Formation des noyaux planétaires; convection et changements de phase à l'intérieur des planètes telluriques

Renaud Deguen

Université Claude Bernard Lyon 1

Laboratoire de Géologie de Lyon – Terre, Planètes, Environnement

Mémoire présenté pour obtenir
L'Habilitation à Diriger des Recherches

Formation des noyaux planétaires ; convection et changements de phase à l'intérieur des planètes telluriques

---

Renaud DEGUEN

Composition du jury :

Gaël CHOBLET	LPG Nantes	Rapporteur
Edouard KAMINSKI	IPGP Paris	Rapporteur
Michael LE BARS	IRPHE Marseille	Rapporteur
James BADRO	IPGP Paris	Examinateur
Cathy QUANTIN-NATAF	LGL-TPE Lyon	Examinateur

Soutenu le 6 décembre 2018.

Table des matières

Chapitre 1

Introduction

Ces dernières années mes activités scientifiques se sont focalisées principalement sur deux axes :

i) Le premier concerne **la formation et la différentiation des planètes telluriques**. Je travaille sur ces questions depuis mon post-doctorat à l'université Johns Hopkins (Baltimore, USA) avec Peter Olson. Mes travaux sur ce sujet se font maintenant dans le cadre d'un projet financé par l'ERC depuis avril 2017. Ce projet vise à mieux comprendre les processus physiques ayant permis la séparation du manteau et du noyau, afin de proposer un cadre quantitatif pour l'interprétation des données géochimiques (entre autres des éléments radioactifs permettant d'estimer la durée de la formation de la Terre) et la prédiction de quantités clefs pour l'évolution et la dynamique globale de la Terre (température et composition du noyau). Bien que le contexte soit géologique et planétologique, les questions posées dans ce projet incluent des problèmes de mécanique des fluides fondamentale (fragmentation liquide-liquide et mélange dans des écoulements turbulents). Mon travail se base principalement sur des expériences de mécanique des fluides en laboratoire et des simulations numériques, mais aussi sur des modèles géochimiques. Mes travaux sur ce sujet ont bénéficié de collaborations récurrentes avec Maylis Landeau (IPGP), Peter Olson, et Frédéric Risso (IMFT). J'encadre depuis septembre 2017 la thèse de Victor Lherm sur les échanges chimiques et thermiques entre métal et silicates lors de la formation de la Terre, et depuis septembre 2018 le post-doctorat de Vincent Clesi (modélisation géochimique).

ii) Mon second axe de recherche concerne la **convection naturelle dans les intérieurs planétaires**, et plus particulièrement dans les couches solides en interaction avec une couche liquide. Une part importante de mes activités dans cette thématique ont portés sur la dynamique du noyau interne, en continuité avec mes travaux de thèse (collaborations avec Thierry Alboussière, Philippe Cardin, Marine Lasbleis, Sébastien Merkel, Ainhoa Lincot, Stéphane Labrosse, Ludovic Huguet), mais j'ai depuis élargi mes activités à l'étude de la convection dans les manteaux planétaires silicatés en contact avec un océan magmatique, un sujet sur lequel je travaille en collaboration avec Stéphane Labrosse et Thierry Alboussière, et qui fait l'objet de la thèse d'Adrien Morison, encadrée par Stéphane Labrosse. Dans plusieurs contextes géophysiques ou planétologiques, une couche solide mais déformable cristallise à partir d'une couche liquide. La graine terrestre, qui cristallise à partir du noyau externe, est un exemple, mais on peut penser aussi au cas d'un manteau silicaté cristallisant à partir d'un océan magmatique, superficiel ou basal, ou à certains des satellites de glace de Jupiter ou Saturne, qui présentent un manteau de glace en contact avec un océan d'eau liquide profond. L'interface séparant les couches cristallines et liquides doit être très proche de l'équilibre thermodynamique, et une déformation de cette interface peut entrainer fusion ou cristallisation. L'interface est alors "semi-permeable", et des conditions limites adaptées doivent être utilisées pour modéliser la convection dans la coquille sphérique. Nous avons développé un jeu de conditions limites “semi-permeables” permettant de prendre en compte de manière simple la fusion ou la cristallisation

induits par des déformations de l'interface [Deguen *et al.*, 2013]. Dans le cas de la graine terrestre, de telles conditions limites permettent l'émergence d'un mode de convection consistant en une translation de la graine, sans déformation interne. Dans les prochaines années, nous comptons : (i) généraliser ces conditions limites pour les adapter à des problèmes de convection thermo-solutale, (ii) étudier de manière systématique l'effet de ces conditions limites sur la morphologie et la vigueur de la convection, (iii) appliquer nos résultats à plusieurs problèmes géophysiques (effet d'un océan magmatique basal sur la convection mantellique et l'évolution thermique de la Terre) et planétologiques (le "degré 1" d'Encélade par exemple).

Lors de l'écriture de ce document, j'ai pris le parti de me focaliser uniquement sur les travaux pour lesquels je pense avoir eu un rôle moteur. J'ai préféré exposer ma compréhension actuelle de ces problèmes plutôt que de faire une présentation exhaustive de mes travaux. Je ne discuterai pas en détails de projets auxquels j'ai participé de manière plus ponctuelle, et notamment des travaux menés par Peter Olson sur l'évolution couplée du manteau et du noyau terrestre [Olson *et al.*, 2013, 2015], la texturation de la graine (thèse d'Ainoha Lincot encadrée par Sébastien Merkel et Philippe Cardin [Lincot *et al.*, 2014, 2016]), ou la convection dans une zone dendritique (thèse de Ludovic Huguet, encadrée par Thierry Alboussière [Huguet *et al.*, 2016]). Une liste de mes publications est disponible dans l'annexe B, et une sélection de mes articles dans l'annexe C.

Chapitre 2

Formation des noyaux planétaires

La Terre s'est formée il y a environ 4.5 Gy par l'accrétion de corps pour la plupart déjà massifs ($\sim 100 - 1000$ km de diamètre), constitués majoritairement de fer et de roches silicatées. Les modèles d'accrétion planétaires suggèrent que la distribution de la masse dans le système solaire au cours de la formation des planètes telluriques est rapidement dominée par des embryons planétaires dont la masse peut varier de celle de la Lune à celle de Mars, et qui sont pour la plupart déjà différenciés. L'évolution de cette population d'embryons planétaires est ensuite beaucoup plus lente (10-100 My), stochastique, et caractérisée par des collisions et impacts géants entre embryons planétaires, le dernier de ces impacts étant vraisemblablement à l'origine de la Lune. Ces évènements catastrophiques, très énergétiques, induisent un chauffage intense des embryons planétaires : la dissipation de l'énergie gravitationnelle libérée lors de l'accrétion et de la différentiation suffit en effet à provoquer une augmentation de la température de la Terre de plusieurs milliers de Kelvin au cours de sa formation, et assurer la fusion répétée d'une fraction significative de la planète.

La structure actuelle de la Terre et des corps telluriques du système solaire est pour une part importante héritée des épisodes de différentiation ayant ponctués le processus d'accrétion :

(i) La formation du noyau a induit un fractionnement chimique entre métal et silicates, qui dépend du mode de ségrégation (diapirisme, fracturation hydraulique, percolation, pluie de fer dans un océan magmatique, ...) et des conditions physico-chimiques auxquelles la ségrégation a eu lieu. En raison du très lent transfert de matière entre noyau et manteau, ceux-ci sont aujourd'hui toujours en déséquilibre thermodynamique, ce qui implique que la composition chimique de la Terre silicatée a gardé une mémoire de la différentiation et peut être utilisée pour contraindre les processus physiques mis en jeu [*e.g.* Wood *et al.*, 2006]. Ce fractionnement chimique a aussi des implications géodynamiques fortes. En particulier, la nature et l'abondance dans le noyau d'éléments radioactifs [Gessmann & Wood, 2002; Corgne *et al.*, 2007; Bouhifd *et al.*, 2007], du magnésium [O'Rourke & Stevenson, 2016; Badro *et al.*, 2016; O'Rourke *et al.*, 2017], ou des éléments légers (O,S,Si,...) dépendent des conditions de pression P, de température T, et d'oxydoréduction (fugacité d'oxygène f_{O_2}) auxquelles métal et silicates ont été équilibrés [Siebert *et al.*, 2012; Badro *et al.*, 2015; Fischer *et al.*, 2015].

(ii) Tout comme les éléments chimiques, la chaleur dégagée lors de l'accrétion a été partitionnée entre le manteau et le noyau, d'une manière qui dépend des mécanismes physiques de séparation des phases. La répartition de cette chaleur a défini la valeur du contraste de température entre le manteau et le noyau à la fin de l'accrétion, un paramètre clé pour la dynamique de la planète, et notamment pour l'existence d'un océan de magma basal [Labrosse *et al.*, 2007], l'existence d'une dynamo précoce [Williams & Nimmo, 2004; Monteux *et al.*, 2011], et de manière plus générale pour l'évolution thermique et magnétique de la planète.

En combien de temps se sont formés les corps telluriques ? Peut-on estimer la partitionnement entre noyau et manteau des éléments chimiques et de la chaleur libérée lors de l'accrétion ? Quel était l'état de la Terre à la fin de l'accrétion ? Les données apportées par la géochimie sont critiques pour répondre à ces questions, mais l'interprétation de ces données en terme de processus physiques est loin d'être triviale. Un effort significatif a été dédié ces dernières

années à la détermination du fractionnement entre métal et silicates de beaucoup d'éléments en fonction des conditions physico-chimiques. En comparaison les modèles physiques utilisés pour interpréter les données géochimiques ont peu évolué. L'exposé qui suit est divisé en trois parties. Je commencerai par discuter des contraintes apportées par la géochimie sur la formation du noyau, avant d'exposer ma compréhension actuelle des mécanismes physiques de ségrégation et d'équilibrage du métal dans un océan de magma. Une dernière partie est dédiée à mes travaux en cours et à mes projets.

2.1 Contraintes géochimiques

L'interprétation des données géochimiques pertinentes pour la différentiation noyau/manteau peut être vue comme un problème inverse pouvant être formalisé comme suit :

$$\begin{cases} \blacktriangleright \text{ Geochronomètres} \\ \text{(Hf-W, U-Pb, ...)} \\ \blacktriangleright \text{ Fractionnement chimique} \\ \text{estimé entre noyau et manteau} \end{cases} \xrightarrow{\text{inversion}} \begin{cases} \blacktriangleright \text{ Durée d'accrétion } \tau_a \text{ et} \\ \text{forme de la courbe d'accrétion } M(t/\tau_a) \\ \blacktriangleright \text{ conditions } P, T, fO_2 \text{ d'équilibrage} \\ \blacktriangleright \text{ degré d'équilibrage} \end{cases}$$

Les données comprennent :

1. des géochronomètres tels que les systèmes Hf-W ou U-Pb, qui permettent d'estimer la durée de l'accrétion [*e.g.* Kleine *et al.*, 2002; Yin *et al.*, 2002; Halliday, 2004; Kleine *et al.*, 2004; Kleine *et al.*, 2009; Rudge *et al.*, 2010] ;

2. le fractionnement chimique estimé entre noyau et manteau. La plupart des éléments sidérophiles sont plus abondants dans la Terre silicatée que ce que suggèreraient leurs coefficients de partage métal/silicates à basse pression et température modérée, ce que Ringwood [1966] a appelé le *problème de l'excès des éléments sidérophiles*. La résolution la plus plausible de ce problème semble être un équilibrage chimique métal-silicates à hautes température et pression, où les coefficients de partage thermodynamique de ces éléments peuvent expliquer le fractionnement noyau/manteau estimé. La comparaison entre le fractionnement noyau/manteau estimé et les coefficients de partage déterminés en laboratoire permet de contraindre les conditions de pression P, température T, et fugacité d'oxygène fO_2 auxquelles métal et silicates ont été équilibrés lors de chaque épisode de différentiation [Murthy, 1991; Li & Agee, 1996; Chabot *et al.*, 2005; Wood *et al.*, 2006; Siebert *et al.*, 2011, 2013].

Les quantités cibles incluent la durée d'accrétion τ_a, la forme de la courbe d'accrétion $M = M(t/\tau_a)$ (où M est la masse de la planète), les conditions de pression, température, et degré d'oxydation auxquelles métal et silicates se sont équilibrés, et le degré d'équilibrage – une mesure de l'efficacité avec laquelle métal et silicates ont pu échanger des éléments chimiques.

Ce problème est un problème inverse *mal posé*, au sens où le nombre de degrés de libertés est (beaucoup) plus grand que le nombre de contraintes. Il n'y a donc pas de solution unique. En pratique, l'inversion est souvent réalisée en faisant des hypothèses permettant de contraindre l'inversion et rendre le problème (artificiellement) bien posé : pression d'équilibrage à une fraction constante de la limite noyau-manteau (CMB), température d'équilibrage fixée au liquidus de la phase silicatée, forme de la courbe d'accrétion imposée [par exemple $M(t) = M_f(1 - \mathrm{e}^{-t/\tau_a})$], efficacité d'équilibrage constante, etc... Cette approche est raisonnable, et certaines hypothèses peuvent être justifiées, mais le nombre important d'hypothèses nécessaires pose la question de la robustesse de l'inversion.

Ce problème de non-unicité des solutions est particulièrement bien illustré par le chronomètre Hf-W. L'excès de tungstène radiogénique dans la Terre silicatée peut être expliqué par deux modèles extrêmes : (i) une durée d'accrétion et de différentiation similaire au temps de

demi-vie de l'isotope ^{182}Hf, permettant la génération de ^{182}W dans le manteau après la fin de la différentiation, ou (ii) une accrétion plus longue mais avec un équilibrage métal/silicates imparfait, permettant de conserver dans le manteau une partie du ^{182}W radiogénique malgré son caractère sidérophile. La réalité est sans doute entre ces deux limites. Sous l'hypothèse d'un équilibrage parfait entre les phases métal et silicates, le système Hf-W prédit une durée d'accrétion de l'ordre d'une dizaine de millions d'années [Kleine *et al.*, 2002; Yin *et al.*, 2002]. La durée d'accrétion déduite du système Hf-W augmente si l'équilibrage est supposé ne pas être parfait [Halliday, 2004; Kleine *et al.*, 2004; Kleine *et al.*, 2009; Rudge *et al.*, 2010] : il y a une tendance inverse marquée entre la durée de l'accrétion estimée et le degré d'équilibrage supposé, jusqu'à une limite où Hf-W ne contraint plus la durée de l'accrétion, mais uniquement le degré d'équilibrage [Rudge *et al.*, 2010]. Le système Hf-W permet donc d'obtenir une borne inférieure pour le degré d'équilibrage k (défini ici comme la fraction de métal équilibrée avec les silicates) ; Rudge *et al.* [2010] obtiennent $k \geq 0.36$.

Mes contributions sur ces questions, détaillées dans les paragraphes ci-dessous, incluent : (i) le développement et la mise en équation d'un modèle géochimique de différentiation permettant un équilibrage partiel de la phase métallique et de la phase silicate, et l'introduction d'une mesure de l'équilibrage (définie par les équations (2.2) et (2.3)) prenant en compte un équilibrage partiel du manteau, (ii) l'utilisation de ce modèle pour proposer une borne inférieure au degré de dispersion moyen du métal dans les silicates au cours de la différentiation, et (iii) le développement d'une méthode d'interprétation du fractionnement chimique noyau/manteau en termes de conditions d'équilibrage permettant d'une part de s'affranchir de l'hypothèse d'une pression d'équilibrage égale à une fraction fixe de la pression à la CMB, et d'autre part de proposer des bornes sur l'évolution des température et pression d'équilibrage au cours de l'accrétion.

Efficacité d'équilibrage et modèle de différentiation hors équilibre

Les premiers modèles géochimiques de différentiation noyau-manteau développés pour prendre en compte un équilibrage imparfait ont été construit en faisant l'hypothèse que seule une fraction k de la phase métallique est équilibrée avec la phase silicatée, la fraction $1-k$ restante atteignant le noyau sans échange chimique avec le manteau [*e.g.* Halliday, 2004; Kleine *et al.*, 2004; Kleine *et al.*, 2009; Nimmo *et al.*, 2010; Rudge *et al.*, 2010]. Ces modèles ont été appliqués au système Hf-W et ont montré l'effet d'un équilibrage partiel de la phase métallique sur la durée estimée de l'accrétion. Cependant, ces modèles supposent que l'intégralité du manteau est équilibré avec chaque volume de métal ajouté au noyau, ce qui est peu probable [Deguen *et al.*, 2011*b*; Morishima *et al.*, 2013]. Afin de quantifier l'effet d'un équilibrage partiel du manteau, j'ai développé un modèle en boîte, décrit sur la figure 2.1. Dans ce modèle, seule une fraction k du métal est équilibré (comme dans les modèles précédents), mais l'équilibrage partiel du manteau est maintenant pris en compte : on introduit pour cela un paramètre Δ défini comme

$$\Delta = \frac{\text{masse de métal équilibré}}{\text{masse de silicates équilibrés}}. \tag{2.1}$$

Δ est une mesure du degré de dilution de la phase métallique dans la phase silicatée.

Une bonne manière de définir une mesure de l'équilibrage d'un élément x est la suivante,

$$\mathscr{E}_x = \frac{\text{masse d'élément } x \text{ échangée entre métal et silicates}}{\text{masse optimale d'élément } x \text{ échangée entre métal et silicates}} \tag{2.2}$$

où la "masse optimale d'élément x échangée" correspond à la masse échangée lorsque l'équilibre thermodynamique est atteint, dans le cas d'une dilution infinie ($\Delta \to \infty$) de la phase métallique [Deguen *et al.*, 2014*a*]. Dans le cadre du modèle en boîte décrit figure 2.1, on peut démontrer que l'efficacité d'équilibrage s'écrit

$$\mathscr{E}_x = \frac{k}{1 + D_x/\Delta}, \tag{2.3}$$

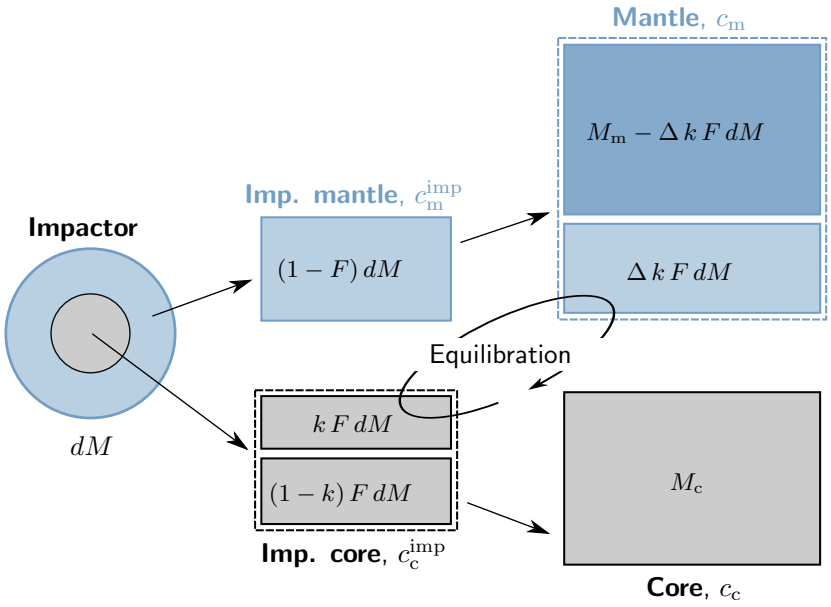

Figure 2.1

Modèle géochimique de différentiation noyau/manteau. Après chaque addition de masse dM apportée par un impacteur, une fraction k de la masse de métal de l'impacteur est équilibré avec une masse de silicates Δ fois plus grande, avant de rejoindre le noyau de la proto-Terre. La fraction restante $1-k$ rejoint le noyau sans échanger d'éléments avec le manteau. On note F la fraction massique de métal dans la proto-Terre et les impacteurs.

où $D_x(P, T, fO_2)$ est le coefficient de partage thermodynamique de l'élément x. On peut voir que $\mathscr{E}_x$ tend vers k lorsque $\Delta/D_x \to \infty$, ce qui fait de cette définition une simple généralisation de la définition classique du degré d'équilibrage. Une différence importante est la présence du coefficient de partage thermodynamique D_x dans l'expression de l'efficacité d'équilibrage, qui dépend donc de l'élément considéré. L'efficacité d'équilibrage d'un élément sidérophile est en général plus faible que celle d'un élément lithophile.

Système Hf-W

L'application du modèle de différentiation présenté ci-dessus au chronomètre Hf-W a permis de généraliser de manière très simple les travaux supposant un équilibrage parfait du manteau. J'ai en effet pu montrer que le système d'équations obtenu en prenant en compte un équilibrage partiel du manteau est identique au sytème d'équations utilisé par Rudge *et al.* [2010] pour étudier le système Hf-W si l'on remplace le paramètre k par $\mathscr{E}_W$ [Deguen *et al.*, 2014*a*]. Une conséquence directe est que la borne inférieure sur k obtenue par Rudge *et al.* [2010] est en fait une borne sur $\mathscr{E}_W$: $\mathscr{E}_W \geq 0.36$. On en déduit que $k \geq 0.36$, comme obtenu par Rudge *et al.* [2010], mais aussi que $\Delta \geq D_W/(k/0.36-1) \geq 0.56\, D_W$. En prenant pour $D_W \simeq 30$ (la valeur estimée pour le rapport de composition entre noyau et manteau, généralement utilisée pour interpréter le chronomètre Hf-W), on obtient $\Delta \geq 17$. Cela suggèrerait que le métal apporté par chaque impact a dû être équilibré "en moyenne" avec une quantité de silicates de plus de 17 fois sa masse [Deguen *et al.*, 2014*a*], ce qui indiquerait une dispersion importante de la phase métallique au cours de la différentiation, une contrainte potentiellement forte sur les mécanismes de séparation des phases.

Interprétation du fractionnement chimique estimé entre noyau et manteau

La mise en équation pour des éléments non-radioactifs du modèle décrit figure 2.1 donne deux équations différentielles du premier ordre à coefficients variables pour l'évolution de la

concentration d'un élément donné (x) dans le manteau et le noyau. Les solutions de ces deux équations peuvent être écrites littéralement en faisant intervenir des intégrales mettant en jeu l'évolution au cours de l'accrétion du coefficient de partage thermodynamique aux conditions d'équilibrage, de l'efficacité d'équilibrage, et du fractionnement noyau/manteau des impacteurs [Deguen, in prep.]. Le coefficient de partage effectif final noyau/manteau, $D^{\text{final}}_{x,\text{c/m}}$, est obtenu en formant le rapport des concentrations dans le noyau et le manteau. On obtient

$$D^{\text{final}}_{x,\text{c/m}} = \frac{1-F}{F}\frac{1-\mathcal{I}_x}{\mathcal{I}_x}, \tag{2.4}$$

où

$$\mathcal{I}_x = \int_0^1 \frac{1+\mathscr{E}_x R^{\text{imp}}_{x,\text{c/m}}}{1+R^{\text{imp}}_{x,\text{c/m}}} \exp\left(-\int_f^1 \frac{\mathscr{E}_x R_x}{f'} df'\right) df, \tag{2.5}$$

F est la fraction massique de phase métallique dans la planète (supposée ici constante au cours de l'accrétion), $R_x = F/(1-F)D_x$, et $R^{\text{imp}}_{x,\text{c/m}} = F/(1-F)D^{\text{imp}}_{x,\text{c/m}}$, où $D^{\text{imp}}_{x,\text{c/m}}$ est le rapport des concentrations dans le noyau et le manteau de l'impacteur [Deguen, in prep.].

La première conclusion qui s'impose est que l'expression obtenue pour $D^{\text{final}}_{\text{c/m}}$ est loin d'être transparente, et son interprétation ardue. Le fractionnement final n'est pas donné par une simple moyenne pondérée des coefficients de partage aux conditions rencontrées lors de chaque ajout de métal au noyau. La raison en est que le transfert d'éléments chimiques entre métal et silicates dépend de la composition chimique du manteau de la planète, qui elle même est fonction des épisodes précédents de différentiation.

À travers l'équation (2.4), l'estimation du fractionnement final entre le noyau et le manteau apporte des contraintes intégrales (une par élément) sur l'évolution au cours de l'accrétion de la valeur du coefficient de partage auquel se fait l'équilibrage, et de l'efficacité d'équilibrage et du fractionnement noyau/manteau des impacteurs. En faisant l'hypothèse que les coefficients de partage ont évolué de manière monotone (croissants ou décroissants) au cours de l'accrétion, j'ai pu obtenir à partir de ces intégrales des bornes inférieure et supérieure sur la valeur de D_x en fonction de la fraction accrétée. En utilisant les expressions de D_x en fonction de P, T, fO_2 obtenues expérimentalement, on peut convertir ces bornes sur D_x en des bornes sur la pression et la température d'équilibrage $P_{eq}(f)$ et $T_{eq}(f)$. Cette approche permet de s'affranchir de l'hypothèse d'une pression d'équilibrage égale à une fraction fixe de la pression à la CMB (fonction de la taille de la proto-Terre). Cette hypothèse a à ma connaissance toujours été faite dans les modèles d'accretion permettant une évolution des conditions d'équilibrage [*e.g.* Rudge *et al.*, 2010; Rubie *et al.*, 2011; Siebert *et al.*, 2012; Rubie *et al.*, 2015; Badro *et al.*, 2015; Fischer *et al.*, 2015].

Je n'ai jusqu'ici considéré que les éléments Ni, Co, V, et Cr, qui sont à ce jour les seuls éléments donc le comportement est bien connu jusqu'à des pressions proches de celle de la CMB actuelle [Siebert *et al.*, 2012; Fischer *et al.*, 2015]. En faisant de plus l'hypothèse que l'équilibrage a lieu à la base d'un océan de magma dont la température est au liquidus du manteau primitif [Andrault *et al.*, 2011], j'ai pu obtenir les bornes représentées sur la figure 2.2, pour plusieurs valeurs de k et Δ. Par souci de simplicité, la fugacité d'oxygène est ici supposée constante (ΔIW$= -2.3$). Sur cette figure, sont représentées en couleur les bornes inférieures et supérieures correspondant aux quatre éléments considérés. Les zones colorées en bleu correspondent aux domaines interdits de l'espace (f, P_{eq}), ou, de manière équivalente, (f, T_{eq}). D'après ces bornes, la pression et la température d'équilibrage ont nécessairement évolué dans la zone blanche située entre les courbes colorées.

Dans le cas d'un équilibrage parfait, la figure 2.2 montre que la pression d'équilibrage a dû être inférieure à environ la moitié de la pression de la CMB jusqu'à ce que la Terre atteigne une masse d'environ 90% de sa masse finale, excepté au début de l'accrétion. En revanche, la pression et la température d'équilibrage ne sont plus bornées par le haut pendant les 10 derniers % de l'accrétion. Les bornes obtenues sont donc naturellement cohérentes avec le scénario

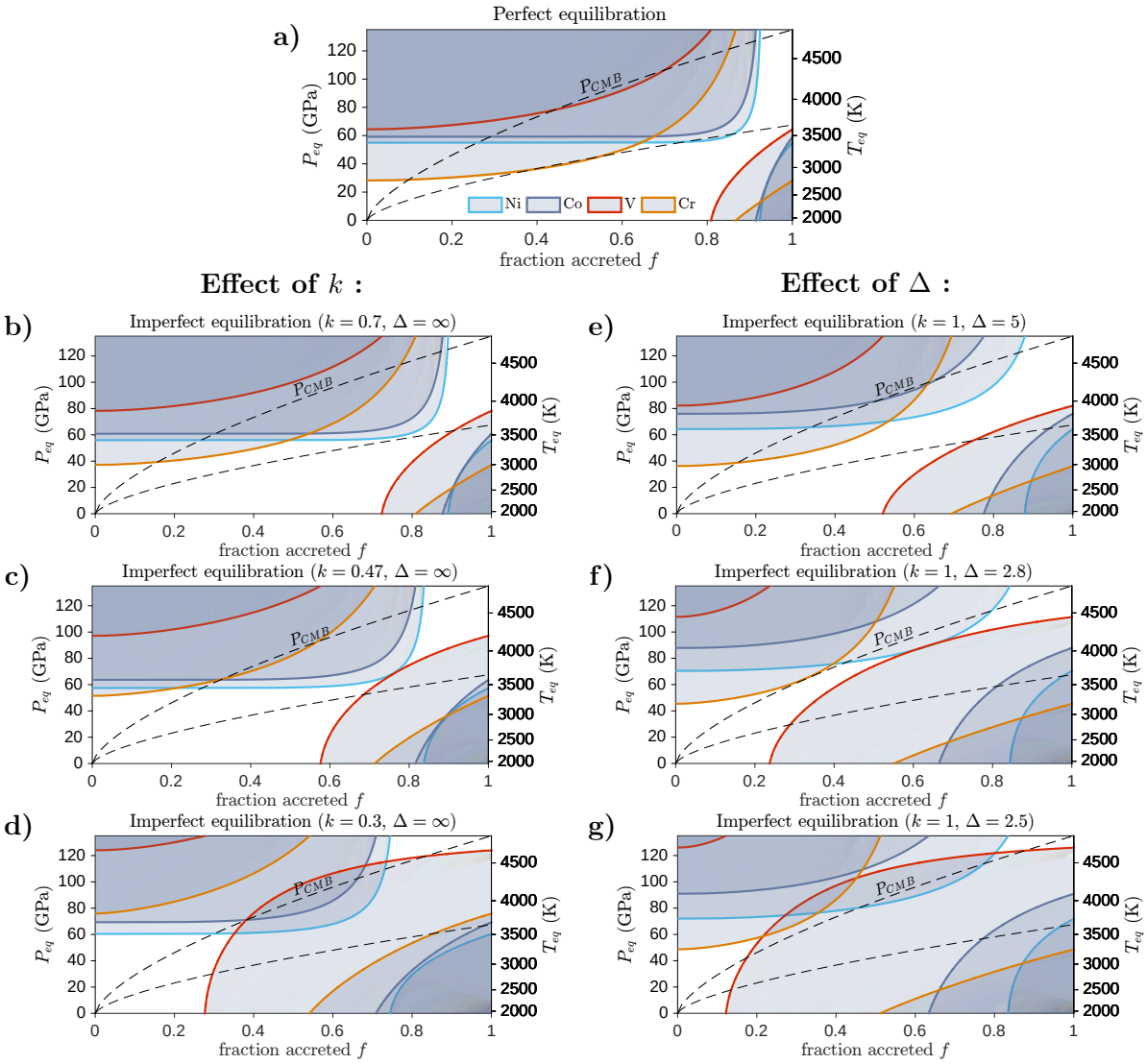

Figure 2.2

Bornes inférieures et supérieures sur le chemin $P_{eq}(f)$ obtenues à partir des éléments Ni, Co, V, et Cr sous l'hypothèse d'un équilibrage parfait (Fig. **a)**) ou imparfait : **b)** $k = 0.7$, $\Delta = \infty$, **c)** $k = 0.47$, $\Delta = \infty$, **c)** $k = 0.3$, $\Delta = \infty$, **e)** $k = 1$, $\Delta = 5$, **f)** $k = 1$, $\Delta = 2.8$, et **g)** $k = 1$, $\Delta = 2.5$. Sont aussi représentés pour référence la pression à la CMB en fonction de f (ligne noire tiretée) et la moitié de la pression à la CMB (ligne tiretée grise).

canonique de formation de la Lune à l'issue de la collision de la proto-Terre avec un corps de la taille de Mars (soit environ 10% de la masse de la Terre) [Canup *et al.*, 2000]. C'est un résultat important, qui ne pouvait émerger des contraintes géochimiques qu'en autorisant une évolution libre de la pression d'équilibrage. On peut noter que les bornes obtenues autorisent (de justesse !) une accrétion où la pression d'équilibrage est une fraction fixe de la pression de la CMB (ici environ 50%).

Un équilibrage imparfait ($k < 1$ ou Δ fini) privilégie généralement des conditions d'équilibrage de plus hautes pression et température. En outre, la fraction accrétée à laquelle la pression et la température d'équilibrage ne sont plus bornées par le haut est plus petite que dans le cas d'un équilibrage parfait. Cela autorise donc une collision finale avec un corps plus massif.

Un point important pour finir : lorsque l'on diminue k ou Δ, la borne inférieure de certains éléments se rapproche de la borne supérieure d'autres éléments. Lorsque ces bornes finissent par se rejoindre, aucun trajet $P_{eq}(f)$ ne peux expliquer les données. Ceci démontre qu'une efficacité d'équilibrage minimale est nécessaire pour pouvoir expliquer le fractionnement noyau/manteau

estimé de ces éléments. On obtient donc des bornes inférieures pour les valeurs de k et Δ : $k > 0.47$ et $\Delta > 2.8$. Ces bornes dépendent cependant assez fortement du modèle de composition supposé, et la prise en compte d'incertitudes plus fortes sur la composition du manteau et du noyau peut diminuer de manière significative la valeur de ces bornes. En revanche, l'utilisation d'éléments supplémentaires, qui devrait être possible dans le futur, permettra d'apporter des contraintes plus fortes sur l'évolution des conditions d'équilibrage au cours de l'accrétion.

2.2 Séparation métal/silicates dans un océan magmatique

Malgré l'inversion simultanée de plusieurs systèmes isotopiques et du fractionnement des éléments sidérophiles, les modèles géochimiques de différentiation restent sous-contraints, et pâtissent d'une compréhension insuffisante des processus physiques mis en jeux. Un des paramètres clef pour l'interprétation de ces données est l'efficacité d'équilibrage chimique métal-silicates – l'efficacité avec laquelle métal et silicates ont pu échanger des éléments chimiques au cours de la formation du noyau. La discussion de la partie 2.1 a montré l'importance du paramètre d'efficacité d'équilibrage $\mathscr{E}_x$ pour l'interprétation des données géochimiques. Plus précisément, l'expression de $\mathscr{E}_x$ (equation (2.3)) montre que l'estimation de $\mathscr{E}_x$ nécessite d'une part une compréhension des mécanismes de transfert chimique (paramètre k du modèle en boîte), et d'autre part d'estimer le rapport Δ des masses de silicates et métal ayant interagi. Ces paramètres, même s'il peuvent être contraints dans une certaine mesure par la géochimie [Halliday, 2004; Nimmo *et al.*, 2010; Rudge *et al.*, 2010; Fischer & Nimmo, 2018], dépendent de processus de mélange gouvernés par la mécanique des fluides.

L'efficacité d'équilibrage dépend de l'aire spécifique de l'interface séparant métal-silicate (aire de l'interface/volume de métal et silicates en jeu), et de l'efficacité du transport diffusif et convectif dans les deux phases. Les modèles de formation des planètes du système solaire indiquent qu'une fraction importante de la masse de la Terre a probablement été apportée sous la forme d'embryons planétaires déjà différenciés, lors d'impacts suffisamment énergétiques pour assurer la fusion d'une fraction significative de la planète. Il est généralement supposé que l'équilibrage métal/silicates nécessite la fragmentation de la phase métallique en gouttes [*e.g.* Stevenson, 1990; Karato & Murthy, 1997; Rubie *et al.*, 2003]. Toute la question est alors de savoir si le métal issu des noyaux des impacteurs (diamètre 10-1000 km) peut se fragmenter lors de sa migration à travers le manteau fondu, jusqu'à des échelles suffisamment petites (< 10 cm ?) pour permettre un ré-équilibrage efficace.

Un des objectifs de mes recherches sur ce sujet est de quantifier les échanges chimiques et thermiques entre métal et silicates au cours de la différentiation, et de proposer des estimations des paramètres d'équilibrage à partir de modélisation dynamique des processus de séparation de phase. L'intérêt est double : (i) d'une part ce type de modèle permettrait d'interpréter en termes de processus physiques les contraintes obtenues par la géochimie sur l'efficacité d'équilibrage ; (ii) et d'autre part il est aussi possible d'utiliser les prédictions des modèles dynamiques pour fixer l'efficacité d'équilibrage dans les modèles géochimiques plutôt que le considérer comme un paramètre libre. Je me suis jusqu'ici concentré sur les processus de ségrégation dans un océan magmatique, qui est la configuration la plus propice à des échanges chimiques et thermiques entre métal et silicates.

2.2.1 Nombres sans-dimension

Considérons dans un premier temps un volume de métal, de forme initialement sphérique, chutant dans un océan magmatique (figure 2.3). On note U sa vitesse de chute et R_0 son rayon, $\rho_{m,s}$ et $\nu_{m,s}$ les masses volumiques et viscosités cinématiques des phases métal (indice "m") et silicate (indice "s"), γ la tension interfaciale entre les deux phases, et g l'accélération

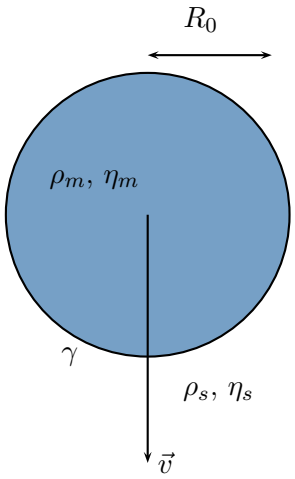

Figure 2.3

Définition de la géométrie d'étude : un volume d'un liquide de masse volumique ρ_m (la phase métallique) et de viscosité dynamique η_m chute à une vitesse verticale U dans un second liquide (l'océan magmatique) de masse volumique $\rho_s < \rho_m$ et de viscosité dynamique η_s. On note γ la tension interfaciale entre les deux liquides.

de la gravité. Ce problème est caractérisé par les nombres sans dimensions suivants :

$$\mathrm{Re} = \frac{UR_0}{\nu_s}, \quad \mathrm{We} = \frac{\rho_s U^2 R_0}{\gamma}, \quad \mathrm{Bo} = \frac{(\rho_m - \rho_s) g R_0^2}{\gamma}, \quad \frac{\rho_m}{\rho_s}, \quad \frac{\nu_m}{\nu_s}, \tag{2.6}$$

où le nombre de Reynolds Re compare l'inertie aux forces visqueuses, le nombre de Weber We compare l'inertie à la tension de surface, et le nombre de Bond Bo compare la flottabilité à la tension de surface. Le problème décrit par la figure 2.3 – un volume d'un fluide chutant dans un autre fluide – est un problème classique de mécanique des fluides, qui peut sembler simple au premier abord. Cependant, le nombre important de nombres sans-dimension indépendants (5) suggère que des dynamiques variées peuvent être possibles en fonction des valeurs de ces nombres sans-dimension. C'est effectivement le cas, et une partie non négligeable de l'espace des paramètres a été explorée, montrant des facettes variées du problème formalisé par la figure 2.3 : chute et fragmentation d'une goutte de pluie [Villermaux & Bossa, 2009], remontée de "grandes" bulles d'air [Davies & Taylor, 1950], diapirs métalliques migrant à travers un manteau cristallisé [Samuel & Tackley, 2008; Monteux *et al.*, 2009; Samuel *et al.*, 2010], etc... La gamme de paramètres pertinents pour la chute d'un volume de métal dans un océan magmatique n'a cependant été approché que récemment [Deguen *et al.*, 2014*a*; Landeau *et al.*, 2014; Wacheul *et al.*, 2014; Wacheul & Le Bars, 2017]. La difficulté de ce problème vient des conditions dynamiques extrêmes des processus d'accrétion et de différentiation. Un volume de fer de rayon 10 km chutant à une vitesse de 100 m/s (des valeurs modestes pour un impact planétaire) a un nombre de Reynolds de l'ordre de 10^{11}, un nombre de Weber de l'ordre de 10^{12} et un nombre de Bond de l'ordre de 10^{12}. Re, We et Bo sont tous trois très grands : il s'agit donc d'un processus probablement extrêmement turbulent, pour lequel la tension interfaciale et la viscosité ont un effet négligeable sur une grande gamme d'échelles spatiales. Ceci suggère que la dispersion de la phase métallique pourrait être prédite par des modèles ignorant la tension interfaciale. En revanche, la tension interfaciale jouera un rôle important pour la structure de l'écoulement à petites échelles, qui est déterminante pour le transfert d'éléments chimiques entre métal et silicates.

Des conditions de similitude parfaite avec un impact planétaire sont impossibles à atteindre, que ce soit par le biais de simulations numériques ou d'expériences en laboratoire, mais des expériences dans des conditions de grands nombres de Weber, Bond et Reynolds peuvent permettre de comprendre la physique en jeu et de développer des modèles de fragmentation et de transfert chimique applicables au cas d'impacts planétaires. Ces conditions sont difficiles à

atteindre dans des simulations numériques, car nécessitant une résolution spatiale et temporelle très fine, et les simulations numériques réalisées à ce jour se sont limitées à des nombres de Reynolds, Weber et Bond modérés pour lesquels l'écoulement reste laminaire [Ichikawa *et al.*, 2010; Samuel, 2012]. Nous avons pu en revanche réaliser une série d'expériences, utilisant des solutions aqueuses pour modéliser la phase métallique et une huile de silicone de faible viscosité pour modéliser l'océan magmatique, qui ont permis d'atteindre des conditions que l'on pense pertinentes pour le problème de la différentiation manteau/noyau [Deguen *et al.*, 2014*a*; Landeau *et al.*, 2014, 2016; Deguen & Risso, in prep.]. Le choix de ces liquides permet d'atteindre des nombres de Reynolds, Weber et Bond grand devant 1 (de l'ordre de 10^4, soit 2 à 3 ordres de grandeur plus grand que dans les simulations numériques publiées à ce jour), tout en ayant un rapport de densité similaire au couple fer/silicates.

2.2.2 Dispersion – entrainement turbulent

Au vu des valeurs extrêmement grandes de Bo et We, il est pertinent d'ignorer dans un premier temps tout effet de la tension interfaciale, et de s'intéresser au cas de liquides immiscibles, qui peut être vu comme la limite $Bo, We \to \infty$. Ce type d'écoulement constitue ce qu'on appelle communément en mécanique des fluides un *thermique turbulent* (même si la théorie peut s'appliquer aussi bien à une flottabilité d'origine compositionnelle que d'origine thermique [1]).

La figure 2.4a illustre l'évolution d'un tel thermique : un volume d'une solution aqueuse de NaI colorée ($\rho = 1502$ kg.m^{-3}) est lâché dans un grand volume d'eau. Les cinq clichés successifs de la figure 2.4a montrent que la zone colorée grandit au cours de sa chute, ce qui indique un mélange entre la solution colorée et l'eau environnante. En mesurant le rayon moyen de la zone colorée, on observe que celui-ci augmente linéairement avec la distance verticale parcourue [Batchelor, 1954; Morton *et al.*, 1956].

Un modèle prédisant l'évolution de la dimension du thermique et de sa vitesse peut classiquement être obtenu soit par analyse dimensionnelle [Batchelor, 1954], soit à partir des lois de conservation de la masse et de la quantité mouvement en faisant l'hypothèse dite d'*entrainement turbulent*, qui suppose que le flux de liquide ambiant entrainé dans le thermique est proportionnel à la vitesse verticale moyenne du thermique. Le coefficient de proportionnalité est le coefficient d'entrainement usuellement noté α [Morton *et al.*, 1956]. Ce type de modèle permet de prédire une croissance linéaire du rayon moyen du thermique,

$$R = R_0 + \alpha(z - z_0), \tag{2.7}$$

où z_0 est l'*origine virtuelle* (qui peut être différente de la position initiale du thermique), et une vitesse verticale de la forme

$$v_z = \frac{B^{1/2}}{R_0} f\left(\frac{z - z_0}{R_0}, \alpha\right) \tag{2.8}$$

$$\to \left(\frac{B}{2\alpha^3}\right)^{1/2} z^{-1} \quad \text{lorsque } R \gg R_0 \tag{2.9}$$

où

$$B = \frac{\rho_m - \rho_s}{\rho_s} g R_0^3 \tag{2.10}$$

est la flottabilité totale de la phase métallique. L'expression de la fonction f peut par exemple être trouvée dans Deguen *et al.* [2014*a*] ou Landeau *et al.* [2014] pour une différence de densité $\rho_m - \rho_s$ qui n'est pas nécessairement petite devant ρ_s.

1. Le terme *thermique*, ou *thermal* en anglais fait référence aux *thermiques atmosphériques* bien connus des amateurs de vol à voile ou parapente. On peut d'ailleurs noter à ce sujet les travaux de Betsy Woodward, amatrice de vol à voile, qui a réalisé à bord de son planeur des observations sur la structure du champ de vitesse à l'intérieur de thermiques atmosphériques [Woodward, 1958] et les a ensuite comparé à des expériences en laboratoire qu'elle a réalisé à Imperial College [Woodward, 1959].

a) Thermique turbulent miscible

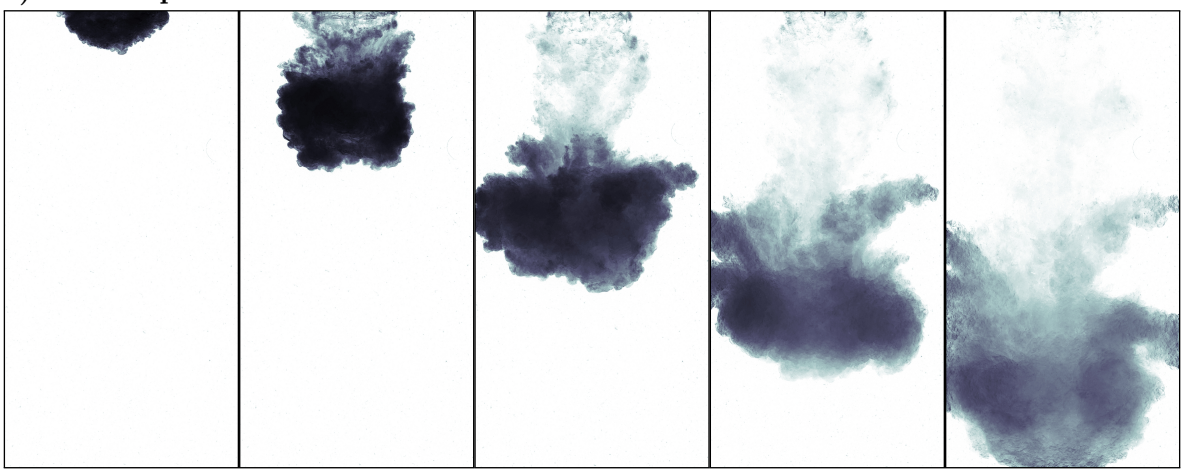

b) Thermique turbulent immiscible

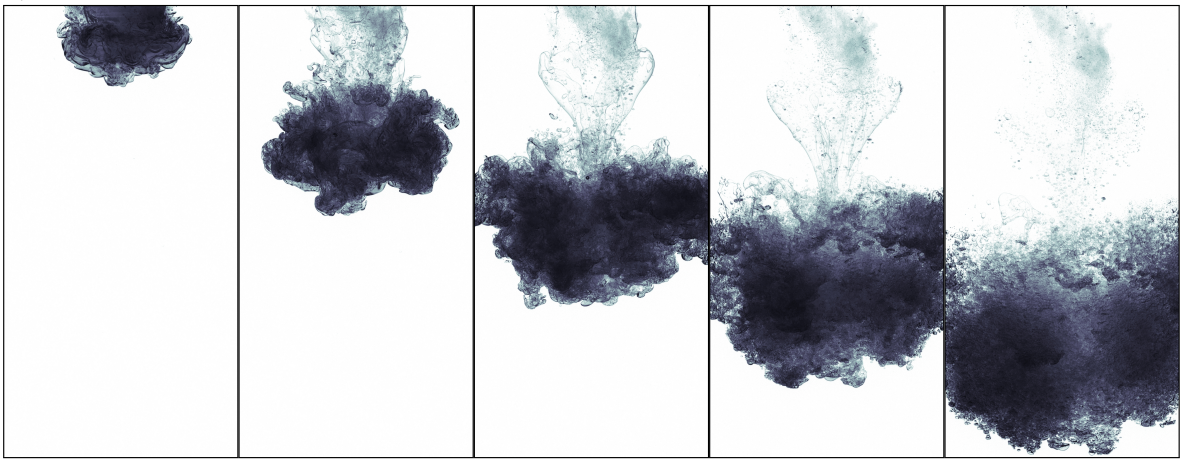

Figure 2.4

Thermiques turbulents *miscible* (**a**) et *immiscible* (**b**). L'échelle spatiale des deux séries de photos est la même, la largeur de chaque image étant de 19 cm. **a)** Évolution d'un volume de 169 mL d'une solution aqueuse de NaI ($\rho = 1502$ kg.m^{-3}) chutant dans de l'eau, à Re $= 4 \times 10^4$, $\rho_m/\rho_s = 1.5$, $\eta_m/\eta_s = 1$. L'intervalle de temps entre chaque image est de 0.3 s. **b)** Évolution d'un volume de 169 mL d'une solution aqueuse de NaI ($\rho = 1601$ kg.m^{-3}) chutant dans de l'huile de silcone ($\rho = 821$ kg.m^{-3}, $\eta = 8.2 \times 10^{-4}$ Pa.s), à $Bo = 3.4 \times 10^4$, Re $= 5.5 \times 10^4$, $\rho_m/\rho_s = 1.95$, $\eta_m/\eta_s = 1.2$. L'intervalle de temps entre chaque image est de 0.2 s.

Dans l'article Deguen *et al.* [2011*b*], nous avons fait l'hypothèse que le modèle d'entrainement turbulent pouvait être appliqué au cas d'un volume de fer chutant dans un océan magmatique, malgré l'immiscibilité des deux phases. Nous avons ensuite pu tester cette hypothèse dans deux articles [Deguen *et al.*, 2014*a*; Landeau *et al.*, 2014] où nous avons démontré expérimentalement la validité des lois (2.7) et (2.8) dans le cas de liquides immiscibles lorsque le nombre de Weber est suffisamment grand. La figure 2.4b montre une série de clichés d'une telle expérience, où un volume de 169 mL d'une solution aqueuse de NaI ($\rho = 1601$ kg.m^{-3}) est lâché dans une cuve remplie d'huile de silicone de faible viscosité (1cst). On peut noter la similitude qualitative entre ce *thermique turbulent immiscible* et le thermique miscible de la figure 2.4a. L'analogie tient aussi de manière quantitative : les lois prédisant l'évolution du rayon moyen et de la vitesse (équations (2.7) et (2.8)) sont vérifiées expérimentalement pour des valeurs du coefficient d'entrainement ($\alpha = 0.25 \pm 0.5$) similaires aux valeurs typiquement obtenues avec des fluides miscibles. Le mécanisme d'entrainement ne semble donc pas être affecté par la tension de surface lorsque $We \gg 1$. Ce régime d'entrainement turbulent a aussi été observé par Wacheul *et al.* [2014] et Wacheul & Le Bars [2017] dans des expériences utilisant du gallium et des solutions de glycerol de différentes viscosités.

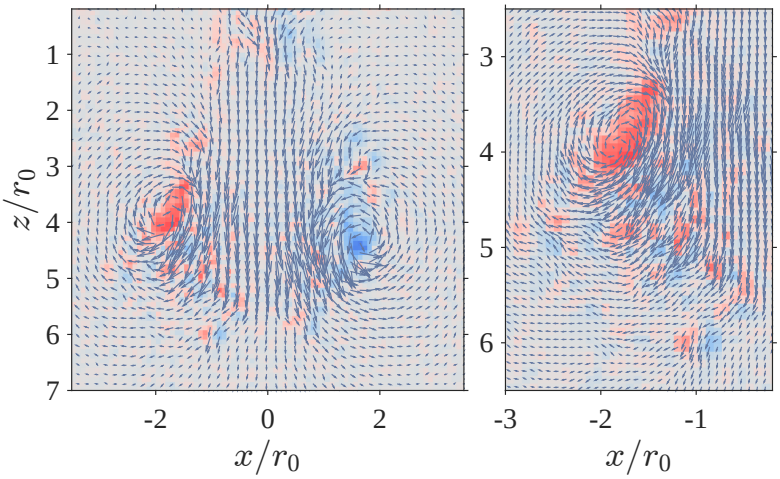

Figure 2.5

Champs de vitesse (flèches) et de vorticité (échelle de couleur) obtenus par vélocimétrie PIV durant une expérience semblable à la figure 2.4b, où 169 mL d'une solution aqueuse de NaI à $\rho = 1280$ kg.m^{-3} chute dans une huile de silicone à 1cst, Bo $= 2 \times 10^4$, Re $= 4.2 \times 10^4$, $\rho_m/\rho_s = 1.56$, $\eta_m/\eta_s = 1.2$. La concentration de NaI a été choisie pour que son indice optique soit le même que celui de l'huile de silicone, pour éviter toute déformation optique des images utilisées pour déterminer le champ de vitesse. La figure de droite montre un agrandissement de la figure de gauche, avec le champ de vitesse représenté sur une grille spatiale plus dense. Les distances sont normalisées par le rayon initial $r_0 = 3.4$ cm de la solution de NaI.

Il est important de bien noter que l'évolution du rayon moyen de la zone occupée par le liquide dense ne reflète pas une simple dispersion de la phase dense, mais bien un entrainement du liquide ambiant, qui se déplace ensuite avec le liquide dense. En d'autres termes, il n'y a dans ce régime pas (ou peu) de vitesse différentielle entre le liquide dense et le liquide ambiant entrainé. Ce point est vérifié de manière indirecte par le fait que la vitesse expérimentalement déterminée vérifie bien l'équation (2.8), qui fait l'hypothèse que le liquide entrainé a la même vitesse verticale moyenne que le liquide dense. Nous avons pu aussi le vérifier expérimentalement de manière plus directe via : (i) la détermination du champ de vitesse [Deguen, in prep.] qui montre que l'écoulement prend la forme de celui d'un anneau de vorticité (figure 2.5), sans différence apparente de vitesse entre les deux phases, et (ii) qualitativement par ombroscopie : les deux liquides sont initialement portés à des températures différentes, et on visualise les variations spatiales d'indice optique (dues aux variations spatiales de température) en éclairant la cuve avec une source de lumière parallèle. Dans ces expériences, on observe que les fluctuations spatiales d'indice optique sont localisées pour l'essentiel à l'intérieur du thermique, ce qui montre que seul le liquide entrainé échange de la chaleur avec le liquide dense, et que ce liquide chute bien à la même vitesse que le liquide dense.

Le point discuté dans le paragraphe précédent est important pour l'application aux modèles géochimiques, car il permet d'estimer le paramètre Δ introduit dans la partie 2.1 (le rapport entre masse de silicates équilibré et métal équilibré, equation (2.1)). Si l'on suppose en effet que la masse de silicates équilibrée est égale à la masse entrainée, le paramètre Δ peut être obtenu directement à partir de l'équation (2.7) donnant l'évolution du rayon de la zone de mélange :

$$\Delta = \frac{\rho_s}{\rho_m} \left[\left(1 + \alpha \frac{z - z_0}{R_0} \right)^3 - 1 \right]. \tag{2.11}$$

Cette paramétrisation a depuis été utilisée dans plusieurs modèles géochimiques de différentiation [Rubie *et al.*, 2015, 2016; Badro *et al.*, 2016; Jacobson *et al.*, 2017; Suer *et al.*, 2017; Siebert *et al.*, 2018; Mahan *et al.*, 2018*a*,*b*].

Cette paramétrisation est valable jusqu'à ce que la phase métallique se sépare des silicates entrainés, ce qui est possible une fois la phase métallique fragmentée si la vitesse de sédimen-

a) Fragmentation par instabilité capillaire

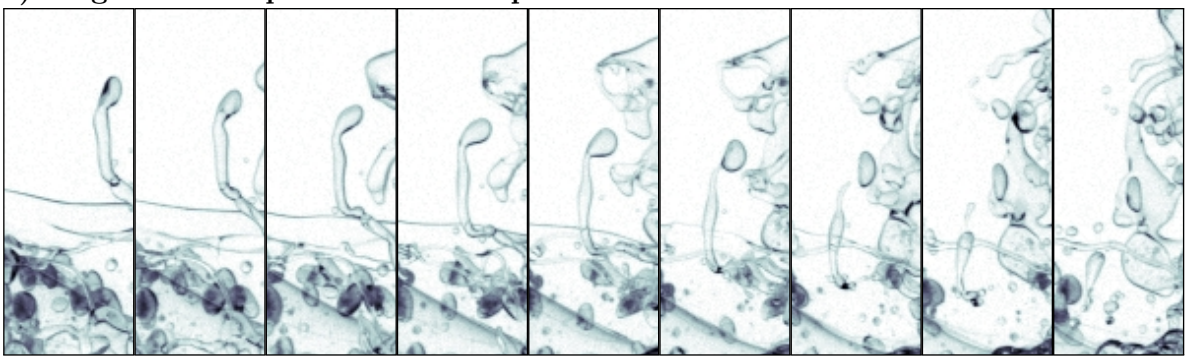

b) Fragmentation de nappe

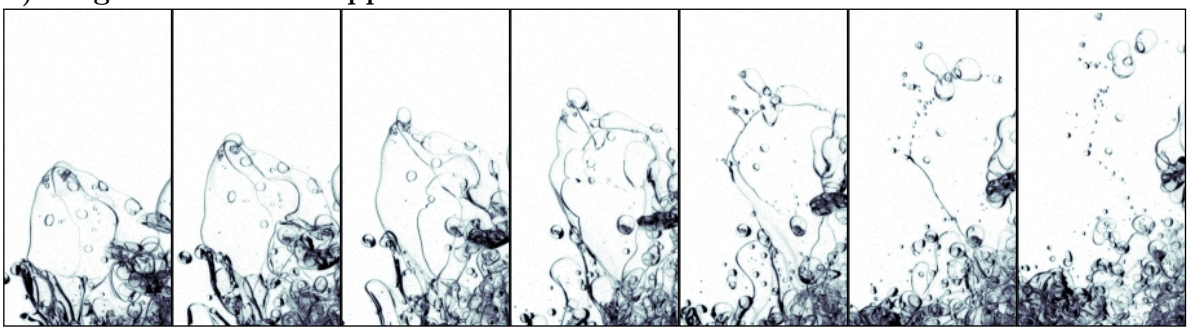

Figure 2.6

Deux mécanismes de fragmentation extraits de photographies de l'expérience montrée dans la figure 2.4b [Deguen & Risso, in prep.]. **a)** Séquence d'images (pas de temps $\Delta t = 10$ ms) montrant la fragmentation d'un ligament par instabilité capillaire. La largeur de chaque image est de 1 cm. **b)** Séquence d'images (pas de temps $\Delta t = 20$ ms) montrant la fragmentation d'une nappe. La largeur de chaque image est de 1.8 cm.

tation des fragments est inférieure à la vitesse du thermique. La vitesse du thermique finit toujours par diminuer (equation (2.9)) en raison de l'incorporation du fluide entrainé, dont la quantité de mouvement est initialement nulle, et cette condition peut donc finir par être vérifiée si la profondeur de l'océan magmatique est suffisamment grande. Lorsque la vitesse d'ensemble devient inférieure à la vitesse de sédimentation des fragments, l'écoulement ne peut plus porter ces fragments, qui perdent alors leur mouvement collectif et se séparent du thermique [Noh & Fernando, 1993; Buehler & Papantoniou, 2001; Bush *et al.*, 2003; Deguen *et al.*, 2011*b*]. D'après l'équation (2.9), cela a lieu à une profondeur $z_{\text{sep}} \sim B^{1/2}/v_{\text{sed}}$, où v_{sed} est la vitesse de sédimentation des fragments. Nous n'avons pas à ce jour de prédiction théorique de la profondeur à laquelle cette séparation de phases peut avoir lieu (il nous manque pour cela un modèle robuste de fragmentation), mais dans le contexte de la différentiation noyau/manteau il semble assez peu probable que ce phénomène ait été important. Pour une taille de fragments de l'ordre du centimètre (vitesse terminale de sédimentation de l'ordre de ~ 0.3 m/s) et un rayon initial $R_0 \gtrsim 10$ km, on trouve $z_{\text{sep}} \gtrsim 60\,000$ km, soit une distance très supérieure à l'épaisseur du manteau.

2.2.3 Fragmentation, brassage, et mélange

Fragmentation

L'observation des expériences décrites dans la partie 2.2.2 montre que la fragmentation du liquide dense en gouttelettes se produit pour l'essentiel lors d'un évènement global et localisé dans le temps. Dans la figure 2.4b, la phase dense est essentiellement continue jusqu'au troisième cliché, et presque entièrement fragmentée en gouttelettes au quatrième cliché. La formation de gouttes ne résulte donc pas d'une cascade de fragmentation telle qu'envisagée

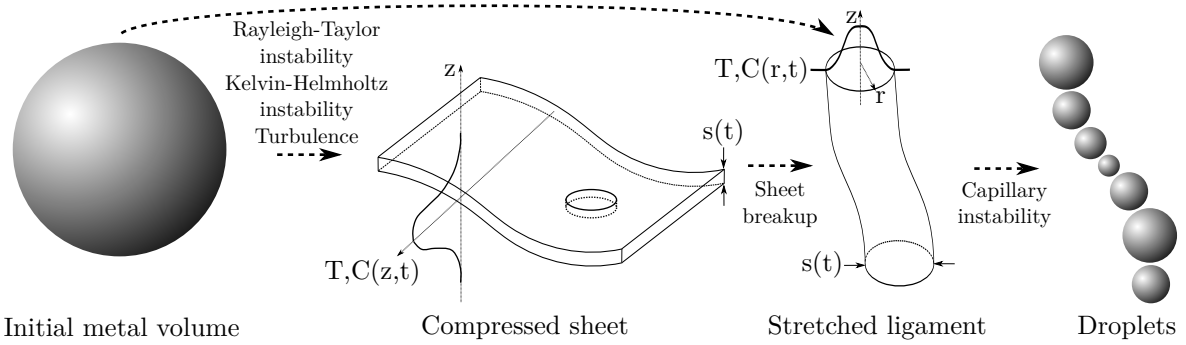

Figure 2.7

Modèle conceptuel d'évolution d'une masse de métal liquide chutant dans un océan magmatique [Lherm & Deguen, submitted].

par Rubie *et al.* [2003] et Samuel [2012], où une suite d'épisodes de fragmentation induirait une diminution progressive de la taille des fragments, jusqu'à une taille d'équilibre où la tension de surface ou la viscosité empêcherait toute fragmentation supplémentaire. Nous n'avons pas observé de fragmentation secondaire ou de coalescence entre gouttes, ce qui implique que la distribution de taille des fragments est fixée par cet évènement de fragmentation.

L'analyse d'images obtenues grâce à une caméra rapide (1000 images/s) montre que la formation de gouttelettes résulte de deux mécanismes [Deguen & Risso, in prep.] :

1. la fragmentation de structures cylindriques – que l'on appellera *ligaments* par la suite – via l'instabilité capillaire de Rayleigh-Plateau, comme illustré par la séquence de clichés de la figure 2.6a.

2. la fragmentation de films de liquide dense, tel qu'illustré par les clichés de la figure 2.6b. Ce régime de fragmentation passe par la formation et l'étirement d'un film de liquide dense qui, une fois percé, se rétracte très rapidement pour former des ligaments se fragmentant ensuite par instabilité capillaire.

Ces deux modes de fragmentation sont classiquement observés dans des problèmes de fragmentation liquide, dans des contextes très variés. En fait, il semblerait que la fragmentation liquide passe nécessairement par une instabilité capillaire [Villermaux, 2007], quelque soit la nature de l'écoulement. Ce qui varie d'un problème à l'autre est la séquence de mécanismes aboutissant à la formation de ligaments susceptibles de fragmenter par instabilité capillaire. Dans nos expériences, la séquence observées est la suivante (figure 2.7) : (i) l'interface est déstabilisée et déformée par l'effet combiné du cisaillement et du contraste de densité entre les phases (instabilité mixte Rayleigh-Taylor / Kelvin-Helmoltz) ; (ii) les structures tridimensionnelles générées par la déstabilisation de l'interface sont étirées et brassées par l'écoulement moyen et les fluctuations du champ de vitesse (figure 2.5) ; (iii) ce brassage produit ligaments et nappes, qui se fragmenteront ensuite pour produire une population de gouttes.

Dans ce scénario, l'instabilité capillaire se développe sur des ligaments étirés par l'écoulement. C'est un point important car l'étirement est connu pour retarder significativement la fragmentation [Taylor, 1934; Tomotika, 1936; Mikami *et al.*, 1975; Eggers & Villermaux, 2008]. La raison principale est la suivante. Supposons un ligament étiré, de rayon moyen $r_0(t)$, dont la surface est modulée par une perturbation longitudinale de longueur d'onde λ (ou de nombre d'onde $k = 2\pi/\lambda$). L'étirement du ligament affectera aussi la perturbation, qui verra sa longueur d'onde augmenter en proportion de l'étirement. Si l'on suppose que la longueur d'onde initiale correspond à la longueur d'onde optimale pour la croissance de l'instabilité capillaire, l'augmentation de la longueur d'onde aura pour conséquence de diminuer le taux de croissance de la perturbation. La croissance de l'instabilité jusqu'à fragmentation nécessite donc que le taux d'étirement soit suffisamment faible pour laisser le temps à une perturbation d'une longueur d'onde initiale donnée de grandir avant que sa longueur d'onde n'ait significativement augmenté. En pratique, cela nécessite que le taux de croissance σ de l'instabilité

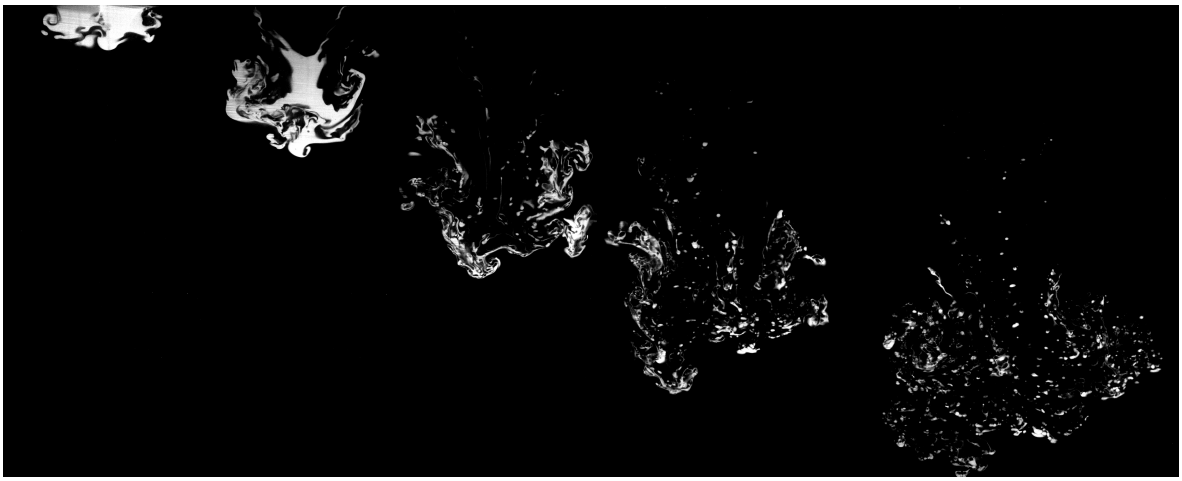

Figure 2.8

Expérience de fragmentation d'un thermique immiscible visualisée grâce à une technique de fluorescence induite (PLIF) : un colorant fluorescent (Rhodamine B) est ajouté à la solution de NaI, et est excité par un plan laser vertical. L'expérience a été réalisée dans des conditions identiques à l'expérience de la figure 2.5 : 169 mL d'une solution aqueuse de NaI à $\rho = 1280$ kg.m^{-3} chutant dans une huile de silicone à 1cst, Bo $= 2 \times 10^4$, Re $= 4.2 \times 10^4$, $\rho_m/\rho_s = 1.56$, $\eta_m/\eta_s = 1.2$. Le pas de temps séparant chaque image est égal à 0.2 s.

Rayleigh-Plateau, qui est donné par

$$\sigma = \left(\frac{\gamma}{2\rho r_0^3}\right)^{1/2} \left[(kr_0)^2 - (kr_0)^4\right]^{1/2} \tag{2.12}$$

si $\lambda > 2\pi r_0$ [*e.g.* Eggers & Villermaux, 2008], soit supérieur au taux d'étirement $\dot{\epsilon}$:

$$\left(\frac{\gamma}{2\rho r_0^3}\right)^{1/2} \left[(kr_0)^2 - (kr_0)^4\right]^{1/2} > \dot{\epsilon}.$$

La prédiction de la distance de fragmentation nécessite donc le développement d'un modèle pour l'évolution du taux de déformation $\dot{\epsilon}$ et pour la formation des ligaments et l'évolution de leur rayon. Le taux de déformation $\dot{\epsilon}$ dépend à la fois de l'écoulement moyen, qui est bien compris (partie 2.2.2), et des fluctuations du champs de vitesse, qui restent à quantifier et modéliser. Une analyse dimensionnelle suggère une loi de la forme $\dot{\epsilon} \sim \frac{v_z}{R} We(z)^{3/5}$ (R et v_z étant donnés par les équations (2.7) et (2.8)). Cette loi d'échelle s'avère être en raisonnablement bon accord avec nos résultats expérimentaux, mais la gamme de valeurs testées (Bo et We) est encore insuffisante pour la valider.

Brassage et mélange

Commençons par un point de vocabulaire. Pour les spécialistes de la mécanique des fluides du mélange, le *mélange* (*mixing* en anglais) comprend l'ensemble des étapes menant à l'homogénéisation *à l'échelle moléculaire* d'un champ, généralement scalaire, tel que la température ou la concentration. L'état final mélangé correspond à un état de température ou composition uniforme. Le mélange est un processus irréversible, impliquant nécessairement un effet de la diffusion pour atteindre un état final mélangé où la température et la composition sont uniformes à l'échelle moléculaire. L'agitation et la déformation du champ scalaire constitue ce qu'on appellera *brassage* (*stirring*). Le brassage, contrairement au mélange, est un processus réversible : même s'il peut mener à une homogénéisation apparente du système, chaque particule fluide garde ses température et composition initiales, et il est possible mécaniquement de revenir à l'état initial.

Dans le cadre de cette définition, il peut sembler incongru de parler de mélange dans un écoulement diphasique, mais l'utilisation de ce terme est cependant pertinente si l'on s'intéresse à l'évolution d'un champ scalaire (température ou concentration) défini dans les deux phases. L'état final mélangé correspond dans ce cas à l'état d'équilibre thermodynamique du système, c'est à dire à une température et un potentiel chimique uniformes. On parlera donc de brassage pour l'évolution de l'interface métal/silicates, et bien de mélange pour l'évolution de la température ou de la composition (homogénéisation de la température et du potentiel chimique).

Nous avons vu dans la sous-partie précédente que la fragmentation de la phase métallique nécessite la formation de nappes et de ligaments. Cela implique donc une évolution de la topologie de la phase métallique permettant de passer d'une géométrie compacte (un noyau d'impacteur proche d'une sphère, ou le volume de solution aqueuse libéré dans nos expériences) à un ensemble de ligaments et de nappes de métal pouvant se fragmenter. Nos expériences suggèrent que cette évolution de la topologie résulte de l'interaction entre des instabilités de l'interface (Rayleigh-Taylor / Kelvin-Helmoltz), l'écoulement moyen, et les fluctuations du champ de vitesse. Aux temps intermédiaires entre l'initiation de la déformation et la fragmentation, la phase métallique se trouve sous la forme de nappes et de ligaments étirés par le champ de vitesse ambiant. Des expériences où une technique de visualisation par fluorescence induite a été utilisée montrent clairement que la phase dense est vigoureusement étirée avant qu'elle ne se fragmente (figure 2.8). L'équilibrage chimique et thermique entre métal et silicates pourrait débuter lors de cette phase : l'étirement de la phase métallique pourrait permettre un transfert chimique/thermique efficace en augmentant l'aire spécifique de l'interface métal/silicates et en maintenant des gradients forts au niveau des interfaces, *via* le mécanisme de *stretching enhanced diffusion* bien connu dans le domaine du mélange [Ranz, 1979; Ottino *et al.*, 1979; Olson *et al.*, 1984; Gurnis, 1986; Kellogg & Turcotte, 1987; Ottino, 1989; Villermaux, 2004; Coltice & Schmalzl, 2006; Ricard, 2007].

Le mécanisme de *stretching enhanced diffusion* est le suivant : Supposons une tache de colorant, initialement localisée, dans un fluide en mouvement. A moins que l'écoulement ne soit uniforme, la tache de colorant sera déformée en fonction des propriétés locales du tenseur des déformations, et en particulier des directions principales de déformation. En 2D, la tache sera étirée dans l'une des directions principale de déformation, et compressée dans l'autre. En 3D, la tache sera soit étirée dans l'une des directions principale de déformation et compressée dans les deux autres (ce qui mènera à la formation d'un filament de forme $\sim$ cylindrique), soit compressée dans l'une des directions principales et étirée dans les deux autres (ce qui mènera à la formation d'une nappe). Ce changement de topologie peut accélérer de manière drastique l'homogénéisation du colorant, et ce pour deux raisons : (i) d'une part l'étirement augmente l'aire de la surface d'échange entourant la tache de colorant, et (ii) la compression, qui est essentiellement parallèle au gradient de concentration, maintient un gradient de concentration fort, ce qui permet un transport diffusif efficace. L'effet de l'étirement sur le temps caractéristique d'homogénéisation du colorant est important si le temps caractéristique d'étirement (l'inverse du taux d'étirement) est petit devant le temps caractéristique de diffusion basé sur la taille initiale de la tache de colorant. Dans cette limite, le temps d'homogénéisation dépend peu de la diffusivité du colorant, et est fixé par le temps caractéristique d'étirement [*e.g.* Ranz, 1979; Kellogg & Turcotte, 1987; Villermaux, 2004].

Au cours de son stage de M2 et de sa première année de thèse, Victor Lherm a généralisé le formalisme de ce mécanisme au cas de l'homogénéisation d'un scalaire dans un écoulement biphasique, dans le but d'appliquer ensuite ce formalisme au transfert de masse et de chaleur entre métal et silicates [Lherm & Deguen, submitted]. On considère donc un champ scalaire distribué dans deux phases immiscibles. Ce champ scalaire peut varier de manière continue (température) ou discontinue (composition) au niveau de l'interface séparant les deux phases (lorsque l'on ignore les phénomènes de dissipation visqueuse et de compressibilité, une équivalence mathématique stricte existe entre le problème thermique et le problème chimique [Lherm

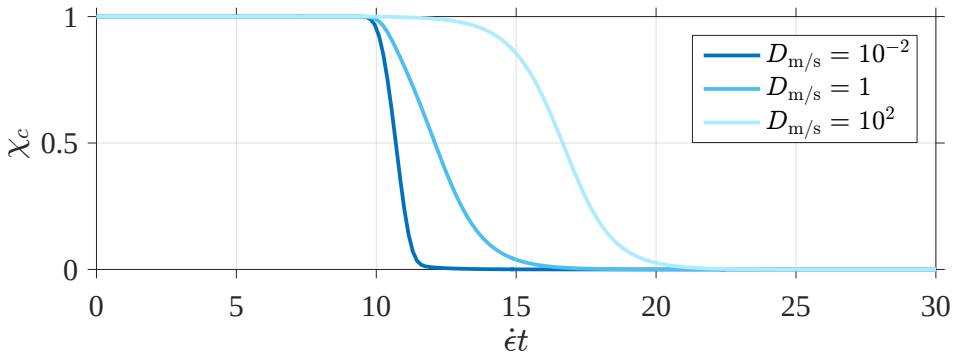

Figure 2.9

Évolution en fonction du temps normalisé $\dot{\epsilon}t$ de la concentration (normalisée) au centre d'une nappe étirée, à $\mathrm{Pe_m} = 10^{10}$ et $\mathrm{Pe_s} = 10^9$, et un coefficient de partage $D_{\mathrm{m/s}}$ égal à 10^{-2}, 1, ou 10^2.

& Deguen, submitted]). Victor a considéré les deux géométries pertinentes pour le mécanisme de *stretching enhanced diffusion* : (i) le cas d'une nappe de métal compressée perpendiculairement à sa surface, et (ii) le cas d'un cylindre de métal étiré parallèlement à son axe de symétrie. On note $\dot{\epsilon}$ la déformation principale, qui peut être au choix un taux d'élongation (dans le cas du cylindre, déformation principale parallèle à l'axe du cylindre), ou un taux de compression (dans le cas de la nappe, déformation principale perpendiculaire à la surface de la nappe). Le problème est caractérisé par deux nombres de Péclet définis à partir du taux d'étirement ou de compression $\dot{\epsilon}$, de l'épaisseur initiale e_0 de la nappe, et des diffusivités chimique $\kappa_{\mathrm{m}}^{\chi}$ (dans la phase métal) et $\kappa_{\mathrm{s}}^{\chi}$ (dans la phase silicate) :

$$\mathrm{Pe_m} = \frac{e_0^2 \dot{\epsilon}}{\kappa_{\mathrm{m}}^{\chi}}, \quad \mathrm{Pe_s} = \frac{e_0^2 \dot{\epsilon}}{\kappa_{\mathrm{s}}^{\chi}}. \tag{2.13}$$

Ces nombres mesurent l'importance relative de l'advection et de la diffusion de l'élément chimique considéré.

Victor Lherm a pu obtenir des solutions analytiques pour l'évolution du champ scalaire au cours du temps dans un cylindre étiré et une nappe compressée, dans le cas général où les propriétés des deux phases (diffusivités thermique ou chimique, capacité calorifique) sont différentes. La figure 2.9 montre l'évolution en fonction du temps de la concentration (normalisée) au centre d'une nappe de métal étirée, pour des nombre de Péclet valant $\mathrm{Pe_m} = 10^{10}$ et $\mathrm{Pe_s} = 10^9$, et un coefficient de partage $D_{\mathrm{m/s}}$ égal à 10^{-2}, 1, ou 10^2. Le temps est normalisé par le temps caractéristique de déformation $1/\dot{\epsilon}$. Il suffit de diviser ce temps par le nombre de Péclet $\mathrm{Pe_m}$ pour obtenir un temps normalisé par le temps de diffusion e_0/κ_s^{χ}. À ces valeurs de Péclet, la concentration tend donc vers sa valeur d'équilibre en un temps très petit devant le temps de diffusion $\tau_{\kappa_s^{\chi}} = e_0/\kappa_s^{\chi}$, de l'ordre de $10^{-9} \times \tau_{\kappa_s^{\chi}}$! Un second point important à noter est que le transfert d'éléments chimiques se fait sur un intervalle de temps resserré : dans le cas $D_{\mathrm{m/s}} = 10^{-2}$ par exemple, le transfert d'éléments chimiques est insignifiant jusqu'à $\dot{\epsilon}t \simeq 10$, et l'intégralité du transfert se fait entre $\dot{\epsilon}t = 10$ et $\dot{\epsilon}t = 12$. Ce n'est pas aussi drastique dans le cas d'un coefficient de partage $\gtrsim 1$, mais cette observation reste vraie : l'intégralité du transfert d'éléments se fait pendant sur un intervalle de temps petit par rapport au temps de latence durant lequel le transfert est négligeable. Dans le contexte de la formation du noyau, une implication est qu'un équilibrage partiel serait moins probable qu'un équilibrage négligeable ou presque parfait (*i.e.* $k = 0$ ou $k = 1$ dans le formalisme des modèles géochimiques).

On peut partir de la loi donnant l'évolution du champ scalaire en fonction du temps pour obtenir des expressions analytiques pour le temps d'équilibrage $t_{1/2}$, défini ici par le temps auquel l'écart entre la valeur maximale de la température ou composition dans la phase métallique et la valeur d'équilibre a été divisé par deux. Sous l'hypothèse d'un taux de compression $\dot{\epsilon}$ constant, l'expression générale obtenue pour $t_{1/2}$ dans le cas compositionnel [2] admet deux ex-

2. Des expressions équivalentes existent pour le problème de transfert de la chaleur [Lherm & Deguen,

pressions approchées dans les limites $D_{m/s} \gg 1$ (éléments sidérophiles) et $D_{\mathrm{m/s}} \lesssim 1$ (éléments lithophiles) :

$$t_{1/2} \simeq \frac{1}{2\dot{\epsilon}} \ln\left(2\mathrm{Pe_s} D_{\mathrm{m/s}}^2 + 1\right) \qquad \text{si } D_{\mathrm{m/s}} \gg 1, \tag{2.14}$$

$$t_{1/2} \simeq \frac{1}{2\dot{\epsilon}} \ln\left(2\mathrm{Pe_m} + 1\right) \qquad \text{si } D_{\mathrm{m/s}} \lesssim 1. \tag{2.15}$$

On peut d'ores et déjà noter que le temps d'équilibrage dépend du coefficient de partage (cela est vrai aussi pour l'équilibrage d'une goutte de métal [Ulvrová *et al.*, 2011; Lherm & Deguen, submitted]), ce qui est un point potentiellement important pour l'interprétation des données géochimiques. Le point le plus important à noter est cependant l'effet du nombre de Péclet. Lorsque $\mathrm{Pe_s} D_{\mathrm{m/s}}^2 \ll 1$ et $\mathrm{Pe_m} \ll 1$, les équations (2.14) et (2.15) se réduisent à $t_{1/2} \simeq D_{\mathrm{m/s}}^2 e_0^2/\kappa_{\mathrm{s}}^\chi$ et $t_{1/2} \simeq e_0^2/\kappa_{\mathrm{m}}^\chi$, ce qui correspond simplement aux temps caractéristiques de diffusion basés sur l'épaisseur initiale de la nappe de métal, comme attendu dans la limite de petites valeurs des nombres de Péclet. En revanche, le comportement change drastiquement dans la limite de grands nombres de Péclet. Les équations (2.14) et (2.15) tendent alors vers

$$t_{1/2} \simeq \frac{1}{2\dot{\epsilon}} \ln\left(\mathrm{Pe_s} D_{\mathrm{m/s}}^2\right) \qquad \text{si } D_{\mathrm{m/s}} \gg \sqrt{\frac{\kappa_{\mathrm{s}}^\chi}{\kappa_{\mathrm{m}}^\chi}}, \tag{2.16}$$

$$t_{1/2} \simeq \frac{1}{2\dot{\epsilon}} \ln \mathrm{Pe_m} \qquad \text{si } D_{\mathrm{m/s}} \ll \sqrt{\frac{\kappa_{\mathrm{s}}^\chi}{\kappa_{\mathrm{m}}^\chi}}. \tag{2.17}$$

Dans cette limite, le temps d'équilibrage dépend faiblement (logarithmiquement) des diffusivités. À titre d'exemple, les temps d'équilibrage de deux espèces chimiques ayant une diffusivité de 10^{-6} m^2.s^{-1} (l'ordre de grandeur de la diffusivité thermique) et 10^{-12} m^2.s^{-1} ne diffèrerent que d'un facteur 2, malgré les 6 ordres de grandeur de différence de leurs diffusivité ! Le temps d'équilibrage est donc essentiellement contrôlé par le taux d'étirement.

L'expression du champ de température ou de concentration permet aussi d'obtenir l'expression de l'épaisseur de la nappe de métal au temps $t = t_{1/2}$, ce qui permet de donner une idée du degré de brassage nécessaire pour permettre l'homogénéisation par diffusion. On obtient ainsi

$$\ell_\chi \sim \frac{2}{D_{\mathrm{m/s}}} \left(\frac{\kappa_s^\chi}{\dot{\epsilon}}\right)^{1/2} \tag{2.18}$$

dans le cas de l'homogénéisation d'un élément sidérophile, et

$$\ell_T \sim \left(\frac{\kappa_s}{\dot{\epsilon}}\right)^{1/2} \tag{2.19}$$

dans le cas de l'homogénéisation de la température, où κ_s est la diffusivité thermique dans la phase silicate. Le rapport $\ell_\chi/\ell_T \sim D_{\mathrm{m/s}} \left(\kappa_s/\kappa_s^\chi\right)^{1/2}$ est en général grand : avec par exemple $\kappa_s^\chi \sim 10^{-10}$ m.s^{-2}, $\kappa_s \sim 10^{-6}$ m.s^{-2}, et $D_{\mathrm{m/s}} = 100$, on obtient $\ell_\chi/\ell_T \sim 10^4$, ce qui indique que l'équilibrage chimique est significativement plus tardif que l'équilibrage thermique. Des lois similaires peuvent être obtenues dans le cas d'un cylindre étiré [Lherm & Deguen, submitted]. L'équilibrage y est un peu plus rapide et l'échelle d'équilibrage un peu plus grande, pour des raisons géométriques.

Il est intéressant de tenter une estimation de ces longueurs, et de les comparer à des estimations de la taille des gouttes de métal qui résulteraient de la fragmentation. Le modèle d'entrainement de la partie 2.2.2 (équations (2.7) et (2.8)) permet d'estimer le taux de déformation associé à l'écoulement moyen, qui est typiquement $> 10^{-4}$ s^{-1}. (Le véritable taux d'étirement est probablement plus grand en raison des fluctuations du champ de vitesse ; nos

submitted].

estimations seront donc probablement surestimées). Avec $\dot{\epsilon} = 10^{-4}$, on obtient ℓ_χ entre 5 mm et 0.05 mm pour $D_{\mathrm{m/s}}$ comprit entre 1 et 100, et $\ell_T \sim 15$ cm. L'implication est que l'équilibrage sera insignifiant si le brassage n'est pas suffisamment vigoureux pour étirer la phase métallique jusqu'à ce point. Ces estimations sont données à titre indicatif : dans ce type de problème, l'histoire de la déformation compte et les temps et longueurs d'équilibrage dépendent de la dépendance temporelle de $\dot{\epsilon}$, qui reste à modéliser.

2.3 Travaux en cours et perspectives

2.3.1 Dynamique

Brassage, mélange, et fragmentation

Thèse de Victor Lherm

Les discussions de la partie 2.2.3 montrent que, dans la limite $(\mathrm{Bo}, \mathrm{Re}) \gg 1$, les processus de fragmentation et d'homogénéisation sont contrôlés pour une part importante par le brassage (ou, plus généralement, par le tenseur taux de déformation $\underline{\dot{\epsilon}}(\vec{x}, t)$ et son évolution temporelle). Avec Victor Lherm, nous avons dans un premier temps étudié ce problème avec un point de vue cinématique, en imposant le taux d'élongation des structures et en calculant leur temps d'homogénéisation (partie 2.2.3). Mais la dynamique du brassage reste à élucider : nous pensons comprendre qualitativement la séquence de mécanismes permettant d'aller jusqu'à la fragmentation de la phase métallique (figure 2.7), mais nous avons besoin d'un modèle quantitatif pour pouvoir être prédictif.

Victor a réalisé une première étude numérique de la déformation et de l'équilibrage d'un volume de métal chutant dans un océan magmatique, dans des conditions de Reynolds et Bond relativement grands. Pour des raisons de coût numérique, ces simulations ont été réalisées en 2D (ce qui ne permet pas l'étude de la fragmentation), mais un régime de brassage vigoureux a pu néanmoins être atteint, qualitativement similaire aux expériences réalisées dans le régime d'entrainement turbulent. Cette première étude numérique sera suivie par plusieurs études expérimentales du mélange dans des écoulements que l'on rendra progressivement de plus en plus proche de l'écoulement suivant un impact planétaire :

1. Dans un premier temps, on s'intéressera à l'homogénéisation dans des thermiques turbulents *miscibles* (obtenus en libérant un volume d'eau salée dans de l'eau douce). Bien qu'il s'agisse d'un écoulement "classique" de mécanique des fluides [*e.g.* Morton *et al.*, 1956; Scorer, 1957; Turner, 1957], cet écoulement a été assez peu étudié avec des techniques expérimentales modernes et l'analyse de cet écoulement a pour l'instant été essentiellement limité à la quantification de grandeurs intégrales – vitesse verticale, entrainement, circulation – [Morton *et al.*, 1956; Scorer, 1957; Turner, 1957; Bond & Johari, 2005, 2010], ou à celle de la structure moyenne des champs de concentration et de vorticité [Zhao *et al.*, 2013]. L'utilisation simultanée de vélocimétrie PIV et de mesure de concentration par fluorescence induite PLIF (en ajourant un colorant fluorescent à l'eau salée, et en éclairant l'expérience avec un plan laser) permettra de quantifier en fonction du nombre de Reynolds le champ de vitesse et ses fluctuations, l'évolution de la topologie des hétérogénéités de concentration du traceur fluorescent, la distribution spatiale (pdf) de ce traceur, et le temps caractéristique d'homogénéisation.

2. On cherchera ensuite à quantifier le brassage et l'homogénéisation dans des thermiques turbulents *immiscibles* tels que discutés dans la partie 2.2.2 : un volume d'une solution aqueuse libérée sans vitesse initiale dans un bain d'huile de silicone de faible viscosité (figures 2.4 et 2.8). Comme dans le cas miscible, l'utilisation de vélocimétrie PIV permettra de mesurer le champ de vitesse, et l'ajout d'un colorant fluorescent dans la phase aqueuse permettra d'étudier l'évolution et l'étirement de l'interface entre les deux liquides. Pour

être utilisées dans un écoulement diphasique, ces deux techniques nécessitent de minimiser au maximum la différence d'indices optiques entre les deux liquides pour éviter de trop fortes distorsion optiques des champs de vitesse et de concentration. L'utilisation d'une huile de silicone et d'une solution aqueuse de NaI permet un ajustement fin des indices optiques en jouant sur la concentration de NaI (figures 2.5 et 2.8). L'étude de l'homogénéisation d'un champ scalaire entre les deux phases sera plus difficile dans le cas immiscible. On peut s'intéresser au transfert thermique entre les deux phases, en libérant la solution aqueuse avec une température différente de celle de l'huile [Wacheul & Le Bars, 2017]. Plusieurs techniques expérimentales sont envisageables (cristaux thermochromiques, thermométrie PLIF à 2 couleurs). Une autre approche que j'envisage est de résoudre numériquement l'équation de transport d'un soluté en utilisant comme champ de vitesse des champs de vitesse déterminés expérimentalement par PIV.

Dispersion de la phase métallique par l'impact

Thèse de Victor Lherm, et collaboration avec Maylis Landeau (IPGP).

Les expériences que nous avons réalisées jusqu'ici ont des conditions initiales (liquides initialement au repos) très éloignées de ce que l'on peut attendre après un impact planétaire, et ignorent le brassage, la fragmentation, et le mélange qui pourraient être induits par l'impact lui même.

Ce problème peut être étudié à l'aide d'expériences où un volume liquide est libéré dans l'air et vient impacter un second liquide. Dans le régime de cratérisation qui est pertinent dans notre contexte (*gravity regime*, où les contraintes mises en jeu sont suffisamment grandes comparées au seuil de plasticité ou aux contraintes visqueuses pour que la résistance à la déformation des matériaux ne joue pas de rôle), la dynamique de l'ouverture du cratère d'impact ne dépend que de l'inertie de l'impacteur et des forces de gravité. Le rapport entre ces deux forces est mesuré par un nombre de Froude défini par

$$Fr^* = \frac{\rho_i \, v_i^2}{\rho_t \, g \, d}, \tag{2.20}$$

où v_i est la vitesse d'impact, d le diamètre de l'impacteur, ρ_i et ρ_t les masses volumiques moyennes de l'impacteur et de la cible (le manteau de la proto-Terre). Avec cette définition, Fr^* peut être compris comme le rapport entre l'énergie cinétique du corps impactant ($\sim \rho_i v_i^2 d^3$), et la variation d'énergie gravitationnelle associée à l'ouverture d'un cratère de diamètre d dans la cible ($\sim \rho_t g d^4$). Si l'on suppose que la vitesse d'impact est proche de la vitesse d'échappement, $v_i \simeq v_{\text{esc}} = \sqrt{gD}$, où D est le diamètre de la proto-Terre, on obtient

$$Fr^* \simeq \frac{\rho_i}{\rho_t} \frac{D}{d}. \tag{2.21}$$

Le rapport ρ_i/ρ_t étant de l'ordre de 1, le nombre de Froude Fr^* dépend essentiellement des tailles relatives de l'impacteur et de la proto-Terre. Fr^* est de l'ordre de 1 pour les plus gros impacts planétaires, et peut atteindre des valeurs beaucoup plus grandes dans le cas d'impacts de petits corps. À titre d'exemple, on pense que la météorite à l'origine de Meteor Crater (Arizona) avait un diamètre de l'ordre de 50 m, et a percuté la Terre à une vitesse supérieure à 10 km.s^{-1}, ce qui donne $Fr^* \sim 10^5$. Dans une certaine mesure, les petits impacts sont donc dynamiquement plus extrêmes que les impacts géants – en tout cas du point de vue de l'impacteur – et on peut s'attendre à ce que la déformation de l'impacteur associée à l'ouverture du cratère soit plus modeste dans le cas d'impacts géant que dans le cas de petits impacts. [3]

3. On peut se donner une idée de l'importance de ce point avec le calcul suivant. On peut facilement montrer que la taille du cratère d'impact à son maximum est $\sim dFr^{*1/4}$. Si l'on suppose que le volume de l'impacteur se répartit uniformément à la surface du cratère sous la forme d'une nappe, l'épaisseur moyenne de cette nappe au maximum de l'ouverture sera $\sim dFr^{*-1/2}$. Dans le cas de Meteor Crater, on obtient $h \sim 10$ cm pour une

Il est sans doute dangereux d'extrapoler aux impacts géants l'observation que les impacts météoritiques "récents" ont résulté en la fragmentation presque complète de la météorite. Ces impacts sont sans doute de mauvais analogues des impacts géants car leur nombre de Froude est trop grand.

L'ensemble de la gamme de valeurs de Fr^* pertinentes pour la formation des planètes telluriques (Fr^* de l'ordre de 1 à plusieurs centaines) peut être exploré avec des expériences d'impacts de gouttes de taille millimétrique à pluri-centimétriques relâchées de différentes hauteurs au-dessus d'un bain d'un second liquide moins dense. Nous avons déjà réalisé plusieurs séries d'expériences d'impacts à incidence verticale, qui seront poursuivies et modélisées dans les années à venir. À titre d'exemple, la figure 2.10 montre plusieurs clichés issus de deux expériences d'impacts de gouttes composée d'une solution aqueuse de NaI ($\rho = 1470$ kg.m^{-3}) lâchée au-dessus d'un bain d'eau. Les deux gouttes ont un diamètre de 4.5 mm. L'une des expériences est réalisée à $Fr^* = 1.2$, l'autre à $Fr^* = 65$. Ces expériences (et de nombreuses autres) nous ont permis d'identifier les phases suivantes :

1. L'impact de la goutte induit l'ouverture d'un cratère, qui grandit jusqu'à un rayon de l'ordre de $dFr^{*1/4}$ (à 29 ms dans l'expérience à $Fr^* = 65$, et 20 ms à $Fr^* = 1.2$). Lors de la phase d'ouverture de la cavité, la couche de liquide dense est sujette à une instabilité que l'on interprète comme étant de type Rayleigh-Taylor (à 29 ms dans l'expérience à $Fr^* = 65$, et figure 2.11). Une particularité de cette instabilité dans ce contexte est que l'accélération de l'interface due à l'ouverture du cratère est supérieure à la gravité, ce qui induit une croissance radiale, et non verticale, de la zone de mélange.

2. Le cratère atteint son rayon maximal lorsque l'intégralité de l'énergie cinétique de l'impact a été consommée par le changement d'énergie potentielle de gravité associé à l'ouverture du cratère. Cette énergie potentielle est ensuite convertie à nouveau en énergie cinétique lors de la fermeture du cratère. La convergence de l'écoulement amène à la formation d'un pic central. L'écoulement ascendant et convergent associé à la fermeture du cratère et à la formation du pic central étire fortement la zone de mélange formée par l'instabilité Rayleigh-Taylor.

3. Dans les expériences d'impacts de gouttes millimétriques, on observe (souvent) que le pic central se fragmente en raison du développement d'une instabilité capillaire, un mécanisme qui n'est clairement pas pertinent dans le cas d'un impact planétaire. Ce n'est pas le cas dans les expériences que nous avons réalisées avec des gouttes pluri-centimétriques.

4. L'effondrement du pic central ré-injecte le mélange goutte/liquide ambiant. À des valeurs modérées de Fr^*, ce mélange forme un nuage compact bien défini (78 ms dans l'expérience à $Fr^* = 1.2$). À $Fr^* = 1.2$, le diamètre de ce nuage à $t = 78$ ms est environ le double de celui de la goutte, ce qui indique un brassage déjà significatif (liquide ambiant/goutte en proportion 8 :1 dans le nuage). La dispersion de la goutte est plus importante à $Fr^* = 65$.

5. À des valeurs modérées de Fr^*, le nuage composé d'un mélange de liquide dense et de liquide ambiant évolue ensuite comme un thermique turbulent (de 78 ms à 314 ms à $Fr^* = 1.2$). Dans cette limite, le modèle d'entrainement turbulent (*c.f.* partie 2.2.2) reste applicable et l'évolution du rayon du thermique peut être prédite grâce au modèle d'entrainement, en supposant simplement que l'origine virtuelle z_0 est une fonction de Fr^*. Les choses sont un peu moins claires à plus grand Fr^*. Une partie du liquide de la goutte évolue effectivement comme un thermique turbulent (non visible sur la figure 2.10), mais une partie significative est laissée dans le sillage du thermique.

météorite de diamètre 50 m : on approche de la taille de la longueur capillaire (~ 1 cm) à laquelle la tension de surface peut commencer à jouer un rôle. Dans ces conditions on peut donc imaginer que l'impact résulte en la fragmentation presque totale de la météorite, ce qui semble effectivement avoir été le cas.

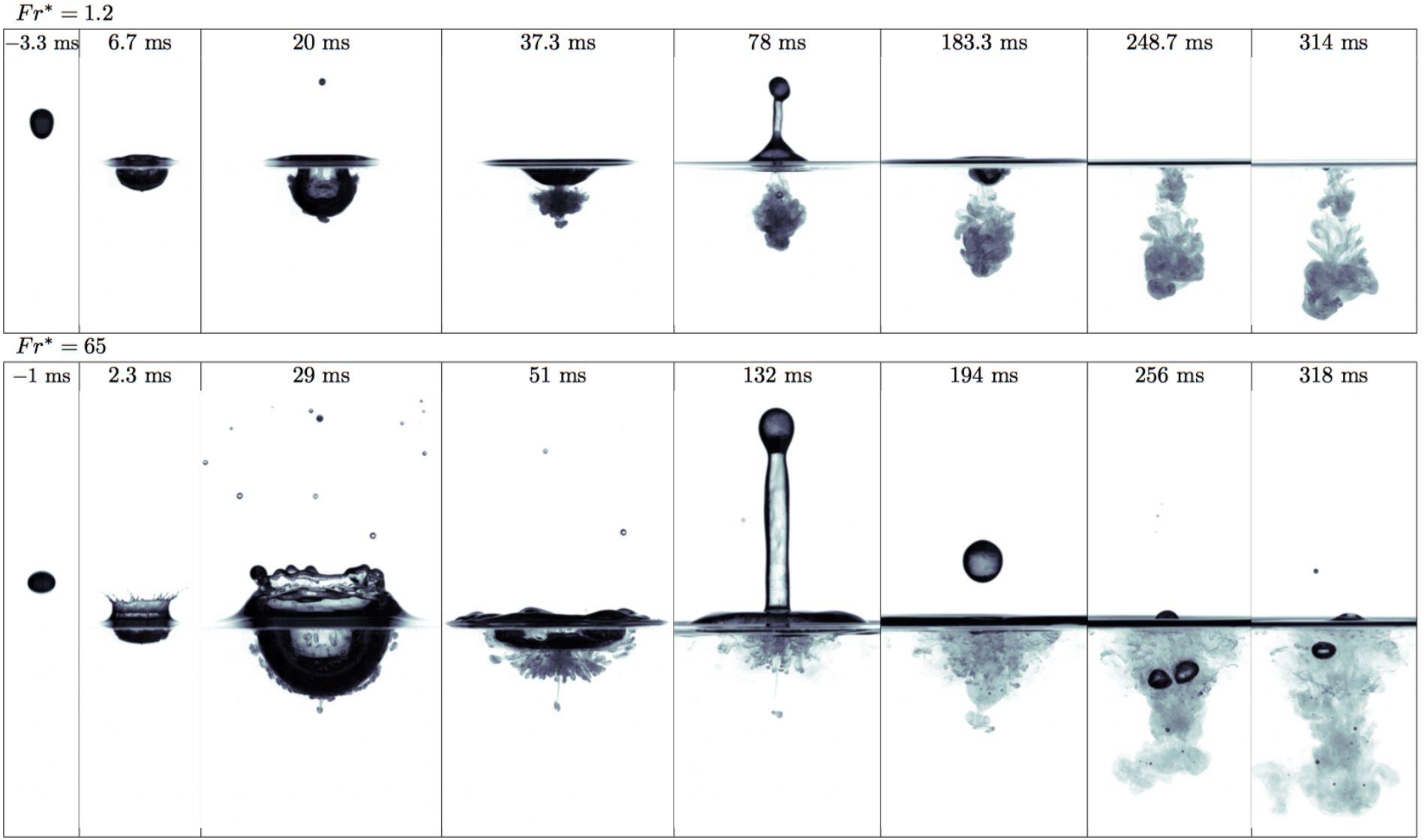

Figure 2.10

Clichés obtenus dans deux expériences d'impact d'une goutte composée d'une solution aqueuse de NaI ($\rho = 1470$ kg.m^{-3}) chutant dans un bain d'eau, à $Fr^* = 1.2$ (haut) et $Fr^* = 65$ (bas). Dans les deux cas la goutte mesure 4.5 mm de diamètre (les images sont toutes à l'échelle). Le temps est compté en ms à partir d'un temps de référence correspondant à l'instant où la goutte entre en contact avec la surface de l'eau. Le rapport de densité est de 1.47, le rapport de viscosité est proche de 1.

Figure 2.11
Cliché tiré de l'expérience d'impact à $Fr^* = 65$ de la figure 2.10, à $t = 25$ ms. La couche de liquide apportée par la goutte est répartie sur toute la surface du cratère, et est sujette à une instabilité que l'on interprète comme étant de type Rayleigh-Taylor.

Nous avons commencé l'étude détaillée de ces différentes phases, dans le but d'obtenir un modèle prédictif de la dispersion induite par l'impact. Nous projetons de plus de développer un dispositif expérimental permettant de réaliser des impacts obliques, plus pertinents que les impacts à incidence verticale. Il est probable que l'angle d'impact joue sur la dispersion de la phase métallique [Kendall & Melosh, 2016].

2.3.2 Modélisation géochimique

Le système Hf-W

Le système Hf-W peut être utilisé pour contraindre les paramètres k et Δ quantifiant l'équilibrage métal-silicates (section 2.1). Par exemple, Rudge *et al.* [2010] a obtenu que la paramètre k devait être supérieur à 0.36, et une généralisation de cette approche permet en plus d'obtenir une borne inférieure pour le paramètre Δ mesurant le rapport silicates/métal équilibrés : $\Delta \geq 17$ [Deguen *et al.*, 2014*a*].

Une limitation majeure de cette prédiction vient de l'hypothèse d'un coefficient de partage du tungstène qui resterait constant au cours de l'accrétion. En réalité le coefficient de partage D_W du tungstène a nécessairement varié en raison de l'évolution des conditions T, P et fO_2 auxquelles métal et silicates ont pu échanger des éléments, et ce potentiellement sur une gamme de plusieurs ordres de grandeurs [Cottrell *et al.*, 2009; Rubie *et al.*, 2011]. Le choix de considérer D_W constant dans l'interprétation du système Hf-W est donc discutable, tout comme l'est la borne obtenue ci-dessus pour Δ.

Un autre point important est la signification de ces valeurs "moyennes" de k et Δ, qui est loin d'être claire. Il s'agit sans aucun doute de moyennes pondérées sur l'ensemble des épisodes de différentiation, mais la nature de cette pondération n'a pour l'instant pas été explicitée. Nous n'avons pas de raison de penser que ces valeurs soient représentatives de l'ensemble du processus d'accrétion. Il est tout à fait possible par exemple que les valeurs obtenues soient plus représentatives de la fin de l'accrétion, où la quantité de tungstène piégée dans le manteau a pu être proportionnellement plus grande qu'en début d'accrétion en raison de la décroissance probable de D_W au cours de l'accrétion.

Nous projetons de reprendre l'étude du système Hf-W en prenant en compte les variations de D_W au cours de l'accrétion, et en quantifiant la sensibilité de la composition isotopique du tungstène aux valeurs de k et Δ en fonction de la fraction de Terre accrétée.

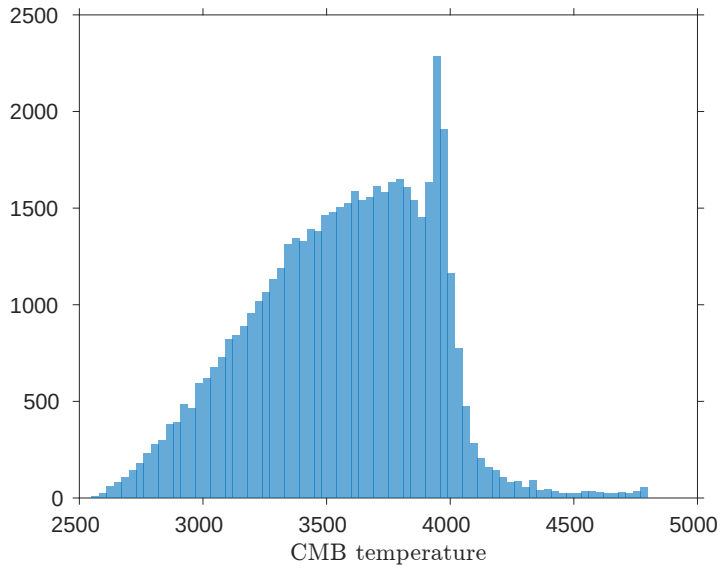

Figure 2.12

Distribution de la température au sommet du noyau à la fin de l'accrétion, telle que prédite par un modèle d'évolution thermique de la phase métallique pour des évolutions de la pression et de la température d'équilibrage compatibles avec la répartition entre noyau et manteau de Ni et Co. Pour comparaison, la température à la CMB aujourd'hui est estimée être supérieure à 4200 K.

2.3.3 Vers des modélisations géochimique et thermique couplées

Post-doctorat de Vincent Clesi

Le fractionnement noyau/manteau estimé des éléments sidérophiles apporte des contraintes sur l'évolution des conditions $(P_{\text{eq}}, T_{\text{eq}})$ d'équilibrage de la phase métallique avec le manteau de la proto-Terre [*e.g.* Wood *et al.*, 2006]. Ces contraintes ont été utilisées pour prédire la concentration dans le noyau d'éléments tels que O et Si [Rubie *et al.*, 2011; Badro *et al.*, 2015; Fischer *et al.*, 2015]. Il est tentant d'essayer de les utiliser pour prédire la quantité de chaleur déposée dans le noyau au cours de sa formation.

On peut tenter de le faire de la manière suivante. La première étape consiste à obtenir par inversion des trajets $(P_{\text{eq}}, T_{\text{eq}})$ qui vérifient les contraintes apportées par les éléments sidérophiles. Si l'on se place dans le cadre du modèle d'ocean magmatique, ces conditions $(P_{\text{eq}}, T_{\text{eq}})$ peuvent être interprétées comme étant celles de la base de l'océan de magma, et donc celles de la phase métallique avant qu'elle ne commence sa migration à travers la partie solide du manteau. On peut ensuite modéliser l'évolution thermique de la phase métallique au cours de sa migration à travers le manteau solide pour prédire sa température lorsqu'elle atteint le noyau, puis prendre en compte la compression associée à la croissance de la Terre pour prédire sa température à la fin de l'accrétion.

À titre d'exemple, la figure 2.12 montre un histogramme de la température à la CMB à la fin de l'accrétion obtenue pour un ensemble de trajets $(P_{\text{eq}}, T_{\text{eq}})$ compatibles avec la concentration dans la Terre silicaté du Nickel et du Cobalt (obtenus grâce à une inversion de type Monte-Carlo). Dans ce calcul, j'ai supposé : (i) un équilibrage chimique métal-silicates parfait ; (ii) que l'intégralité de la dissipation visqueuse a lieu dans le manteau et que l'échange de chaleur métal/silicates est négligeable au cours de la migration du fer à travers le manteau solide (deux hypothèses raisonnables pour un modèle de migration par diapirisme) ; et (iii) que le noyau est mélangé après chaque impact (et donc peut être supposé isentrope).

La figure 2.12 montre que la gamme de températures obtenues est large (de 2500 K à 4800 K pour cette inversion). La forme de la distribution n'a sans doute pas de signification physique (elle doit dépendre de la manière dont l'espace des modèles est échantillonné), mais il est significatif que la température obtenue pour une majorité des histoires d'accrétion soit

plus petite (parfois de beaucoup) que la température actuelle, qui est probablement supérieure à 4000 K [*e.g.* Hirose *et al.*, 2013]. Si l'on fait l'hypothèse assez plausible que la température du noyau à l'issue de l'accrétion a dû être supérieure ou égale à sa température actuelle, la prédiction de la température du noyau peut donc être utilisée pour écarter des trajets $(P_{\text{eq}}, T_{\text{eq}})$ admissibles géochimiquement mais amenant à une température trop basse. Dans ce calcul par exemple, les trajets $(P_{\text{eq}}, T_{\text{eq}})$ donnant une température à la CMB supérieure à 4000 K ont typiquement des pressions d'équilibrage assez faible tant que la Terre n'a pas atteint environ 80% de sa masse actuelle, puis des pressions d'équilibrages proches de celles de la CMB à la fin de l'accrétion.

Il y a clairement beaucoup d'hypothèses et d'incertitudes dans cette approche, que ce soit sur l'interprétation physique des valeurs P_{eq} et T_{eq} [Höink *et al.*, 2006], sur l'efficacité d'équilibrage, sur l'évolution de la fugacité d'oxygène, sur le mécanisme physique de migration du fer à travers la partie solide du manteau, ou sur le devenir du métal liquide une fois le noyau atteint (formation d'une stratification thermique stable, ou mélange radial du noyau ?). En particulier, le résultat dépendra fortement du mécanisme de migration envisagé (diapirisme, fracturation, percolation), dont dépend la répartition entre métal et silicate de la chaleur produite par dissipation, et l'importance du transfert thermique entre le métal et le manteau. Dans la suite de cette étude (post-doctorat de Vincent Clesi depuis septembre 2018), nous envisageons d'explorer l'effet de ces différents facteurs sur la température du noyau à la fin de l'accrétion, tout en incluant plus d'éléments chimiques (V, Cr, W ?) lors de l'inversion pour mieux contraindre les trajets $(P_{\text{eq}}, T_{\text{eq}})$ admissibles géochimiquement.

Chapitre 3

Convection et changements de phase – application au noyau interne de la Terre et aux manteaux planétaires

Une partie de mes activités de recherche après mon doctorat a concerné la dynamique du noyau interne de la Terre, ou graine, et notamment la possibilité que la graine puisse être le siège de convection naturelle. Une particularité importante de la graine est que sa frontière avec le noyau externe (ICB pour Inner Core Boundary) est une limite de phase, probablement très proche de l'équilibre thermodynamique. Par conséquent, une déformation de l'interface solide-liquide induite par des mouvements à l'intérieur de la graine peut s'accompagner de fusion ou de solidification, ce qui implique un flux de matière à travers l'ICB. On a alors des conditions limites que l'on qualifiera de "semi-perméables" ("semi" car la vitesse de changement de phase, et donc le flux de masse à travers l'ICB, sont limités par le transport de chaleur latente de changement de phase). Ceci peut modifier fondamentalement le mode de convection, et nous avons développé avec Thierry Alboussière un jeu de conditions limites permettant de rendre compte de la fusion ou cristallisation induites par une déformation de l'interface [Deguen *et al.*, 2013]. Dans le cas de la graine terrestre, de telles conditions limites modifient radicalement le régime de convection et permettent l'émergence d'un mode de convection consistant en une translation de la graine, sans déformation interne, avec fusion sur un hémisphère et solidification sur l'autre [Alboussière *et al.*, 2010; Monnereau *et al.*, 2010; Deguen *et al.*, 2013].

D'autres objets planétaires présentent, ou ont présenté, une couche solide en équilibre de phase avec une couche liquide : manteau primitif cristallisant à partir d'un océan de magma, océan de magma dans Io, ou couche de glace en contact avec un océan (satellites de glace tels que Europe, Ganymède, Callisto, Titan, Encélade, ...). Bien que développées pour modéliser la dynamique de la graine, nos conditions limites peuvent être appliquées à ces objets.

Dans ce qui suit, je commencerai par présenter les conditions limites que nous avons développées pour prendre en compte la fusion ou la cristallisation à une interface. La dérivation de ces conditions limites est esquissée dans la partie 3.1, et présentée en détails dans l'annexe 3.A de ce chapitre (dans une version plus générale que dans les articles publiés). Je discuterai ensuite brièvement de l'effet de ces conditions limites sur la convection dans la graine (partie 3.2) et sur la convection dans un manteau cristallisant à partir d'un océan de magma (partie 3.3).

3.1 Conditions limites à une interface solide/liquide déformable en équilibre de phase

On considère une couche d'un solide déformable, en contact avec une couche de liquide en équilibre de phase avec le solide. Le solide et le liquide sont des mélanges binaires de compositions différentes. L'interface séparant le solide et le liquide est déformable, de topographie h. L'interface est supposée à l'équilibre thermodynamique et peut se déplacer soit par advection

par le champ de vitesse $\mathbf{v} = (v_r, v_\theta, v_\phi)$, soit par changement de phase en fonction des valeurs locales des flux de chaleur et de soluté de part et d'autre de l'interface, d'après la condition cinématique

$$\frac{Dh}{Dt} = v_r + V_r \tag{3.1}$$

où $D(\cdot)/Dt$ est la dérivée lagrangienne, et V_r est la vitesse de changement de phase dans la direction radiale (l'épaisseur de solide créée ou enlevée par unité de temps). Si on suppose que la topographie est quasi-statique, c'est à dire que $\frac{Dh}{Dt}$ est très petit devant v_r et V_r, alors la vitesse radiale dans le solide est simplement égale à l'opposé de la vitesse de changement de phase,

$$v_r = -V_r. \tag{3.2}$$

La vitesse de changement de phase est déterminée par les équations de conservation de la chaleur (condition de Stefan) et du soluté à l'interface, qui relient V_r aux différences de flux de chaleur et de soluté de part et d'autre de l'interface. L'estimation de V_r nécessite donc la connaissance du flux de chaleur et du flux de soluté du côté liquide, qui dépend de l'écoulement dans le liquide. On pourrait en théorie traiter simultanément la convection dans le liquide et le solide, mais des simulations numériques directes sont impraticables en raison des échelles de temps extrêmement différentes : la résolution temporelle de la convection dans le liquide nécessite un pas de temps extrêmement petit par rapport au temps caractéristique de la convection solide.

L'approche que nous avons développée avec Thierry Alboussière est la suivante : l'idée est de paramétrer l'effet de la convection dans le liquide en reliant la vitesse de changement de phase V_r à l'amplitude h de la topographie. En redistribuant la chaleur et les solutés absorbés ou relâchés par les changements de phase, la convection tend à éroder la topographie, en faisant fondre les bosses et cristalliser les creux. Pour quantifier cet effet, on estime les flux de chaleur et de composition coté liquide en supposant un transport dominé par l'advection, proportionnel aux différences de température potentielle et de composition entre l'interface et le coeur du liquide, qui elles mêmes sont proportionnelles à la topographie. On obtient alors une loi de la forme

$$V_r = -\frac{h}{\tau_\phi} - A\left(\frac{q^s}{\rho_l c_{p,l}} + q^s_\chi\right), \tag{3.3}$$

où τ_ϕ est un temps caractéristique de changement de phase, caractérisant la réponse de la topographie au transport de chaleur et de soluté dans la phase liquide, q^s et q^s_χ les flux de chaleur et de soluté côté solide, ρ_l et $c_{p,l}$ la masse volumique et la capacité calorifique du liquide, et A une fonction dépendant notamment de la chaleur latente de changement de phase. Dans cette approche, l'efficacité avec laquelle la convection liquide peut transporter la chaleur et les solutés est paramétrée par la valeur du temps caractéristique τ_ϕ. Une faible valeur de τ_ϕ signifie un transport efficace et un changement de phase rapide.

À ce stade, la convection dans le liquide est entièrement paramétrée par τ_ϕ. Un jeu complet de conditions limites à l'interface est donné par les équations (3.2) et (3.3), auxquelles il faut ajouter les conditions d'équilibre thermodynamique à l'interface (température égale au liquidus) et de continuité de la contrainte à travers l'interface. La continuité de la contrainte normale exprime un équilibre entre les contraintes verticales induites par la convection solide et le poids de la topographie, et fait donc apparaitre h :

$$-p + 2\eta\frac{\partial v_r}{\partial r} = \Delta\rho g h. \tag{3.4}$$

où p est la pression et η la viscosité du solide. On peut ensuite exprimer h en fonction de v_r (à partir des équations (3.2) et (3.3)) et remplacer h par son expression dans l'équation (3.4),

ce qui donne

$$-p + 2\eta\frac{\partial v_r}{\partial r} = \Delta\rho g\tau_\phi \left[v_r - A\left(\frac{q^s}{\rho_l c_{p,l}} + q^s_\chi\right)\right]. \tag{3.5}$$

On obtient alors un jeu de conditions limites indépendantes de la topographie, qui devient une variable muette du problème. Par rapport à des conditions limites "classiques", la seule condition modifiée par le changement de phase est la continuité de la contrainte normale.

En introduisant R, ΔT et Δc des échelles caractéristiques de longueur, température, et composition du problème, on peut construire une échelle de vitesse κ_T/R et une échelle de pression $\eta\kappa_T/R^2$, où κ_T est la diffusivité thermique dans la phase solide. En adimensionnant les variables du problème à l'aide de ces échelles caractéristiques, l'équation (3.5) devient

$$-\tilde{p} + 2\frac{\partial \tilde{v}_r}{\partial \tilde{r}} = \mathcal{P}\left[\tilde{v}_r - \frac{1}{\mathcal{S}^*}\left(\tilde{q}^s + \frac{\kappa_\chi \Delta c}{\kappa_T \Delta T}\tilde{q}^s_\chi\right)\right] \tag{3.6}$$

où $(\tilde{p}, \tilde{v}_r, \tilde{r}, \tilde{q}^s, \tilde{q}^s_\chi)$ correspondent aux versions adimensionnées de $(p, v_r, r, q^s, q^s_\chi)$, et où

$$\mathcal{P} = \frac{\Delta\rho\, g\, R\, \tau_\phi}{\eta}, \tag{3.7}$$

$$\mathcal{S}^* = A_T\frac{\rho_s L}{\rho_l c_{p,l}\Delta T} + A_\chi\frac{1-k}{k}\frac{m_c c^i_s}{\Delta T}. \tag{3.8}$$

Le nombre $\mathcal{P}$ compare le temps caractéristique de changement de phase τ_ϕ au temps visqueux $\eta/(\Delta\rho\, g\, R)$, qui dans ce contexte peut être interprété comme étant le temps nécessaire à la convection dans la couche solide pour construire une topographie dont le poids équilibre les contraintes normales convectives. Le nombre $\mathcal{S}^*$ s'apparente à un nombre de Stefan dans la limite d'un problème purement thermique (rapport entre chaleur latente de changement de phase L et chaleur spécifique disponible $c_p\Delta T$).

En pratique nous avons jusqu'ici négligé dans l'équation (3.6) la contribution des flux de chaleur et de soluté (limite $\mathcal{S}^* \to \infty$), et dans cette limite l'équation (3.6) se réduit à

$$-\tilde{p} + 2\frac{\partial \tilde{v}_r}{\partial \tilde{r}} = \mathcal{P}\tilde{v}_r, \tag{3.9}$$

qui montre que la vitesse radiale à l'interface (et donc la vitesse de changement de phase) est proportionnelle à la contrainte normale induite par la convection dans la couche solide. Dans la limite $\mathcal{P} \to \infty$, on doit avoir $\tilde{v}_r \to 0$ puisque la contrainte normale (terme à gauche du signe "=") doit rester finie. On tend donc vers une condition d'interface imperméable classique. Dans la limite $\mathcal{P} \to 0$, la contrainte normale tend vers 0 puisque la vitesse $\tilde{v}_r$ doit rester finie, ce qui correspond à une condition limite de type perméable.

3.2 Dynamique du noyau interne de la Terre

La noyau interne terrestre, ou graine, présente une structure d'une complexité étonnante (Fig. 3.1). Son anisotropie sismique [Poupinet *et al.*, 1983] est aujourd'hui généralement acceptée mais la structure fine de la graine et l'origine de cette structure restent très mal comprises. L'exploration sismologique de la graine a permis de significativement affiner notre vision de sa structure et a mis en évidence des variations à la fois radiales et latérales des propriétés sismiques [*e.g.* Tkal***v***cić, 2015; Souriau & Calvet, 2015]. L'anisotropie semble faible ou inexistante dans les 100 à 400 km les plus superficiels. Cette couche 'isotrope' présente une forte atténuation et est asymétrique, l'hémisphère Est étant plus rapide et moins atténuant que l'hémisphère Ouest [Tanaka & Hamaguchi, 1997]. L'anisotropie est plus forte en profondeur, de symétrie cylindrique au premier ordre, et alignée avec l'axe de rotation de la Terre. Une 'sous-graine' de rayon $\sim$ 500 km, présentant des propriétés élastiques encore différentes, pourrait

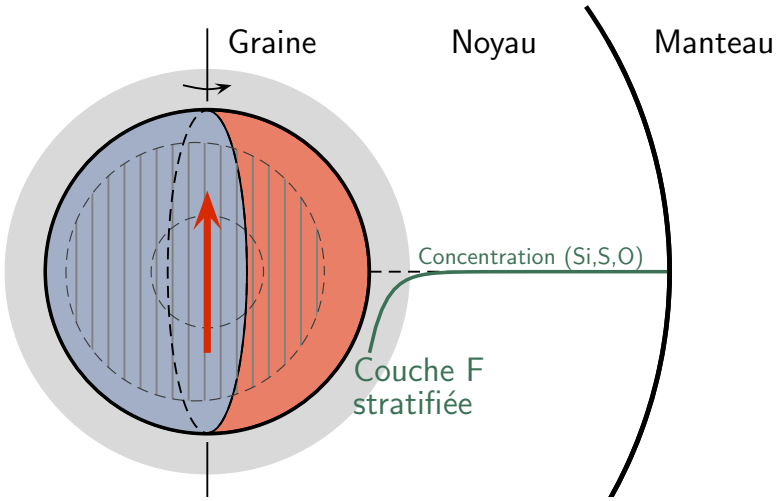

Figure 3.1

Une vue schématique de la structure de la graine déduite de l'interprétation des observations sismologiques. En plus d'une anisotropie élastique globale orientée parallèlement à l'axe de la rotation de la Terre (flèche rouge), la graine présente des variations radiales et horizontales de ses propriétés sismiques (vitesse de propagation et atténuation). La graine présente une asymétrie entre ses hémisphère "ouest" et "est" (à peu de chose près à l'ouest et l'est du méridien de Greenwich), qui présentent des vitesses, atténuation, et degrés d'anisotropie différents. L'anisotropie est faible ou inexistante à proximité de la surface de la graine, et augmente en profondeur. Une "sous-graine" ayant encore des propriétés différentes pourrait occuper la région la plus profonde de la graine. Enfin, la graine est entourée d'une couche semblant être stratifiée de manière stable, la couche F.

être présente au centre de la graine. Enfin, une couche anormale – la "couche F" [1]– stratifiée de manière stable (appauvrie en éléments légers), est observée à la base du noyau liquide [Souriau & Poupinet, 1991; Song & Helmberger, 1992; Yu *et al.*, 2005; Zou *et al.*, 2008; Cormier, 2009; Cormier *et al.*, 2011]. Cette observation est très difficilement explicable dans le cadre de notre vision classique de la convection du noyau, qui prédit au contraire une très fine couche limite instable à la base du noyau.

D'un point de vue dynamique, la complexité du modèle construit par la sismologie pose question. De nombreux modèles ont été proposés, mais aucun ne parvient à expliquer de manière cohérente toutes ces observations [Sumita & Bergman, 2007; Deguen, 2012].

3.2.1 État thermique et chimique de la graine

Le régime dynamique de la graine dépend de manière critique de la stratification en densité (stable ou instable) résultant de la contribution des profils de température et de concentration en éléments légers (Si, S, O, ...).

L'état thermique de la graine résulte d'une compétition entre refroidissement à l'ICB (frontière graine-noyau) et extraction de la chaleur interne de la graine. Une convection thermique peut potentiellement se développer dans la graine si le taux de refroidissement à l'ICB est suffisamment important pour qu'un géotherme superadiabatique puisse s'y développer malgré l'évacuation par diffusion de sa chaleur interne. J'ai développé un modèle d'évolution thermique de la graine couplé à celle du noyau [Deguen & Cardin, 2011] qui permet de prédire l'état thermique de la graine en fonction du flux de chaleur Q_{cmb} à la frontière noyau-manteau (CMB). Le résultat dépend fortement de la conductivité thermique de la graine, dont l'estimation a fortement évolué ces dernières années. Lorsque j'ai commencé à travailler sur le sujet,

1. Un nom hérité des modèles sismologiques de Bullen, dans lesquels les différentes enveloppes terrestres étaient nommées par des lettres allant de A à G. La couche D" et la couche F sont les seuls survivantes de cette nomenclature.

peu d'estimations étaient disponibles. La dernière estimation en date était de 36 $W.m^{-1}.K^{-1}$ [Stacey & Davis, 2008], une valeur plus faible que la valeur de 79 $W.m^{-1}.K^{-1}$ proposée plus tôt par Stacey & Anderson [2001]. Avec ces valeurs, la convection dans la graine est plausible, et même probable si l'on accepte la valeur de 36 $W.m^{-1}.K^{-1}$. Les choses ont changé après 2012, après que plusieurs groupes indépendants aient prédit des valeurs beaucoup plus hautes, typiquement supérieures à 200 $W.m^{-1}.K^{-1}$ dans le noyau interne [Sha & Cohen, 2011; Pozzo *et al.*, 2012; de Koker *et al.*, 2012; Gomi *et al.*, 2013; Seagle *et al.*, 2013; Pozzo *et al.*, 2014; Gomi *et al.*, 2016; Ohta *et al.*, 2016; Zhang *et al.*, 2016]. Avec une telle valeur de conductivité thermique, on prédit un géotherme fortement sous-adiabatique dans la graine, et la convection thermique devient impossible [Deguen & Cardin, 2011; Deguen *et al.*, 2013; Pozzo *et al.*, 2014; Labrosse, 2014; Lythgoe *et al.*, 2015].

Il est cependant encore un peu tôt pour accepter définitivement cette valeur haute de la conductivité thermique [Williams, 2018]. L'étude expérimentale de Konôpková *et al.* [2016] suggère en effet une valeur beaucoup plus faible de la conductivité dans le noyau, entre 18 et 44 $W.m^{-1}.K^{-1}$. Cette exception est notable car il s'agit de la seule étude expérimentale publiée ayant obtenue une estimation directe de la conductivité thermique, et non de la conductivité électrique convertie ensuite en conductivité thermique à l'aide de la loi de Wiedemann-Franz [Gomi *et al.*, 2013; Seagle *et al.*, 2013; Gomi *et al.*, 2016; Ohta *et al.*, 2016].

L'existence d'une stratification chimique et son effet dynamique (stabilisante ou déstabilisante) est aussi sujette à discussion. Si l'on note $D = c_s/c_l$ le coefficient de partage solide/liquide d'un élément donné, la dérivée logarithmique de cette définition permet d'obtenir la relation suivante pour la variation relative de la concentration dans le solide [Deguen & Cardin, 2011] :

$$\frac{dc_s}{c_s} = \frac{dc_l}{c_l} + \frac{dD}{D}. \tag{3.10}$$

Si on ignore les variations de D au cours de la croissance de la graine, l'évolution de la composition du solide cristallisé reflète simplement l'évolution de la composition du liquide à partir duquel il cristallise. Si le noyau externe est supposé bien mélangé, la concentration en éléments légers (incompatibles) augmente au fur et à mesure de la cristallisation de la graine. Si D est constant, la concentration en élément léger dans la graine suit l'évolution du liquide, et on attend donc une stratification stable (augmentation avec la distance au centre de la concentration en éléments légers). Un simple bilan de masse montre que l'augmentation de la concentration en éléments légers est au maximum de l'ordre de 5 % (le rapport entre la masse de la graine et celle du noyau).

La stratification chimique de la graine pourrait s'écarter de ce profil stable, et peut être même jusqu'au point d'être déstabilisante (plus d'éléments légers au centre de la graine qu'à sa périphérie), pour plusieurs raisons :

1. Le coefficient de partage D a pu diminuer au cours de la croissance de la graine, soit en raison de la différence de pression entre le centre de la Terre et la position actuelle de l'ICB, soit pour des raisons dynamiques (efficacité de compaction de la zone de mush probablement présente au niveau de l'ICB). Il semblerait que l'effet de la pression aille effectivement dans le sens d'une diminution du coefficient de partage thermodynamique D, et soit suffisant pour induire des variations de D de l'ordre de plusieurs % qui peuvent être suffisante pour contrebalancer une stratification thermique stabilisante [Gubbins *et al.*, 2013; Labrosse, 2014].

2. Il est possible aussi que l'hypothèse d'un noyau liquide bien mélangé ne soit pas vérifiée : l'étude sismologique du noyau semble indiquer la présence de couches stratifiées à la base (la couche F) et au sommet du noyau. À moins qu'elle n'ait une origine primordiale [Arkani-Hamed, 2017; Jacobson *et al.*, 2017], l'existence de la couche F – une couche appauvrie en éléments légers au dessus de l'ICB – argumente en faveur d'une

diminution au cours de la formation de la graine de la concentration en éléments légers à la base du noyau. Si la formation de cette couche résulte d'une manière ou d'une autre de la croissance de la graine [Gubbins *et al.*, 2008; Alboussière *et al.*, 2010; Gubbins *et al.*, 2011; Deguen *et al.*, 2013], sa formation implique nécessairement une purification progressive du liquide à partir duquel la graine cristallise. Ceci induit une stratification compositionnelle instable dans la graine [Deguen *et al.*, 2013, 2018].

Au vu des incertitudes fortes sur l'état de stratification de la graine et d'autres paramètres importants (la viscosité de la graine en particulier, dont les estimations publiées vont de 10^{11} Pa.s à 10^{22} Pa.s [Yoshida *et al.*, 1996; Buffett, 1997; Van Orman, 2004; Koot & Dumberry, 2011; Reaman *et al.*, 2011, 2012]), j'ai entrepris depuis ma thèse une exploration systématique des différents régimes dynamiques susceptibles d'exister dans la graine. Je me suis ainsi intéressé d'une part au cas d'une stratification instable et au développement de convection naturelle dans la graine [Deguen & Cardin, 2011; Deguen *et al.*, 2013, 2018], et d'autre part au cas d'une stratification stable, en considérant un forçage dû soit à une croissance hétérogène de la graine [Deguen & Cardin, 2009; Deguen *et al.*, 2011*a*; Lincot *et al.*, 2014], soit au champ magnétique diffusé dans la graine [Lasbleis *et al.*, 2015]. La comparaison des différents régimes possibles a fait l'objet d'un article de review [Deguen, 2012], puis d'un second article dans lequel nous avons comparé quantitativement les différents modèles proposés pour expliquer l'anisotropie de la graine, et construit un diagramme de régime de la graine donnant le régime dominant en fonction des deux paramètres les plus important pour ce problème : la nature (stabilisante ou déstabilisante) et l'amplitude de la stratification thermosolutale, et la viscosité de la graine [Lasbleis & Deguen, 2015]. Dans ce qui suit, je me concentrerai sur le régime où le changement de phase à l'ICB a le plus d'effet : la convection naturelle, qu'elle soit d'origine thermique ou thermo-compositionelle (partie 3.2.2).

3.2.2 Convection naturelle

Convection thermique

J'ai étudié le problème de la convection thermique dans une sphère avec des conditions limites permettant la fusion ou la cristallisation à l'ICB en utilisant une combinaison d'approches théoriques (analyses de stabilité linéaire, modèles de convection développée) et numériques. Au vu de la forte viscosité de la graine, l'inertie peut être négligée et le problème ne dépend que de deux nombres sans-dimension, un nombre de Rayleigh Ra et le nombre $\mathcal{P}$ caractérisant les conditions limites à l'ICB.

Nos résultats montrent que les conditions limites peuvent avoir un effet spectaculaire sur le mode de convection. La figure 3.2 montre le nombre de Rayleigh critique en fonction de $\mathcal{P}$, pour des perturbations de degrés harmoniques $l = 1$, 2, 3, et 4, ainsi que la forme (lignes de courant) du premier mode instable pour trois valeurs de $\mathcal{P}$. Suivant la valeur de $\mathcal{P}$, deux régimes très différents sont possibles :

1. Lorsque $\mathcal{P} \gg 1$, les conditions limites approchent les conditions imperméables usuelles et la convection prend une forme similaire à ce qui est observé classiquement pour la convection forcée par chauffage interne. Le premier mode instable consiste en une cellule convective de degré 1 tel qu'obtenu par Chandrasekhar [1961] ; à plus haut Ra, des calculs numériques montrent que la convection devient instationnaire puis chaotique (figure 3.3 à $\mathcal{P} = 10^3$). Nous avons étudié ce régime à l'aide de simulations numériques, et développé des lois d'échelles prédisant la vitesse caractéristique de convection, la largeur des cellules de convection, et le taux de fusion associé à la déformation de l'ICB par la convection [Deguen *et al.*, 2013].
2. Lorsque $\mathcal{P} \ll 1$, la fusion/cristallisation à l'ICB est aisée et l'initiation de la convection s'en trouve facilitée (la valeur du nombre de Rayleigh critique diminue lorsque $\mathcal{P}$ diminue).

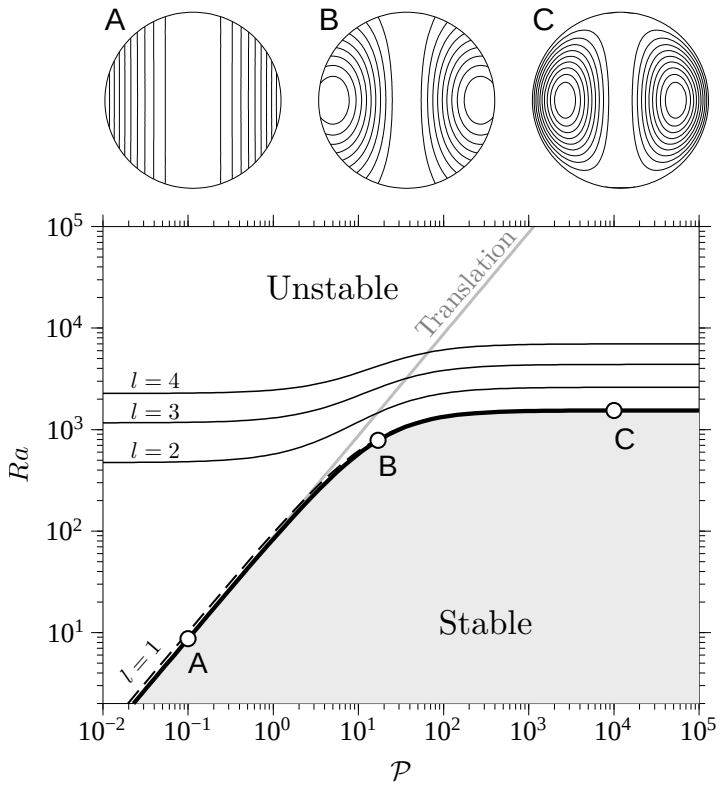

Figure 3.2

Courbes de stabilité marginale pour l'initiation de la convection thermique dans une sphère ayant des conditions limites à sa surface telles que décrites dans la partie 3.1. Les courbes donnent le nombre de Rayleigh critique Ra_c (la valeur du nombre de Rayleigh au dessus duquel une perturbation donnée grandit) en fonction du nombre $\mathcal{P}$, pour des perturbations de degrés harmoniques $l = 1$, 2, 3, et 4. On montre aussi sur cette figure la forme (lignes de courant) du premier mode instable pour trois valeurs de $\mathcal{P}$: $\mathcal{P} = 0.1$ (sous figure A), $\mathcal{P} = 17$ (sous figure B), et $\mathcal{P} = 10^4$ (sous figure C). D'après Deguen *et al.* [2013].

La possibilité d'un changement de phase diminue la valeur du nombre de Rayleigh critique quelque soit le degré harmonique de la perturbation, mais l'effet est particulièrement important pour les perturbations de degré 1.

L'effet d'une diminution de $\mathcal{P}$ est particulièrement drastique pour l'initiation du mode de convection de degré 1, pour lequel on peut montrer que le nombre de Rayleigh critique chute lorsque l'on diminue $\mathcal{P}$. Le premier mode instable prend la forme d'une translation, avec cristallisation sur un hémisphère et fusion sur l'autre. Dans cette limite, l'analyse de stabilité montre que le nombre sans dimension pertinent est le rapport $Ra/\mathcal{P}$, qui est indépendant de la viscosité, un résultat cohérent avec le fait que le premier mode instable est une translation sans déformation. Ce mode reste dominant dans des conditions de plus haut Rayleigh (figure 3.3 à $\mathcal{P} = 1$). Nous avons développé un modèle analytique prédisant la vitesse de translation et le taux de fusion associé en fonction du nombre de Rayleigh et de $\mathcal{P}$, et retrouvé numériquement les prédictions théoriques [Alboussière *et al.*, 2010; Deguen *et al.*, 2013].

Nous avons étudié en détail la transition entre le mode de translation et la convection par panaches, qui a lieu de manière assez abrupte lorsque $\mathcal{P}$ dépasse une valeur de l'ordre de 30. Cette transition est due au caractère barocline du champ de température dans le régime de translation (figure 3.3 à $\mathcal{P} = 1$) : les isothermes n'étant pas parallèles aux surfaces isopotentielles, la distribution de température générée par la translation induit un écoulement secondaire. Cet écoulement modifie le champ de température et diminue l'amplitude de sa composante de degré 1, ce qui diminue la flottabilité disponible pour maintenir la translation. On montre que

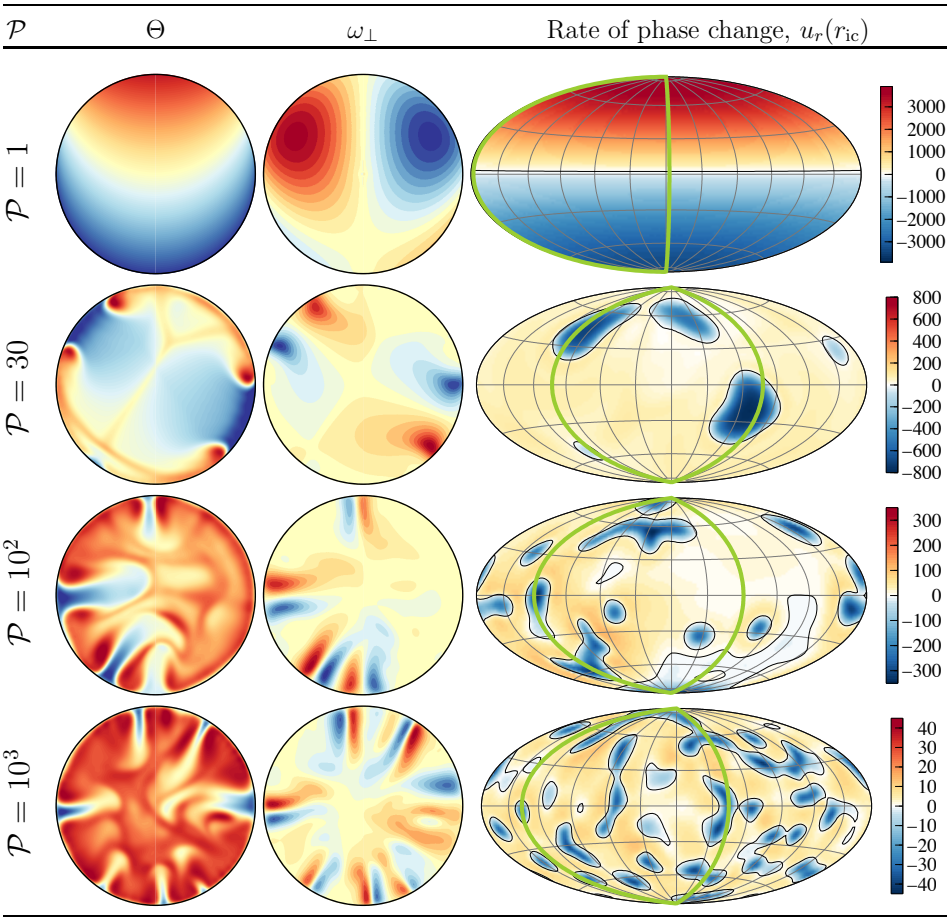

Figure 3.3

Résultats de simulations numériques de convection dans la graine à $Ra = 10^7$ et $\mathcal{P} = 1$, 30, 10^2, et 10^3. Sont représentés les champs de température potentielle Θ et de vorticité $\omega_\perp$ dans une section de la graine (deux premières colonnes), et des cartes du taux de changement de phase à l'ICB (troisième colonne). D'après Deguen *et al.* [2013].

le rapport entre la vitesse de cet écoulement et la vitesse de translation est proportionnel à $\mathcal{P}$, sans dépendance en Ra [Deguen *et al.*, 2013, 2018], ce qui explique pourquoi la transition entre les deux régimes est fixée par la seule valeur de $\mathcal{P}$.

La valeur de $\mathcal{P}$ à laquelle on observe la transition de régime est de l'ordre de 30. En estimant le temps caractéristique de changement de phase τ_ϕ à un millier d'année [Alboussière *et al.*, 2010; Buffett & Matsui, 2015], cette valeur correspond à une viscosité de l'ordre de 10^{18} Pa.s. La graine peut donc translater si sa viscosité est supérieure à $\sim 10^{18}$ Pa.s. La gamme d'estimations publiées de la viscosité s'étendant de 10^{11} Pa.s à 10^{22} Pa.s, il est difficile de conclure. On peut cependant noter que les estimations les plus récentes [Reaman *et al.*, 2011, 2012] favorisent une viscosité haute, de l'ordre de 10^{21} Pa.s à 10^{22} Pa.s, ce qui permettrait l'existence du régime de translation.

Convection double-diffusive

Comme discuté dans la partie 3.2.1, les valeurs hautes de conductivité thermiques obtenues depuis 2012 impliquent que le profil de température dans la graine est sans doute sous-adiabatique, et donc stable vis-à-vis de la convection. En revanche, il semble possible que le profil de composition dans la graine soit déstabilisant [Gubbins *et al.*, 2013; Labrosse, 2014]. Il est connu que dans ces conditions le fort contraste de diffusivité entre les champs de température et de composition peut permettre le développement de mouvements de convection même si l'effet (stabilisant) de la température sur la densité semble plus fort que l'effet (déstabilisant)

de la composition. Ce type de convection, dite *double-diffusive*, a été identifié initialement dans le contexte de la dynamique de l'océan [Stommel *et al.*, 1956; Stern, 1960], puis étudié dans des contextes assez variés [*e.g.* Huppert & Turner, 1981]. Nos travaux montrent qu'un régime de *translation double-diffusive* est possible lorsque $\mathcal{P} \lesssim 30$ et que l'opposé du nombre de Rayleigh thermique, $-Ra$, est inférieur à environ 6×10^3, dès lors que le profil de composition est déstabilisant [Deguen *et al.*, 2018]. Contrairement au cas de la translation d'origine purement thermique, ce régime de translation double-diffusive n'est dominant qu'à des nombres de Rayleigh modérés. En pratique, cela revient à dire que le régime de translation ne peut être dominant que si la viscosité de la graine est suffisamment élevée. Cette valeur limite dépend fortement de la taille de la graine : elle est d'environ 3×10^{21} Pa.s pour la taille actuelle de la graine, et par exemple de 10^{17} Pa.s lorsque la graine ne faisait que 200 km de rayon.

Implications pour la structure de la graine et du noyau externe

La translation de la graine pourrait expliquer plusieurs observations assez énigmatiques :

1. **L'asymétrie hémisphérique de la graine** – Un régime de translation de la graine avec une direction de translation d'Est en Ouest est clairement un candidat intéressant pour expliquer l'asymétrie hémisphérique de la graine. En pratique cependant, le mécanisme qui produirait les variations de vitesse et d'atténuation sismique reste à élucider. Plusieurs propositions ont été faites (croissance des cristaux de fer [Monnereau *et al.*, 2010] ou évolution de la texture acquise lors de solidification [Bergman *et al.*, 2010, 2014; Al-Khatatbeh *et al.*, 2013] au cours de la translation), mais ces propositions sont pour l'instant restées essentiellement qualitatives. La situation est la même pour l'autre famille de modèles, qui propose que l'asymétrie hémisphérique soit le signe d'une croissance hétérogène de la graine, qui serait due à l'effet sur la convection dans le noyau externe des variations spatiales du flux de chaleur à la frontière noyau-manteau [Sumita & Olson, 1999; Aubert *et al.*, 2008; Sreenivasan & Gubbins, 2011]. Un avantage du modèle de translation est qu'il produirait des variations abruptes des propriétés sismiques entre les deux hémisphères, ce qui semble plus cohérent avec les observations sismiques que les variations plus graduelles que l'on attendrait du modèle de croissance hétérogène [Geballe *et al.*, 2013].

2. **La couche F** – Un des attraits du modèle de translation est qu'il permet de proposer un mécanisme de formation de la couche F observée à la base du noyau externe [Souriau & Poupinet, 1991; Song & Helmberger, 1992; Yu *et al.*, 2005; Zou *et al.*, 2008; Cormier, 2009; Cormier *et al.*, 2011]. La présence de cette couche est difficile à réconcilier avec le modèle "classique" de convection dans le noyau externe, dans lequel la cristallisation de la graine s'accompagne d'un flux d'éléments légers à la base du noyau. Dans ce modèle, on attend donc la formation d'une couche compositionnelle instable (plus d'éléments légers en profondeur) et très fine en raison de la faible viscosité du noyau. Ce que semble montrer la sismologie est au contraire la présence d'une couche appauvrie en éléments légers et très épaisse ($\sim$ 200 km), ce qui est en désaccord total avec la vision classique de la convection dans le noyau. Le modèle que nous proposons repose sur l'idée que la graine puisse fondre localement, comme l'ont montré nos modèles de convection dans la graine. Le produit de cette fusion est du fer presque pur, dense, qui s'étend à la surface de la graine par écoulement gravitaire. Dans les zones où la graine cristallise, des panaches de liquide riche en éléments légers entraînent partiellement cette couche et permettent un mélange radial pouvant donner lieu à une variation continue de composition entre l'ICB et le noyau externe. Nous avons testé ce modèle dans une série d'expériences qui ont montré qu'il était possible de maintenir dynamiquement une couche stratifiée si le taux de fusion est comparable au taux de solidification moyen [Alboussière *et al.*, 2010]. Le modèle de translation convective que nous avons proposé s'accompagne de taux de

fusion suffisamment forts pour permettre la formation d'une telle couche [Alboussière *et al.*, 2010; Deguen *et al.*, 2013].

3. **L'existence d'un gyre asymétrique dans le noyau externe** – La translation de la graine impose des conditions limites fortement hétérogène pour la convection du noyau et la géodynamo : le flux de flottabilité à l'ICB est négatif dans l'hémisphère qui fond (formation de liquide appauvri en éléments légers), et positif au niveau de l'hémisphère qui cristallise. Ce forçage asymétrique pourrait avoir des conséquences observables pour le champ magnétique terrestre et l'écoulement dans le noyau. En utilisant des modèles numériques de la géodynamo, nous avons étudié l'effet d'un tel forçage sur la dynamo [Olson & Deguen, 2012; Deguen *et al.*, 2014*b*], et montré que l'écoulement résultant pouvait être qualitativement similaire au gyre asymétrique observé dans le noyau par Gillet *et al.* [2009]. Plus récemment, Aubert *et al.* [2013] et Aubert [2013] ont montré à l'aide de simulations numériques de la géodynamo qu'un flux de flottabilité asymétrique à l'ICB tel que prédit par le modèle de translation permet de mieux rendre compte de la structure du champ magnétique terrestre. Les modèles fonctionnent le mieux pour une vitesse de translation similaire à la vitesse de croissance moyenne de la graine. Cette vitesse de translation est cohérente avec les prédictions dans le cas d'un régime de translation double-diffusive [Deguen *et al.*, 2018], mais faible comparée à ce que l'on prédit dans le cas d'une translation purement thermique [Alboussière *et al.*, 2010; Deguen *et al.*, 2013].

Le modèle de translation de la graine n'a cependant pas que des atouts :

1. Un modèle de translation Est-Ouest cohérent avec l'asymétrie hémisphérique ne permet pas facilement d'expliquer l'anisotropie sismique nord-sud de la graine.

2. Un second point, et peut être le plus important, est que le régime de translation ne peut exister que dans un domaine assez restreint de l'espace des paramètres : (i) Il faut nécessairement que le géotherme ou le profil de concentration dans la graine soit déstabilisant pour permettre l'initiation de la convection. C'est plausible mais incertain (partie 3.2.1). (ii) La viscosité de la graine doit être suffisamment forte (supérieure à 10^{18} Pa.s dans le cas d'une translation thermique, et 10^{21} Pa. dans le cas d'une translation double-diffusive). Là encore, il est possible que cette condition soit vérifiée, mais cela reste très incertain au vu de la gamme de valeurs de viscosité proposées dans la littérature.

3.3 Convection dans les manteaux planétaires primitifs

L'idée d'utiliser les conditions développées pour la graine dans d'autres contextes m'est venue lors d'un workshop organisé par Dave Yuen à Wuhan (Chine) en 2012. Lors de ce workshop, Shijie Zhong a donné une présentation très intéressante sur les structures de degré 1 dans les planètes du système solaire (asymétrie hémisphérique de la Lune et Mars, Encélade, ...). L'intention de Shijie était de suggérer des pistes d'explications de l'asymétrie hémisphérique de la graine à partir d'un panorama des modèles proposés pour expliquer d'autres structures de degré 1 observées dans le système solaire. Mais la transposition de notre approche à d'autres planètes est aussi possible : les conditions limites que l'on a développées pour la graine, et qui ont pour effet d'augmenter l'échelle spatiale horizontale de la convection, peuvent être pertinentes pour d'autres objets du système solaire.

À la suite de ce workshop, j'ai étudié la stabilité linéaire d'une coquille sphérique visqueuse chauffée en volume [Deguen, 2013]. Ces premiers travaux sur ce sujet ont par la suite motivé une collaboration avec Stéphane Labrosse et Thierry Alboussière. Stéphane porte depuis 2016 un projet ANR qui porte entre autres sur l'utilisation de ces conditions limites dans le contexte de la convection mantellique. Deux thèses et un post-doctorat sont en cours dans le cadre de ce projet ANR : les thèses d'Adrien Morison (encadrée par S. Labrosse et co-encadrée par T.

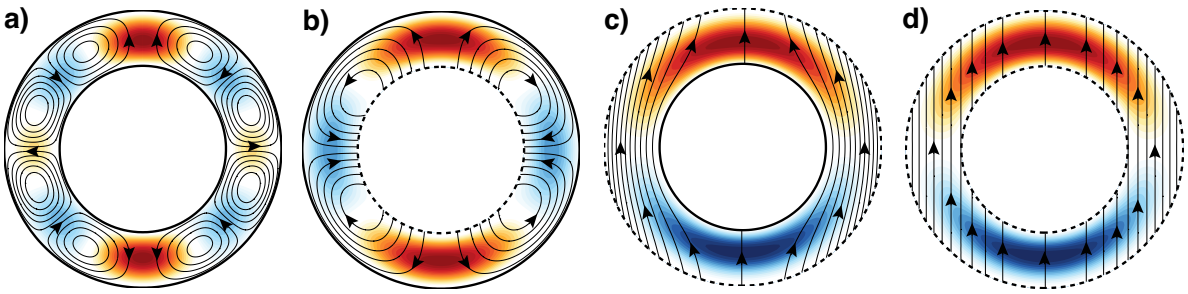

Figure 3.4

Forme (lignes de courant et perturbation du champ de température) du premier mode instable dans une coquille sphérique de rapport d'aspect (rapport rayon interne/rayon externe) égal à 0.6, pour plusieurs configurations de conditions limites : **a)** Frontières interne et externe imperméables : $(\mathcal{P}^-, \mathcal{P}^+) \gg 1$, **b)**Frontière interne perméable et frontière externe imperméable : $\mathcal{P}^- \ll 1, \mathcal{P}^+ \gg 1$, **c)** Frontière interne imperméable et frontière externe perméable : $\mathcal{P}^- \gg 1, \mathcal{P}^+ \ll 1$, et **d)** Frontières interne et externe perméables : $(\mathcal{P}^-, \mathcal{P}^+) \ll 1$. Adapté de Deguen [2013]

Alboussière et moi même), et de Daniela Bolrão (ETH Zurich), et le post-doctorat de Roberto Agrusta.

Analyses de stabilité

On considère ici une coquille sphérique formée d'un solide déformable cristallisant à partir d'une couche de liquide. On utilise les conditions limites présentées dans la partie 3.1 pour les deux interfaces, chacune étant caractérisée par un nombre de changement de phase ($\mathcal{P}^-$ pour la frontière interne, et $\mathcal{P}^+$ pour la frontière externe). Plusieurs configurations intéressantes sont possibles en fonction du mode de cristallisation : chacune des deux interfaces peut être au choix imperméable ($\mathcal{P}^{-,+} \gg 1$) ou perméable ($\mathcal{P}^{-,+} \ll 1$). J'ai donc réalisé une analyse de stabilité linéaire du jeu d'équations décrivant ce problème, pour des valeurs de $\mathcal{P}^-$ et $\mathcal{P}^+$ quelconques. La figure 3.4 montre la forme (lignes de courant et perturbation du champ de température) du premier mode instable dans une coquille sphérique de rapport d'aspect (rapport rayon interne/rayon externe) égal à 0.6, pour plusieurs configurations de conditions limites. Comme dans le cas d'une sphère pleine (partie 3.2.2), la géométrie de la convection dans une coquille sphérique est fortement modifiée par la possibilité d'un changement de phase aux frontières :

1. **Frontières interne et externe imperméables :** $(\mathcal{P}^-, \mathcal{P}^+) \gg 1$ **(figure 3.4a)**. Il s'agit du régime de convection Rayleigh-Bénard classiquement étudié, et qui nous servira de référence. Dans cette limite, le premier mode de convection prend la forme de cellules de convection dont la dimension horizontale est proche de l'épaisseur de la couche.

2. **Frontière interne perméable et frontière externe imperméable :** $\mathcal{P}^- \ll 1, \mathcal{P}^+ \gg 1$ **(figure 3.4b)**. Lorsque l'on rend perméable la limite interne en supposant de $\mathcal{P}^- \ll 1$, la dimension horizontale des cellules de convection devient significativement plus grande (à peu près le double) que dans le cas de référence imperméable. Les lignes de courant traversent la limite interne de la couche, ce qui montre que la convection y induit fusion et cristallisation. Cette configuration peut être pertinente pour l'étude de la dynamique de la couche de glace externe des satellites glacés où la présence d'un océan profond est avéré (Europe, Ganymède, Callisto, Titan, Encélade, ...), mais aussi pour la convection dans le manteau terrestre primitif si un océan de magma basal a été présent [Labrosse *et al.*, 2007].

3. **Frontière interne imperméable et frontière externe perméable :** $\mathcal{P}^- \gg 1, \mathcal{P}^+ \ll 1$ **(figure 3.4c)**. Dans cette situation l'effet d'une condition limite perméable est encore plus importants que dans le cas où c'est la frontière interne qui est ouverte. Malgré le

rapport d'aspect étudié pour lequel la couche solide est relativement fine, le premier mode instable est un mode de degré 1 contournant la frontière interne imperméable. Ce mode de déformation reste le premier à émerger même pour des rapports d'aspect approchant 1. Cette configuration est pertinente dans le cas d'un manteau silicaté cristallisant par le bas à partir d'un océan de magma (manteaux de la Lune ou de Mars pas exemple), ou pour la convection dans les couches de glace profonde de certains satellites glacés.

4. **Frontières internes et externes perméables :** $(\mathcal{P}^-, \mathcal{P}^+) \ll 1$ **(figure 3.4d)**. Lorsque les deux frontières sont perméables, le premier mode de convection est un mode de translation de la coquille sphérique, similaire à celui obtenu dans le cas d'une sphère pleine (partie 3.2.2). Comme dans le cas de la sphère pleine, le nombre de Rayleigh critique de ce régime est beaucoup plus faible que pour des régimes plus classiques, en raison de l'absence de dissipation visqueuse dans la couche solide. Le nombre de Rayleigh critique est proportionnel à la moyenne de $\mathcal{P}^-$ et $\mathcal{P}^+$ pondérée par l'aire des frontières interne et externe.

Pour étendre cette première étude, Adrien Morison a développé pendant son stage de M2 et le début de sa thèse un outil d'analyse de stabilité linéaire utilisant une décomposition en harmoniques sphériques et une décomposition en polynômes de Chebyshev pour la variation radiale des coefficients des harmoniques sphériques. L'approche est numériquement un peu plus lourde que la décomposition en harmoniques sphériques et fonctions de Bessel sphériques que j'ai utilisée [Deguen, 2013], mais a l'avantage de pouvoir être utilisée pour des profils de gravité, température, et composition pouvant avoir une dépendance radiale de forme arbitraire. Avec cette approche, Adrien a pu réaliser l'analyse de stabilité linéaire pour la convection dans une coquille sphérique avec une différence de température imposée entre les deux frontières. Les résultats sont qualitativement similaires à ceux que j'ai obtenus pour de la convection avec chauffage interne. Cette étude pourra être étendue au cas d'un mode de chauffage mixte.

Une analyse faiblement non-linéaire en géométrie cartésienne [Labrosse *et al.*, 2018] et des simulations numériques de convection développée réalisées par Adrien Morison montrent que l'effet des conditions limites reste fort lorsque l'on s'éloigne du seuil de l'instabilité. Le fusion/cristallisation à l'une ou l'autre des frontières favorise l'émergence de mouvements convectifs de plus grande échelle, et tend à augmenter la vigueur de la convection et l'efficacité du transport de chaleur.

3.4 Travaux en cours et perspectives

Effet d'un océan magmatique basal sur la dynamique du manteau solide

Une première perspective concerne l'effet d'un océan magmatique basal sur la dynamique et l'évolution thermique du manteau terrestre. Cette thématique est actuellement portée par Adrien Morison dans le cadre de sa thèse, Roberto Agrusta dans le cadre de son post-doctorat, et Stéphane Labrosse, avec des contributions plus ponctuelles de la part de Thierry Alboussière et de moi même. Adrien Morison a implémenté dans le code StaggYY de Paul Tackley nos conditions limites semi-perméables, ainsi que la prise en compte de l'évolution de l'épaisseur de la partie cristallisée du manteau, et l'évolution thermo-solutale de l'océan de magma basal. Adrien dispose donc maintenant d'un outil permettant de modéliser la dynamique et l'évolution du manteau terrestre sur de longues échelles de temps.

Ce code sera notamment utilisé pour étudier la formation et l'évolution d'hétérogénéités chimiques dans le manteau, et l'évolution thermique à long terme du système manteau solide-océan de magma-noyau.

Généralisation de la formulation des conditions limites semi-perméables

Les conditions limites telles qu'on les a développées et utilisées reposent sur un certain nombres d'hypothèses, dont certaines sont discutables.

1. À cours terme, un premier point à étudier sera l'effet des flux de chaleur et de composition côté solide apparaissant dans l'équation (3.6). Nous avons jusqu'ici négligé ces termes, ce qui est raisonnable pour la graine (nous avons pu le vérifier *a posteriori*), mais peut-être pas dans le cas de la convection développée dans un manteau solide ou une couche de glace (le nombre $\mathcal{S}^*$ peut être d'ordre 1). L'implémentation de ces termes dans un modèle numérique de convection ne devrait pas poser de problème, les flux de chaleur et de composition pouvant être calculés à chaque pas de temps à partir des champs de température et de composition.

2. À plus long terme, il faudra s'attaquer à un point plus délicat, qui est l'hypothèse implicite dans notre formulation de l'absence d'une zone biphasique (zone de mush ou slurry) au niveau de l'interface. La présence d'une zone de mush au niveau de l'interface est probable dans tous les applications envisagées. La solidification de zones de mush est un problème classique [*e.g.* Worster, 1991] mais complexe. Des travaux récents ont proposé des modèles paramétrés de la convection dans une zone de mush, permettant de prédire les flux de chaleur et de composition associés à la convection interstitielle [Wells *et al.*, 2011, 2013; Rees Jones & Worster, 2013*a*,*b*]. La fusion d'une zone de mush a comparativement été moins étudiée que la cristallisation [*e.g.* Hallworth *et al.*, 2004, 2005; Yu *et al.*, 2015; Huguet *et al.*, 2016] et nous sommes encore assez loin d'être en mesure de paramétrer de manière simple la fusion d'une zone de mush.

Annexes

3.A Dérivation des conditions limites

On considère ici une couche d'un solide déformable, en contact avec une couche de liquide en équilibre de phase avec le solide. On suppose que le solide et le liquide sont des mélanges binaires de compositions différentes. On note c_s et c_l les concentrations en soluté des phases solide et liquide. L'interface séparant le solide et le liquide est déformable, de topographie h (définie par rapport à la position de l'isopotentielle coïncidant en moyenne avec l'interface). On se place dans un repère sphérique (r, θ, ϕ) et on note $\mathbf{v} = (v_r, v_\theta, v_\phi)$ le champ de vitesse dans la couche solide. L'interface est supposée à l'équilibre thermodynamique et peut se déplacer soit par advection par le champ de vitesse $\mathbf{v}$, soit par changement de phase en fonction des valeurs locales des flux de chaleur et de soluté de part et d'autre de l'interface. Les conditions limites vérifiées à cette interface sont :

1. une condition cinématique décrivant l'évolution de la topographie $h(\theta, \phi)$ de l'interface :

$$\frac{Dh}{Dt} = v_r + V_r \tag{3.11}$$

où $D(\cdot)/Dt$ est la dérivée lagrangienne, et V_r est la vitesse de changement de phase dans la direction radiale (l'épaisseur de solide créée ou enlevée par unité de temps), par convention comptée positive en cas de solidification, et négative en cas de fusion.

2. les conditions exprimant la conservation de la chaleur (condition de Stefan) et du soluté à l'interface :

$$\rho_s \, L \, V_r = (\mathbf{q}_l - \mathbf{q}_s) \cdot \boldsymbol{e_r}, \tag{3.12}$$

$$(c_s^i - c_l^i) \, V_r = (\mathbf{q}_l^\chi - \mathbf{q}_s^\chi) \cdot \boldsymbol{e_r}, \tag{3.13}$$

où $\rho_{s,l}$ est la masse volumique du solide ou du liquide, L la chaleur latente, $q_{s,l}$ le flux de chaleur à l'interface du côté du solide et du liquide, $c_{s,l}^i$ la concentration de soluté à l'interface dans le solide ou le liquide, et $q_{s,l}^\chi$ le flux de soluté à l'interface du côté du solide et du liquide.

3. deux conditions exprimant l'équilibre thermodynamique à l'interface.

(i) La température de l'interface est égale à la température du liquidus à la pression et à la composition de l'interface :

$$T(h) = T_\mathrm{L}(h), \tag{3.14}$$

$$= T_\mathrm{L}^0 - m_P \rho_l g h - m_c (c_l^i - c_l^0), \tag{3.15}$$

où $m_P = \partial T_L / \partial P$, $m_c = \partial T_L / \partial c$, ρ_l est la masse volumique de la phase liquide, g l'accélération de la gravité, c_l^0 la concentration moyenne de soluté dans le liquide, et T_L^0 la température du liquidus pour une concentration c_l^0 en l'absence de topographie.

(ii) La concentration en soluté varie de manière discontinue à l'interface, le rapport des concentrations étant fixé par le diagramme de phase. En notant k le coefficient de partage du soluté, les concentrations à l'interface côté solide (c_s^i) et côté liquide (c_l^i) sont liées par

$$k = \frac{c_s^i}{c_l^i}. \tag{3.16}$$

4. la continuité de la contrainte à l'interface. Dans le cas d'une topographie h de faible amplitude (par rapport à l'échelle caractéristique des variations latérales de topographie), la continuité de la contrainte normale peut s'écrire

$$-p + 2\eta \frac{\partial v_r}{\partial r} = \Delta\rho g h, \tag{3.17}$$

qui exprime un équilibre entre les contraintes verticales induites par la convection solide et le poids de la topographie. La continuité de la contrainte tangentielle nous permet de supposer pour la convection solide une condition de surface libre (contraintes tangentielles nulles), ce qui est justifié par le très grand contraste de viscosité et par le fait que les contraintes induites par le liquide varient sur une échelle de temps très petite par rapport à celle de la convection solide, et peuvent être supposées de moyenne nulle [2].

L'application de ce jeu de conditions limites à la couche solide nécessite la connaissance du flux de chaleur et du flux de soluté du côté liquide (équations (3.12) et (3.13)), qui dépendent de l'écoulement dans le liquide. On pourrait en théorie traiter simultanément la convection dans le liquide et le solide, mais des simulations numériques directes sont impraticables en raison des échelles de temps extrêmement différentes : la résolution temporelle de la convection dans le liquide nécessite un pas de temps extrêmement petit par rapport au temps caractéristique de la convection solide.

L'approche que nous avons choisie et développée avec Thierry Alboussière est la suivante : l'idée est de paramétrer l'effet de la convection dans le liquide à l'aide d'une loi d'échelle reliant la vitesse de changement de phase V_r à l'amplitude $h(\theta, \phi)$ de la topographie. La condition cinématique sur h permet ensuite d'obtenir une relation entre h et le champ de vitesse, qui peut ensuite être injecté dans l'équation de continuité de la contrainte normale (Eq. (3.17)) pour faire disparaitre la topographie du problème. Pour cela, on estime les flux côté liquide en supposant un transport dominé par l'advection, ce qui permet d'écrire

$$q^l \sim \rho_l c_{p,l} v' \delta\Theta = A_T \rho_l c_{p,l} v' \delta\Theta, \tag{3.18}$$

$$q^l_\chi \sim v' \delta c = A_\chi v' \delta c \tag{3.19}$$

où $\delta\Theta$ est la différence de température potentielle entre l'interface et la couche liquide, supposée bien mélangée et isentropique, et $\delta c = c_l^i - c_l^0$ la différence de concentration en soluté entre l'interface et la couche liquide, v' la magnitude des vitesses convectives dans le liquide. A_T et A_χ sont deux paramètres sans dimension que l'on peut espérer être de l'ordre de 1 si les lois d'échelles (3.18) et (3.19) sont effectivement vérifiées. Dans cette approche, la vigueur de la convection liquide est paramétrée par la valeur de v'. La différence de température potentielle $\delta\Theta$ est obtenue en soustrayant à la température de l'interface, donnée par l'équation (3.15), la différence de température le long d'une isentrope entre l'altitude h de l'interface et la position moyenne de l'interface :

$$\delta\Theta = (m_{\text{is}} - m_P)\rho_l g h - m_c(c_l^i - c_l^0), \tag{3.20}$$

$$= (m_{\text{is}} - m_P)\rho_l g h - m_c\, \delta c, \tag{3.21}$$

où $m_{\text{is}} = \partial T/\partial P|_s$ est la dérivée par rapport à la pression de la température le long d'une isentrope. $\delta\Theta$ est nulle en moyenne, négative dans le cas d'une topographie positive, et positive dans le cas d'une topographie en creux.

En combinant les équations (3.12) et (3.13) avec les estimations des flux côté liquide données par (3.18) et (3.19) et l'expression (3.21) de $\delta\Theta$, on peut obtenir une expression reliant

2. Des exceptions peuvent être envisagées : rotation de la graine, convection dans le liquide forcée par des conditions aux limites hétérogènes, etc...

la vitesse de changement de phase à la topographie, que l'on peut écrire

$$V_r = -\frac{h}{\tau_\phi} - \frac{\dfrac{q^s}{\rho_l c_{p,l}} + q^s_\chi}{A_T \dfrac{\rho_s}{\rho_l}\dfrac{L}{c_{p,l}} + A_\chi (1-k) m_c c_l^i}, \tag{3.22}$$

en introduisant

$$\tau_\phi = \frac{A_T \dfrac{\rho_s L}{\rho_l c_{p,l}} + A_\chi (1-k) m_c c_l^i}{\rho_l g (m_P - m_{\mathrm{is}}) v'} \tag{3.23}$$

le temps caractéristique de changement de phase, caractérisant la réponse de la topographie au transport de chaleur et de soluté dans la phase liquide. La concentration c_l^i à l'interface n'est pas connue (c'est une des variables du problème, qui dépend en particulier de la vigueur de la convection), mais elle doit être assez proche de c_0 si la convection est vigoureuse. Dans le cas de la graine (où $L/c_{p,l} \sim 1000$ K, $m_c \sim 100$ K.wt.%, et $c_l^i \sim 10$ wt.%), les termes thermique et solutal sont du même ordre de grandeur.

En insérant l'équation (3.22) dans la condition limite cinématique (3.11) on obtient une équation pronostique pour l'évolution de la topographie,

$$\frac{Dh}{Dt} = v_r - \frac{h}{\tau_\phi} - \frac{\dfrac{q^s}{\rho_l c_{p,l}} + q^s_\chi}{A_T \dfrac{\rho_s}{\rho_l}\dfrac{L}{c_{p,l}} + A_\chi \dfrac{1-k}{k} m_c c_s^i}, \tag{3.24}$$

ne faisant plus apparaître explicitement de quantités associées à la convection côté liquide. On a donc à ce stade un jeu de conditions limites complet ne faisant intervenir que des quantités associées à la convection côté solide, données par l'équation (3.24) pour l'évolution de la topographie, les équations (3.15) et (3.16) pour la température et la composition à l'interface, et la continuité de la contrainte (équation (3.17) pour la contrainte normale).

On peut simplifier un peu plus ces conditions limites en supposant que la topographie varie lentement par rapport aux temps dynamiques τ_ϕ et h/v_r (topographie quasi-statique). C'est une hypothèse raisonnable pour des problèmes de convection dans des couches solides, où le système convectif varie sur des échelles de temps longues ($1 - 100$ Ma). Dans ces conditions, l'équation (3.24) permet d'obtenir une expression de h en fonction de v_r et des flux de température et de composition côté solide,

$$h = \tau_\phi v_r - \frac{\dfrac{q^s}{\rho_l c_{p,l}} + q^s_\chi}{\rho_l g (m_P - m_{\mathrm{is}}) v'}, \tag{3.25}$$

qui peut ensuite être inséré dans la condition de continuité de la contrainte normale [équation (3.17)],

$$-p + 2\eta \frac{\partial v_r}{\partial r} = \Delta\rho g \tau_\phi v_r - \frac{\Delta\rho}{\rho_l} \frac{\dfrac{q^s}{\rho_l c_{p,l}} + q^s_\chi}{(m_P - m_{\mathrm{is}}) v'}. \tag{3.26}$$

Les conditions limites deviennent alors indépendantes de la topographie, qui devient une variable muette du problème.

En introduisant R, ΔT et Δc des échelles caractéristiques de longueur, température, et composition du problème, on peut construire une échelle de vitesse κ_T/R et une échelle de pression $\eta\kappa_T/R^2$, où κ_T est la diffusivité thermique dans la phase solide. En adimensionnant les variables du problème à l'aide de ces échelles caractéristiques, l'équation (3.26) devient

$$-\tilde{p} + 2\frac{\partial \tilde{v}_r}{\partial \tilde{r}} = \mathcal{P}\left[\tilde{v}_r - \frac{1}{\mathcal{S}^*}\left(\tilde{q}^s + \frac{\kappa_\chi \Delta c}{\kappa_T \Delta T}\tilde{q}^s_\chi\right)\right] \tag{3.27}$$

où $(\tilde{p}, \tilde{v}_r, \tilde{r}, \tilde{q}^s, \tilde{q}^s_\chi)$ correspondent aux versions adimensionnées de $(p, v_r, r, q^s, q^s_\chi)$, et où

$$\mathcal{P} = \frac{\Delta\rho\, g\, R\, \tau_\phi}{\eta}, \tag{3.28}$$

$$\mathcal{S}^* = A_T \frac{\rho_s L}{\rho_l c_{p,l} \Delta T} + A_\chi \frac{1-k}{k} \frac{m_c c_s^i}{\Delta T}. \tag{3.29}$$

Le nombre $\mathcal{P}$ compare le temps caractéristique de changement de phase τ_ϕ au temps visqueux $\eta/(\Delta\rho\, g\, R)$, qui dans ce contexte peut être interprété comme étant le temps nécessaire à la convection dans la couche solide pour construire une topographie dont le poids équilibre les contraintes normales convectives. Le nombre $\mathcal{S}^*$ s'apparente à un nombre de Stefan dans la limite d'un problème purement thermique (rapport entre chaleur latente de changement de phase L et chaleur spécifique disponible $c_p \Delta T$).

En pratique nous avons jusqu'ici négligé dans l'équation (3.27) la contribution des flux de chaleur et de soluté (limite $\mathcal{S}^* \to \infty$), et dans cette limite l'équation (3.27) se réduit à

$$-\tilde{p} + 2\frac{\partial \tilde{v}_r}{\partial \tilde{r}} = \mathcal{P}\tilde{v}_r, \tag{3.30}$$

qui montre que la vitesse radiale à l'interface (et donc la vitesse de changement de phase) est proportionnelle à la contrainte normale induite par la convection dans la couche solide. Dans la limite $\mathcal{P} \to \infty$, on doit avoir $\tilde{v}_r \to 0$ puisque la contrainte normale (terme à gauche du signe =) doit rester finie. On tend donc vers une condition d'interface imperméable classique. Dans la limite $\mathcal{P} \to 0$, la contrainte normale tend vers 0 puisque la vitesse $\tilde{v}_r$ doit rester finie, ce qui correspond à une condition limite de type perméable.

Bibliographie

Al-Khatatbeh, Y., Bergman, M., Lewis, D., Mason, Z., Zhu, L., & Rosenstock, S. Annealing of directionally solidified alloys revisited : No loss of solidification texture in Earth's inner core. *Phys. Earth Planet. Inter.*, **223** :32–39, 2013.

Alboussière, T., Deguen, R., & Melzani, M. Melting induced stratification above the Earth's inner core due to convective translation. *Nature*, **466** :744–747, 2010.

Andrault, D., Bolfan-Casanova, N., Nigro, G.L., Bouhifd, M.A., Garbarino, G., & Mezouar, M. Solidus and liquidus profiles of chondritic mantle : Implication for melting of the earth across its history. *Earth Planet. Sci. Lett.*, **304**(1) :251–259, 2011.

Arkani-Hamed, J. Formation of a solid inner core during the accretion of Earth. *J. Geophys. Res.*, **122**(5) :3248–3285, 2017.

Aubert, J., Amit, H., Hulot, G., & Olson, P. Thermochemical flows couple the Earth's inner core growth to mantle heterogeneity. *Nature*, **454**(7205) :758–761, 2008. ISSN 0028-0836. doi :10.1038/nature07109.

Aubert, J. Flow throughout the Earth's core inverted from geomagnetic observations and numerical dynamo models. *Geophys. J. Int.*, **192**(2) :537–556, 2013.

Aubert, J., Finlay, C.C., & Fournier, A. Bottom-up control of geomagnetic secular variation by the earth's inner core. *Nature*, **502**(7470) :219, 2013.

Badro, J., Brodholt, J.P., Piet, H., Siebert, J., & Ryerson, F.J. Core formation and core composition from coupled geochemical and geophysical constraints. *Proc. Nat. Acad. Sci.s*, **112**(40) :12 310–12 314, 2015.

Badro, J., Siebert, J., & Nimmo, F. An early geodynamo driven by exsolution of mantle components from Earth's core. *Nature*, **536**(7616) :326–328, 2016.

Batchelor, G. Heat convection and buoyancy effects in fluids. *Quart. J. R. Met. Soc.*, **80** :339–358, 1954.

Bergman, M., Lewis, D., Myint, I., Slivka, L., Karato, S., & Abreu, A. Grain growth and loss of texture during annealing of alloys, and the translation of Earth's inner core. *Geophys. Res. Lett.*, **37**(22) :L22 313, 2010. ISSN 0094-8276.

Bergman, M.I., Al-Khatatbeh, Y., Lewis, D.J., & Shannon, M.C. Deformation of directionally solidified alloys : Evidence for microstructural hardening of earth's inner core ? *Comptes Rendus Geoscience*, 2014.

Bond, D. & Johari, H. Effects of initial geometry on the development of thermals. *Experiments in Fluids*, **39** :591–601, 2005. doi :10.1007/s00348-005-0997-1.

Bond, D. & Johari, H. Impact of buoyancy on vortex ring development in the near field. *Experiments in Fluids*, **48** :737–745, 2010. doi :10.1007/s00348-009-0761-z.

Bouhifd, M.A., Gautron, L., Bolfan-Casanova, N., Malavergne, V., Hammouda, T., Andrault, D., & Jephcoat, A.P. Potassium partitioning into molten iron alloys at high-pressure : Implications for Earth's core. *Phys. Earth Planet. Inter.*, **160** :22–33, 2007. doi :10.1016/j.pepi.2006.08.005.

Buehler, J. & Papantoniou, D. On the motion of suspension thermals and particle swarms. *Journal of Hydraulic Research*, pages 643–653, 2001.

Buffett, B.A. Geodynamics estimates of the viscosity of the Earth's inner core. *Nature*, **388** :571–573, 1997.

Buffett, B.A. & Matsui, H. The fluid dynamics of inner-core growth. *Phys. Earth Planet. Inter.*, **243** :22–29, 2015.

Bush, J.W.M., Thurber, B.A., & Blanchette, F. Particle clouds in homogeneous and stratified envi-

ronments. *J. Fluid Mech.*, **489** :29–54, 2003.

Canup, R.M., Righter, K., & et al. *Origin of the earth and moon.* Origin of the earth and moon, edited by R.M. Canup and K. Righter and 69 collaborating authors. Tucson : University of Arizona Press ; Houston : Lunar and Planetary Institute, c2000. (The University of Arizona space science series), 2000.

Chabot, N., Draper, D., & Agee, C. Conditions of core formation in the Earth : Constraints from Nickel and Cobalt partitioning. *Geochimica et Cosmochimica Acta*, **69**(8) :2141–2151, 2005. ISSN 00167037. doi :10.1016/j.gca.2004.10.019.

Chandrasekhar, S. *Hydrodynamic and hydromagnetic stability.* International Series of Monographs on Physics, Oxford : Clarendon, 1961.

Coltice, N. & Schmalzl, J. Mixing times in the mantle of the early earth derived from 2-d and 3-d numerical simulations of convection. *Geophys. Res. Lett.*, **33**(23), 2006.

Corgne, A., Keshav, S., Fei, Y., & McDonough, W.F. How much potassium is in the earth's core ? new insights from partitioning experiments. *Earth planet. Sci. Lett.*, **256** :567–576, 2007.

Cormier, V.F. A glassy lowermost outer core. *Geophys. J. Int.*, **179**(1) :374–380, 2009. ISSN 1365-246X. doi :10.1111/j.1365-246X.2009.04283.x.

Cormier, V.F., Attanayake, J., & He, K. Inner core freezing and melting : Constraints from seismic body waves. *Phys. Earth Planet. Inter.*, **188** :163–172, 2011. ISSN 0031-9201. doi :DOI:10.1016/j.pepi.2011.07.007.

Cottrell, E., Walter, M.J., & Walker, D. Metal-silicate partitioning of tungsten at high pressure and temperature : Implications for equilibrium core formation in Earth. *Earth Planet. Sci. Lett.*, **281** :275–287, 2009. doi :10.1016/j.epsl.2009.02.024.

Davies, R.M. & Taylor, G. The Mechanics of Large Bubbles Rising through Extended Liquids and through Liquids in Tubes. *Royal Society of London Proceedings Series A*, **200** :375–390, 1950.

de Koker, N., Steinle-Neumann, G., & Vlcek, V. Electrical resistivity and thermal conductivity of liquid Fe alloys at high P and T, and heat flux in Earth's core. *Proc. Nat. Acad. Sci.*, **109**(11) :4070–4073, 2012.

Deguen, R. Structure and dynamics of Earth's inner core. *Earth Planet. Sci. Lett.*, **333–334** :211–225, 2012.

Deguen, R. Thermal convection in a spherical shell with melting/freezing at either or both of its boundaries. *Journal of Earth science*, **24**(5) :669–682, 2013.

Deguen, R. Bounds on metal-silicate equilibration conditions during core formation. in prep.

Deguen, R., Alboussière, T., & Cardin, P. Thermal convection in Earth's inner core with phase change at its boundary. *Geophys. J. Int.*, **194**(3) :1310–1334, 2013.

Deguen, R., Alboussière, T., & Labrosse, S. Double-diffusive translation of earth's inner core. *Geophysical Journal International*, **214**(1) :88–107, 2018.

Deguen, R. & Cardin, P. Tectonic history of the Earth's inner core preserved in its seismic structure. *Nature Geoscience*, **2** :419–422, 2009.

Deguen, R. & Cardin, P. Thermo-chemical convection in Earth's inner core. *Geophys. J. Int.*, **187** :1101–1118, 2011.

Deguen, R., Cardin, P., Merkel, S., & Lebensohn, R. Texturing in earth's inner core due to preferential growth in its equatorial belt. *Phys. Earth Planet. Inter.*, **188** :173–184, 2011*a*.

Deguen, R., Landeau, M., & Olson, P. Turbulent metal-silicate mixing, fragmentation, and equilibration in magma oceans. *Earth Planet. Sci. Lett.*, **391**(0) :274 – 287, 2014*a*. ISSN 0012-821X. doi : http://dx.doi.org/10.1016/j.epsl.2014.02.007.

Deguen, R., Olson, P., & Cardin, P. Experiments on turbulent metal-silicate mixing in a magma ocean. *Earth Planet. Sci. Lett.*, **310** :303–313, 2011*b*.

Deguen, R. & Risso, F. Immiscible turbulent thermals. *to be submitted to Journal of Fluid Mechanics*, in prep.

Deguen, R., Olson, P., & Reynolds, E. F-layer formation in the outer core with asymmetric inner core growth. *Comptes Rendus Geoscience*, 2014*b*.

Eggers, J. & Villermaux, E. Physics of liquid jets. *Reports on progress in physics*, **71**(3) :036 601, 2008.

Fischer, R.A., Nakajima, Y., Campbell, A.J., Frost, D.J., Harries, D., Langenhorst, F., Miyajima, N., Pollok, K., & Rubie, D.C. High pressure metal-silicate partitioning of Ni, Co, V, Cr, Si, and O.

Geochimica and Cosmochimica Acta, **167** :177–194, 2015.

Fischer, R.A. & Nimmo, F. Effects of core formation on the hf–w isotopic composition of the earth and dating of the moon-forming impact. *Earth and Planetary Science Letters*, **499** :257 – 265, 2018. ISSN 0012-821X. doi :https://doi.org/10.1016/j.epsl.2018.07.030.

Geballe, Z., Lasbleis, M., Cormier, V., & Day, E. Sharp hemisphere boundaries in a translating inner core. *Geophys. Res. Lett.*, **40**(9) :1719–1723, 2013.

Gessmann, C.K. & Wood, B.J. Potassium in the Earth's core ? *Earth Planet. Sci. Lett.*, **200** :63–78, 2002.

Gillet, N., Pais, M.A., & Jault, D. Ensemble inversion of time-dependent core flow models. *Geochem. Geophys. Geosyst.*, **10** :Q06 004, 2009.

Gomi, H., Hirose, K., Akai, H., & Fei, Y. Electrical resistivity of substitutionally disordered hcp Fe–Si and Fe–Ni alloys : Chemically-induced resistivity saturation in the Earth's core. *Earth Planet. Sci. Lett.*, **451** :51–61, 2016.

Gomi, H., Ohta, K., Hirose, K., Labrosse, S., Caracas, R., Verstraete, M.J., & Hernlund, J.W. The high conductivity of iron and thermal evolution of the earth's core. *Phys. Earth Planet. Inter.*, **224** :88–103, 2013.

Gubbins, D., Alfè, D., & Davies, C. Compositional instability of Earth's solid inner core. *Geophys. Res. Lett.*, **40** :1–5, 2013.

Gubbins, D., Masters, G., & Nimmo, F. A thermochemical boundary layer at the base of Earth's outer core and independent estimate of core heat flux. *Geophys. J. Int.*, **174** :1007–1018, 2008.

Gubbins, D., Sreenivasan, B., Mound, J., & Rost, S. Melting of the Earth's inner core. *Nature*, **473**(7347) :361–363, 2011.

Gurnis, M. Stirring and mixing in the mantle by plate-scale flow : Large persistent blobs and long tendrils coexist. *Geophysical Research Letters*, **13**(13) :1474–1477, 1986.

Halliday, A. Mixing, volatile loss and compositional change during impact-driven accretion of the earth. *Nature*, **427**(6974) :505–509, 2004. ISSN 0028-0836. doi :10.1038/nature02275.

Hallworth, M.A., Huppert, H.E., & Woods, A.W. Crystallization and layering induced by heating a reactive porous medium. *Geophysical research letters*, **31**(13), 2004.

Hallworth, M.A., Huppert, H.E., & Woods, A.W. Dissolution-driven convection in a reactive porous medium. *Journal of Fluid Mechanics*, **535** :255–285, 2005.

Hirose, K., Labrosse, S., & Hernlund, J. Composition and state of the core. *Annual Review of Earth and Planetary Sciences*, **41** :657–691, 2013.

Höink, T., Schmalzl, J., & Hansen, U. Dynamics of metal-silicate separation in a terrestrial magma ocean. *Geochem. Geophys. Geosyst.*, **7** :9008–+, 2006.

Huguet, L., Alboussiere, T., Bergman, M.I., Deguen, R., Labrosse, S., & Lescœur, G. Structure of a mushy layer under hypergravity with implications for earth's inner core. *Geophysical Journal International*, **204**(3) :1729–1755, 2016.

Huppert, H.E. & Turner, J.S. Double-diffusive convection. *Journal of Fluid Mechanics*, **106** :299–329, 1981. doi :10.1017/S0022112081001614.

Ichikawa, H., Labrosse, S., & Kurita, K. Direct numerical simulation of an iron rain in the magma ocean. *J. Geophys. Res.*, **115** :B01 404, 2010.

Jacobson, S.A., Rubie, D.C., Hernlund, J., Morbidelli, A., & Nakajima, M. Formation, stratification, and mixing of the cores of Earth and Venus. *Earth Planet. Sci. Lett.*, **174** :375–386, 2017.

Karato, S. & Murthy, V.R. Core formation and chemical equilibrium in the earth—I. physical considerations. *Phys. Earth Planet. Inter.*, **100**(1-4) :61–79, 1997. ISSN 00319201. doi : 10.1016/S0031-9201(96)03232-3.

Kellogg, L. & Turcotte, D. Homogenization of the mantle by convective mixing and diffusion. *Earth and planetary science letters*, **81**(4) :371–378, 1987.

Kendall, J.D. & Melosh, H. Differentiated planetesimal impacts into a terrestrial magma ocean : fate of the iron core. *Earth and Planetary Science Letters*, **448** :24–33, 2016.

Kleine, T., Mezger, K., Palme, H., & Münker, C. The W isotope evolution of the bulk silicate earth : constraints on the timing and mechanisms of core formation and accretion. *Earth Planet. Sci. Lett.*, **228** :109–123, 2004.

Kleine, T., Münker, C., Mezger, K., & Palme, H. Rapid accretion and early core formation on asteroids

and the terrestrial planets from Hf-W chronometry. *Nature*, **418** :952–955, 2002.

Kleine, T., Touboul, M., Bourdon, B., Nimmo, F., Mezger, K., Palme, H., Jacobsen, S.B., Yin, Q., & Halliday, A.N. Hf-W chronology of the accretion and early evolution of asteroids and terrestrial planets. *Geochimica and Cosmochimica Acta*, **73** :5150–5188, 2009.

Konôpková, Z., McWilliams, R.S., Gómez-Pérez, N., & Goncharov, A.F. Direct measurement of thermal conductivity in solid iron at planetary core conditions. *Nature*, **534**(7605) :99–101, 2016.

Koot, L. & Dumberry, M. Viscosity of the earth's inner core : Constraints from nutation observations. *Earth Planet. Sci. Lett.*, 2011.

Labrosse, S. Thermal and compositional stratification of the inner core. *C. R. Geoscience*, **346** :119–129, 2014.

Labrosse, S., Hernlund, J., & Coltice, N. A crystallizing dense magma ocean at the base of the earth's mantle. *Nature*, **450**(7171) :866–869, 2007. ISSN 0028-0836. doi :10.1038/nature06355.

Labrosse, S., Morison, A., Deguen, R., & Alboussière, T. Rayleigh-Bénard convection in a creeping solid with melting and freezing at either or both its horizontal boundaries. *J. Fluid Mech.*, **846** :5 – 36, 2018.

Landeau, M., Deguen, R., & Olson, P. Experiments on the fragmentation of a buoyant liquid volume in another liquid. *Journal of Fluid Mechanics*, **749** :478–518, 2014.

Landeau, M., Olson, P., Deguen, R., & Hirsh, B.H. Core merging and stratification following giant impact. *Nature Geoscience*, **9**(10) :786, 2016.

Lasbleis, M., Deguen, R., Cardin, P., & Labrosse, S. Earth's inner core dynamics induced by the Lorentz force. *Geophys. J. Int.*, **202** :548–563, 2015.

Lasbleis, M. & Deguen, R. Building a regime diagram for the earth's inner core. *Physics of the Earth and Planetary Interiors*, **247** :80–93, 2015.

Lherm, V. & Deguen, R. Small-scale metal/silicate equilibration during core formation : the influence of stretching enhanced diffusion on mixing. *Journal of Geophysical Research - Solid Earth*, submitted.

Li, J. & Agee, C. Geochemistry of mantle–core differentiation at high pressure. *Nature*, **381**(6584) :686–689, 1996. doi :10.1038/381686a0.

Lincot, A., Cardin, P., Deguen, R., & Merkel, S. Multiscale model of global inner-core anisotropy induced by hcp alloy plasticity. *Geophysical Research Letters*, **43**(3) :1084–1091, 2016.

Lincot, A., Deguen, R., Merkel, S., & Cardin, P. Seismic response and anisotropy of a model *hcp* iron inner core. *Comptes Rendus Geoscience*, 2014.

Lythgoe, K.H., Rudge, J.F., Neufeld, J.A., & Deuss, A. The feasibility of thermal and compositional convection in Earth's inner core. *Geophys. J. Int.*, **201**(2) :764–782, 2015.

Mahan, B., Siebert, J., Blanchard, I., Badro, J., Kubik, E., Sossi, P., & Moynier, F. Investigating earth's formation history through copper & sulfur metal-silicate partitioning during core-mantle differentiation. *Journal of Geophysical Research : Solid Earth*, 2018*a*.

Mahan, B., Siebert, J., Blanchard, I., Borensztajn, S., Badro, J., & Moynier, F. Constraining compositional proxies for earth's accretion and core formation through high pressure and high temperature zn and s metal-silicate partitioning. *Geochimica et Cosmochimica Acta*, **235** :21–40, 2018*b*.

Mikami, T., Cox, R., & Mason, S. Breakup of extending liquid threads. *International Journal of Multiphase Flow*, **2**(2) :113–138, 1975.

Monnereau, M., Calvet, M., Margerin, L., & Souriau, A. Lopsided growth of Earth's inner core. *Science*, **328** :1014–1017, 2010.

Monteux, J., Jellinek, A., & Johnson, C. Why might planets and moons have early dynamos ? *Earth Planet. Sci. Lett.*, **310**(3) :349–359, 2011.

Monteux, J., Ricard, Y., Coltice, N., Dubuffet, F., & Ulvrova, M. A model of metal–silicate separation on growing planets. *Earth Planet. Sci. Lett.*, **287**(3-4) :353–362, 2009. ISSN 0012821X. doi : 10.1016/j.epsl.2009.08.020.

Morishima, R., Golabek, G.J., & Samuel, H. N-body simulations of oligarchic growth of Mars : Implications for Hf–W chronology. *Earth Planet. Sci. Lett.*, **366** :6–16, 2013.

Morison, A., Labrosse, S., Deguen, R., & Alboussière, T. Timescale of overturn in a magma ocean cumulate. *Earth Planet. Sci. Lett.*, sub.

Morton, B.R., Taylor, G., & Turner, J.S. Turbulent gravitational convection from maintained and instantaneous sources. *Proceedings of the Royal Society of London. Series A, Mathematical and*

Physical Sciences, **234** :1–23, 1956.

Murthy, V.R. Early differentiation of the earth and the problem of mantle siderophile elements : A new approach. *Science*, **253**(5017) :303–306, 1991. doi :10.1126/science.253.5017.303.

Nimmo, F., O'Brien, D., & Kleine, T. Tungsten isotopic evolution during late-stage accretion : Constraints on earth–moon equilibration. *Earth Planet. Sci. Lett.*, 2010.

Noh, Y. & Fernando, H. The transition in the sedimentation pattern of a particle cloud. *Phys. Fluids A*, **5**(12) :3049–3055, 1993.

Ohta, K., Kuwayama, Y., Hirose, K., Shimizu, K., & Ohishi, Y. Experimental determination of the electrical resistivity of iron at Earth's core conditions. *Nature*, **534**(7605) :95–98, 2016.

Olson, P. & Deguen, R. Eccentricity of the geomagnetic dipole caused by lopsided inner core growth. *Nature Geoscience*, **5**(8) :565–569, 2012.

Olson, P., Deguen, R., Hinnov, L.A., & Zhong, S. Controls on geomagnetic reversals and core evolution by mantle convection in the phanerozoic. *Physics of the Earth and Planetary Interiors*, **214** :87–103, 2013.

Olson, P., Deguen, R., Rudolph, M.L., & Zhong, S. Core evolution driven by mantle global circulation. *Physics of the Earth and Planetary Interiors*, **243** :44–55, 2015.

Olson, P., Yuen, D.A., & Balsiger, D. Convective mixing and the fine structure of mantle heterogeneity. *Physics of the earth and planetary interiors*, **36**(3-4) :291–304, 1984.

O'Rourke, J.G., Korenaga, J., & Stevenson, D.J. Thermal evolution of earth with magnesium precipitation in the core. *Earth Planet. Sci. Lett.*, **458** :263–272, 2017.

O'Rourke, J.G. & Stevenson, D.J. Powering earth's dynamo with magnesium precipitation from the core. *Nature*, **529**(7586) :387–389, 2016.

Ottino, J., Ranz, W.E., & Macosko, C.W. A lamellar model for analysis of liquid-liquid mixing. *Chemical Engineering Science*, **34**(6) :877–890, 1979.

Ottino, J.M. *The kinematics of mixing : stretching, chaos, and transport*, volume 3. Cambridge university press, 1989.

Poupinet, G., Pillet, R., & Souriau, A. Possible heterogeneity of the Earth's core deduced from PKIKP travel times. *Nature*, **305** :204–206, 1983.

Pozzo, M., Davies, C., Gubbins, D., & Alfè, D. Thermal and electrical conductivity of iron at Earth's core conditions. *Nature*, **485** :355–358, 2012.

Pozzo, M., Davies, C., Gubbins, D., & Alfè, D. Thermal and electrical conductivity of solid iron and iron–silicon mixtures at Earth's core conditions. *Earth Planet. Sci. Lett.*, **393** :159–164, 2014.

Ranz, W.E. Applications of a stretch model to mixing, diffusion, and reaction in laminar and turbulent flows. *AIChE Journal*, **25**(1) :41–47, 1979.

Reaman, D.M., Daehn, G.S., & Panero, W.R. Predictive mechanism for anisotropy development in the Earth's inner core. *Earth Planet. Sci. Lett.*, **312**(3-4) :437 – 442, 2011. ISSN 0012-821X. doi : 10.1016/j.epsl.2011.10.038.

Reaman, D., Colijn, H., Yang, F., Hauser, A., & Panero, W. Interdiffusion of Earth's core materials to 65GPa and 2200K. *Earth Planet. Sci. Lett.*, **349** :8–14, 2012.

Rees Jones, D.W. & Worster, M.G. Fluxes through steady chimneys in a mushy layer during binary alloy solidification. *Journal of Fluid Mechanics*, **714** :127–151, 2013*a*.

Rees Jones, D.W. & Worster, M.G. A simple dynamical model for gravity drainage of brine from growing sea ice. *Geophysical Research Letters*, **40**(2) :307–311, 2013*b*.

Ricard, Y. Physics of mantle convection. In G. Schubert, editor, *Treatise on Geophysics*, volume 7. Elsevier, 2007.

Ringwood, A. Chemical evolution of the terrestrial planets. *Geochimica et Cosmochimica Acta*, **30**(1) :41–104, 1966. ISSN 00167037. doi :10.1016/0016-7037(66)90090-1.

Rubie, D.C., Jacobson, S.A., O'Brien, D.P., Young, E.D., de Vries, J., Nimmo, F., Palme, H., & Frost, D.J. Accretion and differentiation of the terrestrial planets with implications for the compositions of early-formed solar system bodies and accretion of water. *Icarus*, **248** :89–108, 2015.

Rubie, D.C., Laurenz, V., Jacobson, S.A., Morbidelli, A., Palme, H., Vogel, A.K., & Frost, D.J. Highly siderophile elements were stripped from earth's mantle by iron sulfide segregation. *Science*, **353**(6304) :1141–1144, 2016.

Rubie, D., Frost, D., Mann, U., Asahara, Y., Nimmo, F., Tsuno, K., Kegler, P., Holzheid, A., & Palme, H. Heterogeneous accretion, composition and core–mantle differentiation of the earth. *Earth Planet. Sci. Lett.*, **301**(1) :31–42, 2011.

Rubie, D., Melosh, H., Reid, J., Liebske, C., & Righter, K. Mechanisms of metal–silicate equilibration in the terrestrial magma ocean. *Earth Planet. Sci. Lett.*, **205**(3-4) :239–255, 2003. ISSN 0012821X. doi :10.1016/S0012-821X(02)01044-0.

Rudge, J., Kleine, T., & Bourdon, B. Broad bounds on earth's accretion and core formation constrained by geochemical models. *Nature Geoscience*, **3** :439–443, 2010.

Samuel, H. A re-evaluation of metal diapir breakup and equilibration in terrestrial magma oceans. *Earth Planet. Sci. Lett.*, **313** :105–114, 2012.

Samuel, H. & Tackley, P.J. Dynamics of core formation and equilibration by negative diapirism. *Geochem. Geophys. Geosyst.*, **9** :6011–+, 2008. doi :10.1029/2007GC001896.

Samuel, H., Tackley, P.J., & Evonuk, M. Heat partitioning in terrestrial planets during core formation by negative diapirism. *Earth Planet. Sci. Lett.*, **290** :13–19, 2010. doi :10.1016/j.epsl.2009.11.050.

Scorer, R. Experiments on convection of isolated masses of buoyant fluid. *Journal of Fluid Mechanics Digital Archive*, **2**(06) :583–594, 1957. doi :10.1017/S0022112057000397.

Seagle, C.T., Cottrell, E., Fei, Y., Hummer, D.R., & Prakapenka, V.B. Electrical and thermal transport properties of iron and iron-silicon alloy at high pressure. *Geophysical Research Letters*, **40**(20) :5377–5381, 2013.

Sha, X. & Cohen, R. First-principles studies of electrical resistivity of iron under pressure. *Journal of Physics : Condensed Matter*, **23** :075 401, 2011.

Siebert, J., Corgne, A., & Ryerson, F. Systematics of metal–silicate partitioning for many siderophile elements applied to earth's core formation. *Geochimica et Cosmochimica Acta*, **75**(6) :1451–1489, 2011.

Siebert, J., Badro, J., Antonangeli, D., & Ryerson, F.J. Metal–silicate partitioning of Ni and Co in a deep magma ocean. *Earth Planet. Sci. Lett.*, **321** :189–197, 2012.

Siebert, J., Badro, J., Antonangeli, D., & Ryerson, F.J. Terrestrial accretion under oxidizing conditions. *Science*, **339**(6124) :1194–1197, 2013.

Siebert, J., Sossi, P.A., Blanchard, I., Mahan, B., Badro, J., & Moynier, F. Chondritic mn/na ratio and limited post-nebular volatile loss of the earth. *Earth and Planetary Science Letters*, **485** :130–139, 2018.

Song, X. & Helmberger, D.V. Velocity structure near the inner core boundary from waveform modeling. *J. Geophys. Res.*, **97**(B5) :6573–6586, 1992.

Souriau, A. & Calvet, M. *Treatise on Geophysics*, chapter Deep Earth Structure : The Earth's Cores, pages 725 – 757. 2015.

Souriau, A. & Poupinet, G. The velocity profile at the base of the liquid core from PKP(BC+Cdiff) data : An argument in favor of radial inhomogeneity. *Geophys. Res. Lett.*, **18** :2023–2026, 1991.

Souriau, A. & Roudil, P. Attenuation in the uppermost inner core from broad-band GEOSCOPE PKP data. *Geophys. J. Int.*, **123** :572–587, 1995.

Sreenivasan, B. & Gubbins, D. On mantle-induced heat flow variations at the inner core boundary. *Phys. Earth Planet. Inter.*, 2011.

Stacey, F.D. & Anderson, O.L. Electrical and thermal conductivities of Fe-Ni-Si alloy under core conditions. *Phys. Earth Planet. Inter.*, **124** :153–162, 2001.

Stacey, F.D. & Davis, P.M. *Physics of the Earth*. Cambridge University Press, 2008.

Stern, M.E. The salt-fountain and thermohaline convection. *Tellus*, **12**(2) :172–175, 1960.

Stevenson, D.J. *Origin of the Earth*, chapter Fluid dynamics of core formation, pages 231–249. Oxford University Press, 1990.

Stommel, H., Arons, A.B., & Blanchard, D. An oceanographical curiosity : the perpetual salt fountain. *Deep Sea Research (1953)*, **3**(2) :152–153, 1956.

Suer, T.A., Siebert, J., Remusat, L., Menguy, N., & Fiquet, G. A sulfur-poor terrestrial core inferred from metal–silicate partitioning experiments. *Earth and Planetary Science Letters*, **469** :84–97, 2017.

Sumita, I. & Bergman, M.I. Inner-core dynamics. In G. Schubert, editor, *Treatise on Geophysics*, volume 8, pages 299–318. Elsevier, 2007.

Sumita, I. & Olson, P. A laboratory model for convection in Earth's core driven by a thermally heterogeneous mantle. *Science*, **286** :1547–1549, 1999.

Tanaka, S. & Hamaguchi, H. Degree one heterogeneity and hemispherical variation of anisotropy in the inner core from PKP(BC)-PKP(DF) times. *J. Geophys. Res.*, **102** :2925–2938, 1997.

Taylor, G.I. The formation of emulsions in definable fields of flow. *Proc. R. Soc. Lond. A*, **146**(858) :501–523, 1934.

Tkal***v***cić, H. Complex inner core of the earth : The last frontier of global seismology. *Reviews of Geophysics*, **53**(1) :59–94, 2015.

Tomotika, S. Breaking up of a drop of viscous liquid immersed in another viscous fluid which is extending at a uniform rate. *Proc. R. Soc. Lond. A*, **153**(879) :302–318, 1936.

Turner, J. Buoyant vortex rings. *Proceedings of the Royal Society of London.*, **239**(1216) :61–75, 1957.

Ulvrová, M., Coltice, N., Ricard, Y., Labrosse, S., Dubuffet, F., Velímskỳ, J., ***v***Srámek, O., *et al.* Compositional and thermal equilibration of particles, drops and diapirs in geophysical flows. *Geochemistry Geophysics Geosystems*, **12**(10) :1–11, 2011.

Van Orman, J.A. On the viscosity and creep mechanism of Earth's inner core. *Geophys. Res. Lett.*, **31** :20 606–+, 2004.

Villermaux, E. Fragmentation. *Annu. Rev. Fluid Mech.*, **39** :419–446, 2007.

Villermaux, E. & Bossa, B. Single-drop fragmentation determines size distribution of raindrops. *Nature Physics*, **5** :697–702, 2009. doi :10.1038/nphys1340.

Villermaux, E. Unifying ideas on mixing and atomization. *New Journal of Physics*, **6**(1) :125, 2004.

Wacheul, J.B., Le Bars, M., Monteux, J., & Aurnou, J.M. Laboratory experiments on the breakup of liquid metal diapirs. *Earth Planet. Sci. Lett.*, **403** :236–245, 2014.

Wacheul, J.B. & Le Bars, M. Experiments on fragmentation and thermo-chemical exchanges during planetary core formation. *Physics of the Earth and Planetary Interiors*, 2017.

Wells, A., Wettlaufer, J., & Orszag, S. Brine fluxes from growing sea ice. *Geophysical Research Letters*, **38**(4), 2011.

Wells, A.J., Wettlaufer, J.S., & Orszag, S.A. Nonlinear mushy-layer convection with chimneys : stability and optimal solute fluxes. *Journal of Fluid Mechanics*, **716** :203–227, 2013.

Williams, J.P. & Nimmo, F. Thermal evolution of the Martian core : Implications for an early dynamo. *Geology*, **32** :97–+, 2004.

Williams, Q. The thermal conductivity of earth's core : A key geophysical parameter's constraints and uncertainties. *Annual Review of Earth and Planetary Sciences*, **46** :47–66, 2018.

Wood, B., Walter, M., & Wade, J. Accretion of the earth and segregation of its core. *Nature*, **441**(7095) :825–833, 2006. ISSN 0028-0836. doi :10.1038/nature04763.

Woodward, B. *Swiss Aero. Revue, OSTIV Section,*, **6** :131, 1958.

Woodward, B. The motion in and around isolated thermals. *Quarterly Journal of the Royal Meteorological Society*, **85**(364) :144–151, 1959.

Worster, M.G. Natural convection in a mushy layer. *Journal of Fluid Mechanics*, **224** :335–359, 1991.

Yin, Q., Jacobsen, S.B., Yamashita, K., Blichert-Toft, J., Telouk, P., & Albarede, F. A short timescale for terrestrial planet formation from Hf/W chronometry of meteorites. *Nature*, **418**(6901) :949–952, 2002. ISSN 0028-0836. doi :10.1038/nature00995.

Yoshida, S., Sumita, I., & Kumazawa, M. Growth model of the inner core coupled with the outer core dynamics and the resulting elastic anisotropy. *J. Geophys. Res.*, **101** :28 085–28 104, 1996.

Yu, J., Bergman, M.I., Huguet, L., & Alboussiere, T. Partial melting of a pb-sn mushy layer due to heating from above, and implications for regional melting of earth's directionally solidified inner core. *Geophysical Research Letters*, **42**(17) :7046–7053, 2015.

Yu, W., Wen, L., & Niu, F. Seismic velocity structure in the earth's outer core. *J. Geophys. Res. - Solid Earth*, **110**(B2) :B02 302+, 2005.

Zhang, P., Cohen, R., & Haule, K. Retraction : Effects of electron correlations on transport properties of iron at earth's core conditions. *Nature*, 2016.

Zhao, B., Law, A.W.K., Lai, A.C.H., & Adams, E.E. On the internal vorticity and density structures of miscible thermals. *J. Fluid Mech.*, **722, R5**, 2013.

Zou, Z., Koper, K.D., & Cormier, V.F. The structure of the base of the outer core inferred from seismic

waves diffracted around the inner core. *J. Geophys. Res. (Solid Earth)*, **113** :5314–+, 2008.

Annexe A

Curriculum Vitae

Renaud Deguen

Maître de Conférence
Né le 9 avril 1982
Nationalité française
☎ 04 72 44 85 13
✉ renaud.deguen@univ-lyon1.fr

Laboratoire de Géologie de Lyon(LGLTPE)
UMR CNRS 5276 (CNRS, ENS, Université Lyon 1)
Université Claude Bernard, Lyon 1
Campus de la Doua, bât. GEODE
2, rue Raphaël Dubois
69622 Villeurbanne Cedex
France

Cursus universitaire

2009	Doctorat de l'Université Joseph Fourier, Genoble. "Dynamique de la cristallisation de la graine : expériences et modèles" . Encadrants : Thierry Alboussière et Daniel Brito.
2005	Master "Sciences de la Terre, de l'Univers et de l'Environnement", Université Joseph Fourier.
2002-2004	*École Normale Supérieure de Lyon (ENS-Lyon).* Département des Sciences de la Terre.

Parcours professionnel

2013–...	**Maître de conférence** Laboratoire de Géologie de Lyon - Terre, Planètes, Environnement (LGLTPE), Observatoire des Sciences de l'Univers de Lyon, Université Claude Bernard Lyon 1.
jan 2013–sept. 2013	Post-doctorat à l'Institut de Mécanique des Fluides de Toulouse (IMFT) (ANR Retour Post-doctorant).
2009-2012	Postdoctorat à l'université Johns Hopkins University (Baltimore, Maryland), avec Peter Olson.

Activités d'enseignement

2013–...	Maître de Conférence à l'Université Claude Bernard Lyon 1. Matières enseignées : mécanique des fluides, géomagnétisme, planétologie, géodynamique, prospection géophysique et géotechnique, statistiques, algorithmique, introduction aux sciences de la Terre.
2006–2009	Moniteur à l'Université Joseph Fourier (Grenoble).

Participations à des formations doctorales ou post-doctorales :

Oct. 2016	École des Houches sur la Terre Interne
April 2018	CISM School, "Fluid dynamics of planets and stars", Udine, Italie.
Sept. 2018	Formation CNRS Forsterite "La différenciation de la terre et des corps silicatés du système solaire"

Prix

- ◇ Prix Doornbos 2012 (SEDI, Leeds 2012), "for particularly innovative contributions to understanding the dynamics and evolution of the inner core and its interactions with the surrounding fluid".
- ◇ Geophysical Journal International Outstanding reviewer en 2014.

Projets financés (en tant que porteur)

- ◇ 2017–2022 : ERC Starting Grant on the fluid dynamics of core-mantle differentiation and chemical equilibration, 1.25 M€.
- ◇ 2016–2017 : PNP ("Modélisation expérimentale de l'impact d'un planétésimal sur la Terre primitive"), 7k€.
- ◇ 2012–2015 : ANR "Retour post-doctorants", 246 k€.

Responsabilités collectives

- ◇ Membre de l'editorial board de *Physics of the Earth and Planetary Interiors* (2015–...).
- ◇ Reviewer pour *Earth and Planetary Science Letters*, *Journal of Fluid Mechanics*, *Geophysical Journal International*, *Physics of the Earth and Planetary Interiors*, *Geochemistry, Géophysics, Geosystems* (G^3), *International Journal of Heat and Mass Transfer*, *AGU Books*, *Mathematical Geosciences*, *Journal of Earth System Science*.
- ◇ Reviewer pour les agences de financement française et US (NSF).
- ◇ Membre élu du conseil de l'Observatoire des Sciences de l'Univers de Lyon (2016-2017).
- ◇ Responsable chaque année de 2 à 6 Unités d'Enseignement de l'Observatoire des Sciences de l'Univers de Lyon depuis 2014.
- ◇ Interrogateur pour les oraux de physique du concours A d'entrée aux ENS (BCPST) en 2017.

Organisation de conférences

Spring AGU 2009	Co-chairman de la session DI13A, AGU Spring Meeting, Toronto
EGU 2012	Convener de la session GD7.1 "Earth's core dynamics : observations and models"
SEDI 2012	Chairman et "discussion leader" de la session "inner core dynamics".
EGU 2015	Co-convener de la session GD4.1 sur "Earth's core structure and dynamics : observations, models, experiments ".
EGU 2016	Convener de la session GD4.1 sur "Earth's core structure and dynamics : observations, models, experiments ".
2017	Membre du comité d'organisation de la conférence "Compressible Convection Conference 2017", Lyon.
2015-2019	Membre du comité exécutif (Executive Committee) du SEDI (Study of Earth Deep Interiors).

Encadrements

◇ Post-doctorant :

- Vincent Clesi (depuis sept. 2018), sur la modélisation géochimique de la formation du noyau.

◇ Doctorants :

- Victor Lherm (depuis sept. 2017), sur la mécanique des fluides de la séparation du métal et des silicates dans un océan de magma.
- Adrien Morison (depuis sept. 2016) (encadrant principal : Stéphane Labrosse), sur la dynamique de la convection dans un manteau planétaire solide en contact avec un océan de magma.
- J'ai aussi joué un rôle actif, bien qu'officieux, dans l'encadrement des thèses de Maylis Landeau (publication de deux articles) et Marine Lasbleis (publication de deux articles).

◇ Stagiaires de Master : Assane Ndieguene (2008), Charlotte Regnier (2009), Mathilde Roberge (2009), Mawaraba Keita (2014), Adrien Morison (2016), Lola Perruchon-Monge (2017), Victor Lherm (2017).

◇ $\sim$ 10 stages de niveau licence encadrés depuis 2007.

Publications et communications

◇ **12 presentations invitées** dans des conférences internationales (AGU, EGU, SEDI, Gordon Conference) et des workshops, dont des conférences de review à la Gordon Conference "Interior of the Earth" de 2013 et au SEDI de 2014 à Kanagawa (Japan).

◇ **16 séminaires** donnés entre 2009 et 2018.
Bullard Laboratories (Cambridge, UK), HELSI (Tokyo, Japan), Carnegie Institute (Washington, USA), Johns Hopkins University (Baltimore, USA), Rensselaer Polytechnic Institute (Albany, USA), Bard College at Simon's Rock (Great Barrington, USA), University of Colorado (Boulder, USA), IRPHE (Marseille, France), LPG (Nantes), FAST (Orsay), LGL (Lyon), ISTerre (Grenoble), IMFT (Toulouse), IRAP (Toulouse), DTP (Toulouse), IPG Strasbourg.

◇ **25 articles** publiés (h-index =14).

Annexe B

Liste des publications

(Les noms des auteurs étudiants au moment de l'écriture de l'article sont soulignés.)

Articles soumis à des revues de rang A :

- ◇ Morison A., Labrosse S., **Deguen** R., Alboussière T., Timescale of compositional overturn in a magma ocean cumulate. *submitted to Earth and Planetary Sciences Letters*
- ◇ Lherm V. & **Deguen** R., Small scale equilibration processes during core formation. *submitted to Journal of Geophysical Research*

Articles publiés dans des revues de rang A :

25. **Deguen** R., Alboussière T., Labrosse S., Double-diffusive translation of Earth's inner core, *Geophysical Journal International*, **214**, 88 – 107, 2018.
24. Labrosse S., Morison A., **Deguen** R., Alboussière T., Rayleigh-Bénard convection with a phase change at either or both horizontal boundaries, *Journal of Fluid Mechanics*, **846**, 5–36, 2018.
23. Landeau M., Olson P., **Deguen** R., Hirsh B.H., Core merging and stratification following giant impact, *Nature Geoscience*, **9**, 786-789, 2016.
22. Huguet L., Alboussière T., Bergman M.I., **Deguen R.**, Labrosse S., Lesœur G., Structure of a mushy layer under hypergravity with implications for Earth's inner core, *Geophysical Journal International*, **204**, 1729-1755, 2016.
21. Lincot A., Cardin P., **Deguen R.**, Merkel S., Multiscale model of global inner-core anisotropy induced by hcp alloy plasticity, *Geophysical Research Letters*, **43**, 1084-1091, 2016.
20. Lasbleis M., **Deguen R.**, Cardin, P., & Labrosse, S., Inner Core dynamics induced by the Lorentz force. *Geophysical Journal International*. Geophys. J. Int., **202**, 548–563, 2015.
19. Olson, P., **Deguen R.**, Rudolph, M. & Zhong, S., Core evolution driven by mantle global circulation. *Physics of the Earth and Planetary Interiors*, **243**, 44–55, 2015.
18. Lasbleis M., & **Deguen R.**, Building a regime diagram for Earth's inner core. *Physics of the Earth and Planetary Interiors*, **247**, 80–93, 2015.
17. **Deguen R.**, Olson, P. & Reynolds E., F-layer formation in the outer core with asymmetric inner core growth. *C. R. Geoscience*, **346** (5), 101-109, 2014.
16. Lincot A., **Deguen R.**, Merkel S. & Cardin P. Forward Model of Seismic Anisotropy in the Earth's Inner Core. *C. R. Geoscience*, **346** (5), 148-157, 2014.

15. Landeau M., **Deguen R.** & Olson P. Experiments on the fragmentation of a buoyant liquid volume in another liquid. *Journal of Fluid Mechanics*, **749** :478–518, 2014.

14. **Deguen R.**, Landeau M. & Olson P. Turbulent metal-silicate mixing, fragmentation, and equilibration in magma oceans. *Earth and Planetary Science Letters*, **391(0)** :274 – 287, 2014.

13. **Deguen R.** Thermal convection in a spherical shell with melting/freezing at its boundaries. *Journal of Earth Science*, **24**, 669-682, 2013.

12. **Deguen R.**, Alboussière T. & Cardin P. Convection in Earth's inner core with phase change at its boundary. *Geophysical Journal International*, **194(3)** :1310–1334, 2013.

11. Olson P. L., **Deguen R.**, Hinnov L. A. & Zhong S. Controls on geomagnetic reversals and core evolution by mantle convection in the Phanerozoic *Physics of the Earth and Planetary Interiors*, **214**, 87-103, 2012.

10. Alboussière T. & **Deguen R.** Asymmetric Dynamics of the Inner Core and Impact on the Outer Core. *Journal of Geodynamics*, **61**, 172-182, 2012.

9. Olson P. & **Deguen R.** Eccentricity of the geomagnetic dipole caused by lopsided inner core growth. *Nature Geoscience*, **5**, 565–569, 2012.

8. **Deguen R.** Structure and dynamics of Earth's inner core. *Earth and Planetary Science Letters - Frontiers article*, **333–334**, 211–225, 2012.

7. **Deguen R.** & Cardin P., Thermo-chemical convection in Earth's inner core. *Geophysical Journal International*, **187**, 1101-1118, 2011.

6. **Deguen R.**, Cardin P., Merkel S., & Lebensohn R. A. Texturing in Earth's inner core due to preferential growth in its equatorial belt. *Physics of the Earth and Planetary Interiors*, **188**, 173-184, 2011.

5. **Deguen R.**, Olson P. & Cardin P. Experiments on turbulent metal-silicate mixing in a magma ocean. *Earth and Planetary Science Letters*, **310**, 303-313, 2011.

4. Alboussière, T., **Deguen, R.**, & Melzani, M. Melting induced stratification above the Earth's inner core due to convective translation. *Nature*, **466** :744–747, 2010.

3. Venet L., Duffar T & **Deguen R.**, Grain structure of the Earth's inner core. *Comptes Rendus Geosciences*, 341, 513-516, 2009.

2. **Deguen R.** & Cardin P., Tectonic history of the Earth's inner core preserved in its seismic structure. *Nature Geoscience*, 2, 419 - 422, 2009.

1. **Deguen R.**, Alboussière T. & Brito D., On the presence and structure of a mush at the Earth's inner core boundary. *Physics of the Earth and Planetary Interiors*, 164, 36-49, 2007.

Annexe C

Sélection d'articles

C.1 Différentiation noyau-manteau

Earth and Planetary Science Letters 391 (2014) 274–287

Contents lists available at ScienceDirect

Earth and Planetary Science Letters

www.elsevier.com/locate/epsl

Turbulent metal–silicate mixing, fragmentation, and equilibration in magma oceans

Renaud Deguen [a,c,*], Maylis Landeau [b], Peter Olson [a]

[a] Department of Earth and Planetary Sciences, Johns Hopkins University, Baltimore, MD 21218, USA
[b] Dynamique des Fluides Géologiques, Institut de Physique du Globe de Paris, Sorbonne Paris Cité, Université Paris Diderot, CNRS UMR 7154, 1 rue Jussieu, 75238, Paris cedex 05, France
[c] Institut de Mécanique des Fluides de Toulouse, Université de Toulouse (INPT, UPS) and CNRS, Allée C. Soula, Toulouse, 31400, France

ARTICLE INFO

Article history:
Received 19 April 2013
Received in revised form 16 October 2013
Accepted 3 February 2014
Available online 21 February 2014
Editor: C. Sotin

Keywords:
core formation
magma ocean
fragmentation
turbulent mixing
chemical equilibration

ABSTRACT

Much of the Earth was built by high-energy impacts of planetesimals and embryos, many of these impactors already differentiated, with metallic cores of their own. Geochemical data provide critical information on the timing of accretion and the prevailing physical conditions, but their interpretation depends critically on the degree of metal–silicate chemical equilibration during core–mantle differentiation, which is poorly constrained. Efficient equilibration requires that the large volumes of iron derived from impactor cores mix with molten silicates down to scales small enough to allow fast metal–silicate mass transfer. Here we use fluid dynamics experiments to show that large metal blobs falling in a magma ocean mix with the molten silicate through turbulent entrainment, with fragmentation into droplets eventually resulting from the entrainment process. In our experiments, fragmentation of the dense fluid occurs after falling a distance equal to 3–4 times its initial diameter, at which point a sizable volume of ambient fluid has already been entrained and mixed with the dense falling fluid. Contrary to previous assumptions, we demonstrate that fragmentation of the metallic phase into droplets may not be required for efficient equilibration: turbulent mixing, by drastically increasing the metal–silicate interfacial area, may result in fast equilibration even before fragmentation. Efficient re-equilibration is predicted for impactors of size small compared to the magma ocean depth. In contrast, much less re-equilibration is predicted for large impacts in situations where the impactor core diameter approaches the magma ocean thickness.

1. Introduction

The formation of Earth's core produced chemical and isotopic fractionations which have been used to constrain the timing of differentiation (Yin et al., 2002; Kleine et al., 2002) and the physical conditions (Wood et al., 2006; Corgne et al., 2008; Siebert et al., 2011; Rubie et al., 2011) that prevailed early in Earth's history. Hafnium–Tungsten (Hf-W) systematics in particular provide constraints on the timing of accretion, but their interpretation depends critically on the degree to which the metal portion of the impactors equilibrates isotopically with Earth's mantle silicates (Halliday, 2004; Kleine et al., 2004; Nimmo et al., 2010; Rudge et al., 2010). Assuming full equilibration after each impact, Hf-W chronometry implies an accretion timescale of about 10 Myr (Yin et al., 2002; Rudge et al., 2010), whereas relaxing this assumption can increase this timescale by several tens of Myr, or even render it indeterminate (Rudge et al., 2010).

Partial equilibration is usually modeled by assuming that a fraction k of the metal phase delivered by each impact re-equilibrates with the whole mantle, the remaining metal fraction $1-k$ reaching the Earth's core without chemical interaction with the mantle (Halliday, 2004; Kleine et al., 2004; Nimmo et al., 2010; Rudge et al., 2010). However, the compositional transfer between metal and silicate also depends on the quantity of silicates the metal phase equilibrates with. For example, the amount of radiogenic Tungsten extracted from the silicates by the metal will be insignificant if the volume of interacting silicate is small. We thus define a more general measure of equilibration, the equilibration efficiency $\mathscr{E}_i$, as the total mass of element i exchanged between metal and silicates normalized by its maximum possible value, had all the metal re-equilibrated with an infinitely larger silicate reservoir. If a fraction k of the metal phase equilibrates with a mass of silicates equal to Δ times the mass of equilibrated metal, the

* Corresponding author. Current address: Laboratoire de Géologie de Lyon (LGLTPE), Université Lyon 1, ENS Lyon, CNRS, 69622 Villeurbanne, France.
E-mail address: renaud.deguen@univ-lyon1.fr (R. Deguen).

http://dx.doi.org/10.1016/j.epsl.2014.02.007
0012-821X/

equilibration efficiency of an element i with a metal/silicate partition coefficient D_i is, from mass balances,

$$\mathscr{E}_i = \frac{k}{1 + D_i/\Delta} \quad (1)$$

(see Appendix A for the derivation and more discussion of the equilibration efficiency), with the metal dilution Δ defined as

$$\Delta = \frac{\text{mass of equilibrated silicates}}{\text{mass of equilibrated metal}}. \quad (2)$$

$\mathscr{E}_i$ approaches k when $\Delta \gg D_i$, which is the usual assumption of disequilibrium core formation models. Importantly, $\mathscr{E}_i$ is element-dependent, with efficient equilibration of an element i requiring a metal dilution Δ similar or larger than its distribution coefficient. Tungsten, for example, had a mean distribution coefficient around $D_W \simeq 30$ during Earth's differentiation, so that equilibration is efficient only if the metal mixes and equilibrates with more than about 30 times its mass of silicates on average.

Previous disequilibrium geochemical models assuming infinite dilution can be corrected for the effect of finite metal dilution by substituting $\mathscr{E}_i$ in place of k (as demonstrated in Appendix A), which means that previously determined constraints on k actually apply to $\mathscr{E}_i$. In particular, Hf-W systematics imply that the Tungsten equilibration efficiency $\mathscr{E}_W$ must have been larger than about 0.36 on average during Earth's accretion (Rudge et al., 2010), which requires that on average $k \geqslant 0.36$ and $\Delta/D_W \geqslant 0.56$. In practice, the distribution coefficient of W may have changed by several order of magnitude in the course of Earth's accretion due to possible changes in oxygen fugacity (Cottrell et al., 2009; Rubie et al., 2011), and this makes the process of obtaining constraints on metal–silicate mixing from Hf-W systematics a non-trivial matter. As an illustration, assuming an average D_W around 30 (Rudge et al., 2010) implies an average metal dilution Δ larger than about 17, which argues for significant metal–silicate mixing.

Though Hf-W systematics can provide a lower bound on the degree of metal–silicate mixing and equilibration, its use as a core-formation chronometer is still hampered by the lack of stronger constraints on the degree of equilibration: there is an inverse trade-off between the assumed degree of re-equilibration and the Hf-W accretion timescale, which even becomes unbounded when $\mathscr{E}_i$ approaches it's lower acceptable bound (0.36 according to Rudge et al., 2010). Additional constraints on metal–silicate equilibration are needed to properly interpret the data.

During accretion, dissipation of the gravitational and kinetic energies associated with large impacts inevitably results in widespread melting (Melosh, 1990; Tonks and Melosh, 1993; Pierazzo et al., 1997), implying that part of the separation of the core-forming metal phase from the silicates occurred in low-viscosity magma oceans. Under these conditions, efficient chemical equilibration would be expected if the Earth had formed through the accretion of undifferentiated bodies with the metal phase already finely dispersed within a silicate matrix. However, it is now recognized that much of the Earth was accreted from already differentiated bodies with sizes ranging from a few tens of kilometers in diameter to objects the size of Mars (Yoshino et al., 2003; Baker et al., 2005; Bottke et al., 2006; Ricard et al., 2009). It is usually assumed that efficient chemical equilibration between the cores of these impactors and the proto-Earth's mantle requires fragmentation of the metal down to scales of 1 cm to 1 m where efficient metal–silicate chemical equilibration can occur (Stevenson, 1990; Karato and Murthy, 1997; Rubie et al., 2003; Ulvrová et al., 2011), implying a scale reduction by a factor of 10^4–10^8. Smooth Particle Hydrodynamics (SPH) simulations of the Moon-forming impact suggest some degree of disruption of the impactor core into 100–1000 km sized iron blobs (Canup, 2004), but the current resolution of these models is too coarse to give any information about smaller scale mixing and fragmentation. Hence the fate of these large iron blobs, while critical for the interpretation of geochemical data, remains uncertain.

2. Non-dimensional parameters

We consider the evolution of an iron blob, which can be either the core of an impactor or a fragment of an impactor core, falling in a magma ocean. Its dynamics are characterized by the following set of non-dimensional numbers:

$$Re = \frac{wd}{\nu_m}, \qquad We = \frac{\rho_m w^2 d}{\sigma}, \qquad Bo = \frac{\Delta\rho g d^2}{\sigma},$$
$$M = \frac{w}{c}, \qquad \mathrm{P} = \frac{\rho_m}{\rho_s}, \qquad \mathrm{H} = \frac{\eta_m}{\eta_s},$$

where w and d are the velocity and diameter of the falling metal volume, ρ is density, η the dynamic viscosity, $\nu = \eta/\rho$ the kinematic viscosity, g the acceleration of gravity, σ the iron–silicate interfacial tension, and c the sound wave velocity in the dominant phase. Subscripts "m" and "s" refer to metal and silicate, respectively, and $\Delta\rho = \rho_m - \rho_s$. The Reynolds number Re compares the magnitude of inertia to viscous forces, the Weber and Bond numbers, We and Bo, are measures of the relative importances of inertia and buoyancy to interfacial tension at the lengthscale d, and the Mach number M compares the velocity of the flow to the sound wave velocity. A list of the symbols used in the main text and appendices is given in Table 1.

Typical values for these parameters for a metal blob 100 km in diameter falling in a magma ocean with an initial velocity of 1 km s^{-1} are $Re \sim 10^{14}$, $Bo \sim 10^{14}$, $We \sim 10^{14}$, with $\mathrm{P} \simeq 2$ and $\mathrm{H} \sim 0.1$–1. Note that Re, We, Bo and M are all time-dependent.

The huge value of Re implies that the flow must have been extremely turbulent. The Weber and Bond numbers are large as well, which implies that interfacial tension effects were unimportant except at the smallest scales of the flow (Dahl and Stevenson, 2010; Deguen et al., 2011). The Mach number M may be up to $\sim$5 just after the impact (with an impact velocity $\sim$15 km s^{-1} and a speed of sound $\sim$3 km s^{-1}), and then decreases with time as the metal decelerates. The flow is typically supersonic, implying that compressibility effects are important.

3. Turbulent entrainment

Given the extreme values of the Weber and Bond numbers, it is appropriate to first consider the limiting case of miscible fluids, for which We and Bo are formally infinite. Numerous experimental and theoretical studies have shown that the evolution of a turbulent buoyant fluid falling or rising under the action of gravity – what is called a *turbulent thermal* in fluid mechanics – is governed by turbulent entrainment of ambient fluid (Batchelor, 1954; Morton et al., 1956; Turner, 1986). As an illustration, Fig. 1a shows snapshots from an experiment in which a volume of a dense solution is released into a larger volume of pure water. A small amount of fluorescent dye has been added to the solution. The volume of dyed fluid is seen to increase as it falls, which indicates that the negatively buoyant fluid entrains and incorporates ambient fluid, resulting in its gradual dilution (Batchelor, 1954; Morton et al., 1956).

This effect is quantified using the *entrainment hypothesis* of Morton et al. (1956), which states that the rate of entrainment of ambient fluid is proportional to the mean velocity of the buoyant turbulent fluid, and predicts that the radius $r = d/2$ of the buoyant fluid evolves as

Table 1
Symbols used in the main text and appendices.

Latin symbols	
B	Buoyancy of the metal–silicate mixture
$c_{m,s}$	Mean concentration (wt%) of element i in the metal (m) or silicate (s) phase
$c_{m,s}^{\mathrm{imp}}$	Mean concentration (wt%) of element i in the metal (m) or silicate (s) phase of the impactor
$c_{m,s}^{\mathrm{int}}$	Concentration of element i, in the metal (m) or silicate (s) phase at the metal–silicate interface
$\Delta c_{m,s}$	Composition difference across the boundary layer, in the metal (m) or silicate (s) phase
C_d	Drag coefficient
d	Diameter of the metal–silicate mixture
$d_{\max}$	Maximum stable drop diameter
D	Fractal dimension
D_i	Metal/silicate partition coefficient
$\mathscr{E}_i^{\circ}$	Equilibration efficiency
F	Core mass fraction
F_c	Compositional flux across the metal–silicate interface
g	Acceleration of gravity
k	Mass fraction of equilibrated metal
K	Coefficient of added mass
ℓ^*	Cut-off length scale
ℓ_K	Kolmogorov scale
ℓ_σ	Turbulent capillary scale
ℓ_{eq}	Equilibration distance
$\mathcal{M}_i$	Mass exchange of element i between metal and silicates
$\mathcal{M}_i^{\max}$	Maximum possible value of $\mathcal{M}_i$
$M_{m,s}$	Mass of metal (m) or silicate (s)
M	Mass of the Earth at time t
r	Radius of the metal–silicate mixture
S_ℓ	Area of the metal–silicate mixture measured at scale ℓ
S_T	True area of the metal–silicate mixture
u_ℓ	Turbulent velocity fluctuation at scale ℓ
V	Volume of the metal–silicate mixture
w	Vertical velocity of the metal–silicate mixture
Greek symbols	
α	Entrainment coefficient
$\gamma_{m/s}$	$\Delta c_m/\Delta c_s$
$\delta_{m,s}$	Compositional boundary layer thickness in the metal (m) or silicate (s) phase
Δ	Metal dilution, *i.e.* the ratio of the mass of equilibrated silicate over the mass of equilibrated metal
ϵ	Dissipation rate
$\eta_{m,s}$	Dynamic viscosity in the metal (m) or silicate (s) phase
$\kappa_c^{m,s}$	Compositional diffusivity in the metal (m) or silicate (s) phase
$\nu_{m,s}$	Kinematic viscosity in the metal (m) or silicate (s) phase
$\rho_{m,s}$	Density of the metal (m) or silicate (s) phase
$\bar{\rho}$	Mean density of the metal–silicate mixture
$\Delta\rho$	Density contrast $\rho_m - \rho_s$
σ	Metal–silicate interfacial tension
τ_{eq}	Equilibration timescale
ϕ	Metal mass fraction in the metal–silicate mixture
Dimensionless numbers	
Bo	Bond number, $\Delta\rho g d^2/\sigma$
H	Viscosity ratio, η_m/η_s
P	Density ratio, ρ_m/ρ_s
Pe	Compositional Péclet number, $w d/\kappa_c$
Re	Reynolds number, $w d/\nu_m$
Sc	Schmidt number, ν/κ_c
We	Weber number, $\rho_m w^2 d/\sigma$

$$r = r_0 + \alpha z, \tag{3}$$

where α is the entrainment coefficient and $r_0 = d_0/2$ the initial radius of the dense blob. The velocity of the mixture can be calculated from the equations of conservation of momentum and mass (Appendix B), a general expression being given in Eq. (B.12). The velocity law (B.12) has a useful large-z asymptote given by

$$w = \left(\frac{r_0^3 g}{2\alpha^3}\frac{\Delta\rho}{\rho_s}\right)^{1/2}\left(1 + K + \frac{3}{16}\frac{C_d}{\alpha}\right)^{-1/2}\frac{1}{z}, \tag{4}$$

where C_d is the drag coefficient, and K the coefficient of added mass, which accounts for the momentum imparted to the surrounding fluid. These laws have been verified in a wide variety of physical settings, from laboratory experiments using thermally or compositionally buoyant fluids to large scale geophysical flows including explosive volcanic plumes (Terada and Ida, 2007; Yamamoto et al., 2008), underwater gas plumes (Bettelini and Fanneløp, 1993), and atmospheric convective bursts (known as *thermals* – hence the name – by sailplane pilots; Woodward, 1959).

Turbulent entrainment results from a combination of *engulfment* of ambient fluid by large scale, inviscid eddies, which draws large volumes of surrounding fluid into the turbulent region, and *nibbling*, which denotes small scale viscous processes (vorticity diffusion) (Turner, 1986; Mathew and Basu, 2002; Westerweel et al., 2009). The rate at which the ambient fluid is entrained is thought to be controlled by large scale process (Brown and Roshko, 1974; Turner, 1986), while nibbling is responsible for eventually imparting vorticity to the entrained fluid. The entrainment coefficient appears to be independent of Re (Turner, 1969), which is consistent with the rate of turbulent entrainment being controlled by the largest inviscid eddies rather by the small scale viscous effects. In two-fluids systems we would expect that these large-scale eddies remain unaffected by interfacial tension if the Weber number is large enough, in which case turbulent entrainment should still occur, at a rate similar to the case of miscible fluids. We argue here that the concept of turbulent entrainment is indeed also applicable to immiscible fluids like molten metal and silicate, provided Re and We are large. This is demonstrated below in a series of experiments with two immiscible fluids.

4. Experimental set-up

Molten silicate is modeled by a low viscosity silicone oil (density $\rho_s = 820\ \mathrm{kg\,m^{-3}}$, viscosity $\eta_s = 1\ \mathrm{mPa\,s}$) enclosed in a 25.5 cm × 25.5 cm × 47 cm container. A volume of NaI aqueous solution (density $\rho_m = 1580\ \mathrm{kg\,m^{-3}}$, viscosity $\eta_m = 2\ \mathrm{mPa\,s}$), representing a metal blob falling into a magma ocean, is held in a vertically oriented tube whose lower extremity is sealed using a thin latex diaphragm, which is ruptured at the beginning of the experiment. Tube diameters from 1.28 cm to 7.62 cm have been used, with an aspect ratio (height of fluid in the tube/diameter of the tube) kept to 1 in all experiments. A surfactant (Triton X-100) is added to the NaI solution, lowering the interfacial tension of the silicone oil/NaI solution system to about $5\ \mathrm{mJ\,m^{-2}}$. A small amount of $Na_2S_2O_3$ is added to the NaI solution to avoid a yellowish coloration of the solution. In experiments where induced fluorescence is used to image cross-sections (Fig. 3), we use a concentration of the NaI solution for which the refractive index of the NaI solution matches that of the silicone oil, which is necessary to avoid optical distortions. At this concentration, its density is $\rho_m = 1260\ \mathrm{kg\,m^{-3}}$. The exact values of the densities, viscosities and interfacial tension are measured before each series of experiments. The experiments are recorded with a color video camera at 24 frames per second. Using a pixel intensity threshold method, we estimate on each video frame the location of the center of mass z of the oil/NaI solution mixture and the apparent area A of the mixture, from which its equivalent radius is estimated as $r = \sqrt{A/\pi}$.

The dense fluid is released from rest and its vertical velocity is set by the conversion of its gravitational potential energy

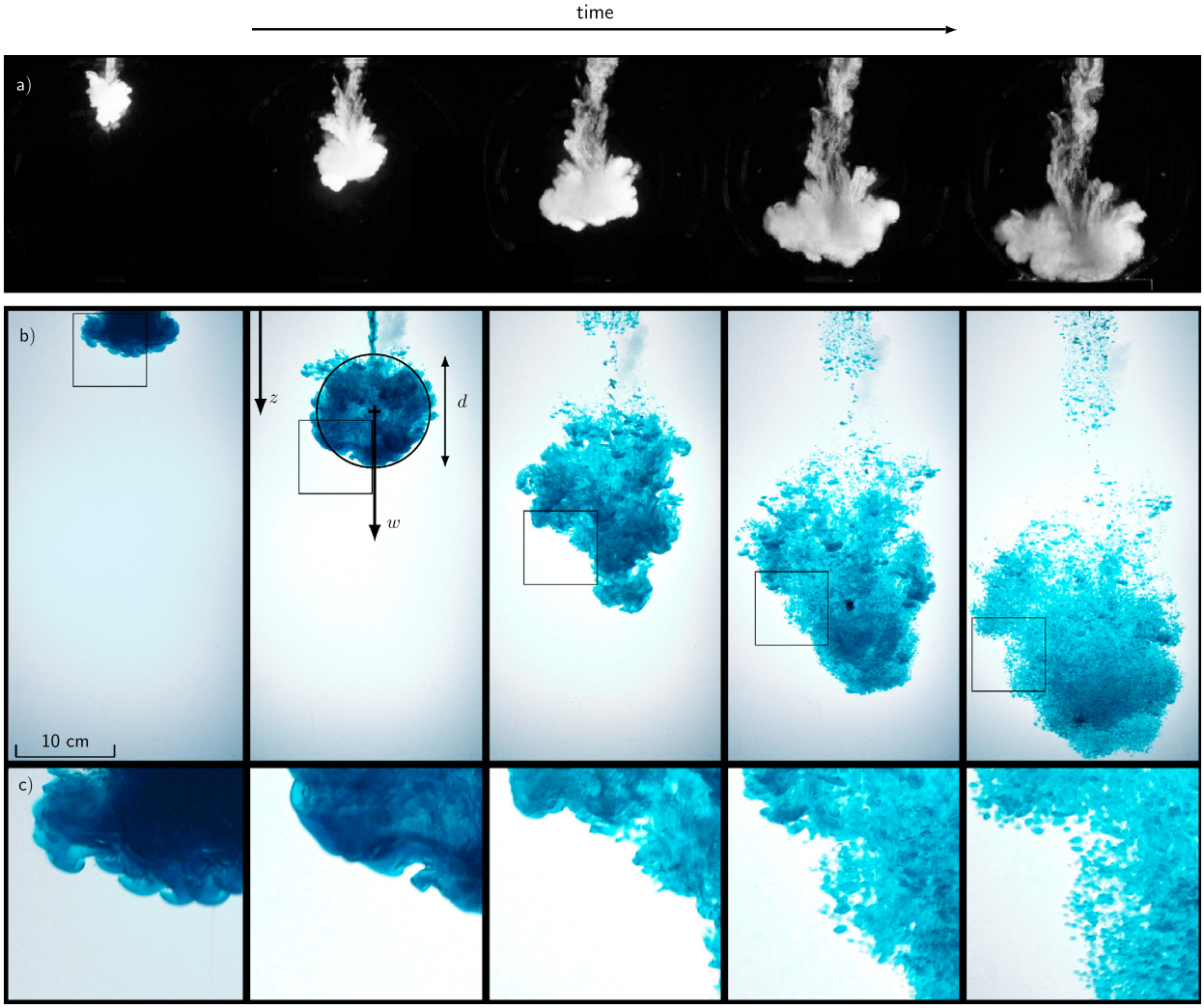

Fig. 1. Analog fluid dynamics experiments on metal–silicate mixing and fragmentation. (a) Growth of a negatively buoyant thermal by turbulent entrainment at $Re = 2 \times 10^3$. Here the buoyancy of the falling fluid is due to very fine dense particles in suspension (modified from Deguen et al., 2011). A small amount of fluorescent dye (fluoresceine) is added to the particle-laden fluid, which appears white in the pictures. (b) Fragmentation of a volume of aqueous solution of NaI salt (dyed in blue) released in silicone oil, at $We = 3 \times 10^3$, $Re = 2 \times 10^4$, $\mathsf{P} = 1.9$, $\mathsf{H} = 2.1$. Fragmentation of the aqueous volume into droplets occurs between the third and fourth snapshots. (c) Close-ups corresponding to the squares in (b). Small scale Rayleigh–Taylor instabilities are apparent in the first close-up. (For interpretation of the colours in this figure, the reader is referred to the web version of this article.)

into kinetic energy, which implies that the vertical velocity initially scales as $w \sim \sqrt{(\Delta\rho/\rho_m)gr}$. Using this scaling for w implies that $We \sim Bo$, using the equivalent diameter of the NaI solution volume as the length scale. The Weber and Reynolds numbers that characterize the experiments are defined using as a velocity scale the vertical velocity of the dense fluid after it has travelled a distance equal to its initial diameter. With this definition, we found that $We \simeq 0.43\,Bo$ in our experiments. Our choice of experimental fluids plus the use of a surfactant to reduce the interfacial tension allows us to reach values of Re larger than 10^4 and We up to 3×10^3, making our experiments far more dynamically similar to planetary accretion than current numerical simulations (Ichikawa et al., 2010; Samuel, 2012).

We have explored a wide range of parameters, with density ratios P from slightly larger than 1 to about 2, and Reynolds and Weber numbers ranging from moderate values to around 10^4 and 3×10^3, respectively. We focus here on the experiments we performed at the largest Reynolds and Weber numbers and a density ratio similar to that of the metal–silicate system, which are the most relevant to the core–mantle differentiation problem. More details about the all set of experiments will be found in a companion paper (Landeau et al., in press).

5. Experimental validation of the turbulent entrainment model

Snapshots from an experiment with Bond number $Bo = 6.9 \times 10^3$, Weber number $We = 3 \times 10^3$, Reynolds number $Re = 2 \times 10^4$, density ratio $\mathsf{P} = 1.9$, and viscosity ratio $\mathsf{H} = 2.1$ are shown in Fig. 1b and c. After release, the dense fluid (dyed in blue) undergoes small scale Rayleigh–Taylor instabilities (apparent on the first snapshot) which, together with shear induced by the global motion of the fluid, generate turbulence. The volume of the falling fluid increases with time much like the miscible fluids case shown in Fig. 1a, indicating that entrainment is occurring in spite of immiscibility.

Fig. 2 shows that the equivalent radius of the NaI solution–silicone oil mixture increases linearly with the distance travelled, in agreement with the turbulent entrainment model predictions (Eq. (3)). The entrainment coefficient α is in the range 0.2–0.3 in our experiments, similar to turbulent thermals in miscible fluids (Morton et al., 1956; Turner, 1969), which suggests that we have indeed reached a regime for which the large scales of the flow are unaffected by interfacial tension effects.

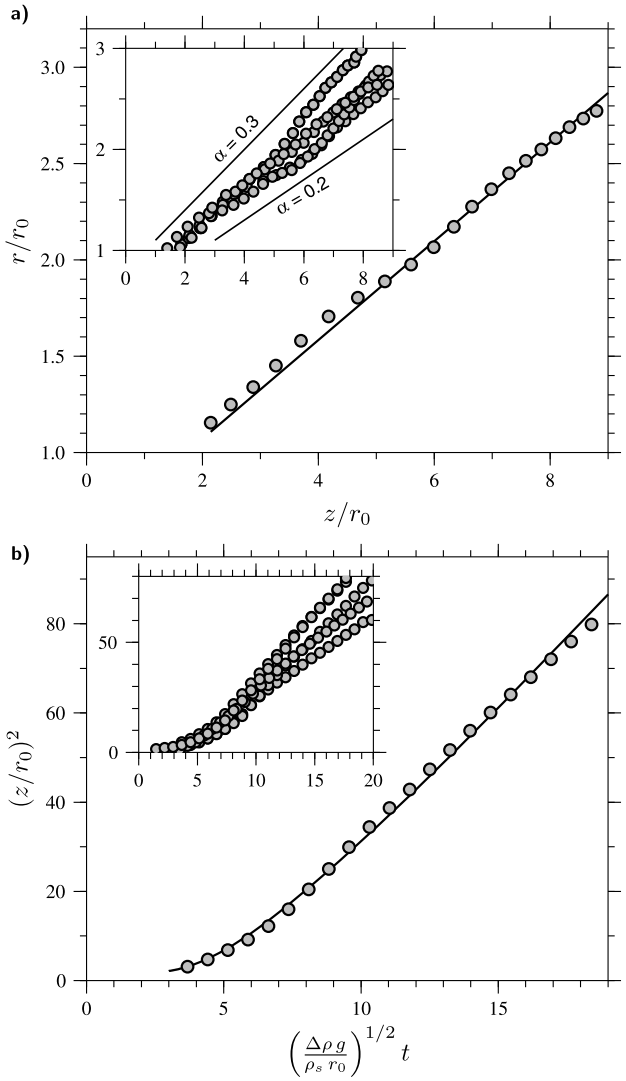

Fig. 2. Time evolution of the mean radius and position of the falling fluid, in experiments where a volume of NaI solution is released into silicone oil (P = 1.9). (a) Mean radius r (normalized by r_0) of the aqueous solution/oil mixture as a function of the position z (normalized by r_0) of its center of mass. (b) Square of the normalized position z of the center of mass of the aqueous solution/oil mixture as a function of time (normalized by $(\Delta\rho g/\rho_s r_0)^{-1/2}$). The results of one experiment are compared with the predictions of our model based on the entrainment assumption shown with black lines in (a) and (b). For this experiment, the model [Eqs. (B.8), (B.9) and (B.10)] best fits the data with $\alpha = 0.26$, a drag coefficient $C_d = 0.53$, and a virtual mass coefficient $K = 0.5$ (see Appendix B for details on the model). The experimental results shown in the inserts illustrate the natural variability seen in our experiments, with α varying between 0.2 and 0.3.

The predicted descent trajectory also compares favorably with the experimental results. Once integrated in time, the asymptotic velocity law equation (4) yields

$$\left(\frac{z}{r_0}\right)^2 = \left(\frac{2\Delta\rho g}{\alpha^3 \rho_s r_0}\right)^{1/2} \left(1 + K + \frac{3}{16}\frac{C_d}{\alpha}\right)^{-1/2} t. \quad (5)$$

Fig. 2b shows that after a short acceleration phase the experiments agree well with the prediction of Eq. (5) that $z^2 \propto t$, although there is some variability in the magnitude of the slope. The full evolution of our experiments can be explained by the model described in Appendix B. Although the drag and virtual mass coefficients are uncertain, the model (black curves in Fig. 2) fits very well the experimental measurements for reasonable values of these coefficients, with the observed variability in our experiments attributable to imperfect control of initial conditions plus natural variability inherent in turbulent flows.

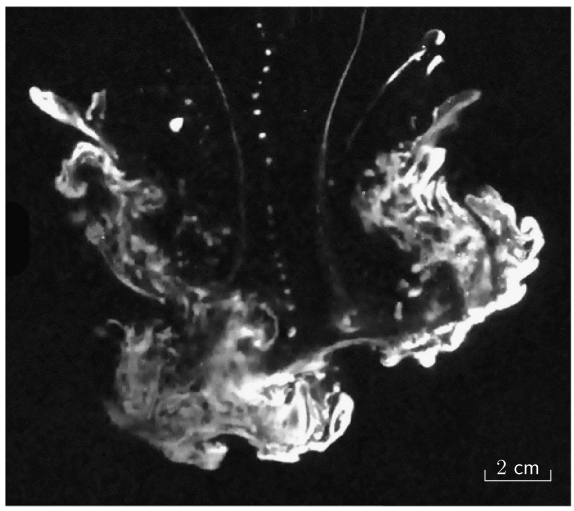

Fig. 3. Cross-section of the NaI solution/silicone oil mixture at a distance $\sim 2d_0$ from the origin. The experiment is illuminated with a thin light sheet exciting a fluorescent dye (Rhodamine B) added to the NaI solution, which appears white in the picture. In this experiment $Bo = 4.6 \times 10^3$, $We = 2 \times 10^3$, P = 1.54, H = 2.1, and $Re = 2 \times 10^4$.

The agreement between our experiments and the entrainment prediction strongly supports our contention that the turbulent entrainment concept can be applied to immiscible fluids when *We* and *Re* are large, and offers a simple way [Eqs. (3), (4), and Appendix B] to model the evolution of large metal masses in a magma ocean. In particular, the linear increase of the buoyant mixture radius provides a measure of metal–silicate mixing, with the metal dilution [Eq. (2)] given by

$$\Delta = \frac{\rho_s}{\rho_m}\left[\left(1 + \alpha\frac{z}{r_0}\right)^3 - 1\right]. \quad (6)$$

6. Fragmentation

Fig. 1b–c reveals that the dense NaI solution entrains and incorporates silicone oil *before* it fragments into droplets. Fragmentation occurs relatively late in the descent process (between the third and fourth pictures in the experiment shown in Fig. 1b–c), at a time when a sizable volume of ambient fluid has already been entrained. Droplets appear in a single global fragmentation event, which is at variance with previously suggested "cascade" processes, in which a succession of fragmentation events lead to the final stable drop size (Rubie et al., 2003; Samuel, 2012), and "erosion" processes, in which metal–silicate mixing occurs predominantly on the boundary with the ambient fluid (Dahl and Stevenson, 2010).

Adding a small amount of fluorescent dye to the NaI solution and illuminating the experiment with a thin light sheet reveals cross-sections of the NaI solution/silicone oil mixture, one example being shown in Fig. 3. Small scale mixing of the phases is evident in this picture, demonstrating that oil has been entrained into the NaI solution and that the two phases are already intimately mixed *before* fragmentation occurs. This striking observation suggests that fragmentation is a consequence of mixing associated with turbulent entrainment of the ambient fluid, with fragmentation into drops ultimately resulting from small scale instabilities, plausibly capillary instabilities developed on filaments stretched by the turbulent flow (Villermaux et al., 2004; Shinjo and Umemura, 2010).

In all our experiments in this turbulent regime, fragmentation into drops is observed to occur after the dense liquid falls a dis-

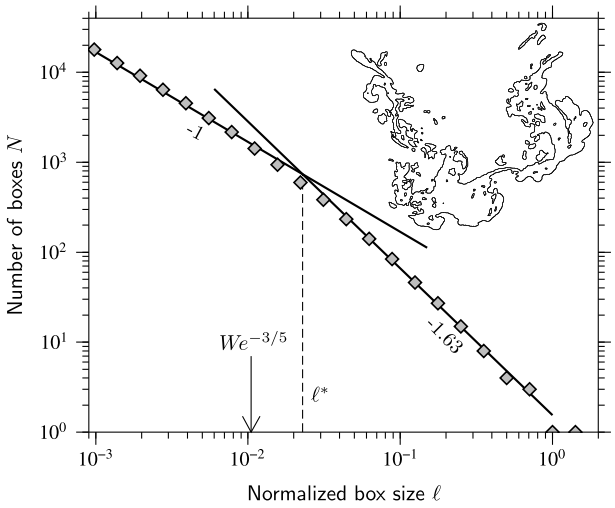

Fig. 4. The fractal dimension of the oil/aqueous solution interface shown in Fig. 3, determined using a box counting algorithm. Shown here is the number $N(\ell)$ of square boxes of size ℓ required to cover the oil/aqueous solution interface as a function of the box size ℓ. Here the box size ℓ is normalized by the size of the smallest box fully enclosing the interface. The slope of the resulting curve is $1-D$, where D is the fractal dimension of the 3D interface. A slope of -1 is expected for a non-fractal surface, as found here for small ℓ. The interface is fractal at scales above $\ell^* \simeq 2.3\times10^{-2}$, which is of the same order of magnitude as $We^{-3/5} \simeq 1.05\times10^{-2}$. Fitting the data for $\ell > \ell^*$ (thick black line) gives a slope of -1.63 ± 0.03 ($\pm1\sigma$), which implies a fractal dimension of 2.63 ± 0.03, slightly smaller than $D = 8/3 = 2.67$.

tance equal to 3–4 times its initial diameter, with no clear trend observed in the explored range of parameters. At this point the volume fraction of the dense fluid in the mixture is of order 5–10%. It is possible that the fragmentation distance becomes independent of *Re* and *We* when these two numbers are large, but the maximum value of *We* obtained in our experiments (3000) is only 6 times larger than its observed critical value for this turbulent regime (∼500), making the explored range of *We* too small to test this possibility.

7. Chemical equilibration before fragmentation – a fractal model

Fragmentation of the metal phase into drops is an important facet of the problem of metal–silicate interactions, because drop formation is an efficient way of increasing the interfacial area between metal and silicate, thus enhancing chemical transfer and equilibration. However, it may not be necessary for chemical equilibration. The small scale mixing observed in our experiments (Fig. 3) results in a highly convoluted interface, which should drastically decrease the timescale of equilibration with the entrained silicate.

To illustrate this point, we consider a model of metal–silicate equilibration prior to drop formation based on the observation that the interface separating the two fluids has a fractal nature once turbulence is well-developed. Theory (Mandelbrot, 1975; Constantin et al., 1991; Constantin and Procaccia, 1994) and experiments (Sreenivasan et al., 1989; Constantin et al., 1991) show that isosurfaces of transported quantities (composition, temperature) in well-developed turbulent flows are fractal – a consequence of the self-similarity of the turbulent flow – with a fractal dimension predicted to be $D = 8/3$ for homogeneous turbulence with Kolmogorov scaling.

It is to be expected that the interface between immiscible fluids in a turbulent flow shares this property over the range of scales in which interfacial tension is unimportant. Experimental support for this assumption is given in Fig. 4, where the interface between the oil and aqueous solution is shown to have a fractal nature

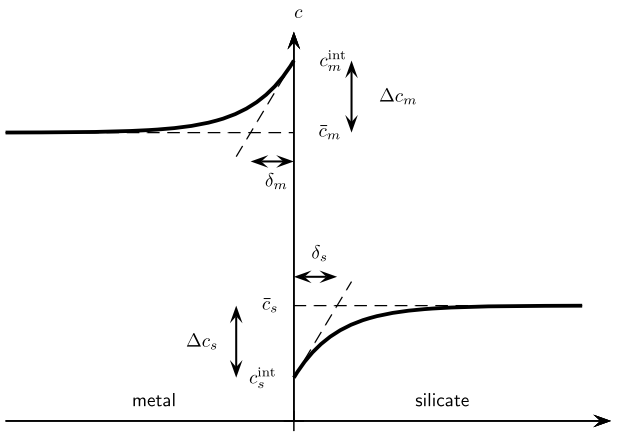

Fig. 5. A sketch of the composition profiles in the vicinity of the metal–silicate interface. The situation depicted here is that of a siderophile element in excess in the silicate phase.

with a fractal dimension at scales larger than a cut-off length ℓ^*. For miscible fluids, Sreenivasan et al. (1989) assumed that the inner cut-off length is the Kolmogorov scale for isovorticity surfaces, and the Batchelor scale for isocompositional surfaces for high Schmidt number fluids. For a surface separating two immiscible fluids, we expect that the inner cut-off length will be the largest of the Kolmogorov scale $\ell_K = d\,Re^{-3/4}$ and the scale $\ell_\sigma = d\,We^{-3/5}$ at which interfacial tension balances local dynamic pressure fluctuations estimated assuming a Kolmogorov cascade (Kolmogorov, 1949; Hinze, 1955, and see Section 8 for more details). Typically $\ell_\sigma \gg \ell_K$, and we expect that $\ell^* \sim \ell_\sigma$. In our experiments, ℓ^* and ℓ_σ are numerically close (within a factor of 2, Fig. 4) and the measured fractal dimension is only slightly smaller than the theoretical value of 8/3. Note that the observed fractal nature of the interface is indicative of self-similarity in the flow, and that the measured fractal dimension is consistent with Kolmogorov type turbulence and a $k^{-5/3}$ kinetic energy spectrum.

Assuming that the metal–silicate interface has a fractal nature offers a convenient way of estimating its area A_T, which according to fractal geometry scales as $A_T \sim A_0(\ell^*/d)^{2-D}$, where $A_0 = \pi d^2$ is the area measured at the scale d. Using $\ell^* \sim \ell_\sigma$, the predicted surface area is $A_T \sim A_0 We^{\frac{3}{5}(D-2)}$. With $D = 8/3$ and $We = 10^{14}$, this implies an increase in interfacial area by five orders of magnitude. A timescale for chemical equilibration, τ_{eq}, can then be found by coupling the estimate for A_T with a local scaling for turbulent mass flux at the metal–silicate interface.

We denote by κ_c the diffusivity of the chemical element of interest. The Schmidt number $Sc^{m,s} = \nu_{m,s}/\kappa_c^{m,s}$, where ν is the kinematic viscosity, is assumed to be large in both phases. Fig. 5 shows a sketch of the composition profiles in the vicinity of the metal–silicate interface, with definitions of the main variables. Thermodynamic equilibrium is assumed at the metal/silicate interface, so that the concentrations by mass c_m^{int} and c_s^{int} at the interface are linked by the partition coefficient $D_i = c_m^{\mathrm{int}}/c_s^{\mathrm{int}}$, but the bulk compositions $\bar{c}_m$ and $\bar{c}_s$ are out of thermodynamic equilibrium, i.e. $\bar{c}_m/\bar{c}_s \neq D_i$. The resulting compositional boundary layers have thicknesses $\delta_{m,s}$, and we denote by $\Delta c_{m,s}$ the composition difference across the boundary layers. The local diffusive compositional flux across the interface scales as $\kappa_c \Delta c/\delta$ and the total mass flux F_c is

$$F_c \sim \rho_m A_T \kappa_c^m \frac{\Delta c_m}{\delta_m} \sim \rho_s A_T \kappa_c^s \frac{\Delta c_s}{\delta_s}. \tag{7}$$

Continuity of the mass flux across the interface implies that the ratio $\gamma_{m/s}$ of Δc_m to Δc_s is

$$\gamma_{m/s} = \frac{\Delta c_m}{\Delta c_s} = \frac{\rho_s}{\rho_m}\frac{\kappa_c^s}{\kappa_c^m}\frac{\delta_m}{\delta_s}. \tag{8}$$

We now relate the compositional jumps Δc_s and Δc_m to the mean composition $\bar{c}_m$ and $\bar{c}_s$ of the metal and silicate phases. Using Eq. (8) together with the assumption of local thermodynamic equilibrium ($D_i = c_m^{\text{int}}/c_s^{\text{int}}$), we obtain the following expressions for Δc_s and Δc_m:

$$\Delta c_s = -\frac{\bar{c}_m - D_i\bar{c}_s}{\gamma_{m/s} + D_i}, \qquad \Delta c_m = -\gamma_{m/s}\frac{\bar{c}_m - D_i\bar{c}_s}{\gamma_{m/s} + D_i}. \tag{9}$$

Using $(\pi/6)\bar{\rho}\,d^3$ for the mass of the metal–silicate mixture, the evolution of composition in the metal and silicate phases are given by

$$\phi\frac{\pi}{6}\bar{\rho}d^3\frac{d\bar{c}_m}{dt} = -F_c, \tag{10}$$

$$(1-\phi)\frac{\pi}{6}\bar{\rho}d^3\frac{d\bar{c}_s}{dt} = F_c, \tag{11}$$

where ϕ is the mass fraction of the metal phase in the mixture. Combining Eqs. (10) and (11) and using the metal dilution $\Delta = (1-\phi)/\phi$ and Eq. (7) for F_c, we obtain

$$\frac{d}{dt}\ln(\bar{c}_m - D_i\bar{c}_s) \sim -\frac{(1+\Delta)(D_i+\Delta)}{\Delta(D_i+\gamma_{m/s})}\frac{\rho_s}{\bar{\rho}}\frac{6\kappa_c^s}{d\delta_s}We^{\frac{3}{5}(D-2)}, \tag{12}$$

from which we obtain an equilibration timescale τ_{eq} given by

$$\tau_{\text{eq}} = f(\Delta, D_i, \gamma_{m/s})\frac{\bar{\rho}}{\rho_s}\frac{d\,\delta_s}{\kappa_c^s}We^{-\frac{3}{5}(D-2)}, \tag{13}$$

where the factor 6 in Eq. (12) has been omitted, on the basis that this expression for τ_{eq} is based on an order of magnitude estimate of the flux across the interface [Eq. (7)], in which an unknown – presumably $\mathcal{O}(1)$ – factor has already been omitted. Keeping this factor would result in a shorter equilibration timescale. In Eq. (13), the function $f(\Delta, D_i, \gamma_{m/s})$ is given by

$$f(\Delta, D_i, \gamma_{m/s}) = \frac{\Delta(D_i+\gamma_{m/s})}{(1+\Delta)(D_i+\Delta)}. \tag{14}$$

The function f is $\mathcal{O}(1)$ for intermediate values of Δ (with a maximum always smaller than 1), but $f \to 0$ if Δ is small compared to $\min(1, D_i)$ or large compared to $\max(1, D_i)$.

We now estimate the boundary layers thicknesses δ in the metal and silicate phases (the subscript m and s will be omitted in what follows, with the understanding that the analysis applies to both phases). Denoting by ℓ the smallest scale of the flow in the vicinity of the interface, then the smallest scale δ of the compositional field is found by balancing the strain rate at scale ℓ with the diffusion rate at the scale δ, i.e. $u_\ell/\ell \sim \kappa_c/\delta^2$. Assuming a Kolmogorov type velocity spectrum, the velocity at scale ℓ is $u_\ell \sim w(\ell/d)^{\frac{1}{3}}$, where w is the large scale velocity. With these assumptions, we obtain

$$\delta = d\,Sc^{-\frac{1}{2}}Re^{-\frac{1}{2}}\left(\frac{\ell}{d}\right)^{\frac{1}{3}}. \tag{15}$$

At this stage, further progress requires assumptions on the small scale structure of the turbulence in the vicinity of the metal–silicate interface:

1. If we assume that the turbulence structure is not affected by the presence of the interface and interfacial tension effects, then ℓ should be the Kolmogorov scale. Eq. (15) with $\ell = \ell_K = dRe^{-3/4}$ gives

$$\delta = d\,Sc^{-\frac{1}{2}}Re^{-3/4}, \tag{16}$$

which is the Batchelor scale ℓ_B. With this estimate for δ, we obtain

$$\gamma_{m/s} = \left(\frac{\rho_s}{\rho_m}\right)^{5/4}\left(\frac{\kappa_c^s}{\kappa_c^m}\right)^{1/2}\left(\frac{\eta_s}{\eta_m}\right)^{1/4} \tag{17}$$

and an equilibration timescale

$$\tau_{\text{eq}} = f(\Delta, D_i, \gamma_{m/s})\frac{\bar{\rho}}{\rho_s}\frac{d^2}{\kappa_c^s}Sc^{-1/2}Re^{-3/4}We^{-\frac{3}{5}(D-2)}. \tag{18}$$

2. Alternatively, one might argue that the turbulent motion in the vicinity of the interface is damped by interfacial tension at scales smaller than ℓ_σ. In this case the smallest scale of the flow is $\ell_\sigma \sim dWe^{-3/5}$ and the boundary layer thickness is

$$\delta = d\,Sc^{-\frac{1}{2}}Re^{-\frac{1}{2}}We^{-\frac{1}{5}}, \tag{19}$$

which gives

$$\gamma_{m/s} = \left(\frac{\rho_s}{\rho_m}\right)^{6/5}\left(\frac{\kappa_c^s}{\kappa_c^m}\right)^{1/2} \tag{20}$$

and an equilibration timescale

$$\tau_{\text{eq}} = f(\Delta, D_i, \gamma_{m/s})\frac{\bar{\rho}}{\rho_s}\frac{d^2}{\kappa_c^s}Sc^{-\frac{1}{2}}Re^{-\frac{1}{2}}We^{-\frac{3}{5}D+1}. \tag{21}$$

Choosing between the two models Eqs. (18) or (21) would require detailed measurement of the small scale structure of the flow, or alternatively, measurements of a tracer concentration in both phases, which are beyond the scope of our current experimental set-up. We therefore choose the more conservative estimate of the equilibration timescale Eq. (21) which assumes that turbulent motions in the vicinity of the interface are damped at scales smaller than ℓ_σ. For comparison, the model assuming no effect of the interface on the turbulence structure would yield an equilibration timescale a factor $We^{1/5}Re^{-1/4}$ smaller (typically a factor of 5 or more smaller).

With $\rho_s/\rho_m \simeq 0.5$, assuming that κ_c^s and κ_c^m are of the same order of magnitude implies that $\gamma_{m/s} = \mathcal{O}(1)$. Since it only appears in $f(\Delta, D_i, \gamma_{m/s})$ as a sum with D_i which is $\gg 1$ for siderophile elements, the exact value of $\gamma_{m/s}$ should be of little importance. The factor $\bar{\rho}/\rho_s$ is also $\mathcal{O}(1)$, and ignoring it as well in Eq. (21) yields the simplified equilibration timescale

$$\tau_{\text{eq}} \simeq f(\Delta, D_i)\frac{d^2}{\kappa_c^s}Sc^{-\frac{1}{2}}Re^{-\frac{1}{2}}We^{-\frac{3}{5}D+1}. \tag{22}$$

From Eq. (22), we obtain an equilibration distance $\ell_{\text{eq}} = w\tau_{\text{eq}}$ given by

$$\ell_{\text{eq}} \simeq f(\Delta, D_i)d\,Sc^{\frac{1}{2}}Re^{\frac{1}{2}}We^{-\frac{3}{5}D+1}, \tag{23}$$

which is the distance travelled by the metal phase during the time τ_{eq} required for equilibration of the metal with the silicate it has mixed with. Metal and silicates equilibrate if the equilibration distance ℓ_{eq} is smaller than the magma ocean depth. Fig. 6 shows ℓ_{eq} as a function of d for various values of w between 100 m s^{-1} and 1 km s^{-1}, calculated with $f(\Delta, D_i) = 0.5$, $\kappa_c^s = 10^{-8}$ m s^{-1}, $\sigma = 1$ J m^{-2} and $\rho_s = 3500$ kg m^{-3}. The equilibration distance is always a fraction of the metal–silicate mixture diameter, which implies that, once turbulence is well-developed, the metal should continuously equilibrate with the entrained silicates.

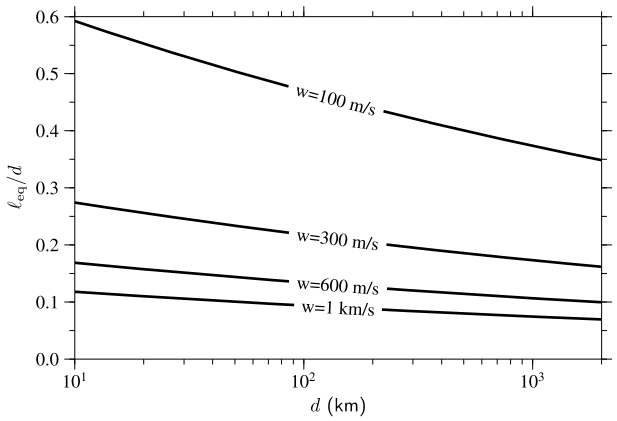

Fig. 6. Equilibration distance ℓ_{eq}/d as functions of the metal–silicate mixture diameter d, for $w = 100$, 300, 600 and 1000 $\mathrm{m\,s^{-1}}$, calculated using Eq. (23) with $f(\Delta, D_i) = 0.5$, $\kappa_c^s \sim 10^{-8}$ $\mathrm{m\,s^{-1}}$, $\sigma = 1$ $\mathrm{J\,m^{-2}}$ and $\rho_s = 3500$ $\mathrm{kg\,m^{-3}}$.

8. Prediction for the stable drop size after fragmentation

After fragmentation, the metal–silicate equilibration timescale depends mostly on the resulting fragments size (Karato and Murthy, 1997; Rubie et al., 2003; Ulvrová et al., 2011). In this section, we propose a scaling for the drop size of the metal phase after fragmentation, as well as a justification for the scaling used in the previous section for the cut-off length scale ℓ^* above which the interface (before fragmentation) is fractal. In a fully turbulent flow, the stable drop size d_d after fragmentation, as well as the cut-off length scale ℓ^* before fragmentation, are expected to depend only on the dissipation rate ϵ, the interfacial tension σ, the densities and viscosities of both phases, and the metal volume fraction:

$$\left(d_d, \ell^*\right) = \mathcal{F}_1(\epsilon, \sigma, \rho_m, \rho_s, \nu_s, \nu_m, \phi). \tag{24}$$

Using the Vashy–Buckingham theorem, we find that ℓ^* must be the solution of an equation of the form

$$\mathcal{F}_2\left[\mathsf{P}, \mathsf{H}, \phi, \frac{\ell^*}{\ell_K}, \frac{\ell^*}{\ell_\sigma}\right] = 0, \tag{25}$$

where we have introduced two length scales,

$$\ell_K = \left(\frac{\nu_s^3}{\epsilon}\right)^{1/4}, \qquad \ell_\sigma = \left(\frac{\sigma}{\rho_s}\right)^{3/5} \epsilon^{-2/5}. \tag{26}$$

ℓ_K is the Kolmogorov scale, at which turbulent kinetic energy is dissipated into heat by the action of viscous forces; ℓ_σ can be shown to be the length scale at which interfacial tension (Laplace pressure) balances turbulent pressure fluctuations and stresses if a Kolmogorov type turbulence is assumed (Kolmogorov, 1949; Hinze, 1955). With $\epsilon \sim w^3/r$ (Tennekes and Lumley, 1972),

$$\ell_K \sim Re^{-3/4} d, \qquad \ell_\sigma \sim We^{-3/5} d. \tag{27}$$

Two end-member cases are possible, depending on the relative values of ℓ_K and ℓ_σ. Let us first compare the magnitude of the viscous stress and Laplace pressure at a given scale ℓ. Assuming a Kolmogorov type turbulence cascade, the velocity fluctuations u_ℓ at a scale $\ell > \ell_K$ is $u_\ell \sim w(\ell/d)^{1/3}$. Using this estimate for u_ℓ, we find that the ratio of the viscous stress to the Laplace pressure at the scale ℓ is

$$\frac{\text{Viscous stress at scale } \ell}{\text{Laplace pressure at scale } \ell} \sim \frac{\eta_s u_\ell/\ell}{\sigma/\ell} \sim \left(\frac{\ell_K}{\ell_\sigma}\right)^{4/3} \left(\frac{\ell}{\ell_\sigma}\right)^{1/3}. \tag{28}$$

Two options are possible:

1. First, if $\ell_K \gg \ell_\sigma$, all the energy input is dissipated at the Kolmogorov scale, at which scale the ratio of viscous stress and Laplace pressure is $\sim (\ell_K/\ell_\sigma)^{5/3} \gg 1$ according to Eq. (28). In this case interfacial tension is unimportant, and d_d and ℓ^* scale as
$$\left(d_d, \ell^*\right) = \mathcal{F}_3(\mathsf{P}, \mathsf{H}, \phi)\left(\frac{\nu_s^3}{\epsilon}\right)^{1/4} \sim \mathcal{F}_3(\mathsf{P}, \mathsf{H}, \phi) d Re^{-3/4}. \tag{29}$$
2. Alternatively, if $\ell_K \ll \ell_\sigma$, then interfacial tension balances turbulent pressure and stress fluctuations at the scale ℓ_σ, with further smaller scale deformation of the interface inhibited by the interfacial tension. According to Eq. (28), the ratio of viscous stress and Laplace pressure is $\sim (\ell_K/\ell_\sigma)^{4/3} \ll 1$ at this scale, which implies that viscous effects are unimportant. As a consequence, the stable drop size does not depend on the viscosity of either phase, nor on the viscosity ratio H, and thus the drop size and the cut-off length scale follow a scaling law of the form:
$$\left(d_d, \ell^*\right) = \mathcal{F}_4(\mathsf{P}, \phi)\left(\frac{\sigma}{\rho_s}\right)^{3/5} \epsilon^{-2/5} \sim \mathcal{F}_4(\mathsf{P}, \phi) d We^{-3/5}. \tag{30}$$

The ratio $\ell_K/\ell_\sigma \sim We^{3/5} Re^{-3/4}$ following an impact is found to be typically smaller than 10^{-2}, which suggests that the drop size or cut-off length will be set by interfacial tension rather than viscosity, and will obey the scaling given by Eq. (30). When ϕ is small, its effect should be negligible, as indeed observed in experiments with dilute dispersions (Hinze, 1955; Chen and Middleman, 1967).

From analysis of Clay's (1940) data, Hinze (1955) found that the maximum drop size $d_{\max}$ in a turbulent flow with $\ell_\sigma \gg \ell_K$ is given by

$$d_{\max} \simeq 0.725 \left(\frac{\sigma}{\rho_s}\right)^{3/5} \epsilon^{-2/5}. \tag{31}$$

Effects of changing the density ratio was not investigated in this study, which focused on fluids with density ratios $\mathsf{P} \simeq 1$. Theory (Levich, 1962) and experiments (Hesketh et al., 1987) argue for a dependence on the density ratio of the form $d_{\max} \propto \mathsf{P}^{-1/5}$. For the metal–silicate system, which has $\mathsf{P} \simeq 2$, this would predict a maximum drop size about 13% smaller than what Eq. (31) predicts, a minor discrepancy in light of the other uncertainties.

Clearly, the size of the drops produced by fragmentation of the metal blob must depend on the details of the fragmentation mechanism, which are not elucidated yet, and the drop size just after fragmentation does not have to match the prediction of Eq. (31) (although a similar scaling is expected). Nevertheless, Eq. (31) should give a reasonable upper bound for the fragment size, since it predicts that larger drops would be disrupted by turbulent dynamic pressure fluctuations.

In a system in statistical steady state, the dissipation rate ϵ must equal the total energy input in the system e_{in}, which here is the rate of work of the buoyancy forces. However, since the metal–silicate mixture is not in statistical steady state (it can be shown using the self-similar regime velocity (Eq. (4)) that the total kinetic energy of the system evolves with time), dissipation does not equal the rate of energy input, but is some fraction f of the work done by the buoyancy forces. The rate of work of the buoyancy forces,

$$e_{\text{in}} = \bar{\phi} \frac{\Delta\rho}{\bar{\rho}} g w, \tag{32}$$

tends towards

$$e_{\text{in}} = 2\left[1 + K + \frac{3}{16}\frac{C_d}{\alpha}\right]^{-1/2} \frac{\rho_s}{\bar{\rho}} \left[\frac{\Delta\rho g r_0^{1/3}}{2\alpha^3 \rho_s}\right]^{3/2} \left(\frac{r_0}{z}\right)^4, \tag{33}$$

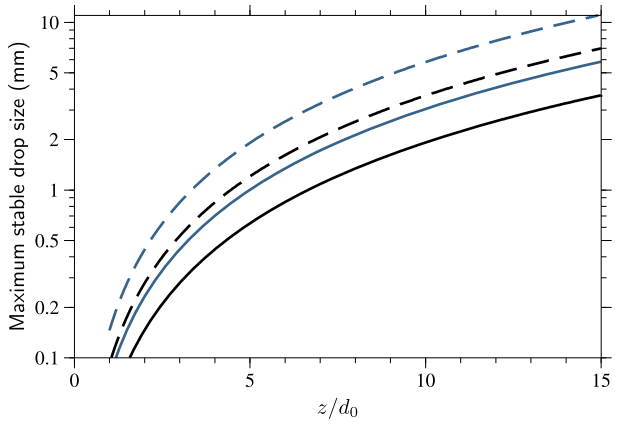

Fig. 7. Maximum stable drop size after fragmentation according to Eq. (34), as a function of the distance travelled (normalized by the initial metal blob diameter d_0), for metal blobs with initial diameter 100 km (blue curves) and 1000 km (black curves) with $f = 0.5$ (solid curves) and $f = 0.1$ (dashed curves). Assumed parameters values are: $\alpha = 0.25$, $K + 3C_d/16\alpha = 1$, $\Delta\rho = 4000\ \mathrm{kg\,m^{-3}}$, $\rho_s = 3500\ \mathrm{kg\,m^{-3}}$, $g = 5\ \mathrm{m\,s^{-2}}$, $\sigma = 1\ \mathrm{J\,m^{-2}}$. (For interpretation of the colours in this figure, the reader is referred to the web version of this article.)

in the self-similar regime, for which w is given by Eq. (4). Using Eq. (33) for e_{in} and writing the dissipation as $\epsilon = f e_{\mathrm{in}}$, we find that

$$\frac{d_{\max}}{d_0} \simeq \frac{3}{f^{2/5}}\left[1 + K + \frac{3}{16}\frac{C_d}{\alpha}\right]^{1/5}\left(\frac{\bar{\rho}}{\rho_s}\right)^{2/5}\frac{\alpha^{9/5}}{Bo_0^{3/5}}\left(\frac{z}{d_0}\right)^{8/5} \quad (34)$$

when the mixture has reached the self-similar regime. Here $Bo_0 = \Delta\rho\, g\, d_0^2/\sigma$. The value of f is difficult to estimate precisely, but shouldn't be much smaller than 1. Fig. 7 shows $d_{\max}$ from Eq. (34) for metal blobs with initial diameter 100 km (blue curves) and 1000 km (black curves) with $f = 0.5$ (solid curves) and $f = 0.1$ (dashed curves), and $\alpha = 0.25$. Smaller values of α would result in smaller drop sizes. Eq. (34) predicts submillimeter-to-centimeter maximum stable drop sizes, which is small enough to ensure fast re-equilibration with the surrounding silicates (Karato and Murthy, 1997; Rubie et al., 2003; Ulvrová et al., 2011).

9. Discussion

9.1. On the relevance of our experiments for the core formation problem

Uncertainties about the applicability of our results to metal–silicate mixing and fragmentation in magma oceans are due mostly to the fact that our experiments are still very far from the impact conditions with *Re*, *We* and *Bo* up to ten orders of magnitude smaller than during Earth accretion. The main obstacles to improving experimental as well as numerical approaches stem from the three dimensional, turbulent nature of the flow at these extreme parameters. Direct numerical simulations of turbulent flows at such high *Re* are prohibitively expensive. The cost[1] of a direct numerical simulation resolving the Kolmogorov scale goes as $\sim Re^{11/4}$, which implies that increasing *Re* by a factor of 10 multiplies the cost by about 500.

Accordingly, a legitimate question is: how close to the dynamical conditions of accretion do we need to go? In boundary free turbulent flows involving fully miscible fluids, it is observed that there is no qualitative change of the flow associated with increasing *Re* once turbulence is "fully-developed", i.e. once there is a range of length scales (the inertial range) for which viscosity effects are negligible (e.g. Mungal and Hollingsworth, 1989). Increasing *Re* further increases the gap between the integral scale (the largest scale of the flow, here the diameter of the blob) and the Kolmogorov scale at which viscous dissipation occurs, but does not change the slope of the kinetic energy spectrum. The entrainment coefficient in turbulent thermals appears to be independent of *Re* (e.g. Turner, 1969) once $Re \gtrsim 10^3$, which is consistent with the rate of turbulent entrainment being controlled by the largest, inviscid eddies (Turner, 1986).

In immiscible fluid systems like metal–silicate, we should expect that a similar asymptotic regime is reached once there is a separation of scales between the integral scale of the flow and the Kolmogorov ($dRe^{-3/4}$) and capillary ($dWe^{-3/5}$) scales, so that there is a range of scales for which viscosity and interfacial tension do not play any role. Increasing further *Re* and *We* will increase the ratio between the largest and smallest scales of the flow, but should not change the phenomenology, nor the slope of the kinetic energy spectrum in the inertial range. By analogy with the miscible fluid case, the entrainment coefficient in the immiscible fluids case should not depend on *We* and *Re* once these numbers are large enough.

While it is difficult to demonstrate without heavier instrumentation and actual velocity measurements that our experiments have indeed reached a large *Re*, large *We* asymptotic regime, there are a number of observations which are consistent with our experiments being at least close to such regime: (i) the measured coefficient of entrainment is similar to that measured in miscible turbulent thermals, consistent with the entrainment rate being independent of the interfacial tension; (ii) the observed fractal nature of the interface is indicative of self-similarity in the flow, and the measured fractal dimension is consistent with a $k^{-5/3}$ spectrum; (iii) the cut-off length observed in cross-sections of the mixture, which presumably corresponds to the capillary scale, is more than a decade smaller than the diameter of the NaI–silicon oil mixture (40 times smaller in Fig. 4).

Together, these observations support our claim that the entrainment model, and the entrainment coefficient value of $\simeq 0.25$ which we observe, should indeed apply to larger values of *Re* and *We*. However, there is one more point which needs to be discussed: compressibility effects, which are absent in our experiments (the Mach number M is $\sim 10^{-4}$), may be significant in the flow following an impact, which can often be supersonic. This is probably the most severe limitation of our experiments. The fact that the flow velocity is similar to the sound velocity has an important qualitative consequence for the structure of the flow: the finite speed of sound introduces a time delay in the transmission of pressure signals from one point to another, which disrupts the coherence of large turbulent eddies where the local Mach number (based on the eddy velocity scale) is of order one or larger (Breidenthal, 1992; Freund et al., 2000; Pantano and Sarkar, 2002). Because the rate of entrainment is thought to be controlled by the process of engulfment of ambient fluid by large scale eddies (Brown and Roshko, 1974; Turner, 1986; Mathew and Basu, 2002), mixing is expected to decrease when M approaches 1. Experiments on compressible turbulent jets and mixing layers show that the entrainment rate indeed decreases significantly with increasing M, before saturating at a value about five times smaller than for incompressible flows (Brown and Roshko, 1974; Freund et al., 2000) when $M \gtrsim 1$. An entrainment coefficient several times smaller than the 0.25 ± 0.05 value of our experiments might therefore be expected when the Mach number of the metal–silicate mixture is $\mathcal{O}(1)$.

[1] In a turbulent flow, the smallest scale which has to be resolved is the Kolmogorov scale $\ell_K \sim d\,Re^{-3/4}$. This therefore requires $\sim Re^{3/4}$ grid points in each direction, or $\sim Re^{9/4}$ grid points for a 3D simulations. The typical timescale corresponding to the Kolmogorov scale is $\tau_K = Re^{-1/2} d/w$, which means that $\sim Re^{1/2}$ timesteps are needed for a simulation time corresponding to d/w. The total cost therefore scales as $\sim Re^{9/4} \times Re^{1/2} \sim Re^{11/4}$.

9.2. Comparison with previous work

The reduction of a large metal blob to a drop size has been investigated by Dahl and Stevenson (2010) and Samuel (2012). Two different scenarios have been considered by Dahl and Stevenson (2010). In the first model, metal–silicate mixing is assumed to occur through gradual erosion of the metal blobs by small scale Rayleigh–Taylor instabilities. The model predicts that only relatively small metal blobs (less than 10 km in diameter) efficiently mix with silicates, so that larger blobs reach the core of the growing planet without significant chemical interactions with the surrounding silicates. In the second model, Dahl and Stevenson (2010) considered the possibility of metal–silicate mixing through turbulent entrainment, similar to the model we present here, but their analysis of the structure of the turbulence lead them to conclude that mixing associated with the entrainment process does not proceed to length scales small enough to permit efficient chemical re-equilibration. Our experiments suggest that mixing does proceed down to the capillary scale at which surface tension balances dynamic pressure fluctuations, and our model for the kinetics of equilibration predicts fast re-equilibration, implying that the metal should continuously equilibrate with the entrained silicates once turbulence is well-developed. However, fast equilibration between the metal and entrained silicates does not necessarily imply a significant flux of elements from one phase to the other, because this also depends on the amount of metal–silicate mixing. Although the entrainment model predicts significantly more mixing than the Rayleigh–Taylor erosion model of Dahl and Stevenson (2010), chemical re-equilibration remains problematic for the largest impacts (see further discussion in Section 10).

Numerical models of the evolution of a metal blob falling in molten silicates by Samuel (2012) indicate metal fragmentation occurs through a sequence of events leading to the final stable drop size, which is quite different from the picture our experiments and analysis suggest. A major limitation of Samuel (2012) study is the assumption of axisymmetry of the flow, a constraint that inhibits the development of turbulence.

Regarding the size of the fragments resulting from the metal fragmentation process, models for the maximal stable drop size have been discussed by Stevenson (1990), Karato and Murthy (1997), and Rubie et al. (2003). Although we argue for a different scaling for the stable drop size (Section 8), the implications are essentially the same: metal phase fragmentation to stable drop size ensures fast chemical re-equilibration between the drops and surrounding silicates.

10. Implications for planetary core formation

As shown in the introduction section [see Eq. (1)], efficient chemical re-equilibration requires that two necessary conditions are met: (i) that the metal phase is capable of equilibrating with the silicates it has mixed with (i.e. that the parameter k in Eq. (1) is of order 1), and (ii) that the metal phase equilibrates with a silicate mass at least a factor D_i larger (i.e. that the metal dilution $\Delta \gtrsim D_i$).

With a velocity w in the range 0.1–1 $\mathrm{km\,s^{-1}}$ and diameter $d > 10$ km, our model predicts that the equilibration distance ℓ_{eq} (the distance travelled by the metal phase during the time needed for equilibration) is always smaller than about $0.6d$ (Fig. 6). For example, Eq. (23) yields $\ell_{eq} \simeq 50$ km for $d = 100$ km and $w = 100\ \mathrm{m\,s^{-1}}$, and $\ell_{eq} \simeq 75$ km for $d = 1000$ km and $w = 1\ \mathrm{km\,s^{-1}}$, assuming $\kappa_c = 10^{-8}\ \mathrm{m^2\,s^{-1}}$, $\rho_s = 3500\ \mathrm{kg\,m^{-3}}$, $\sigma = 1\ \mathrm{J\,m^{-2}}$, and $f(\Delta, D_i) = 0.5$. The corresponding equilibration timescales are $\tau_{eq} \simeq 8$ min and $\simeq$75 s, respectively. Since ℓ_{eq} is smaller than the metal–silicate mixture diameter, and small compared with the typical depth of a magma ocean, the metal phase

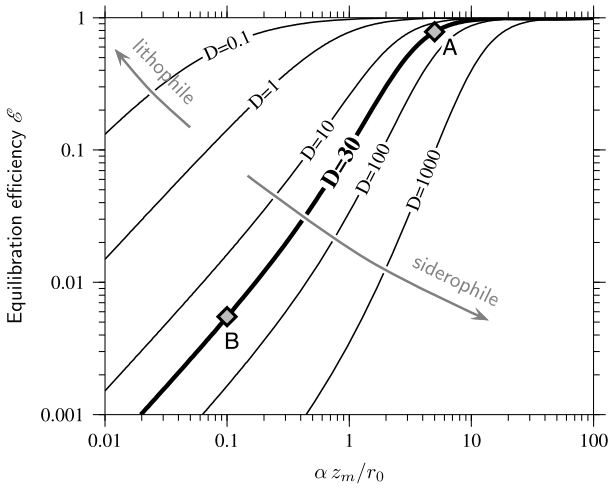

Fig. 8. Equilibration efficiency $\mathscr{E}_i$ as a function of $\alpha z_m/r_0$ (where z_m is the depth of the magma ocean) and various values of the partition coefficient D, estimated for metal–silicate mixing in a magma ocean as predicted by the turbulent entrainment model (Eq. (6)). Point A corresponds to the case of a metal blob falling through a magma ocean of depth ten times its diameter, with $\alpha = 0.25$. Point B corresponds to the case of a giant impact with $r_0 = 0.5 z_m$ and $\alpha = 0.05$.

and the entrained silicate should readily equilibrate once turbulence is fully developed, which typically requires one advection time $\sim d/w$, or a distance of fall $\sim d$. Re-equilibration should be efficient as well once the metal phase is fragmented: the maximum stable size of the resulting fragments is expected to scale as $d\,We^{-3/5}$ (Kolmogorov, 1949; Hinze, 1955; Risso, 2000), which predicts submillimeter-to-centimeter size drops, small enough for fast re-equilibration (Karato and Murthy, 1997; Rubie et al., 2003; Ulvrová et al., 2011). This suggests that once turbulence is well-developed, most of the metal indeed equilibrates with the surrounding silicates and k should be close to 1. Whether or not metal–silicate equilibration has a significant geochemical fingerprint then depends on the ratio Δ/D_i. Assuming that metal–silicate mixing occurs through turbulent entrainment, Fig. 8 shows that the equilibration efficiency $\mathscr{E}_i$, calculated using Eqs. (1) and (6) with $k = 1$, depends strongly on the quantity $\alpha z_m/r_0$, where z_m is the depth of the magma ocean.

The above considerations suggest that efficient metal–silicate equilibration should have been the norm for impacts in which the magma ocean is much deeper than the impactor core diameter. As an example, Eq. (6) predicts that a molten iron blob falling through a magma ocean of depth ten times its diameter mixes with about 100 times its mass of silicate, assuming $\alpha = 0.25$ (a relevant value here because the large value of z_m/r_0 ensures deceleration of the metal phase to subsonic velocity, irrespectively of the initial conditions). The large value of z_m/r_0 also ensures well-developed turbulence and fast equilibration. The resulting Tungsten equilibration efficiency is $\mathscr{E}_W \simeq 0.78$ (point A in Fig. 8), assuming $D_W = 30$.

The cases of impacts for which z_m/r_0 is not much larger than one, which includes the Moon-forming event, are not as clear. First, it is not obvious that the time needed for the impactor core material to reach the base of the magma ocean would allow enough turbulence to develop and the metal–silicate interfacial area to increase sufficiently for fast equilibration. Second, and as discussed in Section 9.1, the effect of compressibility on α may significantly reduce the entrainment rate, allowing only a small mass of silicate to mix with the metal. Assuming, as for turbulent jets, a fivefold decrease of the entrainment rate due to compressibility, $\alpha = 0.25/5 = 0.05$, the core of an impactor with $\simeq$10% the mass of the proto-Earth ($r_0 \simeq 0.5\, z_m$) would mix with only about 17% its mass of silicate before it reaches the proto-Earth's core, giving $\mathscr{E}_W \simeq 5.5 \times 10^{-3}$ (point B in Fig. 8). However, the actual

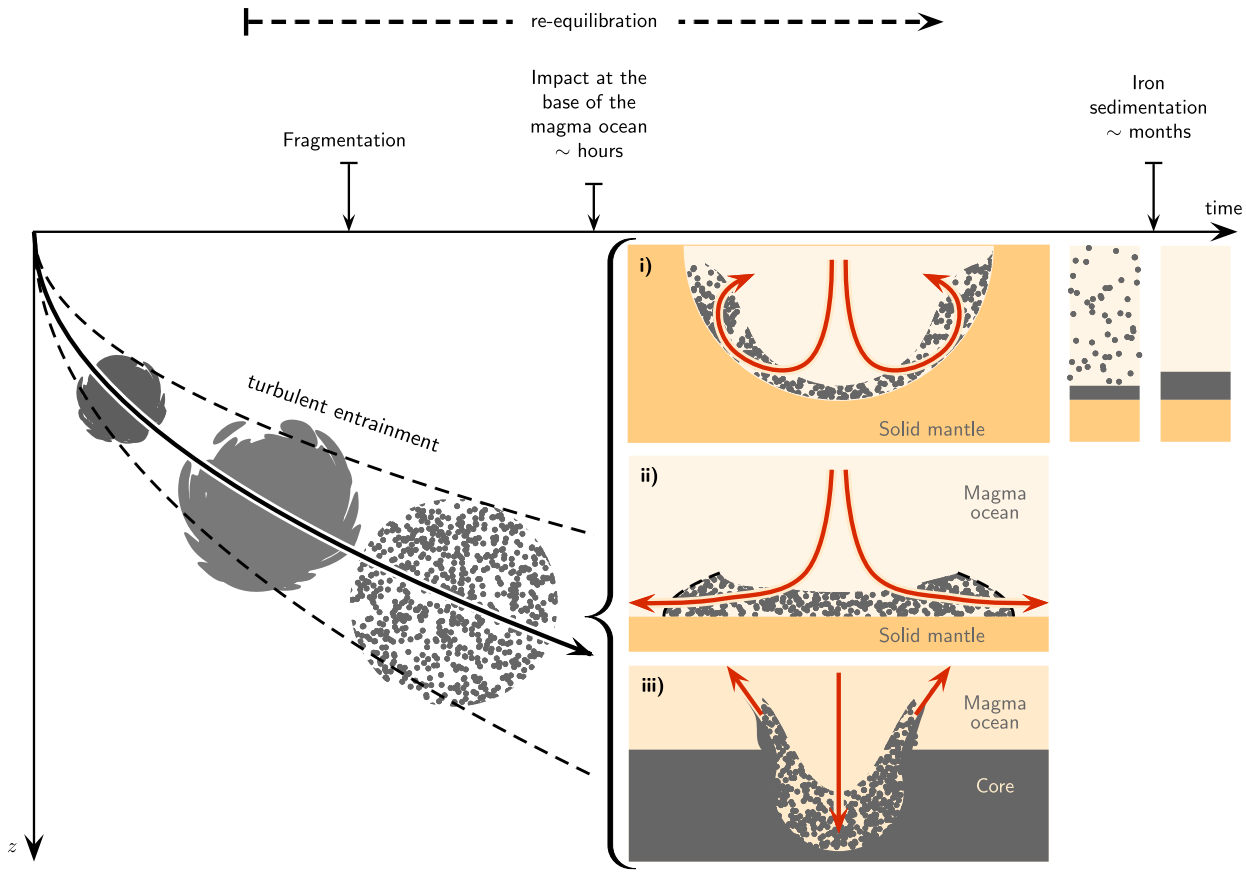

Fig. 9. Possible scenarios for metal–silicate mixing and segregation following a large impact involving a previously differentiated impactor. The metal is shown in grey, molten silicate in light orange, and solid silicate in dark orange. The metal phase gradually mixes with the silicates through turbulent entrainment, with efficient chemical equilibration resulting from small-scale mixing. Additional mixing may be caused by the impact of the metal–silicate mixture at the base of the magma ocean. (For interpretation of the references to colour in this figure legend, the reader is referred to the web version of this article.)

equilibration efficiency may depend on the details of the impact dynamics. SPH simulations of the Moon-forming impact suggest that in the likely case of an oblique impact, a fraction of the impactor including most of its core would be sheared past the planet before re-impacting Earth's mantle (Canup, 2004). Some degree of disruption of the impactor core during this process might be sufficient to allow subsequent metal–silicate equilibration by increasing the value of $\alpha z_m/r_0$ for individual blobs.

Lastly, we point out that core–mantle segregation is a complex, multi-step process and additional equilibration is possible at other stages. In particular, the velocity of the metal–silicate mixture may easily exceed hundreds of $\mathrm{m\,s^{-1}}$, implying an energetic "secondary impact" when it reaches the bottom of the magma ocean, which, as sketched in Fig. 9, could cause significant additional metal–silicate mixing (Deguen et al., 2011). (i) In the case of an impact forming its own semi-spherical magma pool, the inertia of the mixture can drive an upward flow, re-suspending iron fragments (Deguen et al., 2011) which, in spite of likely vigorous convection, sediment out on a timescale similar to Stokes' sedimentation time (Martin and Nokes, 1988; Lavorel and Le Bars, 2009). (ii) In a pre-existing global magma ocean with a horizontal lower boundary, the metal–silicate mixture will rather spread laterally as a turbulent gravity current – analogous to a pyroclastic flow – with possibly significant additional entrainment of molten silicate (Hallworth et al., 1993). (iii) If the mantle is fully molten, the metal–silicate mixture directly impacts the proto-Earth's core, with splashing and entrainment of mantle material into the core (Storr and Behnia, 1999) providing additional metal–silicate mixing.

Acknowledgements

We would like to thank H.J. Melosh, David Rubie, and an anonymous reviewer for helpful comments and suggestions. This research was supported by NSF grants EAR-110371 and EAR-1135382 (FESD).

Appendix A. Equilibration efficiency

Definition. Let c_m and c_s denote the concentrations (in weight %) of element i in either the metal or silicate phases, respectively. The metal and silicate are fully equilibrated when the two phases have reached thermodynamic equilibrium, for which the equilibrium concentration c_m^{eq} and c_s^{eq} are linked through the metal/silicate partition coefficient D_i by $c_m^{eq} = D_i c_s^{eq}$.

Consider a mass M_m of metal, in which we assume that a fraction $k M_m$ has been mixed and equilibrated with a mass M_s of silicates. We define the metal dilution Δ as the ratio of the mass of equilibrated silicate over the mass of equilibrated metal,

$$\Delta = \frac{M_s}{kM_m}. \tag{A.1}$$

Given the initial values c_m^0 and c_s^0 of the concentration in the metal and silicate phases, the concentration in the equilibrated metal c_m^{eq} and equilibrated silicate c_s^{eq} are found from mass conservation,

$$c_m^{eq} + \Delta c_s^{eq} = c_m^0 + \Delta c_s^0, \tag{A.2}$$

which, together with the assumption of thermodynamic equilibrium, $c_m^{eq} = D_i\, c_s^{eq}$, gives

$$c_m^{eq} = \frac{c_m^0 + \Delta c_s^0}{1 + \Delta/D_i}, \qquad c_s^{eq} = \frac{c_m^0 + \Delta c_s^0}{D_i + \Delta}. \tag{A.3}$$

The net mass exchange $\mathcal{M}_i$ of element i between the metal and silicate phases can be written as

$$\mathcal{M}_i = kM_m\left|c_m^{eq} - c_m^0\right| = M_s\left|c_s^{eq} - c_s^0\right| \tag{A.4}$$

$$= kM_m \frac{|c_m^0 - D_i c_s^0|}{1 + D_i/\Delta}. \tag{A.5}$$

$\mathcal{M}_i$ reaches a maximum value $\mathcal{M}_i^{max} = M_m|c_m^0 - D_i c_s^0|$ when all the metal phase is equilibrated ($k = 1$) and is infinitely diluted in the silicate phase ($\Delta \to \infty$). We thus define the equilibration efficiency $\mathscr{E}_i$ of element i as the actual mass exchange $\mathcal{M}_i$ normalized by the maximum possible mass exchange $\mathcal{M}_i^{max}$. From Eq. (A.5) and the value of $\mathcal{M}_i^{max}$, the equilibration efficiency is found to be

$$\mathscr{E}_i = \frac{k}{1 + D_i/\Delta}, \tag{A.6}$$

which reduces to k when $\Delta/D_i \gg 1$, the limit that is usually assumed in continuous accretion models (e.g. Rudge et al., 2010).

As shown by Eq. (A.6), the equilibration efficiency $\mathscr{E}_i$ depends critically on the ratio Δ/D_i, and is small, even when $k = 1$, if Δ is small compared to D_i. Efficient re-equilibration requires the metal dilution to be similar to or larger than the partition coefficient of the element considered. For Tungsten, which has $D_W \simeq 30$, efficient re-equilibration thus requires that the metal re-equilibrates with at least 30 times its mass of silicate.

Use of $\mathscr{E}_i$ in geochemical models. We demonstrate here that geochemical models assuming partial equilibration of the metal phase but infinite dilution can be generalized by using the equilibration efficiency $\mathscr{E}_i$ in place of k. We consider the case of continuous accretion, according to the formulation of Rudge et al. (2010) (see their Supplementary Information). Discontinuous accretion can be treated in the same way.

We note $c_m(t)$ and $c_s(t)$ the concentration in Earth's mantle and core at time t, and $c_m^{imp}(t)$ and $c_s^{imp}(t)$ the composition of the metal and silicate phase of the impacting bodies. The mass of the Earth is denoted by $M(t)$, and, using F for the mass fraction of metal in the Earth (assumed constant), then the masses of the core and mantle are $FM(t)$ and $(1-F)M(t)$, respectively. We assume for simplicity that all impactors have the same metal mass fraction F.

Conservation of mass of element i in Earth's core implies that

$$\frac{d}{dt}[FMc_m] = \underbrace{(1-k)Fc_m^{imp}\frac{dM}{dt}}_{\text{Flux of non-equilibrated metal}} + \underbrace{kFc_m^{eq}\frac{dM}{dt}}_{\text{Flux of equilibrated metal}} \tag{A.7}$$

where c_m^{eq} is the concentration in the re-equilibrated fraction of the impactor core. One complication is that the metal of the impactor may equilibrate with silicates from both the impactor mantle and Earth's mantle, in unknown proportion (Rubie et al., 2012). If $\tilde{c}_s$ denotes the mean composition of the equilibrated silicate, Eq. (A.3) yields

$$c_m^{eq} = \frac{c_m^{imp} + \Delta\tilde{c}_s}{1 + \Delta/D_i}. \tag{A.8}$$

For siderophile elements such as Tungsten, $\tilde{c}_s$ can be approximated by $c_s(t)$. As discussed above in Definition section, the effect of re-equilibration is significant only if the metal re-equilibrates with a mass of silicates about D_i times larger (e.g. about 30 times larger for Tunsten). Since the mass of the impactor mantle is only about twice the mass of its core, efficient re-equilibration of siderophile elements requires that the impactor metal equilibrates with a mass of Earth's mantle significantly larger than the impactor's mantle. This implies that, in cases where equilibration is efficient, the mean concentration of the equilibrated silicate is close to $c_s(t)$. The approximation $\tilde{c}_s \simeq c_s(t)$ is not valid if the equilibration efficiency is small, but in that situation it has little effect on the results.

Substituting Eq. (A.8) into Eq. (A.7) yields the following equation for the compositional evolution of the core:

$$\frac{d}{dt}(Mc_m) = \left[\mathscr{E}_i D_i\tilde{c}_s + (1-\mathscr{E}_i)c_m^{imp}\right]\frac{dM}{dt}, \tag{A.9}$$

while conservation of element i in the mantle yields the following equation for the mantle:

$$\frac{d}{dt}(Mc_s) = \left[c_s^{imp} + \mathscr{E}_i\frac{F}{1-F}\left(c_m^{imp} - D_i\tilde{c}_s\right)\right]\frac{dM}{dt}. \tag{A.10}$$

If $\tilde{c}_s$ is taken to be equal to $c_s(t)$, Eqs. (A.9) and (A.10) are the same as used by Rudge et al. (2010) for stable species if $\mathscr{E}_i$ is substituted for k (see their equations A.3 and A.4 in the Supplementary Information). The equivalence also holds if radioactive or radiogenic species are considered (see the Supplementary Information of Rudge et al. (2010) for a detailed derivation of the relevant equations). Results of previous accretion models, including the bounds on Earth's accretion derived by Rudge et al. (2010) from Hf-W and U-Pb systematics, can therefore be generalized to include the effect of finite dilution by using $\mathscr{E}_i$ in place of k.

Implications. Previous studies (Kleine et al., 2004; Nimmo et al., 2010; Rudge et al., 2010) have shown that Hf-W systematics can be used to infer a lower bound for the mean degree of re-equilibration during Earth's accretion. Assuming infinite dilution of the metal phase, Rudge et al. (2010) found that Hf-W systematics constrains the fraction of equilibrated metal k to be larger than about 0.36 on average during Earth's accretion. If finite metal dilution is considered, the implication is that $\mathscr{E}_W \geqslant \mathscr{E}_W^{min} = 0.36$, which requires that $k > 0.36$ and, assuming $D_W \simeq 30$, $\Delta \geqslant \Delta^{min} = D_W/(1/\mathscr{E}_W^{min} - 1) \simeq 17$.

A possibly important implication for modeling the abundance of siderophile elements in the mantle is that the equilibration efficiency $\mathscr{E}_i$ is element-dependent. One consequence is that constraints on the equilibration efficiency from Hf-W systematics do not apply directly to other elements. The equilibration efficiency of an element i with partition coefficient D_i differs from the Tungsten equilibration efficiency $\mathscr{E}_W$ according to

$$\mathscr{E}_i = g(D_W, D_i, \Delta)\mathscr{E}_W, \tag{A.11}$$

where

$$g(D_W, D_i, \Delta) = \frac{1 + D_W/\Delta}{1 + D_i/\Delta}.$$

In Eq. (A.11), the function g is an increasing function of Δ if $D_i > D_W$, and a decreasing function of Δ if $D_i < D_W$. Thus the lower bounds on k and Δ deduced from Hf-W systematics imply the following lower bound on the equilibration efficiency of an element i:

$$\mathscr{E}_i \geqslant \mathscr{E}_i^{min} = \begin{cases} \frac{1+D_W/\Delta^{min}}{1+D_i/\Delta^{min}}\mathscr{E}_W^{min} & \text{if } D_i \geqslant D_W, \\ \mathscr{E}_W^{min} & \text{if } D_i \leqslant D_W. \end{cases} \tag{A.12}$$

The constraint on the equilibration efficiency becomes weaker for elements that are more siderophile. For example, the lower bound on the equilibration efficiency is $\mathscr{E}_i^{min} \simeq 0.14$ for an element with $D_i = 100$, and only $\mathscr{E}_i^{min} \simeq 0.017$ for an element with $D_i = 10^3$.

Thus low equilibration efficiency should be considered when modeling the core/mantle partitioning of highly siderophile elements (e.g. Wood et al., 2006; Corgne et al., 2008).

Appendix B. Turbulent entrainment model

Integral relationships. We consider a buoyant spherical mass of initial radius r_0 and density $\rho_m = \rho_s + \Delta\rho$ released with an initial (downward) velocity w_0 in a fluid of density ρ_s. Owing to entrainment, the mean density of the metal–silicate mixture evolves with time according to

$$\bar{\rho}(t) = \rho_s + (\rho_m - \rho_s)\phi = \rho_s\left[1 + \frac{\Delta\rho}{\rho_s}\phi\right], \tag{B.1}$$

where $\phi = r_0^3/r^3$ is the metal phase volume fraction. The buoyancy of the metal–silicate mixture,

$$B = g\frac{\bar{\rho} - \rho_s}{\rho_s}V = g\frac{\Delta\rho}{\rho_s}\phi V, \tag{B.2}$$

is conserved in absence of density stratification in the ambient fluid. Here V is the volume of the turbulent fluid and r is its mean radius.

We adopt the standard entrainment assumption of Morton et al. (1956) for which the local inward entrainment velocity u_e is proportional to the magnitude of the mean vertical velocity w of the mixture,

$$u_e = \alpha|w|, \tag{B.3}$$

where α is the entrainment coefficient. With this assumption, the equation of conservation of mass becomes

$$\frac{4\pi}{3}\frac{d(\bar{\rho}r^3)}{dt} = 4\pi r^2\rho_s\alpha|w|, \tag{B.4}$$

while conservation of momentum becomes (e.g. Bush et al., 2003)

$$\frac{4\pi}{3}\frac{d}{dt}\left[(\bar{\rho} + K\rho_s)r^3 w\right] = \rho_s B - \frac{1}{2}C_d\rho_s\pi r^2 w^2. \tag{B.5}$$

Here K is the coefficient of added mass, which accounts for the momentum imparted to the surrounding fluid (Escudier and Maxworthy, 1973). The second term on the right hand side of Eq. (B.5) is the hydrodynamic drag F_d, with C_d the drag coefficient.

Using Eq. (B.1) to write $\bar{\rho}$ as a function of ϕ, Eqs. (B.4) and (B.5) become

$$\frac{dr}{dt} = \alpha|w|, \tag{B.6}$$

$$\left[(1+K)r^3 + \frac{\Delta\rho}{\rho_s}r_0^3\right]\frac{dw}{dt} = g\frac{\Delta\rho}{\rho_s}r_0^3 - 3\alpha\left[1 + K + \frac{C_d}{8\alpha}\right]r^2w^2. \tag{B.7}$$

Noting that $w = dz/dt$, Eq. (B.6) implies that $dr/dz = \alpha$.

We now non-dimensionalize lengths by r_0, time by $[\rho_s r_0/(\Delta\rho\, g)]^{1/2}$, and velocity by $(r_0\, g\, \Delta\rho/\rho_s)^{1/2}$. In non-dimensional form, equations (B.6), (B.7) then become

$$\frac{d\tilde{r}}{d\tilde{t}} = \alpha|w|, \tag{B.8}$$

$$\left[(1+K)\tilde{r}^3 + \frac{\Delta\rho}{\rho_s}\right]\frac{d\tilde{w}}{d\tilde{t}} = 1 - 3\alpha\left[1 + K + \frac{C_d}{8\alpha}\right]\tilde{r}^2\tilde{w}^2, \tag{B.9}$$

where the tilde ('∼') denotes non-dimensional variables. The initial conditions are

$$\tilde{r} = 1, \qquad \tilde{z} = 0, \quad \text{and} \quad \tilde{w} = \frac{w_0}{(r_0\, g\, \frac{\Delta\rho}{\rho_s})^{1/2}} \quad \text{at } \tilde{t} = 0. \tag{B.10}$$

In Fig. 2, we use a least-square inversion procedure to find the values of α, K and C_d for which the model described by Eqs. (B.8)–(B.10) best fits our experimental data on the position of the center of mass $\tilde{z}$ and radius of the mixture $\tilde{r}$ as a function of time.

Analytical solutions. Using $d\tilde{r}/d\tilde{t} = \alpha\, d\tilde{z}/d\tilde{t} = \alpha\tilde{w}$, Eq. (B.9) can be re-written as

$$\left[(1+K)\tilde{r}^3 + \frac{\Delta\rho}{\rho_s}\right]\frac{\alpha}{2}\frac{d\tilde{w}^2}{dr} = 1 - 3\alpha\left[1 + K + \frac{C_d}{8\alpha}\right]\tilde{r}^2\tilde{w}^2, \tag{B.11}$$

the solution of which is

$$\tilde{w}^2 = \frac{2}{\alpha}\int_1^{\tilde{r}}\frac{(\frac{\Delta\rho}{\rho_s} + (1+K)x^3)^{\gamma-1}}{(\frac{\Delta\rho}{\rho_s} + (1+K)\tilde{r}^3)^{\gamma}}\,dx + \left(\frac{\frac{\Delta\rho}{\rho_s} + 1 + K}{\frac{\Delta\rho}{\rho_s} + (1+K)\tilde{r}^3}\right)^{\gamma}\tilde{w}_0^2, \tag{B.12}$$

where

$$\gamma = 2 + \frac{C_d}{4(1+K)\alpha} = \frac{2}{1+K}\left(1 + K + \frac{C_d}{8\alpha}\right). \tag{B.13}$$

The integral on the RHS of Eq. (B.12) can be calculated analytically if $C_d = 0$, or if $\Delta\rho/\rho_s \to 0$ (for arbitrary K and C_d).

The solution (B.12) has a large-z asymptote given by

$$\tilde{w} = \left[2\left(1 + K + \frac{3}{16}\frac{C_d}{\alpha}\right)\alpha^3\right]^{-1/2}\frac{1}{\tilde{z}}, \tag{B.14}$$

which corresponds to the self-similar regime of a turbulent thermal, consistent with the form given in Eq. (2) of the paper. Once integrated, Eq. (B.14) yields

$$\tilde{z}^2 = \left[\left(1 + K + \frac{3}{16}\frac{C_d}{\alpha}\right)\frac{\alpha^3}{2}\right]^{-1/2}\tilde{t}. \tag{B.15}$$

K and C_d act in exactly the same way in the self-similar regime. Furthermore, $3/(16\alpha) \sim 1$ if $\alpha \simeq 0.25$, which implies that K and C_d have a quantitatively similar effect.

References

Baker, J., Bizzarro, M., Wittig, N., Connelly, J., Haack, H., 2005. Early planetesimal melting from an age of 4.5662 Gyr for differentiated meteorites. Nature 436, 1127–1131.

Batchelor, G., 1954. Heat convection and buoyancy effects in fluids. Q. J. R. Meteorol. Soc. 80, 339–358.

Bettelini, M., Fanneløp, T., 1993. Underwater plume from an instantaneously started source. Appl. Ocean Res. 15, 195–206.

Bottke, W.F., Nesvorný, D., Grimm, R.E., Morbidelli, A., O'Brien, D.P., 2006. Iron meteorites as remnants of planetesimals formed in the terrestrial planet region. Nature 439, 821–824.

Breidenthal, R., 1992. Sonic eddy—a model for compressible turbulence. AIAA J. 30, 101–104.

Brown, G.L., Roshko, A., 1974. On density effects and large structure in turbulent mixing layers. J. Fluid Mech. 64, 775–816.

Bush, J.W.M., Thurber, B.A., Blanchette, F., 2003. Particle clouds in homogeneous and stratified environments. J. Fluid Mech. 489, 29–54.

Canup, R., 2004. Simulations of a late lunar-forming impact. Icarus 168, 433–456.

Chen, H., Middleman, S., 1967. Drop size distribution in agitated liquid–liquid systems. AIChE J. 13, 989–995.

Clay, P., 1940. The mechanism of emulsion formation in turbulent flow. Proc. Sect. Sci. 43, 852–965.

Constantin, P., Procaccia, I., 1994. The geometry of turbulent advection: Sharp estimates for the dimensions of level sets. Nonlinearity 7, 1045.

Constantin, P., Procaccia, I., Sreenivasan, K.R., 1991. Fractal geometry of isoscalar surfaces in turbulence: theory and experiments. Phys. Rev. Lett. 67, 1739–1742.

Corgne, A., Keshav, S., Wood, B.J., McDonough, W.F., Fei, Y., 2008. Metal silicate partitioning and constraints on core composition and oxygen fugacity during Earth accretion. Geochim. Cosmochim. Acta 72, 574–589.

Cottrell, E., Walter, M.J., Walker, D., 2009. Metal–silicate partitioning of tungsten at high pressure and temperature: Implications for equilibrium core formation in Earth. Earth Planet. Sci. Lett. 281, 275–287.

Dahl, T., Stevenson, D., 2010. Turbulent mixing of metal and silicate during planet accretion — and interpretation of the Hf-W chronometer. Earth Planet. Sci. Lett. 295, 177–186.
Deguen, R., Olson, P., Cardin, P., 2011. Experiments on turbulent metal–silicate mixing in a magma ocean. Earth Planet. Sci. Lett. 310, 303–313.
Escudier, M., Maxworthy, T., 1973. On the motion of turbulent thermals. J. Fluid Mech. 61, 541–552.
Freund, J.B., Lele, S.K., Moin, P., 2000. Compressibility effects in a turbulent annular mixing layer. Part 1. Turbulence and growth rate. J. Fluid Mech. 421, 229–267.
Halliday, A., 2004. Mixing, volatile loss and compositional change during impact-driven accretion of the Earth. Nature 427, 505–509.
Hallworth, M., Phillips, J., Huppert, H., Sparks, R., 1993. Entrainment in turbulent gravity currents. Nature 362, 829–831.
Hesketh, R., Fraser Russell, T., Etchells, A., 1987. Bubble size in horizontal pipelines. AIChE J. 33, 663–667.
Hinze, J., 1955. Fundamentals of the hydrodynamic mechanism of splitting in dispersion processes. AIChE J. 1, 289–295.
Ichikawa, H., Labrosse, S., Kurita, K., 2010. Direct numerical simulation of an iron rain in the magma ocean. J. Geophys. Res. 115, B01404.
Karato, S., Murthy, V.R., 1997. Core formation and chemical equilibrium in the Earth—I. Physical considerations. Phys. Earth Planet. Inter. 100, 61–79.
Kleine, T., Mezger, K., Palme, H., Münker, C., 2004. The W isotope evolution of the bulk silicate earth: constraints on the timing and mechanisms of core formation and accretion. Earth Planet. Sci. Lett. 228, 109–123.
Kleine, T., Münker, C., Mezger, K., Palme, H., 2002. Rapid accretion and early core formation on asteroids and the terrestrial planets from Hf-W chronometry. Nature 418, 952–955.
Kolmogorov, A., 1949. On the breakage of drops in a turbulent flow. Dokl. Akad. Nauk SSSR, 825–828.
Landeau, M., Deguen, R., Olson, P., in press. Experiments on the fragmentation of a liquid volume in another liquid. J. Fluid Mech.
Lavorel, G., Le Bars, M., 2009. Sedimentation of particles in a vigorously convecting fluid. Phys. Rev. E 80, 046324.
Levich, V., 1962. Physicochemical Hydrodynamics. Chap. VI, 60. Prentice-Hall, Englewood Cliffs, NJ, p. 355.
Mandelbrot, B., 1975. On the geometry of homogeneous turbulence, with stress on the fractal dimension of the iso-surfaces of scalars. J. Fluid Mech. 72, 401–416.
Martin, D., Nokes, R., 1988. Crystal settling in a vigorously converting magma chamber. Nature 332, 534–536.
Mathew, J., Basu, A.J., 2002. Some characteristics of entrainment at a cylindrical turbulence boundary. Phys. Fluids 14, 2065–2072.
Melosh, H.J., 1990. Giant Impacts and the Thermal State of the Early Earth, pp. 69–83.
Morton, B.R., Taylor, G., Turner, J.S., 1956. Turbulent gravitational convection from maintained and instantaneous sources. Proc. R. Soc. Lond. Ser. A, Math. Phys. Sci. 234, 1–23.
Mungal, M.G., Hollingsworth, D.K., 1989. Organized motion in a very high Reynolds number jet. Phys. Fluids A, Fluid Dyn. 1, 1615–1623.
Nimmo, F., O'Brien, D., Kleine, T., 2010. Tungsten isotopic evolution during late-stage accretion: Constraints on Earth–Moon equilibration. Earth Planet. Sci. Lett 292, 363–370.
Pantano, C., Sarkar, S., 2002. A study of compressibility effects in the high-speed turbulent shear layer using direct simulation. J. Fluid Mech. 451, 329–371.
Pierazzo, E., Vickery, A.M., Melosh, H.J., 1997. A reevaluation of impact melt production. Icarus 127, 408–423.
Ricard, Y., Šrámek, O., Dubuffet, F., 2009. A multi-phase model of runaway core–mantle segregation in planetary embryos. Earth Planet. Sci. Lett. 284, 144–150.
Risso, F., 2000. The Mechanisms of Deformation and Breakup of Drops and Bubbles. Multiphase Science and Technology, vol. 12.
Rubie, D., Melosh, H., Reid, J., Liebske, C., Righter, K., 2003. Mechanisms of metal–silicate equilibration in the terrestrial magma ocean. Earth Planet. Sci. Lett. 205, 239–255.
Rubie, D., Frost, D., Mann, U., Asahara, Y., Nimmo, F., Tsuno, K., Kegler, P., Holzheid, A., Palme, H., 2011. Heterogeneous accretion, composition and core–mantle differentiation of the Earth. Earth Planet. Sci. Lett. 301 (1), 31–42.
Rubie, D., Nimmo, F., Morbidelli, A., Frost, D.J., 2012. Extent of metal–silicate disequilibrium during accretion and early differentiation of the Earth. Abstract presented at 2012 Fall Meeting. AGU, San Francisco, CA, pp. 3–7.
Rudge, J., Kleine, T., Bourdon, B., 2010. Broad bounds on Earth's accretion and core formation constrained by geochemical models. Nat. Geosci. 3, 439–443.
Samuel, H., 2012. A re-evaluation of metal diapir breakup and equilibration in terrestrial magma oceans. Earth Planet. Sci. Lett. 313, 105–114.
Shinjo, J., Umemura, A., 2010. Simulation of liquid jet primary breakup: Dynamics of ligament and droplet formation. Int. J. Multiph. Flow 36, 513–532.
Siebert, J., Corgne, A., Ryerson, F.J., 2011. Systematics of metal–silicate partitioning for many siderophile elements applied to Earth's core formation. Geochim. Cosmochim. Acta 75, 1451–1489.
Sreenivasan, K.R., Ramshankar, R., Meneveau, C., 1989. Mixing, entrainment and fractal dimensions of surfaces in turbulent flows. Proc. R. Soc. Lond. A 421, 79–107.
Stevenson, D.J., 1990. Fluid dynamics of core formation. In: Origin of the Earth. Oxford University Press, pp. 231–249.
Storr, G., Behnia, M., 1999. Experiments with large diameter gravity driven impacting liquid jets. Exp. Fluids 27, 60–69.
Tennekes, H., Lumley, J.L., 1972. First Course in Turbulence. MIT Press.
Terada, A., Ida, Y., 2007. Kinematic features of isolated volcanic clouds revealed by video records. Geophys. Res. Lett. 34, L01305.
Tonks, W.B., Melosh, H.J., 1993. Magma ocean formation due to giant impacts. J. Geophys. Res. 98, 5319–5333.
Turner, J., 1969. Buoyant plumes and thermals. Annu. Rev. Fluid Mech. 1, 29–44.
Turner, J.S., 1986. Turbulent entrainment – The development of the entrainment assumption, and its application to geophysical flows. J. Fluid Mech. 173, 431–471.
Ulvrová, M., Coltice, N., Ricard, Y., Labrosse, S., Dubuffet, F., Velímskỳ, J., Šrámek, O., et al., 2011. Compositional and thermal equilibration of particles, drops and diapirs in geophysical flows. Geochem. Geophys. Geosyst. 12, 1–11.
Villermaux, E., Marmottant, P., Duplat, J., 2004. Ligament-mediated spray formation. Phys. Rev. Lett. 92, 74501.
Westerweel, J., Fukushima, C., Pedersen, J.M., Hunt, J.C.R., 2009. Momentum and scalar transport at the turbulent/non-turbulent interface of a jet. J. Fluid Mech. 631, 199–230.
Wood, B., Walter, M., Wade, J., 2006. Accretion of the Earth and segregation of its core. Nature 441, 825–833.
Woodward, B., 1959. The motion in and around isolated thermals. Q. J. R. Meteorol. Soc. 85, 144–151.
Yamamoto, H., Watson, M., Phillips, J.C., Bluth, G.J., 2008. Rise dynamics and relative ash distribution in vulcanian eruption plumes at Santiaguito Volcano, Guatemala, revealed using an ultraviolet imaging camera. Geophys. Res. Lett. 35, L08314.
Yin, Q., Jacobsen, S.B., Yamashita, K., Blichert-Toft, J., Telouk, P., Albarede, F., 2002. A short timescale for terrestrial planet formation from Hf/W chronometry of meteorites. Nature 418, 949–952.
Yoshino, T., Walter, M.J., Katsura, T., 2003. Core formation in planetesimals triggered by permeable flow. Nature 422, 154–157.

LETTERS
PUBLISHED ONLINE: 12 SEPTEMBER 2016 | DOI: 10.1038/NGEO2808
nature geoscience

Core merging and stratification following giant impact

Maylis Landeau[1]*, Peter Olson[1], Renaud Deguen[2] and Benjamin H. Hirsh[1]

A stratified layer below the core–mantle boundary has long been suspected on the basis of geomagnetic and seismic observations[1–3]. It has been suggested that the outermost core has a stratified layer about 100 km thick[3–6] that could be due to the diffusion of light elements[7,8]. Recent seismological evidence, however, supports a layer exceeding 300 km in thickness of enigmatic origin[9–11]. Here we show from turbulent mixing experiments that merging between projectile and planetary core following a giant impact can lead to a stratified layer at the top of the core. Scaling relationships between post-impact core structure and projectile properties suggest that merging between Earth's protocore and a projectile core that is enriched in light elements and 20 times less massive can produce the thick stratification inferred from seismic data. Our experiments favour Moon-forming impact scenarios involving a projectile smaller than the proto-Earth[12,13] and suggest that entrainment of mantle silicates into the protocore led to metal–silicate equilibration under extreme pressure–temperature conditions. We conclude that the thick stratified layer detected at the top of Earth's core[9,10] can be explained as a vestige of the Moon-forming giant impact during the late stages of planetary accretion.

Giant impacts have been implicated in the formation of Earth's Moon[12–14] and the crustal dichotomy on Mars[15]. The energy released by giant impacts allows the liquid metallic core of the projectile to fall through a fully molten magma ocean and merge with the protocore of the accreting planet under extreme turbulence conditions[16,17] (Fig. 1a). Accretion scenarios predict the metal added to the protocore after each collision was either enriched or depleted in light elements depending on the oxidation state of the projectile and on the thermodynamic conditions during metal–silicate equilibration[18], implying that compositional stratification in the post-impact core is most probable. Numerical simulations of giant impacts[12–14,17] capture large-scale dynamics of core formation, but not the turbulence, which is crucial for predicting the post-impact stratification of the core.

Figure 1b,c is the schematic of the first experiments on merging and turbulent mixing following impacts aimed at predicting the post-impact structure of the core. A liquid volume of radius R, representing the projectile core, is released into a two-layer liquid, the upper layer representing an impact-induced magma ocean that extends to the core–mantle boundary (CMB, the interface in our experiment), the lower layer representing the protocore. The released liquid, whose density is varied relative to the lower liquid, is immiscible with the upper liquid but miscible with the lower, with which it eventually merges. The upper layer depth z_u, analogue for the magma ocean depth, is fixed so that the aspect ratio $Z = z_u/R$ is smaller than 4, as expected for giant impacts. Details of the experimental set-up and dimensionless parameters are given in the Methods.

Figure 2 shows the first steps of the merging process for both positive and negative values of the density ratio $P = (\rho_l - \rho_r)/(\rho_r - \rho_u)$, where the subscripts u, l, r indicate the upper, lower and released liquids, respectively (previous core formation studies[19,20] use the term merging to signify absence of chemical equilibration; here it refers to the dynamical sequence in Fig. 2). As the released volume sinks in the upper liquid, it entrains liquid drops, generating a turbulent cloud of the two immiscible liquids, intermingled at small scales (right column in Fig. 2). The cloud penetrates deep in the lower layer, forming a turbulent fountain that collapses and spreads beneath the interface as a turbulent gravity current. Unexpectedly, the volume of upper liquid entrained into the lower liquid is comparable to the released volume. During the gravity current stage, the released liquid mixes with a significant volume of the lower liquid, while drops of entrained upper liquid sediment upward toward the interface. Collapse of the cloud mixture below the interface, irrespective of the sign of P, demonstrates that entrainment of upper liquid has transiently reduced the cloud density to below that of the lower liquid. Turbulent fountaining (Fig. 2) implies that, during Earth's accretion, metal–silicate mixtures penetrated into the protocore, collapsed, and spread below the CMB, whereupon the entrained silicates sedimented upwards as drops toward the magma ocean.

Figure 3 illustrates the longer-term behaviour in our experiments, following sedimentation of the immiscible drops. For released liquids denser than the lower liquid ($P < 0$, Fig. 3b), the collapsing fountain destabilizes into plumes, initiating an overturn event that yields a global stratification throughout the entire lower liquid. In contrast, following releases lighter than the lower liquid ($P > 0$, Fig. 3a), a turbulent gravity current spreads and settles at the top of the lower liquid, producing a localized stratified layer below the immiscible interface and unstratified conditions below.

For lighter releases ($P > 0$), we quantify turbulent mixing and residual stratification in the lower liquid in terms of V/V_0, where V denotes the volume of the residual stratified layer (see Methods for details) and V_0 denotes the initial volume of the released liquid. Efficient mixing occurs wherever the gravity current is turbulent: the more efficient the mixing, the larger the ratio V/V_0. Our experimental results reveal that V/V_0 depends on both the density ratio P and the aspect ratio Z, such that the least-squares best-fitting power law is $V/V_0 = c_1 P^{c_2} Z^{c_3}$, where $c_1 = 1.13 \pm 0.3$, $c_2 = -0.34 \pm 0.02$ and $c_3 = 0.89 \pm 0.08$, as shown in Fig. 4a. The signs of these power-law exponents are consistent with previous studies on entrainment at a density interface and with force balance arguments (Supplementary Information). Our experimental scaling for V/V_0 means that fountain collapse induces extensive mixing and

[1]Department of Earth and Planetary Sciences, Johns Hopkins University, Baltimore, Maryland 21218, USA. [2]Univ. Lyon, Université Claude Bernard Lyon 1, Ens de Lyon, CNRS, UMR 5276 LGL-TPE, F-69622 Villeurbanne, France. *e-mail: landeau@jhu.edu

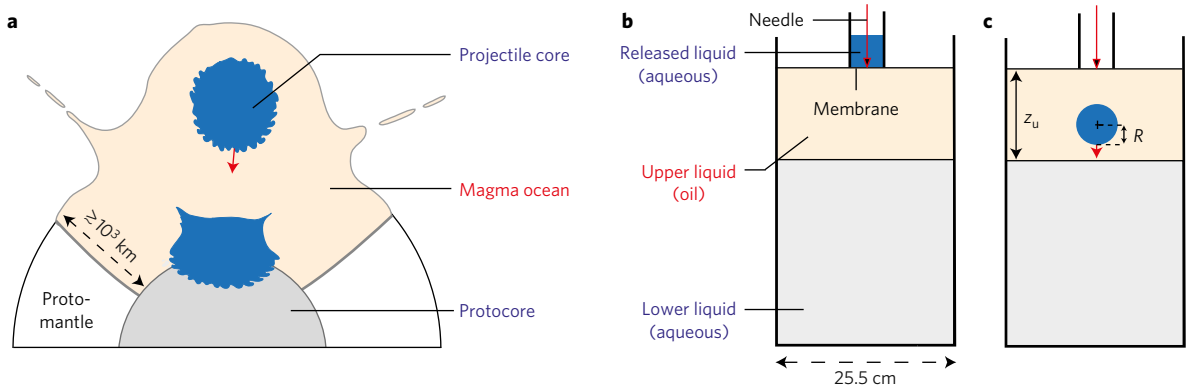

Figure 1 | Turbulent core merging after a giant impact. a, Sketch of the merging of the core of a projectile and a protoplanet after a giant impact. **b**, Experimental set-up at time $t = 0$ (side view). The upper, lower and released liquids are analogues for the magma ocean, the protocore and the projectile core, respectively. **c**, Sketch of an experiment at times $t > 0$.

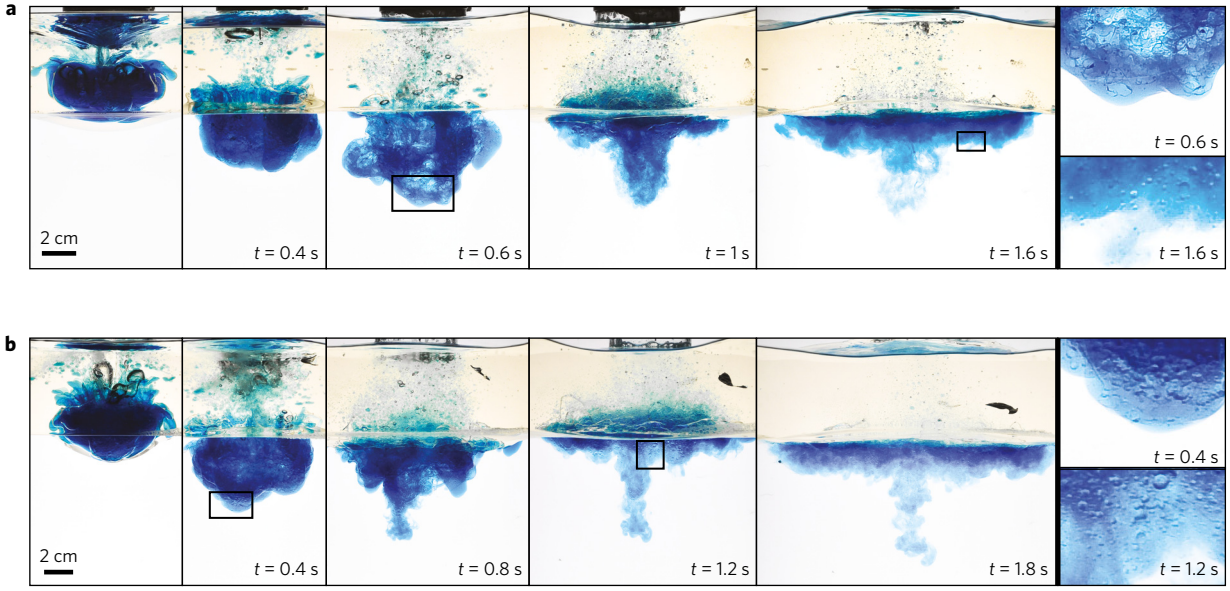

Figure 2 | Collapsing fountain during the first steps of the merging process. a, Released liquid lighter than the lower liquid, $P \approx 1.68 \times 10^{-2}$, $Z = 2$. **b**, Released liquid denser than the lower liquid, $P \approx -1.63 \times 10^{-2}$, $Z = 2$. The first five columns are photographs at different times t in a single experiment. The right column displays close-ups of the rectangular sub-regions in **a** and **b**, showing turbulent intermingling between entrained upper liquid and released liquid.

produces a stratified layer 20 or more times as voluminous as the projectile core.

Extrapolated to giant impacts, our experiments with $P < 0$ suggest that merging with a projectile core depleted in light elements produces global stratification throughout the protocore whereas experiments with $P > 0$ demonstrate that localized stratification can be produced at the top of the protocore after merging with a projectile core enriched in light elements. In the latter situation, the final structure of the protocore depends on the mass ratio and the density difference between the protocore and the projectile core, as shown by the regime diagram in Fig. 4b, obtained from our experimental scaling law for mixing (Fig. 4a). For each giant impact, Z depends on the size of the projectile core but also on the excavation mechanism[16] and the deformation of the projectile core, processes that are poorly constrained. However, we find that allowing for variations in Z has little effect on our conclusions (Supplementary Information) and therefore, in Fig. 4b, we assume a constant value $Z = 2$, typical of giant impacts.

Dashed and solid contours in Fig. 4b quantify the amount of mixing between the merged cores. Regions below the solid curve correspond to impacts that mix the entire protocore with the projectile core, yielding no distinct layers, whereas for impacts above the solid curve a residual stratified layer is produced at the top of the protocore by incomplete mixing. Blue dotted contours in Fig. 4b show the density deficit of this residual layer, obtained from mass balance, using the initial core density difference and the amount of mixing predicted by the scaling law in Fig. 4a.

Results of planetary accretion simulations[21,22] suggest that most giant impacts involve projectile cores smaller than 0.2 Earth's protocore mass. Such impacts correspond to the blue shaded regions in Fig. 4b, assuming an upper bound of 10% for the core density contrast[23]. The darker blue region comprises core density contrasts on the order of these found in geochemical models of core formation by reduced projectiles[18]. Nearly all impacts in the darker blue region lie within the incomplete mixing regime, implying that, in the aftermath of most Earth-building giant impacts with reduced projectiles, the core was left with compositional stratification at its top.

Therefore, Earth's present-day core structure offers clues about the last great impact that our planet experienced. On the basis of

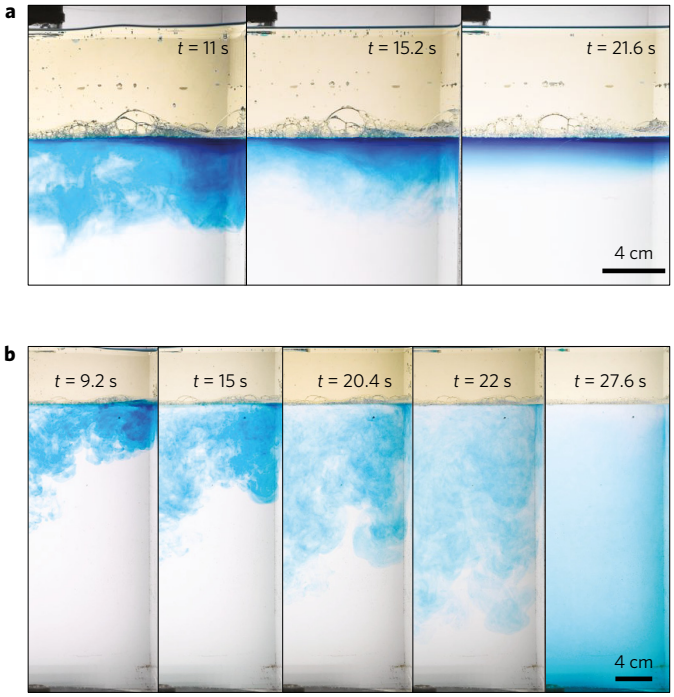

Figure 3 | Long-term dynamics after fountain collapse. a, Formation of a stratified layer for released liquids less dense than the lower liquid ($P \approx 1.68 \times 10^{-2}$, $Z = 2$). **b**, Overturn of the entire lower liquid for releases denser than the lower liquid ($P \approx -1.63 \times 10^{-2}$, $Z = 2$).

seismic evidence, the authors of ref. 9 have argued for a density anomaly of 0.75% distributed over a 300-km-thick layer at the top of Earth's core. In order for this layer to date from planetary accretion, it must have withstood erosion by convective motions underneath (Supplementary Information), and may have thickened by 10–100 km by molecular diffusion since its time of formation (Supplementary Information), suggesting an initial layer thickness of 200–300 km. The red filled rectangle in Fig. 4b corresponds to projectiles capable of producing such a stratified layer by turbulent core merging following a giant impact; such projectiles have a core mass ratio in the range 0.04–0.05 and an initial density 3.8%–5.0% smaller than the protocore. The possible range of core mass ratios extends to 0.04–0.07 when allowing for density differences due to temperature or multiple impacts (Supplementary Information). A Moon-forming projectile in this size range is consistent with impact simulations on a fast-spinning Earth[13] and with predictions from accretion simulations[22].

At the other extreme, the green shaded region in Fig. 4b corresponds to collisions between two bodies of comparable size, an alternative scenario[14] for the Moon-forming impact. Such impacts are located below the solid curve in Fig. 4b, suggesting that the entire protocore mixes with the projectile core, erasing any pre-existing layering and implying that heterogeneity below the CMB developed after the main phase of accretion was over. Our experiments with $P < 0$ suggest similar outcomes after merging with a projectile core depleted in lighter elements[18]. Yet, it is difficult to explain how a 300 km stratified layer would develop without invoking substantial post-accretional mass transfer into or out of the core. According to our experiments, it is easier to explain the present-day core stratification as a primordial layer produced by the Moon-forming collision involving a Mars-sized or smaller projectile[12,13], with a core enriched in light elements. This Moon-forming impact scenario is also supported by geochemical properties of the Earth and the Moon, which can be explained by a Mars-sized, reduced projectile[24].

Core merging in the aftermath of giant impacts has far-reaching implications for composition and dynamics of planetary cores. The extent of metal–silicate equilibration after giant impacts is crucial in interpreting isotopic and geochemical data[18–20]. Previous fluid dynamical studies[25–27] concluded that, in the aftermath of giant impacts, the projectile core does not emulsify significantly within the magma ocean, implying little or no geochemical signature. In contrast, fountain collapse below the CMB (Fig. 2) suggests that chemical equilibration is not restricted to the magma ocean but extends deep inside the core, where silicate drops are entrained during the core merging process, allowing for significant signatures on mantle composition (Supplementary Information).

During fountain collapse, the magnetic Reynolds number (ratio of flow-produced induction to diffusion of magnetic field) probably exceeded 10^8, large enough for a short-lived but intense dynamo

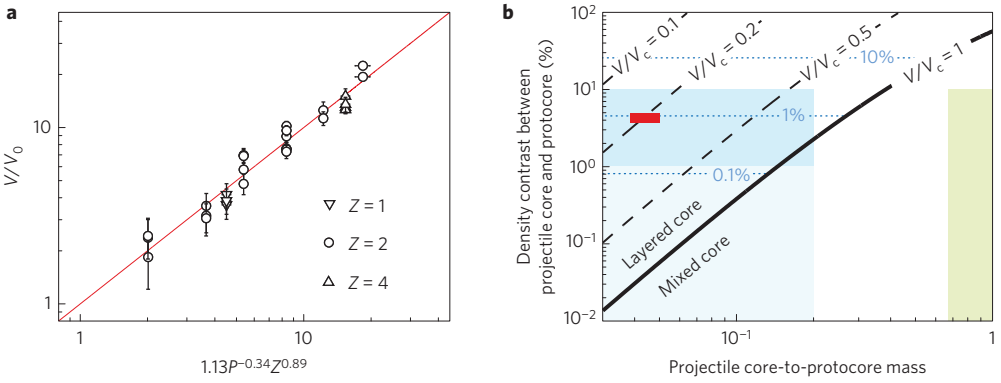

Figure 4 | Core stratification after merging with a projectile core enriched in light elements. a, Experimentally measured volume of the residual stratified layer normalized by the released volume versus least-squares best-fit power-law scaling in terms of the density ratio P (varying from 1.7×10^{-3} to 1.1) and the aspect ratio Z. Error bars indicate measurement uncertainties. **b**, Regime diagram for the final structure of the core from Fig. 4a, assuming $Z = 2$ (see text). Black curves are contours of the stratified layer-to-core volume ratio V/V_c as a function of the core mass ratio and the core density contrast (normalized by the protocore density). Blue dotted curves are contours of the mean density deficit in the stratified layer (normalized by the protocore density). We assume the density contrast between metal and silicates is half the metal density, and we equate volume and mass ratios, neglecting compressibility effects. The red rectangle locates projectiles that produce a 200–300 km layer with a 0.75%–1.10% density contrast. Blue regions: likely domain for giant impacts (see text) including a Moon-forming impact with a Mars-sized or smaller projectile[12,13]. Density contrasts of the order of those found in geochemical models of core formation[18] are depicted in darker blue. Green region: Moon-forming impact between two objects of comparable size[14], assuming constant core–mantle mass ratio.

capable of magnetizing crustal rocks (Supplementary Information). After dissipation of the impact kinetic energy and death of this transient dynamo, stabilizing compositional stratification inherited from giant impacts delayed, and perhaps suppressed, core convection and dynamo action. This scenario is consistent with the previously reported relationship between large impacts and the cessation of the dynamo on Mars[28]. A compositional layer at the top of Earth's core produced after a giant impact would have prevented dynamo action within the layer and could have delayed the initiation of a convective geodynamo underneath by a few thermal diffusion times. The thermal diffusion timescale through a 300-km-thick layer is approximately 0.14 Gyr, which is consistent with the presence of an early dynamo 3.4 Gyr ago, as recorded by palaeomagnetic observations[29].

Finally, we note that stratification observed in the F-layer at the base of the outer core may be another vestige of core formation[30], the residue from a merger with an impactor core depleted in light elements (Supplementary Fig. 2b). In this report we consider only projectile cores falling vertically under their own buoyancy. Additional simulations and experiments using a range of projectile shapes, velocities and compositions would be needed to model the full history of core formation.

Methods

Methods, including statements of data availability and any associated accession codes and references, are available in the online version of this paper.

Received 16 February 2016; accepted 10 August 2016; published online 12 September 2016

References

1. Braginsky, S. I. Mac-oscillations of the hidden ocean of the core. *J. Geomagn. Geoelectr.* **45,** 1517–1538 (1993).
2. Whaler, K. Does the whole of the Earth's core convect? *Nature* **287,** 528–530 (1980).
3. Lay, T. & Young, C. The stably-stratified outermost core revisited. *Geophys. Res. Lett.* **17,** 2001–2004 (1990).
4. Tanaka, S. Possibility of a low p-wave velocity layer in the outermost core from global smks waveforms. *Earth Planet. Sci. Lett.* **259,** 486–499 (2007).
5. Gubbins, D. Geomagnetic constraints on stratification at the top of Earth's core. *Earth Planet. Space* **59,** 661–664 (2007).
6. Buffett, B. Geomagnetic fluctuations reveal stable stratification at the top of the Earth's core. *Nature* **507,** 484–487 (2014).
7. Buffett, B. & Seagle, C. Stratification of the top of the core due to chemical interactions with the mantle. *J. Geophy. Res.* **115,** B04407 (2010).
8. Gubbins, D. & Davies, C. The stratified layer at the core–mantle boundary caused by barodiffusion of oxygen, sulphur and silicon. *Phys. Earth Planet. Int.* **215,** 21–28 (2013).
9. Helffrich, G. & Kaneshima, S. Outer-core compositional stratification from observed core wave speed profiles. *Nature* **468,** 807–810 (2010).
10. Tang, V., Zhao, L. & Hung, S. Seismological evidence for a non-monotonic velocity gradient in the topmost outer core. *Sci. Rep.* **5,** 8613 (2015).
11. Helffrich, G. & Kaneshima, S. Causes and consequences of outer core stratification. *Phys. Earth Planet. Inter.* **223,** 2–7 (2013).
12. Canup, R. M. Simulations of a late lunar-forming impact. *Icarus* **168,** 433–456 (2004).
13. Ćuk, M. & Stewart, S. Making the Moon from a fast-spinning Earth: a giant impact followed by resonant despinning. *Science* **338,** 1047–1052 (2012).
14. Canup, R. Forming a moon with an Earth-like composition via a giant impact. *Science* **338,** 1052–1055 (2012).
15. Marinova, M. M., Aharonson, O. & Asphaug, E. Mega-impact formation of the Mars hemispheric dichotomy. *Nature* **453,** 1216–1219 (2008).
16. Tonks, W. B. & Melosh, H. J. Magma ocean formation due to giant impacts. *J. Geophys. Res.* **98,** 5319–5333 (1993).
17. Nakajima, M. & Stevenson, D. J. Melting and mixing states of the Earth's mantle after the moon-forming impact. *Earth Planet. Sci. Lett.* **427,** 286–295 (2015).
18. Rubie, D. *et al*. Heterogeneous accretion, composition and core–mantle differentiation of the Earth. *Earth Planet. Sci. Lett.* **301,** 31–42 (2011).
19. Nimmo, F. & Agnor, C. Isotopic outcomes of n-body accretion simulations: constraints on equilibration processes during large impacts from Hf/W observations. *Earth Planet. Sci. Lett.* **243,** 26–43 (2006).
20. Rudge, J. F., Kleine, T. & Bourdon, B. Broad bounds on Earth's accretion and core formation constrained by geochemical models. *Nat. Geosci.* **3,** 439–443 (2010).
21. Wetherill, G. W. Occurrence of giant impacts during the growth of the terrestrial planets. *Science* **228,** 877–879 (1985).
22. Jacobson, S. & Morbidelli, A. Lunar and terrestrial planet formation in the grand tack scenario. *Phil. Trans. R. Soc. A* **372,** 20130174 (2014).
23. Poirier, J. P. Light elements in the Earth's outer core: a critical review. *Phys. Earth Planet. Int.* **85,** 319–337 (1994).
24. Wade, J. & Wood, B. The oxidation state and mass of the moon-forming impactor. *Earth Planet. Sci. Lett.* **442,** 186–193 (2016).
25. Dahl, T. W. & Stevenson, D. J. Turbulent mixing of metal and silicate during planet accretion - And interpretation of the Hf-W chronometer. *Earth Planet. Sci. Lett.* **295,** 177–186 (2010).
26. Deguen, R., Landeau, M. & Olson, P. Turbulent metal-silicate mixing, fragmentation, and equilibration in magma oceans. *Earth Planet. Sci. Lett.* **391,** 274–287 (2014).
27. Landeau, M., Deguen, R. & Olson, P. Experiments on the fragmentation of a buoyant liquid volume in another liquid. *J. Fluid Mech.* **749,** 478–518 (2014).
28. Roberts, J., Lillis, R. & Manga, M. Giant impacts on early Mars and the cessation of the martian dynamo. *J. Geophys. Res.* **114,** E04009 (2009).
29. Tarduno, J. A. *et al*. Geodynamo, solar wind, and magnetopause 3.4 to 3.45 billion years ago. *Science* **327,** 1238–1240 (2010).
30. Hernlund, J., Rubie, D. & Labrosse, S. Primordial stratification of the Earth's core. *AGU Fall Meeting Abstracts* DI33C–01 (AGU, 2013).

Acknowledgements

We gratefully acknowledge support from grant EAR-110371 and Frontiers in Earth System Dynamics grant EAR-1135382 from the National Science Foundation.

Author contributions

M.L., R.D., P.O. and B.H.H. designed and conducted the experiments; M.L. analysed the experimental data; M.L. and P.O. wrote the paper.

Additional information

Supplementary information is available in the online version of the paper. Reprints and permissions information is available online at www.nature.com/reprints. Correspondence and requests for materials should be addressed to M.L.

Competing financial interests

The authors declare no competing financial interests.

Methods

A tank of width $L = 25.5$ cm and height 47 cm is filled with two immiscible liquids: an aqueous solution (density $\rho_l = 999 \pm 1\,\mathrm{kg\,m^{-3}}$, viscosity $\mu_l = 1 \pm 0.1$ mPa s) below a low-viscosity silicone oil (density $\rho_u = 819 \pm 1\,\mathrm{kg\,m^{-3}}$, viscosity $\mu_u = 1 \pm 0.1$ mPa s), referred to as the lower liquid and the upper liquid, with thicknesses z_l and z_u, respectively. A volume $V_0 = 103$ ml is released at time $t = 0$ following the procedure used in an earlier study[27]. A blue dye (food colouring) is added in the released liquid. The flow is visualized using back-illumination through a diffusive screen and recorded by a colour video camera at 24 frames per second.

We release aqueous solutions of ethanol and sodium chloride of various concentrations such that the density contrast between the released and lower liquid varies between $-95\,\mathrm{kg\,m^{-3}}$ and $105\,\mathrm{kg\,m^{-3}}$. The viscosity μ_r of the released liquid varies in the range 1 ± 0.1–2.9 ± 0.1 mPa s. A surfactant (Triton X-100, concentration $2\,\mathrm{ml\,l^{-1}}$) is added to the lower and released liquids to lower their interfacial tension with the upper liquid to values in the range 2.6 ± 0.1–$5.5 \pm 0.1\,\mathrm{mN\,m^{-1}}$.

At the end of each experiment, the image intensity provides information about the dye concentration, and hence the final distribution of released liquid in the lower layer. Since the released liquid has a different density from the lower liquid, the image intensity also provides information about the shape of the final stratification in the lower layer.

If the light is monochromatic and the released and lower liquids have the same refractive index, the concentration in released liquid averaged in the direction perpendicular to the image is related to the image intensity through the Beer–Lambert law

$$C(x,z) = a \log \frac{I(x,z)}{I_0(x,z)} \tag{1}$$

where a is a constant, z is the distance to the upper–lower interface, x is the coordinate in the horizontal direction, $I(x,z)$ is the intensity at location (x,z) in the final image, and $I_0(x,z)$ is the intensity at location (x,z) in the back field image taken before the release. Integrating equation (1) over the entire image, and remembering that the total mass in released fluid is conserved and equal to $\rho_r V_0$, we obtain

$$a = \frac{\rho_r V_0}{L \int_0^L \int_0^{z_l} \log(I/I_0)\,\mathrm{d}z'\,\mathrm{d}x'} \tag{2}$$

For releases lighter than the lower liquid, a stratified layer eventually forms at the top of the lower liquid. For each experiment, we use the profile $C(x,z)$ to estimate the characteristic layer volume V such that V comprises 96% of the released liquid mass, assuming a flat, uniform layer in the horizontal direction. We measure V before molecular diffusion affects the layer thickness.

In our experiments, the light is not monochromatic and deviations from the Beer–Lambert law (1) cause errors in the released liquid concentration and in V/V_0. By calibrating $\log(I/I_0)$ against known released liquid concentrations, we estimate that discrepancies between C and the concentration in released liquid are of about 15%, uncertainties on the exponents c_2 and c_3 in our scaling law for V/V_0 are smaller than 10%, and uncertainties on the prefactor c_1 are less than 30%.

The dimensionless control parameters are:

$$Z = \frac{z_u}{R}, \quad P = \frac{\rho_l - \rho_r}{\rho_r - \rho_u}$$

$$\mathrm{Bo} = \frac{(\rho_r - \rho_u) g R^2}{\sigma_r}, \quad \mathrm{Oh} = \frac{\sqrt{\rho_r}\nu_r}{\sqrt{\sigma_r R}}$$

$$\frac{\rho_l}{\rho_u}, \quad \frac{z_l}{R}, \quad \frac{L}{R}, \quad \frac{\nu_r}{\nu_u}, \quad \frac{\nu_l}{\nu_u}, \quad \frac{\sigma_r}{\sigma_l}$$

where g is the acceleration due to gravity, R is the equivalent spherical radius of the released volume, ν is kinematic viscosity, ρ is density, and σ is the interfacial tension with the upper liquid. The subscripts r, u and l denote the released, upper and lower liquids, respectively. Values for P, Z, Bo, Oh, ρ_l/ρ_u and ν_l/ν_u in our experiments are compared with plausible values after giant impacts in Supplementary Table 1. In all of our experiments, the ratios ν_r/ν_u and σ_r/σ_l lie in the range 0.7–2.6 and 0.7–1.5, respectively. The ratio z_l/R is in the range 5–14 such that z_l is larger than the depth at which the released liquid penetrates in the lower layer (equal to $2R$ at most in our experiments), the relevant regime for most giant impacts (blue regions in Fig. 4b); this ensures that z_l/R does not significantly affect the dynamics of the impact at the immiscible interface separating the upper and lower liquids. The dimensionless tank width L/R is equal to 9.1. Experiments at the two largest density ratios P, where mixing stops before the gravity current reaches the tank walls, fit on the same scaling law as the other experiments (Supplementary Fig. 1), suggesting that the dimensionless tank width L/R does not significantly affect the amount of mixing.

The Bond number Bo measures the importance of the buoyancy force versus interfacial forces and the Ohnesorge number Oh measures the importance of viscous forces to inertial forces. In this study, Bo and Oh are kept larger than 190 and smaller than 0.01, respectively. According to our previous studies[26,27], such values ensure that, in all of our experiments, the released liquid produce turbulence during its fall through the upper liquid, forming a self-similar cloud. Turbulence is a key ingredient for giant impacts, missing in impact simulations[12–14,17]. We assume that, within this asymptotic, turbulent regime, Bo and Oh do not affect the mixing rate (as detailed in Supplementary Information).

Within this turbulent cloud regime, we study the effect of the density difference ratio and the dimensionless depth of the upper fluid Z. Applied to giant impacts, Z represents the dimensionless depth of the magma ocean.

Data availability. The authors declare that any additional data supporting the findings of this study are available from the corresponding author on request.

C.2 Convection, changement de phase, dynamique du noyau interne

LETTERS

Melting-induced stratification above the Earth's inner core due to convective translation

Thierry Alboussière[1,2], Renaud Deguen[1,3] & Mickaël Melzani[1]

In addition to its global North–South anisotropy[1], there are two other enigmatic seismological observations related to the Earth's inner core: asymmetry between its eastern and western hemispheres[2–6] and the presence of a layer of reduced seismic velocity at the base of the outer core[6–12]. This 250-km-thick layer has been interpreted as a stably stratified region of reduced composition in light elements[13]. Here we show that this layer can be generated by simultaneous crystallization and melting at the surface of the inner core, and that a translational mode of thermal convection in the inner core can produce enough melting and crystallization on each hemisphere respectively for the dense layer to develop. The dynamical model we propose introduces a clear asymmetry between a melting and a crystallizing hemisphere which forms a basis for also explaining the East–West asymmetry. The present translation rate is found to be typically 100 million years for the inner core to be entirely renewed, which is one to two orders of magnitude faster than the growth rate of the inner core's radius. The resulting strong asymmetry of buoyancy flux caused by light elements is anticipated to have an impact on the dynamics of the outer core and on the geodynamo.

The original observation[7] of seismic compressional (P)-wave velocities slower than the adiabatic PREM[14] model in the lower outer core has since been confirmed and incorporated in one-dimensional global models AK135 (ref. 10) and PREM2 (ref. 11). That discrepancy from the adiabatic profile could result from a wrong interpretation caused by the nearby complex inner core, because sensitivity kernels have a width of several hundred kilometres at body-wave frequencies[15], or might also be attributed to floating crystals[12,16]. Gubbins *et al.*[13] show that this last explanation is not possible but that the observed seismic velocities can be explained by a stratification in light elements (and temperature). However, the stratification mechanism by crystallization and melting of crystals at different depths has not been completely elucidated.

We propose that a dense layer can develop when melting and crystallization occur only at the inner-core boundary (ICB). Where crystallization takes place, light elements are released, providing light fluid; where melting takes place, dense fluid is produced. It is possible to quantify these effects in terms of flux of buoyancy. Let us denote $\Delta\rho$ as the fraction of density jump across the ICB that is due to composition partition between solid and liquid phases. For a rate of crystallization V, the buoyancy flux is $\Delta\rho g_c V$, where g_c is the magnitude of gravity[17] on the ICB (subscript c is for 'core'). For melting, the buoyancy flux is $-\Delta\rho g_c V$. The idea is that part of the heavy fluid would remain at the bottom, while the rest would be entrained by the light fluid. Conversely, part of the light fluid would mix with the dense fluid in the dense layer while the rest would cross the dense layer and contribute to convection within the main part of the outer core. This idea has been validated experimentally as follows.

The experiments consist of simultaneously injecting constant fluxes of light and dense fluids at the bottom of a fluid cavity. The cavity is a box of perspex 20 cm high and with a 15 cm × 15 cm horizontal cross-section. It is initially filled with salted water (initial concentration χ_0, in wt% NaCl). At the bottom of the cavity, there is a porous layer (sponge) below which the cross-section is divided into two disconnected parts: on one side light fluid is injected ($\chi_l < \chi_0$) and on the other side heavy fluid is injected ($\chi_h > \chi_0$), where χ_l and χ_h are the salt concentrations of the light and heavy fluids in wt% NaCl. Both density differences $\chi_0 - \chi_l$ and $\chi_h - \chi_0$ and both flow rates are controlled and set to be constant during the experiment. The injections of fluids start simultaneously through pipes from reservoirs with the desired concentration. The excess fluid is removed through an overflow at the top of the cavity.

The geophysically relevant case is when the positive buoyancy flux exceeds the negative one, because on average the inner core is growing. When the negative buoyancy flux induced by the heavy fluid is less than 80% of the amplitude of the light fluid, no dense layer is observed: the entrainment caused by the rise of light plumes is sufficient to mix the heavy fluid as it is released by the bottom boundary. However, when the heavy buoyancy flux is more than 80% of the light buoyancy flux, a dense layer grows at the bottom of the cavity. It has been observed experimentally that the condition for the existence of the dense layer is really a condition for the buoyancy fluxes, as described above; it does not specifically depend either on the volume flow rates or on the density differences between the fluids. This justifies our convection experiment as an appropriate model of a melting/crystallization process for the inner core.

On Fig. 1, an experimental run is shown. This experiment corresponds to a case in which the heavy fluid buoyancy flux was 83% that of the light fluid. The initial concentration and concentrations of the dense and light injected fluids were $\chi_0 = 4$ wt%, $\chi_h = 6$ wt% and $\chi_l = 1.65$ wt% NaCl respectively. The volume flow rate of the dense fluid was $Q_h = 3.9 \times 10^{-7}\,m^3\,s^{-1}$ and that of the light fluid was $Q_l = 4.0 \times 10^{-7}\,m^3\,s^{-1}$. The experiment was run twice under the same conditions: in the first instance, the injected dense fluid was coloured with potassium permanganate and photographs of the set-up were taken at different times after the beginning of the injections. A dense coloured layer forms at the bottom and its thickness grows linearly with time. It is also possible to see convection plumes going up on the right-hand side, carrying along some of the heavy coloured fluid in the upper part of the cavity. In the second instance, the synthetic schlieren method has been used[18,19], providing a quantitative two-dimensional field of refraction index with which to visualize the concentration gradients: their horizontal components are shown on the middle row of Fig. 1, showing convection plumes of light fluid on the right-hand side of the cavity, while their vertical components are shown on the bottom row, visualizing the dense layer and its

[1]Laboratoire de Géophysique Interne et Tectonophysique, CNRS, Observatoire de Grenoble, Université Joseph Fourier, Maison des Géosciences, BP 53, 38041 Grenoble Cedex 9, France. [2]Université de Lyon, CNRS UMR5570, site UCB Lyon 1, 2 rue Raphaël Dubois, bâtiment Géode, 69622 Villeurbanne, Université Lyon 1, ENS de Lyon, France. [3]Department of Earth and Planetary Sciences, Johns Hopkins University, Baltimore, Maryland 21218, USA.

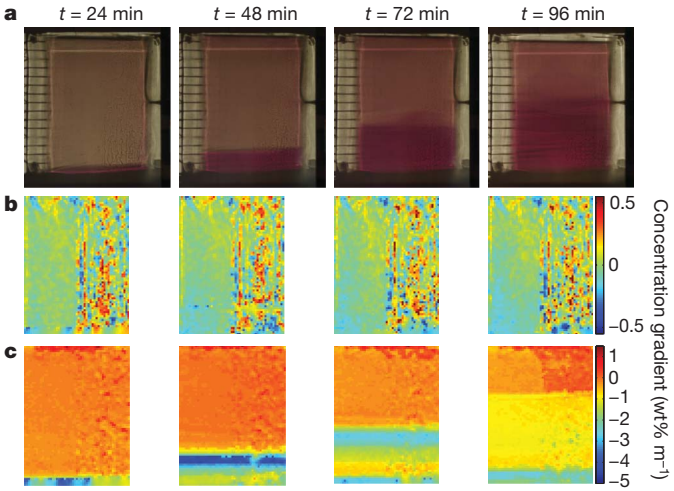

Figure 1 | Visualization of the growth of a dense layer in an experimental run. We used dye injection (**a**) and measurement of horizontal (**b**) and vertical (**c**) density gradients. The experimental cavity is initially filled with a 4 wt% NaCl water solution. From $t = 0$, a constant flux of 1.65 wt% NaCl solution is injected at the bottom on the right-hand side of the cavity while a 6 wt% NaCl solution is injected on the left-hand side. The dense fluid is coloured with potassium permanganate (**a**), visualizing a growing dense layer at the bottom, at four different times after the injection of the dye. The synthetic schlieren method is used in a second identical experiment: the horizontal gradient of refraction index in **b** highlights the convective plumes and the vertical gradient in **c** reveals the dense layer.

growth. The concentration field is computed from its gradient, and averaged along the horizontal direction: the resulting stratification profile is shown in Fig. 2. There is clearly a region of stratified fluid, above which density is nearly uniform. The thickness of this layer grows linearly with time, its volume being 50% to 90% that of the total volume generated by the light and heavy fluxes.

Melting part of the inner core at a significant rate is difficult while it is crystallizing (on average over its surface) as a result of secular cooling. The most plausible mechanism is that a topography is formed dynamically on the ICB so that the temperature of the adjacent fluid of the outer core exceeds the melting temperature. That excess temperature is then responsible for heat transfer from the outer core to the ICB, providing latent heat for fusion: in this way topography can be related to the rate of melting.

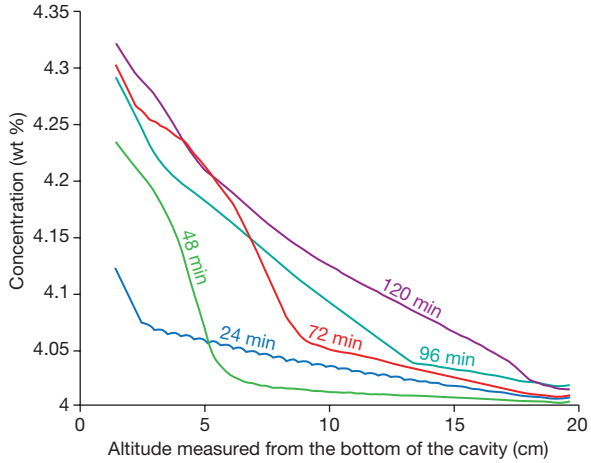

Figure 2 | Evolution of the concentration profile during the growth of a dense layer. The concentration field is extracted from the gradient of refraction index. It is averaged along the horizontal direction and shows the time evolution of the dense layer since injection of the dye.

The dynamical model we put forward to account for significant melting on the ICB results from the combination of three physical elements: the thermal state of a superadiabatic inner core, gravitational equilibrium and finite heat exchange of latent heat with the outer core. In superadiabatic conditions, a uniform velocity in the inner-core V, say from west to east along the x-axis (see Fig. 3), generates a global superadiabatic temperature gradient in the same direction proportional to the residence time in the inner core; such a gradient would hence be inversely proportional to V, and proportional to a positive source term $S \approx 10^{-15}\,\mathrm{K\,s^{-1}}$ defined by secular cooling and thermal conduction along the adiabat (see Methods and ref. 20):

$$\frac{\partial \Theta}{\partial x} = \frac{S}{V} \qquad (1)$$

where Θ is the temperature relative to the adiabat T_{ad} in the inner core anchored to the ICB[17]. It follows from the volume expansion coefficient[21] $\alpha = 1.1 \times 10^{-5}\,\mathrm{K^{-1}}$ and inner-core density (on the ICB[17]) $\rho_s = 1.28 \times 10^4\,\mathrm{kg\,m^{-3}}$ (subscript s is for 'solid') that there exists a density gradient $-\alpha\rho_s\partial\Theta/\partial x$. The resulting gravity field and density distribution generate unbalanced forces on the inner core, so that it is displaced a distance δ in the x direction. In the Methods, we derive the gravitational field and potential associated with this mass distribution, from which it is possible to calculate the net gravitational force $\mathbf{F}_G$ exerted on the inner core and the net pressure force $\mathbf{F}_P$ exerted by the outer core on the inner core

$$\mathbf{F}_G + \mathbf{F}_P = \frac{16\,\pi^2}{9} G\,\rho_l c^3 \left[\alpha \frac{\partial \Theta}{\partial x}\rho_s \frac{c^2}{5} - (\rho_s - \rho_l)\delta\right] \mathbf{e}_x \qquad (2)$$

where G is the universal gravitational constant, $c = 1{,}220$ km is the radius of the inner core[17], $\rho_l = 1.22 \times 10^4\ \mathrm{kg\,m^{-3}}$ is the outer core density on the ICB[17] and $\mathbf{e}_x$ is the unit vector in the direction of the

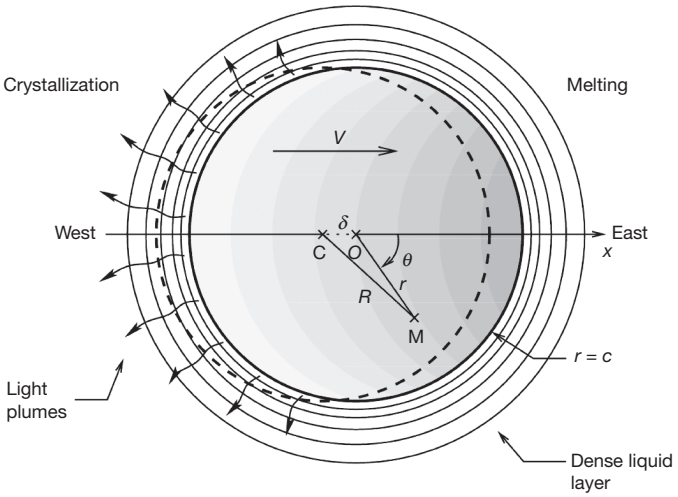

Figure 3 | A schematic representation of the translational convective mode. The centre of the inner core O is shifted by a distance δ away from the centre of the Earth C, which would be its equilibrium position if its density were uniform. That shift causes a thermal departure from the adiabat at the ICB, generating melting on one side and crystallization on the other side. Hence a uniform flow exists in the inner core (arrow labelled V): in the case of a superadiabatic regime, a gradient of temperature develops, as represented by greyscale shading. Its associated changes in density and gravitational potential lead to a new mechanical equilibrium for the inner core, corresponding to a shift in position in the same direction as initially assumed. r is the distance from the centre O of the inner core and θ is the angle between the x axis and the direction of the point where Θ is evaluated. V is the rate of crystallization, and c is the radius of the core. R is the distance between the point at which the gravitational potential U is calculated and the centre of the Earth C. M is a dummy point, used to define r, Θ and R. The dotted circle is the position of the ICB in the absence of density gradient (centred on C). See Methods.

temperature gradient. The equilibrium condition that both forces balance provides the shift δ as a function of the thermal gradient $\partial\Theta/\partial x$

$$\delta = \frac{\alpha \frac{\partial \Theta}{\partial x} \rho_s c^2}{5(\rho_s - \rho_l)} \quad (3)$$

Then, the displacement δ is associated with a non-uniform pressure distribution on the ICB (see Methods), yielding a small temperature departure δT from the adiabat (see Fig. 4)

$$\delta T = \rho_l g_c \, \delta \cos\theta \, (m_P - m_{ad}) \quad (4)$$

where $m_P = 8.5 \times 10^{-9}\,\mathrm{K\,Pa^{-1}}$ is the Clapeyron slope[22], $m_{ad} = (\alpha T_{ad})/(\rho c_p) = 6 \times 10^{-9}\,\mathrm{K\,Pa^{-1}}$ is the adiabatic gradient, $g_c = G\frac{4\pi}{3}\rho_s c$ is the gravity on the ICB and $c_p = 850\,\mathrm{J\,kg^{-1}\,K^{-1}}$ is the specific heat capacity[23]. That departure is accommodated by a thermal boundary layer in the outer core, with a corresponding heat transfer of typical magnitude $u' c_p \delta T$, where $u' = 10^{-4}\,\mathrm{m\,s^{-1}}$ is a typical velocity scale in the outer core. That heat transfer must be balanced by the release or absorption of latent heat

$$L\, V \cos\theta = u' c_p \delta T \quad (5)$$

where $L = 900\,\mathrm{kJ\,kg^{-1}}$ is the latent heat coefficient[24,25]. Finally, combining equations (1), (3), (4) and (5), we can express the translational velocity as

$$V^2 = \frac{4\pi G}{15} \frac{u'\, c_p\, \rho_s^2 \rho_l\, \alpha\, (m_P - m_{ad})\, S}{L\,(\rho_s - \rho_l)} c^3 \quad (6)$$

Depending on the heat flux at the core–mantle boundary, the history of the inner core shows a first phase dominated by growth $\dot{c} \propto c^{-1}$, followed by the development of the translational instability (see Supplementary Information), when its radius was around 400 km, leading to the dominant present translation $V \propto c^{3/2}$ of the order of $5 \times 10^{-10}\,\mathrm{m\,s^{-1}}$, while the growth rate is of the order of $10^{-11}\,\mathrm{m\,s^{-1}}$ (Fig. 5).

The latter scaling law implies that the translational convection is faster along a long axis of the inner-core oblate spheroid (see Supplementary Information), that is, perpendicular to the rotation axis. It follows that the temperature gradient is preferentially aligned with such a long axis, which again reinforces convection in that direction. Moreover, the Earth's aspherical mass distribution—which has essentially a degree 2, order 2 geometry[26]—is responsible for elongating the inner core slightly along an east–west axis and induces a degree 1 translational convection in the inner core through a bifurcation produced by instability (see Supplementary Information). We propose that the translational flow has a west to east orientation, which is responsible for the observed hemispherical asymmetry of the inner core: grain growth during the transit from the western hemisphere to the eastern hemisphere may explain the difference in seismic properties[27]. The temperature difference of a few kelvin between the hemispheres is another source of asymmetry.

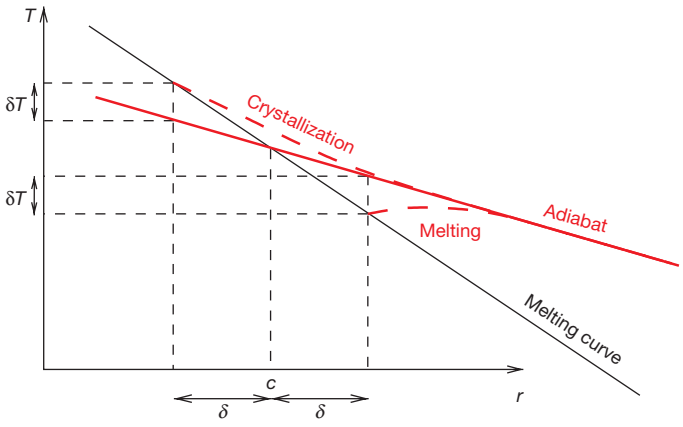

Figure 4 | Thermal departure from the adiabat due to the displacement of the inner core and heat transfer at the ICB. A thermal boundary layer forms in the outer core to adjust to the different radii of the ICB on the melting and crystallization sides.

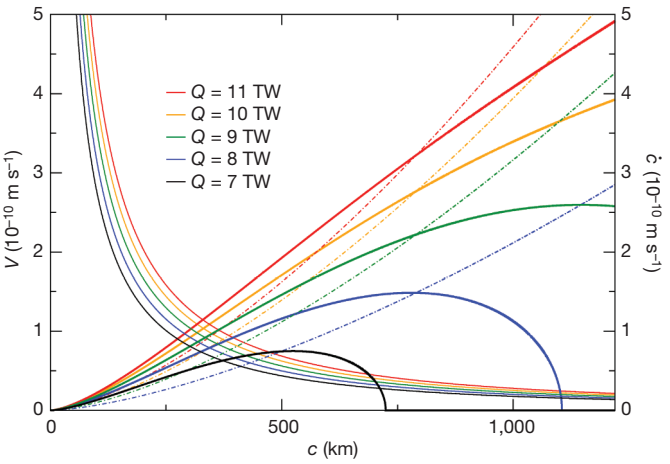

Figure 5 | Growth rate of the radius of the inner core and uniform convective velocity as functions of the inner-core radius. They are plotted for different values of the heat flux Q at the core–mantle boundary. Thin solid lines show the mean solidification (crystallization) rates $\dot{c}$ of the inner core. Dash-dotted lines show the translation velocities V, calculated with the assumption of a constant S. Thick solid lines show the translation velocities V, with $S(t)$ calculated (see Supplementary Information) from the core thermal evolution model of ref. 30.

According to our experiments, a melting rate above 80% of the crystallization rate is necessary for a dense layer to form, which geometrically implies that the translation velocity V is more than 20 times that of the inner-core growth rate. From Fig. 5, we see that this happens only when the core–mantle boundary heat flux exceeds 10 TW, and only since the inner-core radius was 1,100 km, some 200 million years ago. Extrapolating from our experiments, 50% of the volume of melt produced since then would correspond to a layer 250 km thick. The experimental excess concentration is found to be 10% of the concentration difference between light and heavy injected fluids. In the Earth's core, where the concentration of light elements is about 10%, a difference in concentration of around 1% across the dense layer is expected. This is indeed coherent with the observed seismic velocities[13].

Our convection mechanism ignores deformation in the inner core and compositional buoyancy. With a finite effective viscosity, temperature variations along gravity isopotentials induce an internal flow with deformation that affects the translational mode. We have estimated that the internal flow is weak compared to translation for an effective viscosity above 10^{18} Pa s. Enrichment in light elements of the outer core (a few per cent) has been invoked[28,29] to imagine a stabilizing mechanism for convection in the inner core. This is speculative, however, because the fraction of light elements incorporated in the inner core may have decreased more rapidly than the fraction of light elements incorporated into the outer core increased, given that gravity on the ICB is getting larger, reinforcing convection and compaction in the mush.

Invoking an excessively asymmetric buoyancy flux on the ICB calls for further study of the dynamics of the outer core and the geodynamo. The stratified layer is expected to be dynamically isolated and to act as a filter between the inner core and the rest of the outer core, but there might subsist some hemispherical asymmetry in the outer-core dynamics.

METHODS SUMMARY

The mode of convection associated with the translation of the inner core is not standard. Therefore, it is presented in the Methods. Thermal buoyancy is the driving force; however, unlike classical convection, the damping is not due to

viscous and/or thermal diffusion. Damping is set by the capacity of the outer core to extract or supply latent heat on the ICB.

Full Methods and any associated references are available in the online version of the paper at www.nature.com/nature.

Received 7 December 2009; accepted 7 June 2010.

1. Poupinet, G., Pillet, R. & Souriau, A. Possible heterogeneity of the Earth's core deduced from PKIKP travel times. *Nature* **305,** 204–206 (1983).
2. Tanaka, S. & Hamaguchi, H. Degree one heterogeneity and hemispherical variation of anisotropy in the inner core from PKP(BC)-PKP(DF) times. *J. Geophys. Res.* **102,** 2925–2938 (1997).
3. Creager, K. C. Large-scale variations in inner core anisotropy. *J. Geophys. Res.* **104,** 309–314 (1999).
4. Garcia, R. & Souriau, A. Inner core anisotropy and heterogeneity level. *Geophys. Res. Lett.* **27,** 3121–3124 (2000).
5. Niu, F. & Wen, L. Hemispherical variations in seismic velocity at the top of the Earth's inner core. *Nature* **410,** 1081–1084 (2001).
6. Yu, W.-c., Wen, L. & Niu, F. Seismic velocity structure in the earth's outer core. *J. Geophys. Res.* **110,** B02302, doi 10.1029/2003JB002928 (2005).
7. Souriau, A. & Poupinet, G. The velocity profile at the base of the liquid core from PKP(BC+Cdiff) data: an argument in favor of radial inhomogeneity. *Geophys. Res. Lett.* **18,** 2023–2026 (1991).
8. Kennett, B. L. N. & Engdahl, E. R. Traveltimes for global earthquake location and phase identification. *Geophys. J. Int.* **105,** 429–465 (1991).
9. Souriau, A. & Roudil, P. Attenuation in the uppermost inner core from broad-band GEOSCOPE PKP data. *Geophys. J. Int.* **123,** 572–587 (1995).
10. Kennett, B. L. N., Engdahl, E. R. & Buland, R. Constraints on seismic velocities in the earth from traveltimes. *Geophys. J. Int.* **122,** 108–124 (1995).
11. Song, X. & Helmberger, D. V. A. P wave velocity model of Earth's core. *J. Geophys. Res.* **100,** 9817–9830 (1995).
12. Zou, Z., Koper, K. D. & Cormier, V. F. The structure of the base of the outer core inferred from seismic waves diffracted around the inner core. *J. Geophys. Res.* **113,** B05314, doi 10.1029/2007JB005316 (2008).
13. Gubbins, D., Masters, G. & Nimmo, F. A thermochemical boundary layer at the base of Earth's outer core and independent estimate of core heat flux. *Geophys. J. Int.* **174,** 1007–1018 (2008).
14. Dziewonski, A. M. & Anderson, D. L. Preliminary reference Earth model. *Phys. Earth Planet. Inter.* **25,** 297–356 (1981).
15. Calvet, M., Chevrot, S. & Souriau, A. P-wave propagation in transversely isotropic media: II. Application to inner core anisotropy: effect of data averaging, parametrization and a priori information. *Phys. Earth Planet. Inter.* **156,** 21–40 (2006).
16. Loper, D. & Roberts, P. A study of conditions at the inner core boundary of the Earth. *Phys. Earth Planet. Inter.* **24,** 302–307 (1981).
17. Dziewonski, A. M. & Anderson, D. L. Preliminary reference Earth model. *Phys. Earth Planet. Inter.* **25,** 297–356 (1981).
18. Dalziel, S. B., Hughes, G. O. & Sutherland, B. R. Whole-field density measurements by 'synthetic schlieren'. *Exp. Fluids* **28,** 322–335 (2000).
19. Gostiaux, L. & Dauxois, T. Laboratory experiments on the generation of internal tidal beams over steep slopes. *Phys. Fluids* **19,** 028102, doi 10.1063/1.2472511 (2007).
20. Stacey, F. D. & Davis, P. M. *Physics of the Earth* Ch. 19 (Cambridge University Press, 2008).
21. Vočadlo, L. in *Treatise on Geophysics* (ed. Schubert, G.) Vol. 2, 91–120 (2007).
22. Alfè, D., Price, G. D. & Gillan, M. J. Iron under Earth's core conditions: liquid-state thermodynamics and high-pressure melting curve from ab initio calculations. *Phys. Rev. B* **65,** 165118, doi 10.1103/PhysRevB.65.165118 (2002).
23. Poirier, J.-P. Physical properties of the Earth's core. *C. R. Acad. Sci.* **318,** 341–350 (1994).
24. Poirier, J.-P. & Shankland, T. J. Dislocation melting of iron and the temperature of the inner core boundary, revisited. *Geophys. J. Int.* **115,** 147–151 (1993).
25. Anderson, O. L. & Duba, A. Experimental melting curve of iron revisited. *J. Geophys. Res.* **102,** 22659–22670 (1997).
26. Masters, G., Jordan, T. H., Silver, P. G., &. Gilbert, F. Aspherical Earth structure from fundamental spheroidal-mode data. *Nature* 298 609–613 (1982).
27. Calvet, M. & Margerin, L. Constraints on grain size and stable iron phases in the uppermost inner core from multiple scattering modeling of seismic velocity and attenuation. *Earth Planet. Sci. Lett.* **267,** 200–212 (2008).
28. Buffett, B. A. Onset and orientation of convection in the inner core. *Geophys. J. Int.* **179,** 711–719 (2009).
29. Deguen, R. & Cardin, P. Tectonic history of the Earth's inner core preserved in its seismic structure. *Nature Geosci.* **2,** 419–422 (2009).
30. Labrosse, S. Thermal and magnetic evolution of the earth's core. *Phys. Earth Planet. Inter.* **140,** 127–143 (2003).

Supplementary Information is linked to the online version of the paper at www.nature.com/nature.

Acknowledgements This work has benefited from discussions during the CNRS-INSU SEDIT meetings. We thank M. Bergman for discussions regarding inner-core crystallization. The LGIT and the ANR (Agence Nationale de la Recherche) (ANR-08-BLAN-0234-01) have provided financial support for the experiments.

Author Contributions M.M., R.D. and T.A. ran and analysed the experiments. T.A. designed the experimental study and built the dynamical model. R.D. and T.A. worked out the thermal conditions on the ICB and assessed the geophysical relevance of the dynamical model. R.D. computed the different scenarios of thermal history. R.D., T.A. and M.M. applied the experimental results to the geophysical context. T.A. and R.D. wrote the paper.

Author Information Reprints and permissions information is available at www.nature.com/reprints. The authors declare no competing financial interests. Readers are welcome to comment on the online version of this article at www.nature.com/nature. Correspondence and requests for materials should be addressed to T.A. (thierry.alboussiere@ens-lyon.fr).

METHODS

We present here in some detail an analytical model of inner-core translation. The model results from the combination of three physical phenomena: the thermal state of the inner core, gravitational equilibrium and phase change restrictions due to finite heat exchange with the outer core.

Thermal evolution of the inner core. In the inner core, owing to secular cooling, any parcel of matter experiences a decrease in temperature with respect to its initial curve of constant entropy. However, as the inner core grows, newly solidified material is set to a lower and lower entropy value. Hence the inner core is thermally stable if formerly solidified matter is colder than the current adiabatic profile attached to the liquidus temperature at the ICB, as a result of diffusion. If not, it is unstable to thermal convection.

It is convenient to introduce a potential temperature $\Theta(\mathbf{r}, t) = T - T_{ad}(r, t)$, where the adiabat $T_{ad}(r, t)$ is anchored at the ICB (that is, $\Theta = 0$ at the ICB). At inner-core conditions, the equation of conservation of entropy can be simplified (see Supplementary Information) and written as

$$\frac{\partial \Theta}{\partial t} + (\mathbf{v}\cdot\nabla)\Theta = \kappa\nabla^2\Theta + S(t) \tag{7}$$

where κ is the thermal diffusivity of solid iron. This form of the entropy equation captures first-order effects of compressibility by retaining the contribution of adiabatic heating or cooling during vertical advection[31]. The source term is

$$S(t) = \kappa\nabla^2 T_{ad} - \dot{T}_{ad} \tag{8}$$

where $\dot{T}_{ad} = \partial T_{ad}/\partial t$ is the difference between thermal diffusion along the adiabat and secular cooling and is independent of space. The sign of S determines whether or not the inner core is superadiabatic and likely to convect. It is uncertain because S is the difference between two poorly constrained quantities of comparable magnitude. A young inner core (large secular cooling) and small thermal diffusivity favour a superadiabatic temperature regime (positive S) and instability. The low estimate of thermal conductivity given recently by Stacey and Davis[20] together with the young inner core age favoured by recent core thermal models[30, 32,33] make it plausible: with a conductivity $k = 36\,\mathrm{W\,m^{-1}\,K^{-1}}$ as suggested by ref. 20, the inner core would be superadiabatic if its age is of the order of a billion years or less. $S(t)$ can be calculated for any given thermal history of the core (see Supplementary Information); it is a decreasing function of time, with typical values of 10–100 K per billion years. In what follows, we assume that S is indeed positive, and will use a nominal value of $S = 10^{-15}\,\mathrm{K\,s^{-1}} \approx 30\,\mathrm{K}$ per billion years.

If it is superadiabatic, the inner core is mechanically unstable. Classical thermal convection will develop if the inner-core viscosity is not too large[34–36], but the fact that the ICB is not fixed allows for a new instability consisting of a translation (see Supplementary Information for a linear stability analysis). Under the assumption that the viscosity of the inner core is large enough, this mode becomes dominant and the motion is effectively restricted to be a translation, with velocity V. Assuming that the Péclet number ($\mathrm{Pe} = Vc/\kappa$, where c is the radius of the inner core) is very large, the terms $\partial\Theta/\partial t$ and $\kappa\nabla^2\Theta$ can be neglected in equation (7), which now takes the simple form

$$\frac{\partial \Theta}{\partial x} = \frac{S}{V} \tag{9}$$

for a uniform velocity V in the direction of the x axis (see Fig. 3). With a boundary condition of $\Theta = 0$ on the crystallization side, the solution is

$$\Theta = \left(r\cos\theta + \sqrt{c^2 - r^2\sin^2\theta}\right)\frac{S}{V} \tag{10}$$

where r is the distance from the centre O of the inner core and θ is the angle between the x axis and the direction of the point where Θ is evaluated (see Fig. 3). The component Θ goes back to zero on the melting side within a thin boundary layer (not visible on the schematic Fig. 3) of thickness $\kappa/V \ll c$, which can be resolved when thermal diffusion is considered. The maximal temperature deviation from spherical symmetry is thus $\Delta T = 2cS/V$.

Mechanical equilibrium. The thermal asymmetry induced by a translation of the inner core is accompanied by a density asymmetry and it is anticipated that the inner core as a whole will be shifted in the direction of the thermal gradient in an attempt to move the centre of mass of the inner core towards the centre of the Earth: the light part is emerging while the dense part is sinking. We show here that a new equilibrium state with the inner core translated by a distance δ in the x direction results from a balance between the gravitational forces applied on the inner core and the pressure forces on the ICB. A correct estimate of the position of the inner core requires the evaluation of the change in self-gravitational potential resulting from the change in mass distribution.

For the sake of simplicity and tractability, density in the outer core is supposed to be uniform. In the inner core, density variations in the direction of the uniform velocity are kept in the analysis, but perpendicular variations are ignored. They would lead to degree 2 spherical harmonic contributions with little contribution to the displacement δ. Adiabatic spherical symmetric density variations are ignored because they contribute to δ only by slightly changing the average density of the inner core. Density in the inner core is thus expressed as

$$\rho = \rho_l + (\rho_s - \rho_l) - \alpha\frac{S}{V}\rho_s r\cos\theta \tag{11}$$

where α is the volume thermal expansion coefficient of the inner core, and ρ_l and ρ_s are the density of the liquid outer core and solid inner core. In equation (11), the first term on the right-hand side (that is, ρ_l) is the contribution of the liquid core, centred on C, and the other two terms on the right-hand side are the contributions of the inner core, centred on O, separated from C by a distance δ. Let us introduce the gravitational potential U, such that gravity is $g = -\nabla U$, obeying the Poisson equation $\nabla^2 U = 4\pi G\rho$, with G the universal gravitational constant. From equation (11), the corresponding gravitational potential is found to be

$$\frac{U}{4\pi G} = \rho_l\frac{R^2}{6} + (\rho_s - \rho_l)\frac{r^2}{6} - \alpha\frac{S}{V}\rho_s\left(\frac{r^3}{10} - \frac{c^2 r}{6}\right)\cos\theta \tag{12}$$

where r denotes the distance between the point at which U is calculated and the centre of the inner core O and R the distance between the same point and the centre of the Earth C (see Fig. 3). In the derivation of equation (12), the potential had to be determined inside and outside the inner core, whereas potential and gravity are continuous across the ICB. The formula (12) is the gravitational potential within the inner core. Noting that $R^2 = r^2 + 2\delta r\cos\theta + \delta^2$, equation (12) becomes

$$\frac{U}{4\pi G} = \rho_s\frac{r^2}{6} + \rho_l\frac{\delta^2}{6} - \alpha\frac{S}{V}\rho_s\left(\frac{r^3}{10} - \frac{c^2 r}{6}\right)\cos\theta + \delta\,\rho_l\frac{r}{3}\cos\theta \tag{13}$$

The total gravitational forces exerted on the inner core can be readily evaluated as

$$\mathbf{F}_G = -\int_{\text{inner core}}\rho\nabla U\,\mathrm{d}V = -4\pi G\delta\,\rho_l\rho_s\int_{\text{inner core}}\nabla\left(\frac{r}{3}\cos\theta\right)\mathrm{d}V \tag{14}$$

Only the contribution from the last term in equation (13) remains, because the other terms cancel out or have no contribution. Indeed, the distribution of masses within the inner core exerts no net gravity force on the inner core itself and only the outer core has a non-zero contribution when the inner core is not centred. We finally obtain

$$\mathbf{F}_G = -\frac{16\,\pi^2}{9}G\,\delta\,\rho_l\rho_s c^3\,\mathbf{e}_x \tag{15}$$

Within the liquid outer core, we assume hydrostatic equilibrium $-\nabla P - \rho_l\nabla U = 0$, which provides a simple relationship between pressure P and the potential U evaluated in equation (13)

$$P = -\rho_l\,U \tag{16}$$

up to an additive constant. It is then possible to evaluate the net pressure force exerted by the outer core on the ICB

$$\mathbf{F}_P = -\oint_{\text{ICB}}P\mathbf{e}_r\mathrm{d}S = \frac{16\,\pi^2}{9}G\,\rho_l c^3\left[\alpha\frac{S}{V}\rho_s\frac{c^2}{5} + \rho_l\delta\right]\mathbf{e}_x \tag{17}$$

The net force exerted on the inner core is then

$$\mathbf{F} = \mathbf{F}_P + \mathbf{F}_G = \frac{16\,\pi^2}{9}G\rho_l c^3\left[\alpha\frac{S}{V}\rho_s\frac{c^2}{5} - (\rho_s - \rho_l)\delta\right]\mathbf{e}_x \tag{18}$$

Static equilibrium of the inner core ($\mathbf{F} = \mathbf{0}$) is reached when the inner core is translated by a distance equal to

$$\delta = \frac{\alpha\frac{S}{V}\rho_s c^2}{5(\rho_s - \rho_l)} \tag{19}$$

Kinetics of phase change at the ICB. The displacement of the inner core implies that pressure is no longer uniform on the ICB. This corresponds to a temperature difference δT between the adiabat and the liquidus temperature along the interface:

$$\delta T = -\delta P(m_P - m_{ad}) \tag{20}$$

where δP denotes the pressure variation on the ICB and m_P and m_{ad} are the Clapeyron slope and adiabatic gradient (in the liquid phase) respectively. Pressure variations on the ICB can readily be determined from the previous calculations on gravitational equilibrium. Pressure in the liquid is related to the gravitational potential (through equation (16)). The gravitational potential (13) is evaluated on the ICB $r = c$, with equation (19) taken into account

$$\frac{U}{4\pi G} = \frac{\rho_s}{6}\left[c^2 + \delta^2 + 2\ \delta c \cos\theta\right] \quad (21)$$

Hence, the pressure variation on the ICB follows from equations (16) and (21)

$$\delta P = -\rho_l g_c \delta \cos\theta \quad (22)$$

where $g_c = G\frac{4\pi}{3}\rho_s c$ is the gravitational acceleration in $r = c$. From equation (20), the temperature departure from the adiabat is

$$\delta T = \rho_l g_c\ \delta\ \cos\theta\ (m_P - m_{ad}) \quad (23)$$

The adiabat is thus higher than thermodynamic equilibrium on the eastern side and lower by the same amount on the western side. We do not assume that the actual temperature of the solid–liquid interface is dependent on the rate of melting or crystallization, dynamic undercooling being very small for metals. We consider instead that a thermal boundary layer develops in the outer core, which is the cause of heat exchange, that is, supply or extraction of latent heat (see Fig. 4). Heat conduction in the solid and in the liquid are smaller contributions and are fairly equal and opposite. Moreover, it is assumed that the rate of crystallization (and melting on the other side) is much bigger than the growth rate of the inner-core $\mathrm{d}c/\mathrm{d}t$, where $c(t)$ is the radius of the inner core. Fusion and crystallization are thus supposed to be of equal magnitude: this can be expressed in a single form $V\cos\theta$, where V is the assumed uniform velocity of the inner core. Heat transfer in the liquid outer core is related to the amplitude of velocity fluctuations u' in the outer core: we have little knowledge regarding u' near the ICB, so we take them to be of the same order of magnitude as the velocity at the core–mantle boundary estimated from the secular variation of the magnetic field, which is $10^{-4}\,\mathrm{m\,s^{-1}}$. The simplest estimate for the heat transfer coefficient is $c_p u'$. Hence, the heat budget at the ICB is

$$L\ V \cos\theta = u'\ c_p\ \delta T \quad (24)$$

where L is the latent heat. This equation relates the velocity V (rate of crystallization on one side, melting on the other side) to the thermal departure from the adiabat δT at the interface, which is itself related to the displacement δ of the inner core by equation (23).

Results of the model. All elements of the model have been analysed and now we put them together. Equations (23) and (24) provide a relationship between δ and V

$$L\ V = u' c_p \rho_l g_c (m_P - m_{ad})\delta \quad (25)$$

corresponding to the thermal aspect of the problem. Using the independent mechanical equation (19), the displacement δ can be eliminated and the solution for the translation velocity V can be obtained as

$$V^2 = \frac{4\pi G}{15}\frac{u'\ c_p \rho_s^2 \rho_l\ \alpha(m_P - m_{ad})S}{L(\rho_s - \rho_l)}\, c^3 \quad (26)$$

Representative values of the parameters involved are $G = 6.67 \times 10^{-11}\,\mathrm{m^3\,kg^{-1}\,s^{-2}}$, $u' = 10^{-4}\,\mathrm{m\,s^{-1}}$, $c_p = 850\,\mathrm{J\,kg^{-1}\,K^{-1}}$ (ref. 23), $\rho_s = 12{,}800\ \mathrm{kg\ m^{-3}}$ and $\rho_l = 12{,}200\ \mathrm{kg\ m^{-3}}$ (ref. 17), $\alpha = 1.1 \times 10^{-5}\,\mathrm{K^{-1}}$ (ref. 21), $m_P = 8.5 \times 10^{-9}\,\mathrm{K\,Pa^{-1}}$ (ref. 22), $m_{ad} = (\alpha T)/(\rho_l c_p) = 6 \times 10^{-9}\ \mathrm{K\ Pa^{-1}}$, $L = 900\,\mathrm{kJ\,kg^{-1}}$ (refs 24, 25), and $c = 1{,}221\,\mathrm{km}$ (ref. 17). With $S = 10^{-15}\,\mathrm{K\,s^{-1}}$, the translation velocity obtained for the present state of the inner core is found to be $V \simeq 7.7 \times 10^{-10}\ \mathrm{m\ s^{-1}}$, which is faster than the growth rate of the radius of the inner core by a factor of around 70. This is a justification for neglecting the growth of the inner core in the analysis. The associated displacement is derived from equations (25) or (19). Its value is $\delta \simeq 95$ m. The maximal temperature disequilibrium is $\delta T \simeq 0.01$ K, while the non-adiabatic temperature difference across the inner core is $\Delta T = 2cS/V \simeq 3.2$ K. Because δT is very small compared to ΔT, the boundary condition $\Theta = 0$ is justified to a good approximation from the point of view of the inner core. It is also possible to determine the maximal time of residence in the solid inner core, which is $2c/V \simeq 100$ million years.

31. Tritton, D. J. *Physical Fluid Dynamics* 1–536 (Oxford, Clarendon Press, 1988).
32. Gubbins, D., Alfè, D., Masters, G., Price, G. D. & Gillan, M. Gross thermodynamics of two-component core convection. *Geophys. J. Int.* **157,** 1407–1414 (2004).
33. Nimmo, F. in *Treatise on Geophysics* (ed. Schubert, G.) Vol. 2, 31–65, 2007).
34. Jeanloz, R. & Wenk, H.-R. Convection and anisotropy of the inner core. *Geophys. Res. Lett.* **15,** 72–75 (1988).
35. Weber, P. & Machetel, P. Convection within the inner-core and thermal implications. *Geophys. Res. Lett.* **19,** 2107–2110 (1992).
36. Wenk, H.-R., Baumgardner, J. R., Lebensohn, R. A. & Tomé, C. N. A convection model to explain anisotropy of the inner core. *J. Geophys. Res.* **105,** 5663–5678 (2000).

Earth and Planetary Science Letters 333–334 (2012) 211–225

Contents lists available at SciVerse ScienceDirect

Earth and Planetary Science Letters

journal homepage: www.elsevier.com/locate/epsl

Frontiers Paper

Structure and dynamics of Earth's inner core

Renaud Deguen

Department of Earth and Planetary Sciences, Johns Hopkins University, Baltimore, MD 21218, USA

ARTICLE INFO

Article history:
Accepted 8 April 2012
Editor: Y. Ricard

Keywords:
inner core
anisotropy
solidification texturing
deformation texturing
F-layer
differential rotation

ABSTRACT

The seismological exploration of the Earth's inner core has revealed unexpected and puzzling structural complexities. Its elastic anisotropy is now well established, and has been shown to vary spatially. There is a well defined hemispherical dichotomy in anisotropy and attenuation, and significant variations in the radial direction, with weaker anisotropy in the uppermost regions, and possibly different properties in an "innermost inner core" of radius 300–600 km. Perhaps even more puzzling is the observation of a stably stratified layer at the base of the outer core, which has recently been proposed to result from melting of inner core material. If confirmed, the presence of this layer has major implications for our understanding of convection in the outer core. Inner core differential rotation with respect to the mantle remains controversial. We will review here recent progress in understanding the dynamics of the inner core. A number of different models have been proposed for the development of the inner core's structure and formation of the stable layer at the base of the outer core, and particular care will be taken to clarify under which conditions the proposed mechanisms can be active.

1. Introduction

The existence of the Earth's inner core was inferred by Lehmann (1936) from the observation of P-waves in the core shadow zone, which she interpreted as being due to the reflection of P-waves at a deep seismological discontinuity, the inner core boundary (ICB). Although the solidity of the inner core was initially debated—and formally proved rather recently (Dziewonski and Gilbert, 1971), it was soon suggested that the inner core is made of solid iron, and results from the crystallization of the outer core (Birch, 1940; Jacobs, 1953). It has been long recognized that crystallization of the inner core has a key role in powering the Earth's dynamo (Verhoogen, 1961; Braginsky, 1963; Gubbins, 1977; Loper, 1978). The idea that the inner core could be internally dynamic emerged later, one of the triggers being the discovery that the inner core is elastically anisotropic: body waves travel faster along the Earth's rotation axis than perpendicularly to it (Poupinet et al., 1983).

The seismological exploration of the inner core is a difficult task. The inner core is a small target (its volume is less than 1% of the Earth), and is concealed from our view by the mantle and the highly heterogeneous D″ layer of the lowermost mantle. PKP-waves can be used as reference phases to minimize the effect of D″ heterogeneities, but this is effective for only a limited range of epicentral distances (see Fig. 1 for a description of the main P-wave phases in the core). Normal modes are only sensitive to large scale structures, and their sensitivity to the deepest part of the inner core is weak. Body waves are sensitive to much smaller scales, but at 1 Hz the Fresnel zones are typically ~300 km wide (Calvet et al., 2006), which means they sample and average relatively large regions as well.

In spite of all these difficulties, an increasingly complex picture of the inner core is emerging (see Souriau, 2007;Tkalcić and Kennett, 2008 for recent reviews). Significant radial and lateral variations of seismological properties, including anisotropy, have been identified, and the unexpected complexity of the inner core remains a challenge to explain.

Although some of the main results of seismology and mineral physics will be reviewed briefly in Sections 2 and 3, the emphasis of this review is on the dynamics of the inner core. After discussing the thermal and compositional state of the inner core in Section 4, we will discuss the role of solidification (Section 5) and deformation (Section 6) in the development of the inner core internal structure, before discussing possible models of formation of an anomalous layer at the base of the outer core (Section 7), and the possibility and implications of inner core differential rotation (Section 8).

2. The main questions

2.1. What is the origin of inner core anisotropy? Of its radial and lateral variations?

P-waves sampling the inner core travel faster along the direction of Earth's rotation than perpendicular to it (Poupinet et al., 1983). This observation, together with the anomalous splitting of core sensitive modes, has been interpreted as elastic anisotropy of the inner core (Morelli et al., 1986; Woodhouse et al., 1986).

E-mail addresses: rdeguen1@jhu.edu, rdeguen@gmail.com

0012-821X/$ - see front matter © 2012 Elsevier B.V. All rights reserved.
http://dx.doi.org/10.1016/j.epsl.2012.04.038

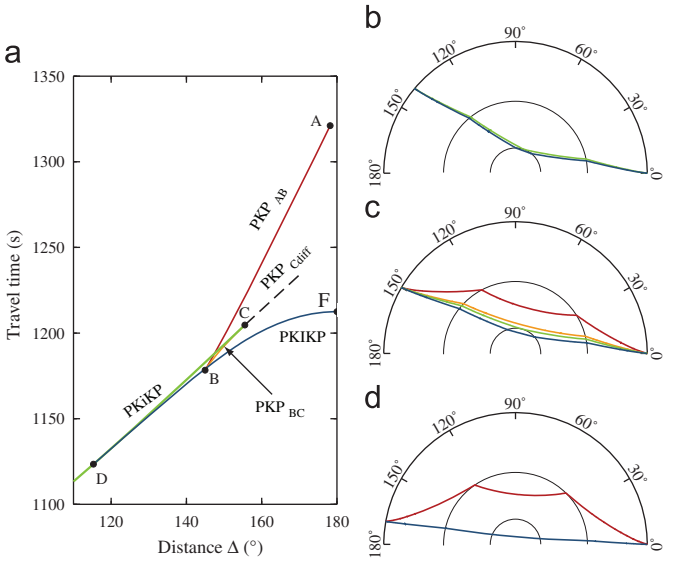

Fig. 1. (a) Traveltimes of the main core phases as a function of epicentral distance Δ. (b)–(d) Ray paths of the main core phases with epicentral distance equal, respectively, to 140°, 150°, and 170°. In the epicentral distance range 145–155°, two different PKP phases coexist: PKP_{AB} (red) samples mostly the outer part of the outer core, while PKP_{BC} (orange) samples the base of the outer core. Whenever possible, PKIKP-waves (also called PKP_{DF}) are compared to a reference PKP phase, either PKP_{AB} or PKP_{BC}, to minimize the effect of source mislocation and mantle heterogeneities. This is possible for only a limited range of epicentral distances (or equivalently, of the depth of the ray turning point). The PKP_{BC} phase exists only for epicentral distances between 145° and 155°, which correspond to a turning point <400 km below the ICB. For deep ray paths (epicentral distance $>155°$, turning point >400 km below the ICB), PKIKP and the reference phase PKP_{AB} sample quite different regions in D″, as can be seen in (d). PKP_{Cdiff} is a compressional wave diffracted around the inner core boundary. (For interpretation of the references to color in this figure caption, the reader is referred to the web version of this article.)

Heterogeneities in D″ may explain part of the traveltimes anomalies (Bréger et al., 2000a,b; Romanowicz and Bréger, 2000), but differential traveltimes of PKP_{DF} and PKP_{BC} waves have provided compelling evidences that the anomalies indeed originate from the inner core (Shearer et al., 1988; Creager, 1992; Song and Helmberger, 1993). Shear-waves traveling in the inner core are extremely difficult to observe, but there is one report of observation of shear-wave splitting in the inner core, which suggests an average shear-wave anisotropy of 1% in the western hemisphere (Wookey and Helffrich, 2008). The inner core also exhibits a clear attenuation anisotropy, P-waves traveling parallel to the Earth's rotation axis being more attenuated (Souriau and Romanowicz, 1996, 1997; Cormier et al., 1998; Oreshin and Vinnik, 2004; Yu and Wen, 2006). The positive correlation between velocity and attenuation is the opposite of what is observed in the mantle, thus suggesting a different attenuation mechanism.

There is a general agreement about weaker anisotropy in the eastern hemisphere than in the western hemisphere (Tanaka and Hamaguchi, 1997; Creager, 1999; Garcia and Souriau, 2000; Niu and Wen, 2001; Deuss et al., 2010; Leykam et al., 2010; Irving and Deuss, 2011), the two hemispheres being defined in reference to the Greenwich meridian. The uppermost inner core is isotropic or weakly anisotropic and highly attenuating (Shearer, 1994; Song and Helmberger, 1995b; Creager, 1999; Garcia and Souriau, 2000), with again a hemispherical structure, the eastern hemisphere being faster and more attenuating. The hemispherical pattern of traveltime anomalies can be explained by either a different anisotropy level (Creager, 1999), or by a hemispherical variation of the thickness of the isotropic layer, with a thickness of $\sim$100 km and $\sim$400 km in the eastern and western hemispheres, respectively (Creager, 2000; Garcia and Souriau, 2000).

The depth dependence of anisotropy in the deeper inner core is more controversial. There are evidences for the presence of an innermost inner core of radius 300–600 km exhibiting a possibly different anisotropy geometry (Ishii and Dziewoński, 2002, 2003; Beghein and Trampert, 2003; Sun and Song, 2008a,b; Niu and Chen, 2008) and a lower attenuation (Li and Cormier, 2002; Cormier and Li, 2002; Cormier and Stroujkova, 2005).

The North–South orientation of the anisotropy suggests that either Earth's rotation or the magnetic field plays a role in the development of inner core anisotropy, which in turn suggests possible couplings with the outer core and the dynamo. A number of models have been proposed so far (Sections 3–6), but we are still short of a model able of explaining all the complexities of the inner core structure in a self-consistent way.

2.2. Is there a stably stratified layer at the base of the outer core? If yes, how has it been formed and sustained?

Model PREM (Dziewonski and Anderson, 1981) exhibits only very slight deviations from a well-mixed adiabatic state in the outer core. This is consistent with the idea of vigorous core convection, which is expected to allow only minute deviations from an adiabatic profile (e.g. Stevenson, 1987) except in very thin boundary layers at the top and bottom of the core. Yet Souriau and Poupinet (1991) have found evidences of significant deviations from PREM of the P-wave velocity profile at the base of the outer core. Traveltimes of PKP_{BC} and PKP_{Cdiff} (P-waves diffracted along the ICB) suggest the presence of a region of low P-wave velocity gradient in the bottom $\sim$150 km of the outer core. This observation has then been confirmed by a number of studies (Song and Helmberger, 1992; Yu et al., 2005; Zou et al., 2008; Cormier, 2009; Cormier et al., 2011), and has been included in global models AK 135 (Kennett et al., 1995) and PREM2 (Song and Helmberger, 1995a). Yu et al. (2005) suggested that this layer exhibits an hemispherical structure, with the P-wave velocity profile being closer to PREM in the eastern hemisphere. This is problematic from a geodynamical point of view, because of the difficulty to sustain large lateral density variations in the outer core, unless the viscosity in this region is significantly larger than usually thought (Cormier, 2009). Cormier et al. (2011) demonstrated however that the hemispherical structure proposed by Yu et al. (2005) is not required by the data.

The observation of this anomalous layer, sometimes called the 'F-layer',[1] is puzzling, and seems very difficult to reconcile with our current view of outer core convection, where crystallization of the inner core is thought to drive convection through the release of buoyant, light element rich liquid. The low P-wave velocity gradient is most probably indicative of a stable density stratification, which is just the opposite of what we expect. The layer is also much thicker than what we can expect for a convective thermo-chemical boundary layer. Models for the formation of this layer are discussed in Section 7.

2.3. Is the inner core differentially rotating? What does it imply?

Following theoretical (Gubbins, 1981) and numerical (Glatzmaier and Roberts, 1996) predictions of inner core differential rotation with respect to the mantle, a number of seismological observations have

[1] In reference to a layer present in early seismological models between the outer core and the inner core, the E and G layers in Bullen's nomenclature (Jeffreys, 1939; Bullen, 1947). The original F-layer had much more dramatic features, including a strong P-wave velocity discontinuity at its boundary with the outer core. The PKiKP precursors interpreted as a discontinuity at the top of the F-layer were later shown to be due to scattering of PKP-waves in D″ (Cleary and Haddon, 1972; King et al., 1973), and the F-layer disappeared from global Earth models.

been reported, with most recent studies indicating a rotation rate between 0.0 and 0.3°/yr. In addition of being fascinating in its own right, differential rotation can have profound consequences for other aspects of inner core dynamics, as well as outer core dynamics. For example, the strength of the toroidal magnetic field at the ICB, a potentially critical parameter for inner core internal dynamics (Section 6.3), depends in part on the rate of differential rotation (Aurnou et al., 1996). The observed rate of differential rotation can be used to put constraints on inner core viscosity (Buffett, 1997), another key parameter for inner core dynamics. Finally, one important question is whether or not differential rotation is compatible with the observed hemispherical structure of the inner core (Section 8).

2.4. Why is the inner core so attenuating? Why is the S-wave velocity so low?

Body waves indicate that the inner core is highly attenuating, with the P-wave quality factor $Q_\alpha \simeq 100-400$ in the upper half of the inner core, but possibly higher, ~ 600, deeper (Li and Cormier, 2002; Cormier and Li, 2002; Oreshin and Vinnik, 2004). Some normal modes seem to indicate very low attenuation in shear, with the shear quality factor Q_μ in the range 1000–4000 (Masters and Gilbert, 1981; Fukao and Suda, 1989), while others require a much lower $Q_\mu \simeq 90-110$ (Widmer et al., 1991; Durek and Ekstrom, 1996; Resovsky, 2005). Andrews et al. (2006) have shown however that the high apparent Q_μ of some normal modes is likely to be an artifact due to anelastic mode coupling, which argues for the low value of Q_μ.

Note that the low value of Q_μ would make the observation of shear waves in the inner core (the PKJKP phase) unlikely (Shearer et al., 2011). Reported observations of PKJKP, if correct, may indicate a much higher Q_μ, at least for certain paths (Wookey and Helffrich, 2008; Shearer et al., 2011).

Even with the low value of the normal mode estimate of Q_μ, there is a disagreement between the attenuation derived from normal modes and body waves. P-waves attenuation results from a combination of attenuation in bulk (compression, quality factor Q_κ) and attenuation in shear (Q_μ). In the mantle, the attenuation in bulk is negligible (Q_κ high), which seems to be also the case in the inner core (Resovsky, 2005). In this case, the P-wave quality factor is related to Q_μ through $Q_\alpha \simeq (3/4)(V_P/V_S)^2 Q_\mu \simeq 7 \times Q_\mu$, where V_P and V_S are the velocity of P and S-waves, respectively (e.g. Souriau, 2007). Thus $Q_\mu \simeq 100$ would imply $Q_\alpha \simeq 700$, which is about twice higher than its observed mean value. Possible explanations include a finite Q_κ or a frequency dependence of Q_μ. Another possibility is that the observed attenuation of body waves is partly due to scattering by kilometer scale heterogeneities, as suggested by the observation of PKiKP waves coda (Vidale and Earle, 2000).

The S-wave velocity is constrained by normal modes, and appear to be much slower ($\sim 3.5\ \mathrm{km\,s^{-1}}$) than the P-wave velocity, which indicates a low rigidity. Both the high attenuation and the low S-wave velocity may be indicative of the presence of melt deep in the inner core (Section 5.2).

3. Origin of elastic anisotropy in the inner core

Seismic anisotropy can originate from either the preferred orientation of elastically anisotropic iron crystals (lattice preferred orientation, LPO), or from the anisotropic distribution of two phases with different elastic properties (shape preferred orientation, SPO). Both are possible in the inner core. As discussed below, iron is likely to be elastically anisotropic at inner core conditions, which makes LPO a natural candidate for explaining the anisotropy of the inner core. Another possibility is that the seismic anisotropy results from the preferential orientation of elongated liquid inclusions (Singh et al., 2000).

It is generally accepted that the stable phase of pure iron at inner core conditions is hexagonal close packed (*hcp*) (Tateno et al., 2010). However, it is clear that both the outer and inner cores are alloyed with nickel and some lighter elements, possibly Si, S, O (Alfè et al., 2002; Badro et al., 2007). Although the concentration of light elements is smaller in the inner core (Jephcoat and Olson, 1987), the presence of both nickel and light elements may stabilize cubic phases (either body-centered cubic, *bcc*, of face-centered cubic, *fcc*) at the expense of the *hcp* phase (Vočadlo et al., 2003; Dubrovinsky et al., 2007; Côté et al., 2008; Kuwayama et al., 2008).

The elastic properties of the candidate iron phases remain subject to debate. Even the sense of anisotropy of *hcp* iron is unclear. Low temperature, high pressure calculations (Stixrude and Cohen, 1995; Laio et al., 2000) suggest that P-wave propagation is faster along the *c*-axis than along the *a*-axis, in agreement with low pressure/low temperature *hcp* analogs. Experimental determination of the elastic constants have suggested a fast direction lying at an intermediate angle between the *a*- and *c*-axis (Mao et al., 1998; Merkel et al., 2005), but this is now thought to be an artifact due to texturing of iron aggregates in diamond anvil cells due to non-hydrostatic stress (Antonangeli et al., 2006). In the first published *ab initio* study of iron at pressure and temperature of the inner core, Steinle-Neumann et al. (2001) found that the sense of anisotropy reverses at high temperature, with the *a*-axis being faster than the *c*-axis. The validity of their treatment of temperature effects has been questioned (Gannarelli et al., 2003, 2005), and a fast *c*-axis is still generally thought to be more likely (Antonangeli et al., 2006). Yet recent *ab initio* calculations at inner core pressure and temperature (Vočadlo et al., 2009) again suggest that the sense of anisotropy reverses at high temperature. Recent studies favour a *c*-axis slightly faster than the *a*-axis, with a pronounced velocity minimum at an intermediate direction (Sha and Cohen, 2010; Chen et al., 2011). Fewer studies have addressed the elastic anisotropy of cubic phases, but they suggest a large anisotropy of up to $\sim 12\%$ with the $\langle 111 \rangle$ directions being the fastest and the $\langle 100 \rangle$ being the slowest (Belonoshko et al., 2008).

It should be clear from the above discussion that there is still no consensus on the nature of the stable phase in the inner core and on the elastic properties of the candidate phases. It is significant however that all candidate phases appear to be elastically anisotropic—although sometimes only weakly (Sha and Cohen, 2010), which supports the idea that seismic anisotropy in the inner core results from the lattice preferred orientation of iron crystals. Most models of inner core anisotropy therefore rely on the preferential alignment of iron crystals, either through solidification texturing where LPO is acquired at the ICB as a result of crystallization (Section 5), or deformation texturing resulting from plastic flow within the inner core (Section 6).

4. Inner core thermal and chemical evolution

Understanding the thermal and chemical evolution of the inner core is a prerequisite for understanding its internal dynamics. As discussed further in Section 6, the viability of a number of possible dynamical models of the inner core depends critically on the thermal and chemical density stratification of the inner core. An unstable density profile promotes natural convection, while a stable density profile in most cases inhibits vertical motions because deformation of isodensity surfaces would induce restoring buoyancy forces.

The core crystallizes from the center outward because the melting temperature of the core mixture increases with depth faster than the (adiabatic) core geotherm (Jacobs, 1953). As the core cooled from an initially fully molten state, the geotherm crossed the melting temperature profile first at the center of the core and the inner core nucleated. Further cooling results in outward crystallization, at a rate which is controlled by heat extraction from the core by mantle convection. One consequence of this unusual solidification mode is that the inner core is effectively cooled from above, a configuration which is potentially prone to thermal convection. Thermal convection further requires that cooling is such that the inner core temperature profile is superadiabatic. This depends on a competition between extraction of the inner core internal heat by diffusion and advection, and cooling at the ICB (Sumita et al., 1995; Yukutake, 1998; Buffett, 2009; Deguen and Cardin, 2011). It can be shown that inner core superadiabaticity depends on the sign of

$$S(t) = \kappa \nabla^2 T_{\mathrm{ad}} - \frac{dT_{\mathrm{ad}}}{dt}, \tag{1}$$

where T_{ad} is the inner core adiabat anchored at the ICB and κ the thermal diffusivity (Deguen and Cardin, 2011). Here $dT_{\mathrm{ad}}/dt < 0$ and $\kappa \nabla^2 T_{\mathrm{ad}} < 0$. Fast cooling and a low inner core thermal diffusivity ($S > 0$) promotes superadiabaticity; slow cooling and high thermal diffusivity ($S < 0$) results in a stable thermal stratification. Although radiogenic heating has been initially proposed as the chief energy source for inner core convection (Jeanloz and Wenk, 1988), its role is probably secondary compared to secular cooling (Yukutake, 1998; Deguen and Cardin, 2011). Note that the cooling rate $|dT_{\mathrm{ad}}/dt|$ most probably decreases with time—even if the heat flux at the core–mantle boundary (CMB) remains constant—because, as the inner core grows, the latent heat and gravitational energy released by inner core growth take an increasingly important part in the heat budget of the core. Superadiabaticity is therefore more likely early in the inner core history.

The thermal state of the inner core is directly controlled by the core thermal history and, ultimately, by the magnitude of the CMB heat flow. The requirement for inner core superadiabaticity can be written as a function of either CMB heat flow or inner core age (Sumita et al., 1995; Yukutake, 1998; Buffett, 2000, 2009; Deguen and Cardin, 2009, 2011). From Eq. (1), it can be shown that a good first order criterion for superadiabaticity of the inner core is that its age τ_{ic} is smaller than a critical age

$$\tau_{\mathrm{ic}}^{c} = \tau_{\kappa}\left(\frac{dT_s}{dT_{\mathrm{ad}}} - 1\right), \tag{2}$$

where $\tau_{\kappa} = r_{\mathrm{ic}}^2/(6\kappa)$ is the timescale of thermal diffusion in the inner core, and dT_s/dT_{ad} is the ratio of the Clapeyron slope dT_s/dP over the adiabat dT_{ad}/dP (Deguen and Cardin, 2009, 2011). It is also to some extent useful to think in terms of deviations from superadiabatic heat flux at the CMB: It can indeed be shown that the requirement for inner core superadiabaticity is close to the requirement for a superadiabatic CMB heat flux when the inner core is small. This would be an exact criterion if the cooling rate of the core and its thermo-physical properties were uniform in the outer core and inner core. This is not exactly true, but a detailed calculation shows that the above criterion is still a useful and relatively accurate rule of thumb when the inner core is young and the contributions of latent heat and gravitational energy to the core heat budget is small.

The advantage of thinking in terms of deviations from adiabatic gradient at the CMB lies in the fact that we do have some constraints on CMB superadiabaticity. Before the nucleation of the inner core, the only significant energy source for core convection and dynamo action was cooling from the CMB. Dynamo action at this time implies that the CMB heat flux was larger than adiabatic, by a factor which depends on how dissipative the Earth's dynamo is. Since there is no evidence from paleomagnetism for a period with no dynamo in the past ~ 3.5 Gyr, it seems likely that the CMB heat flux has been superadiabatic prior to the nucleation of the inner core. According to the discussion of the previous paragraph, this suggests that the conditions for superadiabaticity in the inner core were likely met as well early in its history.

Keeping a superadiabatic inner core geotherm up to now is significantly more difficult. It is still quite plausible if the core thermal conductivity is as low as suggested by Stacey and Davis (2008). With a thermal conductivity of $k = 28\ \mathrm{W\ m^{-1}\ K^{-1}}$, this requires a CMB heat flow of 7–15 TW, which is plausible according to the most recent estimates (Lay et al., 2008). On the other hand, the very high values estimated by Sha and Cohen (2011) for *hcp* iron at inner core conditions ($\sim 160\ \mathrm{W\ m^{-1}\ K^{-1}}$) and by de Koker et al. (2012) for liquid iron alloys at core condition (140–220 $\mathrm{W\ m^{-1}\ K^{-1}}$ at the ICB), would almost certainly imply that the inner core is thermally stably stratified. Given the very large range in published thermal conductivity estimates (Stacey and Davis, 2008; Konopkova et al., 2011; Sha and Cohen, 2011; de Koker et al., 2012), whether the inner core is thermally unstable or not remains an open question.

In addition, the inner core may have developed a compositional stratification due to the gradual enrichment of the outer core in light elements expelled during crystallization. Since the concentration of a given element is related through the partition coefficient D to the concentration in the liquid from which it crystallizes, we expect the development of a stable compositional stratification in the inner core (Stacey, 1992; Deguen and Cardin, 2009; Buffett, 2009). The reality may be more complicated however: the effective partition coefficient D is likely to change during the course of inner core crystallization, because the efficiency of interstitial melt extraction by compaction and convection is expected to increase as the inner core grows and the gravity increases. This may weaken to some extent the compositional stratification (Alboussière et al., 2010; Deguen and Cardin, 2011). Also, the compositional evolution of the inner core would be very different if a stable iron rich layer form at the base of the outer core (see Section 7).

5. Crystallization of the inner core, and solidification texturing

5.1. Solidification regime

In multicomponent systems, such as metallic alloys or sea water, preferential release of incompatible solutes during solidification results in the build up of a solute-enriched boundary layer ahead of the solidification front. Because incompatible solutes generally depress the freezing point, the liquid in the vicinity of the solidification front can become supercooled (see Fig. 2 and its caption). Crystallization of the inner core is unusual in the sense that, because of the effect of pressure on the solidification temperature, the solid is hotter than the liquid and heat flows from solid to liquid, contrary to what is typical in metallurgy and laboratory experiments. As is apparent in Fig. 2, this situation actually favours supercooling because the temperature gradient at the ICB is negative rather than positive.

In practice, this supercooled region usually does not persist. The system evolves toward thermodynamic equilibrium through the formation of a two-phase region, with the solid phase being in the form of either a rigid matrix of dendrites (dendritic or mushy layer) or isolated crystals in suspension (slurry layer), a process called *equiaxed solidification* in metallurgy. Dendritic growth

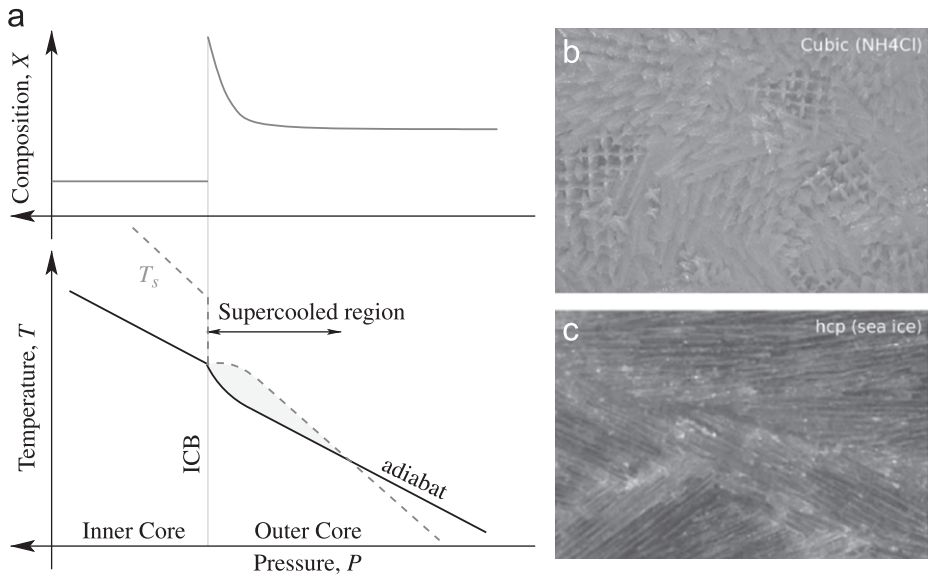

Fig. 2. (a) Compositional and thermal conditions near the ICB in the case of planar solidification. Preferential release of incompatible light elements results in the formation of a compositional boundary layer, with higher light element concentration χ (thick grey line, upper panel) near the ICB. The profile of solidification temperature T_s (grey dashed line) results from the combined effect of variations in composition (T_s decreases with increasing χ) and pressure (T_s decreases with decreasing P). T_s must be compared with the geotherm (thick line), which is adiabatic in the outer core far from the ICB, and connects to the ICB through a thermal boundary layer. The region ahead of the ICB where $T < T_s$ is supercooled. (b) and (c) Solidification textures due to dendritic growth of cubic crystals (b, ammonium chloride aqueous solution) and *hcp* crystals (c, ice grown from an aqueous NaCl solution). The view is parallel to the growth direction. (c) was modified from Bergman et al. (2002).

results from a morphological instability of the solidification front, and is the most common solidification regime in metallurgy. The morphology of the dendrites depends on the crystal symmetry. A good example of cubic materials dendrites is given by ammonium chloride solutions as shown in Fig. 2b. In contrast, *hcp* materials such as ice or zinc produce dendrites in the form of elongated platelets as shown in Fig. 2c. In alloy castings, equiaxed crystallization usually becomes predominant only when the bulk of the fluid is supercooled (Kurz and Fisher, 1989).

The possibility of constitutional supercooling at the ICB was first discussed by Schloessin (1974). Loper and Roberts (1981) and Fearn et al. (1981) have shown that the conditions for constitutional supercooling at the ICB are likely met, thus suggesting dendritic crystallization. Linear stability analysis (Shimizu et al., 2005; Deguen et al., 2007) also support dendritic solidification. Shimizu et al. (2005) have investigated the possibility of formation of a slurry layer at the ICB, but found dendritic growth to be more likely. However, as advocated by Morse (1986, 2002), a possibly important limitation of these studies is that the effect of convection is not, or only partially, included in the stability analysis. Alexandrov and Malygin (2011) have included the effect of vertical, laminar advection in their stability analysis, and predict morphological instability and dendritic growth under downwellings, and possibly a slurry layer localized below upwellings. The effect of vigorous convection and mixing in the melt on the solidification regime remains poorly understood however.

5.2. Trapped melt in the inner core?

One possible consequence of either dendritic or equiaxed solidification is that some light element rich liquid can be trapped within the inner core, a possible explanation for its high Poisson ratio and high attenuation (Doornbos, 1974; Cormier, 1981; Loper and Fearn, 1983). Fearn et al. (1981) have shown that light element rich melt can be thermodynamically stable deep in the inner core: Even at the center of the Earth, the temperature is quite close to the liquidus at core composition (about 100 K below if the inner core geotherm is adiabatic, and at most $\sim$300 K in the unlikely limit of an isothermal inner core), and may be above the solidus (Fearn et al., 1981; Deguen et al., 2007). However, the actual melt fraction depends on the efficiency of melt extraction through interstitial convection (Worster, 1997) and compaction of the solid matrix (Sumita et al., 1996). An analytical model by Loper (1983) suggests that the solid fraction should increase to essentially one in less than a kilometre due to convection in the melt. The compaction length is probably smaller than 1 km as well (Sumita et al., 1996), which implies that compaction should expel most of the interstitial fluid within a few kilometres. It does not mean necessarily that the melt fraction tends to zero after a few compaction lengths because: (1) permeability generally decreases with melt fraction, so that it is increasingly difficult to extract the last melt and (2) depending of the dihedral angle of the partial melt in the iron matrix, the permeability can vanish at a finite melt fraction.

Observational evidences for partial solidification in the inner core are inconclusive. The presence of melt deep in the inner core was first proposed as a possible explanation for the high attenuation in the inner core (Doornbos, 1974), and later on the basis of its high Poisson ratio. Recent *ab initio* calculations (Vočadlo, 2007a) confirm that partial solidification can explain the inner core Poisson ratio if it contains about 8% liquid, but other studies suggest that the low rigidity of the inner core might actually be an intrinsic property of solid iron at high pressure and temperature (Falzone and Stacey, 1980) or due to defects and grain boundaries (Belonoshko et al., 2007).

5.3. Solidification texturing

Karato (1993) has advocated that iron crystals may align with the magnetic field during solidification. He argues that iron is expected to be paramagnetic at inner core conditions. This is supported by the calculations of Grechnev et al. (2003), although the magnetic susceptibility is expected to decrease with temperature and vanish at the melting point. Noting that *hcp* metals (but not cubic metals) usually have anisotropic magnetic susceptibility, Karato (1993) proposed that small crystals nucleated

ahead of the ICB would align with the ambient magnetic field during sedimentation because of their induced magnetic moment, as observed in experiments by De Rango et al. (1991). Effective alignment requires that grain rotation is faster than sedimentation, which is expected to depend on the magnitude of the susceptibility anisotropy and magnetic field, the crystal size, and flow conditions, including turbulence. No quantitative model has been formulated yet.

Solidification texturing is likely if the inner core crystallizes dendritically (Bergman, 1997; Bergman et al., 2000). Dendrites usually grow along preferred crystallographic direction, because of anisotropy in melting entropy, and tend to align with the local heat flux (e.g. Chalmers, 1964). This results in a preferred texture, and elastic anisotropy (Bergman, 1997), dictated by the heat flow. Experiments involving non-dendritic solidification also shows solidification texturing (Brito et al., 2002).

Bergman (1997) suggested that solidification texturing can be a key ingredient of inner core texture and anisotropy. Noting that heat transport in the outer core is expected to be more efficient in the cylindrically radial direction due to the effect of rotation on convection, Bergman (1997) suggested that crystals would grow preferentially in that direction, which would result in a cylindrical elastic anisotropy. Such texture also results in attenuation anisotropy (Bergman et al., 2000), with the direction perpendicular to the growth direction being more attenuating. In a cylindrically growing inner core, this would result in a stronger attenuation along the rotation axis, in agreement with seismological inferences (Bergman, 1997). A potential difficulty of this model is that, even if the ICB heat flux is larger in the equatorial belt than in the polar region (Fig. 3), the local heat flux might still be predominantly radial, parallel to the local gravity field. In this case, solidification texturing would lead at first order to a spherically symmetric radial texture and anisotropy. Note that such a radial texture may not be incompatible with the isotropic layer inferred from body-wave seismology: with a radial anisotropy, the traveltime of PKP_{DF} would depend on the depth of the turning point, but not on the direction of the ray, so that the layer would appear as seismically isotropic.

Additional solidification texturing may come from interactions with the flow in the outer core (Bergman et al., 2002, 2003). Hydrodynamic interactions would be limited if iron has a cubic symmetry because of the axisymmetric morphology of cubic dendrites, but may be important if iron is *hcp* and crystallizes as platelets. In the Arctic, sea ice often exhibits a strong preferred crystal orientation, with the *c*-axis having a similar orientation over areas of sometimes several hundred of square kilometers (Cherepanov, 1971). The *c*-axis appears to align with the mean direction of oceanic currents (Weeks and Gow, 1978, 1980), which suggests alignment results from hydrodynamic interaction with the ice platelets. This has been confirmed in experiments demonstrating that ice crystals having platelets perpendicular to the flow (*c*-axis parallel to the flow) grow at the expense of the others (Langhorne, 1983; Langhorne and Robinson, 1986). This supports the idea that persistent large scale flow in the outer core, controlled by an heterogeneous CMB heat flux (Sumita and Olson, 1999; Aubert et al., 2008) or by the CMB topography (Calkins et al., 2012), may induce a preferred orientation of *hcp* iron crystals over large areas (Bergman et al., 2002; Aubert et al., 2008). Unfortunately, there is no systematic theoretical or experimental results including the effect of platelet spacing and solidification rate, making an extrapolation to inner core conditions hazardous. Bergman et al. (2002, 2003) have shown experimentally that flow *within* the dendritic layer can also lead to strong textures, with the platelets now oriented preferentially parallel to the flow (*c*-axis perpendicular to the flow).

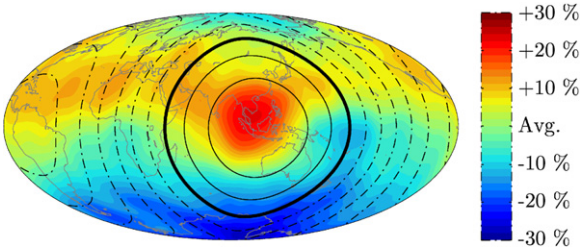

Fig. 3. Time averaged solidification rate at the ICB in a numerical dynamo model with heterogeneous CMB heat flow, adapted from Aubert et al. (2008). The color scale shows the relative deviation (in %) of the averaged solidification rate from the spatial mean. (For interpretation of the references to color in this figure caption, the reader is referred to the web version of this article.)

Variations of the solidification rate can also result in variations in texture and melt content, as proposed by Aubert et al. (2008) to explain the hemispherical structure of the inner core (Fig. 3). For example, interdendritic spacing typically changes with the solidification rate V as $V^{-1/4}$ (Kurz and Fisher, 1989), which means that a $\sim 30\%$ variation in solidification rate would induce a $\sim 7\%$ variation in interdendritic spacing. It remains to be shown how sensitive the seismic properties are to such texture variations.

As discussed above, some degree of solidification texturing seems likely, and it is important to know how such texture subsequently evolves with time. Deformation (see Section 6) can probably rework a solidification texture. Spontaneous evolution seems likely as well according to Bergman et al.'s (2010) experiments on annealing of directionally solidified alloy. In these experiments, Zinc–Tin ingots with an initially strong solidification texture were kept for several days at a temperature high enough to allow for partial melting of the alloy, thus modeling the evolution of a portion of a dendritic layer buried below the ICB. The unexpected result is a dramatic loss of texture and decrease in grain size during annealing. This would limit the importance of solidification texturing to the uppermost inner core.

6. Dynamical regimes

We now turn to a discussion of the various dynamical models of the inner core involving large scale deformation. The study of inner core dynamics is made difficult by the very large uncertainties on several key parameters. We have already discussed in Section 4 the thermo-chemical evolution of the inner core and its implications for the density stratification—stable or unstable—of the inner core. The implications would become more apparent in the discussion below. A second critical point is the inner core rheology. This is obviously of primary importance for at least two reasons. (i) LPO development depends on the microscopic deformation mechanism. Since diffusion-controlled creep does not induce LPO, deformation texturing requires that deformation is accommodated for a significant part by dislocation creep. (ii) The dynamics of the inner core depends critically on its effective viscosity. Published estimates from mineral physics (Yoshida et al., 1996; Van Orman, 2004; Reaman et al., 2011) and geodynamics (Buffett, 1997; Mound and Buffett, 2006; Koot and Dumberry, 2011) span roughly ten order of magnitudes, with estimates ranging from 10^{11} Pa s to 10^{22} Pa s. Note that since the rheology can be stress-dependent, the inner core 'viscosity' is not a fully intrinsic property of the iron aggregate, but should in general be a function of the flow considered. Recent discussions of the inner core rheology can be found in Sumita and Bergman (2007), Vočadlo (2007b) and Reaman et al. (2011).

6.1. Thermal convection

Thermal convection has been the first model proposed for the origin of the inner core anisotropy (Jeanloz and Wenk, 1988;

Wenk et al., 1988), in analogy with convectively induced anisotropy in the upper mantle. As already mentioned in Section 4, the first key question is the thermal and chemical state of the inner core. Natural convection requires that the inner core is unstably stratified. Inner core thermal convection is forced by the core thermal evolution, and as noted in Section 4, the inner core is more likely to be superadiabatic—and convect—early in its history (Buffett, 2009; Deguen and Cardin, 2011; Cottaar and Buffett, 2012).

An important property of inner core convection is that the ICB is a phase boundary, which implies that solidification or melting can occur if the interface is displaced away from equilibrium. Convection, or any internal dynamic process, would induce a dynamic topography at the ICB, with the topographic stress balancing the viscous stress and dynamic pressure associated with convective motion. This results in lateral variations of the freezing rate, with higher than average solidification rate in troughs and lower solidification rate, or even melting, at crests. In practice, phase change is rate limited by the ability of outer core convection to supply or evacuate the heat absorbed or released by melting or solidification. Equating the rate of latent heat release or absorption with an estimate of the convective heat flux in the outer core, Alboussière et al. (2010) estimated that a topography of amplitude h will evolve at a rate

$$\frac{dh}{dt} = -\frac{h}{\tau_\phi}, \tag{3}$$

where the timescale of phase change τ_ϕ is

$$\tau_\phi = \frac{L}{c_p \overline{u}\left(\frac{dT_{ad}}{dr} - \frac{dT_s}{dr}\right)}. \tag{4}$$

Here L is the latent heat, $\overline{u}$ is the typical convective velocity in the outer core, dT_{ad}/dr is the adiabatic gradient in the outer core at the ICB, and dT_s/dr is the gradient of solidification temperature at the ICB. τ_ϕ is found to be of the order of 1000 years.

Inner core thermal convection depends on two non-dimensional numbers. One is a Rayleigh number

$$Ra = \frac{\alpha \rho g S r_{ic}^5}{6\kappa^2 \eta}, \tag{5}$$

where S is the effective heating rate defined in Eq. (1), α is the thermal expansion coefficient, g the gravity at the ICB, r_{ic} the inner core radius, κ the thermal diffusivity, and η the dynamic viscosity of the inner core. Ra is related to the age of the inner core through S, with fast inner core crystallization leading to higher values of Ra. Because of the possibility of phase change at the ICB, inner core convection depends also on a second number defined as

$$\mathcal{P} = \frac{\Delta \rho g r_{ic} \tau_\phi}{\eta}. \tag{6}$$

$\mathcal{P}$ is the ratio of the phase change timescale τ_ϕ to the timescale of viscous relaxation of a topography of wavelength $\sim r_{ic}$, $\eta/(\Delta \rho g r_{ic})$, where $\Delta\rho$ is the density jump at the ICB. Two very different regimes are possible depending on the value of $\mathcal{P}$.

In the limit of large $\mathcal{P}$, phase change can be neglected and the ICB can be considered as an effectively impermeable boundary. At high Rayleigh number, the regime is typical of large Prandtl number, high Rayleigh number internally heated convection, with cold plumes falling down from the ICB and a passive return flow (Fig. 4b) (Weber and Machetel, 1992; Deguen and Cardin, 2011; Cottaar and Buffett, 2012). In this regime, the convective velocity scales as $U \sim (\kappa/r_{ic}) Ra^{1/2}$ and is typically of order 10^{-9} m s^{-1} or larger (Deguen and Cardin, 2011; Cottaar and Buffett, 2012).

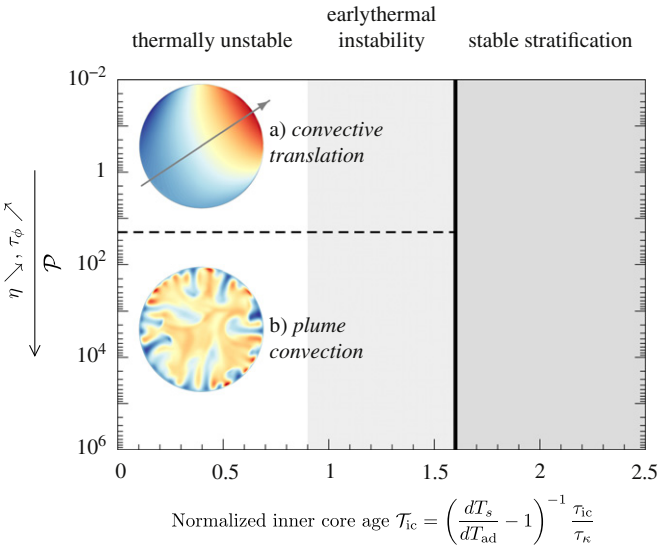

Fig. 4. Regime diagram for thermal convection in the inner core. The age of the inner core is normalized by the critical age for superadiabaticity introduced in Eq. (2). The inner core is stably stratified if $\mathcal{T}_{ic} > 1.6$, unstable early in its history but stable now if $0.9 < \mathcal{T}_{ic} < 1.6$, and unstable up to now if $\mathcal{T}_{ic} < 0.9$. If the inner core is superadiabatic, the mode of convection depends primarily on the parameter $\mathcal{P}$ defined in Eq. (6). Convective translation is the preferred mode if $\mathcal{P} \lesssim 20$, while plume convection dominates if $\mathcal{P}$ is large (η small, τ_ϕ large). The temperature field is shown in the case of convective translation in **a** and chaotic plume convection in (b) (red is hot, blue is cold). (For interpretation of the references to color in this figure caption, the reader is referred to the web version of this article.)

A successful model of inner core dynamics must be able to explain the large scale North–South seismic anisotropy. This may be problematic for this convection regime, because (i) it is likely dominated by relatively small scale, time-dependent motion and (ii) it is not obvious why a North–South orientation should be preferred. In the inner core, the effect of the Coriolis force is vanishingly small and cannot affect the flow. Buffett (2009) has shown however that another consequence of Earth's rotation, the centrifugal acceleration, may favour a degree one pattern aligned with the rotation axis. The limitation is that effective alignment requires the convection to be only slightly supercritical. Buffett (2009) argued that if convection stops, the last active mode would be a degree one convection aligned with the rotation axis. In simulations with an evolving inner core where convection stops, Deguen and Cardin (2011) found that the transition from convection to quiescence is often abrupt, and that the last motions are dominated by relaxation of small scale density heterogeneities left behind by convection. Another possibility is to envision some degree of coupling between convection and other forcings (see discussions in Sections 6.2 and 6.3).

When phase change is fast compared to viscous deformation ($\mathcal{P}$ small), a new regime called 'convective translation' is possible (Monnereau et al., 2010; Alboussière et al., 2010). Perhaps surprisingly, it can be shown that a rigid inner core ($\eta \to \infty$, $\mathcal{P} \to 0$) is unstable if its temperature profile is superadiabatic (Alboussière et al., 2010), the result of the instability being a global translation of the inner core with melting in one hemisphere and solidification in the other (Monnereau et al., 2010; Alboussière et al., 2010). The rate of translation, found to be equal to $(\kappa/r_{ic})\sqrt{\frac{6}{5}(Ra/\mathcal{P})}$ by Alboussière et al. (2010), is set by the magnitude of S and the ability of outer core convection to supply or evacuate the latent heat absorbed or released by melting and solidification. It may be significantly larger than the mean growth rate of the inner core. When the assumption of inner core rigidity is relaxed and finite viscosity is considered, the translation mode still dominates as long as $\mathcal{P} \lesssim 30$, the plume

convection regime being dominant when $\mathcal{P}$ is larger (Deguen et al., 2011a; Mizzon and Monnereau, 2011). With a phase change timescale $\tau_\phi \simeq 1000$ year, this corresponds to a critical viscosity of a little more than 10^{18} Pa s.

Convective translation cannot by itself explain the N–S anisotropy, but has been proposed as a possible explanation for the hemispherical dichotomy of the inner core. There is almost no deformation associated with the translation, so deformation texturing is not expected. However, Monnereau et al. (2010) have suggested that grain growth during the migration from the crystallizing hemisphere to the melting hemisphere results in hemispherical variations in grain size which may be at the origin of the hemispherical asymmetry. Multiple-scattering due to differences of orientation between iron grains can indeed produce the velocity and attenuation variations required to explain the data (Calvet and Margerin, 2008; Monnereau et al., 2010), with solidification in the Western hemisphere and melting in the Eastern hemisphere. Grains, or regions of similar grain orientation, must reach a size roughly comparable to P-wave wavelengths for scattering to have a significant effect on velocity and attenuation (Calvet and Margerin, 2008). Monnereau et al.'s (2010) model requires typical grain size of several hundred of meters in the crystallizing hemisphere and ~ 10 km in the melting hemisphere. One other possible source of texture variations has been suggested by Bergman et al. (2010) on the basis of annealing experiments already discussed in Section 5.3. In the context of convective translation of the inner core, these experiments suggest that the strong solidification texture of newly crystallized iron would be gradually lost during translation toward the melting side of the inner core (Bergman et al., 2010). In this model, the crystallizing side would be strongly textured, while the melting side would be essentially elastically isotropic (Bergman et al., 2010). Finally, one possible way to explain the presence of an innermost inner core in the context of convective translation is to assume the presence of a phase change within the inner core. This is possible, but the range of composition at which this can occur is tight (Kuwayama et al., 2008).

The possible development of a compositional stratification in the inner core add yet another complication to the problem of inner core convection. If strong enough, a stabilizing compositional stratification can shut off thermally driven convection (Buffett, 2009; Cottaar and Buffett, 2012) or localize it in the deep inner core (Deguen and Cardin, 2011). However, a stabilizing compositional stratification may not develop if the base of the outer core becomes enriched in iron as a result of melting (Section 7), or, in the translation regime, if the translation is fast enough.

6.2. Topography relaxation

Given the difficulties that faces thermal convection, Yoshida et al. (1996) have proposed a model in which heterogeneous growth of the inner core drives a large scale axisymmetric flow. Since the inner core crystallizes in response to outer core convection, its local instantaneous solidification rate must reflect the structure of outer core convection, and be spatially heterogeneous. Solid iron being denser than liquid iron, the topography resulting from non-uniform growth must relax viscously, with a timescale $\tau_\eta \sim \eta/(\Delta\rho g\lambda)$, where λ is the horizontal length scale of topography. τ_η is at most ~ 10 kyr for $\lambda \sim r_{ic}$. Provided that the growth pattern persists on a timescale larger than τ_η, heterogeneous growth will drive a flow in the inner core (Yoshida et al., 1996). Yoshida et al. (1996) argue that the inner core is expected to grow faster in the equatorial region owing to the influence of rotation on outer core convection. This would sustain a flow from the equator to the poles, as shown in Fig. 5a. Stress and strain rate

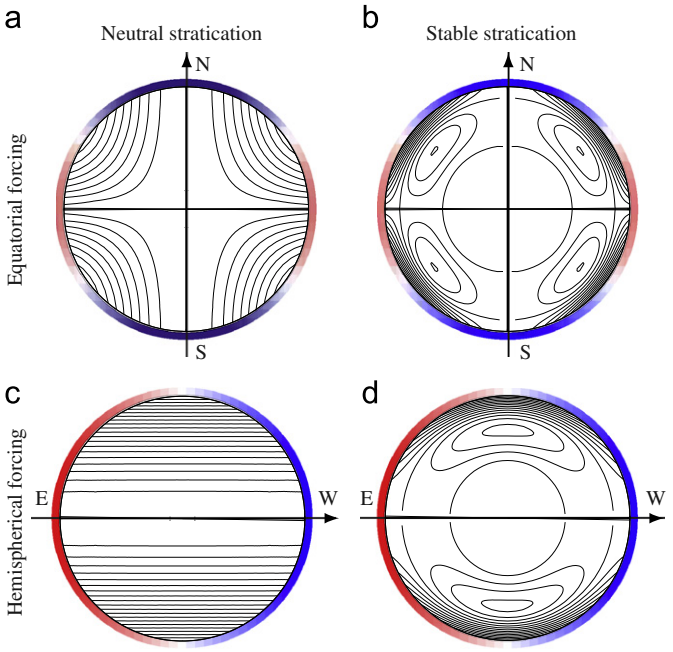

Fig. 5. Flow associated with the continuous relaxation of a topography sustained by outer core convection. Red denotes regions of rapid solidification, and blue regions of slow solidification. (a) and (c) show the flow in the case of a neutrally buoyant inner core, with axisymmetric degree 2 forcing (a) and hemispherical forcing (c). (b) and (d) show the effect of a stable density stratification ($\mathcal{B} = -10^4$) on the flow pattern, with the same forcing as in (a) and (c). Streamlines (isocontours of a streamfunction). (For interpretation of the references to color in this figure caption, the reader is referred to the web version of this article.)

associated with this flow are rather small however, and deformation texturing is expected to be negligible (Yoshida et al., 1996). Rather, Yoshida et al. (1996) proposed that the inner core anisotropy results from recrystallization under the stress field associated with the residual ICB topography. The model correctly predicts the global orientation of the seismic anisotropy, but the preferred orientation is found to develop very slowly, on a Gyr timescale if $\eta \sim 10^{21}$ Pa s (Yoshida et al., 1996). Anisotropy development would be even slower if the viscosity is smaller, because the stress level is commensurate with viscosity in this model.

The geometry and magnitude of the flow forced by heterogeneous solidification depend critically on the density stratification in the inner core (Deguen and Cardin, 2009). If the inner core is stably stratified, the flow depends on the amplitude of the growth rate anomaly and on the 'buoyancy number' $\mathcal{B}$ defined as

$$\mathcal{B} = \frac{g r_{ic}^3}{\eta u_{ic}} \left\langle \frac{\partial \rho}{\partial r} \right\rangle, \tag{7}$$

which compares the effect of buoyancy and viscous forces (Deguen and Cardin, 2009). Here $\langle \partial\rho/\partial r \rangle$ denotes the mean density gradient in the inner core after subtraction of the effect of adiabatic compression. As an example, the geometry of the flow is shown in Fig. 5b for $\mathcal{B} = -10^4$ and a solidification rate twice larger at the equator than at the poles. The stable stratification inhibits radial motion and force the flow to be quasi-horizontal, localizing it in a shear layer of thickness $\sim r_{ic}|\mathcal{B}|^{-1/5}$. An interesting consequence is that strain rates are higher than in the absence of stratification because of the localization of the flow. This implies that deformation texturing can be effective (Deguen et al., 2011b). The flow geometry calculated by Yoshida et al. (1996) remains valid only if $\mathcal{B} \gtrsim -10^2$, which requires a viscosity probably higher than 10^{22} Pa s (Deguen et al., 2011b).

A possibly important point is that $|\mathcal{B}|$ increases dramatically with time, suggesting an evolution of the flow during inner core

history (Deguen and Cardin, 2009). The effect of the stratification was negligible when the inner core was small, but becomes progressively more important as the inner core grows. This can result in a layered structure, with the deep inner core only very weakly affected by deformation, and the upper layers with a strong deformation texture (Deguen et al., 2011b). Deguen and Cardin (2009) suggested that the deepest part of the inner core may preserve a fossil solidification texture acquired when $|\mathcal{B}|$ was small and the deformation weak. This is not supported by the annealing experiments of Bergman et al. (2010), which suggest that solidification textures would be quickly lost.

Deformation induced by heterogeneous growth of the inner core can be forced by a topography of any geometry, as long as there is some degree of persistence of the growth pattern. If the CMB heat flux was spatially homogeneous, the pattern of inner core growth would be zonal on average. However, the CMB heat flux is likely to exhibit strong lateral heterogeneities, as inferred from seismology and predicted by numerical models of mantle convection (van der Hilst et al., 2007; Nakagawa and Tackley, 2008). Sumita and Olson (1999, 2002) and Aubert et al. (2008) have shown that heterogeneous CMB heat flow can produce a long-term deviation from axisymmetry in inner core growth rate. More recently, Calkins et al. (2012) have shown that the effect of the CMB topography on the outer core flow can also result in large scale lateral variations of the mean inner core growth rate. Fig. 3 shows an example of the time averaged inner core growth rate in a dynamo simulation with an heterogeneous CMB heat flow by Aubert et al. (2008). The first order result is that the solidification rate is higher in the equatorial belt than in the polar regions in accordance with Yoshida et al.'s (1996) hypothesis (although the region of highest growth rate is shifted toward higher latitudes in this particular simulation). In addition, the pattern of ICB heat flux also shows longitudinal variations, with faster crystallization in the Eastern hemisphere. Based on this prediction, Aubert et al. (2008) interpreted the seismological hemispherical dichotomy as resulting from texture variations due to the difference of solidification rate. Another possibility is to invoke deformation associated with the continuous relaxation of the resulting hemispherical topography (Regnier, 2009). A degree 1, order 1 growth rate anomaly would induce a translation (Fig. 5c) if the stratification is weak. If the inner core is stratified, deformation would be localized in thin shear layers (Fig. 5d), as in the case of equatorial forcing.

If the inner core is unstable against thermal convection, convective velocities would probably be significantly (orders of magnitude) larger than the flow driven by topography relaxation, as suggested by numerical simulations of inner core convection. Topography relaxation might promote the emergence of large scale convective modes, but convection would probably still be dominated by small scales.

6.3. Magnetic field

Karato (1999, 2000) considered the effect of the Maxwell stress on the ICB associated with the toroidal magnetic field, and showed that latitudinal variations of the Maxwell stress can drive an axisymmetric flow within the inner core (Fig. 6). Buffett and Bloxham (2000) considered the direct volumetric effect of the Lorentz force associated with the toroidal magnetic field diffused in the inner core. In both cases, the geometry of the flow reflects that of the toroidal field B_ϕ near the ICB, and its magnitude is set by a balance between magnetic and viscous forces, with typical velocity scaling as $U \sim B_\phi^2 r_{ic}/(\mu_0 \eta)$, where μ_0 is the magnetic permeability of the vacuum. Karato (1999, 2000) assumed that melting and solidification occurs almost instantaneously in response to deformation of the inner core boundary, which in the model results in very large radial velocities and phase change rate at the ICB. As discussed above (Section 6.1), the rate of phase change at the ICB is limited by the ability of outer core convection to transport heat and solute, and it is a relatively slow process. Use of more realistic boundary conditions would probably weaken the predicted flow to some extent, and this should be investigated.

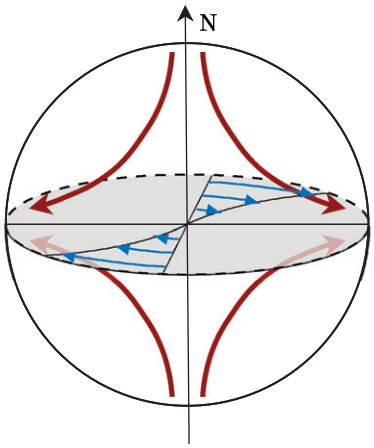

Fig. 6. The Lorentz force is expected to drive a flow in the inner core which is a combination of a poloidal flow [red arrows, (Karato, 1999)], due to the toroidal component of the magnetic field, and an azimuthal flow induced by a combination of the toroidal and poloidal components of the magnetic field [blue arrows, Buffett and Wenk (2001)]. (For interpretation of the references to color in this figure caption, the reader is referred to the web version of this article.)

Karato (1999, 2000) used a rather large value for B_ϕ at the ICB (10^{-2}–10^{-1} T) which is based on the idea of a strong toroidal field in the core. However, systematic exploration of numerical dynamo models support the idea of equipartition of magnetic energy between poloidal and toroidal fields (Christensen and Aubert, 2006), and scaling theories predict typical intensities of a few mT for both poloidal and toroidal field within the core (Christensen and Aubert, 2006; Aubert et al., 2009). Indirect estimates of the intensity of the magnetic field within the core yield values of a few mT (Gillet et al., 2010; Buffett, 2010), in agreement with scaling theories. These estimates are not sensitive to the toroidal field, so the presence of a strong toroidal field near the ICB, if not supported by numerical simulations, is not precluded by the observations. In particular, differential rotation of the inner core can induce a strong toroidal field at the ICB, in proportion to the rate of the differential rotation. With a rotation rate $\sim 0.2^\circ$/yr as currently favoured, analytical models and numerical simulations (Aurnou et al., 1996, 1998) predict ICB toroidal field peak values of order 10^{-2} T at most. As a consequence typical stresses and velocities might be two order of magnitude smaller than estimated by Karato (1999, 2000) for his choice of viscosity value. The flow can still be quite vigorous if the viscosity is small enough.

If the inner core has a stable density stratification, Buffett and Bloxham (2000) have shown that the flow induced by the toroidal field becomes vanishingly small, because the Lorentz force can to a large extent be balanced by buoyancy forces induced by tilting of isodensity surfaces. The realization that a stable stratification would impede radial flow has been a motivation for the search of predominantly horizontal flows, which are not affected by a stable stratification. Buffett and Wenk (2001) suggested that the azimuthal component of the Lorentz force, which results from a combination of the poloidal and toroidal magnetic field, can produce such a flow (Fig. 6), with a typical azimuthal velocity $u_\phi \simeq 0.1 B_z B_\phi r^3/(\mu_0 \eta r_{ic}^2)$, where B_z is the component of the magnetic field aligned with the rotation axis. Being horizontal, this

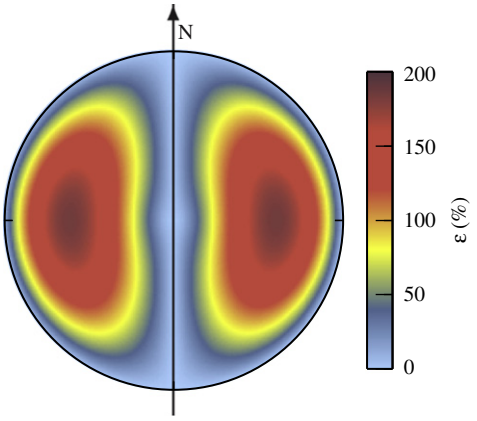

Fig. 7. Cumulated deformation in the inner core due to the azimuthal Lorentz force in the inner core, calculated from the model of Buffett and Wenk (2001) with the assumption of a constant magnetic field intensity at the ICB and an inner core radius increasing as the square root of time. Assuming the same magnetic field geometry as in Buffett and Wenk (2001), the strain rate $\dot{\epsilon}_{r\phi}$ can be integrated in time to give the strain as $\epsilon(r,\theta)=\frac{1}{10}(B_z B_\phi \tau_{ic}/\mu_0\eta)\sin\theta(r/r_{ic})^2\ln(r/r_{ic})$. The strain has a maximum $(1/20e)(B_z B_\phi/\mu_0\eta)\tau_{ic}$ in the equatorial plane at $r=r_{ic}/\sqrt{e}\simeq 740$ km. We assume here $\eta=10^{16}$ Pa s, $B_z=2$ mT and $B_\phi=20$ mT as in Buffett and Wenk (2001), and an age of the inner core of $\tau_{ic}=1$ Gyr.

flow is unaffected by the presence of a stable stratification. This mechanism has sometimes been criticized on the basis that deformation is more vigorous in the uppermost inner core, which may lead to a stronger anisotropy in the upper part of the inner core. However, the smaller strain rate in depth can be compensated by a longer deformation history. As an illustration, Fig. 7 shows the cumulated strain predicted by Buffett and Wenk's (2001) model over the inner core history, calculated with the assumption that B_ϕ and B_z at the ICB are constant in time. This may not be a very good assumption, so this should be understood as illustrative rather than quantitative. Still, it does make the point that the most deformed material in this model is at an intermediate depth rather than at the surface of the inner core.

If the inner core is unstable against thermal convection, the Hartmann number, defined as

$$Ha=\frac{B^2 r_{ic}}{\mu_0\eta U}, \tag{8}$$

can be used to asses the importance of the Lorentz force for the convection style.[2] A large value of Ha means that magnetic drag dominates over viscous drag, at least at the largest scales, which suggest that the Lorentz force may impose its symmetry to the large scale modes of the convection. Conversely, the effect of the Lorentz force is expected to be negligible if $Ha\ll 1$. With $U\sim(\kappa/r_{ic})Ra^{1/2}$ as predicted for thermal convection, and assuming $B\simeq 3$ mT and $S\simeq 10$ K/Gyr, the Lorentz forces are expected to alter significantly the convection pattern if the viscosity is smaller than $\sim 10^{16}$ Pa s. "Magneto-convection" is an interesting candidate to explain inner core anisotropy, since it is expected to have both the correct symmetry and high strain rates. This has yet to be explored in details.

More recently, Takehiro (2010) has proposed that heterogeneous Joule heating associated with the magnetic field diffused within the inner core can force a relatively vigorous flow, with typical velocity $\sim 10^{-11}$ m s^{-1} for a toroidal magnetic field of 10^{-2} T. The forcing has the correct geometry to explain a North–South axisymmetric anisotropy. An appealing feature of this model is that, being driven by horizontal variations in heating rate, it is not impeded by a stable stratification. However, as in Karato (1999, 2000), a limitation of this study is that phase change at the ICB was assumed to be instantaneous. Again, use of more realistic boundary conditions is expected to weaken the flow. If the inner core is convecting, such differential heating may promote axisymmetric convective modes.

6.4. Discussion

All models discussed above are physically sound, and may be active if the inner core is in the correct parameters regime. One key step for understanding inner core dynamics is therefore to estimate the magnitude of the non-dimensional parameters introduced above, which is in some cases extremely challenging. Various combinations of these mechanisms are possible in theory, but the above discussion suggests two main families of dynamical models for the inner core:

(i) If the inner core has an unstable density profile, thermal convection (or possibly thermo-chemical convection) is likely to be the main source of motion within the inner core, with possible coupling with the magnetic field or ICB topography relaxation. Thermal convection alone, whether in the plume regime or in the convective translation regime, is unlikely to produce a N–S oriented anisotropy, unless it remains slightly supercritical (Buffett, 2009). Coupling with either the magnetic field of differential inner core growth may be at the origin of the N–S anisotropy.

(ii) If the inner core is stably stratified, a very different dynamic is expected. The stable stratification in most cases inhibits radial motions, and tend to confine deformation in the uppermost inner core. Mechanisms possibly active include deformation induced by the zonal component of the Lorentz force (Buffett and Wenk, 2001), topography relaxation (Yoshida et al., 1996; Deguen and Cardin, 2009), or deformation induced by Joule heating within the inner core (Takehiro, 2010).

An important point is that all of the non-dimensional parameters introduced above are time-dependent, which implies that the dynamics of the inner core can evolve with time, with possibly a transition from one dominant mechanism to another at some time in the inner core history. In particular, it is possible that the inner core has been superadiabatic early in its history, and has become thermally stable later (Fig. 4). In this case, the inner core dynamical regime would have switched from a convective dynamic to a stably stratified dynamic, a possible explanation for the layered structure of the inner core.

7. The anomalous layer at the base of the outer core—an evidence for inner core melting?

The seismological observation of a stably stratified ~ 150 km thick layer at the base of the outer core is obviously difficult to reconcile with the classical picture of outer core convection, where buoyant liquid is released at the ICB by inner core crystallization. This is an extremely puzzling observation, but seismological evidences have been accumulating and seem robust. Gubbins et al. (2008) have convincingly shown that, if real, the stratification must be of compositional origin. Thermal stratification or the presence of a suspension of solid particles are unlikely to result in P-waves velocity variations of the correct magnitude

[2] Note that the definition of the Hartmann number used here is different from the one usually used in magnetohydrodynamics, $Ha=\sqrt{\sigma/\mu}BL$, where σ is the electrical conductivity and L a length scale of the flow, which assumes that the electric current $\mathbf{j}$ is dominated by the contribution of the motion-induced current $\sigma\mathbf{u}\times\mathbf{B}$. In the inner core, the motion-induced electric current is negligible compared to the electric current diffused from the outer core to the inner core. Using Ampère's law $\mathbf{j}=\mu_0^{-1}\nabla\times\mathbf{B}$ gives the expression of Ha used in Eq. (8).

(Gubbins et al., 2008). The thickness of this layer is much larger than diffusion length scales, even on a gigayear timescale: The process at its origin therefore must rely on advective transport.

Ideas about how to form an anomalous layer at the base of the outer core date back to a dynamical model by Braginsky (1963) of the F-layer present in early seismological models. Braginsky (1963) considered the core to be Sulphur rich, with a Sulphur concentration above that of the eutectic, an assumption now thought to be incorrect. Cooling of the core would then result in the crystallization of a Sulphur rich solid lighter than the surrounding liquid. These light crystals would rise and remelt, thus releasing some Sulphur upper in the layer. This implies a net outward transport of S which results in the formation of a compositionally stratified layer.

Although Braginsky's theory has been abandoned when the evidences for Jeffrey's F-layer disappeared, the model is in qualitative agreement with the properties of the stratified layer inferred from modern seismology (Souriau and Poupinet, 1991). Gubbins et al. (2008) proposed a model which is dynamically similar to that of Braginsky (1963), except that the core was assumed to be on the iron-rich side of the eutectic, in accordance with current models. The underlying idea is that an iron-rich liquid can be produced through a two-step purification process, involving crystallization followed by melting. Because light elements are incompatible, solidification results in an iron-rich solid, which gives an iron-rich liquid when melted. Gubbins et al. (2008) envisaged a model in which iron freezes ahead of the ICB, at the top of the stratified layer, and melts back while sedimenting. This process results in a net inward transport of iron, with preferential release of light elements at the top of the layer and melting of iron rich solid within the layer. Gubbins et al. (2008) demonstrated that the structure of the resulting stratified layer can be compatible with seismological observations. Although thermodynamically consistent, the model suffers from a number of dynamical issues. It is plausible that crystallization takes place in a slurry layer ahead of the ICB (Section 5.1), but it remains to be shown how such a layer can evolve toward a state where crystals melt back while falling toward the ICB.

Two more recent models (Alboussière et al., 2010; Gubbins et al., 2011) are again based on Gubbins et al.'s (2008) idea that melting is required to produce an iron rich melt, although here melting is assumed to occur directly at the ICB rather than within the stratified layer. Alboussière et al. (2010) suggested that the layer has been generated by simultaneous melting and crystallization at the ICB. Melting inner core material produces a dense iron-rich liquid which spreads at the surface of the inner core, while crystallization produces a buoyant liquid which may carry along part of the dense melt as it rises. The stratified layer results from a dynamic equilibrium between production of iron rich melt and entrainment and mixing associated with the release of buoyant liquid. Laboratory experiments in an idealized configuration show that the concept is viable (Alboussière et al., 2010), but suggest that a large rate of melt production is required to sustain a stable layer. Possibly important ingredients are absent from these exploratory experiments (rotation, thermal convection above the stable layer, …) and their effects on the formation and dynamics of the layer need to be properly investigated.

Melting part of the inner core at a significant rate while the core is cooling and the inner core crystallizing on average is obviously difficult. Alboussière et al. (2010) proposed that melting occurs in response to inner core internal dynamics through the formation of a dynamical topography at the ICB (see also discussion in Section 6.1). The melting rate is then limited by the ability of outer core convection to provide the latent heat absorbed by melting, and only a significant topography can lead to a non-negligible melting rate. A number of the mechanisms described in Section 6 could in theory produce a dynamic topography susceptible to induce melting, but most of them are too weak to induce significant melting. For example, although Karato (1999) has predicted very large melting rates associated with Maxwell stress induced deformation, this was due to the assumption of instantaneous melting and solidification when the ICB is deformed. Thermal convection appears to be the mechanism the most susceptible of producing a large dynamical topography and significant melting. In the convective translation regime, the melting rate can be very large as shown in Fig. 8a, up to several tens of times larger than the mean growth rate of the inner core (Alboussière et al., 2010). In the low viscosity convection regime, the melt production can still be significant if the viscosity is not too small, and has a positive feedback on the vigour of convection, with freezing localized above plumes roots and melting above upwellings (Fig. 8b). The main limitations of this mechanism are: (i) thermal convection requires fast inner core growth and a low thermal conductivity, (ii) the viscosity must be large enough ($\eta \gtrsim 10^{17}$ Pa s) to yield a melt production high enough to sustain a stable layer according to Alboussière et al.'s (2010) experiments, (iii) the kinetics of phase change (the timescale τ_ϕ defined in Section 6.1) is uncertain, and might slow down once the stable layer is formed.

Gubbins et al. (2011) proposed that melting occurs in response to outer core convection. They presented dynamo simulations

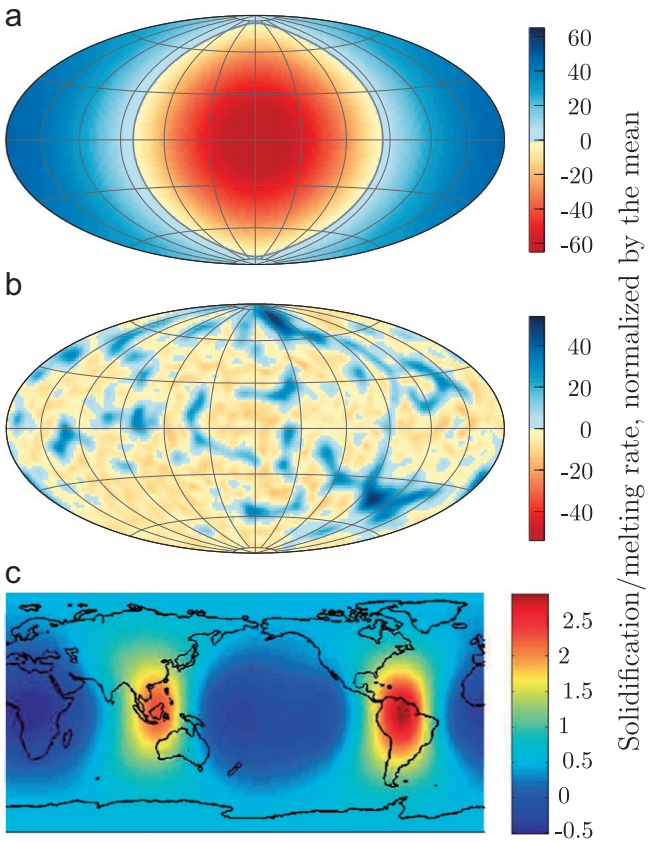

Fig. 8. Melting and solidification at the ICB. (a) Rate of phase change at the ICB associated with convective translation ($S=30$ K/Gyr, $\eta=10^{20}$ Pa s), normalized by the mean growth rate of the inner core. Red is melting, blue is solidification. The boundary between melting and solidifying regions is contoured in dark gray. (b) Same as (a), but when convection is in the turbulent plume convection regime ($S=30$ K/Gyr, $\eta=3\times10^{17}$ Pa s). (c) Instantaneous solidification (>0) and melting (<0) rate, normalized by the mean inner core growth rate, due to outer core convection in a simulation by Gubbins et al. (2011). (c) was modified from Gubbins et al. (2011). (For interpretation of the references to color in this figure caption, the reader is referred to the web version of this article.)

with a strongly heterogeneous CMB heat flux, in which the ICB heat flow was observed to be locally inward, thus inducing melting (Fig. 8c). Melting of the inner core by outer core convection requires the temperature of the liquid close to the ICB to be locally above the ICB temperature, which is possible if the liquid cooling rate is locally smaller than at the ICB. Inward ICB heat flux is not observed in many other dynamo simulations with heterogeneous CMB heat flux (e.g. Aubert et al., 2008; Olson et al., 2010), which raises the question of the robustness of this mechanism. In particular, the possibility of inner core melting by outer core convection must depend on the vigour of the convection and the efficiency of turbulent mixing. Gubbins et al.'s (2011) simulations are only slightly supercritical, and it is not clear yet that this behaviour would persist for conditions more similar to Earth's core. Another difficulty of this model is that it may not be self-sustaining. Assuming a stable layer indeed develops, it would probably be at least partially decoupled from outer core convection and melting at the ICB may become more problematic.

Cormier et al. (2011) explored the possibility that melting and freezing regions can be identified from elastic and anelastic properties of the top of the inner core. Large scale variations of velocity, attenuation, coda can be interpreted as regions of melting or solidification, but the interpretation remains ambiguous, in part because of our incomplete understanding of the expected effect of solidification or melting on the texture and seismological properties.

8. Inner core differential rotation, and the hemispherical dichotomy

Inner core differential rotation has been predicted by Gubbins (1981) from considerations of the torque balance on the inner core. The basic idea behind inner core rotation is that persistent zonal flow in the outer core can entrain the inner core through magnetic and (to a lesser extent) viscous coupling (Gubbins, 1981; Glatzmaier and Roberts, 1996; Aurnou et al., 1996; Aubert and Dumberry, 2011). The moment of inertia of the inner core is so small that, to avoid unbounded acceleration, its differential rotation must adjust so that the net torque applied on the inner core remains essentially zero (Gubbins, 1981). This implies that the inner core must on average corotate with the overlying fluid.

An additional torque comes from the gravitational interaction between the mantle and the inner core. Large scale density heterogeneities in the mantle induce perturbations of the isopotential surface coinciding with the ICB. The torque arising from the gravitational interaction between the mantle heterogeneities and the ICB topography would balance the magnetic torque if the inner core rotates by more than half a degree (Buffett, 1997), which implies that the inner core must be effectively locked to the mantle, unless the ICB topography adjust sufficiently rapidly, most plausibly through viscous relaxation, to avoid an excessively high gravitational torque.

The occurrence of inner core differential rotation in numerical simulations by Glatzmaier and Roberts (1995a,b, 1996) has prompted a search for inner core differential rotation from the seismological community. By the mid-nineties, the seismological models of the inner core had acquired complexities (tilted cylindrical anisotropy, lateral heterogeneities) that could in principle be used to track a possible differential rotation. The rate of super-rotation predicted ($\sim 1^\circ$/yr) was large enough to be potentially observable on a decadal timescale. Various approaches have been used to infer the rate of inner core differential rotation, with varied degree of success and sometimes conflicting results. Early seismological studies inferred an eastward differential rotation at a rate $\sim 1^\circ$/yr, in accordance with the results of the Glatzmaier–Roberts dynamo (Song and Richards, 1996; Su et al., 1996). Later studies yielded smaller rotation rates (Creager, 1997; Vidale et al., 2000; Poupinet et al., 2000; Laske and Masters, 2003; Zhang et al., 2005), with the preferred value being now between 0 and $\sim 0.3^\circ$/yr (see discussion in Souriau, 2007). Note that a number of these studies are compatible with no net differential rotation (Makinen and Deuss, 2011).

Inner core differential rotation may be difficult to reconcile with the presence of an hemispherical dichotomy in seismic properties (Sumita and Bergman, 2007; Aubert et al., 2008; Waszek et al., 2011). If longitudinal variations in seismic properties are related in some way to inner core/mantle coupling, then rotation of the inner core at the seismologically inferred rate would be expected to average out lateral texture variations and result in almost perfect axisymmetry. If the hemispherical asymmetry results from solidification texturing as proposed by Aubert et al. (2008), then the net differential rotation during the time needed to grow the layer, about 100–300 Myr, must have been only a fraction of a full revolution (Aubert et al., 2008). The texturation timescale might be smaller if the asymmetry is due to deformation texturing rather than solidification texturing, but this might still be too large.

Possible solutions of this apparent paradox include:

(i) The observed super-rotation is part of an oscillation rather than a steady differential rotation. This is supported in particular by a recent study of inner core differential rotation in numerical dynamo calculations, which predicts a very small mean rate of differential rotation, of the order of 1°/Myr, but fluctuations of amplitude similar to the seismologically inferred super rotation (Aubert and Dumberry, 2011). This is also supported by some seismological studies which suggest that the mean super rotation is much smaller (Waszek et al., 2011; Makinen and Deuss, 2011) than previously thought. An additional complication, pointed out by Dumberry (2010), is that longitudinal variations of inner core solidification rate (Aubert et al., 2008) can result in differential rotation of the inner core. In this model, differential rotation results from the likely misalignment of the ICB topography associated with heterogeneous crystallization and the mantle-induced longitudinal variations of ICB geoid, which induce a torque applied by mantle mass heterogeneities on the inner core. Using a solidification pattern from Aubert et al. (2008) and models of the CMB geoid, Dumberry (2010) predicts a retrograde (westward) differential rotation, and estimates that this gravitationally driven inner core differential rotation can result in a full rotation of the inner core in a few Myr. This is too slow to explain the seismologically inferred rotation rate, but still fast enough to make the existence of the hemispherical dichotomy problematic.

(ii) The mechanism at the origin of the hemispherical dichotomy is internally driven, rather than being forced by heat flux variations at the CMB. This is the case of the convective translation proposed by Monnereau et al. (2010) and Alboussière et al. (2010), although complications might arise from gravitational interactions between mantle mass heterogeneities and the ICB topography associated with the translation.

9. Summary

Seismology has provided an increasingly refined—but enigmatic—picture of the inner core, and this trend is likely to

continue, as new datasets become available (e.g. Leykam et al., 2010) and new methods are developed (e.g. Irving et al., 2009). In parallel, there is a need to confront more quantitatively dynamical models to seismological observations. This requires the knowledge of the stable mineralogical phase at inner core conditions, as well as its elastic and rheological properties. Calculating the deformation-induced texture has been done for a number of models (Jeanloz and Wenk, 1988; Yoshida et al., 1996; Buffett and Wenk, 2001; Wenk et al., 2000; Deguen et al., 2011b), but the result is extremely dependent on the choice of mineralogy, elastic properties, and dominant slip systems. Because we are far from a consensus on these questions, it has not been attempted here to discuss the ability of each of the deformation mechanisms to explain quantitatively the elastic anisotropy of the inner core. For solidification texturing models, one difficulty is that the sensitivity of seismological properties to the texture and melt content is difficult to estimate. Analogue solidification experiments using ultrasounds might help (Bergman, 1997; Bergman et al., 2000; Brito et al., 2002).

Although numerous models have been proposed for the inner core dynamics, most of them can exist only under certain conditions. The dynamical regime of the inner core depends on only a few key parameters, the most important being:

(i) the density stratification, which depends mainly on the inner core growth rate (hence on the CMB heat flow) and on its thermal diffusivity,
(ii) the viscosity (and more generally the rheology),
(iii) the magnitude of the magnetic field, and its toroidal component in particular, at the ICB,
(iv) the deviation from isotropic growth of the inner core.

Progress made in both computational and experimental high pressure mineral physics have been such that we can be optimistic about the determination of the stable mineralogical phase and its elastic, rheological and thermal properties. Some of the points above also require a better understanding of mantle and core dynamics on a global scale, including D″ dynamics and CMB heat flux, core–mantle coupling, and magnetic field generation. Indeed, perhaps one of the most important messages concerning the inner core is that it cannot be understood independently of core and mantle dynamics and evolution.

Acknowledgements

I am grateful to the editor, Yanick Ricard, for giving me the opportunity of writing this paper. I also thank Thierry Alboussière, Philippe Cardin, Daniel Brito, Peter Olson and Mickael Bergman for many helpful discussions, Mickael Bergman and Julien Aubert for providing Figs. 2c and 4, and Peter Olson and three anonymous reviewers for helpful comments on the manuscript. Ray paths and traveltimes in Fig. 1 have been calculated using the TauP Toolkit (Crotwell et al., 1999), available at www.seis.sc.edu/TauP/. R. Deguen was supported by NSF grant EAR 0909622 and by Frontiers in Earth System Dynamics grant EAR-1135382 from the National Science Foundation.

References

Alboussière, T., Deguen, R., Melzani, M., 2010. Melting induced stratification above the Earth's inner core due to convective translation. Nature 466, 744–747.
Alexandrov, D., Malygin, A., 2011. Coupled convective and morphological instability of the inner core boundary of the Earth. Phys. Earth Planet. Inter. 189, 134–141.
Alfè, D., Gillan, M.J., Price, G.D., 2002. Ab initio chemical potentials of solid and liquid solutions and the chemistry of the Earth's core. J. Chem. Phys. 116, 7127–7136.
Andrews, J., Deuss, A., Woodhouse, J., 2006. Coupled normal-mode sensitivity to inner-core shear velocity and attenuation. Geophys. J. Int. 167, 204–212.
Antonangeli, D., Merkel, S., Farber, D.L., 2006. Elastic anisotropy in hcp metals at high pressure and the sound wave anisotropy of the Earth's inner core. Geophys. Res. Lett. 33, L24303.
Aubert, J., Amit, H., Hulot, G., Olson, P., 2008. Thermochemical flows couple the Earth's inner core growth to mantle heterogeneity. Nature 454, 758–761.
Aubert, J., Dumberry, M., 2011. Steady and fluctuating inner core rotation in numerical geodynamo models. Geophys. J. Int. 184, 162–170.
Aubert, J., Labrosse, S., Poitou, C., 2009. Modelling the palaeo-evolution of the geodynamo. Geophys. J. Int. 179, 1414–1428.
Aurnou, J., Brito, D., Olson, P., 1998. Anomalous rotation of the inner core and the toroidal magnetic field. J. Geophys. Res. 103, 9721–9738.
Aurnou, J.M., Brito, D., Olson, P.L., 1996. Mechanics of inner core super-rotation. Geophys. Res. Lett. 23, 3401–3404.
Badro, J., Fiquet, G., Guyot, F., Gregoryanz, E., Occelli, F., Antonangeli, D., D'Astuto, M., 2007. Effect of light elements on the sound velocities in solid iron: Implications for the composition of Earth's core. Earth Planet. Sci. Lett. 254, 233–238.
Beghein, C., Trampert, J., 2003. Robust normal mode constraints on inner-core anisotropy from model space search. Science 299, 552–555.
Belonoshko, A., Skorodumova, N., Davis, S., Osiptsov, A., Rosengren, A., Johansson, B., 2007. Origin of the low rigidity of the Earth's inner core. Science 316, 1603–1605.
Belonoshko, A.B., Skorodumova, N.V., Rosengren, A., Johansson, B., 2008. Elastic Anisotropy of Earth's Inner Core. Science 319, 797–800.
Bergman, M., Lewis, D., Myint, I., Slivka, L., Karato, S., Abreu, A., 2010. Grain growth and loss of texture during annealing of alloys, and the translation of Earth's inner core. Geophys. Res. Lett. 37, L22313.
Bergman, M.I., 1997. Measurements of elastic anisotropy due to solidification texturing and the implications for the Earth's inner core. Nature 389, 60–63.
Bergman, M.I., Agrawal, S., Carter, M.S., 2003. Transverse solidification textures in hexagonal close-packed alloys. J. Crystal Growth 255, 204–211.
Bergman, M.I., Cole, D., Jones, J., 2002. Preferred crystal orientations due to melt convection during directional solidification. J. Geophys. Res. 107, 2201.
Bergman, M.I., Giersch, L., Hinczewski, M., Izzo, V., 2000. Elastic and attenuation anisotropy in directionally solidified (hcp) zinc, and the seismic anisotropy in the Earth's inner core. Phys. Earth Planet. Inter. 117, 139–151.
Birch, F., 1940. The alpha–gamma transformation of iron at high pressures, and the problem of the Earth's magnetism. Am. J. Sci. 238, 192–211.
Braginsky, S., 1963. Structure of the F layer and reasons for convection in the Earth's core. Dokl. Akad. Nauk. SSSR Engl. Trans. 149, 1311–1314.
Bréger, L., Romanowicz, B., Rousset, S., 2000a. New constraints on the structure of the inner core from P'P'. Geophys. Res. Lett. 27, 2781–2784.
Bréger, L., Tkalčić, H., Romanowicz, B., 2000b. The effect of D″ on PKP(AB-DF) travel time residuals and possible implications for inner core structure. Earth Planet. Sci. Lett. 175, 133–143.
Brito, D., Elbert, D., Olson, P., 2002. Experimental crystallization of gallium: ultrasonic measurements of elastic anisotropy and implications for the inner core. Phys. Earth Planet. Inter. 129, 325–346.
Buffett, B.A., 1997. Geodynamics estimates of the viscosity of the Earth's inner core. Nature 388, 571–573.
Buffett, B.A., 2000. Dynamics of the Earth's core. In: Karato, S., Forte, A., Lieberman, R., Masters, G., Stixrude, L. (Eds.), Earth's Deep Interior: Mineral Physics and Seismic Tomography From the Atomic to Global Scale. Geophysical Monograph, vol. 117. American Geophysical Union, Washington, DC, pp. 37–62.
Buffett, B.A., Bloxham, J., 2000. Deformation of Earth's inner core by electromagnetic forces. Geophys. Res. Lett. 27, 4001–4004.
Buffett, B.A., Wenk, H.R., 2001. Texturing of the Earth's inner core by Maxwell stresses. Nature 413, 60–63.
Buffett, B.A., 2009. Onset and orientation of convection in the inner core. Geophys. J. Int. 179, 711–719.
Buffett, B.A., 2010. Tidal dissipation and the strength of the Earth's internal magnetic field. Nature 468, 952–954.
Bullen, K., 1947. An Introduction to the Theory of Seismology. Cambridge (Eng.).
Calkins, M. A., Noir, J., Eldredge, J.D., Aurnou, J.M., 2012. The effects of boundary topography on convection in Earths core. Geophys. J. Int. http://dx.doi.org/10.1111/j.1365-246X.2012.05415.x.
Calvet, M., Chevrot, S., Souriau, A., 2006. P-wave propagation in transversely isotropic media: II. Application to inner core anisotropy: Effects of data averaging, parameterization and a priori information. Phys. Earth Planet. Inter. 156, 21–40.
Calvet, M., Margerin, L., 2008. Constraints on grain size and stable iron phases in the uppermost inner core from multiple scattering modeling of seismic velocity and attenuation. Earth Planet. Sci. Lett. 267, 200–212.
Chalmers, B., 1964. Principles of Solidification. J. Wiley & Sons, NY 319 pp.
Chen, X., Zeng, Z., Liu, Z., Cai, L., Jing, F., 2011. Elastic anisotropy of Fe under conditions at the Earth's inner core. Phys. Rev. B 83, 132102.
Cherepanov, N., 1971. Spatial arrangement of sea ice crystal structure. Probl. Arkt. Antarkt 38, 176–181.
Christensen, U., Aubert, J., 2006. Scaling properties of convection-driven dynamos in rotating spherical shells and application to planetary magnetic fields. Geophys. J. Int. 166, 97–114.

Cleary, J.R., Haddon, R.A.W., 1972. Seismic wave scattering near the core–mantle boundary: a new interpretation of precursors to PKP. Nature 240, 549–551.
Cormier, V.F., 1981. Short-period PKP phases and the anelastic mechanism of the inner core. Phys. Earth Planet. Inter. 24, 291–301.
Cormier, V.F., 2009. A glassy lowermost outer core. Geophys. J. Int. 179, 374–380.
Cormier, V.F., Attanayake, J., He, K., 2011. Inner core freezing and melting: constraints from seismic body waves. Phys. Earth Planet. Inter. 188, 163–172.
Cormier, V.F., Li, X., 2002. Frequency-dependent seismic attenuation in the inner core 2. A scattering and fabric interpretation. J. Geophys. Res (Solid Earth) 107 (B12), 2362.
Cormier, V.F., Stroujkova, A., 2005. Waveform search for the innermost inner core. Earth Planet. Sci. Lett. 236, 96–105.
Cormier, V.F., Xu, L., Choy, G.L., 1998. Seismic attenuation of the inner core: viscoelastic or stratigraphic? Geophys. Res. Lett. 25, 4019–4022.
Côté, A.S., Vočadlo, L., Brodholt, J.P., 2008. Light elements in the core: effects of impurities on the phase diagram of iron. Geophys. Res. Lett. 35, L05306.
Cottaar, S., Buffett, B., 2012. Convection in the Earth's inner core. Phys. Earth Planet. Inter. 198–199, 67–78.
Creager, K.C., 1992. Anisotropy of the inner core from differential travel times of the phases PKP and PKIKP. Nature 356, 309–314.
Creager, K.C., 1997. Inner core rotation rate from small-scale heterogeneity and time-varying travel times. Science 278, 1284–1288.
Creager, K.C., 1999. Large-scale variations in inner core anisotropy. J. Geophys. Res. 104, 23127–23139.
Creager, K.C., 2000. Inner core anisotropy and rotation. In: Dehant, V. (Ed.), Core Dynamics, Structure and Rotation. American Geophysical Union, pp. 89–114.
Crotwell, H.P., Owens, T.J., Ritsema, J., 1999. The TauP toolkit: flexible seismic travel-time and ray-path utilities. Seismol. Res. Lett. 70, 154–160.
De Rango, P., Lees, M., Lejay, P., Sulpice, A., Tournier, R., Ingold, M., Germi, P., Pernet, M., 1991. Texturing of magnetic materials at high temperature by solidification in a magnetic field. Nature 349, 770–773.
Deguen, R., Alboussière, T., Brito, D., 2007. On the presence and structure of a mush at the inner core boundary of the Earth. Phys. Earth Planet. Inter. 274, 1887–1891.
Deguen, R., Cardin, P., 2009. Tectonic history of the Earth's inner core preserved in its seismic structure. Nat. Geosci. 2, 419–422.
Deguen, R., Cardin, P., 2011. Thermo-chemical convection in Earth's inner core. Geophys. J. Int. 187, 1101–1118.
Deguen, R., Alboussière, T., Cardin, P., Melzani, M., 2011a. Convection melting and the structure of the inner core and lowermost outer core. EGU General Assembly.
Deguen, R., Cardin, P., Merkel, S., Lebensohn, R., 2011b. Texturing in Earth's inner core due to preferential growth in its equatorial belt. Phys. Earth Planet. Inter. 188, 173–184.
de Koker, N., Steinle-Neumann, G., Vlcek, V., 2012. Electrical resistivity and thermal conductivity of liquid Fe alloys at high *P* and *T*, and heat flux in Earth's core. Proc. Natl. Acad. Sci. USA 109, 4070–4073.
Deuss, A., Irving, J., Woodhouse, J., 2010. Regional variation of inner core anisotropy from seismic normal mode observations. Science 328, 1018–1020.
Doornbos, D.J., 1974. The anelasticity of the inner core. Geophys. J. Int. 38, 397–415.
Dubrovinsky, L., Dubrovinskaia, N., Narygina, O., Kantor, I., Kuznetzov, A., Prakapenka, V.B., Vitos, L., Johansson, B., Mikhaylushkin, A.S., Simak, S.I., Abrikosov, I.A., 2007. Body-centered cubic iron-nickel alloy in Earth's core. Science 316, 1880–1883.
Dumberry, M., 2010. Gravitationally driven inner core differential rotation. Earth Planet. Sci. Lett. 297, 387–394.
Durek, J., Ekstrom, G., 1996. A radial model of anelasticity consistent with long-period surface-wave attenuation. Bull. Seismol. Soc. Am. 86, 144–158.
Dziewonski, A.M., Anderson, D.L., 1981. Preliminary reference Earth model. Phys. Earth Planet. Inter. 25, 297–356.
Dziewonski, A.M., Gilbert, F., 1971. Solidity of the inner core of the Earth inferred from normal mode observations. Nature 234, 465–466.
Falzone, A., Stacey, F., 1980. Second order elasticity theory: explanation for the high Poisson's ratio of the inner core. Phys. Earth Planet. Inter. 21, 371–377.
Fearn, D., Loper, D., Roberts, P., 1981. Structure of the Earth's inner core. Nature 292, 232–233.
Fukao, Y., Suda, N., 1989. Core modes of the Earth's free oscillations and structure of the inner core. Geophys. Res. Lett. 16, 401–404.
Gannarelli, C.M.S., Alfè, D., Gillan, M.J., 2003. The particle-in-cell model for ab initio thermodynamics: implications for the elastic anisotropy of the Earth's inner core. Phys. Earth Planet. Inter. 139, 243–253.
Gannarelli, C.M.S., Alfè, D., Gillan, M.J., 2005. The axial ratio of hcp iron at the conditions of the Earth's inner core. Phys. Earth Planet. Inter. 152, 67–77.
Garcia, R., Souriau, A., 2000. Inner core anisotropy and heterogeneity level. Geophys. Res. Lett. 27, 3121–3124.
Gillet, N., Jault, D., Canet, E., Fournier, A., 2010. Fast torsional waves and strong magnetic field within the Earths core. Nature 465, 74–77.
Glatzmaier, G.A., Roberts, P.H., 1995a. A three-dimensional self-consistent computer simulation of a geomagnetic field reversal. Nature 377, 203–209.
Glatzmaier, G.A., Roberts, P.H., 1995b. A three-dimensional convective dynamo solution with rotating and finitely conducting inner core and mantle. Phys. Earth Planet. Inter. 91, 63–75.
Glatzmaier, G.A., Roberts, P.H., 1996. Rotation and magnetism of Earth's inner core. Science 274, 1887–1891.
Grechnev, G., Ahuja, R., Eriksson, O., 2003. Magnetic susceptibility of hcp iron and the seismic anisotropy of Earth's inner core. Phys. Rev. B 68, 064414.
Gubbins, D., 1977. Energetics of the Earth's core. J. Geophys., Z. Geophys. 43, 453–464.
Gubbins, D., 1981. Rotation of the inner core. J. Geophys. Res. 86, 11695–11699.
Gubbins, D., Masters, G., Nimmo, F., 2008. A thermochemical boundary layer at the base of Earth's outer core and independent estimate of core heat flux. Geophys. J. Int. 174, 1007–1018.
Gubbins, D., Sreenivasan, B., Mound, J., Rost, S., 2011. Melting of the Earth's inner core. Nature 473, 361–363.
Irving, J., Deuss, A., 2011. Hemispherical structure in inner core velocity anisotropy. J. Geophys. Res. 116, B04307.
Irving, J., Deuss, A., Woodhouse, J., 2009. Normal mode coupling due to hemispherical anisotropic structure in Earth's inner core. Geophys. J. Int. 178, 962–975.
Ishii, M., Dziewoński, A.M., 2002. The innermost inner core of the Earth: evidence for a change in anisotropic behavior at the radius of about 300 km. Proc. Natl. Acad. Sci. USA 99, 14026–14030.
Ishii, M., Dziewoński, A.M., 2003. Distinct seismic anisotropy at the centre of the Earth. Phys. Earth Planet. Inter. 140, 203–217.
Jacobs, J., 1953. The Earth's inner core. Nature 172, 297–298.
Jeanloz, R., Wenk, H.R., 1988. Convection and anisotropy of the inner core. Geophys. Res. Lett. 15, 72–75.
Jeffreys, H., 1939. The times of the core waves (second paper). Mon. Not. R. Astron. Soc., Geophys. Suppl 4, 594–615.
Jephcoat, A., Olson, P., 1987. Is the inner core of the Earth pure iron? Nature 325, 332–335.
Karato, S.I., 1993. Inner core anisotropy due to the magnetic field-induced preferred orientation of iron. Science 262, 1708–1711.
Karato, S.I., 1999. Seismic anisotropy of the Earth's inner core resulting from flow induced by Maxwell stresses. Nature 402, 871–873.
Karato, S.I., 2000. Dynamics and anisotropy of the Earth's inner core. Importance of the magnetic coupling with the outer core. Proc. Jpn. Acad. Ser. B 76, 1–6.
Kennett, B.L.N., Engdahl, E.R., Buland, R., 1995. Constraints on seismic velocities in the Earth from traveltimes. Geophys. J. Int. 122, 108–124.
King, D., Haddon, R., Cleary, J., 1973. Evidence for seismic wave scattering in the D″ layer. Earth Planet. Sci. Lett. 20, 353–356.
Konopkova, Z., Lazor, P., Goncharov, A., Struzhkin, V., 2011. Thermal conductivity of hcp iron at high pressure and temperature. High Pressure Res. 31, 228–236.
Koot, L., Dumberry, M., 2011. Viscosity of the Earth's inner core: Constraints from nutation observations. Earth Planet. Sci. Lett. 308, 343–349.
Kurz, W., Fisher, D., 1989. Fundamentals of Solidification. Trans Tech Publications, Switzerland (305pp).
Kuwayama, Y., Hirose, K., Sata, N., Ohishi, Y., 2008. Phase relations of iron and iron–nickel alloys up to 300 GPa: implications for composition and structure of the Earth's inner core. Earth Planet. Sci. Lett. 273, 379–385.
Laio, A., Bernard, S., Chiarotti, G.L., Scandalo, S., Tosatti, E., 2000. Physics of iron at Earth's core conditions. Science 287, 1027–1030.
Langhorne, P., 1983. Laboratory experiments on crystal orientation in NaCl ice. Ann. Glaciol. 4, 163–169.
Langhorne, P., Robinson, W., 1986. Alignment of crystals in sea ice due to fluid motion. Cold Regions Sci. Technol. 12, 197–214.
Laske, G., Masters, G., 2003. The Earths free oscillations and the differential rotation of the inner core. In: Dehant, V., et al. (Eds.), Earths Core: Dynamics Structure, Rotation, Geodynamic Series, vol. 31. American Geophysical Union, Washington, DC, pp. 5–21.
Lay, T., Hernlund, J., Buffett, B.A., 2008. Core–mantle boundary heat flow. Nat. Geosci. 1, 25–32.
Lehmann, I., 1936. P'. Bureau Central Sismologique International, vol. 14, pp. 87–115.
Leykam, D., Tkalčić, H., Reading, A.M., 2010. Core structure re-examined using new teleseismic data recorded in Antarctica: evidence for, at most, weak cylindrical seismic anisotropy in the inner core. Geophys. J. Int. 180, 1329–1343.
Li, X., Cormier, V.F., 2002. Frequency-dependent seismic attenuation in the inner core, 1. A viscoelastic interpretation. J. Geophys. Res. (Solid Earth) 107, 2361.
Loper, D., Roberts, P., 1981. A study of conditions at the inner core boundary of the Earth. Phys. Earth Planet. Inter. 24, 302–307.
Loper, D.E., 1978. The gravitationally powered dynamo. Geophys. J. Int. 54, 389–404.
Loper, D.E., 1983. Structure of the inner core boundary. Geophys. Astrophys. Fluid Dyn. 25, 139–155.
Loper, D.E., Fearn, D.E., 1983. A seismic model of a partially molten inner core. J. Geophys. Res. 88, 1235–1242.
Makinen, A.M., Deuss, A., 2011. Global seismic body-wave observations of temporal variations in the Earth's inner core, and implications for its differential rotation. Geophys. J. Int. 187, 355–370.
Mao, H.K., Shu, J., Shen, G., Hemley, R.J., Li, B., Singh, A.K., 1998. Elasticity and rheology of iron above 220 GPa and the nature of the Earth's inner core. Nature 396, 741–743.
Masters, G., Gilbert, F., 1981. Structure of the inner core inferred from observations of its spheroidal shear modes. Geophys. Res. Lett. 8, 569–571.
Merkel, S., Shu, J., Gillet, P., Mao, H.K., Hemley, R.J., 2005. X-ray diffraction study of the single-crystal elastic moduli of ϵ-Fe up to 30 GPa. J. Geophys. Res. (Solid Earth) 110, 5201.

Mizzon, H., Monnereau, M., 2011. Implications of the Lopsided Growth for the Viscosity of the Earth's Inner Core. AGU Fall Meeting Abstracts.
Monnereau, M., Calvet, M., Margerin, L., Souriau, A., 2010. Lopsided growth of Earth's inner core. Science 328, 1014–1017.
Morelli, A., Dziewonski, A.M., Woodhouse, J.H., 1986. Anisotropy of the inner core inferred from PKIKP travel times. Geophys. Res. Lett. 13, 1545–1548.
Morse, S.A., 1986. Adcumulus growth of the inner core. Geophys. Res. Lett. 13, 1466–1469.
Morse, S.A., 2002. No mushy zones in the Earth's core. Geochim. Cosmochim. Acta 66, 2155–2165.
Mound, J.E., Buffett, B.A., 2006. Detection of a gravitational oscillation in length-of-day. Earth Planet. Sci. Lett. 243, 383–389.
Nakagawa, T., Tackley, P.J., 2008. Lateral variations in CMB heat flux and deep mantle seismic velocity caused by a thermal chemical-phase boundary layer in 3D spherical convection. Earth Planet. Sci. Lett. 271, 348–358.
Niu, F., Wen, L., 2001. Hemispherical variations in seismic velocity at the top of the Earth's inner core. Nature 410, 1081–1084.
Niu, F.L., Chen, Q.F., 2008. Seismic evidence for distinct anisotropy in the innermost inner core. Nat. Geosci. 1, 692–696.
Olson, P.L., Coe, R.S., Driscoll, P.E., Glatzmaier, G.A., Roberts, P.H., 2010. Geodynamo reversal frequency and heterogeneous core–mantle boundary heat flow. Phys. Earth Planet. Inter. 180, 66–79.
Oreshin, S., Vinnik, L., 2004. Heterogeneity and anisotropy of seismic attenuation in the inner core. Geophys. Res. Lett. 31, L02613.
Poupinet, G., Pillet, R., Souriau, A., 1983. Possible heterogeneity of the Earth's core deduced from PKIKP travel times. Nature 305, 204–206.
Poupinet, G., Souriau, A., Coutant, O., 2000. The existence of an inner core superrotation questioned by teleseismic doublets. Phys. Earth Planet. Inter. 118, 77–88.
Reaman, D.M., Daehn, G.S., Panero, W.R., 2011. Predictive mechanism for anisotropy development in the Earth's inner core. Earth Planet. Sci. Lett. 312, 437–442.
Regnier, C., 2009. Croissance et anisotropie de la Graine. Master's thesis. Université Joseph Fourier.
Resovsky, J., 2005. Error bars for the global seismic Q profile. Earth Planet. Sci. Lett. 230, 413–423.
Romanowicz, B., Bréger, L., 2000. Anomalous splitting of free oscillations: a reevaluation of possible interpretations. J. Geophys. Res. 105, 21559–21578.
Schloessin, H.H., 1974. Corrugations on the core boundary interfaces due to constitutional supercooling and effects on motion in a predominantly stratified liquid core. Phys. Earth Planet. Inter. 9, 147–156.
Sha, X., Cohen, R., 2010. Elastic isotropy of-fe under Earth's core conditions. Geophys. Res. Lett. 37, L10302.
Sha, X., Cohen, R., 2011. First-principles studies of electrical resistivity of iron under pressure. J. Phys. Condens. Matter 23, 075401.
Shearer, P.M., 1994. Constraints on inner core anisotropy from PKP(DF) travel times. J. Geophys. Res. 99, 19647.
Shearer, P.M., Rychert, C.A., Liu, Q., 2011. On the visibility of the inner-core shear wave phase PKJKP at long periods. Geophys. J. Int. 185, 1379–1383.
Shearer, P.M., Toy, K.M., Orcutt, J.A., 1988. Axi-symmetric Earth models and inner-core anisotropy. Nature 333, 228–232.
Shimizu, H., Poirier, J.P., Le Mouël, J.L., 2005. On crystallization at the inner core boundary. Phys. Earth Planet. Inter. 151, 37–51.
Singh, S.C., Taylor, M.A.J., Montagner, J.P., 2000. On the presence of liquid in Earth's inner core. Science 287, 2471–2474.
Song, X., Helmberger, D.V., 1992. Velocity structure near the inner core boundary from waveform modeling. J. Geophys. Res. 97, 6573–6586.
Song, X., Helmberger, D.V., 1993. Anisotropy of Earth's inner core. Geophys. Res. Lett. 20, 2591–2594.
Song, X., Helmberger, D.V., 1995a. A P wave velocity model of Earth's core. J. Geophys. Res. 100, 9817–9830.
Song, X., Helmberger, D.V., 1995b. Depth dependence of anisotropy of Earth's inner core. J. Geophys. Res. 100, 9805–9816.
Song, X., Richards, P.G., 1996. Seismological evidence for differential rotation of the Earth's inner core. Nature 382, 221–224.
Souriau, A., 2007. The Earth's cores. In: Schubert, G. (Ed.), Treatise on Geophysics, vol. 1.
Souriau, A., Poupinet, G., 1991. The velocity profile at the base of the liquid core from PKP(BC+Cdiff) data: an argument in favor of radial inhomogeneity. Geophys. Res. Lett. 18, 2023–2026.
Souriau, A., Romanowicz, B., 1996. Anisotropy in inner core attenuation: a new type of data to constrain the nature of the solid core. Geophys. Res. Lett. 23, 1–4.
Souriau, A., Romanowicz, B., 1997. Anisotropy in the inner core: relation between P-velocity and attenuation. Phys. Earth Planet. Inter. 101, 33–47.
Stacey, F.D., 1992. Physics of the Earth, 3rd ed. Brooksfield Press, Queensland.
Stacey, F.D., Davis, P.M., 2008. Physics of the Earth. Cambridge University Press.
Steinle-Neumann, G., Stixrude, L., Cohen, R.E., Gülseren, O., 2001. Elasticity of iron at the temperature of the Earth's inner core. Nature 413, 57–60.
Stevenson, D., 1987. Limits on lateral density and velocity variations in the Earth's outer core. Geophys. J. R. Astron. Soc. 88, 311–319.
Stixrude, L., Cohen, R.E., 1995. High-pressure elasticity of iron and anisotropy of Earth's inner core. Science 267, 1972–1975.
Su, W.J., Dziewonski, A.M., Jeanloz, R., 1996. Planet within a planet: rotation of the inner core of Earth. Science 274, 1883–1887.
Sumita, I., Bergman, M.I., 2007. Inner-core dynamics. In: Schubert, G. (Ed.), Treatise on Geophysics, vol. 8. Elsevier, pp. 299–318.
Sumita, I., Olson, P., 1999. A laboratory model for convection in Earth's core driven by a thermally heterogeneous mantle. Science 286, 1547–1549.
Sumita, I., Olson, P., 2002. Rotating thermal convection experiments in a hemispherical shell with heterogeneous boundary heat flux: implications for the Earth's core. J. Geophys. Res. (Solid Earth) 107, 2169.
Sumita, I., Yoshida, S., Hamano, Y., Kumazawa, M., 1995. A model for the structural evolution of the Earth's core and its relation to the observations. In: Yukutake, T. (Ed.), The Earth's Central Part: its Structure and Dynamics, pp. 232–260.
Sumita, I., Yoshida, S., Kumazawa, M., Hamano, Y., 1996. A model for sedimentary compaction of a viscous media and its application to inner-core growth. Geophys. J. Int. 124, 302–324.
Sun, X., Song, X., 2008a. The inner core of the Earth: texturing of iron crystals from three-dimensional seismic anisotropy. Earth Planet. Sci. Lett. 269, 56–65.
Sun, X., Song, X., 2008b. Tomographic inversion for three-dimensional anisotropy of Earth's inner core. Phys. Earth Planet. Inter. 167, 53–70.
Takehiro, S., 2010. Fluid motions induced by horizontally heterogeneous Joule heating in the Earth's inner core. Phys. Earth Planet. Inter. 184, 134–142.
Tanaka, S., Hamaguchi, H., 1997. Degree one heterogeneity and hemispherical variation of anisotropy in the inner core from PKP(BC)-PKP(DF) times. J. Geophys. Res. 102, 2925–2938.
Tateno, S., Hirose, K., Ohishi, Y., Tatsumi, Y., 2010. The structure of iron in Earths inner core. Science 330, 359.
Tkalcić, H., Kennett, B.L.N., 2008. Core structure and heterogeneity: a seismological perspective. Aust. J. Earth Sci. 55, 419–431.
van der Hilst, R.D., de Hoop, M.V., Wang, P., Shim, S.H., Ma, P., Tenorio, L., 2007. Seismostratigraphy and thermal structure of Earth's core–mantle boundary region. Science 315, 1813–1817.
Van Orman, J.A., 2004. On the viscosity and creep mechanism of Earth's inner core. Geophys. Res. Lett. 31, L20606.
Verhoogen, J., 1961. Heat balance of the Earth's core. Geophys. J. R. Astron. Soc. 4, 276–291.
Vidale, J.E., Dodge, D.A., Earle, P.S., 2000. Slow differential rotation of the Earth's inner core indicated by temporal changes in scattering. Nature 405, 445–448.
Vidale, J.E., Earle, P.S., 2000. Fine-scale heterogeneity in the Earth's inner core. Nature 404, 273–275.
Vočadlo, L., Dobson, D., wood, I., 2009. Ab initio calculations of the elasticity of hcp-Fe as a function of temperature at inner-core pressure. Earth Planet. Sci. Lett. 288, 534–538.
Vočadlo, L., 2007a. Ab initio calculations of the elasticity of iron and iron alloys at inner core conditions: evidence for a partially molten inner core? Earth Planet. Sci. Lett. 254, 227–232.
Vočadlo, L., 2007b. Mineralogy of the Earth–the Earth's core: Iron and iron alloys. In: Schubert, G. (Ed.), Treatise on Geophysics, vol. 1, pp. 91–120.
Vočadlo, L., Alfè, D., Gillan, M.J., Wood, I., Brodholt, J., Price, G.D., 2003. Possible thermal and chemical stabilization of body-centred-cubic iron in the Earth's core. Nature 424, 536–539.
Waszek, L., Irving, J., Deuss, A., 2011. Reconciling the hemispherical structure of Earth's inner core with its super-rotation. Nat. Geosci. 4, 264–267.
Weber, P., Machetel, P., 1992. Convection within the inner-core and thermal implications. Geophys. Res. Lett. 19, 2107–2110.
Weeks, W., Gow, A., 1978. Preferred crystal orientations in the fast ice along the margins of the arctic ocean. J. Geophys. Res. 83, 5105–5121.
Weeks, W., Gow, A., 1980. Crystal alignments in the fast ice of Arctic Alaska. J. Geophys. Res. 85, 1137–1146.
Wenk, H.R., Baumgardner, J.R., Lebensohn, R.A., Tomé, C.N., 2000. A convection model to explain anisotropy of the inner core. J. Geophys. Res. 105, 5663–5678.
Wenk, H.R., Takeshita, T., Jeanloz, R., Johnson, G.C., 1988. Development of texture and elastic anisotropy during deformation of hcp metals. Geophys. Res. Lett. 15, 76–79.
Widmer, R., Masters, G., Gilbert, F., 1991. Spherically symmetric attenuation within the Earth from natural mode data. Geophys. J. Int. 104, 541–553.
Woodhouse, J.H., Giardini, D., Li, X.D., 1986. Evidence for inner core anisotropy from free oscillations. Geophys. Res. Lett. 13, 1549–1552.
Wookey, J., Helffrich, G., 2008. Inner-core shear-wave anisotropy and texture from an observation of PKJKP waves. Nature 454, 873–876.
Worster, M.G., 1997. Convection in Mushy Layers. Ann. Rev. Fluid Mech. 29, 91–122.
Yoshida, S., Sumita, I., Kumazawa, M., 1996. Growth model of the inner core coupled with the outer core dynamics and the resulting elastic anisotropy. J. Geophys. Res. 101, 28085–28104.
Yu, W., Wen, L., 2006. Inner core attenuation anisotropy. Earth Planet. Sci. Lett. 245, 581–594.
Yu, W., Wen, L., Niu, F., 2005. Seismic velocity structure in the Earth's outer core. J. Geophys. Res. (Solid Earth) 110, B02302.
Yukutake, T., 1998. Implausibility of thermal convection in the Earth's solid inner core. Phys. Earth Planet. Inter. 108, 1–13.
Zhang, J., Song, X., Li, Y., Richards, P.G., Sun, X., Waldhauser, F., 2005. Inner core differential motion confirmed by earthquake waveform doublets. Science 309, 1357–1360.
Zou, Z., Koper, K.D., Cormier, V.F., 2008. The structure of the base of the outer core inferred from seismic waves diffracted around the inner core. J. Geophys. Res. (Solid Earth) 113, 5314.

Geophysical Journal International

Geophys. J. Int. (2013) **194,** 1310–1334
Advance Access publication 2013 June 21

doi: 10.1093/gji/ggt202

Thermal convection in Earth's inner core with phase change at its boundary

Renaud Deguen,[1] Thierry Alboussière[2] and Philippe Cardin[3]

[1] *Department of Earth and Planetary Sciences, Johns Hopkins University, Baltimore, MD* 21218, *USA. E-mail: rdeguen@gmail.com*
[2] *LGL, Laboratoire de Géologie de Lyon, CNRS, Université Lyon* 1, *ENS-Lyon, Géode,* 2 *rue Raphaël Dubois,* 69622 *Villeurbanne, France*
[3] *ISTerre, Université de Grenoble* 1, *CNRS, B.P.* 53, 38041 *Grenoble, France*

Accepted 2013 May 14. Received 2013 April 22; in original form 2012 November 17

SUMMARY

Inner core translation, with solidification on one hemisphere and melting on the other, provides a promising basis for understanding the hemispherical dichotomy of the inner core, as well as the anomalous stable layer observed at the base of the outer core—the so-called F-layer—which might be sustained by continuous melting of inner core material. In this paper, we study in details the dynamics of inner core thermal convection when dynamically induced melting and freezing of the inner core boundary (ICB) are taken into account.

If the inner core is unstably stratified, linear stability analysis and numerical simulations consistently show that the translation mode dominates only if the viscosity η is large enough, with a critical viscosity value, of order $\sim 3 \times 10^{18}$ Pa s, depending on the ability of outer core convection to supply or remove the latent heat of melting or solidification. If η is smaller, the dynamic effect of melting and freezing is small. Convection takes a more classical form, with a one-cell axisymmetric mode at the onset and chaotic plume convection at large Rayleigh number. η being poorly known, either mode seems equally possible. We derive analytical expressions for the rates of translation and melting for the translation mode, and a scaling theory for high Rayleigh number plume convection. Coupling our dynamic models with a model of inner core thermal evolution, we predict the convection mode and melting rate as functions of inner core age, thermal conductivity, and viscosity. If the inner core is indeed in the translation regime, the predicted melting rate is high enough, according to Alboussière *et al.*'s experiments, to allow the formation of a stratified layer above the ICB. In the plume convection regime, the melting rate, although smaller than in the translation regime, can still be significant if η is not too small.

Thermal convection requires that a superadiabatic temperature profile is maintained in the inner core, which depends on a competition between extraction of the inner core internal heat by conduction and cooling at the ICB. Inner core thermal convection appears very likely with the low thermal conductivity value proposed by Stacey & Loper, but nearly impossible with the much higher thermal conductivity recently put forward by Sha & Cohen, de Koker *et al.* and Pozzo *et al.* We argue however that the formation of an iron-rich layer above the ICB may have a positive feedback on inner core convection: it implies that the inner core crystallized from an increasingly iron-rich liquid, resulting in an unstable compositional stratification which could drive inner core convection, perhaps even if the inner core is subadiabatic.

Key words: Numerical solutions; Instability analysis; Seismic anisotropy; Heat generation and transport.

1 INTRODUCTION

In the classical model of convection and dynamo action in Earth's outer core, convection is thought to be driven by a combination of cooling from the core–mantle boundary (CMB) and light elements (O, Si, S, . . .) and latent heat release at the inner core boundary (ICB). Convection is expected to be vigorous, and the core must therefore be very close to adiabatic, with only minute lateral temperature variations (Stevenson 1987), except in very thin, unstable boundary layers at the ICB and CMB. To a large extent,

seismological models are consistent with the bulk of the core being well-mixed and adiabatic, which supports the standard model of outer core convection. Yet seismological observations indicate the existence of significant deviations from adiabaticity in the lowermost ∼200 km of the outer core (Souriau & Poupinet 1991). This layer, sometimes called F-layer for historical reasons, exhibits an anomalously low V_P gradient which is most probably indicative of stable compositional stratification (Gubbins *et al.* 2008), implying that the lowermost 200 km of the outer core are depleted in light elements compared to the bulk of the core. This is in stark contrast with the classical model of outer core convection sketched above: in place of the expected thin unstable boundary layer, seismological models argues for a very thick and stable layer. Note also that the thickness of the layer, ∼200 km, is much larger than any diffusion length scales, even on a Gy timescale, which means that if real this layer must have been created, and be sustained, by a mechanism involving advective transport.

Because light elements are partitioned preferentially into the liquid during solidification, iron-rich melt can be produced through a two-stage purification process involving solidification followed by melting (Gubbins *et al.* 2008). Based on this idea, Gubbins *et al.* (2008) have proposed a model for the formation of the F-layer in which iron-rich crystals nucleate at the top of the layer and melt back as they sink towards the ICB, thus implying a net inward transport of iron which results in a stable stratification. In contrast, Alboussière *et al.* (2010) proposed that melting occurs directly at the ICB in response to inner core internal dynamics, in spite of the fact that the inner core must be crystallizing on average. Assuming that the inner core is melting in some regions while it is crystallizing in others, the conceptual model proposed by Alboussière *et al.* (2010) works as follow: melting inner core material produces a dense iron-rich liquid which spreads at the surface of the inner core, while crystallization produces a buoyant liquid which mixes with and carries along part of the dense melt as it rises. The stratified layer results from a dynamic equilibrium between production of iron-rich melt and entrainment and mixing associated with the release of buoyant liquid. Analogue fluid dynamics experiments demonstrate the viability of the mechanism, and show that a stratified layer indeed develops if the buoyancy flux associated with the dense melt is larger (in magnitude) than a critical fraction (≃80 per cent) of the buoyancy flux associated with the light liquid. This number is not definitive because possibly important factors were absent in Alboussière *et al.* (2010)'s experiments (Coriolis and Lorentz force, entrainment by thermal convection from above, . . .) but it seems likely that a high rate of melt production will still be required.

A plausible way to melt the inner core is to sustain dynamically a topography that will bring locally the ICB at a potential temperature lower than that of the adjacent liquid core, which allows heat to flow from the outer core to the inner core. The melting rate is then limited by the ability of outer core convection to provide the latent heat absorbed by melting, and only a significant ICB topography can lead to a non-negligible melting rate. More recently, Gubbins *et al.* (2011) and Sreenivasan & Gubbins (2011) have proposed that localized melting of the inner core might be induced by outer core convection, but the predicted rate of melt production is too small to produce a stratified layer according to Alboussière *et al.* (2010)'s experiments. Furthermore, it is not clear that the behaviour observed in numerical simulations at slightly supercritical conditions would persist at Earth's core conditions.

Among the different models of inner core dynamics proposed so far (Jeanloz & Wenk 1988; Yoshida *et al.* 1996; Karato 1999; Buffett & Wenk 2001; Deguen *et al.* 2011), only thermal convection (Jeanloz & Wenk 1988; Weber & Machetel 1992; Buffett 2009; Deguen & Cardin 2011; Cottaar & Buffett 2012) is potentially able to produce a large dynamic topography and associated melting. Thermal convection in the inner core is possible if the growth rate of the inner core is large enough and its thermal conductivity low enough (Sumita *et al.* 1995; Buffett 2009; Deguen & Cardin 2011). One possible mode of inner core thermal convection consists in a global translation with solidification on one hemisphere and melting on the other (Monnereau *et al.* 2010; Alboussière *et al.* 2010; Mizzon & Monnereau 2013). The translation rate can be such that the rate of melt production is high enough to explain the formation of the F-layer (Alboussière *et al.* 2010). In addition, inner core translation provides a promising basis for understanding the hemispherical dichotomy of the inner core observed in its seismological properties (Tanaka & Hamaguchi 1997; Niu & Wen 2001; Irving *et al.* 2009; Tanaka 2012). Textural change of the iron aggregate during the translation (Bergman *et al.* 2010; Monnereau *et al.* 2010; Geballe *et al.* 2013) may explain the hemispherical structure of the inner core. Inner core translation, by imposing a highly asymmetric buoyancy flux at the base of the outer core, is also a promising candidate (Aubert 2013; Davies *et al.* 2013) for explaining the existence of the planetary scale eccentric gyre which has been inferred from quasi-geostrophic core flow inversions (Pais *et al.* 2008; Gillet *et al.* 2009).

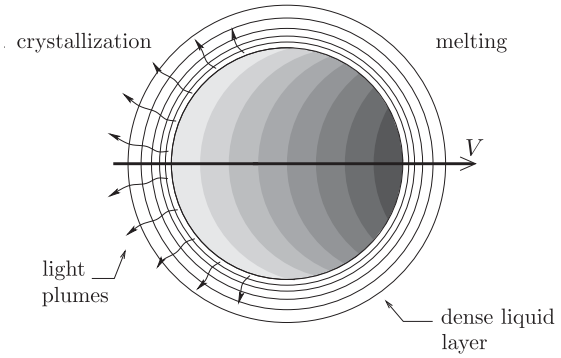

Figure 1. A schematic representation of the translation mode of the inner core, with the grey shading showing the potential temperature distribution (or equivalently the density perturbation) in a cross-section including the translation direction (adapted from Alboussière *et al.* 2010).

However, inner core translation induces horizontal temperature gradients (see Fig. 1), and Alboussière *et al.* (2010) noted that finite deformation associated with these density gradients is expected to weaken the translation mode if the inner core viscosity is too small. They estimated from an order of magnitude analysis that the threshold would be at $\eta \sim 10^{18}$ Pa s. Below this threshold, thermal convection is expected to take a more classical form, with cold plumes falling down from the ICB and warmer upwellings (Deguen & Cardin 2011). Published estimates of inner core viscosity range from $\sim 10^{11}$ to $\sim 10^{22}$ Pa s (Yoshida *et al.* 1996; Buffett 1997; Van Orman 2004; Koot & Dumberry 2011; Reaman *et al.* 2011, 2012) implying that both convection regime seem possible.

The purpose of this paper is twofold: (i) to precise under what conditions the translation mode can be active, and (ii) to estimate the rate of melt production associated with convection, in particular when the effect of finite viscosity becomes important. To this aim, we develop a set of equations for thermal convection in the inner core with phase change associated with a dynamically sustained topography at the inner core boundary (Section 3). The kinetics of phase change is described by a non-dimensional number, noted $\mathcal{P}$ for 'phase change

number', which is the ratio of a phase change timescale (introduced in Section 2) to a viscous relaxation timescale. The linear stability analysis of the set of equations (Section 4) demonstrates that the first unstable mode of thermal convection consists in a global translation when $\mathcal{P}$ is small. When $\mathcal{P}$ is large, the first unstable mode is the classical one cell convective mode of thermal convection in a sphere with an impermeable boundary (Chandrasekhar 1961). An analytical expression for the rate of translation is derived in Section 5. We then describe numerical simulation of thermal convection, from which we derive scaling laws for the rate of melt production (Section 6). The results of the previous sections are then applied to the inner core, and used to predict the convection regime of the inner core and the rate of melt production as functions of the inner core growth rate and thermophysical parameters (Section 7).

2 PHASE CHANGE AT THE ICB

Any phase change at the ICB will release or absorb latent heat, with the rate of phase change v being determined by the Stefan condition,

$$\rho_s L v = -[\![q]\!]_{\mathrm{icb}}, \tag{1}$$

which equates the rate of latent heat release or absorption associated with solidification or melting with the difference of heat flux $[\![q]\!]_{\mathrm{icb}}$ across the inner core boundary. Here ρ_s is the density of the solid inner core just below the ICB, and L is the latent heat of melting. The heat conducted along the adiabatic gradient on the outer core side is to a large extent balanced by the heat flow conducted on the inner core side, the difference between the two making a very small contribution to $[\![q]\!]_{\mathrm{icb}}$. Convective heat transport in the inner core is small as well. Convection in the liquid outer core is a much more efficient way of providing or removing latent heat and $-[\![q]\!]_{\mathrm{icb}}$ is dominated by the contribution of the advective heat flux $\Phi(\theta, \phi)$ on the liquid side, which scales as

$$\Phi \sim \rho_l c_{pl} u' \delta\Theta, \tag{2}$$

where $\delta\Theta$ is the difference of potential temperature between the inner core boundary and the bulk of the core (Fig. 2), u' is a typical velocity scale in the outer core, and ρ_l and c_{pl} are the density and specific heat capacity of the liquid outer core in the vicinity of the inner core boundary (Alboussière *et al.* 2010).

We choose as a reference radius the intersection of the mean outer core adiabat with the solidification temperature curve (Fig. 2), and note $h(\theta, \phi)$ the distance from this reference to the inner core boundary. At a given location on the ICB, the difference of potential temperature between the ICB and the outer core is $\delta\Theta(\theta, \phi) = (m_p - m_{\mathrm{ad}})\delta p(\theta, \phi)$, where $\delta p(\theta, \phi)$ is the pressure difference between the ICB and the reference surface (see Fig. 2), $m_p = \mathrm{d}T_s/\mathrm{d}p$ is the Clapeyron slope, and $m_{\mathrm{ad}} = \mathrm{d}T_{\mathrm{ad}}/\mathrm{d}p$ is the adiabatic gradient in the outer core. Taking into account the local anomaly Ψ' of the gravitational potential (due to the ICB topography and internal density perturbations), we have from hydrostatic equilibrium $\delta p = -\rho_l(g_{\mathrm{icb}} h + \Psi')$, which gives

$$\delta\Theta = -(m_p - m_{\mathrm{ad}})\rho_l g_{\mathrm{icb}} \left(h + \frac{\Psi'}{g_{\mathrm{icb}}}\right), \tag{3}$$

where g_{icb} is the average gravity level on the surface of the inner core. The surface $h_{\mathrm{eq}}(\theta, \phi) = -\Psi'/g_{\mathrm{icb}}$ is the equipotential surface which on average coincides with the ICB.

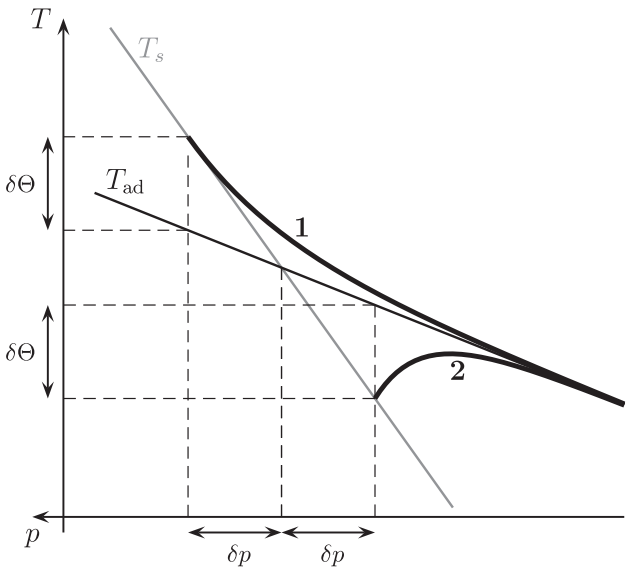

Figure 2. Temperature profiles (thick black lines) in the vicinity of the inner core boundary. Profile 1 corresponds to a crystallizing region, while profile 2 corresponds to a melting region. The thin black line is the outer core adiabat T_{ad} and the thin grey line is the solidification temperature profile.

If the inner core is convecting, with a velocity field $\mathbf{u}(r, \theta, \phi, t) = (u_r, u_\theta, u_\phi)$, then the total rate of phase change is

$$v = \dot{r}_{\mathrm{ic}} + \frac{\partial h}{\partial t} - u_r, \tag{4}$$

where $\dot{r}_{\mathrm{ic}}$ is the mean inner core growth rate, $r_{\mathrm{ic}}(t)$ being the inner core radius. Using eqs. (2)–(4), the heat balance (1) at the inner core boundary can be written as

$$u_r - \dot{r}_{\mathrm{ic}} - \frac{\partial h}{\partial t} \sim \frac{h + \Psi'/g_{\mathrm{icb}}}{\tau_\phi}, \tag{5}$$

where the timescale τ_ϕ is

$$\tau_\phi = \frac{\rho_s L}{\rho_l^2 c_{pl} \left(m_p - m_{\mathrm{ad}}\right) g_{\mathrm{icb}} u'}. \tag{6}$$

With $u' \sim 10^{-4}\,\mathrm{m\,s^{-1}}$ and typical values for the other parameters (Table1), the phase change timescale τ_ϕ is found to be of the order of 10^3 years, which will turn out to be short compared to the dynamic timescale of thermal convection in the inner core (∼1 Myr or more). Noting $\Delta\rho = \rho_s - \rho_l$, the viscous relaxation timescale $\tau_\eta = \eta/(\Delta\rho\, g_{\mathrm{icb}}\, r_{\mathrm{ic}})$ is at most ∼0.1 Myr (for $\eta = 10^{22}$ Pa s), small as well compared to the inner core dynamic timescale. We therefore adopt the hypothesis of isostasy and neglect $\partial h/\partial t$ in (5), the heat transfer boundary condition finally adopted being written

$$u_r - \dot{r}_{\mathrm{ic}} = \frac{h + \Psi'/g_{\mathrm{icb}}}{\tau_\phi}, \tag{7}$$

where the unknown proportionality constant in eq. (2) has been absorbed in τ_ϕ, and will be treated as an additional source of uncertainty.

Table 1. Thermophysical parameters used in this study.

Parameter	Symbol	Value
Inner core radius[a]	$r_{\rm icb}$	1221 km
Solidification temperature[b]	$T_{\rm icb}$	5600 ± 500 K
Gruneisen parameter[c]	γ	1.4 ± 0.1
Thermal expansion[c]	α	$(1.1 \pm 0.1) \times 10^{-5}$ K^{-1}
Heat capacity[d]	c_p	800 ± 80 J kg^{-1} K^{-1}
Latent heat of melting[d, e]	L	600–1200 kJ kg^{-1}
Density jump at the ICB[a]	$\Delta\rho$	600 kg m^{-3}
Density in the inner core[a]	ρ_s	12 800 kg m^{-3}
Density in the outer core at the ICB[a]	ρ_l	12 200 kg m^{-3}
Gravity at the ICB[a]	$g_{\rm icb}$	4.4 m s^{-2}
Radial gravity gradient[a]	g'	3.6×10^{-6} s^{-2}
Thermal conductivity[f]	k	36–150 W m^{-1} K^{-1}
Isentropic bulk modulus[a]	K_S	1400 GPa
Clapeyron/adiabat slopes ratio[g]	dT_s/dT_{ad}	1.65 ± 0.11

[a]From PREM (Dziewonski & Anderson 1981).
[b]Alfè *et al.* (2002).
[c]Vočadlo (2007).
[d]Poirier (1994).
[e]Anderson & Duba (1997).
[f]Stacey & Anderson (2001), Stacey & Davis (2008), Sha & Cohen (2011), de Koker *et al.* (2012) and Pozzo *et al.* (2012).
[g]Deguen & Cardin (2011).

3 GOVERNING EQUATIONS

3.1 Equations within the inner core

The starting point for the dynamics of thermal convection in the inner core is expressed as general entropy, momentum, continuity and gravitational equations:

$$\rho T \frac{\mathrm{D}s}{\mathrm{D}t} = \boldsymbol{\nabla}\cdot(k\boldsymbol{\nabla}T) + \tau : \epsilon, \tag{8}$$

$$\mathbf{0} = -\boldsymbol{\nabla}p - \rho\boldsymbol{\nabla}\Psi + \boldsymbol{\nabla}\cdot\tau, \tag{9}$$

$$0 = \frac{\partial\rho}{\partial t} + \boldsymbol{\nabla}\cdot(\rho\mathbf{u}), \tag{10}$$

$$\nabla^2\Psi = 4\pi\mathcal{G}\rho, \tag{11}$$

where ρ, T, s, k, τ, ϵ, p, Ψ and $\mathbf{u}$ denote density, temperature, specific entropy, thermal conductivity, shear-stress tensor, rate of deformation tensor, pressure, gravitational potential and velocity fields, respectively and where $\mathcal{G}$ is the universal gravitational constant. In eq. (9), inertia has been neglected and the gravity field $\mathbf{g}$ has been written using the gravitational potential $\mathbf{g} = -\boldsymbol{\nabla}\Psi$.

These equations are then linearized around a state of well-mixed uniform but time dependent entropy, $\overline{s}$, hydrostatic pressure $\overline{p}$, density $\overline{\rho}$, gravity $\overline{\mathbf{g}}$ and gravitational potential $\overline{\Psi}$ depending only on radius and time, such that $\partial\overline{p}/\partial r = -\overline{\rho}\,\overline{g}$, with $\overline{\mathbf{g}}$ satisfying the gravitational equation $\nabla^2\overline{\Psi} = 4\pi\mathcal{G}\overline{\rho}$ and $\overline{\mathbf{g}} = -\boldsymbol{\nabla}\overline{\Psi}$. Linearized variables are introduced such that $s = \overline{s} + s'$, $\rho = \overline{\rho} + \rho'$, $T = \overline{T} + \Theta$, $p = \overline{p} + p'$, $\Psi = \overline{\Psi} + \Psi'$ and $\mathbf{g} = \overline{\mathbf{g}} + \mathbf{g}'$. $\overline{T}(r)$ corresponds to an adiabatic profile, and $\Theta = T - \overline{T}(r)$ is a potential temperature. The linearized governing equations take the form

$$\overline{\rho}\,\overline{T}\frac{Ds'}{Dt} = \boldsymbol{\nabla}\cdot(k\boldsymbol{\nabla}\Theta) + \tau : \epsilon - \overline{\rho}\,\overline{T}\frac{\partial\overline{s}}{\partial t} + \boldsymbol{\nabla}\cdot\left(k\boldsymbol{\nabla}\overline{T}\right), \tag{12}$$

$$\mathbf{0} = -\boldsymbol{\nabla}p' - \overline{\rho}\boldsymbol{\nabla}\Psi' - \rho'\boldsymbol{\nabla}\overline{\Psi} + \boldsymbol{\nabla}\cdot\tau, \tag{13}$$

$$\frac{\partial\rho'}{\partial t} = -\frac{\partial\overline{\rho}}{\partial t} - \boldsymbol{\nabla}\cdot(\overline{\rho}\mathbf{u}), \tag{14}$$

$$\nabla^2\Psi' = 4\pi\mathcal{G}\rho'. \tag{15}$$

Using Maxwell relations, we obtain a linearized expression of ρ' in terms of s' and p'

$$\rho' = \left(\frac{\partial\rho}{\partial s}\right)_P s' + \left(\frac{\partial\rho}{\partial P}\right)_s p' = -\frac{\overline{\alpha}\,\overline{\rho}\,\overline{T}}{\overline{c_p}}s' - \frac{1}{\overline{\rho}\,\overline{\mathbf{g}}}\frac{\partial\overline{\rho}}{\partial r}p', \tag{16}$$

where $\overline{\alpha}$ and $\overline{c_p}$ are the volume expansion coefficient and specific heat capacity corresponding to the reference adiabatic state. With this expression for density fluctuations, eq. (13) can be written as

$$\mathbf{0} = -\overline{\rho}\boldsymbol{\nabla}\left(\frac{p'}{\overline{\rho}} + \Psi'\right) + \frac{\overline{\alpha}\,\overline{\rho}\,\overline{g}\,\overline{T}}{\overline{c_p}}s'\,\mathbf{e_r} + \boldsymbol{\nabla}\cdot\tau, \tag{17}$$

where $\mathbf{e_r}$ is the unit radial vector. The equation of entropy fluctuations (12) can be rewritten as

$$\overline{\rho}\,\frac{D\,\overline{T}s'}{Dt} = -\frac{\overline{\alpha g}\,\overline{T}}{\overline{c_p}}s'u_r + \boldsymbol{\nabla}\cdot(k\boldsymbol{\nabla}\Theta) + \tau : \epsilon - \overline{\rho}\,\overline{T}\frac{\partial\overline{s}}{\partial t} + \boldsymbol{\nabla}\cdot\left(k\boldsymbol{\nabla}\overline{T}\right). \tag{18}$$

Then, the anelastic liquid approximation (Schubert *et al.* 2001; Anufriev *et al.* 2005) can be made, which consists in replacing the general linearized expression for entropy,

$$s' = \frac{\overline{c_p}}{\overline{T}}\Theta - \frac{\overline{\alpha}}{\overline{\rho}}p', \tag{19}$$

by its first term only,

$$s' \simeq \frac{\overline{c_p}}{\overline{T}}\Theta, \tag{20}$$

under the condition $\overline{\alpha}\,\overline{T}\,Di \ll 1$ (Anufriev *et al.* 2005), where $Di = \overline{\alpha}\,g_{\rm icb}\,r_{\rm ic}/\overline{c_p}$ is the dimensionless dissipation number, which compares the inner core radius $r_{\rm ic}$ with the natural length scale for adiabatic temperature variations, $\overline{c_p}/(\overline{\alpha}\,g_{\rm icb})$. In the inner core, $Di \simeq 0.07 \times (r_{\rm ic}/1221\ \mathrm{km})^2$ and $\overline{\alpha}\,\overline{T} \simeq 5 \times 10^{-2}$, so that the anelastic liquid approximation can be made safely. An alternative analysis (Alboussière & Ricard 2013) indicates that $c_p/c_v - 1 \ll 1$, where c_v is the specific heat at constant volume, is the relevant criterion for the anelastic liquid approximation. Since $c_p/c_v - 1 = \gamma\alpha T$ and the Gruneisen parameter γ is of order unity, this criterion is well satisfied. Under the liquid anelastic approximation, the momentum eq. (17) and entropy eq. (18) can then be written as

$$\mathbf{0} = -\overline{\rho}\,\boldsymbol{\nabla}\left(\frac{p'}{\overline{\rho}} + \Psi'\right) + \overline{\alpha}\,\overline{\rho}\,\overline{g}\,\Theta\,\mathbf{e_r} + \boldsymbol{\nabla}\cdot\tau, \tag{21}$$

$$\overline{\rho}\,\frac{\mathrm{D}\left(\overline{c_p}\Theta\right)}{\mathrm{D}t} = -\overline{\alpha\rho g}\Theta u_r + \boldsymbol{\nabla}\cdot(k\boldsymbol{\nabla}\Theta) + \tau : \epsilon - \overline{\rho}\,\overline{c_p}\frac{\partial\overline{T}}{\partial t} + \boldsymbol{\nabla}\cdot\left(k\boldsymbol{\nabla}\overline{T}\right), \tag{22}$$

where terms involving $\partial\overline{c_p}/\partial t$ and $\partial\overline{\rho}/\partial t$ have been neglected in (22).

The importance of self-gravitation is best estimated by analyzing its effect in terms of vorticity production. We form the vorticity equation by taking the curl of eq. (13), which gives

$$\mathbf{0} = \boldsymbol{\nabla}\bar{\rho}\times\boldsymbol{\nabla}\Psi' + \boldsymbol{\nabla}\rho'\times\bar{\mathbf{g}} + \boldsymbol{\nabla}\times(\boldsymbol{\nabla}\cdot\tau), \tag{23}$$

$$= \frac{\mathrm{d}\bar{\rho}}{\mathrm{d}r}\mathbf{e_r}\times\boldsymbol{\nabla}_h\Psi' - \bar{g}\,\boldsymbol{\nabla}_h\rho'\times\mathbf{e_r} + \boldsymbol{\nabla}\times(\boldsymbol{\nabla}\cdot\tau), \tag{24}$$

where ∇_h denotes the horizontal part of the gradient. The first term on the right-hand side originates from the interaction between the mean radial density gradient and the horizontal gradient in Ψ', and is to be compared with the second term, which results from the interaction between horizontal density gradients and the mean radial gravity field. From the gravitational equation, $\nabla^2\Psi' = 4\pi\mathcal{G}\rho'$, we find that $\Psi' \sim 4\pi\mathcal{G}\rho'\lambda^2$, where λ is the typical length scale of the temperature and gravitational potential perturbations. Using this estimate for Ψ' the ratio of the first two terms in eq. (24) is

$$\frac{|\nabla\bar{\rho}\times\nabla\Psi'|}{|\nabla\rho'\times\bar{\mathbf{g}}|} \sim \frac{\mathrm{d}\bar{\rho}}{\mathrm{d}r}\frac{\Psi'}{\bar{g}\rho'} \sim \frac{\mathrm{d}\bar{\rho}}{\mathrm{d}r}\frac{4\pi\mathcal{G}\lambda^2}{\bar{g}}. \tag{25}$$

Noting that $\mathrm{d}\bar{\rho}/\mathrm{d}r = -(\mathrm{d}\bar{\rho}/\mathrm{d}p)\bar{\rho}\bar{g} = -\bar{\rho}^2\bar{g}/K_S$ and that $\bar{g}_{\mathrm{icb}} = (4\pi/3)\mathcal{G}\bar{\rho}\, r_{\mathrm{ic}}$, we obtain

$$\frac{|\nabla\bar{\rho}\times\nabla\Psi'|}{|\nabla\rho'\times\bar{\mathbf{g}}|} \sim 3\frac{\bar{\rho}\bar{g}_{\mathrm{icb}}r_{\mathrm{ic}}}{K_s}\frac{\lambda^2}{r_{\mathrm{ic}}^2} \sim 3\frac{Di}{\gamma}\frac{\lambda^2}{r_{\mathrm{ic}}^2}, \tag{26}$$

where the Grüneisen parameter $\gamma \simeq 1.4$ is equal to $\bar{\alpha}K_S/(\bar{c}_p\bar{\rho})$.

Since $Di/\gamma \simeq 0.05$, the vorticity source arising from self-gravitation effects might be up to ~15 per cent of the total vorticity production if the length scale of convection is similar to the inner core radius, but has a much smaller contribution when λ/r_{ic} is small. Although the approximation might not be very good in cases where λ is comparable to r_{ic}, we will ignore here the radial variations of $\bar{\rho}$, without which the force arising from self-gravitation is potential, and is therefore balanced by the pressure field. The density in the inner core is assumed to be uniform: $\overline{\rho} = \rho_s$. To be consistent, $\overline{g}$ is assumed to be a linear function of radius, $\overline{g} = g_{\mathrm{icb}}r/r_{\mathrm{ic}}$. Density in the liquid outer core is assumed to be uniform as well: $\overline{\rho_l} = \rho_l$. This is not correct for the outer core as a whole, but this is an excellent approximation within the depth range of the expected topography of the inner core boundary, so that ρ_l is the density of the outer core close to the inner core for our purpose.

The rheology is assumed to be Newtonian, with uniform effective viscosity η. Furthermore, viscous and adiabatic heating can be neglected since the dissipation number is small (Tritton 1988). We further assume that the thermal conductivity and thermal expansion are uniform. With $\kappa = k/(\rho_s\,\overline{c_p})$ the thermal diffusivity, our final set of equation is

$$\nabla\cdot\mathbf{u} = 0, \tag{27}$$

$$\mathbf{0} = -\nabla\left(p' + \rho_s\Psi'\right) + \frac{\overline{\alpha}\,\rho_s\,g_{\mathrm{icb}}}{r_{\mathrm{ic}}}\Theta\, r\,\mathbf{e_r} + \eta\nabla^2\mathbf{u}, \tag{28}$$

$$\frac{\mathrm{D}\Theta}{\mathrm{D}t} = \kappa\nabla^2\,\Theta + S(t), \tag{29}$$

where the effective heating rate $S(t)$ is defined as the difference between secular cooling and heat conducted down the adiabat:

$$S(t) = \kappa\nabla^2\overline{T} - \frac{\partial\overline{T}}{\partial t}. \tag{30}$$

S can be shown to depend mainly on time, not radius. When this term is positive (strong secular cooling and/or weak conduction), the inner core is superadiabatic and natural convection may develop.

3.2 Expression of boundary conditions

Despite the fact that we have stressed the necessity for a non uniform temperature on the inner core boundary when phase changes occur (in Section 2), we shall now argue that the boundary condition for thermal convection within the inner core is well approximated by $\Theta = 0$ at $r = r_{\mathrm{ic}}$. Indeed, the lateral variations of potential temperature associated with the ICB dynamic topography will be found to be of order 10^{-2} K or smaller (corresponding to a dynamic topography $\lesssim$100 m), while potential temperature variations within the inner core will be found to be of order 1 K or larger. We thus assume

$$\Theta(r = r_{\mathrm{ic}}) = 0. \tag{31}$$

The mechanical boundary conditions are tangential stress-free conditions (the fluid outer core cannot sustain tangential stress) and continuity of the normal stress at the inner core boundary. With the assumption of small topography, the normal vector is very close to the radial unit vector and the stress-free tangential conditions can be written as

$$\tau_{r\theta} = \eta\left[r\frac{\partial}{\partial r}\left(\frac{u_\theta}{r}\right) + \frac{1}{r}\frac{\partial u_r}{\partial\theta}\right] = 0, \tag{32}$$

$$\tau_{r\phi} = \eta\left[r\frac{\partial}{\partial r}\left(\frac{u_\phi}{r}\right) + \frac{1}{r\sin\theta}\frac{\partial u_r}{\partial\phi}\right] = 0, \tag{33}$$

where the spherical coordinates (r, θ, ϕ) are used, while the continuity of the normal stress gives

$$\left[\!\left[2\eta\frac{\partial u_r}{\partial r} - p\right]\!\right]_{\mathrm{icb}} = 0, \tag{34}$$

where $[\![\ldots]\!]_{\mathrm{icb}}$ denotes the difference of a quantity across the ICB. Using again the decomposition $p = \overline{p} + p'$, this becomes

$$\rho_l g_{\mathrm{icb}}h - p'^{+} - 2\eta\frac{\partial u_r}{\partial r} - \rho_s g_{\mathrm{icb}}h + p'^{-} = 0, \tag{35}$$

where the subscripts $+$ and $-$ denote the liquid and solid sides respectively and where overlapping adiabatic hydrostatic states have been used for the liquid and solid regions. This condition can also be written as

$$-\Delta\rho\, g_{\mathrm{icb}}\, h + \rho_l\Psi' - 2\eta\frac{\partial u_r}{\partial r} + p'^{-} = 0, \tag{36}$$

because integrating the hydrostatic equation in the liquid outer core leads to $p + \rho_l\Psi$ constant, which applies also to perturbation quantities.

Finally, the radial velocity u_r at the ICB is related to the topography h and gravitational potential perturbation Ψ' through the heat balance at the ICB (eq. 7).

3.3 Set of equations

Introducing two new variables,

$$\hat{h} = h + \frac{\Psi'}{g_{\mathrm{icb}}}, \tag{37}$$

$$\hat{p} = p'^{-} + \rho_s\Psi', \tag{38}$$

one can write the momentum and entropy equation, together with the boundary conditions relevant when phase change is allowed between solid inner core and liquid outer core:

$$\nabla\cdot\mathbf{u} = 0, \tag{39}$$

$$\mathbf{0} = -\nabla\hat{p} + \frac{\overline{\alpha}\,\rho_s\,g_{\mathrm{icb}}}{r_{\mathrm{ic}}}\Theta\, r\,\mathbf{e_r} + \eta\nabla^2\mathbf{u}, \tag{40}$$

$$\frac{\mathrm{D}\Theta}{\mathrm{D}t} = \kappa\nabla^2\Theta + S(t), \tag{41}$$

with boundary conditions at $r = r_{\rm ic}$ from (31), (32), (33), (36) and (7):

$$\Theta = 0, \tag{42}$$

$$\tau_{r\theta} = \eta\left[r\frac{\partial}{\partial r}\left(\frac{u_\theta}{r}\right) + \frac{1}{r}\frac{\partial u_r}{\partial\theta}\right] = 0, \tag{43}$$

$$\tau_{r\phi} = \eta\left[r\frac{\partial}{\partial r}\left(\frac{u_\phi}{r}\right) + \frac{1}{r\sin\theta}\frac{\partial u_r}{\partial\phi}\right] = 0, \tag{44}$$

$$-\Delta\rho\, g_{\rm icb}\,\hat{h} - 2\eta\frac{\partial u_r}{\partial r} + \hat{p} = 0, \tag{45}$$

$$u_r - \dot{r}_{\rm ic} = \frac{\hat{h}}{\tau_\phi}. \tag{46}$$

It can be seen from (45) and (46), that $\hat{h}$ is not necessary for the resolution of the equations, although it can be recovered once the problem is solved, and can be eliminated between these two equations, leaving only one boundary condition:

$$-\Delta\rho g_{\rm icb}\tau_\phi(u_r - \dot{r}_{\rm ic}) - 2\eta\frac{\partial u_r}{\partial r} + \hat{p} = 0, \tag{47}$$

Incidently, it can also be seen that there is no need to explicitly solve the gravitational eq. (15), since Ψ' has been absorbed in the modified pressure (38).

The governing equations and boundary conditions are now made dimensionless using the age of the inner core $\tau_{\rm ic}$, its time dependent radius $r_{\rm ic}(t)$, $\kappa/r_{\rm ic}(t)$, $\eta\kappa/r_{\rm ic}^2(t)$ and $S(t)r_{\rm ic}^2(t)/(6\kappa)$ as scales for time, length, velocity, pressure and potential temperature, respectively. Using the same symbols for dimensionless quantities, dimensionless equations can be written as

$$\boldsymbol{\nabla}\cdot\mathbf{u} = 0, \tag{48}$$

$$\mathbf{0} = -\boldsymbol{\nabla}\hat{p} + Ra(t)\,\Theta\,\mathbf{r} + \boldsymbol{\nabla}^2\mathbf{u}, \tag{49}$$

$$\xi(t)\frac{\partial\Theta}{\partial t} = \nabla^2\Theta - [\mathbf{u} - Pe(t)]\cdot\boldsymbol{\nabla}\Theta + 6 - \left[\xi(t)\frac{\dot{S}(t)\tau_{\rm ic}}{S(t)} + 2\,Pe(t)\right]\Theta, \tag{50}$$

where $\mathbf{r} = r\,\mathbf{e_r}$ and $\dot{S}(t) = \mathrm{d}S(t)/\mathrm{d}t$. The last terms in (50) are due to dependency of the temperature scale on time, when used to make the equations dimensionless. Three dimensionless parameters are needed

$$\xi(t) = \frac{r_{\rm ic}^2(t)}{\kappa\,\tau_{\rm ic}}, \tag{51}$$

$$Pe(t) = \frac{r_{\rm ic}(t)\dot{r}_{\rm ic}(t)}{\kappa}, \tag{52}$$

$$Ra(t) = \frac{\alpha\rho_s g_{\rm icb}(t)S(t)r_{\rm ic}^5(t)}{6\kappa^2\eta}. \tag{53}$$

The dimensionless boundary conditions, at $r = 1$, can be written

$$\Theta = 0, \tag{54}$$

$$\tau_{r\theta} = r\frac{\partial}{\partial r}\left(\frac{u_\theta}{r}\right) + \frac{1}{r}\frac{\partial u_r}{\partial\theta} = 0, \tag{55}$$

$$\tau_{r\phi} = r\frac{\partial}{\partial r}\left(\frac{u_\phi}{r}\right) + \frac{1}{r\sin\theta}\frac{\partial u_r}{\partial\phi} = 0, \tag{56}$$

$$-\mathcal{P}(t)(u_r - \dot{r}_{\rm ic}) - 2\frac{\partial u_r}{\partial r} + \hat{p} = 0, \tag{57}$$

where we have introduced the 'phase change number' $\mathcal{P}$ characterizing the resistance to phase change:

$$\mathcal{P}(t) = \frac{\Delta\rho\, g_{\rm icb}(t)\, r_{\rm ic}(t)\,\tau_\phi(t)}{\eta}. \tag{58}$$

$\mathcal{P}$ is the ratio between the phase change timescale τ_ϕ and the viscous relaxation timescale $\tau_\eta = \eta/(\Delta\rho\, g_{\rm icb}\, r_{\rm ic})$ (equivalent to postglacial rebound timescale). $\mathcal{P} = 0$ corresponds to instantaneous melting or freezing, while $\mathcal{P}\to\infty$ corresponds to infinitely slow melting or freezing. In the limit of infinite $\mathcal{P}$, the boundary condition (57) reduces to the condition $u_r = 0$, which corresponds to impermeable conditions. In contrast, when $\mathcal{P}\to 0$, eq. (57) implies that the normal stress tends towards 0 at the boundary, which corresponds to fully permeable boundary conditions. The general case of finite $\mathcal{P}$ gives boundary conditions for which the rate of phase change at the boundary (equal to u_r) is proportional to the normal stress induced by convection within the spherical shell.

A steady state version of the set of eqs (48)–(58) is found by using $r_{\rm ic}^2/\kappa$ as a timescale instead of $\tau_{\rm ic}$, and keeping $r_{\rm ic}$ and S constant. All the equation remain unchanged except the heat equation which now writes

$$\frac{\partial\Theta}{\partial t} = \nabla^2\Theta - \mathbf{u}\cdot\boldsymbol{\nabla}\Theta + 6. \tag{59}$$

This will be used in Section 6 where numerical simulations with constant inner core radius and thermal forcing will be used to derive scaling laws.

With the assumptions made so far, the velocity field is known to be purely poloidal (Ribe 2007), and we introduce the poloidal scalar P defined such that

$$\mathbf{u} = \boldsymbol{\nabla}\times\boldsymbol{\nabla}\times(P\mathbf{r}). \tag{60}$$

Taking the curl of the momentum eq. (49) gives

$$Ra(t)L^2\Theta = \left(\nabla^2\right)^2 L^2 P, \tag{61}$$

where the angular momentum operator L^2 is

$$L^2 = -\frac{1}{\sin\theta}\frac{\partial}{\partial\theta}\left(\sin\theta\frac{\partial}{\partial\theta}\right) - \frac{1}{\sin^2\theta}\frac{\partial^2}{\partial\phi^2}. \tag{62}$$

Horizontal integration of the momentum equation (see Forte & Peltier 1987; Ribe 2007, where this is done component-wise in spherical harmonics) shows that, on $r = 1$

$$-\hat{p} + \frac{\partial}{\partial r}\left(r\nabla^2 P\right) = C^{\rm st}. \tag{63}$$

This expression can be used to eliminate $\hat{p}$ in the boundary condition (57). Noting that

$$u_r = \frac{1}{r}L^2 P, \tag{64}$$

continuity of the normal stress at the ICB (eq. 57) gives the following boundary condition at $r = 1$:

$$\frac{\partial}{\partial r}\left(r\nabla^2 P - \frac{2}{r}L^2 P\right) - \mathcal{P}(t)\left(\frac{1}{r}L^2 P - \dot{r}_{\rm ic}\right) = C^{\rm st}, \tag{65}$$

while the stress-free conditions (55) and (56) take the form

$$r\frac{\partial}{\partial r}\left[\frac{1}{r^2}\frac{\partial}{\partial r}(rP)\right] + \frac{1}{r^2}L^2 P = C^{\rm st}, \tag{66}$$

which can be rewritten as

$$\frac{\partial^2 P}{\partial r^2} + \left(L^2 - 2\right)\frac{P}{r^2} = C^{\rm st}. \tag{67}$$

At this stage, there are two unknown scalar field variables, Θ and P. They are expanded as

$$\Theta = t_l^m(r,t)\, Y_l^m, \tag{68}$$

$$P = p_l^m(r,t)\, Y_l^m, \quad l \geq 1, \tag{69}$$

where $Y_l^m(\theta,\phi)$, for $l \geq 0$, $m \in [-l; l]$ are surface spherical harmonics, which satisfy $L^2 Y_l^m = l(l+1)Y_l^m$. The momentum eq. (61) takes the form

$$Ra(t)t_l^m = \mathcal{D}_l^2 p_l^m, \tag{70}$$

where

$$\mathcal{D}_l = \frac{\mathrm{d}^2}{\mathrm{d}r^2} + \frac{2}{r}\frac{\mathrm{d}}{\mathrm{d}r} - \frac{l(l+1)}{r^2}. \tag{71}$$

The stress-free boundary condition (67) can be written as

$$\frac{\mathrm{d}^2 p_l^m}{\mathrm{d}r^2} + [l(l+1) - 2]\frac{p_l^m}{r^2} = 0, \quad l \geq 1, \tag{72}$$

and the boundary condition (65), derived from normal stress balance, as

$$\frac{\mathrm{d}}{\mathrm{d}r}\left[r\mathcal{D}_l p_l^m - 2l(l+1)\frac{p_l^m}{r}\right] = l(l+1)\mathcal{P}(t)\frac{p_l^m}{r}, \quad l \geq 1. \tag{73}$$

With (72), the equation above can also be written:

$$r^2\frac{\mathrm{d}^3 p_l^m}{\mathrm{d}r^3} - 3l(l+1)\frac{\mathrm{d}p_l^m}{\mathrm{d}r} = \left[l(l+1)\mathcal{P}(t) - \frac{6}{r}\right]p_l^m, \quad l \geq 1. \tag{74}$$

The thermal equation is also written in spherical harmonic expansion but cannot be solved independently for each degree and order due to the non-linearity of the advection term, which is evaluated in the physical space and expanded back in spherical harmonics.

4 LINEAR STABILITY ANALYSIS

We investigate here the linear stability of the system of equations describing thermal convection in the inner core with phase change at the ICB, as derived in Section 3. The calculation given here is a generalization of the linear stability analysis of thermal convection in an internally heated sphere given by Chandrasekhar (1961). The case considered by Chandrasekhar (1961), where a non-deformable, impermeable outer boundary is assumed, corresponds to the limit $\mathcal{P} \to \infty$ of the problem considered here.

We assume constant Ra and $\mathcal{P}$ (and $\xi = 1$, $Pe = \dot{S} = 0$), thus ignoring that the base diffusive solution itself is time-dependent. This assumption is essentially correct when the growth rate of the fastest unstable disturbance is much larger than the growth rate of the radius of the inner core. The basic state of the problem is then given by

$$\bar{\Theta} = 1 - r^2, \tag{75}$$

$$\bar{\mathbf{u}} = \mathbf{0}, \tag{76}$$

which is the steady conductive solution of the system of equation developed in Section 3. We investigate the stability of this conductive state against infinitesimal perturbations of the temperature and velocity fields. The temperature field is written as the sum of the conductive temperature profile given by eq. (75) and infinitesimal disturbances $\tilde{\Theta}$, $\Theta(r,\theta,\phi,t) = \bar{\Theta}(r) + \tilde{\Theta}(r,\theta,\phi,t)$. The velocity field perturbation is noted $\tilde{\mathbf{u}}(r,\theta,\phi,t)$, and has an associated poloidal scalar $\tilde{P}(r,\theta,\phi,t)$. We expand the temperature and poloidal disturbances in spherical harmonics,

$$\tilde{\Theta} = \sum_{l=0}^{\infty}\sum_{m=-l}^{l}\tilde{t}_l^m(r)Y_l^m(\theta,\phi)\,\mathrm{e}^{\sigma_l t}, \tag{77}$$

$$\tilde{P} = \sum_{l=1}^{\infty}\sum_{m=-l}^{l}\tilde{p}_l^m(r)Y_l^m(\theta,\phi)\,\mathrm{e}^{\sigma_l t}, \tag{78}$$

where σ_l is the growth rate of the degree l perturbations (note that since m does not appear in the system of equations, the growth rate is function of l only, not m).

The only non-linear term in the system of equations is the advection of heat $\mathbf{u}\cdot\nabla\Theta$ in eq. (59), which is linearized as

$$\tilde{u}_r\frac{\partial\bar{\Theta}}{\partial r} = -2r\tilde{u}_r = -2L^2\tilde{P}. \tag{79}$$

The resulting linearized transport equation for the potential temperature disturbance is

$$\left(\frac{\partial}{\partial t} - \nabla^2\right)\tilde{\Theta} = 2L^2\tilde{P}. \tag{80}$$

Using the decompositions (77) and (78), the linearized system of equations is then, for $l \geq 1$,

$$Ra\,\tilde{t}_l^m = \mathcal{D}_l^2\tilde{p}_l^m, \tag{81}$$

$$(\sigma_l - \mathcal{D}_l)\tilde{t}_l^m = 2l(l+1)\tilde{p}_l^m, \tag{82}$$

with the boundary conditions given by eqs (72) and (73), with $\tilde{t}_l^m(r=1) = 0$.

Developing the $\tilde{t}_l^m$ in series of spherical Bessel functions and solving for $\tilde{p}_l^m$, we obtain an infinite set of linear equations in perturbation quantities, which admits a non trivial solution only if its determinant is equal to zero (see Appendix A for the details of the calculation). This provides the following dispersion equation,

$$\left|\left|\left[q_3^l(\mathcal{P})\alpha_{l,i}^2 + q_4^l(\mathcal{P})\right]\left[1 - \frac{4l+6}{\alpha_{l,j}^2}\right] - \left[q_1^l(\mathcal{P})\alpha_{l,i}^2 + q_2^l(\mathcal{P})\right] + \left(\frac{\sigma_l\alpha_{l,i}^4 + \alpha_{l,i}^6}{2l(l+1)Ra} - 1\right)\frac{1}{2}\delta_{ij}\right|\right| = 0, \quad \text{with } i,j = 1,2,\ldots \tag{83}$$

where $||\cdots||$ denotes the determinant. Here $\alpha_{l,i}$ denotes the ith zero of the spherical Bessel function of degree l. The functions $q_1^l(\mathcal{P})$ to $q_4^l(\mathcal{P})$ are given in Appendix A by eqs (A24), (A25), (A27) and (A28).

Solving eq. (83) for a given value of l and $\sigma_l = 0$ gives the critical value Ra_c of the Rayleigh number for instability of the

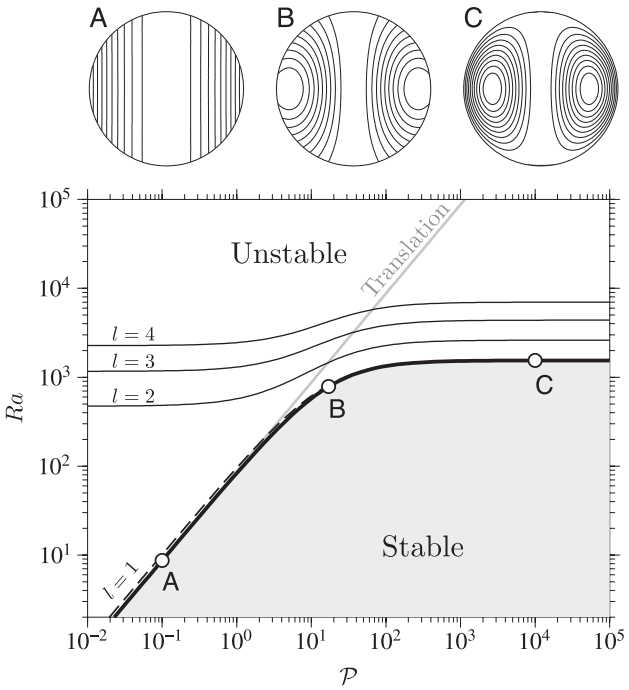

Figure 3. Stability diagram for convection in a sphere with phase change at its outer boundary. The neutral stability curve ($l = 1$) obtained by solving eq. (84) with $\sigma_1 = 0$ is shown by the thick black line. The dashed line shows the approximate stability curve given by eq. (86). The neutral stability curves of higher modes ($l = 2, 3, 4$) obtained by solving eq. (83) with $\sigma_l = 0$ are shown by the annotated thin black lines. The neutral stability curves for $l \geq 5$ are not shown to avoid overcrowding the figure. The thick grey curve annotated 'Translation' is the neutral stability curve of the translation mode, given by eq. (94). Streamlines of the first unstable mode at points A ($\mathcal{P} = 0.1$), B ($\mathcal{P} = 17$) and C ($\mathcal{P} = 10^4$) are shown in the upper figure.

degree l mode, as a function of $\mathcal{P}$. The resulting marginal stability curves for $l = 1$–4 are shown in Fig. 3. The first unstable mode is always the $l = 1$ mode, for which eq. (83) reduces to

$$\left|\left| \left(Ra - \frac{\alpha_{1,i}^6 + \sigma_1 \alpha_{1,i}^4}{4} \right) \delta_{ij} + \alpha_{1,i}^2 \frac{Ra}{\mathcal{P}} + \frac{20}{3\,\alpha_{1,j}^2} Ra \right|\right| = 0. \tag{84}$$

A useful first approximation is obtained by keeping only the $i = j = 1$ terms, thus setting the (1, 1) component of the matrix to zero. This gives a simple analytical form for the growth rate,

$$\sigma_1 = \left(\frac{4}{\alpha_{1,1}^4} + \frac{80}{3\,\alpha_{1,1}^6} \right) Ra + \frac{4}{\alpha_{1,1}^2} \frac{Ra}{\mathcal{P}} - \alpha_{1,1}^2 \tag{85}$$

and for the critical Rayleigh number,

$$Ra_c = \frac{\alpha_{1,1}^6}{4} \left[1 + \frac{\alpha_{1,1}^2}{\mathcal{P}} + \frac{20}{3} \frac{1}{\alpha_{1,1}^2} \right]^{-1}, \tag{86}$$

with $\alpha_{1,1} \simeq 4.4934$. When $\mathcal{P} \ll 1$ or $\mathcal{P} \gg 1$, Ra_c and σ_l have the following limits:

$$Ra_c \longrightarrow \begin{cases} \dfrac{\alpha_{1,1}^8}{4\alpha_{1,1}^2 + 80/3} \simeq 1547 & \text{when } \mathcal{P} \to \infty, \\ \dfrac{\alpha_{1,1}^4}{4} \mathcal{P} \simeq 101.9\,\mathcal{P} & \text{when } \mathcal{P} \to 0, \end{cases} \tag{87}$$

$$\sigma_1 \longrightarrow \begin{cases} \left(\dfrac{4}{\alpha_{1,1}^4} + \dfrac{80}{3\,\alpha_{1,1}^6} \right) Ra - \alpha_{1,1}^2 & \text{when } \mathcal{P} \to \infty, \\ \dfrac{4}{\alpha_{1,1}^2} \dfrac{Ra}{\mathcal{P}} - \alpha_{1,1}^2 & \text{when } \mathcal{P} \to 0, \end{cases} \tag{88}$$

Higher order approximations can be obtained by retaining more terms in the determinant. For $\mathcal{P} \gg 1$, the critical value of Ra converges towards

$$Ra_c = 1545.6, \tag{89}$$

in agreement with Chandrasekhar (1961)'s result (the value given by Chandrasekhar (1961) is twice the value given here, because of different definitions of Ra). When $\mathcal{P} \ll 1$, the relevant non-dimensional parameter is the ratio $Ra/\mathcal{P}$, which is independent of the viscosity and of the thermal diffusivity. An exact value of the critical value of $Ra/\mathcal{P}$ will be given below (eq. 94).

The pattern of the first unstable mode can be calculated by solving the system (A39) given in Appendix A for given $\mathcal{P}$ and Ra. The first unstable modes calculated in this way for points A, B and C ($\mathcal{P} = 0.1$, 17 and 10^4) in the stability diagram are shown in Fig. 3. As shown in Appendix A, the $l = 1$, $m \in [-1, 0, 1]$ components of the poloidal scalar can be written as

$$\tilde{p}_1^m = \sum_{i=1}^{\infty} A_{1,i} \left[\frac{j_1(\alpha_{1,i} r)}{\alpha_{1,i}} + \frac{j_2(\alpha_{1,i})}{3} (r - r^3) + \frac{j_2(\alpha_{1,i}) \alpha_{1,i}^2}{2\,\mathcal{P}} r \right], \tag{90}$$

where the coefficients $A_{1,i}$ are found by solving the system of eqs (A39). Here j_1 and j_2 denote the spherical Bessel functions of the first kind of order 1 and 2, respectively. From eq. (90), it can be seen that

$$\tilde{p}_1^m \to \left(\sum_{i=1}^{\infty} A_{1,i}\, j_2(\alpha_{1,i}) \alpha_{1,i}^2 \right) \frac{2}{\mathcal{P}} r \quad \text{when } \mathcal{P} \to 0, \tag{91}$$

which corresponds to a translation (it can be verified that a $l = 1$ flow with $p_1^m \propto r$ corresponds to a flow with uniform velocity). This is the dominant mode when $\mathcal{P}$ is small, as illustrated in Fig. 3 (point A, $\mathcal{P} = 0.1$). There is no deformation associated with this mode.

At high $\mathcal{P}$, the term in $1/\mathcal{P}$ in eq. (90) becomes negligible, and the first unstable mode is identical to the classical single cell degree one mode of thermal convection with shear-free boundary and no phase change (Chandrasekhar 1961), as illustrated in Fig. 3 (point C, $\mathcal{P} = 10^4$). There is no melting or solidification associated with this mode, which is apparent from the fact that the streamlines of the flow are closed. At intermediate values of $\mathcal{P}$, the first unstable mode is a linear combination of the high-$\mathcal{P}$ convection mode and of the small-$\mathcal{P}$ translation mode.

Allowing only for the translation (i.e. keeping only the $p_{1,i} \propto r/\mathcal{P}$ terms), the dispersion relation (84) reduces to

$$\left|\left| \delta_{ij} - \frac{4}{\alpha_{1,i}^4} \frac{Ra}{\mathcal{P}} \right|\right| = 0. \tag{92}$$

Using Sylvester's determinant theorem, we find that

$$\left|\left| \delta_{ij} - \frac{4}{\alpha_{1,i}^4} \frac{Ra}{\mathcal{P}} \right|\right| = 1 - 4 \frac{Ra}{\mathcal{P}} \sum_{i=1}^{\infty} \frac{1}{\alpha_{1,i}^4}, \tag{93}$$

which allows to write the critical value of $Ra/\mathcal{P}$ as

$$\left(\frac{Ra}{\mathcal{P}} \right)_c = \frac{1}{4} \left(\sum_{i=1}^{\infty} \frac{1}{\alpha_{1,i}^4} \right)^{-1} = \frac{175}{2} = 87.5, \tag{94}$$

where we have used Sneddon (1960)'s result that $\sum_{i=1}^{\infty} \alpha_{1,i}^{-4} = 1/350$. The critical value 175/2 is exact, and is to be preferred to the approximate value (101.9) obtained in eq. (87). Eq. (94) gives the marginal stability curve shown in grey in Fig. 3. Although the translation mode can be unstable at all value of $\mathcal{P}$ provided that Ra is large enough, it is apparent in Fig. 3 that the one cell convection mode is the first unstable mode whenever $\mathcal{P}$ is larger than $\simeq Ra_c/(Ra/\mathcal{P})_c \simeq 17$ (point B in Fig. 3).

Finally, it can be seen in Fig. 3 that the critical Rayleigh number Ra_c^l for higher order modes ($l > 1$) is also lowered when $\mathcal{P} \lesssim 17$. However, the decrease in Ra_c^l is not as drastic as it is for the $l = 1$ mode because, whatever the value of $\mathcal{P}$, viscous dissipation always limits the growth of these modes. The effect of $\mathcal{P}$ on Ra_c^l becomes increasingly small as l increases. This suggests that allowing for phase change at the ICB would generally enhance large scale motions at the expense of smaller scale motions.

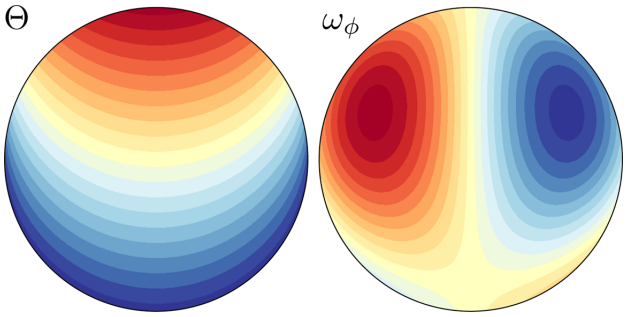

Figure 4. Temperature field (left, red = hot, blue = cold) and vorticity field at $\mathcal{O}(\mathcal{P})$ (right, blue = negative, red = positive) in a meridional cross-section (the direction of translation is arbitrary).

5 ANALYTICAL SOLUTIONS FOR SMALL $\mathcal{P}$

We now search for a finite amplitude solution of inner core convection at small $\mathcal{P}$. In the limit of infinite viscosity ($\mathcal{P} \to 0$), the only possible motions of the inner core are rotation, which we do not consider here, and translation. Guided by the results of the linear stability analysis, we search for a solution in the form of a translation. Alboussière *et al.* (2010) found a solution for the velocity of inner core translation from a global force balance on the inner core, under the assumption that the inner core is rigid. One of the goal of this section is to verify that the system of equations developed in Section 3 indeed leads to the same solution when $\mathcal{P} \to 0$.

If the viscosity is taken as infinite and $\mathcal{P}$ is formally put to zero, searching for a pure translation solution and ignoring any deformation in the inner core leads to an undetermined system. Translation is an exact solution of the momentum equation, but the translation rate is left undetermined, because all the terms in the boundary conditions (55), (56) and (57) (zero tangential stress and continuity of the normal stress) vanish. This of course does not mean that the stress magnitude vanishes, but rather that the rheological relationship between stress and strain via the viscosity becomes meaningless if the viscosity is assumed to be infinite. The ICB topography associated with the translation is sustained by the non-hydrostatic stress field which, even if $\eta \to \infty$, must remain finite. One way to calculate the stress field is to evaluate the flow induced by the lateral temperature variations associated with the translation, for small but non-zero $\mathcal{P}$, and then take the limit $\mathcal{P} \to 0$. If only the 'rigid inner core' limit is wanted, it suffices to calculate the flow at $\mathcal{O}(\mathcal{P})$. The effect of finite viscosity on the translation mode can be estimated by calculating the velocity field at a higher order in $\mathcal{P}$.

5.1 Translation velocity at zeroth order in $\mathcal{P}$

Noting V_0 the translation velocity at zeroth order in $\mathcal{P}$, the poloidal scalar takes the form

$$p_1^0 = \frac{V_0}{2} r, \tag{95}$$

with $Y_1^0 = \cos\theta$, in a cylindrical coordinate system of axis parallel to the velocity translation. If V_0 is large enough, the temperature eq. (50) has a fast convective solution whereby $\mathbf{u} \cdot \nabla\Theta$ balances the constant 6. Imposing $\Theta = 0$ at the ICB on the crystallizing hemisphere, and ignoring a thin boundary layer below the ICB on the melting hemisphere, the temperature field, shown in Fig. 4, is

$$\Theta = \frac{6}{V_0}\left(r\,\cos\theta + \sqrt{1 - r^2\sin^2\theta}\right) \tag{96}$$

(Alboussière *et al.* 2010). This results in a uniform temperature gradient in the translation direction, with the $l = 1, m = 0$ component of the temperature field being

$$t_1^0 = \frac{6}{V_0} r. \tag{97}$$

This temperature field induces a secondary $l = 1, m = 0$ flow which must vanish when $\mathcal{P} \to 0$. We therefore write p_1^0 as

$$p_1^0 = \frac{V_0}{2}\left[r + \hat{p}_{1,1}^0 \mathcal{P} + \mathcal{O}(\mathcal{P}^2)\right]. \tag{98}$$

Inserting this form for p_1^0 and the temperature degree one component t_1^0 into the momentum eq. (70) gives

$$12\frac{Ra}{\mathcal{P}}\frac{1}{V_0^2} r = \mathcal{D}_1^2 \hat{p}_{1,1}^0, \tag{99}$$

from which we can already infer that

$$V_0 \sim \sqrt{\frac{Ra}{\mathcal{P}}}. \tag{100}$$

Eq. (99) has a general solution of the form

$$\hat{p}_{1,1}^0 = Ar + Br^3 + Cr^5, \tag{101}$$

where A, B and C are constants to be determined.

From the momentum eq. (99), we obtain

$$C = \frac{3}{70}\frac{Ra}{\mathcal{P}}\frac{1}{V_0^2}. \tag{102}$$

The stress-free boundary condition (72) for a degree one component,

$$\left.\frac{d^2 p_1^0}{dr^2}\right|_{r=1} = 0, \tag{103}$$

leads to

$$B = -\frac{10}{3}C = -\frac{1}{7}\frac{Ra}{\mathcal{P}}\frac{1}{V_0^2}. \tag{104}$$

Finally, the condition of continuity of the normal stress (74) leads to

$$(-3B + 18C - 1)\mathcal{P} - 2\mathcal{P}^2(A + B + C) + \mathcal{O}(\mathcal{P}^2) = 0, \tag{105}$$

which implies that

$$-3B + 18C - 1 = 0. \tag{106}$$

Note that the constant A is left undetermined: considerations of the velocity field at order $\mathcal{P}^2$ and of the temperature field at order $\mathcal{P}$ are required to determine it. With B and C given by eqs (104) and (102), eq. (106) gives the translation velocity V_0 as

$$V_0 = \sqrt{\frac{6}{5}\frac{Ra}{\mathcal{P}}}. \tag{107}$$

In dimensional unit, the translation rate is given by

$$\frac{\kappa}{r_{\rm ic}}\sqrt{\frac{6}{5}\frac{Ra}{\mathcal{P}}} = \left(\frac{1}{5}\frac{\rho_s}{\Delta\rho}\frac{\alpha S}{\tau_\phi}\right)^{1/2} r_{\rm ic} \tag{108}$$

which, with τ_ϕ given by eq. (6), is exactly the same solution as that found in Alboussière *et al.* (2010) from an analysis of the global force balance on the inner core. As expected, the translation rate is independent of the inner core viscosity η and of the thermal diffusivity, and is an increasing function of the heating rate S and a decreasing function of the phase change timescale.

The potential temperature difference across the inner core is $12/V_0$ in non-dimensional units, and

$$12\frac{Sr_{\rm ic}^2}{6\kappa}\left(\frac{5}{6}\frac{\mathcal{P}}{Ra}\right)^{1/2} = \left(20\frac{\Delta\rho\,\tau_\phi\,S}{\rho_s\,\alpha}\right)^{1/2} \tag{109}$$

in dimensional units.

5.2 Translation velocity at $\mathcal{O}(\mathcal{P})$

The translation velocity at $\mathcal{O}(\mathcal{P})$ can be obtained by calculating the temperature field at $\mathcal{O}(\mathcal{P})$ and the velocity field at $\mathcal{O}(\mathcal{P}^2)$, which allows to determine the constant A in the expression of the poloidal scalar at $\mathcal{O}(\mathcal{P})$ (eq. 101). The procedure, detailed in Appendix B, is complicated by the non-linearity of the heat equation: coupling of higher order harmonics component of the temperature and velocity fields contribute to the $l = 1$ component of the temperature field. Taking into account the effect of the non-linear coupling of the $l = 2$ components of the temperature and velocity fields, we obtain

$$V = \sqrt{\frac{6}{5}\frac{Ra}{\mathcal{P}}}\left[1 - 0.0216\,\mathcal{P} + \mathcal{O}(\mathcal{P}^2)\right]. \tag{110}$$

which suggests that the effect of deformation becomes important when $\mathcal{P}$ is a significant fraction of $1/0.0216 \simeq 46$, in agreement with the prediction of the linear stability analysis.

The temperature field and the ϕ-component of the vorticity field at $\mathcal{O}(\mathcal{P})$, as calculated in Appendix B, are shown in figure (4).

5.3 The effect of the boundary layer

Let us finally discuss the influence of the thermal boundary layer that must develop in the solid inner core near the melting side when a convective translation exists. From the thermal eq. (50), and with the boundary condition (54), a thermal boundary layer of thickness V^{-1} results from the balance between convective and diffusive terms, so that the degree one temperature component (97) may be approximated by

$$t_1^0 \simeq \frac{6}{V}\left[r - e^{V(r-1)}\right]. \tag{111}$$

We now note that

$$\mathcal{D}_1\left[\mathrm{e}^{V(r-1)}\right] = \left(1 + \frac{2}{Vr} - \frac{2}{V^2r^2}\right)V^2\mathrm{e}^{V(r-1)}, \tag{112}$$

so that to a good approximation,

$$\mathcal{D}_1\left[\mathrm{e}^{V(r-1)}\right] \simeq V^2\mathrm{e}^{V(r-1)} \quad \text{and} \quad \mathcal{D}_1^2\left(\mathrm{e}^{Vr}\right) \simeq V^4\mathrm{e}^{V(r-1)} \tag{113}$$

when $V \gg 1$. Under this assumption, the resulting general solution for the velocity poloidal component (101) becomes

$$p_1^0 \simeq \frac{V_0}{2}\left\{r + \left[Ar + Br^3 + Cr^5 - 10\frac{V_0^2}{V^6}\mathrm{e}^{V(r-1)}\right]\mathcal{P} + \mathcal{O}(\mathcal{P}^2)\right\}. \tag{114}$$

Following the same path as above, in the limit of infinite viscosity, the translation velocity V is found to be

$$V \simeq V_0\left(1 - \frac{5}{V_0} - \frac{5}{V_0^2} + \frac{30}{V_0^3} - \frac{30}{V_0^4}\right) \tag{115}$$

when the effect of the boundary layer is taken into account.

5.4 Melt production

We define the rate of melt production $\dot{M}$ as the volume of melt produced at the surface of the inner core by unit area and unit of time, averaged over the ICB. In the case of a pure translation, the volume of melt produced by unit of time is simply given by the translation velocity V multiplied by the cross-section $\pi r_{\rm ic}^2$ of the inner core, so $\dot{M}$ is given by

$$\dot{M} = \frac{V \times \pi r_{\rm ic}^2}{4\pi r_{\rm ic}^2} = \frac{V}{4}. \tag{116}$$

For a more general inner core flow, $\dot{M}$ can be calculated from the radial velocity at the ICB as

$$\dot{M} = \frac{1}{2}\overline{|u_r(r_{\rm ic}) - \dot{r}_{\rm ic}|} = \frac{1}{8\pi}\int_{\theta,\phi}|u_r(r_{\rm ic}) - \dot{r}_{\rm ic}|\sin\theta\,\mathrm{d}\theta\mathrm{d}\phi, \tag{117}$$

where the overbar $\overline{\cdots}$ denotes the average over a spherical surface. In the case of a $l = 1$, $m = 0$ flow, this reduces to

$$\dot{M} = \frac{1}{4\pi}\int_{\theta,\phi}|p_1^0\cos\theta|\sin\theta\,\mathrm{d}\theta\mathrm{d}\phi = \frac{1}{2}|p_1^0| \tag{118}$$

and gives $\dot{M} = V/4$ for a pure translation, which has $p_1^0 = V/2$.

6 NUMERICAL RESULTS AND SCALING LAWS

6.1 Method

The code is an extension of the one used in Deguen & Cardin (2011), with the boundary condition derived in Section 3 now implemented. The system of equations derived in Section 3 is solved in 3-D, using a spherical harmonic expansion for the horizontal dependence and a finite difference scheme in the radial direction. The radial grid can be refined below the ICB if needed. The non-linear part of the advection term in the temperature equation is evaluated in the physical space at each time step. A semi-implicit Crank- Nickolson scheme is implemented for the time evolution of the linear terms and an Adams–Bashforth procedure is used for the non-linear advection term in the heat equation. The temperature field is initialized with a random noise covering the full spectrum. We use up to 256 radial points and 128 spherical harmonics degree. Care has been taken that the ICB thermal boundary layer, which can be very thin in the translation mode, is always well resolved.

The code has the ability to take into account the growth of the inner core and the evolution of the internal heating rate $S(t)$, which is

calculated from the thermal evolution of the outer core (Deguen & Cardin 2011). In this section, we will first focus on simulations with a constant inner core radius and steady thermal forcing (internal heating rate S constant). Simulations with an evolving inner core will be presented in Section 7.

Each numerical simulation was run for at least 10 overturn times r_{ic}/U_{rms}, where U_{rms} is the rms velocity in the inner core.

6.2 Overview

As already suggested by the linear stability analysis (Section 4) and the small $\mathcal{P}$ analytical model (Section 5), the translation mode is expected to be dominant when $\mathcal{P}$ is small. This is confirmed by our numerical simulations. As an example, Fig. 5 shows outputs of simulations with the same Rayleigh number value of $Ra = 10^7$ and $\mathcal{P} = 1, 30, 10^2$ and 10^3. Snapshots of cross-sections of the potential temperature field and vorticity (its component perpendicular to the cross-section plane) are shown in the first and second columns, and maps of radial velocity $u_r(r_{ic})$ at the ICB are shown in the third column. $u_r(r_{ic})$ is equal to the local phase change rate, with positive values corresponding to melting and negative values corresponding to solidification.

At the lowest $\mathcal{P}$ ($\mathcal{P} = 1$), the translation mode is clearly dominant, with the pattern of temperature and vorticity similar to the predictions of the analytical models of Section 5 shown in Fig. 4. In contrast, the convection regime at the largest $\mathcal{P}$ ($\mathcal{P} = 10^3$) appears to be qualitatively similar to the regime observed with impermeable boundary conditions (Weber & Machetel 1992; Deguen & Cardin 2011), which corresponds to the limit $\mathcal{P} \to \infty$. At the Rayleigh number considered here, convection is chaotic and takes the form of cold plumes originating from a thin thermal boundary layer below the ICB, with a passive upward return flow. At intermediate values of $\mathcal{P}$ ($\mathcal{P} = 30$ and 10^2), phase change has still a significant effect on the pattern of the flow, with large scale components of the flow enhanced by phase change at the ICB, in qualitative agreement with the prediction of the linear stability analysis. Note that at $\mathcal{P} = 10^2$, there is still a clear hemispherical pattern, with plumes originating preferentially from one hemisphere.

More quantitative informations on the structure of convection can be found by estimating a characteristic length scale of the flow. We calculate here the mean degree $\bar{\ell}_u$ of the flow from the time averaged

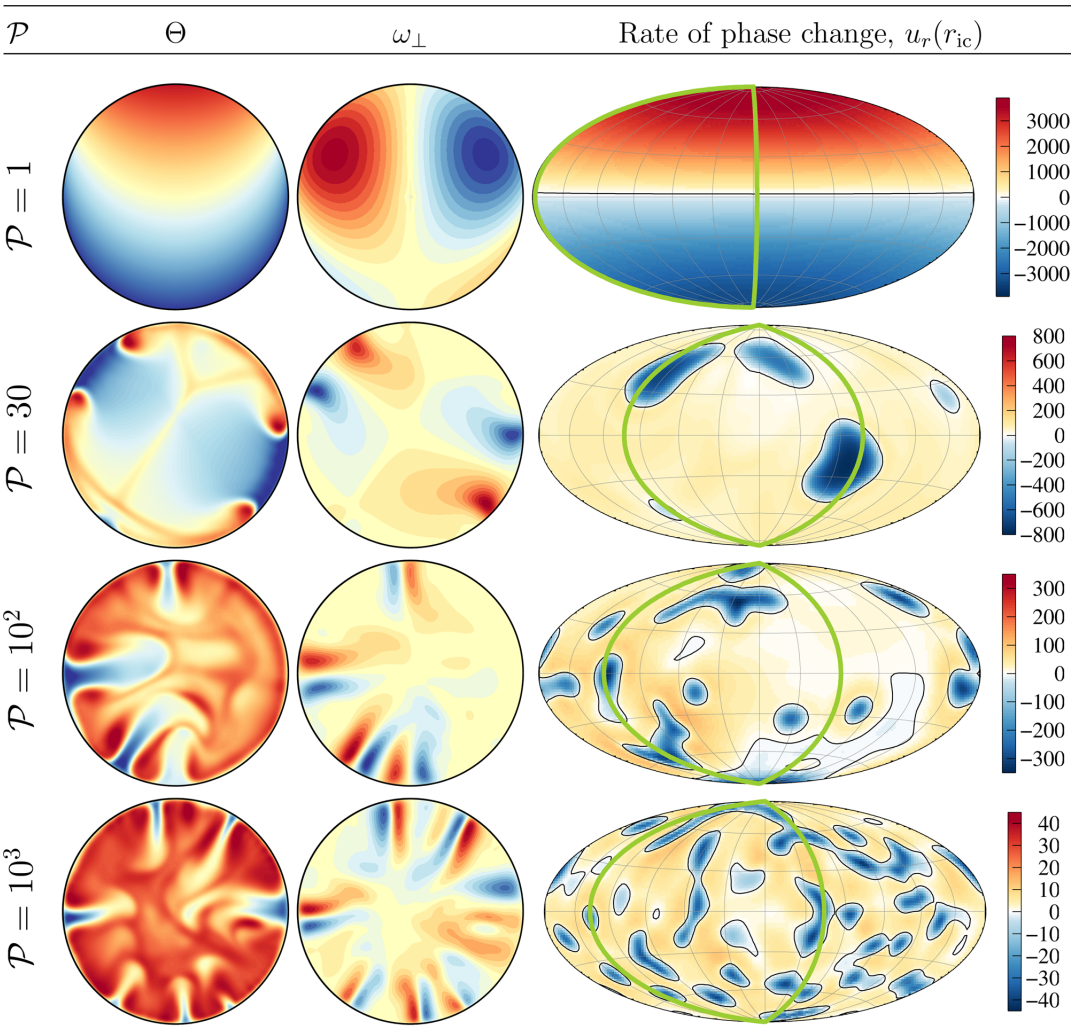

Figure 5. Snapshots from numerical simulations with $Ra = 10^7$ and $\mathcal{P} = 1$, 30, 100 and 10^3, showing potential temperature Θ (first column), azimuthal vorticity $\omega_\perp$ (second column) and radial velocity $u_r(r_{ic})$ at the outer boundary (third column).

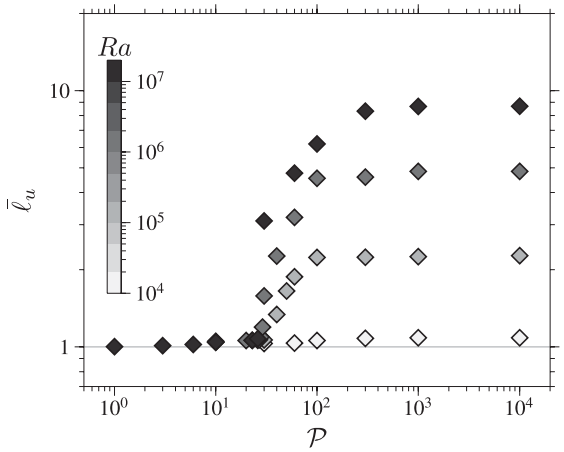

Figure 6. Mean degree $\bar{\ell}_u$ of the kinetic energy (as defined in eq. 119), as a function of $\mathcal{P}$, for simulations with $Ra = 10^4$, 10^5, 10^6 and 10^7. The grey scale of the markers give the Rayleigh number of the simulation. $\bar{\ell}_u$ is close to 1 for $\mathcal{P} \lesssim 29$ for all Ra, although the departure from 1 increases with Ra when $\mathcal{P}$ approaches 29 from below.

kinetic energy spectrum, defined by Christensen & Aubert (2006) as

$$\bar{\ell}_u = \frac{\sum_\ell \ell E_k^\ell}{E_k}, \tag{119}$$

where

$$E_k^\ell = \frac{1}{2}\sum_m (u_\ell^m)^2 \quad \text{and} \quad E_k = \sum_\ell E_k^\ell. \tag{120}$$

With this definition, $\bar{\ell}_u \to 1$ if the flow is dominated by degree 1 components, as in the translation mode, and increases as the characteristic length scale of the flow decreases.

Fig. 6 shows the calculated value of $\bar{\ell}$ for $Ra = 10^4$, 10^5, 10^6 and 10^7 as a function of $\mathcal{P}$. $\bar{\ell}$ remains very close to 1 as long as $\mathcal{P}$ is smaller than a transitional value $\mathcal{P}_t \simeq 29$. There is a rapid increase of $\bar{\ell}_u$ above $\mathcal{P}_t$, showing the emergence of smaller scale convective modes at the transition between the translation mode and the high-$\mathcal{P}$ regime. We interpret this sharp transition as being due to the negative feedback that the secondary flow and smaller scale convection have on the translation mode: advection of the potential temperature field by the secondary flow decreases the strength of its degree one component and therefore weakens the translation mode, which in turn give more time for smaller scale convection to develop, weakening further the degree one heterogeneity. The value of $\mathcal{P}_t$ does not seem to depend on Ra in the range explored here. Fig. 6 further shows that ICB phase change has a strong influence on the flow up to $\mathcal{P} \simeq 300$, which is confirmed by direct visualization of the flow structure.

Fig. 7a shows the translation rate V (circles) and time averaged rms velocity (triangles) as a function of $\mathcal{P}$ for various values of Ra. Here both V and $U_{\rm rms}$ are multiplied by $Ra^{-1/2}$. The grey dashed line shows the analytical prediction for the translation rate in the rigid inner core limit. Below $\mathcal{P}_t$, there is a good quantitative agreement between the numerical results and the analytical model. The fact that $U_{\rm rms} \simeq V$ for $\mathcal{P} < \mathcal{P}_t$ indicates that there is, as expected, negligible deformation in this regime. V and $U_{\rm rms}$ diverge for $\mathcal{P} > \mathcal{P}_t$, the translation rate becoming rapidly much smaller than the rms velocity. As already suggested by the evolution of $\bar{\ell}$, phase change at the ICB has still an effect on the convection for $\mathcal{P}$ up to ~300. Phase change at the ICB has a positive feedback on the vigor of the convection: melting occurs preferentially above upwelling, where the dynamic topography is positive, which enhances upward motion. Conversely, solidification occurs preferentially above downwellings, thus enhancing downward motions. This effect becomes increasingly small as $\mathcal{P}$ is increased, and the rms velocity reaches a plateau when $\mathcal{P} \gtrsim 10^3$, at which the effect of phase change at the ICB on the internal dynamics becomes negligible.

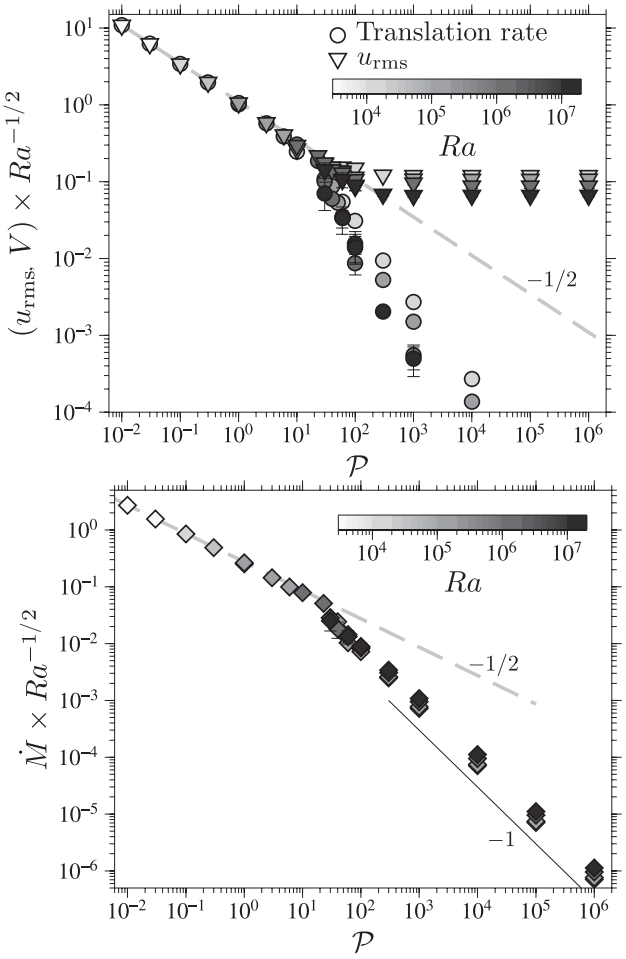

Figure 7. (a) Rms velocity (triangles) and translation velocity (circles) as a function of $\mathcal{P}$, for Rayleigh numbers between 3×10^3 and 10^7 (grey scale). The inner core translation rate is found by first calculating the net translation rate $V_{i=x,y,z}$ of the inner core in the directions x, y, z of a cartesian frame, given by the average over the volume of the inner core of the velocity component $u_{i=x,y,z}$ [which can be written as functions of the degree 1 components of the poloidal scalar at the ICB, see eq. (B42) in Appendix B]. We then write the global translation velocity as $V = \sqrt{V_x^2 + V_y^2 + V_z^2}$. The grey dashed line shows the prediction of the rigid inner core model. (b) $\dot{M} \times Ra^{-1/2}$ as a function of $\mathcal{P}$, the grey scale of the markers giving the value of Ra. The grey dashed line shows the prediction of the rigid inner core model, showing excellent agreement between the theory and the numerical calculations for $\mathcal{P}$ small.

Fig. 7(b) shows the rate of melt production (defined in eq. 117), multiplied by $Ra^{-1/2}$, as a function of $\mathcal{P}$ for various values of Ra. Again, the prediction of the rigid inner core model (eq. 116, grey dashed line in Fig. 7 b) is in very good agreement with the numerical results as long as $\mathcal{P} < \mathcal{P}_t$. For $\mathcal{P} > \mathcal{P}_t$, the rate of melt production appears to be inversally proportional to $\mathcal{P}$.

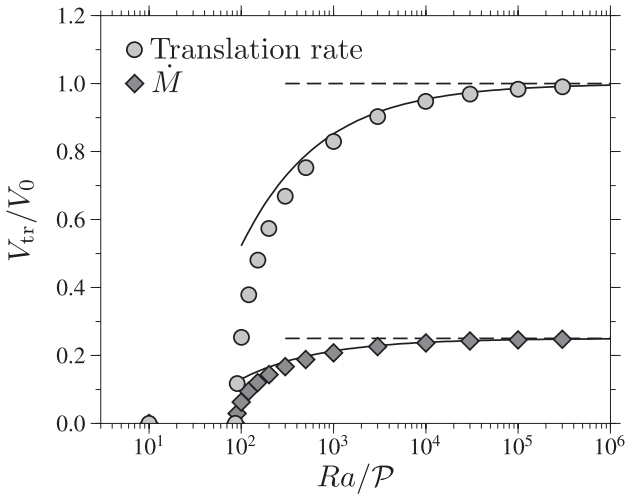

Figure 8. Translation rate and melt production, normalized by the low $\mathcal{P}$ limit estimate given by eq. (107), as a function of $Ra/\mathcal{P}$, for $\mathcal{P} = 10^{-2}$.

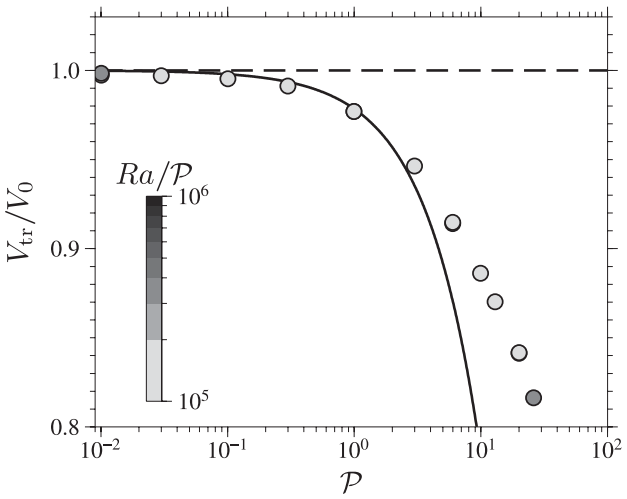

Figure 9. Translation rate (normalized by the low $\mathcal{P}$ limit estimate given by eq. (107)) as a function of $\mathcal{P}$, for different values of $Ra/\mathcal{P}$. The thick black line show the prediction of the $\mathcal{O}(\mathcal{P})$ model given by eq. (110).

6.3 Scaling of translation rate, convective velocity and melt production

We now turn to a more quantitative description of the small-$\mathcal{P}$ and large-$\mathcal{P}$ regimes. We first compare the results of numerical simulations at $\mathcal{P} < \mathcal{P}_t$ with the analytical models developed in Section 5. We then focus on the large-$\mathcal{P}$ regime, and develop a scaling theory for inner core thermal convection in this regime, including a scaling law for the rate of melt production.

6.3.1 Translation mode

Fig. 8 shows the translation rate (circles) and the rate of melt production $\dot{M}$ (diamonds), normalized by the rigid inner core estimate given by eq. (107), as a function of $Ra/\mathcal{P}$, for $\mathcal{P} = 10^{-2}$. The translation rate increases from zero when $Ra/\mathcal{P}$ is higher than a critical value $(Ra/\mathcal{P})_c$ which is found to be in excellent agreement with the prediction of the linear stability analysis. Increasing $Ra/\mathcal{P}$ above $(Ra/\mathcal{P})_c$, the translation rate increases before asymptoting towards the prediction of the rigid inner core model (dashed line). The prediction of our model including a boundary layer correction (eq. 115, black line in Fig. 8) is in good agreement with the numerical results for $Ra/\mathcal{P} \gtrsim 10^3$, demonstrating that our analytical model captures fairly well the effect of the thermal boundary layer. As expected (see Section 5.4), the rate of melt production is equal to 1/4 of the translation rate.

Fig. 9 shows the effect of increasing $\mathcal{P}$ on the translation rate. In this figure, we have kept only simulations with $Ra/\mathcal{P}$ larger than 10^5 to minimize the effect of the boundary layer, and further corrected the translation velocity with the boundary layer correction (eq. 115) found in Section 5.3, in order to isolate as much as possible the effect of $\mathcal{P}$ on the translation mode. The $\mathcal{O}(\mathcal{P})$ model developed in Section 5.2 (eq. 110, black line) agrees with the numerical simulations within 1 per cent for $\mathcal{P}$ up to $\sim$3, but fails to explain the outputs of the numerical simulations when $\mathcal{P}$ is larger, which indicates that higher order terms in $\mathcal{P}$ become important.

Overall, our analytical results (stability analysis and finite amplitude models) are in very good agreement with our numerical simulations when $\mathcal{P}$ is small, which gives support to both our theory and to the validity of the numerical code.

6.3.2 Plume convection

If $\mathcal{P}$ is large, the translation rate of the inner core becomes vanishingly small, but, as long as $\mathcal{P}$ is finite, there is still a finite rate of melt production associated with the smaller scale topography arising from plume convection. A scaling for the melt production in the limit of large $\mathcal{P}$ and large Ra can be derived from scaling relationship for infinite Prandtl number convection with impermeable boundaries. Parmentier & Sotin (2000) derived a set of scaling laws for high Rayleigh number internally heated thermal convection in a cartesian box, in the limit of infinite Prandtl number, but we found significant deviations from their model in our numerical simulations, which we ascribe to geometrical effects due to the spherical geometry. We therefore propose a set of new scaling laws for convection in a full sphere with internal heating.

Quantities of interest are the horizontal and vertical velocities u and w, the mean inner core potential temperature $\langle\Theta\rangle$, the thermal boundary layer thickness δ, the thermal radius of the plumes a, the average plume spacing λ_h, and a length scale for radial variations of the velocity, which we note λ_r (see Fig. 10). The horizontal length scale λ_h is related to the number N of plumes per unit area by $N \sim 1/\lambda_h^2$.

Outputs of numerical simulations ($\langle\Theta\rangle$, δ, rms velocity $U_{\rm rms}$, rms radial velocity $w_{\rm rms}$, rms horizontal velocity $u_{\rm rms}$, N) are shown in Figs 11(a)–(d) for Ra between 10^5 and 3×10^8. The boundary layer thickness δ is estimated as the ratio of the mean potential temperature in the inner core, $\langle\Theta\rangle$, over the time and space averaged potential temperature gradient at the ICB: $\delta = -\langle\Theta\rangle / \langle\partial\Theta/\partial r\rangle_{\rm icb}$. The time-averaged number N of plume per unit area is estimated by counting plumes on horizontal surfaces on typically 50 different snapshots. Both $\langle\Theta\rangle$ and δ follow well-defined power law behaviours over this range of Ra. In contrast, the rms velocities and plume density N seem to indicate a change of behaviour at Ra close to 10^7. For $Ra < 10^7$, the vertical velocity increases faster than the horizontal velocity, while at larger Ra horizontal and vertical velocities increase with Ra at roughly the same rate.

We start our analysis by first noting that under statistically steady state conditions, the heat flux at the ICB must be equal, in a time-averaged sense, to the heat production within the inner core. In the

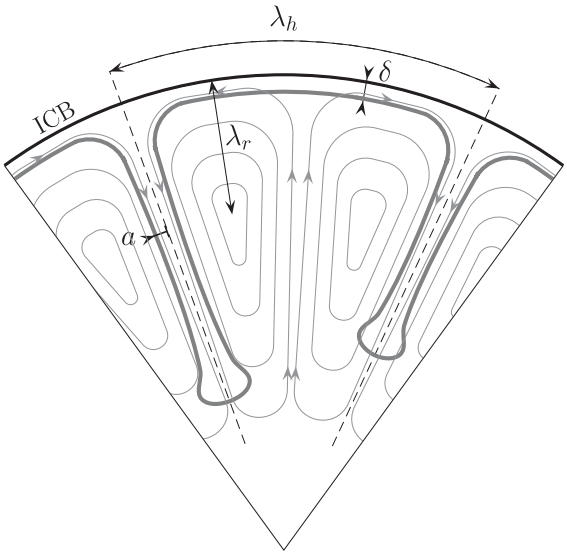

Figure 10. A schematic of inner core plume convection, and definition of the length scales used in the scaling analysis. Streamlines of the flow are shown with thin arrowed grey lines.

thermal boundary layer, heat transport is dominated by conduction and the non-dimensional heat flux $-\langle\partial\Theta/\partial r\rangle_{\rm icb}$ is equal to $\langle\Theta\rangle/\delta$. This must be in balance with the non-dimensional internal heat production. With our scaling, the mean potential temperature gradient should be equal to –2 on average, which implies that δ should be equal to $\langle\Theta\rangle/2$. We can therefore write

$$\delta = \frac{\langle\Theta\rangle}{2} \sim Ra^{\beta}, \tag{121}$$

where β is to be determined. We further assume that the thickness of the thermal boundary layer is set by a local stability criterion, that is, that the boundary layer Rayleigh number $Ra_\delta = (\alpha\rho_s g_{\rm icb}\Theta\delta^3)/(\kappa\eta)$ is on average equal to some constant, which is equivalent to state that $Ra_\delta \sim 1$. Using non-dimensional $\langle\Theta\rangle$ and δ, Ra_δ is related to the inner core Rayleigh number Ra by $Ra_\delta = Ra\,\langle\Theta\rangle\delta^3$. Given that $\langle\Theta\rangle \sim \delta$, this implies that $Ra\langle\Theta\rangle\delta^3 \sim Ra\,\delta^4 \sim 1$, which gives $\beta = -1/4$.

The best fit of the numerical results (Figs 11a and b) gives $\langle\Theta\rangle \sim Ra^{-0.240\pm0.005}$ and $\delta \sim Ra^{-0.236\pm0.003}$, in fair agreement with the predicted scaling. In Cartesian geometry, Parmentier & Sotin (2000) found $\beta = -0.2448$. Deschamps *et al.* (2012) found $\beta = -0.238$ for thermal convection in internally heated spherical shells.

The vertical plume velocity w is set by a balance between the buoyancy stress, $\sim Ra\langle\Theta\rangle a$, and the viscous stress, $\sim w/\lambda_h$. This gives

$$\frac{w}{\lambda_h} \sim Ra\,\langle\Theta\rangle\,a. \tag{122}$$

In addition, the heat flux advected by the plumes, $Nw\langle\Theta\rangle a^2$, must scale as the ICB heat flux, which, as already discussed above, must be $\sim$1. Since the number of plumes per unit area is $N \sim 1/\lambda_h^2$, this

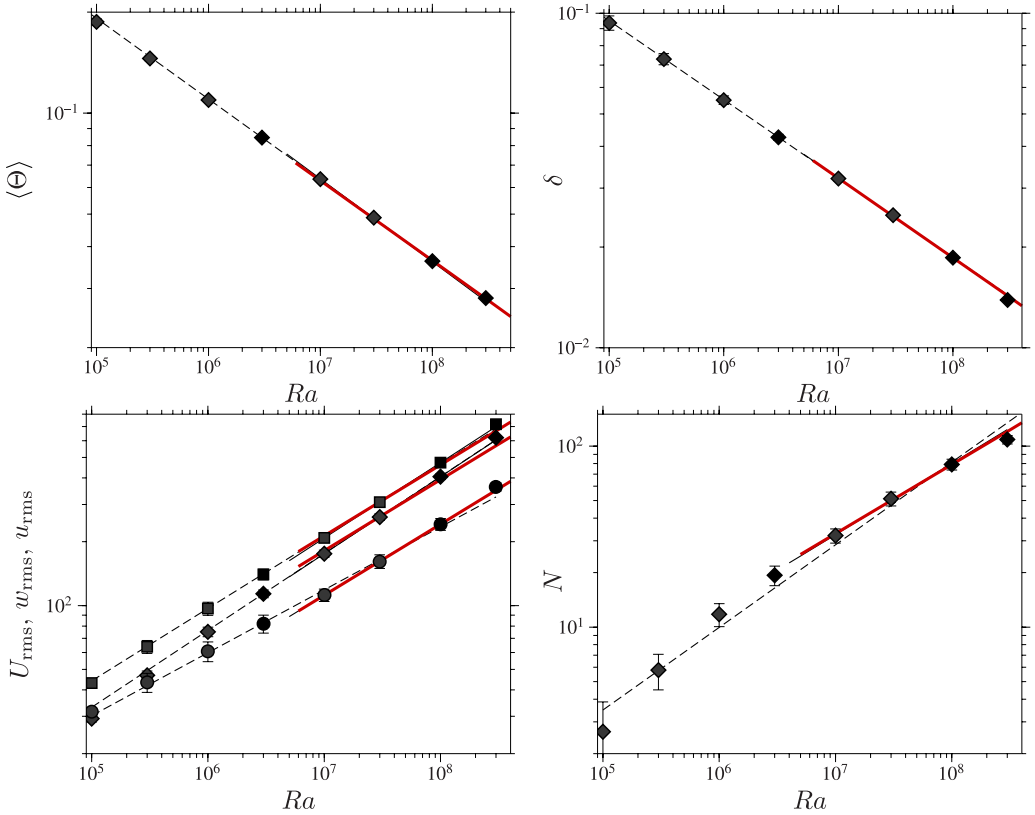

Figure 11. (a) Mean potential temperature $\langle\Theta\rangle$ as a function of Ra for $\mathcal{P}$ larger than 10^3. (b) Boundary layer thickness δ. (c) RMS velocity $U_{\rm rms}$ (squares), rms vertical velocity $w_{\rm rms}$ (diamonds), and rms horizontal velocity $u_{\rm rms}$ (circles). (d) Number of plumes N per unit surface. In figures (a) to (d), the thick red lines show the predictions of the scaling theory developed in Section 6.3.2 with $\beta = -0.238$. The dashed lines show the result of the individual least square inversion for each quantity for $Ra \geq 10^5$.

gives

$$1 \sim \frac{a^2}{\lambda_h^2}\langle\Theta\rangle w. \tag{123}$$

The plume thermal radius a is related to the thermal boundary layer thickness through the conservation of mass, which when applied at the roots of the plumes implies that

$$\delta u \sim a w. \tag{124}$$

Finally, conservation of mass in one convective cell implies that

$$\frac{u}{\lambda_h} \sim \frac{w}{\lambda_r}. \tag{125}$$

This gives four eqs (122)–(125) for five unknowns (u, w, a, λ_h, λ_r). The system can be solved if additional assumptions are made on the scaling of λ_r. For high Pr, low Re convection, a natural choice would be to assume that radial variations of w occur at the scale of the radius of the inner core. This implies $\lambda_r \sim 1$, and solving the system of eqs (122)–(125) with $\beta = -0.24$ gives $a \sim Ra^{-0.14}$, $u \sim Ra^{0.82}$, $w \sim Ra^{0.72}$ and $N \sim Ra^{-0.2}$, which agrees very poorly with the numerical results.

This poor agreement might be due to the spherical geometry. In a sphere, plumes converge towards each others while sinking, which is not the case in cartesian boxes, and is not a very significant effect in a spherical shell for which, like in Earth's mantle, the radius of the inner shell is a significant fraction of that of the outer shell. If Ra is large and the average plume spacing is small compared to the inner core radius, we might expect that the geometry of the convective cells becomes self-similar, with $\lambda_r \sim \lambda_h$. With this assumption, we obtain

$$\lambda_h \sim \lambda_r \sim Ra^{1+5\beta}, \tag{126}$$

$$u \sim w \sim Ra^{2+7\beta}, \tag{127}$$

$$a \sim \delta \sim \langle\Theta\rangle \sim Ra^{\beta}. \tag{128}$$

Assuming a scaling of the form given by eqs (126)–(128), it is possible to inverse simultaneously all variables for β, the result of the inversion being $\beta = -0.238 \pm 0.003$ ($\pm 1\sigma$). The prediction of eqs (126)–(128) with this value of β are shown with red lines in Fig. 11a–d for $Ra \geq 10^7$. They agree with the numerical outputs almost as well as individual inversions, which demonstrates the self-consistency of our scaling theory.

We can now derive a scaling for the rate of melt production $\dot{M}$. The starting point is the continuity of the normal stress at the ICB, given by eq. (57). The local melting/solidification rate is given by the value of $u_r - \dot{r}_{\rm ic}$ at the ICB ($u_r - \dot{r}_{\rm ic} > 0$ means melting, and $u_r - \dot{r}_{\rm ic} < 0$ means solidification) which, according to eq. (57), can be written as

$$u_r - \dot{r}_{\rm ic} = \mathcal{P}^{-1}\left(-2\frac{\partial u_r}{\partial r} + \hat{p}\right). \tag{129}$$

As discussed above, we have

$$\left.\frac{\partial u_r}{\partial r}\right|_{\rm icb} \sim \frac{w}{\lambda_r} \sim Ra^{1+2\beta}. \tag{130}$$

The dynamic pressure is given by the horizontal component of the Stokes equation,

$$0 = -\nabla_H \hat{p} + (\Delta u)_H \tag{131}$$

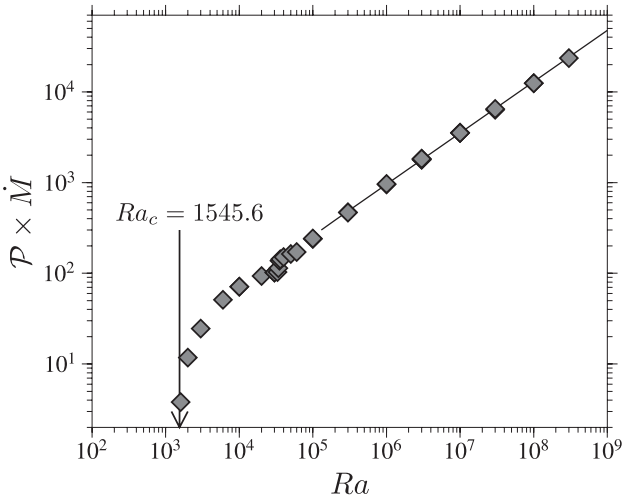

Figure 12. Rate of melt production (multiplied by $\mathcal{P}$) as a function of Ra, for numerical simulations with $\mathcal{P} \geq 10^3$. The value of the critical Rayleigh number as predicted by the linear stability analysis in the limit of infinite $\mathcal{P}$ (eq. 89, $Ra_c = 1545.6$) is indicated by the arrow.

which implies that

$$\hat{p} \sim \frac{u}{\lambda_h} \sim Ra^{1+2\beta}. \tag{132}$$

Both terms follow the same scaling, which implies that the global rate of melt production scales as

$$\dot{M} \sim Ra^{1+2\beta}\mathcal{P}^{-1}. \tag{133}$$

With $\beta = -0.238 \pm 0.003$, we obtain $\dot{M} \sim Ra^{0.524\pm0.006}\mathcal{P}^{-1}$.

Fig. 12(b) shows $\mathcal{P}\dot{M}$ as a function of Ra, for $\mathcal{P} \geq 10^3$ corresponding to the plume convection regime. There is an almost perfect collapse of the data points, which supports the fact that $\dot{M} \propto \mathcal{P}$ in this regime. The kink in the curve at $Ra \simeq 3 \times 10^4$ corresponds to the transition from steady convection to unsteady convection. Above this transition, the data points are well fitted by a power law of the form $\dot{M} = a\mathcal{P}^{-1}Ra^b$. Least-square regression for $Ra \geq 3 \times 10^5$ gives $a = 0.46 \pm 0.04$ and $b = 0.554 \pm 0.006$, in reasonable agreement with the value found above. In dimensional terms, $\dot{M} \simeq a(\kappa/r_{\rm ic})\mathcal{P}^{-1}Ra^b$ and the mass flux of molten material is $\rho_{\rm ic}\dot{M} \simeq ak/(c_p r_{\rm ic})\mathcal{P}^{-1}Ra^b$.

7 APPLICATION

7.1 Evolutive models

The analytical model for the translation mode and the scaling laws for large-$\mathcal{P}$ convection derived in the previous sections strictly apply only to convection with $r_{\rm ic}$ and S constant. We therefore first check that our models correctly describe inner core convection when $r_{\rm ic}$ and S are time-dependent, by comparing their predictions with the outcome of numerical simulations with inner core growth and thermal history determined from the core energy balance.

To account for the inner core secular evolution, we follow the procedure explained in Deguen & Cardin (2011), where the growth of the inner core and its cooling rate are determined from the core energy balance. In this framework, a convenient way to write $S(t)$ is

$$S = \frac{\rho_s g' \gamma T}{K_S} 3\kappa \left[f(r_{\rm ic})\,\mathcal{T}_{\rm ic}^{-1} - 1\right], \tag{134}$$

Table 2. Correspondence between τ_{ic} and $\mathcal{T}_{ic}$ for three values of inner core thermal conductivity, assuming $dT_s/dT_{ad} = 1.65 \pm 0.11$ (Deguen & Cardin 2011).

		k (W m^{-1} K^{-1})		
		36	79	150
$\mathcal{T}_{ic} =$	0.8	1.18 ± 0.23 Gy	0.54 ± 0.11 Gy	0.28 ± 0.06 Gy
	1.0	1.48 ± 0.29 Gy	0.68 ± 0.13 Gy	0.36 ± 0.07 Gy
	1.2	1.77 ± 0.35 Gy	0.81 ± 0.16 Gy	0.43 ± 0.08 Gy

where $f(r_{ic})$ is a decreasing order one function of r_{ic} defined in Deguen & Cardin (2011) (eq. 19, p. 1104), $g' = dg/dr$, K_S is the isentropic bulk modulus, γ the Grüneisen parameter, and

$$\mathcal{T}_{ic} = \left(\frac{dT_s}{dT_{ad}} - 1 \right)^{-1} \frac{\tau_{ic}}{\tau_\kappa}, \tag{135}$$

where τ_{ic} is the age of the inner core, $\tau_\kappa = r_{ic}^{*2}/(6\kappa)$ is the current inner core thermal diffusion time, and dT_s/dT_{ad} is the ratio of the Clapeyron slope dT_s/dP to the adiabat dT_{ad}/dP. The non-dimensional inner core age $\mathcal{T}_{ic}$ is a convenient indicator of the thermal state of the inner core, with $\mathcal{T}_{ic} < 1$ implying unstable stratification for most of inner core history (see Deguen & Cardin 2011, fig. 3a). We give for reference in Table 2 the values of the age of the inner core τ_{ic} corresponding to $\mathcal{T}_{ic} = 0.8$, 1 and 1.2, for a thermal conductivity equal to 36, 79 and 150 W m^{-1} K^{-1}. With the inner core growth history determined from the core energy balance and $S(t)$ calculated from eq. (134), the evolution of $Ra(t)$ and $\mathcal{P}(t)$ can then be calculated.

Fig. 13(a) shows the trajectories of the inner core state in a $Ra - \mathcal{P}$ space for four different scenarios, superimposed on a regime diagram for inner core thermal convection. According to eq. (6), the ICB phase change timescale scales as $\tau_\phi \propto r_{ic}^{-1}$, and therefore $\mathcal{P} \propto r_{ic}$ always increases during inner core history. In contrast, the evolution of $Ra(t)$ is non monotonic, with the effect of the increasing inner core radius and gravity opposing the decrease with time of the effective heating rate $S(t)$. Because S eventually becomes negative at some time in inner core history, Ra reaches a maximum before decreasing and eventually becoming negative, resulting in a bell shaped trajectory of the inner core in the $Ra - \mathcal{P}$ space. The maximum in Ra may or may not have been reached yet, depending on the value of $\mathcal{T}_{ic}$.

The scenarios A–D shown in Fig. 13a have been chosen to illustrate four different possible dynamic histories of the inner core. In cases A and C, which have $\mathcal{T}_{ic} = 0.8$, Ra remains positive and supercritical up to today, thus always permitting thermal convection. In cases B and D, which have $\mathcal{T}_{ic} = 1$, Ra has reached a maximum early in inner core history, before decreasing below supercriticality, at which point convection is expected to stop. In these two cases, only an early convective episode is expected (Buffett 2009; Deguen & Cardin 2011). In cases A and B, which have $\eta = 10^{20}$ Pa s, $\mathcal{P}(t)$ is always smaller than the transitional $\mathcal{P}_t$ and thermal convection therefore should be in the translation regime; Cases C and D, which have $\eta = 10^{17}$ Pa s, have $\mathcal{P}(t) > 10^2 > \mathcal{P}_t$ and thermal convection should be in the plume regime.

Fig. 13(b) shows outputs from numerical simulations corresponding to the inner core histories shown in Fig. 13(a). The numerical results are compared to the predictions for the rms velocity U_{rms}

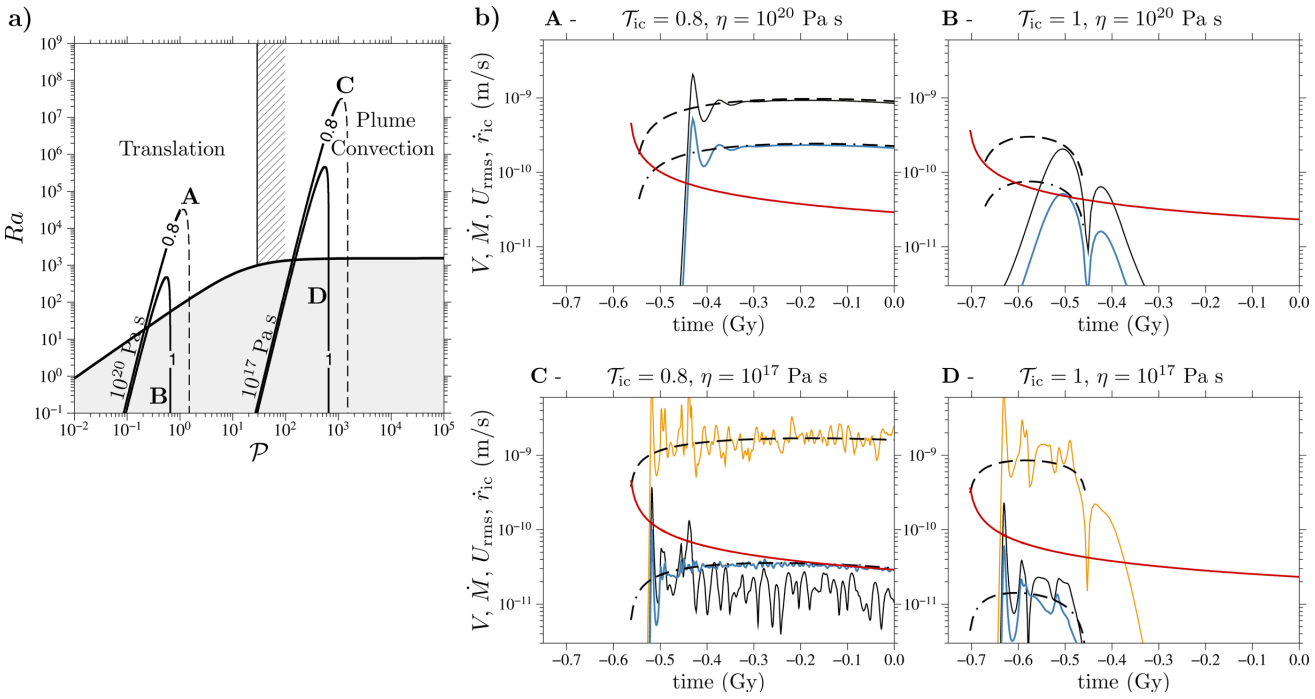

Figure 13. (a) Trajectories of the inner core state in a $Ra - \mathcal{P}$ space, for the four cases A, B, C and D discussed in the text. The line annotations give the value of $\mathcal{T}_{ic}$ for each case. The dashed lines shows the future trajectory of the inner core. (b) Time evolution of V, $\dot{M}$, U_{rms} and $\dot{r}_{ic}$ for cases A to D. Red line: inner core growth rate $\dot{r}_{ic}$. Black line: translation rate V. Orange line-: rms velocity U_{rms}. Blue line: dimensional melting rate $(\kappa/r_{ic})\dot{M}$. Predictions for the rms velocity (or translation velocity in the translation regime) and melting rate $\dot{M}$ are shown with thick dashed and dash-dotted lines, respectively. In the $\eta = 10^{20}$ Pa s cases, the translation model (eq. 115) is used to predict V and $\dot{M}$. In the $\eta = 10^{17}$ Pa s case, the high-$\mathcal{P}$ scaling is used for U_{rms} and $\dot{M}$. In the $\eta = 10^{20}$ Pa s, $\mathcal{T}_{ic} = 0.8$ and $\mathcal{T}_{ic} = 1$ cases, the translation rate and the rms velocity are equal. For these simulations, the Rayleigh number was calculated assuming a thermal conductivity $k = 79$ W m^{-1} K^{-1} and a phase change timescale $\tau_\phi = 1000$ yr. Values of other physical parameters used for these runs are summarized in Table 1.

(equal to the translation rate V_{tr} in the translation regime) and melting rate $\dot{M}$ from the analytical translation model (eq. 116) and the large-$\mathcal{P}$ scaling laws (eq. 133). The agreement is good in both the translation and plume convection regimes, except at the times of initiation and cessation of convection.

There is always a lag between when conditions become supercritical and when the amplitude of convective motions become significant, due to the finite growth rate of the instability. From eq. (88), the timescale for instability growth, $\tau = 1/\sigma$, is approximately (in dimensional form)

$$\tau \simeq 5\frac{r_{\rm ic}^2}{\kappa}\left(\frac{Ra}{\mathcal{P}} - \frac{Ra}{\mathcal{P}}\bigg|_c\right)^{-1} \simeq \left(\frac{r_{\rm ic}}{600\ \text{km}}\right)^2 \frac{90\ \text{Myr}}{\frac{Ra}{\mathcal{P}}\frac{Ra}{\mathcal{P}}\big|_c} - 1 \qquad (136)$$

in the translation regime, and

$$\tau \simeq 77\frac{r_{\rm ic}^2}{\kappa}(Ra - Ra_c)^{-1} \simeq \left(\frac{r_{\rm ic}}{600\ \text{km}}\right)^2 \frac{80\ \text{Myr}}{Ra/Ra_c - 1} \qquad (137)$$

in the large-$\mathcal{P}$ regime. In both cases, the timescale for the growth of the instability will typically be a few tens of Myr, thus explaining the delayed initiation of convection seen in the numerical simulations.

In cases B and D, the flow occurring after $t \simeq -0.46$ Gy, at a time where the models predict no motion (because $S < 0$), corresponds to a slow relaxation of the thermal heterogeneities left behind by the convective episode.

Apart during the initiation and cessation periods of convection, the models developed for steady internal heating and constant inner core radius agree very well with the full numerical calculations, and can therefore be used to predict the dynamic state of the inner core and key quantities including rms velocity and melt production rate.

7.2 Melt production

Experiments by Alboussière *et al.* (2010) have shown that the development of a stably stratified layer above the ICB by inner core melting is controlled by the ratio Φ_B of the buoyancy fluxes arising from the melting and freezing regions of the ICB. By using the analytical translation model and the scaling laws for plume convection developed in the last two sections, we can now estimate today's value of Φ_B as a function of the state and physical properties of the inner core, and assess the likelihood of the origin of the F-layer by inner core melting.

With $\dot{M}$ being the non-dimensional rate of melt production defined in eq. (117), the mean solidification rate is $(\kappa/r_{\rm ic})\dot{M} + \dot{r}_{\rm ic}$ from conservation of mass. The buoyancy flux associated with the release of dense fluid by melting can be written as $-\Delta\rho_\chi\, g_{\rm icb}(\kappa/r_{\rm ic})\dot{M}$, while the buoyancy flux associated with the solidification is $\Delta\rho_\chi\, g_{\rm icb}[(\kappa/r_{\rm ic})\dot{M} + \dot{r}_{\rm ic}]$, where $\Delta\rho_\chi$ is the fraction of the ICB density jump due to the compositional difference. According to Alboussière *et al.* (2010)'s experiments, a stratified layer is expected to form above the ICB if the magnitude of the buoyancy flux associated with melting is more than 80 per cent of the buoyancy flux associated with solidification, that is, if

$$\Phi_B = \frac{\Delta\rho_\chi\, g_{\rm icb}(\kappa/r_{\rm ic})\dot{M}}{\Delta\rho_\chi\, g_{\rm icb}[(\kappa/r_{\rm ic})\dot{M} + \dot{r}_{\rm ic}]} = \frac{\dot{M}}{\dot{M} + \dot{r}_{\rm ic}\, r_{\rm ic}/\kappa} > 0.8, \qquad (138)$$

which requires that

$$\frac{\kappa}{r_{\rm ic}}\dot{M} > 4\dot{r}_{\rm ic}. \qquad (139)$$

In the translation regime, in which $\dot{M} = V/4$, this requires that the rate of translation is at least 16 times larger than the mean solidification rate of the inner core.

The current inner core growth rate can be expressed as

$$\dot{r}_{\rm ic} = \frac{3\kappa}{r_{\rm ic}} \frac{f(r_{\rm ic})}{\left(\frac{dT_s}{dT_{\rm ad}} - 1\right)\mathcal{T}_{\rm ic}} \qquad (140)$$

where the function $f(r_{\rm ic}) \simeq 0.8$ at the current inner core radius (Deguen & Cardin 2011). Using this expression, the buoyancy ratio Φ_B is

$$\Phi_B = 1 - \left[1 + \left(\frac{dT_s}{dT_{\rm ad}} - 1\right)\frac{\mathcal{T}_{\rm ic}}{3f(r_{\rm ic})}\frac{V}{4}\right]^{-1} \qquad (141)$$

in the translation regime, with the translation velocity V given by eq. (115), and

$$\Phi_B = 1 - \left[1 + \left(\frac{dT_s}{dT_{\rm ad}} - 1\right)\frac{\mathcal{T}_{\rm ic}}{3f(r_{\rm ic})}a\mathcal{P}^{-1}Ra^b\right]^{-1} \qquad (142)$$

in the high-$\mathcal{P}$ regime.

7.3 Today's inner core regime and rate of melt production

The inner core dynamic regime depends mostly on the value of its non-dimensional age $\mathcal{T}_{\rm ic}$ and of $\mathcal{P}$, both parameters being very poorly constrained. The value of $\mathcal{T}_{\rm ic}$ dictates whether the inner core has a stable or unstable temperature profile, and the parameter $\mathcal{P}$ determines the convection regime if the inner core is unstable against thermal convection. Other parameters have a comparatively small influence on the inner core dynamics, and on the value of Φ_B. With this idea in mind, it is useful to rewrite the Rayleigh number as a function of $\mathcal{P}$ and $\mathcal{T}_{\rm ic}$:

$$Ra = \frac{\alpha\rho_s g_{\rm icb} S r_{\rm ic}^5}{6\kappa^2\eta}$$

$$= \mathcal{A}\left[f(r_{\rm ic})\,\mathcal{T}_{\rm ic}^{-1} - 1\right]\mathcal{P}, \quad \text{with } \mathcal{A} = \frac{\alpha^2\rho_s^2 g_{\rm icb} r_{\rm ic}^3 T}{2\,k\,\Delta\rho\,\tau_\phi}. \qquad (143)$$

The exact value of the pre-factor $\mathcal{A}$ affects the value of Φ_B, but not the inner core regime (stably stratified inner core, translation, or plume convection) which is determined by $\mathcal{P}$ and $\mathcal{T}_{\rm ic}$. The uncertainty on $\mathcal{A}$ comes mostly from the uncertainty on τ_ϕ, which is difficult to estimate without a better understanding of the dynamics of the F-layer. If $\mathcal{P}$ and $\mathcal{T}_{\rm ic}$ are kept constants, changing $\mathcal{A}$ by an order of magnitude would change the translation velocity and melting rates (in both regimes) by a factor of ~3. Fig. 14 shows Φ_B as a function of $\mathcal{T}_{\rm ic}$ and $\mathcal{P}$, calculated from eqs (141) and (142) with Ra given by eq. (143) and $\mathcal{A} = 3 \times 10^5$ (corresponding to parameters values given in Table 1). Fig. 14 serves both as a regime diagram for the inner core, and as a predictive map for Φ_B and the likelihood of the development of a stratified layer at the base of the outer core.

The inner core has currently an unstable thermal profile only if $\mathcal{T}_{\rm ic}$ is smaller than ≃0.87. The mode of thermal convection then depends on $\mathcal{P}$, with the translation regime (small $\mathcal{P}$) being the most efficient at producing melt. Plume convection generates less melt, but the rate of melt production still remains significant as long as $\mathcal{P}$ is not too large (η not too small). The critical value of $\Phi_B = 0.8$ (white contour in Fig. 14) suggested by the experiments of Alboussière *et al.* (2010) is almost always reached in the translation regime, but only in a small part of the parameter space in the plume convection regime.

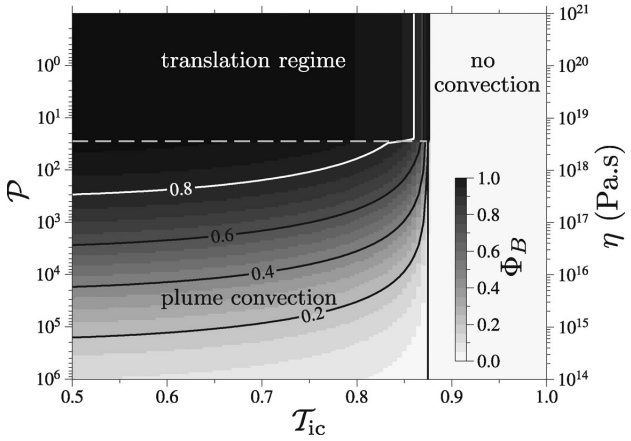

Figure 14. Inner core regime diagram and map of the buoyancy ratio Φ_B, as functions of $\mathcal{P}$ and $\mathcal{T}_{ic}$. The corresponding values of η assuming $\tau_\phi = 1000$ yr are given on the right hand size vertical axis. According to Alboussière *et al.* (2010)'s experiments, inner core melting can produce a stably stratified layer at the base of the outer core if $\Phi_B > 0.8$ (white contour).

8 COMPOSITIONAL EFFECTS

We have so far left aside the possible effects of the compositional evolution of the outer and inner core on the inner core dynamics. We will argue here that the development of an iron rich layer above the inner core can have a possibly important positive feedback on inner core convection: irrespectively of the exact mechanism at the origin of the F-layer (Gubbins *et al.* 2008, 2011; Alboussière *et al.* 2010), its interpretation as an iron rich layer implies a decrease with time of light elements concentration in the liquid just above the ICB. This in turn implies that the newly crystallized solid is increasingly depleted in light elements, and intrinsically denser, which may drive compositional convection in the inner core. The reciprocal coupling between the inner core and the F-layer may create a positive feedback loop which can make the system (inner core + F-layer) unstable. The mechanism releases more gravitational energy than purely radial inner core growth with no melting, and should therefore be energetically favored.

We note c^s and c^l the light element concentration in the inner and outer core, respectively, $c^{s,l}_{icb}$ their values at the ICB, and $\dot{c}^{s,l}_{icb} = \mathrm{d}c^{s,l}_{icb}/\mathrm{d}t$ their time derivatives at the ICB. The concentration in the liquid and solid sides of the ICB are linked by the partition coefficient k, $c^s_{icb} = k\, c^l_{icb}$. Introducing $\tilde{c} = c - c^s_{icb}$, the equation of transport of light element can be written as

$$\frac{\mathrm{D}\tilde{c}}{\mathrm{D}t} = \kappa_c \nabla^2 \tilde{c} + S_c, \quad \tilde{c}(r_{ic}) = 0, \tag{144}$$

with

$$S_c = -\dot{c}^s_{icb} = -k\,\dot{c}^l_{icb} - c^l_{icb}\frac{\mathrm{d}k}{\mathrm{d}t}, \tag{145}$$

which is an exact analogue of the potential temperature transport eq. (29). The only—but important—difference is that the source term S_c is a dynamic quantity which depends on the convective state of the inner core and on the dynamics of the F-layer rather than being externally imposed like the effective heating rate S, which means that the dynamics of the inner core and F-layer must be considered simultaneously.

In general, the fact that the thermal and compositional diffusivities are different can be of importance, and would lead to double-diffusive type convection. However this is not the case in the translation regime, for which diffusion does not play any role as long as the translation rate is large enough (i.e. if the Péclet number $Pe = V r_{ic}/\kappa \gg 1$). Thanks to the potential temperature/composition analogy noted above, the translation model developed for thermal convection can be extended to include compositional effects, the translation rate being given by

$$V = \left[\frac{1}{5}\frac{\rho_s}{\Delta\rho}\frac{(\alpha S + \alpha_c S_c)}{\tau_\phi}\right]^{1/2} r_{ic} \tag{146}$$

when compositional effects are accounted for. We therefore need to compare the magnitudes of αS and $\alpha_c S_c = -\alpha_c k\,\dot{c}^l_{icb} - \alpha_c c^l_{icb}\,\mathrm{d}k/\mathrm{d}t$. Assuming (Gubbins *et al.* 2008) that the light element concentration at the base of the F-layer is currently about twice smaller than the outer core mean concentration, $c_{oc} \simeq 5$ wt. per cent, we obtain $\dot{c}^l_{icb} \sim -0.5\, c_{oc}/\tau_{ic} \sim -10^{-18}$ wt. per cent s^{-1} with $\tau_{ic} \sim 1$ Gy. With $\alpha_c \simeq 1$, this gives $-\alpha_c k\,\dot{c}^l_{icb} \sim 10^{-19}$ s^{-1} if $k \simeq 0.1$ and $-\alpha_c k\,\dot{c}^l_{icb} \sim 10^{-20}$ s^{-1} if $k \simeq 0.01$, which is similar or larger than the thermal contribution $\alpha S \sim 10^{-5} \times 10^{-15} \sim 10^{-20}$ s^{-1}. The term $-\alpha_c c^l_{icb}\,\mathrm{d}k/\mathrm{d}t$ might be positive as well. According to calculations by Gubbins *et al.* (2013), the variation with temperature of the partitioning behaviour of Oxygen can produce an unstable compositional gradient. As discussed in Alboussière *et al.* (2010) and Deguen & Cardin (2011), the effective partition coefficient may also decrease with time because of dynamic reasons (the efficiency of melt expulsion from the inner core increases with inner core size), which would also imply that this term is positive.

There is an additional feedback, this time negative, which comes from the effect of composition on the solidification temperature, which increases with decreasing light element concentration. The decreasing light element concentration at the base of the F-layer implies that the ICB temperature decreases with time at a slower rate than if the composition is fixed, which results in a smaller effective heating rate S (eq. 30). For a fixed inner core growth rate, this decreases the ICB cooling rate by an amount equal to $-m_c\,\dot{c}^l_{icb}$, where $m_c = \partial T_s/\partial c \sim -10^4$ K (Alfè *et al.* 2002) is the liquidus slope at the inner core boundary pressure and composition. This adds a term $-\alpha\, m_c\,\dot{c}^l_{icb}$ in eq. (146). If only one light element is considered, the ratio of the stabilizing term $\alpha\, m_c\,\dot{c}^l_{icb}$ over the destabilizing term $-\alpha_c k\,\dot{c}^l_{icb}$ is $\sim \alpha\, m_c/(\alpha_c k) \sim -0.1/k$. The two terms are of the same order of magnitude if $k \sim 0.1$, but the negative feedback dominates if k is smaller.

The above estimates are clearly uncertain, and a dynamic model of the F-layer will be required for assessing in a self-consistent way the effect of the development of the F-layer on inner core convection. There are several feedbacks of the formation of an F-layer on inner core convection, either positive or negative, and it is not clear yet whether the net effect would be stabilizing or destabilizing. Still, it does suggest that the effect could be important, and worth considering in more details.

9 SUMMARY AND CONCLUSIONS

Inner core translation can potentially explain a significant part of the inner core structure, but its existence depends critically on the value of a number of poorly constrained parameters. In this paper, we have studied in details the conditions for and dynamics of inner core thermal convection when melting and solidification at the ICB are allowed. We summarize here the main results and implications of our work:

(i) If the inner core is convectively unstable, linear stability analysis (Section 4), asymptotic calculations (Section 5), and direct

Table 3. Summary of theoretical results and scaling laws for the translation ($\mathcal{P} \lesssim 29$) and plume convection ($\mathcal{P} \gg 29$) regimes. In the plume convection regime, the value of β obtained by fitting the numerical outputs to our scaling theory is $\beta = -0.238 \pm 0.003$.

	Translation regime $\mathcal{P} \lesssim 29$	Plume convection regime $\mathcal{P} \gg 29$
Onset	$(\frac{Ra}{\mathcal{P}})_c = \frac{175}{2}$	$Ra_c = 1545.6$
Velocity scaling , V or U_{rms}	$\frac{\kappa}{r_{\mathrm{ic}}}\sqrt{\frac{6}{5}\frac{Ra}{\mathcal{P}}}$	$0.96\frac{\kappa}{r_{\mathrm{ic}}}Ra^{2+7\beta}$
Rate of melt production, $\dot{M}$	$\frac{1}{4}\frac{\kappa}{r_{\mathrm{ic}}}\sqrt{\frac{6}{5}\frac{Ra}{\mathcal{P}}}$	$0.46\frac{\kappa}{r_{\mathrm{ic}}}Ra^{1+2\beta}\mathcal{P}^{-1}$
$\langle\Theta\rangle$	$\frac{Sr_{\mathrm{ic}}^2}{\kappa}(\frac{10}{3}\frac{\mathcal{P}}{Ra})^{1/2}$	$2.9\frac{Sr_{\mathrm{ic}}^2}{\kappa}Ra^{\beta}$
Number of plumes per unit area, N	–	$\frac{0.07}{r_{\mathrm{ic}}^2}Ra^{-2-10\beta}$
Strain rate $\dot{\epsilon} \sim \frac{U_{\mathrm{rms}}}{\lambda} \sim \sqrt{N}U_{\mathrm{rms}}$	–	$0.25\frac{\kappa}{r_{\mathrm{ic}}^2}Ra^{1+2\beta}$

$Ra = \frac{\alpha\rho_s g_{\mathrm{icb}} Sr_{\mathrm{ic}}^5}{6\kappa^2\eta}$, $\mathcal{P} = \frac{\Delta\rho\, g_{\mathrm{icb}}\, r_{\mathrm{ic}}\, \tau_\phi}{\eta}$.

numerical simulations (Section 6) consistently show that the convection regime depends mostly on a non-dimensional number, the 'phase change number' $\mathcal{P}$, characterizing the resistance to phase change (eq. 58). The convective translation mode dominates only if $\mathcal{P} < 29$, which requires that the inner core viscosity is larger than a critical value estimated to be $\sim 3 \times 10^{18}$ Pa s. If $\mathcal{P}$ is larger (smaller viscosity), melting and solidification at the ICB have only a small dynamic effect, and convection takes the usual form of low Prandtl number internally heated convection, with a one-cell axisymmetric mode at the onset, and chaotic plume convection if the Rayleigh number is large.

(ii) With published estimates of the inner core viscosity ranging from 10^{11} to 10^{22} Pa s (Yoshida *et al.* 1996; Buffett 1997; Van Orman 2004; Mound & Buffett 2006; Koot & Dumberry 2011; Reaman *et al.* 2011, 2012), the question of which mode would be preferred is open (although we note that the latest estimate from mineral physics, 10^{20}–10^{22} Pa s (Reaman *et al.* 2012), would put the inner core, if unstably stratified, well within the translation regime).

(iii) The two convection regimes have been characterized in details in Sections 4–7; a summary of theoretical results and scaling laws for useful dynamic quantities (rms velocity, rate of melt production, mean potential temperature, number of plumes per unit area, and strain rate) is given in Table 3. If the inner core is unstably stratified, the rate of melt production predicted by our models is always large enough to produce an iron-rich layer at the base of the outer, according to Alboussière *et al.* (2010)'s experiments, if the inner core is in the translation regime (Fig. 14). In the plume convection regime, the rate of melt production can still be significant if $\mathcal{P}$ is not too large (η not too small).

(iv) Being driven by buoyancy, a prerequisite for the existence of convective translation is that an unstable density profile is maintained within the inner core. Thermal convection requires that a superadiabatic temperature profile is maintained with the inner core, which is highly dependent on the core thermal history and inner core thermal conductivity. With $k = 36$ W m^{-1} K^{-1} as proposed by Stacey & Davis (2008), this would be very likely (Buffett 2009; Deguen & Cardin 2011). However, several independent groups (Sha & Cohen 2011; de Koker *et al.* 2012; Pozzo *et al.* 2012) have recently argued for a much higher core thermal conductivity, around 150 W m^{-1} K^{-1} or higher. This would make thermal convection in the inner core, whether in the translation mode or in the plume convection mode, impossible unless the inner core is very young ($\simeq$300 Myr or less, which would require a probably excessively high CMB heat flux).

(v) Compositional convection might be a viable alternative to thermal convection, either because the temperature dependency of the light elements partitioning behaviour can produce an unstable compositional profile (Gubbins *et al.* 2013), or because of a possibly positive feedback of the development of the F-layer on inner core convection. As proposed in Section 8, the formation of an iron-rich layer at the base of the outer core over the history of the inner core implies that the inner core crystallizes from a source which is increasingly depleted in light elements. This in turn implies that the newly crystallized solid is increasingly depleted in light element, which results in an unstable density profile. Whether this positive feedback is strong enough to overcome the stabilizing effect of a possibly subadiabatic temperature profile depends on the dynamics of the F-layer, and further work is needed to test this idea.

ACKNOWLEDGEMENTS

We would like to thank the two anonymous referees for many helpful comments and suggestions. All the computations presented in this paper were performed at the Service Commun de Calcul Intensif de l'Observatoire de Grenoble (SCCI). RD was supported by grant EAR-0909622 and Frontiers in Earth System Dynamics grant EAR-1135382 from the National Science Foundation. TA was supported by the ANR (Agence National de la Recherche) within the CrysCore project ANR-08-BLAN-0234-01, and by the program PNP of INSU/CNRS. PC was supported by the program PNP of INSU/CNRS.

REFERENCES

Abramovich, M. & Stegun, I., 1965. *Handbook of Mathematical Functions,* Fourth Printing. Applied Math. Ser. 55, US Government Printing Office, Washington, DC.

Alboussière, T. & Ricard, Y., 2013. Reflections on dissipation associated with thermal convection, *J. Fluid Mech.,* **725,** doi:10.1017/jfm.2013.241.

Alboussière, T., Deguen, R. & Melzani, M., 2010. Melting induced stratification above the Earth's inner core due to convective translation, *Nature,* **466,** 744–747.

Alfè, D., Gillan, M.J. & Price, G.D., 2002. Ab initio chemical potentials of solid and liquid solutions and the chemistry of the Earth's core, *J. Chem. Phys.,* **116,** 7127–7136.

Anderson, O.L. & Wenk Duba, A., 1997. Experimental melting curve of iron revisited, *J. geophys. Res.,* **102,** 22 659–22 670.

Anufriev, A., Jones, C. & Soward, A., 2005. The Boussinesq and anelastic liquid approximations for convection in the Earth's core, *Phys. Earth planet. Inter.,* **12**(3), 163–190.

Aubert, J., 2013. Flow throughout the Earth's core inverted from geomagnetic observations and numerical dynamo models, *Geophys. J. Int.,* **192**(2), 537–556.

Bergman, M., Lewis, D., Myint, I., Slivka, L., Karato, S. & Abreu, A., 2010. Grain growth and loss of texture during annealing of alloys, and the translation of Earth's inner core, *Geophys. Res. Lett.,* **37**(22), L22313, doi:10.1029/2010GL045103.

Buffett, B., 2009. Onset and orientation of convection in the inner core, *Geophys. J. Int.,* **179,** 711–719.

Buffett, B.A., 1997. Geodynamics estimates of the viscosity of the Earth's inner core, *Nature,* **388,** 571–573.

Buffett, B.A. & Wenk, H.-R., 2001. Texturing of the Earth's inner core by Maxwell stresses, *Nature,* **413,** 60–63.

Chandrasekhar, S., 1961. *Hydrodynamic and Hydromagnetic Stability,* International Series of Monographs on Physics, Clarendon, Oxford.

Christensen, U. & Aubert, J., 2006. Scaling properties of convection-driven dynamos in rotating spherical shells and application to planetary magnetic fields, *Geophys. J. Int.,* **166**(1), 97–114.

Cottaar, S. & Buffett, B., 2012. Convection in the Earth's inner core, *Phys. Earth planet. Inter.,* **198-199,** 67–78.

Davies, C.J., Silva, L. & Mound, J., 2013. On the influence of a translating inner core in models of outer core convection, *Phys. Earth planet. Inter.,* **214,** 104–114.

de Koker, N., Steinle-Neumann, G. & Vlcek, V., 2012. Electrical resistivity and thermal conductivity of liquid fe alloys at high p and t, and heat flux in earth's core, *Proc. Natl. Acad. Sci.,* **109**(11), 4070–4073.

Deguen, R. & Cardin, P., 2011. Thermo-chemical convection in Earth's inner core, *Geophys. J. Int.,* **187,** 1101–1118.

Deguen, R., Cardin, P., Merkel, S. & Lebensohn, R., 2011. Texturing in Earth's inner core due to preferential growth in its equatorial belt, *Phys. Earth planet. Inter.,* **188,** 173–184.

Deschamps, F., Yao, C., Tackley, P.J. & Sanchez-Valle, C., 2012. High rayleigh number thermal convection in volumetrically heated spherical shells, *J. geophys. Res.-Solid Earth,* **117,** E09006, doi:10.1029/2012JE004090.

Dziewonski, A.M. & Anderson, D.L., 1981. Preliminary reference Earth model, *Phys. Earth planet. Inter.,* **25,** 297–356.

Forte, A.M. & Peltier, W.R., 1987. Plate tectonics and aspherical Earth structure: the importance of poloidal-toroidal coupling, *J. geophys. Res.,* **92,** 3645–3679.

Geballe, Z.M., Lasbleis, M., Cormier, V.F. & Day, E.A., 2013. Sharp hemisphere boundaries in a translating inner core, *Geophys. Res. Lett.,* **40,** doi:10.1002/grl.50372.

Gillet, N., Pais, M.A. & Jault, D., 2009. Ensemble inversion of time-dependent core flow models, *Geophys. J. Int.,* **10,** Q06004, doi:10.1029/2008GC002290.

Gubbins, D., Masters, G. & Nimmo, F., 2008. A thermochemical boundary layer at the base of Earth's outer core and independent estimate of core heat flux, *Geophys. J. Int.,* **174,** 1007–1018.

Gubbins, D., Sreenivasan, B., Mound, J. & Rost, S., 2011. Melting of the Earth's inner core, *Nature,* **473**(7347), 361–363.

Gubbins, D., Alfè, D. & Davies, D., 2013. Compositional instability of Earth's solid inner core, *Geophys. Res. Lett.,* **40**(1–5), 361–363.

Irving, J., Deuss, A. & Woodhouse, J., 2009. Normal mode coupling due to hemispherical anisotropic structure in Earth's inner core, *Geophys. J. Int.,* **178**(2), 962–975.

Jeanloz, R. & Wenk, H.-R., 1988. Convection and anisotropy of the inner core, *Geophys. Res. Lett.,* **15,** 72–75.

Karato, S.-I., 1999. Seismic anisotropy of the Earth's inner core resulting from flow induced by Maxwell stresses, *Nature,* **402,** 871–873.

Koot, L. & Dumberry, M., 2011. Viscosity of the earth's inner core: constraints from nutation observations, *Earth planet. Sci. Lett.,* **308**(3–4), 343–349.

Mizzon, H. & Monnereau, M., 2013. Implications of the lopsided growth for the viscosity of Earth's inner core, *Earth planet. Sci. Lett.,* **361,** 391–401.

Monnereau, M., Calvet, M., Margerin, L. & Souriau, A., 2010. Lopsided growth of Earth's inner core, *Science,* **328,** 1014–1017.

Mound, J.E. & Buffett, B.A., 2006. Detection of a gravitational oscillation in length-of-day, *Earth planet. Sci. Lett.,* **243,** 383–389.

Niu, F.L. & Wen, L.X., 2001. Hemispherical variations in seismic velocity at the top of the Earth's inner core, *Nature,* **410,** 1081–1084.

Pais, A. & Jault, D., 2008. Quasi-geostrophic flows responsible for the secular variation of the Earth's magnetic field, *Geophys. J. Int.,* **173,** 421–443.

Parmentier, E.M. & Sotin, C., 2000. Three-dimensional numerical experiments on thermal convection in a very viscous fluid: implications for the dynamics of a thermal boundary layer at high Rayleigh number, *Phys. Fluids,* **12,** 609–617.

Poirier, J.-P., 1994. Physical properties of the Earth's core, *C.R. Acad. Sci. Paris,* **318,** 341–350.

Pozzo, M., Davies, C., Gubbins, D. & Alfè, D., 2012. Thermal and electrical conductivity of iron at Earth's core conditions, *Nature,* **485,** 355–358.

Reaman, D., Colijn, H., Yang, F., Hauser, A. & Panero, W., 2012. Interdiffusion of Earth's core materials to 65 GPa and 2200K, *Earth planet. Sci. Lett.,* **349,** 8–14.

Reaman, D.M., Daehn, G.S. & Panero, W.R., 2011. Predictive mechanism for anisotropy development in the Earth's inner core, *Earth planet. Sci. Lett.,* **312**(3–4), 437–442.

Ribe, N.M., 2007. Analytical approaches to mantle dynamics, in *Treatise on Geophysics,* pp. 167–226, eds Gerald, S. & Bercovici, D., Elsevier, New York.

Schubert, G., Turcotte, D. & Olson, P., 2001. *Mantle Convection in the Earth and Planets,* Cambridge University Press, Cambridge, UK.

Sha, X. & Cohen, R., 2011. First-principles studies of electrical resistivity of iron under pressure, *J. Phys.: Conden. Matter,* **23,** 075401, doi:10.1088/0953-8984/23/7/075401.

Sneddon, I., 1960. On some infinite series involving the zeros of bessel functions of the first kind, in *Proceedings of the Glasgow Mathematical Association,* Vol. 4, pp. 144–156, Cambridge University Press, Cambridge, UK.

Souriau, A. & Poupinet, G., 1991. The velocity profile at the base of the liquid core from PKP(BC+Cdiff) data: an argument in favor of radial inhomogeneity, *Geophys. Res. Lett.,* **18,** 2023–2026.

Sreenivasan, B. & Gubbins, D., 2011. On mantle-induced heat flow variations at the inner core boundary, *Phys. Earth planet. Inter,* **187,** 336–341.

Stacey, F. & Loper, D., 2007. A revised estimate of the conductivity of iron alloy at high pressure and implications for the core energy balance, *Phys. Earth planet. Inter.,* **161,** 13–18.

Stacey, F.D. & Anderson, O.L., 2001. Electrical and thermal conductivities of Fe-Ni-Si alloy under core conditions, *Phys. Earth planet. Inter.,* **124,** 153–162.

Stacey, F.D. & Davis, P.M., 2008. *Physics of the Earth,* Cambridge University Press, Cambridge, UK.

Stevenson, D., 1987. Limits on lateral density and velocity variations in the Earth's outer core, *Geophys. J. R. astr. Soc.,* **88**(1), 311–319.

Sumita, I., Yoshida, S., Hamano, Y. & Kumazawa, M., 1995. A model for the structural evolution of the Earth's core and its relation to the observations, in *The Earth's Central Part: Its Structure and Dynamics,* pp. 231–260, ed. Yukutake, T., Terra Scientific Publishing Company (Terrapub), Tokyo.

Tanaka, S., 2012. Depth extent of hemispherical inner core from pkp (df) and pkp (cdiff) for equatorial paths, *Phys. Earth planet. Inter,* **210–211,** 50–62.

Tanaka, S. & Hamaguchi, H., 1997. Degree one heterogeneity and hemispherical variation of anisotropy in the inner core from PKP(BC)-PKP(DF) times, *J. geophys. Res.,* **102,** 2925–2938.

Tritton, D., 1988. *Physical Fluid Dynamics,* Clarendon Press, Oxford.
Van Orman, J.A., 2004. On the viscosity and creep mechanism of Earth's inner core, *Geophys. Res. Lett.,* **31,** L20606, doi:10.1029/2004GL021209.
Vočadlo, L., 2007. Ab initio calculations of the elasticity of iron and iron alloys at inner core conditions: evidence for a partially molten inner core?, *Earth planet. Sci. Lett.,* **254,** 227–232.
Weber, P. & Machetel, P., 1992. Convection within the inner-core and thermal implications, *Geophys. Res. Lett.,* **19,** 2107–2110.
Yoshida, S., Sumita, I. & Kumazawa, M., 1996. Growth model of the inner core coupled with the outer core dynamics and the resulting elastic anisotropy, *J. geophys. Res.,* **101,** 28 085–28 104.

APPENDIX A: LINEAR STABILITY ANALYSIS

We investigate here the linear stability of the system of equations describing thermal convection in the inner core with phase change at the ICB, as derived in Section 3. The calculation given here is a generalization of the linear stability analysis of thermal convection in an internally heated sphere given by Chandrasekhar (1961).

We assume constant Ra and $\mathcal{P}$. The basic state of the problem is then

$$\bar{\Theta} = 1 - r^2, \tag{A1}$$

$$\bar{\mathbf{u}} = \mathbf{0}, \tag{A2}$$

which is the steady conductive solution of the system of equation developed in Section 3. We investigate the stability of this conductive state against infinitesimal perturbations of the temperature and velocity fields. The temperature field is written as the sum of the conductive temperature profile given by eq. (A1) and infinitesimal disturbances $\tilde{\Theta}$, $\Theta(r,\theta,\phi,t) = \bar{\Theta}(r) + \tilde{\Theta}(r,\theta,\phi,t)$. The velocity field perturbation is noted $\tilde{\mathbf{u}}(r,\theta,\phi,t)$, and has an associated poloidal scalar $\tilde{P}(r,\theta,\phi,t)$. We expand the temperature and poloidal disturbances in spherical harmonics,

$$\tilde{\Theta} = \sum_{l=0}^{\infty}\sum_{m=-l}^{l} \tilde{t}_l^m(r) Y_l^m(\theta,\phi)\, \mathrm{e}^{\sigma_l t}, \tag{A3}$$

$$\tilde{P} = \sum_{l=1}^{\infty}\sum_{m=-l}^{l} \tilde{p}_l^m(r) Y_l^m(\theta,\phi)\, \mathrm{e}^{\sigma_l t}, \tag{A4}$$

where σ_l is the growth rate of the degree l perturbations.

The only non-linear term in the system of equations is the advection of heat $\mathbf{u}\cdot\nabla T$, which is linearized as

$$\tilde{u}_r \frac{\partial \bar{\Theta}}{\partial r} = -2r\tilde{u}_r = -2L^2\tilde{P}. \tag{A5}$$

The resulting linearized transport equation for the potential temperature disturbance is

$$\frac{\partial \tilde{\Theta}}{\partial t} = \nabla^2\tilde{\Theta} + 2L^2\tilde{P} + 6. \tag{A6}$$

Using the decompositions (A3) and (A4), the linearized system of equations is then, for $l \geq 1$,

$$Ra\, \tilde{t}_l^m = \mathcal{D}_l^2 \tilde{p}_l^m, \tag{A7}$$

$$(\sigma_l - \mathcal{D}_l)\, \tilde{t}_l^m = 2l(l+1)\tilde{p}_l^m \tag{A8}$$

with the boundary conditions given by eqs (72) and (73), with $\tilde{t}_l^m(r=1) = 0$.

We expand the temperature perturbations $\tilde{t}_l^m(r)$ as a series of spherical Bessel functions of the first kind j_l,

$$\tilde{t}_l^m = \sum_i A_{l,i}\, j_l(\alpha_{l,i} r). \tag{A9}$$

The spherical Bessel functions are defined as

$$j_l(r) = \sqrt{\frac{\pi}{2r}} J_{l+\frac{1}{2}}(r), \tag{A10}$$

where J denotes Bessel functions of the first kind. $\alpha_{l,i}$ is the ith zero of $J_{l+\frac{1}{2}}$, and therefore of j_l as well. The functions $j_l(\alpha_{l,i} r)$ for $i = 1, 2, \ldots, \infty$ and a given l form a complete set of orthogonal functions on [0, 1], and satisfy the orthogonality relation

$$\int_0^1 r^2 j_l(\alpha_{l,i} r) j_l(\alpha_{l,j} r)\mathrm{d}r = \frac{\delta_{i,j}}{2}\left[j_{l+1}(\alpha_{l,j})\right]^2. \tag{A11}$$

The spherical Bessel functions are eigenfunctions of the operator $\mathcal{D}_l$, such that

$$\mathcal{D}_l j_l(\alpha_{l,i} r) = -\alpha_{l,i}^2\, j_l(\alpha_{l,i} r). \tag{A12}$$

Writing the poloidal scalar perturbations $\tilde{p}_l^m$ as

$$\tilde{p}_l^m = \sum_i A_{l,i}\, p_{l,i}, \tag{A13}$$

the functions $p_{l,i}$ are solutions of

$$Ra\, j_l(\alpha_{l,i} r) = \mathcal{D}_l^2 p_{l,i}, \tag{A14}$$

which has a general solution of the form

$$p_{l,i} = \frac{Ra}{\alpha_{l,i}^4} j_l(\alpha_{l,i} r) + B_{l,i} r^l + C_{l,i} r^{l+2}. \tag{A15}$$

We now use the boundary conditions at $r = 1$ to find the constants $B_{l,i}$ and $C_{l,i}$. The condition of zero tangential stress (eq. 72) can be rewritten as

$$\mathcal{D}_l \tilde{p}_l^m - 2\frac{d\tilde{p}_l^m}{dr} + 2\left[l(l+1) - 1\right]\tilde{p}_l^m = 0, \tag{A16}$$

which, recalling that $j_l(\alpha_{l,i}) = 0$ and noting that

$$\mathcal{D}_l \tilde{p}_l^m = \sum_i A_{l,i}\left[-\frac{Ra}{\alpha_{l,i}^2} j_l(\alpha_{l,i} r) + C_{l,i}(4l+6) r^l\right], \tag{A17}$$

gives

$$C_{l,i} = \frac{1-l^2}{l(l+2)} B_{l,i} + \frac{1}{l(l+2)} \frac{Ra}{\alpha_{l,i}^3} j_l'(\alpha_{l,i}). \tag{A18}$$

From the continuity of the normal stress at $r = 1$ (eq. 73), we obtain

$$B_{l,i} = -\left[2(l-1) + \mathcal{P}\right]^{-1}\left[\frac{1}{l(l+1)} + \frac{2}{\alpha_{l,i}^2}\right]\frac{j_l'(\alpha_{l,i})}{\alpha_{l,i}} Ra$$
$$-C_{l,i} + \left[2(l-1) + \mathcal{P}\right]^{-1}\frac{6}{l} C_{l,i}. \tag{A19}$$

The derivative of j_l which appears in eqs (A18) and (A19) can be evaluated from the recurrence relation

$$\frac{n}{r} j_n - \frac{\mathrm{d}j_n}{\mathrm{d}r} = j_{n+1} \tag{A20}$$

(Abramovich & Stegun 1965). Recalling that $j_l(\alpha_{l,i}) = 0$, eq. (A20) with $n = l$ gives

$$j_l'(\alpha_{l,i}) = -j_{l+1}(\alpha_{l,i}). \tag{A21}$$

Inserting eq. (A18) in eq. (A19), we obtain

$$\left\{4l(l+1) - 2 + (2l+1)\mathcal{P} - \frac{6}{l}\right\} B_{l,i} = \left\{\frac{l+2}{l+1} + \left[2(l^2+3l-1) + \mathcal{P} - \frac{6}{l}\right]\frac{1}{\alpha_{l,i}^2}\right\}\frac{j_{l+1}(\alpha_{l,i})}{\alpha_{l,i}} Ra, \tag{A22}$$

which we rewrite as

$$B_{l,i} = \left(q_1^l(\mathcal{P}) + \frac{q_2^l(\mathcal{P})}{\alpha_{l,i}^2}\right)\frac{j_{l+1}(\alpha_{l,i})}{\alpha_{l,i}} Ra, \tag{A23}$$

where

$$q_1^l(\mathcal{P}) = \frac{l+2}{l+1}\left[4l(l+1) - 2 + (2l+1)\mathcal{P} - \frac{6}{l}\right]^{-1}, \tag{A24}$$

$$q_2^l(\mathcal{P}) = \frac{2(l^2+3l-1) + \mathcal{P} - \frac{6}{l}}{4l(l+1) - 2 + (2l+1)\mathcal{P} - \frac{6}{l}}. \tag{A25}$$

With this expression for $B_{l,i}$, the constants $C_{l,i}$ are given by

$$C_{l,i} = -\left(q_3^l(\mathcal{P}) + \frac{q_4^l(\mathcal{P})}{\alpha_{l,i}^2}\right)\frac{j_{l+1}(\alpha_{l,i})}{\alpha_{l,i}} Ra, \tag{A26}$$

where

$$q_3^l(\mathcal{P}) = \frac{(l^2-1)}{l(l+2)} q_1^l(\mathcal{P}), \tag{A27}$$

$$q_4^l(\mathcal{P}) = \frac{(l^2-1)q_2^l(\mathcal{P}) + 1}{l(l+2)}. \tag{A28}$$

Now, using eqs (A13) and (A15) for $\tilde{p}_l^m$ and eq. (A9) for $\tilde{t}_l^m$, the heat eq. (A8) gives

$$\sum_i A_{l,i}\left(\frac{\sigma_l + \alpha_{l,i}^2}{2l(l+1)} - \frac{Ra}{\alpha_{l,i}^4}\right) j_l(\alpha_{l,i} r) = \sum_i A_{l,i}\left(B_{l,i} r^l + C_{l,i} r^{l+2}\right). \tag{A29}$$

Multiplying eq. (A29) by $r^2 j_l(\alpha_{l,j} r)$ where j is an integer in $[0; \infty]$, integrating in r over $[0; 1]$, and using the orthogonality relation (A11), we obtain

$$A_{l,j}\left(\frac{\sigma_l + \alpha_{l,j}^2}{2l(l+1)} - \frac{Ra}{\alpha_{l,j}^4}\right)\frac{1}{2}\left[j_{l+1}(\alpha_{l,j})\right]^2 = \sum_i A_{l,i} B_{l,i}\int_0^1 r^{l+2} j_l(\alpha_{l,j} r)\mathrm{d}r + \sum_i A_{l,i} C_{l,i}\int_0^1 r^{l+4} j_l(\alpha_{l,j} r)\mathrm{d}r, \quad (j = 1, 2, \ldots). \tag{A30}$$

Eq. (A30) forms a set of linear homogeneous equations for the constants $A_{l,j}$, which admits non-trivial solutions only if its secular determinant is equal to zero.

Before calculating the secular determinant of the system of equations, we evaluate the two integrals on the right hand side, starting with the integral of $r^{l+2} j_l(\alpha_{l,j} r)$. Using the formula

$$\left(\frac{1}{x}\frac{d}{dx}\right)^m \left[x^{n+1} j_n(x)\right] = x^{n-m+1} j_{n-m}(x) \tag{A31}$$

(Abramovich & Stegun 1965) with $m = 1$ and $n = k + 1$ gives

$$\frac{\mathrm{d}}{\mathrm{d}x}\left[x^{k+2} j_{k+1}(x)\right] = x^{k+2} j_k(z), \tag{A32}$$

which allows to write, with $k = l$,

$$\int_0^1 r^{l+2} j_l(\alpha_{l,j} r)\mathrm{d}r = \frac{1}{\alpha_{l,j}^{l+3}}\int_0^{\alpha_{l,j}} x^{l+2} j_l(x)\mathrm{d}x = \frac{1}{\alpha_{l,j}^{l+3}}\left[x^{l+2} j_{l+1}(x)\right]_0^{\alpha_{l,j}} = \frac{j_{l+1}(\alpha_{l,j})}{\alpha_{l,j}}. \tag{A33}$$

Now, using the recurrence relation

$$j_{n-1} + j_{n+1} = \frac{2n+1}{r} j_n \tag{A34}$$

(Abramovich & Stegun 1965) with $n = l + 1$, we rewrite the integral of $r^{l+4} j_l(\alpha_{l,j} r)$ as

$$\int_0^1 r^{l+4} j_l(\alpha_{l,j} r)\mathrm{d}r = \frac{1}{\alpha_{l,j}^{l+5}}\int_0^{\alpha_{l,j}} x^{l+4} j_l(x)\mathrm{d}x \tag{A35}$$

$$= -\frac{1}{\alpha_{l,j}^{l+5}}\int_0^{\alpha_{l,j}} x^{l+4} j_{l+2}(x)\mathrm{d}x + \frac{2l+3}{\alpha_{l,j}^{l+5}}\int_0^{\alpha_{l,j}} x^{l+3} j_{l+1}(x)\mathrm{d}x. \tag{A36}$$

The two integrals on the RHS can be calculated using the relation (A32) with $k = l + 2$ and $k = l + 1$, respectively. With further use of the recurrence relation (A34), we finally obtain

$$\int_0^1 r^{l+4} j_l(\alpha_{l,j} r)\mathrm{d}r = \left[1 - \frac{4l+6}{\alpha_{l,j}^2}\right]\frac{j_{l+1}(\alpha_{l,j})}{\alpha_{l,j}}. \tag{A37}$$

With the integrals estimated above, the system of eqs (A30) can be rewritten as

$$A_{l,j}\left(\frac{\sigma_l + \alpha_{l,j}^2}{2l(l+1)Ra} - \frac{1}{\alpha_{l,j}^4}\right)\frac{1}{2}\left[j_{l+1}(\alpha_{l,j})\right]^2 = \sum_i A_{l,i}\left\{\left(q_3^l(\mathcal{P}) + \frac{q_4^l(\mathcal{P})}{\alpha_{l,i}^2}\right)\left[\frac{4l+6}{\alpha_{l,j}^2} - 1\right] + q_1^l(\mathcal{P}) + \frac{q_2^l(\mathcal{P})}{\alpha_{l,i}^2}\right\}\frac{j_{l+1}(\alpha_{l,i})}{\alpha_{l,i}}\frac{j_{l+1}(\alpha_{l,j})}{\alpha_{l,j}}, \quad (j = 1, 2, \ldots). \tag{A38}$$

Introducing $\mathcal{A}_i = (j_{l+1}(\alpha_{l,i})/\alpha_{l,i}^3) A_{l,i}$, and dividing by $j_{l+1}(\alpha_{l,j})/\alpha_{l,j}$, we finally obtain

$$\sum_i \mathcal{A}_i\left\{\left[q_3^l(\mathcal{P})\alpha_{l,i}^2 + q_4^l(\mathcal{P})\right]\left[1 - \frac{4l+6}{\alpha_{l,j}^2}\right] - \left[q_1^l(\mathcal{P})\alpha_{l,i}^2 + q_2^l(\mathcal{P})\right]\left(\frac{\sigma_l \alpha_{l,i}^4 + \alpha_{l,i}^6}{2l(l+1)Ra} - 1\right)\frac{1}{2}\delta_{ij}\right\} = 0, \quad (j = 1, 2, \ldots). \tag{A39}$$

This forms an infinite set of linear equations, which admits a non trivial solution only if its determinant is zero:

$$\left|\left|\left[q_3^l(\mathcal{P})\alpha_{l,i}^2+q_4^l(\mathcal{P})\right]\left[1-\frac{4l+6}{\alpha_{l,j}^2}\right]-\left[q_1^l(\mathcal{P})\alpha_{l,i}^2+q_2^l(\mathcal{P})\right]\right.\right.$$
$$\left.\left.+\left(\frac{\sigma_l\alpha_{l,i}^4+\alpha_{l,i}^6}{2l(l+1)Ra}-1\right)\frac{1}{2}\delta_{ij}\right|\right|=0, \tag{A40}$$

with $i,j=1,2,\ldots$. Solving eq. (A40) for a given value of l and $\sigma_l=0$ gives the critical value Ra_c of the Rayleigh number for instability of the l mode as a function of $\mathcal{P}$. When solving numerically eqs (A40), the precision on Ra_c depends on the maximum value of i and j retained in the calculation, but the value of Ra_c converges relatively fast with i,j.

The pattern of the first unstable mode can be calculated by solving the system (A39) in $\mathcal{A}_i$ for given $\mathcal{P}$ and Ra, which gives $A_{l,i}$ and allows to calculate the poloidal scalar $\tilde{p}_l^m$ from eqs (A13) and (A15). With $l=1$, we have $q_1^1=1/(2\mathcal{P})$, $q_2^1=1/3$, $q_3^1=0$ and $q_4^1=1/3$, so that the functions $p_{1,i}$ can be written as

$$p_{1,i}=\frac{j_1(\alpha_{1,i}r)}{\alpha_{1,i}}+\frac{j_2(\alpha_{1,i})}{3}(r-r^3)+\frac{j_2(\alpha_{1,i})\alpha_{1,i}^2}{2\mathcal{P}}r, \tag{A41}$$

and the general form of the $l=1$, $m\in[-1,0,1]$ components of the poloidal scalar is

$$\tilde{p}_1^m=\sum_{i=1}^{\infty}A_{1,i}\left[\frac{j_1(\alpha_{1,i}r)}{\alpha_{1,i}}+\frac{j_2(\alpha_{1,i})}{3}(r-r^3)+\frac{j_2(\alpha_{1,i})\alpha_{1,i}^2}{2\mathcal{P}}r\right]. \tag{A42}$$

To a good approximation, the first unstable mode is given (to within a multiplicative constant) by keeping only the $i=j=1$ term,

$$\tilde{P}\simeq\left\{\frac{j_1(\alpha_{1,1}r)}{\alpha_{1,1}}+\frac{j_2(\alpha_{1,1})}{3}(r-r^3)+\frac{j_2(\alpha_{1,1})\alpha_{1,1}^2}{2\mathcal{P}}r\right\}\cos\theta. \tag{A43}$$

APPENDIX B: TRANSLATION RATE AT $\mathcal{O}(\mathcal{P})$

In order to estimate the translation velocity at $\mathcal{O}(\mathcal{P})$, we need to determine the parameter A in the $\mathcal{O}(\mathcal{P})$ expansion of p_1 (eq. 101), which was left undetermined. To do so, we need to consider the thermal field at $\mathcal{O}(\mathcal{P})$ and the velocity field at $\mathcal{O}(\mathcal{P}^2)$. This is more challenging because, owing to the non-linearity of the heat equation, coupling of higher order components of the temperature and velocity fields contribute to the $l=1$ component of the temperature field at $\mathcal{O}(\mathcal{P})$, and to the $l=1$ component of the velocity field at $\mathcal{O}(\mathcal{P}^2)$.

As before, we consider a steady state approximation of the heat equation where advection and internal heating balance,

$$\mathbf{u}\cdot\nabla\Theta=u_r\frac{\partial\Theta}{\partial r}+\frac{u_\theta}{r}\frac{\partial\Theta}{\partial\theta}=6. \tag{B1}$$

Using Legendre polynomial expansions of the poloidal and temperature field,

$$\Theta=\sum_{l=0}^{\infty}t_lP_l(\cos\theta),\quad P'=\sum_{l=0}^{\infty}p_lP_l(\cos\theta), \tag{B2}$$

eq. (B1) can be rewritten as

$$6=\left[\sum_l l(l+1)\frac{p_l}{r}P_l(\cos\theta)\right]\times\left[\sum_l\frac{\mathrm{d}t_l}{\mathrm{d}r}P_l(\cos\theta)\right]$$
$$+\frac{1}{r}\left[\sum_l\frac{1}{r}\frac{\mathrm{d}}{\mathrm{d}r}(rp_l)\frac{\mathrm{d}P_l(\cos\theta)}{\mathrm{d}\theta}\right]\times\left[\sum_l t_l\frac{\mathrm{d}P_l(\cos\theta)}{\mathrm{d}\theta}\right] \tag{B3}$$

(We can use Legendre polynomials rather than full spherical harmonics because we restrict the calculation to axisymmetric flows. This gives slightly simpler expressions.) The $l=1$ and $l=2$ component of the temperature field being much larger than higher order components (with odd l components being zero), we consider only the $l=1$ and 2 terms. Multiplying eq. (B3) by $\sin\theta$ and integrating over $[0\,\pi]$ in θ then gives

$$12=\frac{4}{3}\frac{p_1}{r}\frac{\mathrm{d}t_1}{\mathrm{d}r}+\frac{12}{5}\frac{p_2}{r}\frac{\mathrm{d}t_2}{\mathrm{d}r}+\frac{4}{3}\frac{1}{r^2}\frac{\mathrm{d}}{\mathrm{d}r}(rp_1)t_1$$
$$+\frac{12}{5}\frac{1}{r^2}\frac{\mathrm{d}}{\mathrm{d}r}(rp_2)t_2 \tag{B4}$$

which can be rewritten as

$$3r^2=\frac{\mathrm{d}}{\mathrm{d}r}\left(\frac{1}{3}rp_1t_1+\frac{3}{5}rp_2t_2\right). \tag{B5}$$

Integrating eq. (B5) gives

$$r^3+\mathrm{cst}=\frac{1}{3}rp_1t_1+\frac{3}{5}rp_2t_2. \tag{B6}$$

We now expand the Legendre components of the temperature and poloidal scalar fields as

$$t_1=\frac{6}{V_0}\left[r+\hat{t}_{1,1}\mathcal{P}+\mathcal{O}(\mathcal{P}^2)\right],\quad t_2=\frac{1}{V_0}\left[\hat{t}_{2,0}+\mathcal{O}(\mathcal{P})\right]$$
$$p_1=\frac{V_0}{2}\left[r+\hat{p}_{1,1}\mathcal{P}+\mathcal{O}(\mathcal{P}^2)\right],\quad p_2=V_0\left[\hat{p}_{2,1}\mathcal{P}+\mathcal{O}(\mathcal{P}^2)\right] \tag{B7}$$

and insert these expressions in eq. (B6). The zeroth order terms cancel, and eq. (B6) then writes

$$0=\left(r\hat{p}_{1,1}+r\hat{t}_{1,1}+\frac{3}{5}\hat{p}_{2,1}\hat{t}_{2,0}\right)\mathcal{P}+\mathcal{O}(\mathcal{P}^2) \tag{B8}$$

which implies that

$$\hat{t}_{1,1}=-\hat{p}_{1,1}-\frac{1}{r}\frac{3}{5}\hat{p}_{2,1}\hat{t}_{2,0}. \tag{B9}$$

B1 $l=2$ components of the thermal field and velocity field

We now calculate the $l=2$ component of the temperature field at zeroth order in $\mathcal{P}$, which will then be used to find the $l=2$ component of the velocity field at $\mathcal{O}(\mathcal{P})$.

It will be useful to first note that

$$\mathcal{D}_l^2(r^a)=[a(a+1)-l(l+1)]\,[(a-2)(a-1)-l(l+1)]\,r^{a-4}, \tag{B10}$$

from which we find that

$$\left(\mathcal{D}_1^2\right)^{-1}(r^a)=\frac{r^{a+4}}{(a+6)(a+4)(a+3)(a+1)} \tag{B11}$$

and

$$\left(\mathcal{D}_2^2\right)^{-1}(r^a)=\frac{r^{a+4}}{(a+7)(a+5)(a+2)a}. \tag{B12}$$

The $l = 2$ component of the temperature field at zeroth order in $\mathcal{P}$ can be found by direct integration of the temperature field given by eq. (96):

$$\begin{aligned} t_2 &= \frac{5}{2}\frac{6}{V_0}\int_0^\pi \sqrt{1-r^2\sin^2\theta}\, P_2(\cos\theta)\sin\theta \mathrm{d}\theta \\ &= \frac{5}{2}\frac{9}{4V_0}\left\{\frac{1}{r^2}-\frac{1}{3}+\frac{1-r^2}{2r}\left(\frac{1}{3}+\frac{1}{r^2}\right)\log\left(\frac{1-r}{1+r}\right)\right\} \\ &= \frac{15}{8V_0}\sum_{k=1}^{+\infty}\left(\frac{1}{2k-1}+\frac{2}{2k+1}-\frac{3}{2k+3}\right)r^{2k} \\ &= \frac{1}{V_0}\sum_{k=1}^{+\infty}\alpha_k r^{2k} \end{aligned} \tag{B13}$$

with

$$\alpha_k = \frac{30k}{(2k+3)(2k+1)(2k-1)}. \tag{B14}$$

From this, we can calculate the associated velocity field,

$$p_2 = Ra\left(\mathcal{D}_2^2\right)^{-1} t_2 \tag{B15}$$

$$= \frac{Ra}{V_0}\left(\mathcal{D}_2^2\right)^{-1}\left(\sum_{k=1}^{+\infty}\alpha_k r^{2k}\right) \tag{B16}$$

$$= \frac{5}{6}V_0\mathcal{P}\left(\mathcal{D}_2^2\right)^{-1}\left(\sum_{k=1}^{+\infty}\alpha_k r^{2k}\right) \tag{B17}$$

$$= V_0\mathcal{P}\sum_{k=1}^{+\infty}\frac{5}{6}\frac{\alpha_k}{(2k+7)(2k+5)(2k+2)2k}r^{2k+4}. \tag{B18}$$

The general solution for $\hat{p}_{2,1}$ is

$$\hat{p}_{2,1} = A_2 r^2 + B_2 r^4 + \sum_{k=1}^{+\infty}\beta_k r^{2k+4}, \tag{B19}$$

where

$$\beta_k = \frac{5}{6}\frac{\alpha_k}{(2k+7)(2k+5)(2k+2)2k} \tag{B20}$$

$$= \frac{25}{2(2k+7)(2k+5)(2k+3)(2k+2)(2k+1)(2k-1)}, \tag{B21}$$

The constants A_2 and B_2 have to be determined from the boundary conditions. The stress free condition gives

$$3A_2 + 8B_2 + \sum_{k=1}^{+\infty}\beta_k\left[2+(k+2)(2k+3)\right] = 0 \tag{B22}$$

and the continuity of normal stress gives, ignoring $\mathcal{O}(\mathcal{P})$ terms,

$$-15A_2 - 21B_2 + \sum_{k=1}^{+\infty}\beta_k(2k+7)(2k^2+2k-3) = 0. \tag{B23}$$

From eqs (B22) and (B23), we obtain

$$B_2 = -\frac{1}{19}\sum_{k=1}^{+\infty}(k+1)(4k^2+24k+19)\beta_k \simeq -0.0211 \tag{B24}$$

and

$$A_2 = \frac{1}{57}\sum_{k=1}^{+\infty}k(32k^2+186k+211)\beta_k \simeq 0.0346. \tag{B25}$$

B2 $l = 1$ temperature field at $\mathcal{O}(\mathcal{P})$ and velocity field at $\mathcal{O}(\mathcal{P}^2)$

Inserting in eq. (B9) the expression found above for the $l = 2$ component of the velocity field, $\hat{t}_{1,1}$ is now given by

$$\hat{t}_{1,1} = -\hat{p}_{1,1} - \frac{3}{5}\left(A_2 r + B_2 r^3 + \sum_{k=1}^{+\infty}\beta_k r^{2k+3}\right)\left(\sum_{k=1}^{+\infty}\alpha_k r^{2k}\right). \tag{B26}$$

After some rearrangements, we obtain

$$\hat{t}_{1,1} = -\hat{p}_{1,1} - \frac{3}{5}\sum_{k=0}^{+\infty}(A_2\alpha_{k+1} + B_2\alpha_k + \gamma_k - \beta_0\alpha_k)r^{2k+3}, \tag{B27}$$

where

$$\gamma_k = \sum_{i=0}^{k}\alpha_i\beta_{k-i}. \tag{B28}$$

We can now determine the $l = 1$ flow field by integrating the Stokes equation with the above temperature field. Noting

$$p_1 = \frac{V_0}{2}\left[r + \hat{p}_{1,1}\mathcal{P} + \hat{p}_{1,2}\mathcal{P}^2 + \mathcal{O}(\mathcal{P}^3)\right] \tag{B29}$$

the second order contribution is given by

$$\frac{V_0}{2}\mathcal{P}^2\hat{p}_{1,2} = \frac{6}{V_0}\mathcal{P}Ra\left(\mathcal{D}_1^2\right)^{-1}\hat{t}_{1,1}, \tag{B30}$$

or

$$\hat{p}_{1,2} = 10\left(\mathcal{D}_1^2\right)^{-1}\hat{t}_{1,1} + Dr + Er^3. \tag{B31}$$

We obtain

$$\begin{aligned} \hat{p}_{1,2} = &-\frac{1}{28}Ar^5 - \frac{5}{756}Br^7 - \frac{5}{2376}Cr^9 \\ &-\frac{30}{5}\sum_{k=0}^{+\infty}\frac{A_2\alpha_{k+1} + (B_2-\beta_0)\alpha_k + \gamma_k}{(2k+9)(2k+6)(2k+7)(2k+4)}r^{2k+7} \\ &+Dr + Er^3 \end{aligned} \tag{B32}$$

which gives

$$\begin{aligned} \hat{p}_{1,2} = &-\frac{1}{28}Ar^5 + \frac{25}{31752}r^7 - \frac{5}{66528}r^9 \\ &-\frac{30}{5}\sum_{k=0}^{+\infty}\frac{A_2\alpha_{k+1} + (B_2-\beta_0)\alpha_k + \gamma_k}{(2k+9)(2k+6)(2k+7)(2k+4)}r^{2k+7} \\ &+Dr + Er^3. \end{aligned} \tag{B33}$$

The constants A and E can be determined from the boundary conditions. The no-stress condition gives

$$E = \frac{5}{42}A - \frac{115}{24948} + \sum_{k=0}^{+\infty}\frac{A_2\alpha_{k+1} + (B_2-\beta_0)\alpha_k + \gamma_k}{(2k+9)(2k+4)} \tag{B34}$$

and continuity of the normal stress gives

$$\begin{aligned} \frac{23}{7}A = &-6E + \frac{316}{1173} - \frac{30}{5}\sum_{k=0}^{+\infty}\frac{A_2\alpha_{k+1} + (B_2-\beta_0)\alpha_k + \gamma_k}{(2k+9)(2k+6)(2k+7)(2k+4)} \\ &\times 2(k+3)(4k^2+24k+29). \end{aligned} \tag{B35}$$

Using eqs (B34) and (B35), we obtain

$$A = \frac{131}{1764} - \frac{3}{2}\sum_{k=0}^{+\infty} \frac{A_2\alpha_{k+1} + (B_2 - \beta_0)\alpha_k + \gamma_k}{2k+7} \simeq 0.0617. \tag{B36}$$

The average velocity $\bar{u}_x$ in the x direction, defined as

$$\bar{u}_x = \frac{1}{V_{\rm ic}} \int_{V_{\rm ic}} u_x \mathrm{d}V \tag{B37}$$

is less than the infinite viscosity limit (here $V_{\rm ic}$ is the volume of the inner core). Indeed, noting that $u_x = u_r \cos\theta - u_\theta \sin\theta$, and that

$$u_r = \sum_{l,m} l(l+1)\frac{p_l^m}{r} P_l, \tag{B38}$$

$$u_\theta = \sum_{l,m} \frac{1}{r}\frac{\mathrm{d}}{\mathrm{d}r}\left(r p_l^m\right)\frac{\partial P_l}{\partial \theta}, \tag{B39}$$

we find

$$\bar{u}_x = \frac{3}{4\pi}\int_0^1\int_0^\pi \left[2\, p_1 \cos^2\theta + \frac{\mathrm{d}}{\mathrm{d}r}\left(r\ p_1\right)\sin^2\theta\right] r\sin\theta \mathrm{d}r\mathrm{d}\theta\mathrm{d}\phi \tag{B40}$$

$$= \int_0^1 \left[4p_1 + 2r\frac{\mathrm{d}p_1}{\mathrm{d}r}\right] r\,\mathrm{d}r = \int_0^1 2\frac{\mathrm{d}}{\mathrm{d}r}\left(r^2 p_1\right)\,\mathrm{d}r \tag{B41}$$

$$= 2\, p_1(r=1) \tag{B42}$$

$$= V_0\left[1 + (A+B+C)\,\mathcal{P} + \mathcal{O}(\mathcal{P}^2)\right], \tag{B43}$$

which gives

$$\bar{u}_x \simeq \sqrt{\frac{6}{5}\frac{Ra}{\mathcal{P}}}\left[1 - 0.0216\,\mathcal{P} + \mathcal{O}(\mathcal{P}^2)\right]. \tag{B44}$$

Journal of Earth Science, *Vol. 24*, *No. 5*, *p. 669–682*, *October 2013* *ISSN 1674-487X*
Printed in China
DOI: 10.1007/s12583-013-0364-8

Thermal Convection in a Spherical Shell with Melting/Freezing at either or both of Its Boundaries

Renaud Deguen*
Institut de Mécanique des Fluides de Toulouse, *Université de Toulouse* (*INPT*, *UPS*) *and CNRS*, *Allée C. Soula*, *Toulouse* 31400, *France*

ABSTRACT: In a number of geophysical or planetological settings, including Earth's inner core, a silicate mantle crystallizing from a magma ocean, or an ice shell surrounding a deep water ocean—a situation possibly encountered in a number of Jupiter and Saturn's icy satellites—a convecting crystalline layer is in contact with a layer of its melt. Allowing for melting/freezing at one or both of the boundaries of the solid layer is likely to affect the pattern of convection in the layer. We study here the onset of thermal convection in a viscous spherical shell with dynamically induced melting/freezing at either or both of its boundaries. It is shown that the behavior of each interface—permeable or impermeable—depends on the value of a dimensionless number P (one for each boundary), which is the ratio of a melting/freezing timescale over a viscous relaxation timescale. A small value of P corresponds to permeable boundary conditions, while a large value of P corresponds to impermeable boundary conditions. Linear stability analysis predicts a significant effect of semi-permeable boundaries when the number P characterizing either of the boundary is small enough: allowing for melting/freezing at either of the boundary allows the emergence of larger scale convective modes. The effect is particularly drastic when the outer boundary is permeable, since the degree 1 mode remains the most unstable even in the case of thin spherical shells. In the case of a spherical shell with permeable inner and outer boundaries, the most unstable mode consists in a global translation of the solid shell, with no deformation. In the limit of a full sphere with permeable outer boundary, this corresponds to the "convective translation" mode recently proposed for Earth's inner core. As another example of possible application, we discuss the case of thermal convection in Enceladus' ice shell assuming the presence of a global subsurface ocean, and found that melting/freezing could have an important effect on the pattern of convection in the ice shell.
KEY WORDS: planetary mantle, thermal convection, phase change, linear stability analysis.

INTRODUCTION

The seismologically observed hemispherical asymmetry of the inner core (Irving and Deuss, 2011; Niu and Wen, 2001; Tanaka and Hamaguchi, 1997) has recently been interpreted as resulting from a high-viscosity mode of thermal convection, consisting in a translation of the inner core with melting on one hemisphere and solidification on the other (Alboussière et al., 2010; Monnereau et al., 2010). This "convective translation" regime can exist because the

This study was supported by the ANR (Agence Nationale de la Recherche) of France (No. ANR-12-PDOC-0015-01).
*Corresponding author: renaud.deguen@imft.fr

Manuscript accepted March 13, 2013.
Manuscript received June 2, 2013.

boundary between the inner core and the outer core is a phase change interface, which means that deforming the inner core boundary (ICB) by internal stresses can induce melting or freezing. Melting occurs when the ICB is displaced outward, and crystallization occurs when the ICB is displaced inward, at a rate which depends on the ability of outer core convection to supply or evacuate the latent heat of phase change. Because there is no deformation, and therefore no viscous dissipation, associated with it, the translation mode is dominant whenever phase change at the inner core boundary proceeds at a fast enough rate.

The situation where a convective crystalline shell is in contact with its melt is encountered in a number of other geophysical or planetological problems, including convection in a silicate mantle crystallizing from below from a magma ocean, or from a basal magma ocean (Ulvrová et al., 2012; Labrosse et al., 2007), or convection in an ice shell surrounding a deep water ocean, a situation possibly encountered in several of Jupiter and Saturn's icy satellites (Tyler, 2008; Spohn and Schubert, 2003; Kivelson et al., 2000). If one of the boundaries is impermeable, the translation mode predicted for a full sphere obviously cannot exist, but we might anticipate that allowing for phase change at the other boundary will modify the pattern of convection and favor larger scale modes (Monnereau and Dubuffet, 2002). We will study here the onset of thermal convection in a uniformly heated spherical shell with boundary conditions allowing for dynamically induced melting or freezing at either or both of the boundaries.

PROBLEM DEFINITION

We consider a viscous solid spherical shell of outer radius R and inner radius γR, in contact with melt layers either above or below, or both (see Fig. 1). Superscripts "+" or "-" will be used for quantities taken at the outer or inner boundary, respectively. The solid shell has constant density ρ_s, the layers below and above have densities ρ_m^- and ρ_m^+, respectively, and we note $\Delta\rho^+ = \rho_m^+ - \rho_s$ and $\Delta\rho^- = \rho_m^- - \rho_s$. To ensure long term mechanical stability of the solid layer, we must have $\rho_m^- > \rho_s > \rho_m^+$, or $\Delta\rho^+ < 0$ and $\Delta\rho^- > 0$. The inner and outer boundaries are phase change interfaces, and melting and freezing can therefore occur when the interface is displaced by internal stresses. This will be described below with a parametrization of the relationship between the freezing or melting rate and the dynamic topography of the interface, which has been developed for describing convection in Earth's inner core (Deguen et al., 2013; Alboussière et al., 2010).

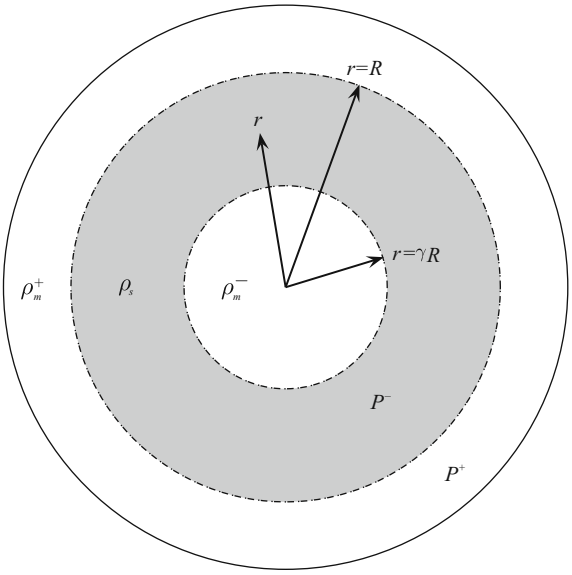

Figure 1. A sketch of the problem considered here.

To be consistent with the assumption of constant density ρ_s, the acceleration of gravity g in the spherical shell is assumed to vary linearly with radius r, $g = -g' r e_r$, where $g' = dg/dr = g^+/R = Cst$ and e_r is the radial unit vector, which is relevant to situations where the depth dependence of the density is too small to have a significant effect on the mean gravity profile. While this is not true in a number of situations of geophysical interest (like in Earth's mantle), we will make this assumption for two reasons: (i) it is (mathematically) the simplest configuration (Chandrasekhar, 1961), and (ii) the case of the inner core, for which g is essentially linear in r, corresponds to the limit $\gamma \to 0$ of the problem discussed here. Considering a more general form for g is likely to give qualitatively similar results.

The spherical shell is heated volumetrically at a rate $\rho_s c_{ps} S$ (with c_{ps} the specific heat capacity of the solid layer, and S the heating rate in K/s). The rheology is assumed to be Newtonian and temperature and pressure independent, with a constant viscosity η. Thermal convection in the spherical shell is then described by the conservation equations for mass, mo-

mentum, and entropy, which take the form

$$\nabla \cdot u = 0 \tag{1}$$

$$0 = -\nabla p - \alpha_s \rho_s \Theta g + \eta \nabla^2 u \tag{2}$$

$$\frac{\partial \Theta}{\partial t} + u \cdot \nabla \Theta = \kappa_S \nabla^2 \Theta + S \tag{3}$$

under the Boussinesq approximation. Here α_S and κ_s are the thermal expansion coefficient and thermal diffusivity in the solid shell, respectively.

Boundary Conditions

The rate of melting/freezing at each interface depends on the ability of convective motion in the melt layer to transport the heat absorbed or released by the phase change. Given a topography $h(\theta,\varphi)$ of the boundary (defined here in reference to the isopotential surface which coincides on average with the boundary), the rate of erosion of the topography by melting or freezing is set by a balance between the rate of latent heat release or absorption, $\rho_S L(u_r^{\pm} - \partial h/\partial t)$, with the convective heat flux on the melt side, which should scale as $\rho^{\pm}_{ll}\ c_{pl}^{\pm} u' \delta\Theta$, where L is the latent heat of melting, $u_r^{\pm}$ is the radial component of the solid layer flow velocity at the boundary, $c_{pl}^{\pm}$ the specific heat capacity of the melt, u' a typical velocity scale for convective motion in the melt layer, and $\delta\Theta(\theta,\phi)$ the difference of potential temperature between the boundary and the adjacent melt. The boundary is assumed to remain very close to thermodynamic equilibrium (more justifications in Deguen et al. (2013)), and is therefore at the melting temperature $T_m^{\pm}$. The potential temperature variation $\delta\Theta(\theta,\phi)$ along the boundary results from the combined effect of the pressure dependency of $T_m^{\pm}$ and of the adiabat in the melt layer, so that a topography h induces a difference of potential temperature between the boundary and the melt layer given by

$$\delta\Theta = -(m_p^{\pm} - m_{ad}^{\pm})\rho_l^{\pm} g^{\pm} h \tag{4}$$

where $m_P^{\pm} = \partial T_s / \partial P$ is the Clapeyron slope, and $m_{ad}^{\pm} = \partial T_{ad} / \partial P$ is the adiabatic gradient in the melt layer at each boundary. With this expression for $\delta\Theta$, the heat balance described above gives

$$u_r^{\pm} - \frac{\partial h}{\partial t} = \frac{h}{\tau_\phi^{\pm}} \tag{5}$$

where the timescale for phase change, $\tau_\phi^{\pm}$, is

$$\tau_\phi^{\pm} \sim \frac{\rho_s L}{\rho_l^{\pm 2} c_{pl}^{\pm} \left| m_P^{\pm} - m_{ad}^{\pm} \right| g^{\pm} u'} \tag{6}$$

with $m_P^{\pm} = T_m^{\pm} \Delta\rho^{\pm} / (\rho_S \rho_l^{\pm} L)$ from the Clapeyron relation, Equation (6) can be rewritten as

$$\tau_\phi^{\pm} \sim \frac{\rho_s^2 L^2}{\rho_l^{\pm} \left| \Delta\rho^{\pm} \right| c_{pl}^{\pm} T_m^{\pm} \left| 1 - m_{ad}^{\pm} / m_P^{\pm} \right| g^{\pm} u'} \tag{7}$$

Assuming that the phase-change timescale $\tau_\phi^{\pm}$ and the viscous relaxation timescale $\tau_\eta^{\pm} = \eta / \left(\left| \Delta\rho^{\pm} \right| g^{\pm} R \right)$ are both small compared to the dynamical timescale of the shell (overturn time), we can neglect $\partial h/\partial t$ in Equation (5), which gives the boundary condition

$$u_r^{\pm} = \frac{h}{\tau_\phi^{\pm}} \tag{8}$$

The mechanical boundary conditions are tangential stress-free conditions and continuity of the normal stress at both boundaries. Under the assumption of small topography, the stress-free tangential condition writes

$$\tau_{r\theta} = \eta \left[r \frac{\partial}{\partial r} \left(\frac{u_\theta}{r} \right) + \frac{1}{r} \frac{\partial u_r}{\partial \theta} \right] = 0 \tag{9}$$

$$\tau_{r\phi} = \eta \left[r \frac{\partial}{\partial r} \left(\frac{u_\phi}{r} \right) + \frac{1}{r \sin\theta} \frac{\partial u_r}{\partial \phi} \right] = 0 \tag{10}$$

at $r=\gamma$ and 1, where $\tau_{r\theta}$ and $\tau_{r\varphi}$ are the (r, θ) and (r, φ) components of the deviatoric stress tensor $\underline{\tau}$ continuity of the normal stress at each boundary is written as

$$\left[\left[\tau_{rr} - p \right] \right]_h = \left[\left[2\eta \frac{\partial u_r}{\partial r} - p \right] \right]_h = 0 \tag{11}$$

where $\left[\left[... \right] \right]$ denotes the difference of a quantity across the boundary. When expanded around the mean position of the boundary, Equation (11) gives

$$-\Delta\rho^{\pm} g^{\pm} h - 2\eta \frac{\partial u_r}{\partial r} + p = 0 \tag{12}$$

under the assumption that pressure fluctuations on the melt side are negligible compared to pressure fluctuations on the solid side (e.g., Ribe, 2007). With h related to u_r by Equation (8), Equation (12) gives a boundary condition for u_r only

$$-\Delta\rho^{\pm} g^{\pm} \tau_\phi^{\pm} u_r - 2\eta \frac{\partial u_r}{\partial r} + p = 0 \tag{13}$$

The topography h is an implicit variable of the problem, and can be calculated a posteriori from the radial velocity at the boundary.

Non-Dimensional Set of Equations

The governing equations and boundary conditions are now made dimensionless using the thermal diffusion timescale κ_s/R^2, the outer radius R, κ_s/R, $\eta\kappa_s/R^2$, and $SR^2/(6\kappa_s)$ as scales for time, length, velocity, pressure and potential temperature, respectively. Using the same symbols for dimensionless quantities, the system of equations (1–3) is then written as

$$\nabla \cdot u = 0 \tag{14}$$

$$0 = -\nabla p - Ra\Theta re_r + \nabla^2 u \tag{15}$$

$$\frac{\partial \Theta}{\partial t} + u \cdot \nabla\Theta = \nabla^2\Theta + 6 \tag{16}$$

where the Rayleigh number is defined as

$$Ra = \frac{\alpha\rho_s g^+ SR^5}{6\eta\kappa_s^2} \tag{17}$$

The Rayleigh number defined here is based on the outer radius R, not the shell thickness $(1-\gamma)R$. Also, note that the Rayleigh number used here is half that defined by Chandrasekhar (1961). The dimensionless boundary conditions at $r=\gamma$ or 1 can be written

$$\Theta(\gamma) = \Theta_\gamma, \quad \Theta(1) = 0 \tag{18}$$

$$r\frac{\partial}{\partial r}\left(\frac{u_\theta}{r}\right) + \frac{1}{r}\frac{\partial u_r}{\partial \theta} = r\frac{\partial}{\partial r}\left(\frac{u_\phi}{r}\right) + \frac{1}{r\sin\theta}\frac{\partial u_r}{\partial \phi} = 0 \tag{19}$$

$$\pm \mathrm{P}^{\pm} u_r + 2\frac{\partial u_r}{\partial r} - p = 0 \tag{20}$$

where the "phase change numbers" P^+ and P^- are defined as (Deguen et al., 2013; Deguen, 2012)

$$\mathrm{P}^{\pm} = \frac{\tau_\phi^{\pm}}{\tau_\eta^{\pm}} \tag{21}$$

where $\tau_\phi^{\pm}$ is the timescale for erosion of a topography by melting or freezing, as defined in Equation (6), and $\tau_\eta^{\pm} = \eta/\left(\left|\Delta\rho^{\pm}\right| g^{\pm} R\right)$ is the viscous relaxation timescale at the length scale R. The phase change numbers P^+ and P^- are measures of the resistance to phase change on each boundary. In the limit of infinite $\mathrm{P}^{\pm}$, the boundary condition (20) reduces to the condition $u_r^{\pm} = 0$, which corresponds to impermeable conditions. In contrast, when $\mathrm{P}^{\pm} \to 0$, Equation (20) implies that the normal stress tends toward 0 at the boundary, which corresponds to fully permeable boundary conditions (e.g., Monnereau and Dubuffet, 2002). The general case of finite $\mathrm{P}^{\pm}$ gives boundary conditions for which the rate of phase change at the boundary (equal to $u_r^{\pm}$) is proportional to the normal stress induced by convection within the spherical shell. Note that we have defined P^+ and P^- using the absolute value of $\Delta\rho^{\pm}$, so that both P^+ and P^- are positive. Because $\Delta\rho^-$ is negative, this introduces a minus sign before P^- in the boundary condition (20) for the inner boundary.

With the assumptions made so far, the velocity field is known to be purely poloidal (Ribe, 2007) and we introduce the poloidal scalar P defined such that $u = \nabla\times\nabla\times(Pre_r)$. Taking the curl of the momentum equation (15) gives

$$RaL^2\Theta = (\nabla^2)^2 L^2 P \tag{22}$$

where the angular momentum operator L^2 is

$$L^2 = -\frac{1}{\sin\theta}\frac{\partial}{\partial\theta}\left(\sin\theta\frac{\partial}{\partial\theta}\right) - \frac{1}{\sin^2\theta}\frac{\partial^2}{\partial\phi^2} \tag{23}$$

Horizontal integration of the momentum equation (15) (Ribe, 2007) shows that, on both boundaries

$$-p + \frac{\partial}{\partial r}\left(r\nabla^2 P\right) = Cst \tag{24}$$

Using this expression to eliminate p in the boundary condition (20), and noting that $u_r = \frac{1}{r}L^2 P$, continuity of the normal stress at each boundary (Equation (20)) gives the following boundary condition for the poloidal scalar at $r=1$ or γ

$$\frac{\partial}{\partial r}\left(r\nabla^2 P - \frac{2}{r}L^2 P\right) - \pm\mathrm{P}^{\pm}\frac{L^2 P}{r} = Cst \tag{25}$$

while the stress-free conditions (19) give

$$\frac{\partial^2 P}{\partial r^2} + (L^2 - 2)\frac{P}{r^2} = Cst \tag{26}$$

at $r=\gamma$ or 1.

STEADY BASIC SOLUTION

The governing equations and boundary conditions presented in the previous section admit a steady solution (denoted by an overbar $\bar{\cdots}$) in which the ve-

locity field is $\bar{u}=0$ and the potential temperature field $\bar{\Theta}$ is given by the steady state, conductive version of Equation (3), which writes

$$0=\nabla^2\bar{\Theta}+6 \tag{27}$$

with $\bar{\Theta}(r=1)=0$, the general solution of Equation (27) is of the form

$$\bar{\Theta}=a+\frac{1-a}{r}-r^2 \tag{28}$$

where the constant a depends on the thermal boundary condition at $r=\gamma$. The stability analysis could be carried out for the general potential temperature profile given by Equation (28), but we will consider only the case a=1. This is mathematically simpler, and, in addition, will allow us to extrapolate easily the results to the case of Earth's inner core, for which the basic diffusive potential temperature profile is given by $\bar{\Theta}=1-r^2$ (Deguen et al., 2013). The potential temperature at $r=\gamma$ is then $\bar{\Theta}(\gamma)=1-\gamma^2$.

LINEAR STABILITY ANALYSIS

We now investigate the stability of the basic conductive state against infinitesimal perturbations of the temperature and velocity fields. The present analysis follows the analysis presented in Chandrasekhar (1961) (Chapter VI-60), where the stability analysis is treated in the case of impermeable boundaries, which corresponds to the limit of infinite P^+ and P^-. The case of thermal convection in a full sphere with boundary conditions as described above, which corresponds to the limit $\gamma\to 0$ of the problem considered here, has been treated in Deguen et al. (2013).

The temperature field is written as the sum of the conductive temperature profile given by Equation (28) with a=1 and infinitesimal disturbances $\tilde{\Theta}:\Theta(r,\theta,\phi,t)=\bar{\Theta}(r)+\tilde{\Theta}(r,\theta,\phi,t)$. The velocity field perturbation is denoted by $\tilde{u}(r,\theta,\phi,t)$, and has an associated poloidal scalar $\tilde{P}(r,\theta,\phi,t)$. We expand the temperature and poloidal disturbances in spherical harmonics

$$\tilde{\Theta}=\sum_{l=0}^{\infty}\sum_{m=-l}^{l}\tilde{t}_l^m(r)Y_l^m(\theta,\phi)e^{\sigma_l t} \tag{29}$$

$$\tilde{P}=\sum_{l=1}^{\infty}\sum_{m=-l}^{l}\tilde{p}_l^m(r)Y_l^m(\theta,\phi)e^{\sigma_l t} \tag{30}$$

where σ_l is the growth rate of the degree l perturbations (note that since m does not appear in the system of equations, the growth rate is function of l only, not m).

The only non-linear term in the system of equations is the advection of heat $u\cdot\nabla\Theta$ in Equation (16), which is linearized as

$$\tilde{u}_r\frac{\partial\bar{\Theta}}{\partial r}=-2r\tilde{u}_r=-2L^2\tilde{P} \tag{31}$$

The resulting linearized transport equation for the potential temperature disturbance is

$$\left(\frac{\partial}{\partial t}-\nabla^2\right)\tilde{\Theta}=2L^2\tilde{P} \tag{32}$$

Using the decompositions (29) and (30), the linearized system of equations is then, for $l\geq 1$

$$Ra\tilde{t}_l^m=D_l^2\tilde{p}_l^m \tag{33}$$

$$\left(\sigma_l-D_l\right)\tilde{t}_l^m=2l(l+1)\tilde{p}_l^m \tag{34}$$

where the operator D_l is defined as

$$D_l=\frac{d^2}{dr^2}+\frac{2}{r}\frac{d}{dr}-\frac{l(l+1)}{r^2} \tag{35}$$

The stress-free boundary condition is written as

$$\frac{d^2\tilde{p}_l^m}{dr^2}+\left[l(l+1)-2\right]\frac{\tilde{p}_l^m}{r^2}=0\quad l\geq 1 \tag{36}$$

with r=1 or γ on the upper or lower boundary, and the boundary conditions derived from the continuity of the normal stress are given by

$$\frac{d}{dr}\left(rD_l\tilde{p}_l^m-2l(l+1)\frac{\tilde{p}_l^m}{r}\right)=+l(l+1)\mathrm{P}^+\frac{\tilde{p}_l^m}{r} \tag{37}$$

$$\frac{d}{dr}\left(rD_l\tilde{p}_l^m-2l(l+1)\frac{\tilde{p}_l^m}{r}\right)=-l(l+1)\mathrm{P}^-\frac{\tilde{p}_l^m}{r} \tag{38}$$

at the outer and inner boundaries, respectively (note the different signs of the right-hand-side terms). We expand the potential temperature perturbation $\tilde{t}_l^m(r)$ as

$$\tilde{t}_l^m(r)=\frac{1}{\sqrt{r}}\sum_j A_{lj}C_{ll}(\alpha_{lj}r) \tag{39}$$

where the functions $C_{ll}(\alpha_{lj}r)$ are defined as

$$C_{ll}(\alpha_{lj}r) = J_{-(l+1/2)}(\alpha_{lj}\gamma)J_{l+1/2}(\alpha_{lj}r) - J_{l+1/2}(\alpha_{lj}\gamma)J_{-(l+1/2)}(\alpha_{lj}r) \tag{40}$$

(Chandrasekhar, 1961). Here J_k denotes the Bessel function of the first kind of degree k, and the constants α_{lj} are the jth zeros of the function $C_{ll}(r)$. By construction, $C_{ll}(\alpha_{li}\gamma)=0$. As discussed by Chandrasekhar (1961), the functions $C_{ll}(\alpha_{li}r)$ form an integral set of functions satisfying the orthogonality relation

$$\int_{\gamma}^{1} C_{ll}(\alpha_{lj}r)C_{ll}(\alpha_{lk}r)rdr = N_{l+1/2,j}\delta_{jk} \tag{41}$$

where

$$N_{l+1/2,j} = \frac{2}{\pi^2\alpha_{lj}^2}\left[\frac{J_{l+1/2}^2(\alpha_{lj}\gamma)}{J_{l+1/2}^2(\alpha_{lj})} - 1\right] \tag{42}$$

Writing the poloidal scalar perturbations $\tilde{p}_l^m(r)$ as

$$\tilde{p}_l^m(r) = \sum_j A_{lj}\, p_{lj}(r) \tag{43}$$

and injecting the expansions of $\tilde{t}_l^m(r)$ and $\tilde{p}_l^m(r)$ given by equations (39) and (43) in the momentum equation (33), the functions p_{lj} are solutions of the equation

$$D_l^2 p_{lj} = Ra\frac{C_{ll}(\alpha_{lj}r)}{\sqrt{r}} \tag{44}$$

Noting that

$$D_l\left(\frac{C_{ll}(\alpha_{lj}r)}{\sqrt{r}}\right) = -\alpha_{lj}^2\frac{C_{ll}(\alpha_{lj}r)}{\sqrt{r}} \tag{45}$$

equation (44) has a general solution of the form

$$p_{lj} = \frac{Ra}{\alpha_{lj}^4}\frac{C_{ll}(\alpha_{lj}r)}{\sqrt{r}} + B_1^j r^l + B_2^j r^{l+2} + B_3^j r^{-(l+1)} + B_4^j r^{-(l-1)} \tag{46}$$

The coefficients $B_{1\ldots4}^j$ are determined by the boundary conditions at the inner and outer boundaries of the shell, as explained in APPENDIX A.

Injecting the above solution for p_{lj} and the potential temperature expansion (39) in the linearized heat Equation (34), we obtain after some manipulations an infinite set of linear equations in A_{lj} (see Chandrasekhar (1961)), which admits a non trivial solution only if its determinant is equal to zero. With our choice of basic state and $g \propto r$, and following Chandrasekhar (1961), we find a characteristic equation of the form

$$\left\| N_{l+1/2,k}\left[\frac{\alpha_{lk}^2}{2l(l+1)} - \frac{Ra}{\alpha_{lk}^4}\right]\delta_{kj} - Q_{kj}\right\| = 0 \tag{47}$$

where $\|...\|$ denotes the determinant, and where the functions Q_{kj} are defined as

$$Q_{kj} = \int_{\gamma}^{1} C_{ll}(\alpha_{lk}r)\left[B_1^j r^l + B_2^j r^{l+2} + B_3^j r^{-(l+1)} + B_4^j r^{-(l-1)}\right] r^{3/2} dr \tag{48}$$

Solving Equation (47) with the $B_{1\ldots4}^j$ determined by the boundary conditions (APPENDIX A) gives the critical Rayleigh number Ra_c^l for a perturbation of degree l. The pattern of the first unstable modes can be calculated by solving the system in A_{lj} for given P^-, P^+, and Ra, which then allows to calculate the poloidal scalar $\tilde{p}_l^m(r)$ from equations (43) and (46).

RESULTS AND APPLICATIONS

Figure 2 shows the critical Rayleigh number corresponding to the degree one mode as a function of P^- and P^+ for three configurations: (i) the outer boundary is impermeable ($P^+ >> 1$) and P^- is varied from permeable to impermeable conditions; (ii) the inner boundary is impermeable ($P^- >> 1$) and P^+ is varied from permeable to impermeable conditions; and (iii) $P^+=P^-$, with boundary conditions varied from permeable to impermeable. For all three configurations, there is a marked change in the critical Rayleigh number at some transitional value of P^- or P^+, with the critical Rayleigh number being significantly smaller when P^- or P^+ are smaller than this transitional value, corresponding to permeable conditions.

In what follow, we will focus on end-members cases, for which each boundary is either permeable ($P^{\pm} << 1$) or impermeable ($P^{\pm} >> 1$), which gives four end-member configurations. Figure 3 shows the critical Rayleigh number as a function of l and γ for the four end-member

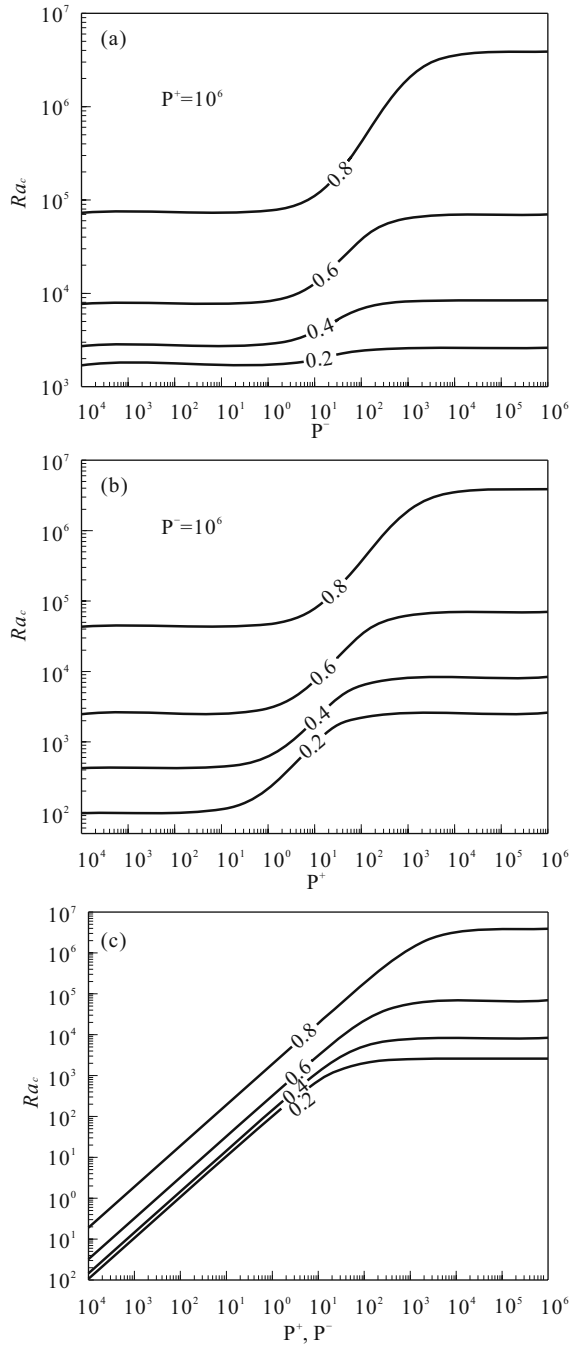

Figure 2. Critical Rayleigh number of the *l*=1 mode for (a) impermeable outer boundary, and variable P^-; (b) impermeable inner boundary, and variable P^+; (c) variable P^- and P^+, with $P^-=P^+$.

cases. The pattern of the first unstable mode (as well as the second for the $P^- \ll 1$, $P^+ \gg 1$ cases) is shown in Fig. 4. The degree l_c of the first unstable mode is shown in Fig. 5 as a function of γ. Each end-member case is described below.

(P^+, P^-)>>1—Impermeable Boundaries

Letting P^+ and P^- tend toward infinity, the problem tends toward the case of Rayleigh-Bénard convection in a spherical shell with impermeable stress free boundaries, as discussed in Chandrasekhar (1961). This will be used as a reference case for the present study. The results found here are identical to that found by Chandrasekhar (1961) (except that, as explained above, the Rayleigh numbers shown here are half that found by Chandrasekhar (1961) because of different definitions). The degree one mode is the first unstable mode for γ smaller than about 0.23. The degree l_c of the first unstable mode then increases rapidly when γ is increased (Fig. 5). The corresponding wavelength is commensurate with the shell thickness $1-\gamma$: assuming a relationship of the form $l_c=a/(1-\gamma)+b$ (which, given that $\lambda_c \sim 1/l_c$ when $l_c \gg 1$, is equivalent to $\lambda_c \sim 1-\gamma$), least square Inversion of $l_c(\gamma)$ gives $l_c=2.17/(1-\gamma)-1.35$, which is shown as a grey dash-dotted line in Fig. 5. The fit is indeed good, consistent with the assumption of a critical wavelength proportional to the layer thickness.

(P^+, P^-)<<1—Permeable Inner and Outer Boundaries

On the other extreme, when both boundaries are fully permeable, the first unstable mode is always the degree one mode (Figs. 3 and 5), which takes the form of a solid translation of the spherical shell (Fig. 4 and APPENDIX B). The limit of a full sphere (γ=0) corresponds to the "convective translation" mode recently proposed for Earth's inner core (Alboussière et al., 2010; Monnereau et al., 2010).

Since this mode consists of a pure translation, there is no deformation, and therefore no viscous dissipation in the shell. This of course does not mean that this is a non-dissipative mode. There is viscous (and magnetic in the case of Earth's inner core) dissipation in the melt layers associated with the redistribution of the latent heat of phase change. The melt layers must provide mechanical work to account for the dissipation associated with the redistribution of the latent heat, which means that this mode of convection is ultimately limited by the vigor of convective motions in the melt layers. It can be shown (APPENDIX B) that the emergence of the translation mode requires that the

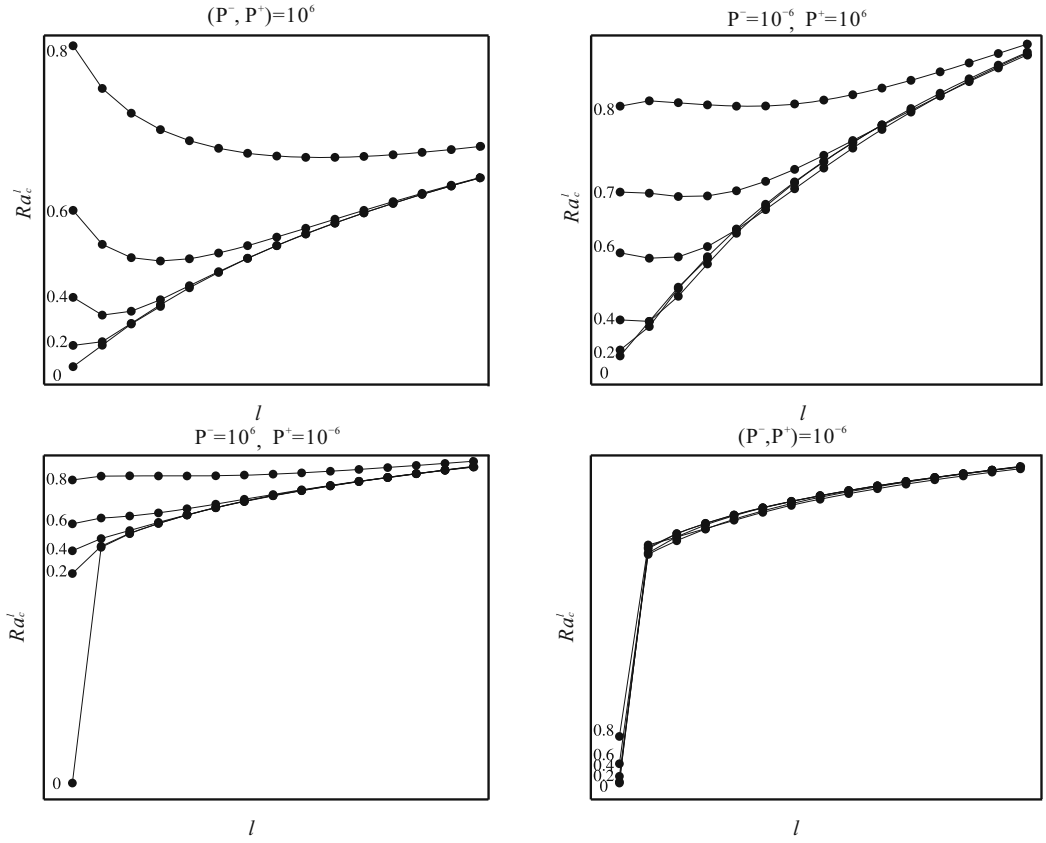

Figure 3. Critical Rayleigh number for convection as a function of degree *l*, for the four end-member cases described in the text, for various values of γ. Note the different scales used for Ra_c^l.

quantity

$$R_P = \frac{Ra}{\mathrm{P}^+ + \gamma^2 \mathrm{P}^-} \tag{49}$$

is higher than a critical value which is a function of γ only. The quantity $\mathrm{P}^+ + \gamma^2 \mathrm{P}^-$ is, save for a factor $1+\gamma^2$, the boundary area weighted mean of P^- and P^+. Figure 6 shows the critical value of R_P for the translational instability as a function of γ calculated using Equation (72) of APPENDIX B. When $\gamma \to 0$, the critical value tends toward the value of $(Ra/\mathrm{P}^+)=175/2=87.5$ found by Deguen et al. (2013) for a full sphere. R_P then increases with γ.

The limit $\gamma \to 0$ is relevant for Earth's inner core dynamics (Deguen et al., 2013; Mizzon and Monnereau, 2013; Alboussière et al., 2010; Monnereau et al., 2010). The case of a spherical shell with phase change at both boundaries might be relevant for the early dynamics of Earth's mantle, which may have started crystallizing at mid-depth from a magma ocean, with a surface magma ocean and a basal magma ocean (Labrosse et al., 2007).

($\mathrm{P}^+ \ll 1$) and ($\mathrm{P}^- \gg 1$)—Permeable Outer Boundary, Impermeable Inner Boundary

When the inner boundary is impermeable ($\mathrm{P}^- \gg 1$) and the outer boundary fully permeable ($\mathrm{P}^+ \ll 1$), the degree one mode is again found to be always the most unstable mode (Figs. 3 and 5), even when γ approaches 1. In contrast with the case where both boundaries are permeable, the degree 1 mode now does involve deformation, and the decrease in Ra_c compared to impermeable boundary conditions is therefore not as drastic as when both boundaries are permeable. The critical Rayleigh number tends toward a finite value when $\mathrm{P}^+ \to 0$, because even with a fully permeable boundary, viscous dissipation always limit the development of the mode.

This configuration could be relevant for the initiation of convection in a silicate mantle crystallizing from below from a magma ocean. The stability analysis predicts that in this configuration the first unstable mode is the degree one mode shown in Fig. 4. However, one key point in this configuration is the lifetime of the magma ocean. Melting/freezing at the interface

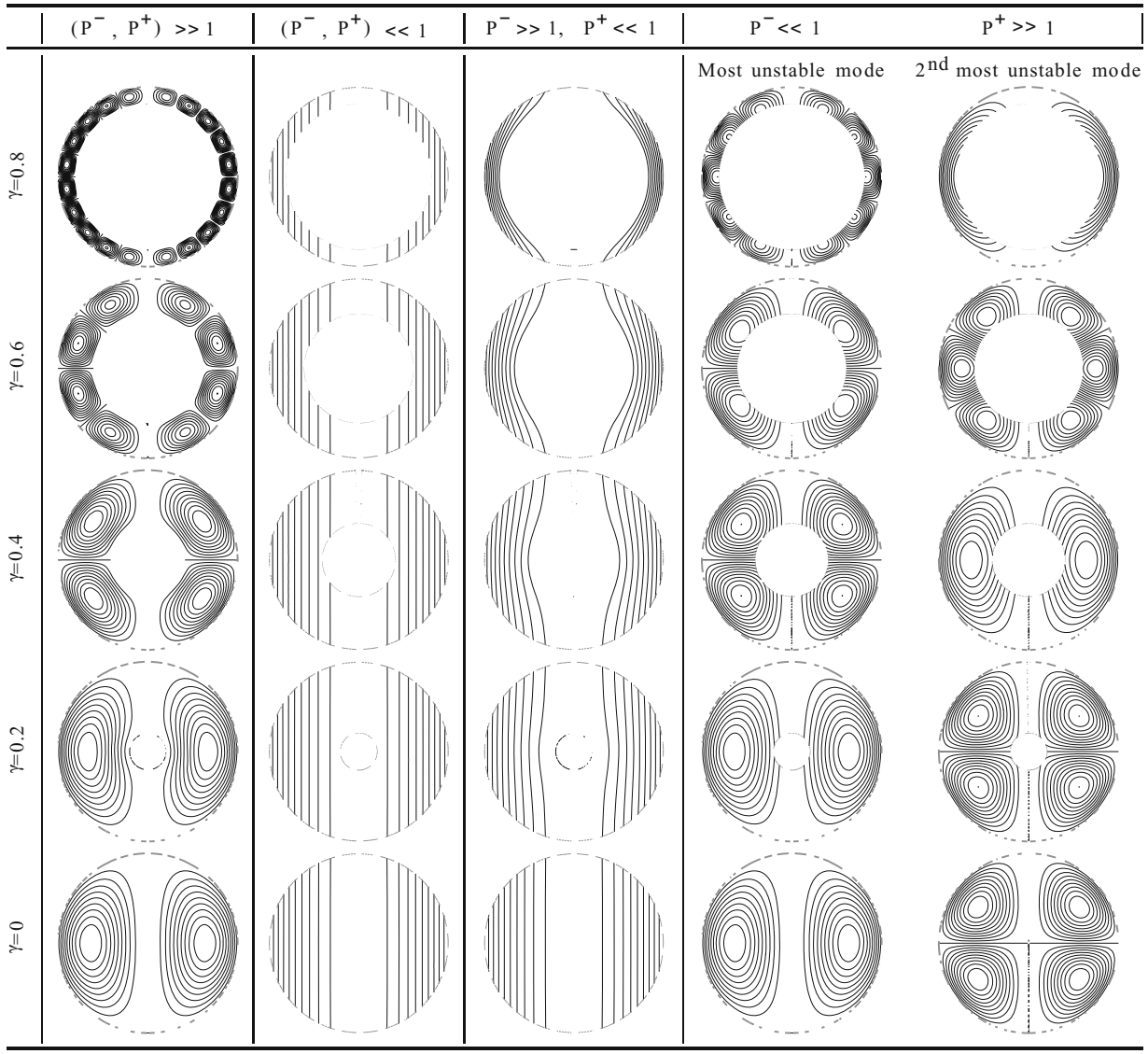

Figure 4. Pattern of the first unstable mode of thermal convection in a spherical shell (streamlines), with aspect ratio γ=0, 0.2, 0.4, 0.6 and 0.8, and P^- and P^+ either small or large compared to 1. Impermeable boundaries ($P^{\pm}>>1$) are shown by a thick line, permeable boundaries ($P^{\pm}<<1$) are shown by a thick dashed line. In the case $P^-<<1$, $P^+>>1$, we also show the second most unstable mode. Only the m=0 modes are shown.

would play a role only if the instability growth is fast enough compared to magma ocean crystallization, which can happen on a ky timescale in the absence of an insulating atmosphere or crystallized lid (Solomatov, 2000).

($P^+>>1$) and ($P^-<<1$)—Impermeable Outer Boundary, Permeable Inner Boundary

When the outer boundary is impermeable ($P^+>>1$) and the inner boundary fully permeable ($P^-<<1$), the relationship between the degree l_c of the most unstable mode and γ becomes non-monotonic (Fig. 5, solid blue line). l_c first increases with γ, similarly to the case of impermeable boundaries (except l_c is smaller when the inner boundary is permeable), but the l=1 mode becomes again the most unstable mode when γ exceeds ≈0.841. Looking at the critical Rayleigh number as a function of l (Fig. 3), there appears to be two local minima, one at l=1 and the other at a higher l, once γ is larger than ≈0.72. The two minima are quite close for all values of γ, which suggests that the l=1 mode would be important even if it is not the most unstable mode. In Fig. 5, we show in blue the degree of the most unstable mode (blue solid line) in this

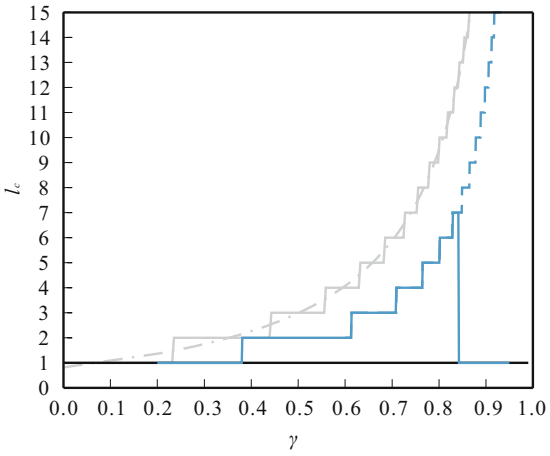

Figure 5. Degree l_c of the first unstable mode as a function of the aspect ratio γ, for different configurations. The solid gray line corresponds to the case of impermeable inner and outer boundaries. The solid blue line corresponds to the case of impermeable outer boundary and fully permeable inner boundary. The dashed blue line shows the degree of the local minimum at l strictly larger than 1 in the case of impermeable outer boundary and fully permeable inner boundary (see text). The solid black line corresponds to the cases of fully permeable inner and outer boundaries, and of fully permeable outer boundary and impermeable inner boundary, for which the most unstable mode is always the degree 1 mode.

configuration, as well as the degree of the local minimum at l strictly larger than 1 (blue dashed line).

The pattern of both the most unstable and second most unstable modes is showed in Fig. 4. The pattern of the degree one mode is found to be close to a truncated version of the pattern of the degree one mode of convection in a full sphere (compare with the γ=0 case).

This configuration may be relevant for the dynamics of icy satellites having an ice mantle overlying a global subsurface water ocean, which might be the case of several of Jupiter and Saturn' moons, including Enceladus (Waite Jr. et al., 2009; Nimmo and Pappalardo, 2006), Europa (Tyler, 2008), Callisto, Ganymede and Titan (Spohn and Schubert, 2003). It might also be relevant for thermal convection in a silicate mantle overlying a basal magma ocean, as might have been the case on Earth early in its history (Ulvrová et al., 2012; Labrosse et al., 2007). The stability analysis suggests that the length scale of convection would be significantly larger if melting/freezing at the interface is important.

DISCUSSION AND CONCLUSION

The linear stability analysis presented here predicts a significant effect of phase-change boundaries when either P^- or P^+ are small enough: allowing for melting/freezing at either of the boundaries results in the emergence of larger scale convective modes. The effect is particularly drastic when the outer boundary is permeable, since the degree 1 mode remains the most unstable even in the case of thin spherical shells. It seems likely that allowing for melting/freezing at one boundary will still result in larger scale convection at supercritical conditions, but the results presented here will clearly have to be supplemented by finite amplitude numerical calculations at supercritical conditions. In addition, the assumption of Newtonian rheology and constant viscosity limits the direct applicability of our results. The effect of variable viscosity would have to be investigated, in particular for application to icy moons, for which order of magnitude variations of viscosity across the layer may be expected. The pattern of convection is also likely to depend on the temperature profile of the basic state (McNamara and Zhong, 2005).

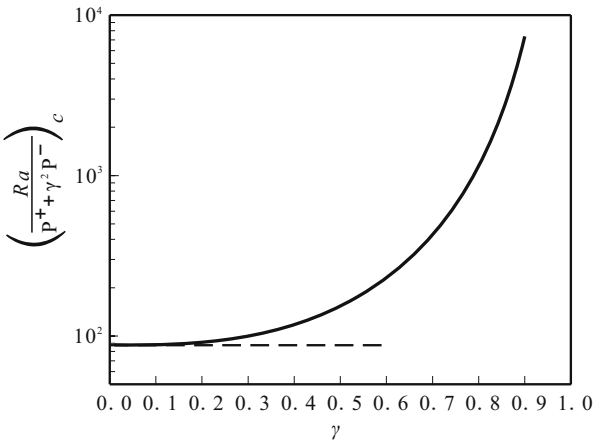

Figure 6. Critical value of the quantity $(Ra/(P^+ + \gamma^2 P^-))_c$ for the translation mode in the limit of small P^- and P^+, as a function of the inner to outer radius ratio γ (solid black line). The dashed black line shows the value of 175/2 found analytically by Deguen et al. (2013) for a full sphere (γ=0).

At this stage, we have suggested some possible geophysical or planetological applications of our results, but specific studies will be needed to assess the applicability of our results in particular settings. In each situation, the value of P of the boundary must be evaluated, which necessitates some understanding of the dynamics of the melt layer in contact with the solid layer.

As an example, let us discuss the case of Enceladus. Enceladus exhibits a strong hemispherical asymmetry, with the Southern Hemisphere being much younger and active that the Northern Hemisphere (Porco et al., 2006). One plausible explanation for the observed asymmetry is degree one convection (Stegman et al., 2009; Grott et al., 2007). Enceladus may have a global subsurface ocean (Tyler, 2009; Waite Jr. et al., 2009; Nimmo and Pappalardo, 2006), and it is therefore legitimate to consider the possible dynamical effect of melting/freezing at the inner boundary of the ice shell. Whether phase change at the inner boundary of the ice shell can alter significantly the pattern of convection depends on the value of P^- with γ=0.6 (Schubert et al., 2007), the effect of phase change would be significant if P^- is smaller than about 10 (Fig. 2). With a viscosity of order 10^{14} Pa·s (which corresponds to the viscosity near the melting point), a radius R=250 km, $\left|\Delta\rho^-\right| = 50\,\mathrm{kg\cdot m^{-3}}$ and $g^-\approx 0.1\ \mathrm{m\cdot s^{-2}}$, we find that $P^-<10$ if the timescale for phase change τ_ϕ^- is smaller than about 25 years. With τ_ϕ^- given by Equation (7), L=300 kJ·kg^{-1}, c_{pl}=4 000 K·kg^{-1}·K^{-1}, T_m=275 K, and $1-m_{ad}/m_P\sim 1$, this would require typical convective velocities around 1 cm·s^{-1} in the melt layer. Tyler (2009) estimates that eccentricity tides would have typical flow amplitude around 1 mm·s^{-1} in a 100 km thick ocean and 1 cm·s^{-1} in a 10 km thick ocean. This would give P^- in the range 10–10^2, so P^- may plausibly be small enough for a significant effect of melting/freezing on the pattern of convection. Including the effect of temperature on viscosity is likely to make the effect of melting/freezing stronger because the effective viscosity for relaxation of a large scale topography would be larger, possibly by several order of magnitude, than the high homologous temperature value of 10^{14} Pa·s assumed here. This would yield a lower effective value of P^-, and a more permeable boundary. Whether or not the effect is strong enough to allow the emergence of a strong degree one convection mode remains an open question. The answer might also depend in part of the dynamical effect of radial viscosity variations in the ice shell (McNamara and Zhong, 2005; Zhong and Zuber, 2001), which will have to be taken into account.

ACKNOWLEDGMENTS

This study was to a large extent motivated by Shijie Zhong's presentation on degree one structures in planetary mantles, given at the 2012 Core Dynamics workshop in Wuhan. I would like to thank David A Yuen and the organizing committee for the invitation, and Shijie Zhong for discussion. I gratefully acknowledge support from the ANR (Agence Nationale de la Recherche) of France (No. ANR-12-PDOC-0015-01).

APPENDIX A - COEFFICIENTS $B_{l\sim 4}^j$

The coefficients $B_{l\sim 4}^j$ introduced in Equation (46) are determined for each degree l by the boundary conditions at the inner and outer boundaries of the shell.

Using expression (46) for p_{lj}, the tangential stress boundary condition (Equation (26)) gives

$$B_1^j\gamma^{l-2}(l^2-1)+B_2^j\gamma^l l(l+2)+B_3^j\gamma^{-l-3}l(l+2)+B_4^j\gamma^{-l-1}(l^2-1)=Ra\frac{C_{ll}'(\alpha_{lj}\gamma)}{\alpha_{lj}^3\gamma^{3/2}} \tag{50}$$

at $r=\gamma$ and

$$B_1^j(l^2-1)+B_2^j l(l+2)+B_3^j l(l+2)+B_4^j(l^2-1)=Ra\frac{C_{ll}'(\alpha_{lj})}{\alpha_{lj}^3} \tag{51}$$

at r=1.

The boundary condition (25) derived from the continuity of the normal stress gives

$$B_1^j\gamma^{l-2}\left(1-l+\frac{\mathrm{P}^-}{2}\gamma\right)+B_2^j\gamma^{l}\left(\frac{3}{l}-l+1+\frac{\mathrm{P}^-}{2}\gamma\right)$$
$$+B_3^j\gamma^{-l-3}\left(l+2+\frac{\mathrm{P}^-}{2}\gamma\right)+B_4^j\gamma^{-l-1}\left(\frac{2l-1}{l+1}+l+\frac{\mathrm{P}^-}{2}\gamma\right) \quad (52)$$
$$=\left[1+\frac{\alpha_{lj}^2\gamma^2}{2l(l+1)}\right]Ra\frac{C_{ll}'(\alpha_{lj}\gamma)}{\alpha_{lj}^3\gamma^{3/2}}$$

at r=γ and

$$B_1^j\left(1-l-\frac{\mathrm{P}^+}{2}\right)+B_2^j\left(\frac{3}{l}-l+1-\frac{\mathrm{P}^+}{2}\right)$$
$$+B_3^j\left(l+2-\frac{\mathrm{P}^+}{2}\right)+B_4^j\left(\frac{2l-1}{l+1}+l-\frac{\mathrm{P}^+}{2}\right) \quad (53)$$
$$=\left[1+\frac{\alpha_{lj}^2}{2l(l+1)}\right]Ra\frac{C_{ll}'(\alpha_{lj})}{\alpha_{lj}^3}$$

at r=1.

Equations (50), (51), (52) and (53) form a linear system of equations for $B_{l\cdots4}^j$ which is solved for each degree l. The $B_{l\cdots4}^j$ are then used to calculate the functions Q_{kj} in the characteristic equation (47).

APPENDIX B – TRANSLATION MODE

We consider here the onset of the degree 1 mode in the limit of small Ra, P^-, and P^+, but finite $Ra/(\mathrm{P}^+{+}\gamma^2\mathrm{P}^-)$. With l=1, the tangential stress free conditions (50) and (51) give

$$B_2^j+B_3^j\gamma^{-5}=Ra\frac{C_{11}'(\alpha_{1j}\gamma)}{3\alpha_{1j}^3\gamma^{5/2}} \quad (54)$$

$$B_2^j+B_3^j=Ra\frac{C_{11}'(\alpha_{1j})}{3\alpha_{1j}^3} \quad (55)$$

while the normal stress continuity conditions (52) and (53) yield

$$B_1^j\mathrm{P}^-+6\gamma\left[B_2^j+\gamma^{-5}B_3^j\right]+\frac{3}{\gamma^2}B_4^j=\left[2+\frac{\alpha_{1j}^2\gamma^2}{2}\right]Ra\frac{C_{11}'(\alpha_{1j}\gamma)}{\alpha_{1j}^3\gamma^{3/2}} \quad (56)$$

$$-B_1^j\mathrm{P}^++6\left[B_2^j+B_3^j\right]+3B_4^j=\left[2+\frac{\alpha_{1j}^2}{2}\right]Ra\frac{C_{11}'(\alpha_{1j})}{\alpha_{1j}^3} \quad (57)$$

when $\mathrm{P}^-<<1$ and $\mathrm{P}^+<<1$. Using equations (54) and (55), the coefficients B_2^j and B_3^j can be eliminated from equations (56) and (57), which give

$$\gamma^2B_1^j\mathrm{P}^-+3B_4^j=\frac{\gamma^{5/2}C_{11}'(\alpha_{1j}\gamma)}{2\alpha_{1j}}Ra \quad (58)$$

$$-B_1^j\mathrm{P}^++3B_4^j=\frac{C_{11}'(\alpha_{1j})}{2\alpha_{1j}}Ra \quad (59)$$

Noting that

$$C_{11}'(\alpha_{1j})=-\frac{2}{\pi\alpha_{1j}}\frac{J_{3/2}(\alpha_{1j}\gamma)}{J_{3/2}(\alpha_{1j})} \quad (60)$$

$$C_{11}'(\alpha_{1j}\gamma)=-\frac{2}{\pi\alpha_{1j}\gamma} \quad (61)$$

(Chandrasekhar, 1961), solving equations (58) and (59) yields

$$B_1^j=\frac{J_{3/2}(\alpha_{1j}\gamma)/J_{3/2}(\alpha_{1j})-\gamma^{3/2}}{\pi\alpha_{1j}^2}\frac{Ra}{\mathrm{P}^++\gamma^2\mathrm{P}^-} \quad (62)$$

$$B_4^j=\left[\frac{1-\gamma^{3/2}J_{3/2}(\alpha_{1j})/J_{3/2}(\alpha_{1j}\gamma)}{1+\gamma^2\mathrm{P}^-/\mathrm{P}^+}-1\right]\frac{1}{3\pi\alpha_{1j}^2}\frac{J_{3/2}(\alpha_{1j}\gamma)}{J_{3/2}(\alpha_{1j})}Ra \quad (63)$$

It can be seen that B_2^j, B_3^j and B_4^j are all ~Ra, while $B_1^j\sim Ra/(\mathrm{P}^++\gamma^2\mathrm{P}^-)$. In the limit of small Ra, P^-, P^+, but finite $Ra/(\mathrm{P}^+{+}\gamma^2\mathrm{P}^-)$, we therefore have $B_1^j>>(B_2^j,B_3^j,B_4^j)$. To a good approximation, p_{1j} is then given [from Equation (46)] by

$$p_{1j}\approx B_1^jr \quad (64)$$

and the poloidal scalar of the first unstable mode is

$$P=\sum_j A_{1j}p_{1j}(r)Y_1^0(\theta,\phi)\approx\left(\sum_j A_{1j}B_1^j\right)rY_1^0(\theta,\phi) \tag{65}$$

which corresponds to a translational motion (it can be verified that a l=1 flow with $P\propto r$ corresponds to a flow with uniform velocity).

In the limit of small Ra, the characteristic equation (47) for l=1 now writes

$$\left\| N_{3/2,k}\frac{\alpha_{1k}^2}{4}\delta_{kj}-Q_{kj}\right\|=0 \tag{66}$$

where

$$Q_{kj}=B_1^j\int_\gamma^1 C_{11}(\alpha_{1k}r)r^{5./2}dr \tag{67}$$

Making use of recurrence relations of the Bessel functions (Abramovich and Stegun, 1965), we find that the integral in Equation (67) can be written as

$$\int_\gamma^1 C_{11}(\alpha_{1k}r)r^{5./2}dr=\frac{2}{\pi\alpha_{1k}^2}\left[\frac{J_{3/2}(\alpha_{1k}\gamma)}{J_{3/2}(\alpha_{1k})}-\gamma^{3/2}\right] \tag{68}$$

which allows to write Q_{kj} as

$$Q_{kj}=\frac{2}{\pi^2\alpha_{1j}^2\alpha_{1k}^2}\left[\frac{J_{3/2}(\alpha_{1j}\gamma)}{J_{3/2}(\alpha_{1j})}-\gamma^{3/2}\right]\left[\frac{J_{3/2}(\alpha_{1k}\gamma)}{J_{3/2}(\alpha_{1k})}-\gamma^{3/2}\right]\frac{Ra}{\mathrm{P}^+ +\gamma^2\mathrm{P}^-} \tag{69}$$

Now, rewriting Equation (66) as

$$\left\|\delta_{kj}-\frac{4}{N_{3/2,k}\alpha_{1k}^2}Q_{kj}\right\|=0 \tag{70}$$

and using Sylvester's determinant theorem, we find that

$$\left\|\delta_{kj}-\frac{4}{N_{3/2,k}\alpha_{1k}^2}Q_{kj}\right\|=1-4\sum_{i=1}^{\infty}\frac{Q_{ii}}{\alpha_{1i}^2N_{3/2,i}}=0 \tag{71}$$

from which, using Equation (69), we obtain the critical value of $Ra/(\mathrm{P}^+ +\gamma^2\mathrm{P}^-)$

$$\left(\frac{Ra}{\mathrm{P}^+ +\gamma^2\mathrm{P}^-}\right)_c=\frac{1}{4}\left\{\sum_{i=1}^{\infty}\frac{1}{\alpha_{1i}^4}\frac{\left[\frac{J_{3/2}(\alpha_{1i}\gamma)}{J_{3/2}(\alpha_{1i})}-\gamma^{3/2}\right]^2}{\frac{J_{3/2}^2(\alpha_{1i}\gamma)}{J_{3/2}^2(\alpha_{1i})}-1}\right\}^{-1} \tag{72}$$

REFERENCES CITED

Abramovich, M., Stegun, I. A., 1965. Handbook of Mathematical Functions. Fourth Printing. Applied Math. Ser. 55, US Government Printing Office, Washington DC

Alboussière, T., Deguen, R., Melzani, M., 2010. Melting Induced Stratification above the Earth's Inner Core due to Convective Translation. *Nature*, 466: 744–747

Chandrasekhar, S., 1961. Hydrodynamic and Hydromagnetic Stability. International Series of Monographs on Physics. Oxford, Clarendon

Deguen, R., 2012. Structure and Dynamics of Earth's Inner Core. *Earth Planet. Sci. Lett.*, 333–334: 211–225

Deguen, R., Alboussière, T., Cardin, P., 2013. Thermal Convection in Earth's Inner Core with Phase Change at Its Boundary. *Geophys. J. Int.*, doi:10.1093/gji/ggt202

Grott, M., Sohl, F., Hussmann, H., 2007. Degree-One Convection and the Origin of Enceladus' Dichotomy. *Icarus*, 191(1): 203–210

Irving, J. C. E., Deuss, A., 2011. Hemispherical Structure in Inner Core Velocity Anisotropy. *Journal of Geophysical Research*, 116(B4): B04307

Kivelson, M. G., Khurana, K. K., Russell, C. T., et al., 2000. Galileo Magnetometer Measurements: A Stronger Case for a Subsurface Ocean at Europa. *Science*, 289(5483): 1340–1343

Labrosse, S., Hernlund, J. W., Coltice, N., 2007. A Crystallizing Dense Magma Ocean at the Base of the Earth's Mantle. *Nature*, 450(7171): 866–869

McNamara, A. K., Zhong, S., 2005. Degree-One Mantle Convection: Dependence on Internal Heating and Temperature-Dependent Rheology. *Geophysical Research Letters*, 32(1): L01301

Mizzon, H., Monnereau, M., 2013. Implication of the Lopsided Growth for the Viscosity of Earth's Inner Core. *Earth Planet. Sci. Lett.*, 361: 391–401

Monnereau, M., Calvet, M., Margerin, L., et al., 2010. Lopsided Growth of Earth's Inner Core. *Science*, 328: 1014–1017

Monnereau, M., Dubuffet, F., 2002. Is Io's Mantle Really Mol-

ten? *Icarus*, 158(2): 450–459

Nimmo, F., Pappalardo, R. T., 2006. Diapir-Induced Reorientation of Saturn's Moon Enceladus. *Nature*, 441(7093): 614–616

Niu, F. L., Wen, L. X., 2001. Hemispherical Variations in Seismic Velocity at the Top of the Earth's Inner Core. *Nature*, 410: 1081–1084

Porco, C. C., Helfenstein, P., Thomas, P. C., et al., 2006. Cassini Observes the Active South Pole of Enceladus. *Science*, 311(5766): 1393–1401

Ribe, N. M., 2007. Analytical Approaches to Mantle Dynamics. In: Schubert, G., ed., Treatise on Geophysics, Vol. 7. 167–226

Schubert, G., Anderson, J. D., Travis, B. J., et al., 2007. Enceladus: Present Internal Structure and Differentiation by Early and Long-Term Radiogenic Heating. *Icarus*, 188(2): 345–355

Solomatov, V. S., 2000. Fluid Dynamics of a Terrestrial Magma Ocean. *Origin of the Earth and Moon*, 1: 323–338

Spohn, T., Schubert, G., 2003. Oceans in the Icy Galilean Satellites of Jupiter? *Icarus*, 161(2): 456–467

Stegman, D. R., Freeman, J., May, D. A., 2009. Origin of Ice Diapirism, True Polar Wander, Subsurface Ocean, and Tiger Stripes of Enceladus Driven by Compositional Convection. *Icarus*, 202(2): 669–680

Tanaka, S., Hamaguchi, H., 1997. Degree One Heterogeneity and Hemispherical Variation of Anisotropy in the Inner Core from PKP(BC)-PKP(DF) Times. *Journal of Geophysical Research*, 102: 2925–2938

Tyler, R. H., 2009. Ocean Tides Heat Enceladus. *Geophysical Research Letters*, 36(15): L15205

Tyler, R. H., 2008. Strong Ocean Tidal Flow and Heating on Moons of the Outer Planets. *Nature*, 456(7223): 770–772

Ulvrová, M., Labrosse, S., Coltice, N., et al., 2012. Numerical Modelling of Convection Interacting with a Melting and Solidification Front: Application to the Thermal Evolution of the Basal Magma Ocean. *Physics of the Earth and Planetary Interiors*, 206(207): 51–66

Waite, Jr. J. H., Lewis, W. S., Magee, B. A., et al., 2009. Liquid Water on Enceladus from Observations of Ammonia and 40ar in the Plume. *Nature*, 460(7254): 487–490

Zhong, S., Zuber, M. T., 2001. Degree-1 Mantle Convection and the Crustal Dichotomy on Mars. *Earth Planet. Sci. Lett.*, 189(1): 75–84

Geophysical Journal International

Geophys. J. Int. (2015) **202,** 548–563
GJI Geodynamics and tectonics

doi: 10.1093/gji/ggv155

Earth's inner core dynamics induced by the Lorentz force

M. Lasbleis,[1] R. Deguen,[1] P. Cardin[2] and S. Labrosse[1]

[1]*Laboratoire de géologie de Lyon, ENS de Lyon, Université Lyon-*1*, Université de Lyon, F-*69007 *Lyon, France. E-mail: marine.lasbleis@ens-lyon.fr*
[2]*ISTerre, University Grenoble Alpes, CNRS, F-*38041 *Grenoble, France*

Accepted 2015 April 8. Received 2015 April 5; in original form 2014 October 29

SUMMARY

Seismic studies indicate that the Earth's inner core has a complex structure and exhibits a strong elastic anisotropy with a cylindrical symmetry. Among the various models which have been proposed to explain this anisotropy, one class of models considers the effect of the Lorentz force associated with the magnetic field diffused within the inner core. In this paper, we extend previous studies and use analytical calculations and numerical simulations to predict the geometry and strength of the flow induced by the poloidal component of the Lorentz force in a neutrally or stably stratified growing inner core, exploring also the effect of different types of boundary conditions at the inner core boundary (ICB). Unlike previous studies, we show that the boundary condition that is most likely to produce a significant deformation and seismic anisotropy is impermeable, with negligible radial flow through the boundary. Exact analytical solutions are found in the case of a negligible effect of buoyancy forces in the inner core (neutral stratification), while numerical simulations are used to investigate the case of stable stratification. In this situation, the flow induced by the Lorentz force is found to be localized in a shear layer below the ICB, whose thickness depends on the strength of the stratification, but not on the magnetic field strength. We obtain scaling laws for the thickness of this layer, as well as for the flow velocity and strain rate in this shear layer as a function of the control parameters, which include the magnitude of the magnetic field, the strength of the density stratification, the viscosity of the inner core and the growth rate of the inner core. We find that the resulting strain rate is probably too small to produce significant texturing unless the inner core viscosity is smaller than about 10^{12} Pa s.

Key words: Numerical solutions; Composition of the core; Seismic anisotropy.

1 INTRODUCTION

The existence of structures within the inner core was first discovered by Poupinet *et al.* (1983), who discussed the possibility of lateral heterogeneity from the observation of *P*-waves traveltime anomalies. These were then attributed to the existence of seismic anisotropy (Morelli *et al.* 1986; Woodhouse *et al.* 1986), with *P*-waves travelling faster in the north–south direction than in the equatorial plane. Since then, more complexities have been discovered in the inner core: a slight tilt in the fast axis of the anisotropy, radial variations of the anisotropy with a nearly isotropic upper layer, hemispherical variations of the thickness of the upper isotropic layer, an innermost inner core with different properties in anisotropy or attenuation and anisotropic attenuation (See Souriau *et al.* 2003; Tkalčić & Kennett 2008; Deguen 2012; Deuss 2014, for reviews, and references therein).

The seismic anisotropy can be explained either by liquid inclusions elongated in some specific direction (shape preferred orientation, SPO; Singh *et al.* 2000) or by the alignment of the iron crystals forming the inner core (lattice preferred orientation, LPO). In the case of LPO, the orientation is acquired either during crystallization (e.g. Karato 1993; Bergman 1997; Brito *et al.* 2002) or by texturing during deformation of the inner core. Several mechanisms have been proposed to provide the deformation needed for texturing: solid state convection (Jeanloz & Wenk 1988; Weber & Machetel 1992; Buffett 2009; Deguen & Cardin 2011; Cottaar & Buffett 2012; Deguen *et al.* 2013), or deformation induced by external forcing, due to viscous adjustment following preferential growth at the equator (Yoshida *et al.* 1996, 1999; Deguen & Cardin 2009), or Lorentz force (Karato 1999; Buffett & Bloxham 2000; Buffett & Wenk 2001).

Thermal convection in the inner core is possible if its cooling rate, related to its growth rate, or radiogenic heating rate is large enough to maintain a temperature gradient steeper than the isentropic gradient. In other words, the heat loss of the inner core must be larger than what would be conducted down the isentrope. However, the thermal conductivity of the core has been recently reevaluated to values larger than 90 W m^{-1} K^{-1} at the core mantle boundary (CMB) and in excess of 150 W m^{-1} K^{-1} in the inner core (de Koker *et al.* 2012; Pozzo *et al.* 2012; Gomi *et al.* 2013; Pozzo *et al.*

2014), and this makes thermal convection in the inner core unlikely (Yukutake 1998; Deguen & Cardin 2011; Deguen *et al.* 2013; Labrosse 2014). Inner core translation, that has been proposed to explain the hemispherical dichotomy of the inner core (Monnereau *et al.* 2010), results from a convection instability (Alboussière *et al.* 2010; Deguen *et al.* 2013; Mizzon & Monnereau 2013) and is therefore also difficult to sustain.

Compositional convection is possible if the partition coefficient of light elements at the inner core boundary (ICB) decreases with time (Deguen & Cardin 2011; Gubbins *et al.* 2013) or if some sort of compositional stratification develops in the outer core (Alboussière *et al.* 2010; Buffett 2000; Gubbins & Davies 2013; Deguen *et al.* 2013) so that the concentration of the liquid that crystallizes decreases with time. However, the combination of both thermal and compositional buoyancy does not favour convection in the inner core (Labrosse 2014).

The strong thermal stability of the inner core resulting from its high-thermal conductivity (Labrosse 2014) is a barrier to any vertical motion and other forcing mechanisms need to work against it. This situation has already been considered in the case of deformation induced by preferential growth in the equatorial belt (Deguen & Cardin 2009), and has been shown to produce a layered structure. Deguen *et al.* (2011) and Lincot *et al.* (2014) evaluated the predictions of anisotropy from this model and found that although it can induce significant deformation, it is difficult to explain the strength and geometry of the anisotropy observed in the inner core.

In this paper, we consider another major external forcing that was proposed, Maxwell stress. This was first proposed by Karato (1999) who considered the action of the Lorentz force assuming the inner core to be neutrally buoyant throughout. This situation is rather unlikely and, as discussed above, we expect the inner core to be stably stratified. Buffett & Bloxham (2000) have shown that in this case the flow is confined in a thin layer at the top of the inner core, similar to the case discussed above for a flow driven by preferential growth at the equator. However, the growth of the inner core gradually buries the deformed iron and this scenario may still produce a texture in the whole inner core. All these previous studies considered a fixed inner core size and infinitely fast phase change at the ICB. The moving boundary brings an additional advection term in the heat balance which can influence the dynamics. In the context of inner core convection Alboussière *et al.* (2010) and Deguen *et al.* (2013) have proposed a boundary condition at the ICB that allows for a continuous variation from perfectly permeable boundary conditions, that was considered in previous studies, to impermeable boundary conditions when the timescale for phase change is large compared to that for viscous adjustment of the topography.

In this paper, we investigate the dynamics of a growing inner core subject to electromagnetic forcing, and include the effects of a stable stratification, of the growth of the inner core and different types of boundary conditions. We propose a systematic study of the dynamics induced by a poloidal Lorentz force in the inner core and develop scaling laws to estimate the strain rate of the flow.

In Section 2, we develop a set of equations taking into account the Lorentz force and a buoyancy force from either thermal or compositional origin. Analytical and numerical results are presented in Section 3, scaling laws for the maximum velocity and strain rate are developed in Sections 4 and 5 and compared to numerical solutions. In Section 6, we use our results to predict the instantaneous strain rates and cumulative strain in the Earth's inner core due to the Lorentz force.

2 GOVERNING EQUATIONS

2.1 Effect of an imposed external magnetic field

The magnetic field produced by dynamo action in the liquid outer core extends up to the surface of the Earth, but also to the centremost part of the core. Considering for example a flow velocity of the order of the growth rate of the inner core gives a magnetic Reynolds number (comparing advection and diffusion of the magnetic field) of the inner core of about 10^{-5}. This shows that the magnetic field in the inner core is only maintained by diffusion from its boundary.

Two dynamical effects need to be taken into account: the Lorentz force and Joule heating. The Lorentz force acts directly on the momentum conservation, while Joule heating is part of the energy budget and modifies the temperature distribution, inducing a flow through buoyancy forces.

In this paper, we will discuss the effect of the Lorentz force in the case of a purely toroidal axisymmetric magnetic field with a simple mathematical form. The effect of Joule heating in the case of a nongrowing inner core was studied by Takehiro (2010) and will not be investigated further here.

The poloidal magnetic field intensity at the CMB can be inferred from surface observations of the field at the Earth's surface, but both poloidal and toroidal components are poorly known deeper in the core. The root mean square (rms) strength of the field at the ICB has been estimated using numerical simulations to be around a few milliteslas (e.g. Glatzmaier & Roberts 1996; Christensen & Aubert 2006). It can be also constrained by physical observations: for example, Koot & Dumberry (2013) give an upper bound of 9–16 mT for the rms field at the ICB by looking at the dissipation in the electromagnetic coupling, while Gillet *et al.* (2010) suggest 2–3 mT from the observation of fast toroidal oscillations in the core. Buffett (2010) obtains similar values from measurements of tidal dissipation. Numerical simulations also predict a strong azimuthal component B_ϕ at the vicinity of the inner core, possibly one order of magnitude higher than the vertical component B_z (Glatzmaier & Roberts 1996), though this depends on the magnitude of inner core differential rotation.

Buffett & Wenk (2001) have considered the effect of the azimuthal component of the Lorentz force resulting from the combination of the B_z and B_ϕ components of the magnetic field. We will focus here on the effect of the azimuthal component of the magnetic field, for which the associated Lorentz force is poloidal and axisymmetric. The flow calculated by Buffett & Wenk (2001) is decoupled from the flow induced by the azimuthal component of the magnetic field, and thus the total axisymmetric flow can be obtained by simply summing the two flows.

One of the most intriguing feature of the Earth's magnetic field is the existence of reversals. However, since the Lorentz force depends quadratically on the magnetic field, its direction is not modified by a reversal of the field. For simplicity, we will consider that the magnetic field is constant in time.

The magnetic field inside the inner core is calculated by diffusing the field from the ICB. The magnetic Reynolds number for the inner core being very small, B is not advected by the flow. Because the seismic observation of anisotropy is of large scale, and also because low-order toroidal component penetrates deeper inside the inner core, only the lowest order of the azimuthal component of the magnetic field is taken into account, following the work of Karato (1999) and Buffett & Bloxham (2000).

We consider a purely toroidal axisymmetric field of degree two in the vicinity of the ICB, of the form $\boldsymbol{B}|_{\mathrm{ICB}} = B_0 \sin\theta \cos\theta \, e_\phi$ (Buffett

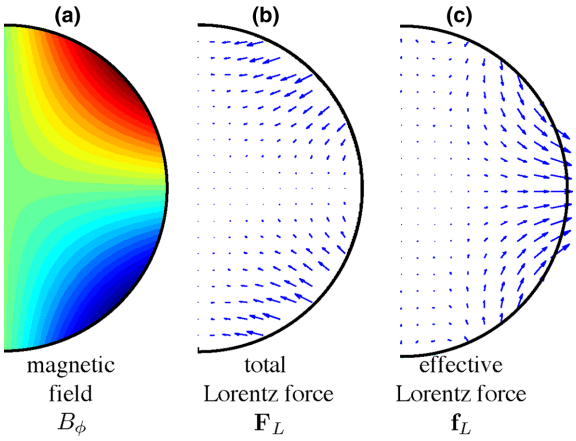

Figure 1. Meridional cross sections showing the intensity of the magnetic field (a), the Lorentz force $\boldsymbol{F}_\mathrm{L}$ (b) and the nonpotential part of the Lorentz force $\boldsymbol{f}_\mathrm{L}$ as defined in eq. (3) (c).

& Bloxham 2000). Solving $\nabla^2 \boldsymbol{B} = 0$, the field inside the inner core is

$$\boldsymbol{B} = B_0 \frac{r^2}{r_{ic}^2} \cos\theta \sin\theta e_\phi, \tag{1}$$

in spherical coordinates, which is associated to an electric current density $\boldsymbol{J} = \frac{1}{\mu_0} \nabla \times \boldsymbol{B}$, where r_{ic} is the radius of the inner core and μ_0 is the magnetic permeability.

The Lorentz force is a volume force given by $\boldsymbol{F}_\mathrm{L} = \boldsymbol{J} \times \boldsymbol{B}$. The Lorentz force can be decomposed as the sum of the gradient of a magnetic pressure and a nonpotential part as $\boldsymbol{F}_L = -\nabla P_\mathrm{m} + \boldsymbol{f}_\mathrm{L}$, which is a unique Helmholtz decomposition for $\nabla \cdot \boldsymbol{f}_\mathrm{L} = 0$. With the magnetic field as defined in eq. (1), we find that P_m and $\boldsymbol{f}_\mathrm{L}$ are given by

$$P_\mathrm{m} = \frac{1}{7} \frac{B_0^2}{\mu_0} \frac{r^4}{r_{ic}^4} \left(\frac{3}{2} \cos^2\theta + \frac{1}{5} \right) \tag{2}$$

and

$$\boldsymbol{f}_L = \frac{B_0^2}{\mu_0 r_{ic}} \frac{r^3}{r_{ic}^3} \left[\left(3\cos^4\theta - \frac{15}{7}\cos^2\theta + \frac{4}{35} \right) e_r + \cos\theta \sin\theta \left(\frac{4}{7} - 3\cos^2\theta \right) e_\theta \right]. \tag{3}$$

The potential part of the Lorentz force can only promote a new equilibrium state but no persisting flow. We are thus only interested in the non potential part of the Lorentz force, shown in Fig. 1. Eq. (3) provides a characteristic scale for the force as $B_0^2/\mu_0 r_{ic}$.

Karato (1999) investigated the effect of the Maxwell stress by applying a given normal stress on the ICB. This is different from our study, where, as in Buffett & Bloxham (2000), we consider a volumetric forcing, as shown on Fig. 1, and not a forcing on the surface of the inner core.

2.2 Conservation equations

2.2.1 Conservation of mass, momentum and energy

We consider an incompressible fluid in a spherical domain, with a newtonian rheology of uniform viscosity η, neglecting inertia. Volume forces considered here are the buoyancy forces, with density variations due to temperature or compositional variations, and the Lorentz force as defined above.

The equations of continuity and conservation of momentum are written as

$$\nabla \cdot \boldsymbol{u} = 0, \tag{4}$$

$$\boldsymbol{0} = -\nabla p' + \Delta\rho\, \boldsymbol{g} + \eta \nabla^2 \boldsymbol{u} + \boldsymbol{f}_\mathrm{L}, \tag{5}$$

where $\boldsymbol{u}$ is the velocity, p' the dynamic pressure that also includes the magnetic pressure, $\Delta\rho$ the density difference compared to the reference density profile, and $\boldsymbol{g} = g_{ic} r / r_{ic} \boldsymbol{e}_r$ the acceleration of gravity with g_{ic} the acceleration of gravity at $r = r_{ic}$.

The density depends on both the temperature T and the light element concentration c. We define a potential temperature as $\Theta = T - T_s(r, t)$, with $T_s(r, t)$ the isentropic temperature profile anchored to the liquidus at the ICB, and introduce a potential composition $C = c - c_{ic}^s(t)$, where $c_{ic}^s(t)$ is the composition of the solid at the ICB. We will consider separately the effects of composition and temperature, but both can induce a density stratification, which is quantified through a variation of density $\Delta\rho$ which is either $\rho\alpha_T\Theta$ or $\rho\alpha_C C$, where ρ is the reference density, and α_T and α_C the coefficients of thermal and compositional expansion, respectively. Because the potential temperature and composition are solutions of mathematically similar equations, we will use a quantity χ which is either the potential temperature Θ or composition C. In this paper, quantities that apply for both cases will have no subscript, whereas we will use $_T$ for quantities referring to the thermal stratification, and $_C$ for compositional stratification.

The momentum conservation eq. (5) is thus written as

$$\boldsymbol{0} = -\nabla p' + \alpha\rho\chi\, g_{ic} \frac{r}{r_{ic}} \boldsymbol{e}_r + \eta \nabla^2 u + \boldsymbol{f}_\mathrm{L}. \tag{6}$$

The equations for the evolution of the potential temperature (energy conservation) and of light element concentration (solute conservation) have a common form, which will be written as

$$\frac{\partial \chi}{\partial t} + \boldsymbol{u} \cdot \nabla \chi = \kappa \nabla^2 \chi + S(t), \tag{7}$$

where κ is the diffusivity of either heat (κ_T) or composition (κ_C) and S a source term given by

$$S_T(t) = \kappa_T \nabla^2 T_s - \frac{\partial T_s}{\partial t} \tag{8}$$

and

$$S_C(t) = -\frac{\partial c_{ic}^s}{\partial t}. \tag{9}$$

As discussed in Deguen & Cardin (2011), the inner core is stably stratified when the source term $S(t)$ is negative, and no convective instability can develop. In this paper, we will focus on this case, with either $S_T(t)$ or $S_C(t)$ negative.

2.2.2 Growth of the inner core

To take into account the growth of the inner core, we use a front fixing approach to solve the moving boundary problem (Crank 1984) by scaling lengths with the inner core radius $r_{ic}(t)$ at time t. We define a new coordinate system with $\tilde{r} = r/r_{ic}(t)$. This modifies slightly the spatial derivatives by bringing a factor $1/r_{ic}(t)$ to radial derivatives, but also adds a radial advection term in the equations where the time derivative is present. In the new coordinate system, we obtain

$$\left.\frac{\partial}{\partial t}\right|_{\tilde{r}} = \left.\frac{\partial}{\partial t}\right|_{r} + \tilde{r} \frac{u_{ic}(t)}{r_{ic}(t)} \left.\frac{\partial}{\partial \tilde{r}}\right|_{t}, \tag{10}$$

where $u_{ic}(t) = dr_{ic}/dt$ is the instantaneous growth rate of the inner core. Eq. (7) becomes

$$\frac{\partial \chi}{\partial t} + \frac{1}{r_{ic}(t)}(u - \tilde{r}\, u_{ic}(t) e_r) \cdot \nabla \chi = \frac{\kappa}{r_{ic}^2(t)} \nabla^2 \chi + S(t), \tag{11}$$

where $\cdot\ \nabla$ and ∇^2 are now spatial derivative operators in the new coordinate system $(\tilde{r}, \theta, \phi)$, with θ and ϕ the colatitude and longitude.

2.3 Dimensionless equations and parameters

2.3.1 Definition of the dimensionless quantities

The set of equations (4), (6), (7) is now made dimensionless, using $r_{ic}(t)$, the age of the inner core $\boldsymbol{\tau}_{ic}$, $\kappa/r_{ic}(t)$, $\eta\kappa/r_{ic}^2(t)$ and $\Delta\rho_\chi$ as characteristic scales for length, time, velocities, pressure and density variations. The density scale $\Delta\rho_\chi$ is the difference of density across the inner core due to either thermal or compositional stratification. The quantity χ is scaled by $\Delta\rho_\chi/\alpha\rho$. The characteristic velocity scale is defined using the diffusion time scale rather than the inner core growth rate, to make it usable in both the growing and non-growing inner core cases. The quantity $S(t)$ is made dimensionless using $r_{ic}^2\alpha\rho/\kappa\Delta\rho_\chi$. Using the same symbols for the dimensionless quantities (including using now r for the dimensionless radius $\tilde{r}$ defined in the last subsection), we obtain

$$\nabla \cdot \boldsymbol{u} = 0, \tag{12}$$

$$\mathbf{0} = -\nabla p' + Ra(t)\, \chi\, r\, \boldsymbol{e}_r + \nabla^2 \boldsymbol{u} + M(t) \boldsymbol{f}_L, \tag{13}$$

$$\xi(t) \frac{\partial \chi}{\partial t} = -(\boldsymbol{u} - Pe(t) r\, \boldsymbol{e}_r) \cdot \nabla \chi + \nabla^2 \chi + S(t) - \chi \xi \frac{\dot{\Delta\rho_\chi}}{\Delta\rho_\chi}, \tag{14}$$

with four dimensionless parameters defined as

$$Ra(t) = \frac{\Delta\rho_\chi(t) g_{ic} r_{ic}^3(t)}{\eta\kappa}, \tag{15}$$

$$M(t) = \frac{B_0^2 r_{ic}^2(t)}{\mu_0 \eta \kappa}, \tag{16}$$

$$\xi(t) = \frac{r_{ic}^2(t)}{\kappa \tau_{ic}}, \tag{17}$$

$$Pe(t) = \frac{u_{ic} r_{ic}(t)}{\kappa}. \tag{18}$$

The last term in eq. (14) comes from the time evolution of the scale for χ, $\Delta\rho_\chi/\alpha\rho$.

$\xi(t)$ and $Pe(t)$ characterize the growth of the inner core. The Péclet number $Pe(t)$ compares the apparent advection from the moving boundary to diffusion. A large Péclet number thus corresponds to a fast inner core growth compared to the diffusion rate. In the case of a nongrowing inner core, $Pe = 0$, $\dot{S}(t) = 0$ and the relevant timescale is no longer τ_{ic} but the diffusion time scale, which gives $\xi = 1$. This approach allows us to treat both nongrowing and growing cases with the same set of dimensionless parameters.

$M(t)$ is an effective Hartmann number, which quantifies the ratio of the Lorentz force to the viscous force, using thermal diffusivity in the velocity scale. This effective Hartmann number is related to the Hartmann number often used in magnetohydrodynamics (Roberts 2007), $Ha = Br/\mu_0\eta\lambda$, through $M = Ha^2\, \lambda/\kappa$, where λ is the magnetic diffusivity.

$Ra(t)$ defined in eq. (15) is the Rayleigh number that characterizes the stratification, and is negative since $\Delta\rho_\chi$ is negative for a stable stratification. The density stratification depends on the importance of diffusion, and on the time-dependence of the inner core radius. Expressions for $\Delta\rho_T$ and $\Delta\rho_c$ will be given in Section 2.3.2.

To solve numerically the momentum eq. (13), the velocity field is decomposed into poloidal and toroidal components. The complete treatment of this equation and the expression of the Lorentz force in term of poloidal and toroidal decomposition are described in Appendix A.

2.3.2 Simplified growth of the inner core

A realistic model for the inner core thermal evolution can be obtained by calculating the time evolution of the source term $S_T(t)$ and the radius $r_{ic}(t)$ from the core energy balance (Labrosse 2003, 2015), as done by Deguen & Cardin (2011). The result is sensitive to the physical properties of the core. To focus on the effect of the Lorentz forces, we choose a simpler growth scenario and assume that the inner core radius increases as the square root of time (Buffett *et al.* 1992). Using $r_{ic}(t) = r_{ic}(\tau_{ic})(t/\tau_{ic})^{1/2}$ with $r_{ic}(\tau_{ic})$ the present radius of the inner core, the growth rate is thus $u_{ic}(t) = r_{ic}(\tau_{ic})/2\sqrt{\tau_{ic} t}$.

This leads to the following expressions for the control parameters:

$$Ra(t) = Ra_0 \frac{\Delta\rho_\chi(t)}{\Delta\rho_{\chi,0}} t^{3/2}, \tag{19}$$

$$M(t) = M_0\, t, \tag{20}$$

$$\xi(t) = 2\, Pe_0\, t, \tag{21}$$

$$Pe(t) = Pe_0, \tag{22}$$

where the subscript 0 corresponds to values for the present inner core, and t is dimensionless.

The Péclet number $Pe(t)$ is constant and equal to $Pe_0 = r_{ic}^2(\tau_{ic})/(2\kappa\tau_{ic})$, and the parameter ξ is proportional to Pe_0. We are left with only three independent dimensionless parameters: the Rayleigh number Ra_0 characterizes the density stratification, the effective Hartman number M_0 the strength of the magnetic field, and the Péclet number Pe_0 the the relative importance of advection from the growth of the inner core and diffusion.

The value and time dependence of $\Delta\rho_\chi(t)$ depends on whether a stratification of thermal or compositional origin is considered:

(i) In the thermal case, the source term for thermal stratification $S_T(t)$ defined in eq. (8) can also be written as

$$S_T(t) = \frac{\rho g' \gamma T}{K_S} \left[\left(\frac{dT_s}{dT_{ad}} - 1 \right) r_{ic}(t) u_{ic}(t) - 3\kappa_T \right], \tag{23}$$

where dT_s/dT_{ad} is the ratio of the Clapeyron slope to the adiabat gradient, $g' = dg/dr = g_{ic}/r_{ic}$, γ the Gruneisen parameter, and K_S the isentropic bulk modulus (Deguen & Cardin 2011). With $r_{ic} \propto t^{1/2}$, the product $r_{ic}(t)u_{ic}(t)$ is constant, and so is S_T.

Solving the energy conservation equation for the potential temperature ($\chi = \Theta$) assuming $u = \mathbf{0}$, $r_{ic} \propto t^{1/2}$, and S_T constant gives

$$\Theta = \frac{S_T r_{ic}^2}{6\kappa_T(1 + Pe_{T0}/3)} \left[1 - \left(\frac{r}{r_{ic}(t)}\right)^2\right] \tag{24}$$

in dimensional form (see Appendix B for the derivation). If $Pe_0 \ll 1$, then the potential temperature difference $\Delta\Theta$ across the inner core is $S_T r_{ic}^2/6\kappa$, which corresponds to a balance between effective heating (S_T) and diffusion. In contrast, $\Delta\Theta$ tends towards $S_T \tau_{ic}$ if diffusion is ineffective and $Pe_0 \gg 1$. From eq. (24), we obtain

$$\Delta\rho_T = \frac{\alpha_T \rho\, S_T r_{ic}^2}{6\kappa_T(1 + Pe_{T0}/3)} \tag{25}$$

and

$$Ra_T = \frac{\alpha_T \rho\, g_{ic} S_T r_{ic}^5}{6\eta\kappa_T^2(1 + Pe_{T0}/3)}. \tag{26}$$

With $g_{ic} \propto r_{ic}$ and $r_{ic} \propto t^{1/2}$, this gives $Ra_T \propto r_{ic}^6 \propto t^3$ and

$$Ra_T(t) = Ra_{T0}\, t^3. \tag{27}$$

(ii) We estimate the density stratification due to composition from the equation of solute conservation, assuming that the outer core is well-mixed and that the partition coefficient is constant. The compositional Péclet number is large ($Pe_C \sim 10^5$ with a diffusivity $\kappa_C \sim 10^{-10}\,\mathrm{m\,s^{-2}}$) and solute diffusion in the inner core is therefore neglected.

The composition of the solid crystallized at time t at the ICB is estimated as

$$c^s_{icb}(t) = k c_0^l \left(1 - \left(\frac{r_{ic}(t)}{r_c}\right)^3\right)^{k-1} \tag{28}$$

(see Appendix C), from which the density difference across the inner core is

$$\Delta\rho_C(t) = \alpha_C \rho \left[c^s_{icb}(t) - c^s_{icb}(t=0)\right], \tag{29}$$

$$= \alpha_C \rho k c_0^l \left[\left(1 - \left(\frac{r_{ic}(t)}{r_c}\right)^3\right)^{k-1} - 1\right]. \tag{30}$$

We take advantage of the smallness of $(r_{ic}(t)/r_c)^3 < 4.3 \times 10^{-2}$ to approximate $\Delta\rho_C$ as

$$\Delta\rho_C(t) \simeq \alpha_C \rho k(1-k) c_0^l \left(\frac{r_{ic}(t)}{r_c}\right)^3, \tag{31}$$

which gives

$$Ra_C = \frac{\Delta\rho_C(t) g_{ic} r_{ic}^3(t)}{\eta\kappa_C} = \frac{\alpha_C \rho k(1-k) c_0^l g_{ic} r_{ic}^6(t)}{\eta\kappa_C r_c^3}. \tag{32}$$

With $g_{ic} \propto r_{ic}$ and $r_{ic} \propto t^{1/2}$, this gives $Ra_C \propto r_{ic}^7 \propto t^{7/2}$ and

$$Ra_C(t) = Ra_{C0}\, t^{7/2}. \tag{33}$$

2.4 Boundary conditions

The Earth's ICB is defined by the coexistence of solid and liquid iron, at the temperature of the liquidus for the given pressure and composition. By construction, the potential temperature Θ and concentration C are both 0 at the ICB : $\Theta(r_{ic}(t)) = C(r_{ic}(t)) = 0$. The mechanical boundary conditions are tangential stress-free conditions and continuity of the normal stress at the ICB.

When allowing for phase change at the ICB, the condition of continuity of the normal stress gives

$$-\mathcal{P}(t)(u_r - u_{ic}) - 2\frac{\partial u_r}{\partial r} + p' = 0 \tag{34}$$

in dimensionless form. The parameter $\mathcal{P}(t)$ was introduced by Deguen *et al.* (2013) to characterize the phase change, and is the ratio of the phase change timescale τ_ϕ to the viscous relaxation timescale $\tau_\eta = \eta/(\delta\rho\, g_{ic} r_{ic})$,

$$\mathcal{P}(t) = \frac{\tau_\phi \delta\rho\, g_{ic} r_{ic}}{\eta}, \tag{35}$$

where $\delta\rho$ is the density difference between liquid and solid iron at the ICB. τ_ϕ has been estimated to be $\sim 10^3$ yr (Alboussière *et al.* 2010; Deguen *et al.* 2013). The limit $\mathcal{P} \to 0$ corresponds to perfectly permeable boundary conditions where the phase change occurs instantaneously, and $\mathcal{P} \to \infty$ corresponds to perfectly impermeable boundary conditions with no phase change allowed at the boundary.

With $r_{ic}(t) \propto t^{1/2}$ and τ_ϕ constant, the parameter $\mathcal{P}(t)$ is expressed using the current value $\mathcal{P}_0 = \mathcal{P}(t = \tau_{ic})$ as

$$\mathcal{P}(t) = \mathcal{P}_0\, t. \tag{36}$$

2.5 Numerical modelling

The code is an extension of the one used in Deguen *et al.* (2013), adding the effect of the magnetic forcing as in eq. (6). The system of equations derived in Appendix A in term of poloidal/toroidal decomposition is solved in axisymmetric geometry, using a spherical harmonic expansion for the horizontal dependence and a finite difference scheme in the radial direction. The nonlinear part of the advection term in the temperature (or composition) equation is evaluated in the physical space at each time step. A semi-implicit Crank-Nicholson scheme is implemented for the time evolution of the linear terms and an Adams-Bashforth procedure is used for the nonlinear advection term in the heat equation.

The boundary conditions are the same as in Deguen *et al.* (2013), but for most of the runs we use $\mathcal{P} = 10^6$, which correspond to impermeable boundary conditions as discussed in Section 2.4.

When keeping the inner core radius constant, the code is run until a steady state is reached. Otherwise, the code is run from $t = 0.01$ to $t = 1$.

3 FLOW DESCRIPTION

3.1 Neutral stratification

In this subsection, we investigate the effect of the boundary conditions on the geometry and strength of the flow by solving analytically the set of equations in the case of neutral stratification. The analytical solution for neutral stratification has also been used to benchmark the code for $Ra = 0$.

In the case of neutral stratification, with $Ra = 0$, the equations for the temperature or composition perturbation (14) and momentum conservation (37) are no longer coupled. The diffusivity is no longer relevant and the problem does not depend on the Péclet number. Eq. (37) is solved in Appendix D using the boundary conditions presented in the previous section. The flow velocity is found to be proportional to the effective Hartman number M times a sigmoid function of $\mathcal{P}$. The solution is shown on Fig. 2, with dimensionless maximum horizontal velocity and root mean square velocity

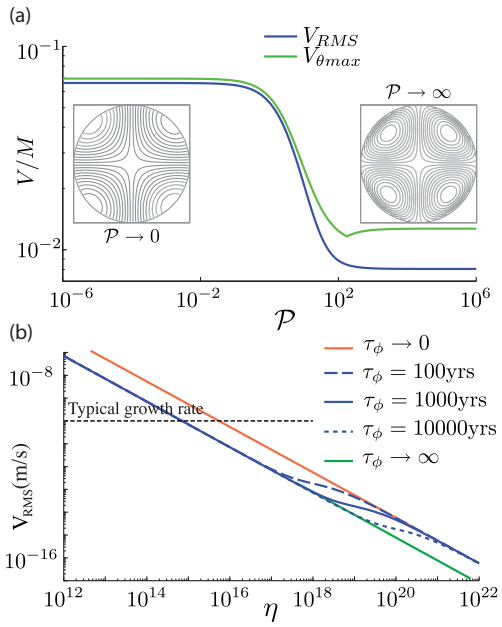

Figure 2. Analytic solution for $Ra = 0$. (a) Evolution of the dimensionless velocity as a function of the phase change number $\mathcal{P}$, with streamlines for $\mathcal{P} \to 0$ (left) and $\mathcal{P} \to \infty$ (right). The rms velocity and the maximum of the horizontal velocity are plotted. (b) Evolution of the rms velocity as a function of η, with velocity in m s^{-1}. Except for the viscosity and the phase change time scale τ_ϕ, the parameters used for definition of $\mathcal{P}$ and M are given in Table 1. The kink in the curves corresponds to the change in regime between large $\mathcal{P}$ (low viscosity) and low $\mathcal{P}$ (large viscosity), and the corresponding viscosity value is a function of the phase change timescale τ_ϕ.

as functions of the phase change number $\mathcal{P}$, as well as streamlines corresponding to the two extreme cases, $\mathcal{P} = 0$ (fully permeable boundary conditions) and $\mathcal{P} \to \infty$ (impermeable boundary conditions).

In the limit $\mathcal{P} \ll 1$, corresponding to permeable boundary conditions, the streamlines of the flow cross the ICB, which indicates significant melting and freezing at the ICB. In contrast, the streamlines in the limit $\mathcal{P} \gg 1$ are closed lines which do not cross the ICB, which indicates negligible melting or freezing at the ICB. The velocity is proportional to the effective Hartmann number M whereas the $\mathcal{P}$ dependence is more complex. The velocities reaches two asymptotic values for low and large $\mathcal{P}$ values, separated by a sharp kink. The discontinuity in the derivative of the maximum horizontal velocity slightly above $\mathcal{P} \sim 10^2$ corresponds to a change of the spatial position of the maximum, when the streamlines become closed and the maximal horizontal velocity is obtained at the top of the cell and no longer at its bottom. The change of behaviour of the boundary from permeable to impermeable induces a significant decrease of the strength of the flow, since the velocity magnitude in the $\mathcal{P} \gg 1$ regime is one order of magnitude smaller than when permeable boundary conditions ($\mathcal{P} \ll 1$) are assumed.

Fig. 2(b) shows the maximum of the velocity, now given in m s^{-1}, as a function of the viscosity, using typical values of the parameters given in Table 1 and five different values for the phase change timescale τ_ϕ, from zero to infinite. In term of dimensionless parameters, a high viscosity corresponds to small Hartmann number M and phase change number $\mathcal{P}$. Changing the timescale τ_ϕ translates the position of the transition between the two regimes, the viscosity value corresponding to the transition being proportional to τ_ϕ, but does not change the general trend of the curve, which is a linear decrease of the velocity magnitude in log-log space, except for the kink between the two regimes. The linear decrease is due to the viscosity dependence of the Hartmann number $M \propto \eta^{-1}$. For typical values of the phase change timescale between 100 and 10 000 yr, the kink between the two regimes occurs at a viscosity in the range 10^{17}–10^{21} Pa s.

In what follows, we will focus on the conditions which are the most favourable to deformation due to the poloidal component of the Lorentz force, and therefore focus on the case of low viscosity and large $\mathcal{P}$. The ICB would act as a permeable boundary only if $\mathcal{P} \lesssim 10^2$ (see Fig. 2), corresponding to $\eta \gtrsim 10^{17}$ Pa s. Under these conditions, the typical flow velocity would be $\lesssim 10^{-12}$ m s^{-1}, that is two orders of magnitude or more smaller than the inner core growth rate, and would be unlikely to result in significant texturing. For this reason, we will let aside the high viscosity/low $\mathcal{P}$ regimes to focus on low viscosity/high $\mathcal{P}$ cases, for which the ICB acts as an impermeable boundary. This gives boundary conditions very different from previous studies, where perfectly permeable boundary

Table 1. Typical values for the parameters used in the text, and typical range of values when useful.

Parameter	Symbol	Typical value	Typical range
Magnetic field	B_0	3×10^{-3} T	10^{-1}–10^{-3} T
Thermal diffusivity[a]	κ_T	1.7×10^{-5} m^2 s	0.33–2.7×10^{-5} m^2 s
Chemical diffusivity[b]	κ_χ	10^{-10} m^2 s	10^{-10}–10^{-12} m^2 s
Viscosity	η	10^{16} Pa s	10^{12}–10^{21} Pa s
Age of IC	τ_{ic}	0.5 Gyr	0.2–1.5 Gyr
Density stratification (thermal case)[c]	$\Delta\rho_T$	6 kg m^{-3}	0.5–25 kg m^{-3}
Density stratification (compositional case)[d]	$\Delta\rho_C$	5 kg m^{-3}	1–10 kg m^{-3}
Phase change timescale	τ_ϕ	10^3 yr	10^2–10^4 yr
Inner core radius[e]	$r_{ic}(\tau_{ic})$	1221 km	
Acceleration of gravity ($r = r_{ic}$)	g_{ic}	4.4 m s^{-2}	
Density of the solid phase[e]	ρ	12 800 kg m^{-3}	
Density difference at the ICB	$\delta\rho_{ic}$	600 kg m^{-3}	
Thermal expansivity	α	10^{-5} K^{-1}	
Permeability	μ_0	$4\pi \times 10^{-7}$ H m^{-1}	

[a]Obtained using $k = 163$ W m^{-1} K^{-1}, $c_p = 750$ J K^{-1} kg^{-1} (Pozzo *et al.* 2012; Gomi *et al.* 2013).
[b]From Gubbins *et al.* (2013).
[c]Assuming $S = 10 - 1000$ K Gyr^{-1} (Deguen & Cardin 2011).
[d]From Deguen & Cardin (2011).
[e]From PREM Dziewoński & Anderson (1981).

conditions were assumed (Karato 1999; Buffett & Bloxham 2000). In particular, this implies that the flow velocity estimated by (Karato 1999) was overestimated by one order of magnitude.

According to eq. (36), the parameter $\mathcal{P}$ varies linearly with time, which means that $\mathcal{P}$ must have been small early in inner core's history. However, this is true for a very short time, when the inner core radius was very small, of the order $r_{ic}(\tau_{ic})/\mathcal{P}_0^{1/2}$, and this episode is unlikely to have observable consequences in the present structure of the inner core.

3.2 Zero growth rate

We first investigate the effect of the Lorentz force without taking into account the secular growth of the inner core ($Pe = 0$). Fig. 3 shows the vorticity and temperature fields obtained for different values of the Rayleigh number, at a given effective Hartmann number $M = 10^4$, for a thermally stratified inner core.

When the Rayleigh number is small, the vorticity field is organized in two symmetric tores wrapped around the N-S axis.The stratification is too weak to alter the flow induced by the Lorentz force and the temperature field is advected and mixed by the flow. The velocity field is equal to the one calculated analytically for $Ra = 0$ (see Section 3.1 and Appendix D).

However, when the Rayleigh number is larger, the flow is altered by the stratification and is confined in an uppermost layer, as found by Buffett & Bloxham (2000). The velocity is smaller than in the case of neutral stratification. The temperature field is strongly stratified and the perturbations due to radial advection are small. The flow obtained here is similar to the flow induced by differential inner core growth with a stable stratification (Deguen *et al.* 2011), with a notable difference: we impose a large $\mathcal{P}$ implying a near zero radial flow v_r across the ICB, whereas Deguen *et al.* (2011) impose a given v_r as the driving force. The confinement of the flow in a thin layer is likely to concentrate the deformation and thus we may expect higher strain rates for a highly stratified inner core, but a different spatial distribution of the deformation.

To explore the parameter space in terms of Rayleigh and effective Hartmann numbers, we computed runs with Rayleigh numbers from -10^3 to -10^7 and effective Hartman number from 10^0 to 10^6. The

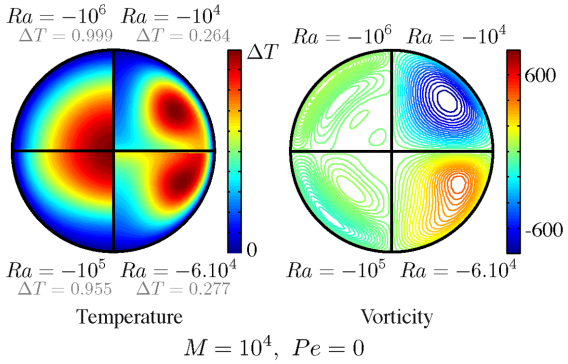

Figure 3. Snapshots of meridional cross-section of the temperature and the vorticity fields for $M = 10^4$ and a constant inner core radius, for four different values of the Rayleigh number (from top right, going clockwise: $Ra = -10^4$, -6×10^4, -10^5, -10^6). When the stratification is large enough ($Ra = -10^6$), the flow is confined at the top of the inner core and the temperature field has a spherical symmetry. When the stratification is weak ($Ra = -10^4$), the flow is similar to the one in Fig. 2 for $Ra = 0$ and the temperature is almost uniform. The vorticity is scaled by κ_T/r_{ic}^2 and the temperature by $Sr_{ic}^2/6\kappa_T$. For $u_{ic} = 0$, $Sr_{ic}^2/6\kappa_T$ reduces to $T_s(0) - T_s(r_{ic})$.

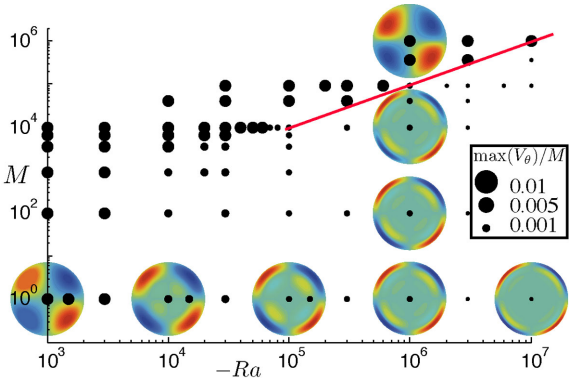

Figure 4. Maximum velocity (normalized by the Hartmann number M) in the upper vorticity layer, for a zero growth rate. The velocity is scaled by the diffusion velocity κ/r_{ic}. The maximum size of the dots corresponds to the value for $Ra = 0$ computed analytically. For some values of (M, $-Ra$), the vorticity field is plotted in the meridional cross section. The red line with a slope of 1 shows the limit between the two regimes.

maximum velocity (normalized by M) is plotted in Fig. 4 as a proxy to determine the regime. The largest velocity coincides with the flow velocity obtained for neutral stratification. The vorticity field corresponding to some of the points in the regime diagram are also shown in Fig. 4.

The systematic exploration of the parameter space reveals two different dynamical regimes, which domains of existence in a ($-Ra$,M) space are shown in Fig. 4. In the upper left part of the diagram (large effective Hartmann number, low Rayleigh number), the flow is very similar (qualitatively and quantitatively) to the analytical solution for a neutral stratification, and deformation extends deep in the inner core. This regime is characterized by a negligible effect of the buoyancy forces, and will therefore be referred to as the *weakly stratified* regime. In the lower right part, the flow is confined in a shallow layer which thickness depends on the Rayleigh number only (not on M) and in which the velocity is smaller than for neutral stratification. This regime will be referred to as the *strongly stratified* regime.

3.3 Growing inner core

To investigate the effect of inner core growth, we compute several runs with a given set of parameters (Ra_0, M_0, Pe_0), with the time t between $t = 0.01$ and $t = 1$. Unlike in Sections 3.1 and 3.2, the dimensionless numbers evolve with time, as described by eqs (19) to (22).

Fig. 5 shows the evolution of the vorticity field in six simulations, for a thermal stratification, with the same Rayleigh and effective Hartman numbers, $Ra_{T0} = -10^6$, $M_{T0} = 10^4$, but different values of the Péclet number, which corresponds to increasing diffusivity from left to right. For each run, snapshots of the vorticity field corresponding to four time steps are shown, from top-right and going clockwise.

Fig. 5 shows that the thickness of the upper layer increases with increasing Péclet number. The transition between the two regimes of strong and weak stratification is shifted towards larger Rayleigh numbers when the Péclet number is increased. At low or moderate Péclet numbers ($Pe_0 \leq 10^2$ in the cases presented here), the magnitude of vorticity is almost constant time, implying that the deformation rate in the uppermost layer is also constant.

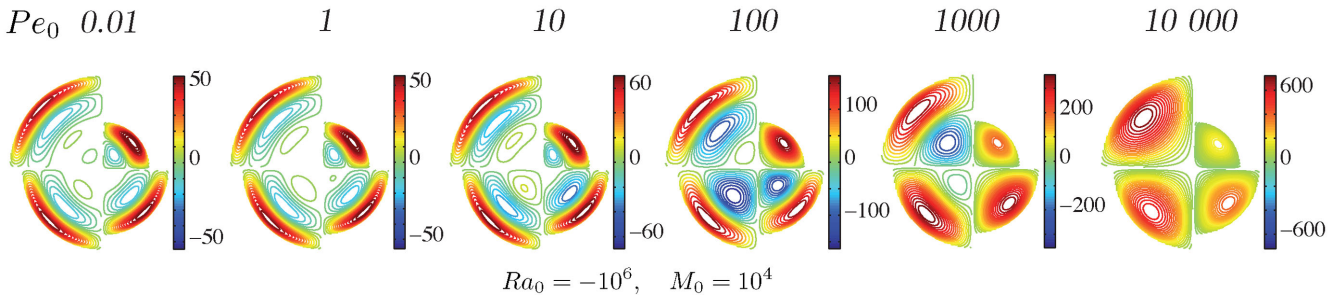

Figure 5. Snapshots of the vorticity field for simulations with dimensionless parameters $M_0 = 10^4$, $Ra_0 = -10^6$ and $Pe_0 = 0.01$, 1, 10, 10^2, 10^3 and 10^4 (from left to right), with $r_{ic} \propto t^{1/2}$. Each panel corresponds to one simulation, with four time steps represented: $t = 0.25$, 0.50, 0.75 and 1 dimensionless time, from top-right and going clockwise. See Fig. 8 for strain rates of corresponding runs.

4 SCALING LAWS

In this section, we determine scaling laws for the thickness of the shallow shear layer and the maximum velocity in the layer in the strongly stratified regime from the set of equations developed in Section 2. We will first discuss the transition between the strongly stratified and weakly stratified regimes discussed in Fig. 4. We will then focus on the strongly stratified regime and estimate the deformation in the uppermost layer. Thermal and compositional stratification are discussed separately. The flow in the weakly stratified regime is given by the analytical model discussed in Section 3.1 and Appendix D for neutral stratification.

4.1 Balance between magnetic forcing and stratification

We start here by discussing the transition between the strongly stratified and weakly stratified regimes. We base our analysis on the vorticity equation obtained by taking the curl of the momentum conservation equation (eq. 13),

$$\mathbf{0} = -Ra(t)\frac{\partial \chi}{\partial \theta}\boldsymbol{e}_\phi + M(t)\nabla \times \boldsymbol{f}_L + \nabla^2 \boldsymbol{\omega}, \tag{37}$$

where $\boldsymbol{\omega} = \nabla \times \boldsymbol{u}$ is the vorticity. The quantity χ (denoting either potential temperature or composition) is split into two parts, $\chi = \bar{\chi}(r,t) + \chi'(r,\theta,t)$, where $\bar{\chi}$ is the reference radial profile corresponding to $u = \mathbf{0}$. The vorticity equation then writes

$$\mathbf{0} = Ra\frac{\partial \chi'}{\partial \theta}\boldsymbol{e}_\phi + M\,\nabla \times \boldsymbol{f}_L + \nabla^2 \boldsymbol{\omega}. \tag{38}$$

In the vorticity equation, the three terms must balance if the effect of stratification is important. Starting from a state with no perturbations, $\chi' = 0$, the flow velocity is initially set by a balance between the Lorentz force and the viscosity force. Isosurfaces of χ are deformed by the resulting flow, and the buoyancy force increases, eventually balancing the magnetic force if the stratification is strong enough. In this case, further radial motion is prevented and the flow tends to be localized in a layer below the ICB, as found in our numerical simulations. Denoting by δ the thickness of the shear layer and u and w the horizontal and vertical velocity, respectively, the vorticity is $\omega \sim u/\delta$. We therefore have, from eq. (38),

$$(-Ra)\chi' \sim M \sim \frac{u}{\delta^3}. \tag{39}$$

The perturbation χ' thus scales as

$$\chi' \sim \frac{M}{-Ra} \tag{40}$$

if the stratification is strong enough for the induced buoyancy forces to balance the Lorentz force.

The effect of the stratification is negligible if the buoyancy forces, which are $\sim -Ra\chi'$, cannot balance the Lorentz force, which is $\sim M$. Since χ' is necessarily smaller than $|\bar{\chi}(r_{ic}) - \bar{\chi}(0)|$, which by construction is equal to 1, the effect of the stratification will therefore be negligible if $M \gg -Ra$. This is consistent with the boundary between the two regimes found from our numerical calculations, as shown in Fig. 4, as well as with the results of Buffett & Bloxham (2000) who found that the Lorentz force can displace isodensity surfaces by $\sim r_{ic}M/(-Ra)$. This estimate is valid for both a growing or nongrowing inner core.

4.2 Scaling laws in the strongly stratified regime

The reference profile $\bar{\chi}$ is solution of

$$\xi\frac{\partial \bar{\chi}}{\partial t} = \nabla^2\bar{\chi} + Pe\,\boldsymbol{r}\cdot\nabla\bar{\chi} + S(t) - \xi\frac{\Delta\dot{\rho}_\chi}{\Delta\rho_\chi}\bar{\chi}. \tag{41}$$

Subtracting eqs (41) to (14), and assuming that $\chi' \ll \bar{\chi}$, we obtain

$$\underbrace{\xi\frac{\partial \chi'}{\partial t}}_{\sim\xi\chi'} = \underbrace{\nabla^2\chi'}_{\sim\chi'/\delta^2} - \underbrace{u\frac{\partial \chi'}{\partial \theta}}_{\sim u\chi'} - \underbrace{w\frac{\partial \chi'}{\partial r}}_{w\chi'/\delta'} - \underbrace{w\frac{\partial \bar{\chi}}{\partial r}}_{\sim w\bar{\chi}\sim w} + \underbrace{Pe\,\boldsymbol{r}\cdot\nabla\chi'}_{\sim Pe\chi'/\delta} - \underbrace{\xi\frac{\dot{\Delta\rho}}{\Delta\rho}\chi'}_{\sim Pe\chi'}. \tag{42}$$

Three of these terms depend on the growth rate: $\xi\,\partial\chi'/\partial t$, $Pe\,\boldsymbol{r}\cdot\nabla\chi'$, and $\xi\,\dot{\Delta\rho}/\Delta\rho\chi'$. With our assumption of $r_{ic} \sim t^{1/2}$, we have $\xi = 2Pe\,t$ and thus $\xi \lesssim Pe$. Thus, the largest term among the growth rate-dependent terms is $Pe\,\boldsymbol{r}\cdot\nabla\chi' \sim Pe\,\chi'/\delta$.

Comparing the effect of the diffusion term, which is $\sim\chi'/\delta^2$, with the inner core growth term, which is $\sim Pe\chi'/\delta$, we find that the effect of the inner core growth is negligible if

$$Pe \ll \frac{1}{\delta}. \tag{43}$$

This suggest the existence of two different regimes depending on whether Pe is small or large. We develop below scaling laws for these two cases.

4.2.1 *Small Pe limit*

Neglecting the growth terms, we have

$$0 = \underbrace{\nabla^2\chi'}_{\sim\chi'/\delta^2} - \underbrace{u\frac{\partial \chi'}{\partial \theta}}_{\sim u\chi'} - \underbrace{w\frac{\partial \chi'}{\partial r}}_{w\chi'/\delta} - \underbrace{w\frac{\partial \bar{\chi}}{\partial r}}_{\sim w\bar{\chi}}. \tag{44}$$

The conservation of mass implies that $u \sim w/\delta$, and with $\chi' \sim M/Ra$, we obtain

$$0 = \underbrace{\nabla^2\chi'}_{\sim M/Ra\delta^2} - \underbrace{u\frac{\partial\chi'}{\partial\theta}}_{\sim uM/Ra} - \underbrace{w\frac{\partial\chi'}{\partial r}}_{uM/Ra} - \underbrace{w\frac{\partial\bar{\chi}}{\partial r}}_{\sim u\delta}. \quad (45)$$

We now assume that the advection of the perturbation χ' is small compared to the vertical advection of the reference state, which requires that $\delta \gg M/(-Ra)$. Balancing the advection and diffusion terms, we obtain

$$\frac{M}{(-Ra)\delta^2} \sim u\delta. \quad (46)$$

Combining this expression with the relation $u/\delta^3 \sim M$ obtained from the vorticity equation (eq. 39), we have

$$\delta \sim (-Ra)^{-1/6}, \quad (47)$$

$$u \sim M(-Ra)^{-1/2}. \quad (48)$$

4.2.2 Large Pe limit

In this limit, the diffusion time is larger than the age of the inner core, which allows us to neglect the diffusion term. Keeping only the largest growth rate-dependent term, and using eq. (39), we have

$$0 = -\underbrace{u\frac{\partial\chi'}{\partial\theta}}_{u\chi'} - \underbrace{w\frac{\partial\chi'}{\partial r}}_{u\chi'} - \underbrace{w\frac{\partial\bar{\chi}}{\partial r}}_{u\delta} + \underbrace{Pe\,\boldsymbol{r}\cdot\nabla\chi'}_{PeM/\delta Ra}. \quad (49)$$

Assuming again that the advection of the perturbation is small compared to the vertical advection of the reference state, the main balance is between the second and third terms, which gives

$$u\,\delta \sim \frac{Pe\,M}{\delta\,(-Ra)}. \quad (50)$$

Combined with $u\delta \sim M\delta^4$ from eq. (39), we find that the thickness and maximum velocity of the upper layer are

$$\delta \sim \left(\frac{Pe}{-Ra}\right)^{1/5}, \quad (51)$$

$$u \sim M\left(\frac{Pe}{-Ra}\right)^{3/5}. \quad (52)$$

Two conditions have to be fulfilled for these scaling laws to be valid. First, we must have $Pe \ll 1/\delta$, which is $Pe \gg (-Ra)^{1/6}$ using eq. (51). Also, we have assumed that the upper layer is thin ($\delta \ll 1$) and that the horizontal advection is small compared to the vertical one.

4.2.3 Time dependence

Our derivation does not make any assumption on the form of the inner core growth $r_{ic}(t)$, and the scaling law validity should not be restricted to the $r_{ic}(t) \propto t^{1/2}$ case assumed in the numerical simulations.

These scaling laws are valid at all time during the growth of the inner core, provided that $Pe \ll 1/\delta$ and $\delta \ll 1$ and that the time dependence of the control parameters is properly taken into account. For example, under the assumption of $r_{ic} \propto t^{1/2}$ and with M, Ra and Pe given by eqs (20), (27) and (22), we obtain

$$\delta \sim (-Ra_{T0})^{-1/6}\,t^{-1/2}, \quad u \sim M_{T0}(-Ra_{T0})^{-1/2}t^{-1/2} \quad (53)$$

for the thermal case (small Pe_T), and

$$\delta \sim \left(\frac{Pe_{C0}}{(-Ra_{C0})}\right)^{1/5} t^{-7/10}, \quad u \sim M_{C0}\left(\frac{Pe_{C0}}{(-Ra_{C0})}\right)^{3/5} t^{-11/10} \quad (54)$$

for the compositional case (large Pe_C).

4.3 Comparison with numerical results

Fig. 6 shows the thickness of the uppermost vorticity layer and the maximum horizontal velocity obtained in numerical simulations with a constant inner core radius, which corresponds to the small Péclet number limit. When $-Ra/M \ll 1$, the flow has the geometry and amplitude predicted by our analytical model for $Ra = 0$. When $-Ra/M \gtrsim 10$ and the thickness of the upper layer is smaller than $\simeq$0.3, the data points align on straight lines in log-log scale, with slopes close to the predictions of the scaling laws developed in Section 4.2.1 (eqs 47 and 48).

Fig. 7 shows the vorticity layer thickness and maximum velocity as functions of $Pe/(-Ra)$, in log-log scale, for runs in the large Péclet limit. The thickness of the upper layer and the maximum velocity align on slopes close to the 1/5 and 3/5 slopes predicted in Section 4.2.2. Fig. 7 has been constructed from runs with $M = 1$, but we have checked that, as long as the condition

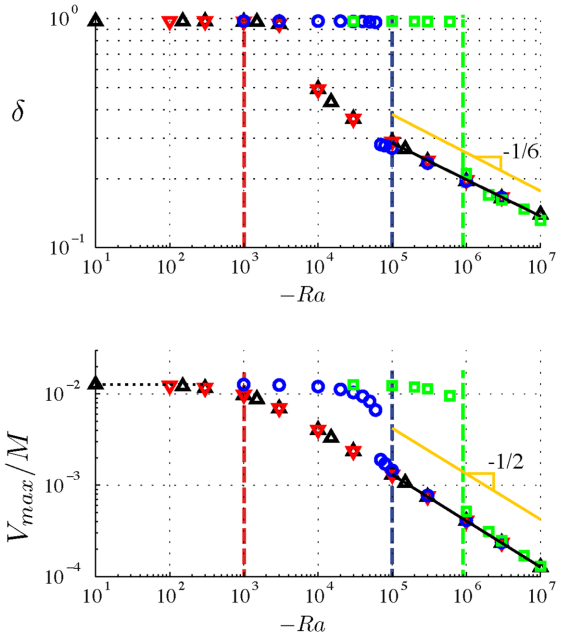

Figure 6. Results from simulations with a constant inner core radius. Evolution of the thickness of the uppermost vorticity layer (a) and maximum horizontal velocity (b) with the absolute value of the Rayleigh number $-Ra$. Colours correspond to different values of the effective Hartmann number M, and dashed lines to the corresponding $-Ra = 10\,M$ line. The velocity has been scaled with the effective Hartman number and the extreme value for low $-Ra$ corresponds to the analytical model with no stratification (black horizontal dotted line). The solid black lines are the best fit for $\delta < 0.3$, $\delta = 1.81(-Ra)^{-0.16\pm0.013}$ and $V_{\max} = 0.44M(-Ra)^{0.506\pm0.002}$. The orange lines show the slopes predicted in Section 4.2.1.

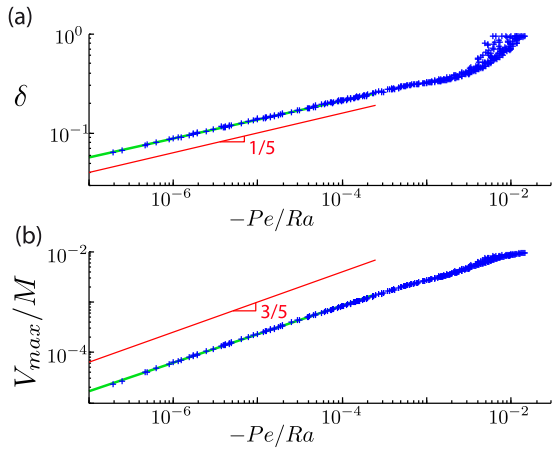

Figure 7. Thickness of the uppermost vorticity layer (a) and maximum velocity (b) as functions of $-Pe/Ra$. 50 runs are plotted, with Ra_0 from -3×10^3 to -10^{10} and Pe_0 from 13 to 5000, with 10 time steps for each runs, and filtered by $Pe_0 \gg 1/\delta$. Solid green lines are the best fit for $\delta < 0.25$, which is $\delta = 1.24\,(-Pe/Ra)^{0.192\pm0.04}$ and $V_{\max} = 0.143\,M\,(-Pe/Ra)^{0.56\pm0.09}$. The red lines are expected scaling laws developed in Section 4.2.2.

$-Ra \gg M$ is verified, the geometry of the flow does not depend on M and that the velocity is proportional to M.

5 STRAIN RATE

Fig. 8 shows the von Mises equivalent strain rate for the runs corresponding to Fig. 5, highlighting regions of high deformation. The von Mises equivalent strain rate is the second invariant of the strain rate tensor, measuring the power dissipated by deformation (Tome *et al.* 1984; Tackley 2000; Wenk *et al.* 2000). Comparing Figs 5 and 8, we see that the deformation and vorticity fields have a similar geometry when the flow is organized in several layers, whereas the location of the regions of high deformation and high vorticity differ when the effect of stratification is small and the flow is organized in one cell only. In this case, which is similar to that studied by Karato (1999), the maximum deformation is at the edges of the cells, whereas in the case of large stratification, the strain is confined in the uppermost layer. In the strongly stratified regime, the deformation can be predicted from the scaling laws discussed in Section 4.2, as $\dot\epsilon \sim u/\delta$ in dimensionless form, or $\dot\epsilon \sim u\kappa/\delta r_{ic}^2$ in dimensional form.

In the small Pe number case, relevant for the Earth's inner core with a thermal stratification, using the scaling laws (47) and (48) for the velocity and shear layer thickness gives

$$\dot\epsilon(t) \sim \frac{\kappa}{r_{ic}^2(t)}\frac{u}{\delta} \simeq 0.2\frac{\kappa}{r_{ic}^2(t)}M(t)(-Ra(t))^{-1/3}. \tag{55}$$

In the large Pe number case, relevant for the Earth's inner core with a compositional stratification, using the scaling laws (51) and (52) for the velocity and shear layer thickness gives

$$\dot\epsilon(t) \sim \frac{\kappa}{r_{ic}^2(t)}\frac{u}{\delta} \simeq 0.1\frac{\kappa}{r_{ic}^2(t)}M(t)\left(\frac{-Ra(t)}{Pe(t)}\right)^{-2/5}. \tag{56}$$

Notice that $\dot\epsilon$ is proportional to $\eta^{-2/3}$ and $\eta^{-3/5}$ in the thermal and compositional cases, and therefore increases with decreasing viscosity in spite of the fact that the velocity in the shear layer decreases with decreasing η. This is because the thickness of the shear layer decreases with viscosity faster than the velocity.

These scaling laws give upper bounds for the actual strain rate in the inner core, which evolves with time because of the time dependence of the parameters. The quantity $1/\dot\epsilon$ is the time needed to deform the shear layer to a cumulated strain $\sim$1.

To estimate the cumulated deformation in the inner core, we assume that the strain rate $\dot\epsilon$ found above is applied only on the uppermost shear layer of thickness δ. The simplest is to assume that both $\dot\epsilon$ and δ are evolving slowly with time, on a timescale long compared to the time δ/u_{ic} over which a layer of thickness δ is crystallized. Assuming that the strain rate $\dot\epsilon(t)$ is given by u/δ within the shear layer of thickness δ and is negligible elsewhere, the cumulated deformation is then

$$\epsilon \sim \frac{\dot\epsilon\delta}{u_{ic}} \sim \frac{u}{Pe}, \tag{57}$$

with u the dimensionless maximum horizontal velocity given by eqs (48) or (52) depending on the value of the Péclet number. With u dimensional, the cumulated strain can also be written as

$$\epsilon \sim \frac{u}{u_{ic}}. \tag{58}$$

The deformation magnitude below the upper shear layer is given by the ratio between the horizontal velocity induced by the Lorentz force and the growth rate of the inner core.

A more elaborated method of estimating ϵ is discussed in Appendix E. The results are close to what eq. (57) predicts for $r > 0.3\,r_{ic}(\tau_{ic})$, but are more accurate for smaller r. The validity of both estimates is restricted to conditions under which the strong stratification scaling laws applies, which requires that $M \ll -Ra$. This is only verified if the inner core radius is larger than $r_{ic}(\tau_{ic})(M_0/Ra_0)^{1/4} \simeq 0.02\,r_{ic}(\tau_{ic})$ in the thermal case, and $r_{ic}(\tau_{ic})(M_0/Ra_0)^{1/5} \simeq 0.07\,r_{ic}(\tau_{ic})$ in the compositional case.

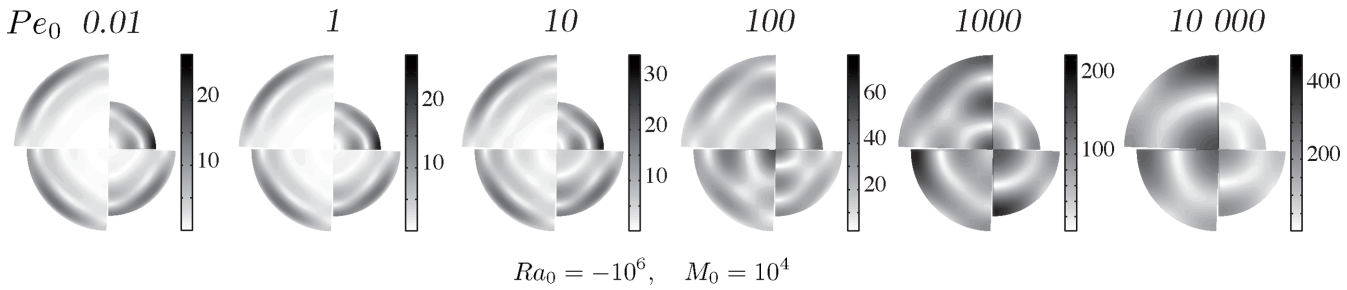

Figure 8. Snapshots of the von Mises equivalent strain rate for simulations with dimensionless parameters $M_0 = 10^4$, $Ra_0 = -10^6$, and $Pe_0 = 0.01$, 1, 10, 10^2, 10^3 and 10^4 (from left to right), with $r_{ic} \propto t^{1/2}$. Each panel corresponds to one simulation, with four time steps represented : $t = 0.25$, 0.50, 0.75 and 1 dimensionless time, from top-right and going clockwise. See Fig. 5 for plots of the vorticity field of corresponding runs.

6 APPLICATION TO THE INNER CORE

To determine in which regime is the inner core, the first step is to estimate the ratio $-Ra/M$

$$\frac{-Ra}{M} = \frac{-\Delta\rho g_{ic} r_{ic} \mu_0}{B_0^2} = \frac{-\Delta\rho}{1\,\mathrm{kg\,m^{-3}}} \left(\frac{3\,\mathrm{mT}}{B_0}\right)^2 7.5 \times 10^5. \quad (59)$$

Notice that this does not depend on the viscosity. Plausible dimensionless numbers for the Earth's inner core are obtained from typical values given in Table 1 and summarized in Table 2. The density stratification is $\Delta\rho \sim 1\,\mathrm{kg\,m^{-3}}$ irrespectively of the nature of the stratification (Deguen & Cardin 2011; Labrosse 2014). Varying the parameters within their uncertainty range can change the ratio $-Ra/M$ by an order of magnitude at most. The ratio $-Ra/M$ is thus unlikely to be smaller than 1, irrespectively of the thermal or compositional origin of the stratification. The inner core is strongly stratified compared to magnetic forcing.

If the stratification is of thermal origin, the Péclet number is on the order of 1 ($Pe_0 = 2.8$). Fig. 5 shows that the low Péclet number scaling laws still agree reasonably well with the numerical results for Péclet numbers around 1; the low Péclet number scaling laws can therefore be used to predict the flow geometry and strength in the thermal stratification case. If the stratification is of compositional origin, the Péclet number is large ($Pe_0 \sim 10^5$) and thus the large Péclet limit scaling laws apply.

Estimates of the thickness of the upper layer, of the maximum velocity in this layer and of the expected strain rate are given in Table 3, using values of parameters of Tables 1 and 2. Because the viscosity is poorly known, we express these estimates as functions of the viscosity. As an example, assuming a viscosity of 10^{16} Pa s gives a shear layer thickness of 94 and 60 km in case of thermal and compositional stratification. The velocity in this layer is expected to be several orders of magnitude lower than the growth rate, and instantaneous deformation due to this flow is small: the typical timescale for the deformation is of order 10^2 Gyr for both cases, for $\eta = 10^{16}$ Pa s. These values are obtained for the present inner core, which means it is the deformation timescale for the present uppermost layer. The deformation $\epsilon \sim u/Pe$ is a decreasing function of the radius, and thus is higher in depth: compared to below the ICB, the strain at $r = 0.5\,r_{ic}$ is multiplied by 2 for thermal stratification, and by 4.6 for compositional stratification.

As can be seen in eqs (55) and (56), the strain rate in the shear layer is a decreasing function of the stratification strength. This is the opposite of what Deguen *et al.* (2011) found in the case of a flow forced by heterogeneous inner core growth (Yoshida *et al.* 1996). The flow geometry is similar to what has been found here if the inner core is stably stratified, with a shear layer below the ICB in which deformation is localized, but, contrary to the case of the Lorentz force, the strength of the flow and strain rate increase with the strength of the stratification. This difference is due to the fact that the velocity is imposed by the boundary conditions at the ICB in the case of heterogeneous inner core growth case, and therefore does not decrease when the stratification strength is increased. In contrast, the velocity in the shear layer produced by the Lorentz force depends on a balance between the Lorentz force and the viscous forces, and decreases with increasing stratification strength.

Using the scaling laws developed above (eqs 55–57), the cumulated strain below the shear layer is given by

$$\epsilon_T \sim 5.6 \times 10^{-4} \left(\frac{10^{16}\,\mathrm{Pa\,s}}{\eta}\right)^{1/2} \left(\frac{B_0}{3\,\mathrm{mT}}\right)^2, \quad (60)$$

and

$$\epsilon_C \sim 2.4 \times 10^{-4} \left(\frac{10^{16}\,\mathrm{Pa\,s}}{\eta}\right)^{2/5} \left(\frac{B_0}{3\,\mathrm{mT}}\right)^2. \quad (61)$$

This shows that a viscosity lower than 10^{10} Pa s is required to obtain a deformation larger than about 1. Such a low viscosity seems unrealistic and this suggests that no detectable anisotropy would be produced in the bulk of the inner core.

Using the method in Appendix E to estimate the strain, the deformation is found to be two orders of magnitude larger close to the centre of the inner core than at the edge. This means a nonnegligible strain for viscosity lower than 10^{12} Pa s.

Table 2. Typical values of the dimensionless parameters discussed in the text for the present inner core, using typical values from Table 1.

Dimensionless parameter	Symbol	Thermal	Compositional
Rayleigh number	Ra	$\frac{10^{16}\,\mathrm{Pa\,s}}{\eta} \times (-2.8 \times 10^8)$	$\frac{10^{16}\,\mathrm{Pa\,s}}{\eta} \times (-8 \times 10^{12})$
Effective Hartmann number	M	$\left(\frac{B_0}{3\times10^{-3}\,\mathrm{T}}\right)^2 \frac{10^{16}\,\mathrm{Pa\,s}}{\eta} \times 63$	$\left(\frac{B_0}{3\times10^{-3}\,\mathrm{T}}\right)^2 \frac{10^{16}\,\mathrm{Pa\,s}}{\eta} \times 1.07 \times 10^7$
Péclet number	Pe	2.8	4.7×10^5
Phase change number	$\mathcal{P}$	$\frac{10^{16}\,\mathrm{Pa\,s}}{\eta} \times 10^4$	$\frac{10^{16}\,\mathrm{Pa\,s}}{\eta} \times 10^4$

See the definitions of the dimensionless parameters in the text.

Table 3. Estimates of the thickness, maximal horizontal velocity and strain rate of the upper layer for thermal stratification (low Pe) and compositional stratification (large Pe).

	Thermal stratification, low Péclet	Compositional stratification, large Péclet
Thickness δ	$\left(\frac{\eta}{10^{16}\,\mathrm{Pa\,s}}\right)^{1/6} \times 94\,\mathrm{km}$	$\left(\frac{\eta}{10^{16}\,\mathrm{Pa\,s}}\right)^{1/5} \times 60\,\mathrm{km}$
Maximal horizontal velocity[a] u	$\left(\frac{10^{16}\,\mathrm{Pa\,s}}{\eta}\right)^{1/2} \times 2.2 \times 10^{-14}\,\mathrm{m\,s^{-1}}$	$\left(\frac{10^{16}\,\mathrm{Pa\,s}}{\eta}\right)^{2/5} \times 0.9 \times 10^{-14}\,\mathrm{m\,s^{-1}}$
Instantaneous strain rate[b] $\dot{\epsilon}$	$\left(\frac{10^{16}\,\mathrm{Pa\,s}}{\eta}\right)^{2/3} \times 7.4 \times 10^{-12}\,\mathrm{yr^{-1}}$	$\left(\frac{10^{16}\,\mathrm{Pa\,s}}{\eta}\right)^{3/5} \times 4.8 \times 10^{-12}\,\mathrm{yr^{-1}}$
Strain $\epsilon = u/Pe$	$\left(\frac{10^{16}\,\mathrm{Pa\,s}}{\eta}\right)^{1/2} \frac{r_{ic}}{r} \times 5.6 \times 10^{-4}$	$\left(\frac{10^{16}\,\mathrm{Pa\,s}}{\eta}\right)^{2/5} \left(\frac{r_{ic}}{r}\right)^{11/5} \times 2.4 \times 10^{-4}$

[a] This value has to be compared with a typical value for the growth rate: $u_{ic}(\tau_{ic}) \approx 10^{-11}\,\mathrm{m\,s^{-1}}$.
[b] At $t = \tau_{ic}$.

The uppermost layer has a different behaviour because it does not have enough time to deform. This could stand for an isotropic layer at the top of the inner core, as observed by seismic studies. We expect this layer to be of the order of one hundred kilometres thick for thermal or compositional stratification.

7 CONCLUSION AND DISCUSSION

Following previous studies (Karato 1999; Buffett & Wenk 2001), we have developed a complete model for evaluating the deformation induced by the Lorentz force in a stratified inner core, investigating the effect of boundary conditions and neutral and strong stratification in the case of thermal or compositional stratification.

Calculating the flow for neutral stratification with different mechanical boundary conditions, we show that the boundary conditions depend on the values of the viscosity. If the viscosity is low, the ICB acts as an impermeable boundary, with no radial flow across the ICB, whereas if the viscosity is large the ICB acts as a permeable boundary, with fast melting and solidification at the ICB. We find that the velocity is larger than the inner core growth rate if the viscosity is lower than 10^{16} Pa s. Unlike previous studies, the boundary conditions assumed here are of impermeable type.

If the inner core has a stable density stratification, then we find that the stratification strongly alters the flow induced by the poloidal component of the Lorentz force. The deformation is concentrated in a thin shear layer at the top of the inner core, which thickness does not depend on the magnetic field strength, but depends on both the density stratification and the Péclet number, which compares the timescales of inner core growth and diffusion.

However, the deformation rate in this regime is predicted to be too small for producing significant LPO in most of the inner core, unless the inner core viscosity is smaller than 10^{10}–10^{12} Pa s. The cumulated deformation can be two orders of magnitude larger close to the centre of the inner core, but remains smaller than 1 if the inner core viscosity is larger than 10^{12} Pa s.

We have made a number of simplifying assumption, but relaxing them is unlikely to significantly alter our conclusions. Our estimated values of the deformation are probably upper bounds. The effective strain in the inner core induced by the poloidal Lorentz force is expected to be even smaller than these values. Indeed, we use assumptions that maximize the strain rate in the inner core.

(i) The geometry and strength of the magnetic field have been chosen to maximize the effect of the Lorentz force: the degree (2,0) penetrates deeper in the inner core than higher orders (smaller length-scales) and is less likely to vary with time. The smaller scale components of the magnetic field vary on a shorter timescale, which make them more sensitive to skin effect.

(ii) We have assumed the magnetic field to be time-independent, a reasonable assumption because the fluctuations associated with outer core dynamics occur on a timescale short compared to the timescale of inner core dynamics. The evolution of the magnetic field strength on the timescale of inner core growth is poorly constrained, but seems unlikely to have involved order of magnitude variations.

(iii) Though a growth law of the form $r_{ic} \propto t^{1/2}$ has been assumed in the numerical simulations, our derivation of the scaling laws (Section 4.2) makes no assumption on the inner core growth law, and our scaling law should therefore also apply if this assumption is relaxed.

Finally, we have focused on the effect of the azimuthal component of the magnetic field, which produces a poloidal Lorentz force in the inner core, and have left aside the combined effect of the azimuthal and $z-$component (parallel to Earth's spin axis), which produce an azimuthal Lorentz force driving an azimuthal flow (Buffett & Wenk 2001). There is no loss of generality involved, because the axisymmetric poloidal flow we have investigated and the azimuthal flow calculated by Buffett & Wenk (2001) are perfectly decoupled, and add up linearly. The azimuthal flow is horizontal, and is therefore not affected by the thermal and compositional fields and their perturbations by the axisymmetric poloidal flow. Conversely, since the flow and density perturbations induced by the axisymmetric poloidal Lorentz force are axisymmetric, they are not affected by an azimuthal flow. The azimuthal flow velocity is

$$v_\phi = -\frac{1}{10}\frac{B_z B_\phi}{\mu_0 \eta}\frac{r^3}{r_{ic}^2}\sin\theta \tag{62}$$

(Buffett & Wenk 2001), and the associated strain rate is

$$\dot{\epsilon}(r,\theta) = \dot{\epsilon}_{r,\phi}(r,\theta) = \frac{1}{10}\frac{B_z B_\phi r^2}{\mu_0 \eta r_{ic}^2}\sin\theta. \tag{63}$$

This is always larger than the strain rate predicted by our scaling laws in the strongly stratified regime (eqs (55) and (56) for thermal and compositional stratification), which implies that this deformation field will dominate over deformation due to the poloidal component of the Lorentz force.

ACKNOWLEDGEMENTS

We would like to thank two anonymous reviewers for their constructive comments, and Christie Juan for her help at a preliminary stage of this project. RD gratefully acknowledges support from grant ANR-12-PDOC-0015-01 of the ANR (Agence Nationale de la Recherche). SL was supported by the Institut Universitaire de France for this work.

REFERENCES

Alboussière, T., Deguen, R. & Melzani, M., 2010. Melting-induced stratification above the Earth's inner core due to convective translation, *Nature,* **466**(7307), 744–747.

Bergman, M.I., 1997. Measurements of electric anisotropy due to solidification texturing and the implications for the Earth's inner core, *Nature,* **389**(6646), 60–63.

Brito, D., Elbert, D. & Olson, P., 2002. Experimental crystallization of gallium: ultrasonic measurements of elastic anisotropy and implications for the inner core, *Phys. Earth planet. Inter.,* **129,** 325–346.

Buffett, B.A., 2000. Sediments at the Top of Earth's Core, *Science,* **290**(5495), 1338–1342.

Buffett, B.A., 2009. Onset and orientation of convection in the inner core, *Geophys. J. Int.,* **179**(2), 711–719.

Buffett, B.A., 2010. Tidal dissipation and the strength of the earth's internal magnetic field, *Nature,* **468**(7326), 952–954.

Buffett, B.A. & Bloxham, J., 2000. Deformation of Earth's inner core by electromagnetic forces, *Geophys. Res. Lett.,* **27**(24), 4001–4004.

Buffett, B.A. & Wenk, H.R., 2001. Texturing of the Earth's inner core by Maxwell stresses, *Nature,* **413**(6851), 60–63.

Buffett, B.A., Huppert, H.E., Lister, J.R. & Woods, A.W., 1992. Analytical model for solidification of the Earth's core, *Nature,* **356**(6367), 329–331.

Christensen, U.R. & Aubert, J., 2006. Scaling properties of convection-driven dynamos in rotating spherical shells and application to planetary magnetic fields, *Geophys. J. Int.,* **166**(1), 97–114.

Cottaar, S. & Buffett, B., 2012. Convection in the Earth's inner core, *Phys. Earth planet. Inter.,* **198–199**(C), 67–78.

Crank, J., 1984. *Free and moving boundary problems,* Oxford University Press.
de Koker, N., Steinle-Neumann, G. & Vlček, V., 2012. Electrical resistivity and thermal conductivity of liquid Fe alloys at high P and T, and heat flux in Earth's core, *Proc. Nat. Acad. Sci.,* **109**(11), 4070–4073.
Deguen, R., 2012. Structure and dynamics of Earth's inner core, *Earth planet. Sci. Lett.,* **333–334**(C), 211–225.
Deguen, R. & Cardin, P., 2009. Tectonic history of the Earth's inner core preserved in its seismic structure, *Nature Geoscience,* **2**(6), 419–422.
Deguen, R. & Cardin, P., 2011. Thermochemical convection in Earth's inner core, *Geophys. J. Int.,* **187**(3), 1101–1118.
Deguen, R., Cardin, P., Merkel, S. & Lebensohn, R.A., 2011. Texturing in Earth's inner core due to preferential growth in its equatorial belt, *Phys. Earth planet. Inter.,* **188**(3–4), 173–184.
Deguen, R., Alboussière, T. & Cardin, P., 2013. Thermal convection in Earth's inner core with phase change at its boundary, *Geophys. J. Int.,* **194**(3), 1310–1334.
Deuss, A., 2014. Heterogeneity and anisotropy of Earth's inner core, *Ann. Rev. Earth Planet. Sci.,* **42**(1), 103–126.
Dziewoński, A.M. & Anderson, D.L., 1981. Preliminary reference Earth model, *Phys. Earth planet. Inter.,* **25**(4), 297–356.
Gillet, N., Jault, D., Canet, E. & Fournier, A., 2010. Fast torsional waves and strong magnetic field within the Earth's core, *Nature,* **465**(7294), 74–77.
Glatzmaier, G.A. & Roberts, P.H., 1996. Rotation and magnetism of Earth's inner core, *Science,* **274**(5294), 1887–1891.
Gomi, H., Ohta, K., Hirose, K., Labrosse, S., Caracas, R., Verstraete, M.J. & Hernlund, J.W., 2013. The high conductivity of iron and thermal evolution of the Earth's core, *Phys. Earth planet. Inter.,* **224**(C), 88–103.
Gubbins, D. & Davies, C.J., 2013. The stratified layer at the core–mantle boundary caused by barodiffusion of oxygen, sulphur and silicon, *Phys. Earth planet. Inter.,* **215,** 21–28.
Gubbins, D., Alfè, D. & Davies, C.J., 2013. Compositional instability of Earth's solid inner core, *Geophys. Res. Lett.,* **40**(6), 1084–1088.
Jeanloz, R. & Wenk, H.R., 1988. Convection and anisotropy of the inner core, *Geophys. Res. Lett.,* **15**(1), 72–75.
Karato, S., 1993. Inner core anisotropy due to the magnetic field—induced preferred orientation of iron, *Science,* **262**(5140), 1708–1711.
Karato, S., 1999. Seismic anisotropy of the Earth's inner core resulting from flow induced by Maxwell stresses, *Nature,* **402**(6764), 871–873.
Koot, L. & Dumberry, M., 2013. The role of the magnetic field morphology on the electromagnetic coupling for nutations, *Geophys. J. Int.,* **195**(1), 200–210.
Labrosse, S., 2003. Thermal and magnetic evolution of the Earth's core, *Phys. Earth planet. Inter.,* **140**(1), 127–143.
Labrosse, S., 2014. Thermal and compositional stratification of the inner core, *C. R. Geosci.,* **346**(5–6), 119–129.
Labrosse, S., 2015. Thermal evolution of the core with a high thermal conductivity, *Phys. Earth planet. Inter.,* doi:10.1016/j.pepi.2015.02.002.
Lincot, A., Deguen, R., Merkel, S. & Cardin, P., 2014. Seismic response and anisotropy of a model hcp iron inner core, *C. R. Geosci.,* **346**(5–6), 148–157.
Mizzon, H. & Monnereau, M., 2013. Implication of the lopsided growth for the viscosity of Earth's inner core, *Earth planet. Sci. Lett.,* **361,** 391–401.
Monnereau, M., Calvet, M., Margerin, L. & Souriau, A., 2010. Lopsided Growth of Earth's Inner Core, *Science,* **328**(5981), 1014–1017.
Morelli, A., Dziewoński, A.M. & Woodhouse, J.H., 1986. Anisotropy of the inner core inferred from PKIKP travel times, *Geophys. Res. Lett.,* **13**(13), 1545–1548.
Poupinet, G., Pillet, R. & Souriau, A., 1983. Possible heterogeneity of the Earth's core deduced from PKIKP travel times, *Nature,* **305,** 204–206.
Pozzo, M., Davies, C., Gubbins, D. & Alfè, D., 2012. Thermal and electrical conductivity of iron at Earth's core conditions, *Nature,* **485**(7398), 355–358.
Pozzo, M., Davies, C., Gubbins, D. & Alfè, D., 2014. Thermal and electrical conductivity of solid iron and iron–silicon mixtures at Earth's core conditions, *Earth planet. Sci. Lett.,* **393,** 159–164.
Ribe, N., 2007. Analytical approaches to mantle dynamics, *Treat. Geophys.,* **7,** 167–226.
Ricard, Y. & Vigny, C., 1989. Mantle dynamics with induced plate tectonics, *J. geophys. Res.,* **94**(B12), 17 543–17 559.
Roberts, P.H., 2007. Theory of the geodynamo, *Treat. Geophys.,* **8,** 67–105.
Singh, S.C., Taylor, M. & Montagner, J.P., 2000. On the presence of liquid in Earth's inner core, *Science,* **287**(5462), 2471–2474.
Souriau, A., Garcia, R. & Poupinet, G., 2003. The seismological picture of the inner core: structure and rotation, *C. R. Geosci.,* **335**(1), 51–63.
Tackley, P.J., 2000. Self-consistent generation of tectonic plates in time-dependent three-dimensional mantle convection simulations, 1. Pseudo-plastic yielding, *Geochem. Geophys. Geosyst.,* **1**(8), 1–45.
Takehiro, S.-I., 2010. Fluid motions induced by horizontally heterogeneous Joule heating in the Earth's inner core, *Phys. Earth planet. Inter.,* **184**(3–4), 134–142.
Tkalčić, H. & Kennett, B. L.N., 2008. Core structure and heterogeneity: a seismological perspective, *Aus. J. Earth Sci.,* **55**(4), 419–431.
Tome, C., Canova, G.R., Kocks, U.F., Christodoulou, N. & Jonas, J.J., 1984. The relation between macroscopic and microscopic strain hardening in FCC polycrystals, *Acta metallurgica,* **32**(10), 1637–1653.
Weber, P. & Machetel, P., 1992. Convection within the innercore and thermal implications, *Geophys. Res. Lett.,* **19**(21), 2107–2110.
Wenk, H.R., Baumgardner, J.R., Lebensohn, R. & Tomé, C.N., 2000. A convection model to explain anisotropy of the inner core, *J. Geophys. Res.,* **105**(B3), 5663–5677.
Woodhouse, J.H., Giardini, D. & Li, X.-D., 1986. Evidence for inner core anisotropy from free oscillations, *Geophys. Res. Lett.,* **13**(13), 1549–1552.
Yoshida, S., Sumita, I. & Kumazawa, M., 1996. Growth model of the inner core coupled with the outer core dynamics and the resulting elastic anisotropy, *J. geophys. Res.,* **101**(B12), 28 085–28 103.
Yoshida, S., Sumita, I. & Kumazawa, M., 1999. Models of the anisotropy of the Earth's inner core, *J. Phys.-Conden. Matter,* **10**(49), 11 215–11 226.
Yukutake, T., 1998. Implausibility of thermal convection in the Earth's solid inner core, *Phys. Earth planet. Inter.,* **108**(1), 1–13.

APPENDIX A: POLOIDAL/TOROIDAL DECOMPOSITION

A1 Momentum equation using poloidal decomposition

Following Ricard & Vigny (1989) and Ribe (2007), a flow induced by internal density anomalies in a constant viscosity fluid is purely poloidal in a spherical shell, if the surface boundary conditions also have a zero vertical vorticity. Considering also that the external forcing by the Lorentz force is purely poloidal ($\boldsymbol{r}\cdot\nabla\times\boldsymbol{F}_L=0$), no toroidal flow is expected in our problem. The velocity field can thus be written by introducing the scalar P defined such that

$$u=\nabla\times\nabla\times(Pr), \tag{A1}$$

where $\boldsymbol{r}=r\boldsymbol{e}_r$ is the position vector.

Applying $\boldsymbol{r}\cdot(\nabla\times\nabla\times)$ to eq. (13) , we obtain that

$$\mathbf{0}=Ra(t)L^2\Theta-(\nabla^2)^2L^2P+M(t)\boldsymbol{r}\cdot(\nabla\times\nabla\times\boldsymbol{F}_L), \tag{A2}$$

where L^2 is the operator defined by

$$L^2=-\frac{1}{\sin\theta}\frac{\partial}{\partial\theta}\left(\sin\theta\frac{\partial}{\partial\theta}\right)-\frac{1}{\sin^2\theta}\frac{\partial^2}{\partial\phi^2}. \tag{A3}$$

The last term of eq. (A2) is computed from the Lorentz force defined in eq. (3) and gives

$$\boldsymbol{r}\cdot(\nabla\times\nabla\times\boldsymbol{F}_L)=8r^2(1-3\cos^2\theta)=-\frac{16}{\sqrt{5}}r^2Y_2^0, \tag{A4}$$

where $Y_2^0=\frac{\sqrt{5}}{2}(3\cos^2\theta-1)$.

Eq. (A2) becomes

$$0=Ra(t)L^2\Theta-(\nabla^2)^2L^2P-M(t)\frac{16}{\sqrt{5}}r^2Y_2^0. \tag{A5}$$

When expanding the two scalar field Θ and P with spherical harmonics $Y_l^m(\theta,\phi)$ that satisfy $L^2 Y_l^m = l(l+1)Y_l^m$, we defined new variables t_l^m and p_l^m by

$$\Theta = t_l^m(r)Y_l^m, \tag{A6}$$

$$P = p_l^m(r)Y_l^m, \qquad l \geq 1. \tag{A7}$$

Eq. (A5) is eventually written as

$$D_l^2 p_l^m + \frac{16}{\sqrt{5}l(l+1)} M(t) r^2 \delta_{2l}\delta_{0m} - Ra(t) t_l^m = 0, \quad l \geq 1, \tag{A8}$$

where δ is the Kronecker symbol and D_l is the second-order differential operator defined by

$$D_l = \frac{d^2}{dr^2} + \frac{2}{r}\frac{d}{dr} - \frac{l(l+1)}{r^2}. \tag{A9}$$

A2 Poloidal decomposition of the boundary conditions

From Deguen *et al.* (2013), the boundary conditions at $r = 1$ are written as:

$$\tau_{r\theta} = \eta\left[r\frac{\partial}{\partial r}\left(\frac{u_\theta}{r}\right) + \frac{1}{r}\frac{\partial u_r}{\partial \theta}\right] = 0, \tag{A10}$$

$$\tau_{r\phi} = \eta\left[r\frac{\partial}{\partial r}\left(\frac{u_\phi}{r}\right) + \frac{1}{r\sin\theta}\frac{\partial u_r}{\partial \phi}\right] = 0, \tag{A11}$$

$$-\mathcal{P}(t)(u_r - u_{ic}) - 2\frac{\partial u_r}{\partial r} + p' = 0. \tag{A12}$$

$\mathcal{P}(t)$ is the dimensionless parameter that characterizes the resistance to phase change as defined in eq. (35).

In term of poloidal decomposition of the velocity field, the set of equations for the boundary conditions at $r = 1$ is modified as

$$\frac{d^2 p_l^m}{dr^2} + [l(l+1) - 2]\frac{p_l^m}{r^2} = 0, \quad l \geq 1, \tag{A13}$$

$$r\frac{d^3 p_l^m}{dr^3} - 3l(l+1)\frac{1}{r}\frac{dp_l^m}{dr} = \left[l(l+1)\mathcal{P}(t) - \frac{6}{r^2}\right]p_l^m, \quad l \geq 1. \tag{A14}$$

APPENDIX B: THERMAL STRATIFICATION

We derive here the expression of the reference diffusive potential temperature profile given in eq. (24), under the assumption of $r_{ic} \propto t^{1/2}$.

The reference potential temperature is the solution of

$$\frac{\partial\Theta}{\partial t} - \tilde{r}\frac{u_{ic}(t)}{r_{ic}(t)}\frac{\partial\Theta}{\partial r} = \frac{\kappa_T}{r_{ic}^2(t)}\frac{1}{\tilde{r}^2}\frac{\partial}{\partial r}\left(\tilde{r}^2\frac{\partial\Theta}{\partial\tilde{r}}\right) + S_T, \tag{B1}$$

obtained from eq. (11) by taking $\chi = \Theta$ and $\boldsymbol{u} = \boldsymbol{0}$. The source term S_T is constant if $r_{ic} \propto t^{1/2}$. The potential temperature Θ is a function of $\tilde{r}$, κ_T, $r_{ic}(t)$, S_T and $u_{ic}(t)$ only. According to the Vaschy-Buckingham theorem, we can form only three independent dimensionless groups from these variables (6-D variables—three independent physical units), one possible set being $\Theta/(S_T r_{ic}^2/\kappa_T)$, $u_{ic}r_{ic}/\kappa_T$ and $\tilde{r}$. With $r_{ic} \propto t^{1/2}$, $u_{ic}r_{ic}/\kappa_T$ is constant and equal to Pe_0. The potential temperature must therefore be of the form

$$\Theta = \frac{S_T r_{ic}^2(t)}{\kappa_T} f(\tilde{r}, Pe_{T0}). \tag{B2}$$

By definition, the potential temperature is equal to 0 at the ICB, which implies $f(\tilde{r} = 1, Pe_{T0}) = 0$. With $r_{ic}(t) = r_{ic}(\tau_{ic})(t/\tau_{ic})^{1/2}$ and noting that $r_{ic}^2(\tau_{ic})/(\kappa_T\tau_{ic}) = \xi_{T0} = 2Pe_{T0}$ (see eqs 17 and 21), inserting eq. (B2) into eq. (B1) yields

$$0 = f'' + f'\left(\frac{2}{\tilde{r}} + Pe_{T0}\tilde{r}\right) - 2Pe_{T0}f + 1, \tag{B3}$$

where f' and f'' stand for the first and second derivatives of f with respect to $\tilde{r}$. Looking for a polynomial solution in $\tilde{r}$ satisfying $f(\tilde{r} = 1, Pe_{T0}) = 0$, we find that $f = (1-\tilde{r}^2)/(6 + 2Pe_{T0})$, which gives

$$\Theta = \frac{S_T r_{ic}^2(t)}{6\kappa_T(1 + Pe_{T0}/3)}\left[1 - \left(\frac{r}{r_{ic}(t)}\right)^2\right]. \tag{B4}$$

APPENDIX C: COMPOSITIONAL STRATIFICATION

The source term S_c of the conservation of light elements is directly related to the evolution of the concentration of light elements in the solid that freezes at the ICB $c_{ic}^s(t)$. Following Gubbins *et al.* (2013) and Labrosse (2014), this term depends both on the evolution of the concentration in the liquid outer core, which increases when the inner core grows because the solid incorporates less light elements than is present in the outer core, and on the evolution of the partition coefficient between solid and liquid.

In this paper, we will focus on the simplest case for which the partition coefficient does not depend on temperature or concentration. Thus, the concentration in the solid is increasing with the radius of the inner core, as the concentration in the liquid increases. This will promote a stably stratified inner core, whereas Gubbins *et al.* (2013) and Labrosse (2014) focused on the potentially destabilizing effects of variations of the partition coefficient.

To estimate the light element concentration, we note $M_c = M_{ic} + M_{oc}$ the total mass of the Earth's core. When increasing the inner core mass by dM_{ic}, the mass of the outer core light elements decreases by $d(c^l M_{oc}) = -c_{ic}^s d M_{ic}$. The total mass of the Earth's core is constant, which gives $dM_{oc} = -dM_{ic}$ and

$$\frac{dc^l}{c^l} = (k-1)\frac{dM_{oc}}{M_{oc}}, \tag{C1}$$

where k is the partition coefficient defined as $k = c_{ic}^s/c^l$.

Eq. (C1) can be integrated with the assumption of a constant partition coefficient. Integration between (c_0^l, M_c) and (c^l, M_{oc}), corresponding to before the inner core formation and any time after, this gives

$$c^l(t) = c_0^l\left(\frac{M_{oc}}{M_c}\right)^{k-1}. \tag{C2}$$

When ignoring radial density variations in the outer core, the ratio M_{oc}/M_c is simply $1 - (r_{ic}/r_c)^3$. Taking into account compressibility (radial density variations in the core) and the density jump at the ICB results in a stratification approximately 15 per cent larger. The light element concentration at the ICB is thus directly obtained from the liquid concentration as

$$c_{ic}^s(t) = kc_0^l\left(1 - \left(\frac{r_{ic}(t)}{r_c}\right)^3\right)^{k-1}. \tag{C3}$$

APPENDIX D: ANALYTIC SOLUTION FOR NEUTRAL STRATIFICATION

We solve eq. (A8) for a neutral stratification, $Ra = 0$, with the boundary conditions (A13) and (A14) described in section (A2).

Eq. (A8) is thus written as

$$D_l^2 p_l^m + \frac{16}{\sqrt{5}l(l+1)} Mr^2 \delta_{2l}\delta_{0m} = 0, \tag{D1}$$

and can be solved analytically.

Except for $(l = 2, m = 0)$, $p_l^m = 0$ is solution of the eq. (D1) and verifies the boundary conditions (A13) and (A14).

For $(l = 2, m = 0)$, we have

$$D_l^2 p_2^0 + \frac{8}{3\sqrt{5}} Mr^2 = 0, \tag{D2}$$

and for $r = 1$

$$\frac{d^2 p_2^0}{dr^2} + 4\frac{p_2^0}{r^2} = 0, \tag{D3}$$

$$r\frac{d^3 p_2^0}{dr^3} - 18\frac{1}{r}\frac{dp_2^0}{dr} = \left[\mathcal{P}(t) - \frac{1}{r^2}\right] 6p_2^0. \tag{D4}$$

Eq. (D2) is solved considering a sum of polynomial functions, and adding the boundary conditions (D3) and (D4), we obtain the coefficient p_2^0 as

$$p_2^0(r) = \frac{M}{3^3 7\sqrt{5}} \left(-r^6 + \frac{14}{5}r^4 - \frac{9}{5}r^2 + \frac{204}{5}\frac{r^4}{19+5P} - \frac{544}{5}\frac{r^2}{19+5P} \right). \tag{D5}$$

From the coefficients p_l^m, the vertical and horizontal velocities are

$$u_r = \sum_{l,m} l(l+1)\frac{p_l^m}{r} Y_l^m, \tag{D6}$$

$$u_\theta = \sum_{l,m} \frac{1}{r}\frac{d}{dr}\left(r p_l^m\right) \frac{\partial}{\partial\theta} Y_l^m, \tag{D7}$$

with Y_l^m the surface spherical harmonics.

The root mean square velocity (V_{rms}) of the system is defined as

$$V_{\text{rms}}^2 = \frac{3}{4\pi}\int_0^{2\phi}\int_0^{\pi}\int_0^1 \left(u_r^2 + u_\theta^2\right)\sin\theta r^2 \,\mathrm{d}r\,\mathrm{d}\theta\,\mathrm{d}\phi. \tag{D8}$$

From eqs (D7) and (D8), we obtain the maximum absolute value of the horizontal velocity and the rms velocity that are shown on Fig. 2. Both graphs have a sigmoid shape, and thus we are mostly interested in the extreme values for each velocity, which are given in Table D1.

Table D1. Extreme values for rms velocity and maximum of the absolute value of the horizontal velocity for two extreme values of $\mathcal{P}$. Velocities are proportional to M and thus only the value v/M is given.

	$\mathcal{P} \to 0$	$\mathcal{P} \to \infty$
V_{rms}/M	0.06609	0.00805
$\max\|u_\theta(r,\theta)\|/M$	0.06944	0.01270

APPENDIX E: INTEGRATION OVER TIME OF THE DEFORMATION

E1 General discussion

In general, the texturation mechanism is a nonlinear process, but an upper bound of the total deformation can be inferred by considering that the strain adds up linearly. The material is deformed at a strain rate $\dot{\epsilon}$ during the time δ/u_{ic} needed to grow a layer of thickness δ, and so

$$\epsilon(r(t)) = \dot{\epsilon}(t)\frac{\delta(t)}{u_{ic}(t)} = \frac{u}{Pe}, \tag{E1}$$

with $Pe = u_{ic}r_{ic}/\kappa$.

This equation leads to simple forms at the low and large Péclet limits, with $\epsilon \propto t^{-1/2}$ for thermal stratification and low Péclet, and $\epsilon \propto t^{-11/10}$ for compositional stratification and large Péclet. In what follows, we will compare the simple estimate given above with results of more elaborate calculations.

The total deformation of a given material during a time τ can be inferred more precisely by $\int_0^\tau \dot{\epsilon}(t)\,\mathrm{d}t$. Using dimensionless quantities described in the main sections, the deformation of a stratified sphere subject to a magnetic forcing is

$$\epsilon(r) = \int_0^1 \dot{\epsilon}(r,t)\,\mathrm{d}t, \tag{E2}$$

with $\dot{\epsilon}$ the strain rate function that will be described by a rectangular function as

$$\dot{\epsilon}(r,t) = \begin{cases} \dot{\epsilon}_{vM}(t)\frac{\kappa}{r_{ic}^2(t)} & \text{if } r_{ic}(t)(1-\delta) < r < r_{ic}(t). \\ 0 & \text{elsewhere.} \end{cases} \tag{E3}$$

The estimations of $\dot{\epsilon}_{vM}$ depend on the scaling laws defined in Section 5, and also on the time dependence of the parameters we have defined.

Because $r_{ic}(t)(1-\delta) < r_{ic}(t)\ \forall t$, integrating over time the function defined by (E3) is equivalent to integrate it between $t_{\min}(r)$ and $t_{\max}(r)$, where $t_{\min}$ and $t_{\max}$ are defined by $r_{ic}(t_{\max})(1-\delta) = r$ and $r_{ic}(t_{\min}) = r$,

$$\epsilon(r) = \int_{t_{\min}}^{t_{\max}} \dot{\epsilon}_{vM}(t)\frac{\kappa}{r_{ic}^2(t)}\,\mathrm{d}t. \tag{E4}$$

E2 Low *Pe*—Thermal stratification

In the low Péclet limit, the dimensionless thickness, maximal horizontal velocity and strain rate of the uppermost layer are given by

$$\delta \sim (-Ra)^{-1/6}, \tag{E5}$$

$$u \sim M(-Ra)^{-1/2}, \tag{E6}$$

$$\dot{\epsilon} \sim M(-Ra)^{-1/3}. \tag{E7}$$

In dimensional form, δ happens to be constant with time for thermal stratification

$$\delta = 1.9643 r_{ic}(\tau_{ic})(-Ra_0)^{-1/6}. \tag{E8}$$

Thus, $t_{\min}$ and $t_{\max}$ are easy to defined as

$$t_{\min}(r) = \tau_{ic}\left(\frac{r}{r_{ic}(\tau_{ic})}\right)^2, \tag{E9}$$

$$t_{\max}(r) = \tau_{ic}\left(\frac{r+\delta}{r_{ic}(\tau_{ic})}\right)^2, \tag{E10}$$

except for time close to τ_{ic} because the inner core has not enough time to be deformed, and $t_{\max} = \tau_{ic}$. For small radius, the limit will be defined by $\delta = 1$, which is here $-Ra(t) = M(t)$, about 28 km for typical values of the parameters.

For thermal stratification and time dependence as defined previously, the instantaneous deformation is

$$\dot{\epsilon}(t)\frac{\kappa}{r_{ic}(t)} = 0.2148\, M_0(-Ra_0)^{-1/3}\frac{\kappa}{r_{ic}^2(\tau_{ic})}\tau_{ic}t^{-1}, \tag{E11}$$

$$= \dot{\epsilon}_0\,\tau_{ic}\,t^{-1}, \tag{E12}$$

with $\dot{\epsilon}_0$ in s^{-1} and t in s.

$$\epsilon(r) = \begin{cases} \dot{\epsilon}_0\tau_{ic}\,2\,\ln\frac{r-\delta}{r}, & \text{for } r < r_{ic}(\tau_{ic}) - \delta, \\ \dot{\epsilon}_0\tau_{ic}\,2\,\ln\frac{r_{ic}(\tau_{ic})}{r}, & \text{for } r > r_{ic}(\tau_{ic}) - \delta, \end{cases} \tag{E13}$$

The strain rate is assumed to be constant over the layer δ whereas we could have used numerical results of the simulations to have the exact repartition and profile of strain over radius and time. But because the von Mises strain rate profile over radius is close to a rectangular function, it is easier to work with an analytic solution such as the one discussed here. It implies a linear increase of the absolute value of the strain, which is unlikely. This will in general overestimate the total strain.

Comparison between the strain computed from (E13) and the simplest solution u/Pe discussed in the text is plotted on Fig. E1. The solution u/Pe is a good approximation for radius larger than $0.3\,\tau_{ic}$, except in the uppermost layer, in which the deformation did not occur completely yet. It is interesting to notice that this magnetic forcing is expected to be several orders of magnitude more efficient when the inner core was younger.

E3 Large *Pe*—Compositional stratification

For compositional stratification,

$$\delta = \left(\frac{Pe}{-Ra_0}\right)^{1/5} r_{ic}(\tau_{ic})\left(\frac{t}{\tau_{ic}}\right)^{-1/5}. \tag{E14}$$

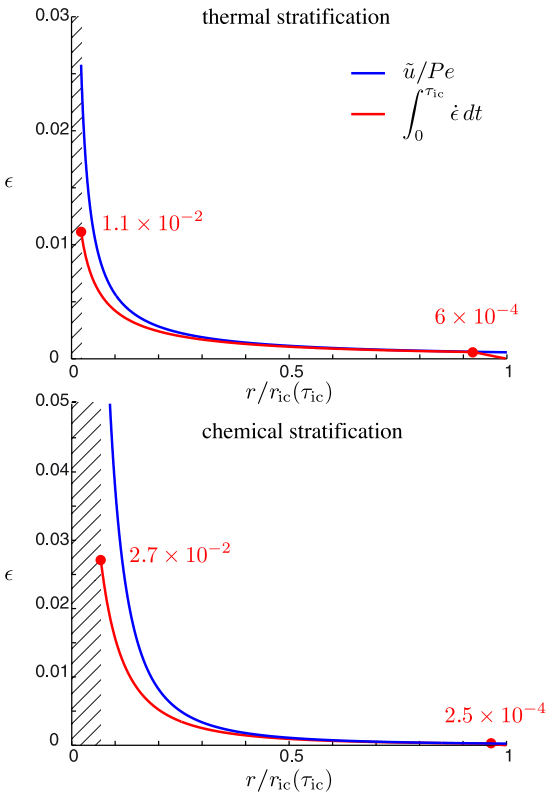

Figure E1. Strain as a function of the radius of the inner core for thermal stratification (a) and compositional stratification (b). Integration from eq. (E4) is the red line (analytical solution for thermal stratification and numerical solution for compositional stratification), and the blue lines stand for the estimation u/Pe, which is valid for $r > 0.5\,r_{ic}$. The minimum radius is computed for $Ra/M = 1$, limit under which the strong stratification approximation is no longer valid.

No exact solution for inverting $r_{ic}(\tau_{ic})(t_{\max}/\tau_{ic})^{1/2} - \delta(\tau_{ic})(t/\tau_{ic})^{-1/5} = r$ can be found. Fig. E1(b) shows the strain rate according to numerical integration and the approximation u/Pe. u/Pe is a good approximation for $r > 0.3\,r_{ic}$.